Masami Sakamoto
Hidehiro Uekusa *Editors*

Advances in Organic Crystal Chemistry

Comprehensive Reviews 2020

Springer

Advances in Organic Crystal Chemistry

Masami Sakamoto · Hidehiro Uekusa
Editors

Advances in Organic Crystal Chemistry

Comprehensive Reviews 2020

Springer

Editors
Masami Sakamoto
Chiba University
Chiba, Japan

Hidehiro Uekusa
Tokyo Institute of Technology
Tokyo, Japan

ISBN 978-981-15-5084-3 ISBN 978-981-15-5085-0 (eBook)
https://doi.org/10.1007/978-981-15-5085-0

This Springer imprint is published by the registered company Springer Nature Singapore Pte Ltd.
The registered company address is: 152 Beach Road, #21-01/04 Gateway East, Singapore 189721, Singapore

Preface

The first volume of this book on the topic of organic crystal chemistry was published in 2015. About 5 years later, this academic area has evolved and diversified significantly in response to the rapid development of various analytical and measurement techniques for organic solid materials. The second volume systematically summarizes and records recent remarkable advances in organic crystal chemistry in a broad sense, including organic–inorganic hybrid materials, liquid crystals, etc., focusing on the topics of organic crystal chemistry achieved during this period. The 25 papers contributed to this volume are broadly classified into five categories, (1) nucleation and crystal growth, (2) structure and design of crystals, (3) function, (4) chirality, and (5) solid-state reaction.

The chapters included herein are by invited members of the Organic Crystal Division of the Chemical Society of Japan (CSJ) and by prominent invited authors from abroad. The Organic Crystal Division of the Chemical Society of Japan (CSJ), founded in 1997, is comprised of the core researchers of organic crystal chemistry in Japan. The division holds a biannual domestic conference (a symposium on organic crystal chemistry in autumn and the Annual Spring Meeting of CSJ in late March) and publishes the *Organic Crystal Division Newsletter* twice a year.

In this exclusive volume on the organic crystal chemistry, leading scientists in the field vividly depict the most recent achievements in this interdisciplinary field of crystal chemistry, which can be applied to a wide variety of science and technology. The chapters herein are up-to-date, comprehensive, and authoritative. We, editors, would like to express our sincerest gratitude to all authors for their great contributions to *Advances in Organic Crystal Chemistry: Comprehensive Review 2020* and we hope that this book is a valuable resource for an advanced course in chemistry, biochemistry, industrial chemistry, and pharmacology.

Chiba, Japan — Masami Sakamoto
Tokyo, Japan — Hidehiro Uekusa

Contents

Part I
Nucleation and Crystal Growth

Chapter 1
X-Ray Birefringence Imaging (XBI): A New Technique for Spatially Resolved Mapping of Molecular Orientations in Materials

Kenneth D. M. Harris, Rhian Patterson, Yating Zhou, and Stephen P. Collins

Abstract The X-ray birefringence imaging (XBI) technique, first reported in 2014, is a sensitive method for spatially resolved mapping of the local orientational properties of anisotropic materials. In the case of organic materials, the technique may be applied to study the orientational properties of individual molecules and/or bonds, including the study of changes in molecular orientations associated with order–disorder phase transitions and characterization of phase transitions in liquid crystalline materials. This chapter presents a basic introduction to the XBI technique, giving a qualitative description of the fundamentals of the technique and discussing experimental aspects of the measurement of XBI data. Several examples are presented to highlight the application of the technique to study the orientational properties of molecules in organic materials.

Keywords X-ray birefringence imaging · Molecular orientations · Solid inclusion compounds · Liquid crystals · Anisotropic materials

1.1 Introduction

The polarizing optical microscope, invented in the nineteenth century, continues to be used extensively to investigate the structural anisotropy of materials across a wide range of scientific disciplines, including mineralogy, crystallography, materials sciences, and biological sciences. The polarizing optical microscope is based on the phenomenon of optical birefringence [1–3]—i.e., for linearly polarized light propagating through an anisotropic material, the refractive index depends on the orientation of the material with respect to the direction of polarization of the incident light.

K. D. M. Harris (✉) · R. Patterson · Y. Zhou
School of Chemistry, Cardiff University, Park Place, Cardiff CF10 3AT, Wales, UK
e-mail: HarrisKDM@cardiff.ac.uk

R. Patterson · S. P. Collins
Diamond Light Source, Harwell Science and Innovation Campus, Didcot, Oxfordshire OX11 0DE, England, UK

M. Sakamoto and H. Uekusa (eds.), *Advances in Organic Crystal Chemistry*,
https://doi.org/10.1007/978-981-15-5085-0_1

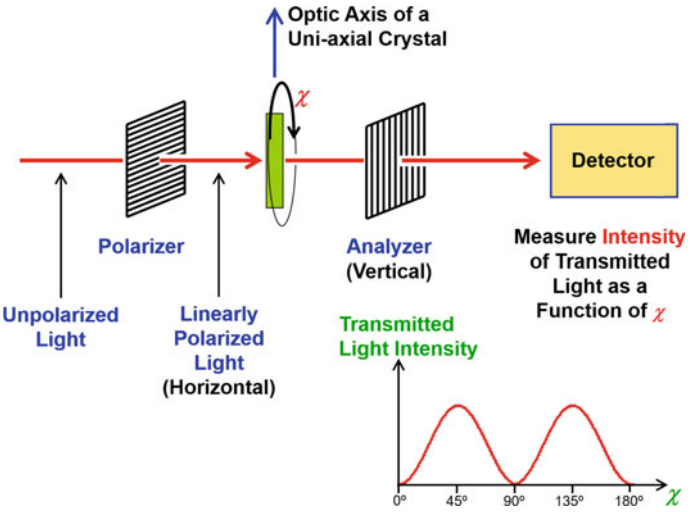

Fig. 1.1 Schematic of the polarizing optical microscope in the "crossed-polarizer" configuration, in which the angle between the orientations of the polarizer and analyzer is 90°. Here, the propagation direction of the incident light is shown as horizontal (clearly, the polarizing optical microscope is usually configured with the light propagating vertically and with the sample stage horizontal). The schematic at the bottom right depicts the sinusoidal variation in the intensity of light transmitted to the detector as a function of the orientation of a uni-axial crystal, which is specified by the angle χ (with $\chi = 0°$ defined as the orientation of the crystal at which the optic axis is parallel to the direction of linear polarization of the incident light)

When an anisotropic material is viewed in a polarizing optical microscope using the standard "crossed-polarizer" configuration (Fig. 1.1), the intensity of light recorded at the detector depends on the orientation of the optic axis (for uni-axial materials, such as high-symmetry crystals) or optic axes (for bi-axial materials, such as triclinic, monoclinic or orthorhombic crystals) of the material relative to the direction of linear polarization of the incident light. For a uni-axial crystal in which the optic axis is perpendicular to the direction of propagation of the incident linearly polarized light, the measured intensity is zero if the optic axis is parallel or perpendicular to the direction of linear polarization of the incident light, and reaches a maximum when the angle between the optic axis and direction of linear polarization of the incident light is 45°. If the material is rotated around the direction of propagation of the incident light (i.e., variation of the angle χ in Fig. 1.1), the measured intensity (I) varies in a sinusoidal manner (see Fig. 1.1) as a function of χ, with $I(\chi) = I_o \sin^2(2\chi)$, where I_o denotes the maximum intensity (observed at $\chi = 45°$). By measuring the intensity of transmitted light for different orientations of the material, the orientation of the optic axis of the material can be established. Furthermore, if the material comprises orientationally distinct domains, the spatial distribution and orientational relationships between the domains may be revealed.

While optical birefringence is widely exploited through the application of the polarizing optical microscope across many different scientific fields, the opportunity

to study birefringence of anisotropic materials using linearly polarized X-rays [4–12] has remained remarkably neglected, despite the fact that linearly polarized X-rays, tunable to any desired X-ray energy, have been readily accessible for the last 50 years or so with the availability of synchrotron radiation facilities. Indeed, the first definitive demonstration of X-ray birefringence was reported only recently [8], as discussed in more detail below.

In recent years, our research group has been exploring the phenomenon of X-ray birefringence (and the related phenomenon of X-ray dichroism), which led to the development of an imaging technique—called *X-ray birefringence imaging* (XBI)—that allows X-ray birefringence of materials to be studied in a spatially resolved manner. In many respects, the XBI technique represents the X-ray analogue of the polarizing optical microscope.

This chapter presents a basic introduction to the XBI technique, giving a qualitative description of the fundamentals of the technique and presenting several examples to demonstrate the utility of the technique to yield information on the orientational properties of anisotropic materials. Several applications of the technique to study organic materials are described, including characterization of changes in molecular orientational ordering associated with solid-state phase transitions, characterization of liquid crystal phases, and studies of materials in which the molecules undergo anisotropic molecular dynamics.

1.2 Background to X-Ray Birefringence Imaging

The phenomenon of X-ray birefringence is closely related to the much more widely studied phenomenon of X-ray dichroism [13–17], both of which concern the interaction of linearly polarized X-rays with anisotropic materials. In particular, X-ray dichroism relates to the way in which X-ray absorption depends on the orientation of a material relative to the direction of polarization of a linearly polarized incident X-ray beam, whereas X-ray birefringence relates to the way in which the real part of the complex refractive index (and hence the speed of wave propagation) depends on the orientation of a material relative to the direction of polarization of a linearly polarized incident X-ray beam. Although X-ray dichroism and X-ray birefringence give rise to different effects on the propagation of linearly polarized X-rays through a material, they are related by a Kramers–Kronig transform [18] and the two phenomena depend on the same structural and symmetry properties of the material.

While X-ray birefringence (as studied using XBI) and optical birefringence (as studied using the polarizing optical microscope) share several common characteristics, they also differ in some fundamentally important aspects. Thus, optical birefringence depends on the anisotropy of the material as a whole (e.g., in the case of a crystal, it depends on the symmetry of the crystal structure), whereas X-ray birefringence, when studied using an X-ray energy close to the absorption edge of a specific type of atom in the material, depends on the *local* anisotropy in the vicinity of the selected type of atom. As X-ray birefringence depends on the orientational

properties of the bonding environment of the X-ray absorbing atom, measurement of X-ray birefringence has the potential to yield information on the orientational properties of individual molecules and/or bonds within an anisotropic material.

X-ray birefringence is significant only when the energy of the incident linearly polarized X-ray beam is close to an X-ray absorption edge of an element in the material. As such, the technique is sensitive to the orientational properties of the local bonding environment of the X-ray absorbing element. Our early applications of the XBI technique focused on materials containing brominated organic molecules, using incident linearly polarized X-rays with energy tuned to the Br K-edge. In this case, it was shown [8] that X-ray birefringence depends specifically on the orientations of C–Br bonds in the material. The strong dependence on the orientation of the C–Br bonds arises because the incident X-ray beam, with energy corresponding to the Br K-edge, can promote a core (1s) electron on the Br atom to the σ* anti-bonding orbital associated with the C–Br bond. Given the directional characteristics of the vacant σ* anti-bonding orbital, the probability of occurrence of this process depends strongly on the orientational relationship between the C–Br bond and the direction of linear polarization of the incident X-ray beam. We note that the phenomenon of X-ray birefringence is "parity even", and thus anti-parallel C–Br bond directions (i.e., C–Br and Br–C) within a material exhibit identical behavior (consequently, X-ray birefringence is observed for centrosymmetric materials).

The capability of X-ray birefringence measurements to yield insights into molecular orientational properties was first demonstrated from studies of a model material with known bond orientations [8], and this capability was then exploited to determine *changes* in molecular orientational distributions associated with an order–disorder phase transition in the solid state [9]. However, these early X-ray birefringence studies used a narrowly focused incident X-ray beam and did not provide spatially resolved mapping of X-ray birefringence across the material. Subsequently, an experimental setup (Fig. 1.2) was proposed [19] to allow X-ray birefringence data to be recorded in "imaging mode", using a large-area linearly polarized incident X-ray beam and recording the X-ray intensity in a spatially resolved manner using an area detector. With this experimental setup, X-rays transmitted through different parts of the sample impinge on different pixels of the detector, allowing the X-ray birefringence of the sample to be mapped in a spatially resolved manner. This development represented the first report [19] of the X-ray birefringence imaging (XBI) technique.

While early XBI experiments focused on studies of brominated materials using linearly polarized X-rays tuned to the Br K-edge, the application of XBI has also been extended to study other X-ray absorption edges, allowing the local bonding environment of other types of element in materials to be probed. However, in the overview presented in this chapter, we focus on XBI studies at the Br K-edge, presenting examples of the application of the technique to determine the orientational properties of C–Br bonds in a range of organic materials.

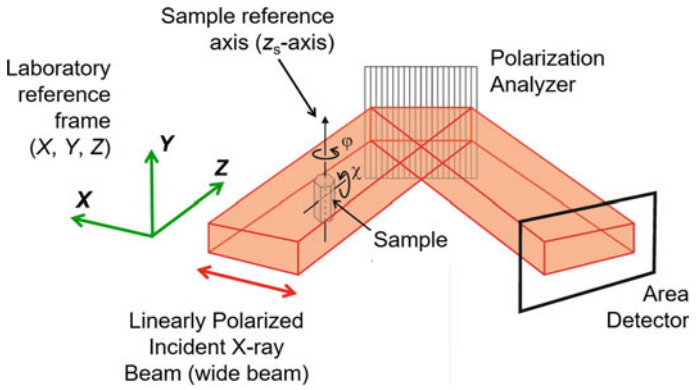

Fig. 1.2 Schematic of the experimental setup for XBI, which uses linearly polarized X-rays (horizontal) from a synchrotron radiation source as the incident radiation. The wide-area incident X-ray beam propagates along the *Z*-axis and is linearly polarized along the *X*-axis. The polarization analyzer is set up to give X-ray diffraction in the horizontal plane at a diffraction angle as close as possible to $2\theta = 90°$, thus selecting the vertical component of linear polarization in the X-ray beam transmitted through the sample. The X-ray beam diffracted at the analyzer is directed towards a two-dimensional X-ray detector

1.3 Experimental Aspects of the XBI Technique

We focus on four aspects of the experimental setup for XBI measurements: (a) the incident X-ray beam, (b) the sample, (c) the polarization analyzer, and (d) the detector. We now discuss each of these components of the experimental assembly in turn. A more detailed discussion of the X-ray optics associated with the XBI experiment has been reported previously [20].

1.3.1 The Incident X-Ray Beam

There are two critical requirements of the incident X-ray beam: (i) it must be linearly polarized, and (ii) it must be tuned to the energy of an X-ray absorption edge of a selected element in the material under investigation.

Synchrotron radiation has a high degree of linear polarization in the plane of the electron orbit (i.e., horizontal). However, as discussed in detail elsewhere [20], the requirement to select a single wavelength from the "white" synchrotron radiation source using a double-crystal monochromator can affect the polarization state of the resultant monochromatic X-ray beam. Nevertheless, for a carefully configured synchrotron beamline (ensuring, for example, that there is no significant component of circular polarization in the incident beam), it is valid to assume, within the context of interpreting XBI results, that the incident X-ray beam has a high degree of linear polarization in the horizontal direction.

As shown in Fig. 1.2, the definition of the laboratory reference frame (X, Y, Z) in the experimental XBI setup is based on the incident X-ray beam; specifically, the direction of propagation of the incident beam is parallel to the Z-axis and the direction of linear polarization of the incident beam is parallel to the X-axis (thus, the XZ-plane is horizontal). For XBI measurements, a wide-area incident beam is used (by appropriate selection of slits on the synchrotron beamline). To date, all our XBI experiments have been carried out on beamline B16 at Diamond Light Source (the UK synchrotron radiation facility), with a beam area that is typically ca. 4 mm horizontally and ca. 1 mm vertically.

Clearly, the range of X-ray energies that can be accessed depends on the characteristics of the beamline used for the XBI experiments. On beamline B16 at Diamond Light Source, X-ray energies corresponding to the K-edges of elements from Cr to Ag in the Periodic Table are readily accessed, including the Br K-edge which was used in recording all the XBI data discussed in this chapter.

After selecting the absorption edge of a particular element in the material of interest, the optimal X-ray energy for the XBI experiment is established by initially measuring X-ray dichroism data for the material, and then using the dichroism data to determine the specific X-ray energy that corresponds to maximum birefringence, following the procedure described previously [8].

1.3.2 The Sample

As X-ray birefringence is sensitive to *local* molecular orientational properties, there is no requirement that the sample under investigation must be crystalline. Thus, in principle, the XBI technique may be applied to probe the distribution of molecular orientations in any anisotropic material, provided it contains a suitable X-ray absorbing element.

The sample is mounted on a goniometer, allowing the orientation of the sample to be changed relative to the direction of propagation (Z-axis) and direction of linear polarization (X-axis) of the incident X-ray beam. First of all, a reference axis for the sample is defined, typically corresponding to: (i) a known crystallographic axis, (ii) a well-defined feature of the sample morphology (e.g., the long axis of a needle-like crystal), or (iii) a well-defined feature of the experimental setup (e.g., the magnetic field in the setup to study liquid-crystal samples discussed in Sect. 1.4.3). It is convenient to define an orthogonal axis system (x_s, y_s, z_s) for the sample, with the z_s-axis taken as the reference axis. The reference axis is maintained in the laboratory XY-plane (i.e., the vertical plane perpendicular to the direction of propagation of the incident X-ray beam) throughout the XBI experiment (Fig. 1.2), and there are two ways in which the orientation of the sample is changed relative to the fixed laboratory reference frame (X, Y, Z), called χ-rotation and ϕ-rotation.

Rotation of the sample around the laboratory Z-axis is called χ-rotation, with the sample rotated in a plane perpendicular to the direction of propagation of the incident

X-ray beam. This rotation changes the orientation of the sample reference axis (z_s-axis) relative to the direction of linear polarization (X-axis) of the incident X-ray beam. Clearly, χ-rotation is analogous to the sample rotation commonly carried out in the polarizing optical microscope (Fig. 1.1). Normally, $\chi = 0°$ is defined as the orientation in which the sample reference axis is horizontal (i.e., with the z_s-axis parallel to the X-axis).

Rotation of the sample *around* the reference axis is called ϕ-rotation. Clearly, ϕ-rotation does not change the orientation of the reference z_s-axis relative to the direction of linear polarization (X-axis) of the incident X-ray beam, but it does change the orientation of the material ($x_s y_s$-plane) relative to the direction of linear polarization of the incident X-ray beam.

In XBI studies, it is common to carry out a complete two-dimensional mapping by recording XBI images as a function of both χ and ϕ. Due to practical limitations in moving the goniometer, the range of values of χ and ϕ that can be accessed is typically about 180° in each case.

1.3.3 The Polarization Analyzer

The role of the polarization analyzer in the XBI experiment (analogous to the function of the analyzer in the polarizing optical microscope shown schematically in Fig. 1.1) is to select the vertical component of linear polarization of the X-ray beam transmitted through the sample. However, unlike the transmission-based polarization analyzer (e.g., a polaroid sheet) used in the polarizing optical microscope, the experimental setup for XBI uses a diffraction-based polarization analyzer. The polarization analyzer is a large single crystal (typically silicon or germanium) positioned and oriented such that the X-ray beam transmitted through the sample is diffracted at the analyzer, with the diffracted beam directed towards the detector. Ideally, the angle of diffraction at the analyzer (in the setup shown in Fig. 1.2) should be exactly $2\theta = 90°$ so that the X-ray beam diffracted from the analyzer comprises only the vertical component of linear polarization. However, as the X-ray wavelength used in the XBI experiment is dictated by selecting a suitable X-ray absorption edge for an element in the material, and as only a relatively restricted set of analyzer crystals are available, it is unlikely that the XBI experiment can be set up such that the diffraction angle at the analyzer is exactly $2\theta = 90°$. Nevertheless, once the wavelength is selected according to the X-ray absorption edge of interest, the analyzer crystal is chosen as the one that gives a diffraction angle as close as possible to $2\theta = 90°$. In practice, provided the diffraction angle is within a few degrees of 90°, the analyzer operates effectively (although not perfectly), selecting predominantly the vertical component of the X-ray beam transmitted through the sample. For XBI experiments in which the X-ray energy corresponds to the Br K-edge ($E \approx 13.474$ keV), suitable analyzer crystals are Si(111) and Ge(111), which gives diffraction angles for the (555) reflection of $2\theta = 94.4°$ and $2\theta = 89.5°$, respectively.

1.3.4 The Detector

The experimental setup for XBI measurements requires a two-dimensional X-ray detector (typically a charge-coupled device detector or a hybrid pixel detector) to allow the X-ray intensity diffracted by the analyzer to be measured in a spatially resolved manner. The resolution of the measured XBI images depends primarily on the resolution of the two-dimensional X-ray detector and is typically of the order of 10 μm (for the charge-coupled device detector currently used in the XBI setup on beamline B16, the pixel size is 6.4 μm, and the image dimensions are 1392 × 1040 pixels). However, the resolution of the XBI images in the horizontal direction also depends on the penetration depth of the X-rays at the polarization analyzer. Ideally, diffraction at the analyzer should occur only close to the surface; however, if the penetration depth at the analyzer is significant, the horizontal resolution of the XBI images is degraded. Minimizing the penetration depth, for example using an analyzer containing heavier elements, is clearly advantageous in terms of optimizing resolution.

1.4 Examples of Applications of the XBI Technique

1.4.1 XBI Study of a Model Material with All C–Br Bonds Parallel

The first XBI experiment [19] studied a thiourea inclusion compound containing 1-bromoadamantane (1-BrA) guest molecules, selected as a model material in which all C–Br bonds are known to be parallel (Fig. 1.3a). This material allowed a test of the hypothesis that X-ray birefringence at the Br K-edge depends specifically on the orientations of the C–Br bonds within the material. In the 1-BrA/thiourea inclusion compound [16], the thiourea molecules are arranged in a tunnel "host" structure, within which the 1-BrA "guest" molecules are located. It is established from X-ray diffraction that the C–Br bonds of all 1-BrA guest molecules in this material are oriented parallel to each other along the tunnel axis of the host structure (Fig. 1.3a).

XBI data for a single crystal of 1-BrA/thiourea, recorded as a function of χ, are shown in Fig. 1.4. The sample reference axis (z_s-axis) is the long axis of the crystal morphology, which is parallel to the thiourea host tunnel (c-axis) and hence parallel to the C–Br bonds in the material. Each image in Fig. 1.4 shows a spatially resolved map of X-ray intensity for a specific orientation of the crystal. Clearly, the X-ray intensity varies significantly as a function of χ, with maximum intensity at $\chi \approx 45°$; in this orientation, the C–Br bonds are oriented at ca. 45° with respect to the direction of linear polarization of the incident X-ray beam. Minimum intensity occurs at $\chi \approx 0°$ and $\chi \approx 90°$, when the C–Br bonds are either parallel ($\chi = 0°$) or perpendicular ($\chi = 90°$) to the direction of linear polarization of the incident X-ray beam. The observed dependence of intensity on χ [i.e., $I(\chi) = I_o \sin^2(2\chi)$] is directly analogous to the

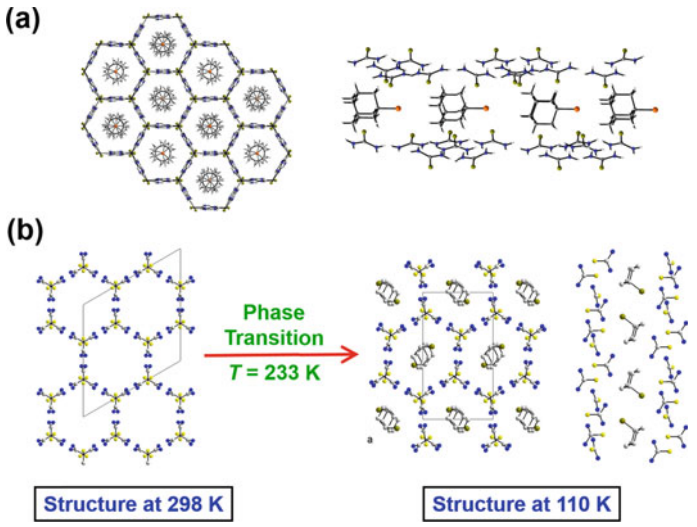

Fig. 1.3 **a** Crystal structure of the 1-BrA/thiourea inclusion compound viewed parallel (left) and perpendicular (right) to the tunnel axis of the thiourea host structure; the C–Br bonds of all 1-BrA guest molecules are parallel to the tunnel axis (*c*-axis), which is also parallel to the long-needle axis of the crystal morphology. **b** Structural changes associated with the phase transition in the BrCH/thiourea inclusion compound (with H atoms omitted for clarity). Left: rhombohedral high-temperature (HT) phase viewed along the tunnel axis of the thiourea host structure (the isotropically disordered BrCH guests are not shown). Middle and right: monoclinic low-temperature (LT) phase viewed along the host tunnels (middle) and perpendicular to the tunnel (right); the C–Br bonds of all BrCH guests form an angle $\psi \approx 52.5°$ with respect to the tunnel axis (vertical in right-hand figure)

behavior of a uni-axial crystal in the polarizing optical microscope. We note that, for each XBI image shown in Fig. 1.4, the crystal exhibits essentially uniform brightness (i.e., the X-ray intensity is the same for all regions of the crystal in the XBI image), indicating that all regions of the crystal have the same orientation of the C–Br bonds.

XBI data recorded for 1-BrA/thiourea as a function of ϕ (with χ fixed) show no significant change in X-ray intensity as a function of ϕ. As variation of ϕ corresponds to rotation of the crystal around the tunnel axis (and hence rotation around the C–Br bond direction), the orientations of the C–Br bonds are not altered by this rotation and the measured X-ray intensity is therefore essentially independent of ϕ.

These XBI measurements [19] on the model material 1-BrA/thiourea (together with earlier X-ray birefringence studies [8] carried out in a non-imaging mode) were crucial for proving that the phenomenon of X-ray birefringence at the Br K-edge depends specifically on the orientational properties of the C–Br bonds in the material of interest.

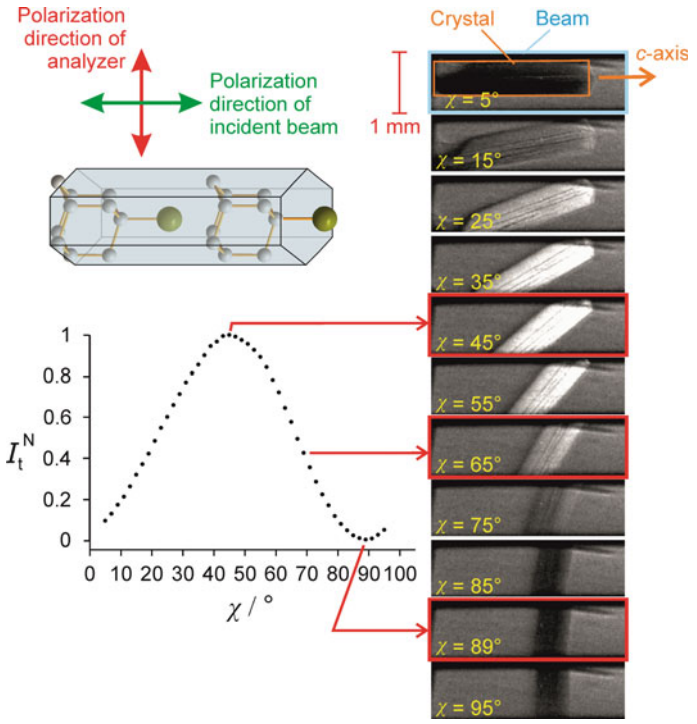

Fig. 1.4 XBI images recorded at 280 K for a single crystal of 1-BrA/thiourea as a function of χ (with ϕ fixed). The images represent spatially resolved maps of X-ray intensity across the crystal. Relative brightness in the images scales with X-ray intensity. The variation of normalized intensity (I_t^N) as a function of χ is shown at the left side, using data from all images recorded in the experiment (with χ varied in steps of 2°). To construct this plot, the X-ray intensity was measured by integrating a region of the image with dimensions 62.5 μm × 192 μm at the center of the crystal, and was normalized to give a value in the range $0 \leq I_t^N \leq 1$

1.4.2 XBI Study of Changes in Molecular Orientation at a Solid-State Phase Transition

As the XBI study of 1-BrA/thiourea proved that the technique is a sensitive probe of molecular orientations in materials, the next application [19] was to explore the use of XBI to characterize changes in molecular orientations as a function of temperature, in particular for a material that undergoes an order–disorder phase transition. To explore this behavior, XBI experiments were carried out on a single crystal of the thiourea inclusion compound containing bromocyclohexane (BrCH) guest molecules (Fig. 1.3b). This material undergoes a phase transition at $T = 233$ K from a high-temperature (HT) phase in which the orientational distribution of the BrCH guest molecules is essentially isotropic (as a result of rapid isotropic molecular motion) to a low-temperature (LT) phase in which the BrCH molecules become orientationally

ordered. In the LT phase, the C–Br bonds of all BrCH molecules are oriented at $\psi \approx 52.5°$ with respect to the tunnel axis of the thiourea host structure (Fig. 1.3b).

XBI images recorded for a single crystal of BrCH/thiourea in the HT phase (298 K; Fig. 1.5a) show essentially zero X-ray intensity for all regions of the crystal, with no variation in intensity as a function of crystal orientation (with variation of both χ and ϕ), confirming that the orientational distribution of the C–Br bonds of the BrCH guest molecules is isotropic in the HT phase. These XBI results for BrCH/thiourea in the HT phase (Fig. 1.5a) provide a clear illustration of the differences between XBI and polarizing optical microscopy; specifically, under the same conditions, a single crystal of BrCH/thiourea exhibits uni-axial behavior in the polarizing optical microscope in crossed-polarizer configuration (see Fig. 1.5b), with minimum intensity arising when the optic axis is parallel to the polarizer or analyzer and maximum intensity arising when the optic axis is at 45° to these directions (for BrCH/thiourea, the optic axis is the *c*-axis of the rhombohedral thiourea host structure, parallel to the long-needle axis of the crystal morphology in Fig. 1.5b). As optical birefringence

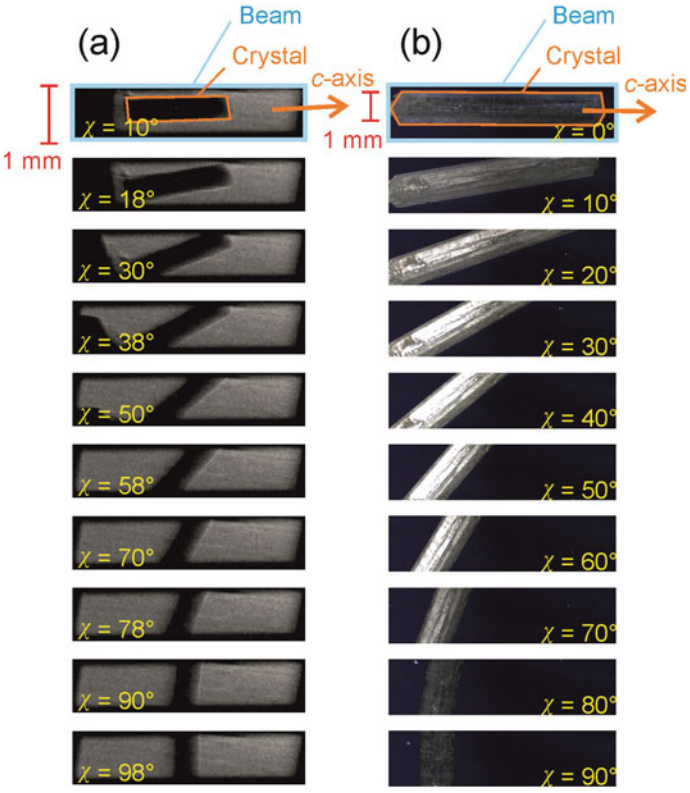

Fig. 1.5 Comparison of images from XBI and polarizing optical microscopy recorded as a function of χ for the same material (in each case, a single crystal of BrCH/thiourea in the HT phase): **a** XBI images (at 298 K), and **b** polarizing optical microscope images (at 293 K)

depends on the overall crystal symmetry, which is rhombohedral for BrCH/thiourea in the HT phase (for a rhombohedral host structure containing guest molecules undergoing isotropic molecular motion, the overall symmetry is rhombohedral), giving uni-axial behavior in optical birefringence (Fig. 1.5b). In contrast, X-ray birefringence at the Br K-edge depends *only* on the orientational properties of the C–Br bonds; as the BrCH guest molecules undergo isotropic reorientational motion in the HT phase, the orientational distribution of the C–Br bonds is isotropic, and no X-ray birefringence is observed (Fig. 1.5a).

For BrCH/thiourea in the LT phase, the XBI behavior [19] (see Fig. 1.6, which shows XBI data recorded at 20 K as a function of χ, with ϕ fixed at $\phi = 0°$) is significantly different from that in the HT phase. First, we consider the large central region of the crystal (i.e., the bright region in the top XBI image in Fig. 1.6); at $\phi = 0°$, the C–Br bonds in this region of the crystal are nearly perpendicular to the direction of propagation of the incident X-ray beam. The X-ray intensity for this region varies significantly as a function of χ, with intensity maxima and minima separated by $\Delta\chi \approx 45°$. In the LT phase, it is known from X-ray diffraction [21] that the C–Br bonds adopt a well-defined orientation within the crystal (see Fig. 1.3b), with an angle $\psi \approx 52.5°$ between the C–Br bond direction and the tunnel axis (c-axis) of the thiourea host structure. For the large central region of the crystal, the maximum intensity in the XBI images in Fig. 1.6 occurs at $\chi \approx 82°$, because for this orientation of the crystal, the angle between the C–Br bond direction and the direction of linear polarization of the incident X-ray beam is ca. 45° (see Fig. 1.6). Similarly, the minimum intensity arises at $\chi \approx 38°$, because for this orientation of the crystal, the angle between the C–Br bond direction and the direction of linear polarization of the incident X-ray beam is ca. 90°. Thus, the χ-dependence of the XBI data for BrCH/thiourea in the LT phase (for $\phi = 0°$) is analogous to the behavior of a uni-axial crystal in the polarizing optical microscope, with the direction of the C–Br bonds representing the "X-ray optic axis." More details of the geometric properties of the BrCH/thiourea inclusion compound in the LT phase that underpin this interpretation of the XBI data are given in the original paper [19].

Furthermore, it is clear from the XBI data in Fig. 1.6 that the crystal of BrCH/thiourea in the LT phase contains orientationally distinct domains, highlighted in Fig. 1.7 (which shows an expanded view of the XBI image recorded for $\chi = 10°$ and $\phi = 0°$ in Fig. 1.6). In Fig. 1.7, the large central region of the crystal comprises a large parallelogram-shaped domain (the bright region), with two smaller domains (dark regions) at each end of the crystal. These distinct domains contain the same crystal structure of the LT phase, but with different orientations relative to the laboratory reference frame. The domain boundaries between the major domain and the two minor domains are parallel to each other and intersect the c-axis at an angle of ca. 136°, allowing the domain boundary to be assigned as the crystallographic $(10\bar{1})$ plane. Further XBI images recorded as a function of temperature indicate that there is

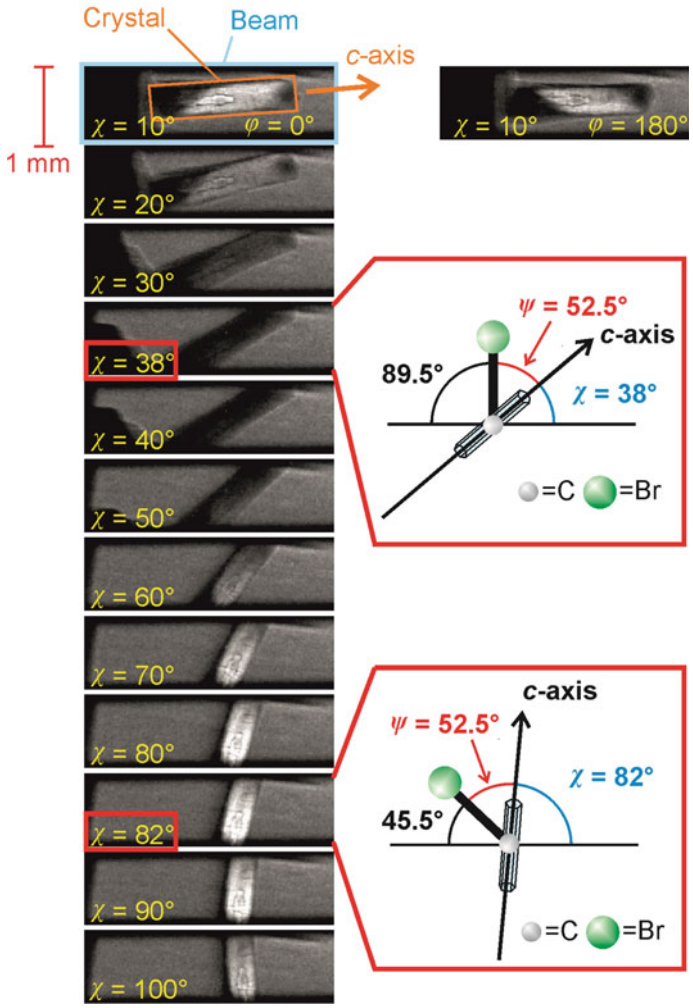

Fig. 1.6 XBI data recorded for a single crystal of BrCH/thiourea in the LT phase (at 20 K) as a function of χ (with ϕ fixed at $\phi = 0°$). Maximum brightness (for the large central domain of the crystal) arises when the C–Br bonds form an angle of 45° with respect to the direction of linear polarization (horizontal) of the incident X-ray beam, which is achieved for the crystal orientation $\chi \approx 82°$. Minimum brightness arises when the C–Br bonds form an angle of 90° with respect to the horizontal direction, which is achieved for the crystal orientation $\chi \approx 38°$

no change in the size and spatial distribution of the domain structure as temperature is varied within the LT phase.

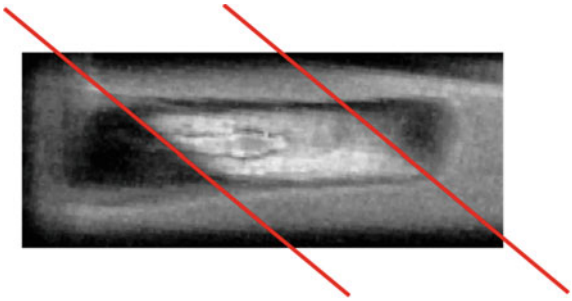

Fig. 1.7 XBI image of a single crystal of BrCH/thiourea in the LT phase (recorded at 20 K with $\chi = 10°$ and $\phi = 0°$), showing that the crystal comprises orientationally distinct domains (corresponding to regions with different levels of brightness). The domain boundaries (indicated by red lines) correspond to the $(10\bar{1})$ plane

1.4.3 XBI Study of Orientational Ordering in Liquid Crystalline Materials

We now describe the application of XBI to study molecular orientational ordering in a non-crystalline material [22], specifically a material that forms several different liquid crystalline phases. The experimental assembly designed specifically to measure XBI data for liquid crystals is shown in Fig. 1.8 and is based on molecular alignment of the liquid crystalline phases in an applied magnetic field. In this setup, the sample cell is mounted on the goniometer of the synchrotron beamline, allowing the orientation of the magnetic field to be changed relative to the direction of linear polarization

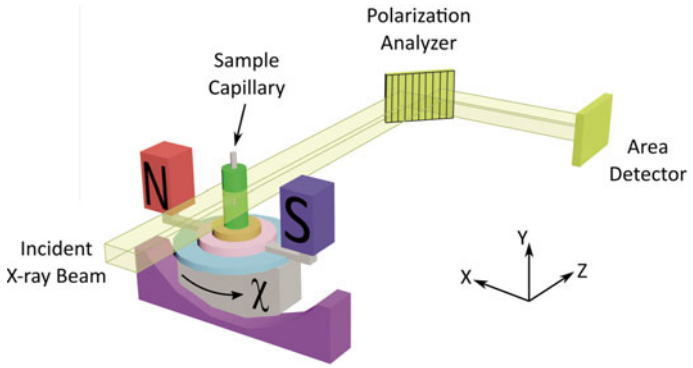

Fig. 1.8 Experimental setup for XBI studies of liquid crystal samples oriented in a magnetic field. The incident X-ray beam propagates along the *Z*-axis and is linearly polarized along the *X*-axis. In this setup, the sample reference axis (z_s-axis) is parallel to the magnetic field; thus, χ is defined as the angle between the magnetic field axis and the direction of linear polarization of the incident X-ray beam (*X*-axis; horizontal)

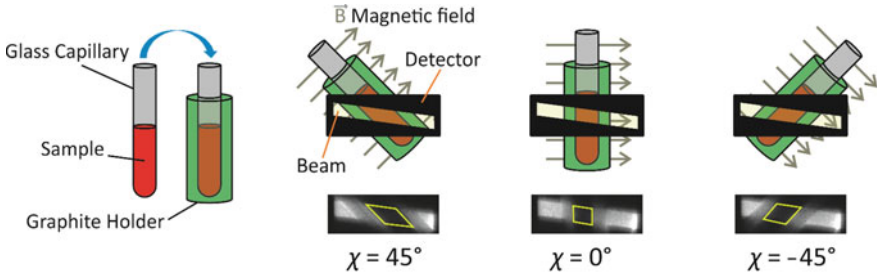

Fig. 1.9 Schematic of the sample assembly for XBI studies of liquid crystal samples. The sample is placed inside a glass capillary, which is inserted inside an outer sample holder made from graphite. The magnetic field is perpendicular to the long axis of the capillary and perpendicular to the direction of propagation of the incident X-ray beam. Here, χ is defined as the angle between the magnetic field axis and the direction of linear polarization of the incident X-ray beam (horizontal). The region of each XBI image corresponding to the sample is highlighted by the yellow box (in the images shown, the sample is an isotropic liquid phase)

(horizontal) of the incident X-ray beam. The sample cell is constructed with a Sm-Co magnet (field strength ca. 1.0 T) to align the liquid crystal phases and a variable temperature capability, controlled by passing an electric current through the graphite outer sample holder (Fig. 1.9), to which a thermocouple is attached for temperature measurement. In this setup, the sample reference axis (z_s-axis) is the direction of the applied magnetic field, so the angle χ (see Figs. 1.8 and 1.9) defines the orientation of the applied magnetic field (i.e., the expected axis of molecular alignment in the liquid crystal phases) relative to the direction of linear polarization of the incident X-ray beam (horizontal). With this experimental assembly, χ may be varied from 45° to –45°, but only very restricted variation of ϕ is possible (for this reason, no experiments involving variation of ϕ are discussed).

We focus on the results of XBI studies to investigate orientational ordering of 4'-octyloxy-[1,1'-biphenyl]-4-yl 4-bromobenzoate (Scheme 1.1; denoted OBBrB), which is known [23] to form liquid crystalline phases. The terminal C–Br bond in this molecule is ideally positioned to "report" on the molecular orientational ordering in the liquid crystal phases from analysis of XBI data recorded at the Br K-edge.

The crystalline phase of this compound melts on heating at 151 °C and exists as an isotropic liquid phase above ca. 216 ºC. On cooling from the isotropic liquid phase, the following sequence of phases occurs, determined from optical microscopy [23] (transition temperatures determined from DSC data [22] are in close agreement):

$$\text{Iso} \cdot 216\,^{\circ}\text{C} \cdot \text{N} \cdot 215\,^{\circ}\text{C} \cdot \text{SmA} \cdot 154\,^{\circ}\text{C} \cdot \text{SmB}$$

Scheme 1.1 Molecular structure of OBBrB

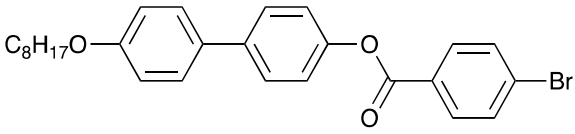

Here, we use the common abbreviations for the different liquid crystal phases: Iso (isotropic liquid), N (nematic), SmA (smectic A), and SmB (smectic B). On cooling the smectic B phase, a transition occurs to a crystalline phase, with the temperature of this transition depending on the experimental conditions as a consequence of supercooling.

The existence of the nematic phase (although over a narrow temperature range) offers the possibility for molecular alignment in the magnetic field on cooling, with the expectation that the terminal C–Br bond should be coincident with, or at least oriented very close to, the director (***n***). As the experimental setup (Figs. 1.8 and 1.9) allows the orientation of the magnetic field to be varied with respect to the direction of linear polarization of the incident X-ray beam, the experimental design gives the opportunity to establish good-quality orientational information from XBI data recorded using an X-ray energy close to the Br K-edge.

Selected XBI images recorded at 220 °C (isotropic liquid), 214 °C (nematic phase and isotropic liquid), and 184 °C (smectic A phase) are shown in Fig. 1.10. The magnetic field was maintained in the *XY*-plane, perpendicular to the direction of propagation (*Z*-axis) of the incident X-ray beam. The angle χ denotes rotation of the magnetic field around the *Z*-axis and thus specifies the direction of molecular alignment in the liquid crystal phases relative to the direction of linear polarization

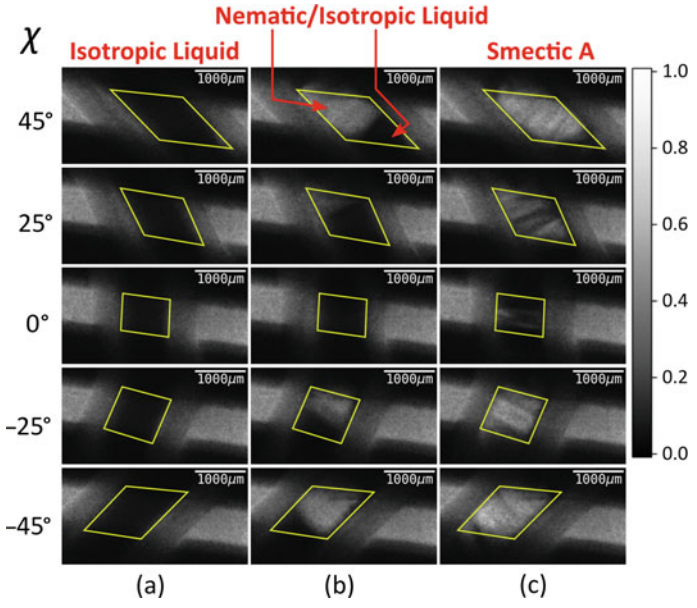

Fig. 1.10 XBI data recorded for OBBrB as a function of orientation of the magnetic field axis (defined by angle χ) at: **a** 220 °C (isotropic liquid phase), **b** 214 °C (both nematic and isotropic liquid phases are present), and **c** 184 °C (smectic A phase). The scale of normalized X-ray intensity is shown on the right-hand side. In each XBI image, the region representing the sample is highlighted by the yellow box

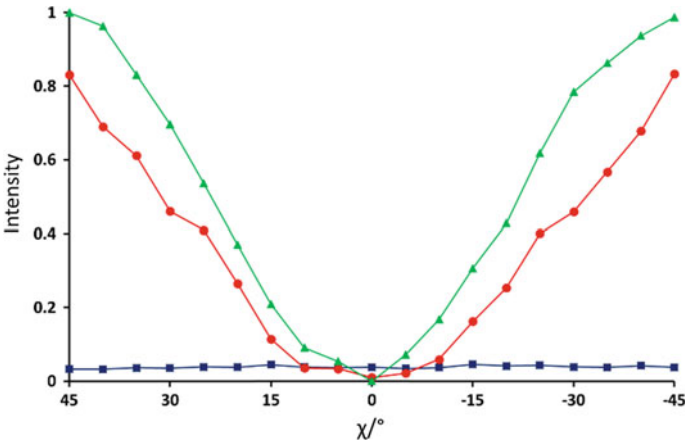

Fig. 1.11 Normalized X-ray intensity as a function of χ for the XBI data recorded for OBBrB at: 220 °C (blue; isotropic liquid); 214 °C (red; nematic), and 184 °C (green; smectic A). Selected XBI images from the same experiment are shown in Fig. 1.10. X-ray intensity (I_{meas}) was measured as the average intensity per pixel across a selected area of the sample region in the XBI image and normalized to give a value in the range $0 \leq I^N \leq 1$, with $I^N = (I_{meas} - I_{min})/(I_{max} - I_{min})$, where I_{max} and I_{min} are the highest and lowest measured intensities in the entire set of data (i.e., for all XBI images recorded at the three temperatures shown). At 214 °C, the sample comprises a region of nematic phase and a region of isotropic liquid (see Fig. 1.10b), and the intensity was measured within the region of the image known to represent the nematic phase

of the incident X-ray beam (*X*-axis). For $\chi = 0°$, the magnetic field is horizontal (parallel to the *X*-axis).

For the isotropic liquid, the XBI images (Fig. 1.10a) are uniformly dark for all sample orientations, with no variation in X-ray intensity as a function of sample orientation (Fig. 1.11). These observations are fully consistent with an isotropic distribution of C–Br bond orientations in this phase. Starting from the isotropic liquid, the sample was oriented at $\chi = 45°$ and cooled in small increments in the temperature region near the phase transition to the nematic phase, until the first change in X-ray intensity was observed in the XBI data. At 214 °C, the XBI image recorded at $\chi = 45°$ (top image in Fig. 1.10b) contains a bright region (upper left) and a dark region (bottom right), representing the first temperature on cooling at which there was evidence of the orientationally ordered nematic phase. From the changes in the XBI data as a function of χ (Fig. 1.10b), it is clear that the region identified as the nematic phase exhibits significant birefringence. In contrast, the other region remains dark in the XBI images at all values of χ and is assigned as the isotropic liquid. The co-existence of both nematic and isotropic liquid phases in the same XBI image is a consequence of a temperature gradient across the sample holder.

For the nematic phase, the X-ray intensity varies in an approximately sinusoidal manner as a function of χ (Fig. 1.11), as expected for a uni-axial system with the optic axis parallel to the magnetic field (giving an intensity minimum at $\chi = 0°$ and intensity maxima at $\chi = 45°$ and $\chi = -45°$). As the effective X-ray optic axis for

XBI at the Br K-edge depends on the *resultant* direction of the C–Br bonds, the XBI behavior for the nematic phase indicates a high degree of molecular orientational ordering, with a *resultant* C–Br bond orientation parallel to the magnetic field.

The XBI data for the smectic A phase (184 °C; Fig. 1.10c) also exhibit a sinusoidal variation in X-ray intensity as a function of χ (Fig. 1.11). Significantly, the maximum intensity (at $\chi = 45°$ and $\chi = -45°$) is higher for the smectic A phase than the nematic phase, indicating that the smectic A phase has a higher degree of ordering of the C–Br bond orientations (i.e., a narrower orientational distribution) in the direction of the magnetic field, as expected for a more ordered phase that has partial translational ordering.

The type of XBI experiment described above in which the orientation of the sample assembly is changed systematically by variation of χ at fixed temperature can be problematic in the case of liquid crystals, as the domain structure can change suddenly and unpredictably on changing the sample orientation due to the fluid nature of these phases under gravity. Under these circumstances, it can be difficult to extract reliable information on the characteristic dependence of X-ray intensity as a function of χ for the different liquid crystal phases.

A more reliable method to explore differences in the degree of ordering between different liquid crystal phases is to record the XBI images with the orientation of the magnetic field *fixed* at $\chi = 45°$ while scanning through the temperature range of interest. Results from this type of experiment are shown in Fig. 1.12, with the XBI data recorded on decreasing temperature from 218 °C (isotropic liquid) to 108 °C (crystalline phase) at a rate of 1 °C min^{-1}, with the XBI images recorded continuously on cooling (time per image, 5 s). At the highest temperature, the intensity is very low as a result of the isotropic distribution of molecular orientations in the isotropic liquid phase. On decreasing temperature, the intensity increases substantially between 216 and 205 °C, representing the transition from the isotropic liquid into orientationally ordered phases (from Iso → N → SmA). Figure 1.12 (top part) shows the evolution of the X-ray intensity measured from the XBI images as a function of temperature. Between 216 and 205 °C, the data show a "first-order" change in intensity at the clearing point as the nematic phase forms, after which there is a small inflection over the approximate temperature range 215–211 °C (corresponding to the intensity range from ca. 0.2 to 0.4). The fact that the sharp rise in intensity between 216 and 205 °C covers a significantly wider temperature range than the Iso → N → SmA events observed by DSC and optical microscopy may reflect a combination of the temperature gradient across the sample plus the kinetics of alignment in the presence of the magnetic field. As temperature decreases within the SmA phase, the intensity increases gradually until a visible transition to the SmB phase is observed from a further sharp (although relatively small) increase in intensity, followed by a significant decrease in intensity upon crystallization.

The orientational order in liquid crystal phases is usually quantified by the orientational order parameter, $S = \langle {}^1\!/_2(3\cos^2\theta - 1)\rangle$, where θ is the angle between the director and the individual long molecular axes. The value of S is often determined by measuring optical birefringence, and it is clear that the X-ray intensity measured in the XBI data is also related to the order parameter S. While our interpretations of

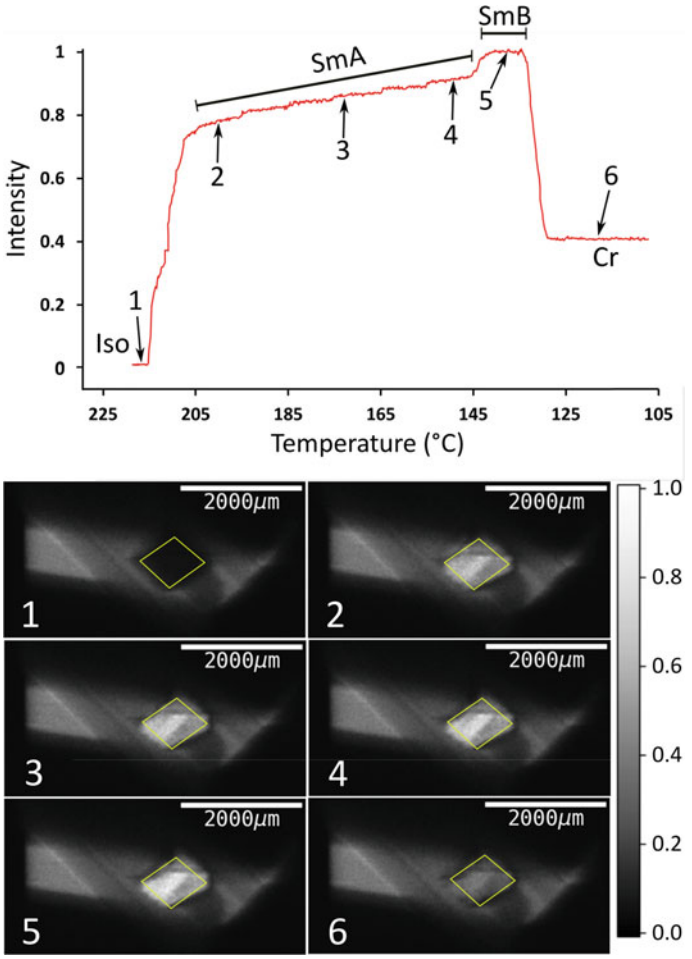

Fig. 1.12 Top: Normalized X-ray intensity in XBI images recorded for OBBrB on decreasing temperature from 218 to 108 °C at 1 °C min^{-1}, with the orientation of the magnetic field fixed at $\chi = 45°$. The phase transitions are associated with abrupt changes in intensity. Bottom: XBI images recorded at different stages of the cooling process (the specific temperature and measured intensity for each image, numbered from 1 to 6, is identified from the plot at the top). The region of each XBI image representing the sample is highlighted by the yellow box

changes in X-ray intensity as a function of temperature have invoked this relation at a qualitative level, our future research aims to derive a more quantitative framework for determining values of order parameters from XBI data.

1.4.4 XBI Study of Materials Undergoing Molecular Reorientational Dynamics

Finally, we consider the application of XBI in studies [24] of materials that undergo *anisotropic* molecular dynamics, focusing on the urea inclusion compounds containing 1,8-dibromooctane [1,8-DBrO; $Br(CH_2)_8Br$] and 1,10-dibromodecane [1,10-DBrD; $Br(CH_2)_{10}Br$] guest molecules. As discussed below, uni-axial reorientational motion of the guest molecules in these materials is well established from a range of experimental techniques.

Conventional urea inclusion compounds [25–27] contain a host tunnel structure [28, 29] constructed from a hexagonal hydrogen-bonded arrangement of urea molecules (Fig. 1.13a; tunnel diameter ca. 5.5–5.8 Å). The tunnels are filled with a dense packing of guest molecules, typically based on long *n*-alkane chains. Along the tunnel axis, the periodic repeat of the guest molecules is usually incommensurate with the periodic repeat of the urea host structure. These materials undergo a low-temperature phase transition, at which the symmetry of the urea host structure [30, 31] changes from hexagonal [high-temperature (HT) phase] to orthorhombic

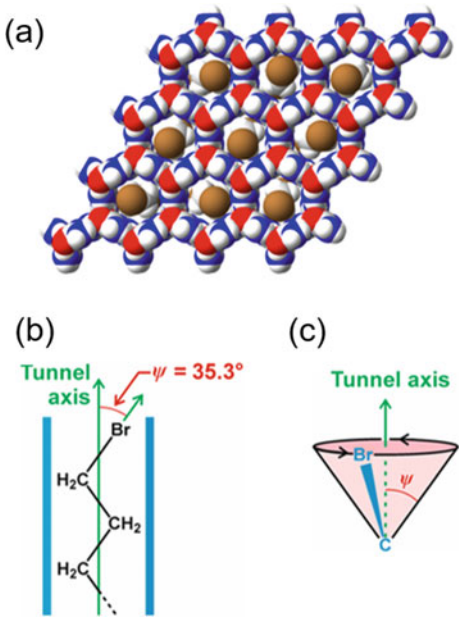

Fig. 1.13 **a** Crystal structure of an α,ω-dibromoalkane/urea inclusion compound viewed along the tunnel axis, showing the hexagonal urea host tunnels occupied by α,ω-dibromoalkane guest molecules. **b** For the guest molecule in the all-*trans* conformation in the host tunnel (vertical), the C–Br bond forms an angle $\psi \approx 35.3°$ with respect to the tunnel axis. **c** The orientational distribution of C–Br bonds resulting from rapid reorientation of the guest molecules about the tunnel axis in the HT phase is described by a cone with semi-angle $\psi \approx 35.3°$

[low-temperature (LT) phase]. The phase transition temperature for 1,8-DBrO/urea is 157 K and for 1,10-DBrD/urea is 140 K. Several techniques have been applied to study the dynamics of the guest molecules in α,ω-dibromoalkane/urea inclusion compounds. Incoherent quasielastic neutron scattering (IQNS) has shown [32] that, in the HT phase, the guest molecules undergo rapid reorientation about the tunnel axis ($\tau \approx 10^{-12} - 10^{-10}$ s; τ denotes the timescale of motion) and restricted translational diffusion along this axis. Solid-state ^{2}H NMR studies (both lineshape analysis and spin-lattice relaxation time measurements) of 1,10-DBrD/urea also indicate [30] that rapid reorientation ($\tau < 10^{-8}$ s) of the guest molecules occurs about the tunnel axis in the HT phase. Polarized Raman spectroscopy [33] has shown that the α,ω-dibromoalkane guest molecules adopt predominantly the all-*trans* conformation within the urea tunnel structure, with only a small proportion (ca. 7%) of *gauche* end-groups. For the predominant (ca. 93%) conformation with *trans* end-groups, the C–Br bonds form an angle $\psi \approx 35.3°$ with respect to the tunnel axis of the urea host structure (Fig. 1.13b).

XBI data were recorded at the Br K-edge for single crystals of 1,8-DBrO/urea and 1,10-DBrD/urea as a function of crystal orientation, specified by angles χ and ϕ. In these measurements, the sample reference axis (z_s-axis) is the long-needle axis of the crystal morphology, which corresponds to the tunnel axis (*c*-axis) of the urea host structure. This axis was maintained in the plane (*XY*-plane) perpendicular to the propagation direction (*Z*-axis) of the incident X-ray beam. Variation of χ refers to rotation of the z_s-axis (*c*-axis of the crystal) around the laboratory *Z*-axis and variation of ϕ refers to rotation of the crystal around the z_s-axis. For $\chi = 0°$, the z_s-axis is parallel to the direction of linear polarization of the incident X-ray beam (*X*-axis; horizontal).

Figure 1.14 shows XBI data recorded at the Br K-edge for single crystals (in the HT phase) of 1,8-DBrO/urea (at 280 K) and 1,10-DBrD/urea (at 170 K) as a function of χ. For both 1,8-DBrO/urea and 1,10-DBrD/urea, the X-ray intensity exhibits sinusoidal variation as a function of χ, with maximum brightness at $\chi \approx 45°$ and minimum brightness at $\chi \approx 0°$ and $\chi \approx 90°$. The X-ray intensity is uniform across the entire crystal, indicating that all regions of the crystal have the same orientational properties of the C–Br bonds.

XBI data recorded as a function of ϕ in the HT phase for single crystals of 1,8-DBrO/urea (at 280 K) and 1,10-DBrD/urea (at 170 K) are shown in Fig. 1.15 (for these measurements, χ was fixed at an orientation close to the maximum intensity in Fig. 1.14). No significant changes in X-ray intensity are observed as a function of ϕ, indicating that the orientational distribution of the C–Br bonds relative to the laboratory frame (*X*, *Y*, *Z*) is not altered by rotating the crystal around the *c*-axis (tunnel axis).

The observed XBI behavior indicates that, for these materials, the effective X-ray optic axis (i.e., the *resultant* C–Br bond orientation) is parallel to the tunnel axis of the urea host structure. For an α,ω-dibromoalkane guest molecule with *trans* end-group conformation inside the urea host tunnel, the C–Br bond forms an angle $\psi \approx 35.3°$ with respect to the tunnel axis (Fig. 1.13b). The fact that the resultant C–Br bond vector is parallel to the tunnel axis for 1,8-DBrO/urea and 1,10-DBrD/urea in the HT

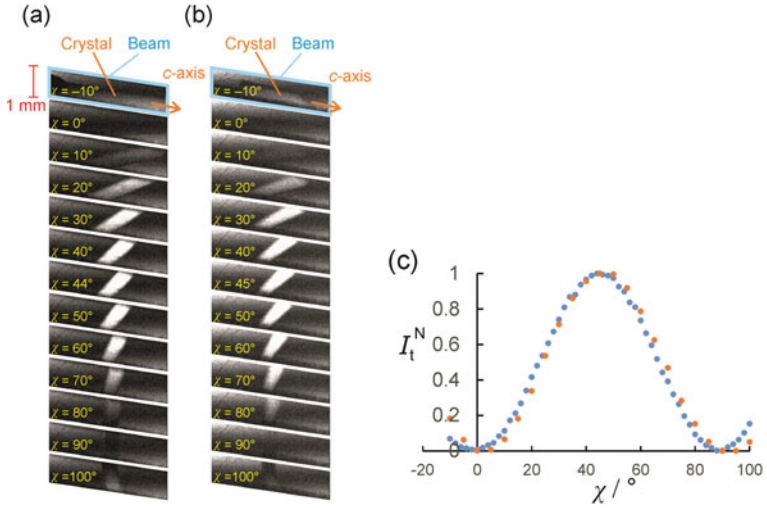

Fig. 1.14 XBI data recorded as a function of χ (with ϕ fixed) in the HT phase for single crystals of: **a** 1,8-DBrO/urea (at 280 K), and **b** 1,10-DBrD/urea (at 170 K). **c** Variation of normalized intensity (I_t^N) as a function of χ for 1,8-DBrO/urea (blue) and 1,10-DBrD/urea (orange). This plot was constructed using data from all images recorded in the experiment (with χ varied in steps of 2° for 1,8-DBrO/urea and steps of 5° for 1,10-DBrD/urea), including the images shown in (**a**) and (**b**). X-ray intensity was measured by integrating across a region of the image [195 μm (vertical) × 169 μm (horizontal)] at the center of the crystal and normalized to give a value in the range $0 \leq I_t^N \leq 1$. The horizontal shift of $\Delta\chi \approx 2°$ between the data for 1,8-DBrO/urea and 1,10-DBrD/urea in (**c**) is attributed to small errors in crystal alignment

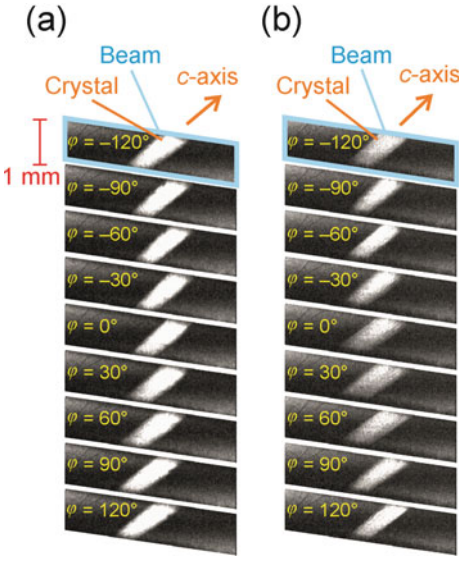

Fig. 1.15 XBI data recorded as a function of ϕ (with χ fixed) in the HT phase for single crystals of: **a** 1,8-DBrO/urea (at 280 K), and **b** 1,10-DBrD/urea (at 170 K)

phase is a consequence of reorientational dynamics of the guest molecules around the tunnel axis, leading to a *time-averaged* projection of the C–Br bond vector along this axis. For this motion, the actual orientational distribution of each C–Br bond is described by a cone with semi-angle ca. 35.3° (Fig. 1.13c) and with the cone axis parallel to the tunnel axis. The relative populations of different C–Br bond orientations on the cone are not necessarily equal, but at a given site along the tunnel axis, the local environment experienced by the guest due to interaction with the host structure is described by a potential with approximately 6-fold rotational symmetry; thus, the distribution of orientations of the C–Br vectors on the cone exhibits approximate 6-fold symmetry. For this orientational distribution, the resultant C–Br bond vector is essentially parallel to the tunnel axis, representing the effective (time-averaged) C–Br bond orientation that defines the X-ray optic axis for XBI. Thus, both 1,8-DBrO/urea and 1,10-DBrD/urea exhibit sinusoidal variation of X-ray intensity as a function of χ and essentially no variation of X-ray intensity as a function of ϕ. While we have focused on the behavior of 1,8-DBrO/urea and 1,10-DBrD/urea in the HT phase, XBI studies of these materials in the LT phase have also been reported [24].

The XBI behavior observed for 1,8-DBrO/urea and 1,10-DBrD/urea demonstrates that, for materials undergoing anisotropic molecular dynamics, the effective X-ray optic axis is the *time-averaged* resultant of the orientational distribution of the C–Br bonds, which represents a basis for the rationalization of XBI behavior of other materials in which the molecules undergo anisotropic dynamic processes.

1.5 Concluding Remarks and Future Prospects

As demonstrated by the results presented above, the XBI technique enables spatially resolved mapping of the orientational properties of specific types of molecule and/or bond in materials. Although several of the samples in these early studies were single crystals, there is no requirement for crystallinity as X-ray birefringence is sensitive to local molecular orientations; thus, XBI could be applied to any material (including liquid phases, liquid crystals, amorphous solids, or molecular assemblies on surfaces) with an anisotropic distribution of molecular orientations. XBI can also be exploited for spatially resolved analysis of orientationally distinct domains in materials (see Fig. 1.7), yielding information on domain sizes, the orientational relationships between domains, and the nature of domain boundaries. Furthermore, as XBI is a full-field imaging technique in which the entire image is recorded simultaneously, XBI data can be measured quickly (typical exposure times for the XBI images shown here were around 1–5 s). Clearly, there are significant opportunities to carry out in situ XBI studies of physical or chemical processes as a function of time, with time resolution of the order of seconds.

Our ongoing research to further develop and apply the XBI technique is extending the initial studies described above by investigating a significantly wider range of materials (including those for which elements other than bromine are selected as the X-ray absorbing element). Given the utility of XBI as a technique for

spatially resolved mapping of the orientational properties of materials, for establishing changes in orientational properties in response to external stimuli, and for *in situ* monitoring of physical or chemical processes as a function of time, we fully anticipate that the XBI technique will find increasing opportunities for applications in several new areas of materials science in the future.

Acknowledgements The contributions of former Ph.D. students (Dr. Benjamin Palmer, Dr. Gregory Edwards-Gau, Dr. Anabel Morte-Ródenas, and Dr. Gin-Keat Lim) and several research collaborators (Dr. Igor Dolbnya, Dr. John Sutter, Dr. Benson Kariuki, Prof. Duncan Bruce, and Mr. Andrew Malandain) to our work on the development and application of the XBI technique are gratefully acknowledged. We are grateful to Diamond Light Source for the award of significant amounts of beamtime for XBI experiments on beamline B16. We thank Cardiff University, EPSRC and Diamond Light Source for financial support.

References

1. Born, M., Wolf, E.: Principles of Optics, 7th edn. Cambridge University Press, Cambridge (1999)
2. Hartshorne, N.H., Stuart, A.: Practical Optical Crystallography. Edward Arnold, London (1969)
3. Kaminsky, W., Claborn, K., Kahr, B.: Polarimetric imaging of crystals. Chem. Soc. Rev. **33**, 514–525 (2004)
4. Templeton, D.H., Templeton, L.K.: X-ray birefringence and forbidden reflections in sodium bromate. Acta Crystallogr. Sect. A **42**, 478–481 (1986)
5. Sauvage, M., Malgrange, C., Petroff, J.-F.: Rotatory power measurements in the X-ray range with synchrotron radiation: experimental set-up and preliminary results for $NaBrO_3$ single crystals. J. Appl. Crystallogr. **16**, 14–20 (1983)
6. Okitsu, K., Oguchi, T., Maruyama, H., Amemiya, Y.: Faraday effect and X-ray birefringence at cobalt K-absorption edge with the tunable X-ray polarimeter. Proc. Soc. Photo-opt. Instrum. Eng. (SPIE) **2873**, 100–104 (1996)
7. Mertins, H.-C., Oppeneer, P.M., Valencia, S., Gudat, W., Senf, F., Bressler, P.R.: X-ray natural birefringence in reflection from graphite. Phys. Rev. B **70**, 235106 (2004)
8. Palmer, B.A., Morte-Ródenas, A., Kariuki, B.M., Harris, K.D.M., Collins, S.P.: X-ray birefringence from a model anisotropic crystal. J. Phys. Chem. Lett. **2**, 2346–2351 (2011)
9. Palmer, B.A., Edwards-Gau, G.R., Morte-Ródenas, A., Kariuki, B.M., Lim, G.K., Harris, K.D.M., Dolbnya, I.P., Collins, S.P.: X-ray birefringence: a new strategy for determining molecular orientation in materials. J. Phys. Chem. Lett. **3**, 3216–3222 (2012)
10. Joly, Y., Collins, S.P., Grenier, S., Tolentino, H.C.N., De Santis, M.: Birefringence and polarization rotation in resonant X-ray diffraction. Phys. Rev. B **86**, 220101(R) (2012)
11. Collins, B.A., Cochran, J.E., Yan, H., Gann, E., Hub, C., Fink, R., Wang, C., Schuettfort, T., McNeill, C.R., Chabinyc, M.L., Ade, H.: Polarized X-ray scattering reveals non-crystalline orientational ordering in organic films. Nature Mater. **11**, 536–543 (2012)
12. Collins, S.P., Dolbnya, I., Palmer, B.A., Edwards-Gau, G.R., Morte-Ródenas, A., Kariuki, B.M., Lim, G.K., Harris, K.D.M., Joly, Y.: X-ray birefringence in highly anisotropic materials. J. Phys. Conf. Ser. **425**, 132015 (2013)
13. Brouder, C.: Angular dependence of X-ray absorption spectra. J. Phys. Condens. Matter **2**, 701–738 (1990)
14. van der Laan, G., Schofield, P.F., Cressey, G., Henderson, C.M.B.: Natural linear dichroism at the Fe 2p absorption edge of Gillespite. Chem. Phys. Lett. **252**, 272–276 (1996)

15. Collins, S.P., Laundy, D., Harris, K.D.M., Kariuki, B.M., Bauer, C.L., Brown, S.D., Thompson, P.: X-ray linear dichroism in an α,ω-dibromoalkane/urea inclusion compound and its application to polarization analysis of magnetic diffraction. J. Phys. Condens. Matter **14**, 123–134 (2002)
16. Chao, M.-H., Kariuki, B.M., Harris, K.D.M., Collins, S.P., Laundy, D.: Design of a solid inclusion compound with optimal properties as a linear dichroic filter for X-ray polarization analysis. Angew. Chemie Int. Ed. **42**, 2982–2985 (2003)
17. Palmer, B.A., Collins, S.P., Hulliger, J., Hughes, C.E., Harris, K.D.M.: Determining molecular orientations in disordered materials from X-ray linear dichroism at the iodine L_1-edge. J. Am. Chem. Soc. **138**, 16188–16191 (2016)
18. Jackson, J.D.: Classical Electrodynamics, 3rd edn. John Wiley & Sons, New York (1998)
19. Palmer, B.A., Edwards-Gau, G.R., Kariuki, B.M., Harris, K.D.M., Dolbnya, I.P., Collins, S.P.: X-ray birefringence imaging. Science **344**, 1013–1016 (2014)
20. Sutter, J.P., Dolbnya, I.P., Collins, S.P., Harris, K.D.M., Edwards-Gau, G.R., Palmer, B.A.: Theoretical analysis of the background intensity distribution in X-ray Birefringence Imaging using synchrotron bending-magnet radiation. J. Appl. Phys. **117**, 164902 (2015)
21. Palmer, B.A., Kariuki, B.M., Morte-Ródenas, A., Harris, K.D.M.: Structural rationalization of the phase transition behavior in a solid organic inclusion compound: bromocyclohexane/thiourea. Cryst. Growth Des. **12**, 577–582 (2012)
22. Zhou, Y., Patterson, R., Palmer, B.A., Edwards-Gau, G.R., Kariuki, B.M., Kumar, N.S.S., Bruce, D.W., Dolbnya, I.P., Collins, S.P., Malandain, A., Harris, K.D.M.: Spatially resolved mapping of phase transitions in liquid-crystalline materials by X-ray birefringence imaging. Chem. Sci. **10**, 3005–3011 (2019)
23. Takeda, H., Sakurai, Y., Takenaka, S., Miyake, H., Doi, T., Kusabayashi, S., Takagi, T.: Molecular structure and smectic properties – the substituent effect on the smectic-A phase in biphenyl ester systems. J. Chem. Soc., Faraday Trans. **86**, 3429–3435 (1990)
24. Palmer, B.A., Edwards-Gau, G.R., Kariuki, B.M., Harris, K.D.M., Dolbnya, I.P., Collins, S.P., Sutter, J.P.: X-ray birefringence imaging of materials with anisotropic molecular dynamics. J. Phys. Chem. Lett. **6**, 561–567 (2015)
25. Harris, K.D.M.: Meldola Lecture: understanding the properties of urea and thiourea inclusion compounds. Chem. Soc. Rev. **26**, 279–289 (1997)
26. Hollingsworth, M.D.: Crystal engineering: from structure to function. Science **295**, 2410–2413 (2002)
27. Harris, K.D.M.: Fundamental and applied aspects of urea and thiourea inclusion compounds. Supramol. Chem. **19**, 47–53 (2007)
28. Smith, A.E.: The crystal structure of the urea-hydrocarbon complexes. Acta Crystallogr. **5**, 224–235 (1952)
29. Harris, K.D.M., Thomas, J.M.: Structural aspects of urea inclusion compounds and their investigation by X-ray diffraction: a general discussion. J. Chem. Soc. Faraday Trans. **86**, 2985–2996 (1990)
30. Aliev, A.E., Smart, S.P., Shannon, I.J., Harris, K.D.M.: Structural and dynamic properties of the 1,10-dibromodecane/urea inclusion compound, investigated by variable-temperature powder X-ray diffraction, solid-state ^{2}H NMR lineshape analysis and solid-state ^{2}H NMR spin-lattice relaxation time measurements. J. Chem. Soc. Faraday Trans. **92**, 2179–2185 (1996)
31. Yeo, L., Harris, K.D.M.: Definitive structural characterization of the conventional low-temperature host structure in urea inclusion compounds. Acta Crystallogr. Sect. B **53**, 822–830 (1997)
32. Guillaume, F., Smart, S.P., Harris, K.D.M., Dianoux, A.J.: Neutron scattering investigations of guest molecular dynamics in α,ω-dibromoalkane-urea inclusion compounds. J. Phys. Condens. Matter **6**, 2169–2184 (1994)
33. Smart, S.P., El Baghdadi, A., Guillaume, F., Harris, K.D.M.: Conformational and vibrational properties of α,ω-dihalogenoalkane/urea inclusion compounds: a Raman scattering investigation. J. Chem. Soc. Faraday Trans. **90**, 1313–1322 (1994)

Chapter 2
Direct Visualization of Crystal Formation and Growth Probed by the Organic Fluorescent Molecules

Fuyuki Ito

Abstract In this chapter, the direct visualization of crystal formation and growth probed by organic fluorescent molecules exhibiting mechanofluorochromism and displaying aggregation-induced emission (AIE) is discussed. The fluorescence observations of the evaporative crystallization can reveal a two-step nucleation model for nuclei formation. The fluorescence from the droplets showed dramatic changes depending on the molecular state, such as monomer, amorphous, and crystal polymorph. The quartz crystal microbalance (QCM) measurement also revealed the changes in the mechanical properties during the solvent evaporation. These methods provide a useful and convenient fluorescence tool for in situ crystal analysis, from which detailed experimental evidence and mechanistic insights into crystal formation and transformation can be obtained through direct fluorescence visualization with real-time, on-site, and nondestructive methods.

Keywords Evaporative crystallization · Fluorescence color changes · Mechanofluorochromism · Aggregation-induced emission (AIE) · Quartz crystal microbalance (QCM) · Two-step nucleation model · Liquid-like cluster

2.1 Introduction

Crystal formation from solution is essential in fundamental science as well as in the fabrication of pharmaceuticals, food, polymers, and organic solid materials; however, it remains poorly understood. In solution crystallization, the formation of crystal nuclei plays an important role in determining the crystal structure, size, and polymorph, controlling crystallization and crystal quality. In classical nucleation theory, molecules are added one-by-one to extend the crystal lattice and form an embryonic nucleus in a one-step process. The classical model for crystallization visualizes the formation of a metastable crystalline nucleus that reaches a critical size through

F. Ito (✉)
Department of Chemistry, Institute of Education, Shinshu University, 6-ro, Nishinagano, Nagano 380-8544, Japan
e-mail: fito@shinshu-u.ac.jp

M. Sakamoto and H. Uekusa (eds.), *Advances in Organic Crystal Chemistry*,
https://doi.org/10.1007/978-981-15-5085-0_2

density fluctuations and grows into a stable crystal. Some computational and experimental results, however, cannot be explained based only on classical nucleation theory [1]. Recently though, a two-step nucleation model involving a liquid-like cluster intermediate prior to nucleation has been developed to explain protein crystallization and has been shown to be of more general validity [2]. It is postulated that liquid-like clusters originate from disordered liquid or amorphous metastable clusters in homogeneous solutions [3]. There have been many reports supporting this two-step nucleation model, in which the intermediated phases play an important role in crystallization.

Nucleation is the initial step of crystallization. The nuclei could not be directly observed because the nuclei exist in the transition state. Understanding and controlling nuclei formation will provide a suitable process for crystallization because the organic molecular crystals generally are formed by weak intermolecular interaction such as van der Waals, π–π interaction, or hydrogen bonding [4]. However, direct observation of such processes under realistic conditions in the real time remains a challenge because of the lack of advanced techniques to discriminate the phase boundaries and capture the intermediate states.

In this chapter, studies of the direct visualization of crystal formation and growth, probed by organic fluorescent molecules by using fluorescence microscopy and spectroscopy, are introduced, with a particular focus on the fluorescence spectral change of a dibenzoylmethane boron difluoride complex exhibiting mechanofluorochromism and a cyanostilbene derivative displaying aggregation-induced emission (AIE).

2.2 Fluorescence Detection of Molecular Assembling

The fluorescence spectra of materials are sensitive to molecular environment and aggregation. In principle, fluorescence spectroscopy can be used to probe the progress of molecular assembly on the scale of just a few molecules or that of a bulk process. In this section, the studies of molecular assembling probed by fluorescence detection are described.

Yu et al. [5] monitored an amorphous-to-crystalline transformation through fluorescence color changes by the in situ microscopic observation of the crystallization of molecular microparticles. As a molecule, tetra-substituted ethene with novel morphology-dependent fluorescence was applied, which can distinguish the interface between the crystalline and amorphous phase by fluorescence color, providing a simple and practical method to probe the inner processes of a molecular microparticle. The fluorescence images of the crystallization due to contact between microparticles were categorized into three cases by monitoring the crystallization evolution of these defective microspheres. This method can clearly record the inhomogeneous crystallization of amorphous microparticles, whereby the perfect microparticles and those with defects demonstrate diverse destinies. The study presents a realistic picture of the microscopic kinetics of not only solid–solid transitions but also crystallizations that occur spontaneously in atmosphere or under external stimuli,

such as mechanochromic behavior. Furthermore, this facile method may provide practical opportunities and utilizations for other molecules employing fluorescence microscopy and fluorescent materials.

Pansu et al. attempted fluorescence lifetime microscopy imaging (FLIM) of the nucleation and growth processes during fluorogenic precipitation in a microflow mapping, the schematic representation of which is as shown in Fig. 2.1 [6]. This is the first observation, enumeration, and mapping of the early stages of crystallization during antisolvent precipitation. As a molecule, (2Z, 2′Z)-2,2′-(1,4-phenylene)-bis-(3-(4-butoxyphenyl)acrylonitrile), DBDCS was chosen, which exhibits aggregation-induced emission enhancement (AIEE), namely, the molecules are non-fluorescent and the nuclei should appear as bright objects on a dark background. THF and water were used as good and poor solvents, respectively, for DBDCS precipitation.

The precipitation of a fluorescent dye in a microfluidic 3D hydrodynamic mixing setup was performed concomitant with the FLIM imaging. The FLIM images of the precipitation process are shown in Fig. 2.2. A short fluorescence lifetime of

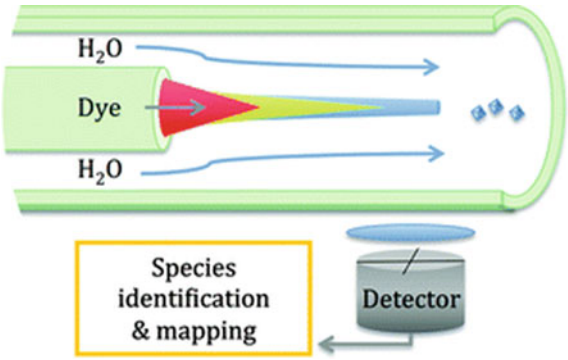

Fig. 2.1 Schematic illustration of FLIM imaging in a 3D hydrodynamic mixing setup. Reproduced from Ref. [6] by permission of The Royal Society of Chemistry (RSC) on behalf of the Centre National de la Recherche Scientifique (CNRS) and the RSC

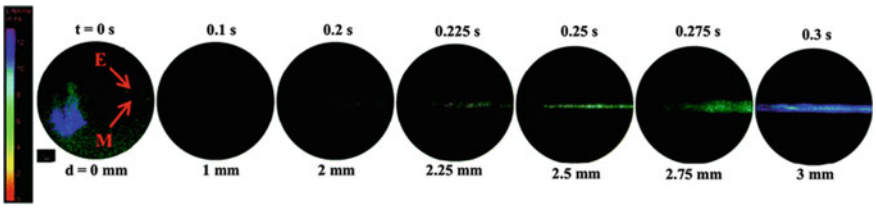

Fig. 2.2 FLIM images of the microprecipitation of DBDCS inside the microfluidic device; $Q_s/Q_c = 10/0.5$ (μL min^{-1}); $C = 0.21 \times 10^{-3}$ mol L^{-1}; inner flow diameter = 30 μm. The color of the pixel codes for the average lifetime. Reproduced from Ref. [6] by permission of The Royal Society of Chemistry (RSC) on behalf of the Centre National de la Recherche Scientifique (CNRS) and the RSC

the DBDCS molecule and the long lifetime of its crystal, with nuclei of intermediate lifetime, are observed. We show that the precipitation is slowed down by the presence of a viscous skin at the interface between water and THF. From the analysis of the decays, we map the concentrations of the three species with over half a million pixels and show that nucleation and growth occur all along the device by the slow diffusion of water into the THF inner flow.

A new method to synthesize and observe the precipitation of sub-micrometer particles was optimized to study and control the early stage of microprecipitation. The developed device is easy to construct and fully compatible with a wide range of solvents. We used fluorescence lifetime imaging microscopy to detect not only the oligomers of molecules that precede the formation of crystals but also the nucleation and growth kinetics simultaneously.

There has been demand for a real-time, on-site, nondestructive, fluorescence imaging technique to monitor the crystal formation and transformation processes of organic fluorescent molecules. Hu and Tang et al. reported the fluorescent visualization of crystal formation and transformation processes of organic luminogens with crystallization-induced emission characteristics [7]. In this work, (Z)-1-phenyl-2-(3-phenylquinoxalin-2(1H)-ylidene)ethanone (PPQE) with crystallization-induced emission properties was reported. Three polymorphs of PPQE with various emission behaviors were obtained with good reproducibility under controlled conditions (Fig. 2.3). With the crystallization-induced emission characteristics and polymorph-dependent luminescence of PPQE, a real-time, on-site, nondestructive fluorescence imaging technique to monitor crystal transformation processes and crystal formation from the amorphous state and dilute solution, respectively, was achieved. This study provides a useful and convenient fluorescence tool for in situ crystal analysis, from which detailed experimental evidence and mechanistic insights into crystal formation and transformation can be obtained through direct fluorescence visualization with real-time, on-site, and nondestructive capabilities. It is a powerful and convenient tool for crystal analysis, providing detailed and valuable information about the crystal formation and transformation processes.

2.3 Evaporative Crystallization of Mechanofluorochromic Molecules

Dibenzoylmethanatoboron difluoride (BF_2DBM) derivatives have excellent optical properties, such as two-photon absorption cross sections [8, 9], high fluorescence quantum yields in the solid state [10], multiple fluorescence colors [11–15], and reversible mechanofluorochromic properties [16, 17]. In particular, BF_2DBM based on the 4-*tert*-butyl-4′-methoxydibenzoylmethane (avobenzone) boron difluoride complex (BF_2AVB) exhibits different emission depending on the crystal phase (polymorph) [18]. BF_2AVB also has excellent fatigue resistance by photoirradiation and a

Fig. 2.3 Crystal formation and transformation processes. A real-time, on-site, nondestructive, fluorescence imaging technique has been reported to monitor the crystal formation and transformation processes of organic luminogens. Reproduced from Ref. [7] by permission of The Royal Society of Chemistry

high fluorescence quantum yield, even in the solid state (~0.5), which is advantageous for photonics applications.

In this chapter, the fluorescence properties of BF_2DBM in PMMA films and solution during evaporative crystallization were investigated to reveal the two-step nucleation model.

2.3.1 Fluorescence Visualization of Crystallization of Dibenzoylmethanatoboron Difluoride Complex

We have investigated the fluorescence properties of 4,4′-di-*tert*-butyldibenzoylmethanatoboron difluoride (BF_2DBMb, Fig. 2.4a) in PMMA films and solution during evaporative crystallization to reveal the two-step nucleation model [19]. BF_2DBMb has a mechanofluorochromic property, [11, 20] which originates from the different emission properties between the amorphous state and

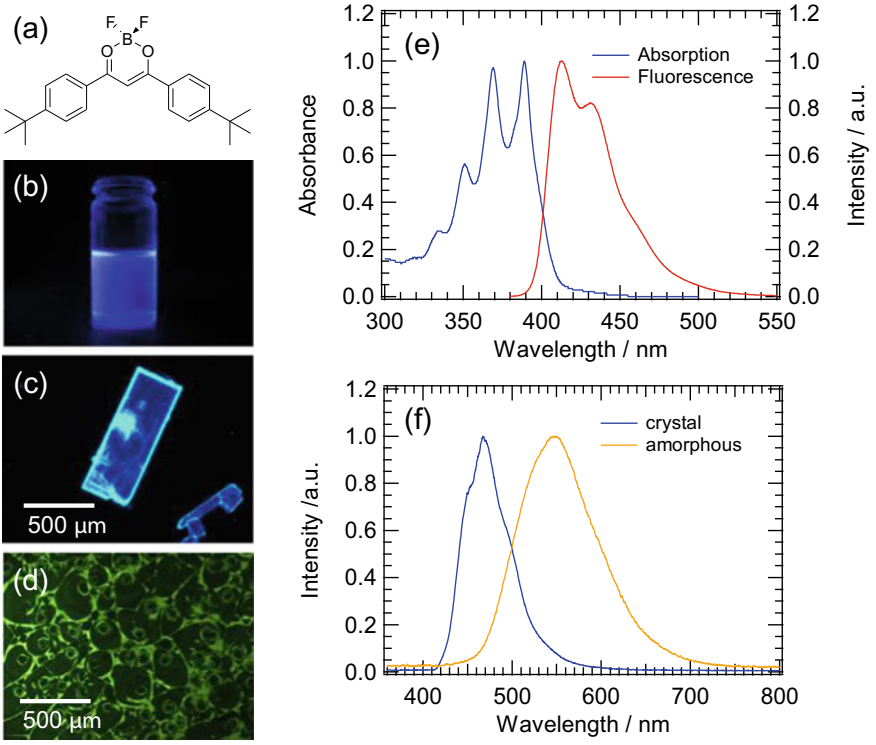

Fig. 2.4 **a** Molecular structure of BF_2DBMb. Fluorescence images of BF_2DBMb in **b** 1,2-dichloromethane, **c** crystalline state, and **d** amorphous state under 365 nm UV irradiation, **e** absorption and fluorescence spectra of BF_2DBMb, and **f** fluorescence spectra of crystal and amorphous states of BF_2DBMb following excitation at 380 nm. Reprinted by permission from Macmillan Publishers Ltd.: Ref. [19], copyright 2016

the crystal one [17]. The two-step nucleation model can be clarified by fluorescence detection, such that the detection of the amorphous state prior to crystallization by fluorescence color change can be expected. As described above, Yu et al. more recently reported the amorphous-to-crystalline transformation monitored by the fluorescence color change [5].

First, we confirmed the fluorescence properties of BF_2DBMb in dilute solution, crystal and amorphous states, the fluorescence images of which are exhibited in Fig. 2.4b–d. The fluorescence exhibits purple, blue, and greenish-orange colors, for the dilute solution, crystal state, and amorphous state, respectively. The absorption and fluorescence spectra of BF_2DBMb in 1,2-dichroloethane are shown in Fig. 2.4e. The absorption peaks were observed at 350, 370, and 390 nm and were in a mirror image of the fluorescence spectra with peaks at 413 and 430 nm and shouldered at 460 nm, which can be assigned to the vibrational modes of BF_2DBMb monomer. The fluorescence showed peaks near 445 and 470 nm for the crystal, and near 550 nm for the amorphous state, as shown in Fig. 2.4f. The crystal and amorphous

states were confirmed by XRD measurement. These findings indicate that molecular forms, such as monomer (isolated state) and aggregated state, can be distinguished by fluorescence color change.

Up to now, we have reported the evolution of the molecular assembling by fluorescence change in polymer matrix, which can provide information on the aggregation and segregation processes. To confirm the molecular assembling of BF_2DBMb in polymer matrix (poly(methyl methacrylate), PMMA) by static trail, the concentration dependence of the fluorescence changes was as shown in Fig. 2.5. The close-up picture of the fluorescence image uniformly shows blue in 0.01 mol%. With increasing concentration, the fluorescence color changes to greenish-orange via light blue until 3.0 mol%. The needle with sky blue emission was confirmed for film of over 4.0 mol%, for which the segregation of BF_2DBMb crystal in the polymer film most probably occurred. At the lower concentrations of 0.01 mol%, BF_2DBMb fluorescence bands were observed near 430 nm, originating from the monomer as shown in Fig. 2.4e. The fluorescence peak was red-shifted until 0.5 mol%. At a concentration of 1.0 mol%, the fluorescence peak was located at 450 nm concomitant with a broad new fluorescence band appearing near 530 nm as a shoulder. Although the broad emission band near 530 nm increased with increasing concentration up to 3.0 mol%, it suddenly disappeared, and the fluorescence peak was shifted to the wavelength near 450 nm. The fluorescence spectrum is identical to that of the emission from the BF_2DBMb crystal shown in Fig. 2.6f. These phenomena imply that the molecular

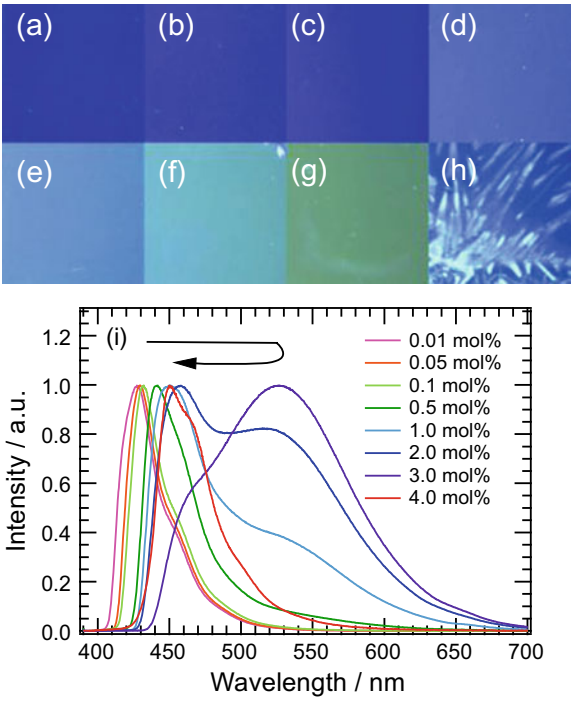

Fig. 2.5 Close-up fluorescence images of BF_2DBMb in PMMA films with a concentration of **a** 0.01, **b** 0.05, **c** 0.1, **d** 0.5, **e** 1, **f** 2, **g** 3, and **h** 4 mol%, and **i** fluorescence spectra as a function of concentration obtained by excitation at 380 nm. Reprinted by permission from Macmillan Publishers Ltd.: Ref. [19], copyright 2016

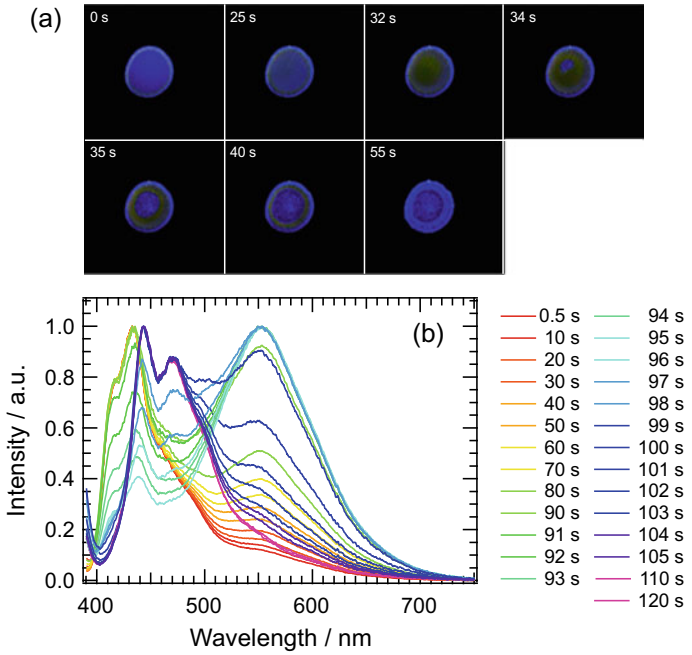

Fig. 2.6 **a** Fluorescence images of a droplet of BF_2DBMb in 1,2-dichloroethane during evaporation under 365 nm UV irradiation. The droplet diameter is approximately 5 mm. **b** Changes in fluorescence spectra of BF_2DBMb in 1,2-dichloroethane during solvent evaporation. Reprinted by permission from Macmillan Publishers Ltd.: Ref. [19], copyright 2016

assembling can be isolated or frozen by the polymer matrix, the dynamics of which revealing the formation of the crystal from the monomer state via the amorphous state of BF_2DBMb. These findings are supported by the XRD results in polymer films. The fluorescence excitation spectra of BF_2DBMb in PMMA films indicate the exciton splitting of the band, suggesting the formation of H- and J-aggregates with increasing concentration. Based on the band splitting, the average number of aggregated molecules was estimated to be 12 molecules.

Next, we attempted to measure the fluorescence change during evaporative crystallization from solution. The detection of the molecular assembling through the fluorescence changes can be expected, particularly liquid-like clusters, such as the amorphous aggregated state. Figure 2.6a shows the fluorescence images during the solvent evaporation from 3.1×10^{-2} mol dm^{-3} BF_2DBMb in a 1,2-dichloroethane droplet, and the movie of which is shown in the supporting information [19]. In this trial, the time origin is set to after the complete focusing of the CCD camera, which describes the reason for the indicated time difference between the movie and the spectral change described below. At a time of 0 s, the fluorescence color is purple. The emission color changes to orange from the edge of droplet after 25 s. With the elapse of time, the emission color transiently becomes orange all over the droplet at

approximately 32 s. The solvent evaporated, which resulted in a doughnut-shaped orange emission formed at approximately 34 s. The region of purple emission shrank from both inside and outside after 34 s. Finally, the entire droplet region turned to blue emission with small parts of the orange emission remaining. The evaporation of solvent from the inner region most probably originates from the analogous mechanism to gas bubbles, which has been reported for the molecular assembling during the evaporation of low vapor pressure solvent [21]. The orange emission is exhibited only in solution with non-equilibrium state. Actually, the concentration dependence of fluorescence spectra of BF_2DBMb in solution does not exhibit orange emission, even under concentrated conditions. It is strongly suggested that the molecular form or assembly with orange emission can be like a supersaturated solution. To obtain the spectroscopic information for solvent evaporation, we observed the fluorescence spectra of BF_2DBMb in 1,2-dichroloethane during evaporation as a function of time, which are shown in Fig. 2.6b. The fluorescence spectrum acquired immediately after applying the droplet exhibits peaks at 433 nm with shoulders at 415, 460, 550 nm, corresponding to the emission spectra of the monomer state. The peak near 550 nm corresponding to the amorphous state monotonically increased with time up to 91 s. The fluorescence peak at 433 nm decreased from 91 to 95 s. After 95 s, the peaks near 445 and 470 nm appeared concomitant with decreasing band intensity near 550 nm. The series of fluorescence spectral changes correspond to the fluorescence image change. Based on the information of the fluorescence properties of BF_2DBMb as described above, we can explain the molecular assembling by solvent evaporative crystallization. The crystal of BF_2DBMb formed from solution via the amorphous state. The dynamic fluorescence change is identical to observations when increasing the concentration in PMMA films during static trials. The Raman spectra of each species were identical to the fluorescence spectral change, which strongly supports the changes in molecular species in the ground state.

The fluorescence spectra were analyzed by nonlinear least squares fitting by six Gaussians. All of the observed spectra matched these values well. Thus, we plotted the relative abundances of monomer, crystal, and amorphous state as a function of time, which is shown in Fig. 2.7a. Afterward, the dropping the fraction of monomer species fell to approximately 0.9. The monomer fraction monotonically decreased, whereas the amorphous fraction increased up to 95 s. The amorphous fraction reached approximately 0.6 at 95 s; then, the fraction decreased considerably. The crystal fraction was not observed before 95 s. The fraction suddenly increased after 95 s, concomitant with the decrease of the amorphous state. These findings indicate that the crystal can be formed from monomer species via the amorphous state, which is presumed to show hierarchical change like a consecutive reaction, as schematically shown in Fig. 2.7b.

Based on the observed phenomena by fluorescence change both depending on the dispersion concentration in PMMA films and during the solvent evaporative crystallization of BF_2DBMb, we can conclude that the direct visualization of proposed a mechanism of the two-step nucleation model. The fluorescence color change from purple to blue via orange corresponds to the molecular formation change from monomer to crystal via amorphous state. The amorphous state is transiently formed

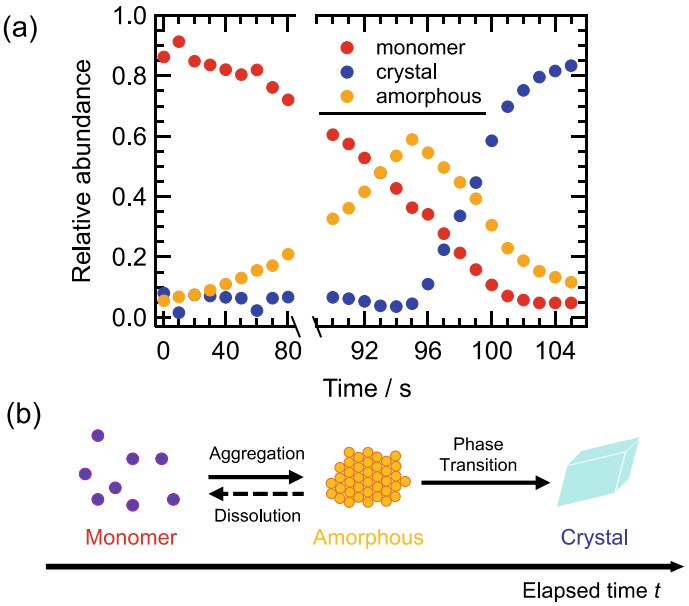

Fig. 2.7 **a** Change in the relative abundance of monomer, amorphous, and crystal states based on time-resolved fluorescence spectral measurements. **b** Schematic representation of the molecular assembly based on the changes in fluorescence spectra. Reprinted by permission from Macmillan Publishers Ltd.: Ref. [19], copyright 2016

prior to the crystal formation. The two-step nucleation model suggests that there is the liquid-like cluster as a crystal nucleus, which has been established based on the induction time of crystal formation [22], NMR spectroscopy [23, 24], electron microscopy [25], and non-photochemical laser-induced crystallization [26]. In the present case, the observed orange emission originating from amorphous species demonstrates the existence of the liquid-like cluster before crystallization, the state of which is only in the supersaturated region during the solvent evaporation, i.e., the non-equilibrium state. The time evolution of the relative abundance of the molecular form of BF_2DBMb clearly reveals that the formation of the amorphous species acts as a precursor to crystal formation. We have verified that the fluorescence visualization during solvent evaporative crystallization agrees with the previously known two-step model for crystal formation [2, 27].

2.3.2 *Changes in Optical and Mechanical Properties During Evaporative Crystallization*

Recently, there have been many reports supporting the two-step nucleation model, which is relatively understood, with the intermediate phases playing an important

role in crystallization [28, 29]. Tsarfati et al. mentioned the crystallization paths involving the three main stages—initial densification from the solvent-rich precursor, early ordering, and concurrent evolution of order and morphology [30]. This finding indicates that the liquid-like cluster state contains the solvent in the solution. It is unknown that the orange emission of BF_2DBM originates from the amorphous phase as either highly dense solvent-rich state or solid aggregates. Based on the above background, we focus on the changes in optical and mechanical properties during evaporative crystallization in real time, particularly to clarify the orange emissive state as the intermediate phase [31].

To assess the optical and mechanical properties of the mutual state during evaporative crystallization in real time, we considered the droplet observation under the crossed Nicol condition [32]. The quartz crystal microbalance (QCM) is a tool that is used to perform real-time monitoring of the mass and the viscoelastic changes based on the change in the frequency (Δf) and resistance (ΔR) from the adsorption onto the quartz substrate [33]. It is utilized in the evaluation of the deposited film thickness in the vacuum deposition.

We first observed the fluorescence images and polarized optical image, simultaneously, during the solvent evaporation. Figure 2.8 shows the photographs of the droplet between the polarizer under the crossed Nicol condition, with (upper side) and without (lower side) UV irradiation during the solvent evaporation. The polarized optical images with UV irradiation correspond to the fluorescence color changes of the droplet, which exhibits a purple color just after the dropping. However, there

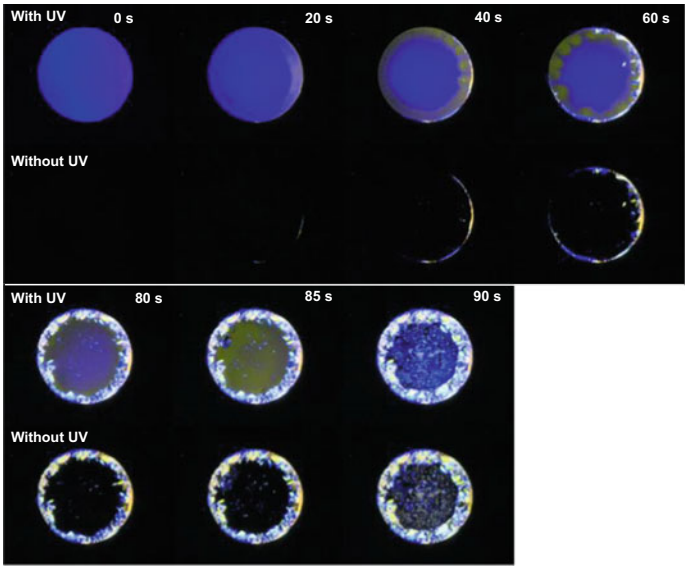

Fig. 2.8 Photographs of the BF_2DBMb in 1,2-DCE droplet between the polarizer arranged under the cross-Nicol condition together with and without UV irradiation during the solvent evaporation. From [31]. Reprinted with permission from Chemical Society of Japan

was no transparency in the image without UV irradiation, indicating that the droplet of BF_2DBMb solution has no crystalline region. With time, the fluorescence color changed to orange from the peripheral of the droplet; this change was associated with the solvent evaporation from 20 to 40 s after the dropping, which can be assigned to the emission of the amorphous phase according to the previous report. After 60 s, birefringence was observed via the polarized optical image, and the texture in both the polarized optical images with and without UV irradiation gradually propagated throughout the droplet. The texture in the images implies the phase transformation of the amorphous state, followed by the formation of a crystalline state. Compared with both images at 85 s, the region with orange emission shows no birefringence, suggesting the optically isotropic phase. We have postulated that the amorphous phase as an intermediate can be identical to the liquid-like cluster state proposed in the two-step nucleation model of the crystallization process. These findings indicate that the photophysical and optical properties of the liquid-like cluster state have an isotropic aggregated state similar to an amorphous phase.

Next, we attempted QCM measurements during the evaporative crystallization of the droplet. Prior to discussing the results of the QCM measurements, to confirm that the Au electrode does not affect the fluorescence behavior in the evaporative crystallization of the droplet, we measured the fluorescence images and spectra during the solvent evaporation on Au-coated AT-cut quartz substrate, simultaneously. The behavior of the fluorescence spectral changes of BF_2DBMb droplet onto Au electrode is almost the same as that in the previous report, indicating that Au electrode does not affect the spectral changes that occur during solvent evaporation, such as the surface plasmon resonance of Au thin film [34, 35].

We attempted the QCM measurements adapted for the evaporative crystallization of the BF_2DBMb droplet, to assess the changes in the dynamic viscoelastic properties. First, to confirm the effects of just solvent evaporation, we measured Δf and ΔR changes by the evaporation of 1,2-DCE as a function of time. Both values indicate the amount of change from before the dropping. Just after dropping, Δf was -2 kHz and began to return to the initial value from approximately 50–156 s. Meanwhile, ΔR exhibited behavior similar to that of Δf just after dropping and then monotonically recovered from 93 to 156 s. Changes in both values correspond to the solvent mass change Δm based on the Sauerbrey equation described below; therefore, recovery to the initial values suggested that the solvent on the Au electrode fully evaporated with time.

Next, we performed the QCM measurements of BF_2DBMb in the 1,2-DCE solution droplet on the Au-coated At-cut quartz electrode. Figure 2.9a shows the changes in Δf and ΔR as a function of time after the dropping of the solution on the Au electrode. Just after dropping, Δf showed a value of -2 kHz until 70 s, which is comparable to that in the 1,2-DCE solvent. From 70 to 86 s, Δf temporarily decreased to -4.5 kHz and then reached -6.9 kHz at 95 s. This value was maintained constant between 95 and 107 s. Afterward, Δf decreased again, ultimately exhibiting a value of -13.8 kHz. Just after dropping, ΔR exhibited a value of 0.37 kΩ until 85 s, which is also comparable to that in the 1,2-DCE solvent. From 85 to 93 s, ΔR temporarily increased to 1.2 kΩ and then steeply increased to 1.6 kΩ until 115 s. Afterward,

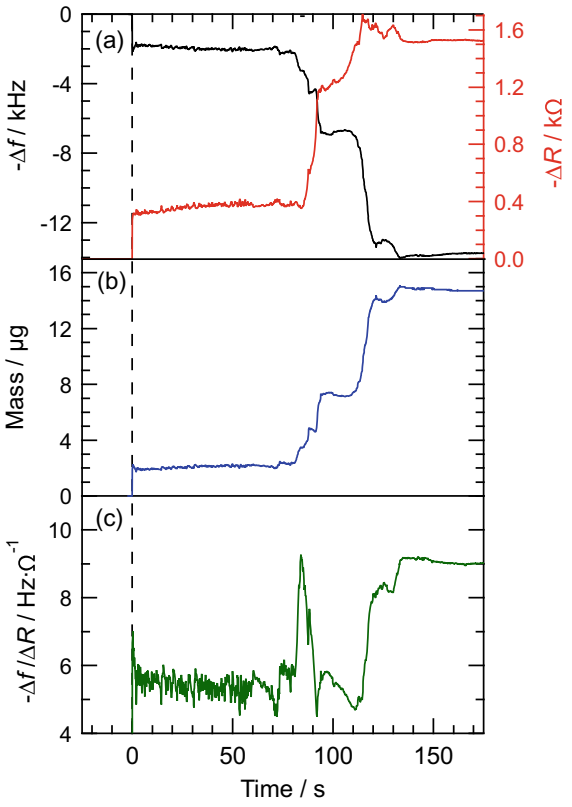

Fig. 2.9 Time evolution of **a** QCM results for Δf and ΔR, **b** the mass change estimated by using the Sauerbrey equation, and **c** $-\Delta f/\Delta R$ during the solvent evaporation of BF_2DBMb in 1,2-DCE solution. From [31]. Reprinted with permission from Chemical Society of Japan

ΔR is slightly decreased to 1.5 kΩ. As an overall trend, it is found that both values changed in two steps during the evaporative crystallization. It is possible to identify the three main stages concerning the fluorescence changes of BF_2DBMb (purple to blue via orange emission).

The change in f is related to the mass change (Δm) based on the Sauerbrey equation as shown in the following equation [36],

$$\Delta m = \frac{\Delta f A \sqrt{\mu_q \rho_q}}{2 f_0} \tag{2.1}$$

where f_0, A, μ_q, and ρ_q are the resonant frequency, piezoelectrically active crystal area, density of quartz, and shear modulus of quartz for AT-cut crystal, respectively. In the present system, we used the following values: $f_0 = 8.947$ MHz, $A = 1.96 \times 10^{-5}$ m^2, $\mu_q = 2.95 \times 10^{10}$ kg m^{-1} s^{-2}, $\rho_q = 2.65 \times 10^3$ kg m^{-3}. Based on Eq. 2.1, we can estimate the Δm of the BF_2DBMb droplet during the evaporative crystallization, the time evolution of which is shown in Fig. 2.9b. Just after dropping, Δm was 2 μg until 80 s, a value comparable with that for just 1,2-DCE solvent, which indicates that the Au electrode can recognize only the mass of the adsorbed solvent. From 80

to 86 s, Δf temporarily decreased to 7.3 μg and then reached 15 μg at 95 s. The increase of Δm is ascribed to the adsorption and precipitation of BF_2DBMb onto the Au electrode. However, the estimated solute mass of the BF_2DBMb solution was 34.65 μg, which is much larger than the estimated Δm value. This causes the spreading out of the effective area of Au electrode and the viscoelastic property of the droplet as described the next paragraph. It is difficult to drop a smaller amount of solution within the electrode area, owing to the surface tension of the droplet.

The QCM results can be used to evaluate not only the Δm but also the viscoelastic properties of the adsorbed materials. Kanazawa et al. reported that the Δf with homogeneous viscous fluids is proportional to the square root of the viscosity coefficients [37]. Muramatsu et al. also represented the linear relation between ΔR and the square root of the viscosity coefficient [38]. However, in terms of Δf for the viscoelastic medium, it is complicated to evaluate both the viscosity and elasticity separately, because Δf depends both on the Δm and viscosity. Based on the above findings, Kubono et al. semi-quantitatively formulated the relation assuming that the Δf is the sum of the two contributions from the ideal frequency shift by adsorbed mass (Δf_m) associated with the elasticity and that by viscous fluid (Δf_v) with constants (a and b) as follows [39],

$$\Delta f = \Delta f_m + \Delta f_v = am + b\sqrt{\eta} \tag{2.2}$$

To estimate the contribution of the elasticity, the ratio $-\Delta f/\Delta R$ can be suitable for the separation of viscoelastic properties from the Δf value

$$-\frac{\Delta f}{\Delta R} = a'\frac{m}{\sqrt{\eta}} + b' \tag{2.3}$$

where a' and b' are constants. If the viscous liquid adsorbs onto the electrode, a' should be zero and $-\Delta f/\Delta R$ is constant, which is independent of the viscosity coefficient. With an increase in elasticity, a' increases, and $-\Delta f/\Delta R$ becomes larger, which indicates that the two contributions (Δf_m and Δf_v) to Δf can be separated as the mass change and viscosity change. If Δf decreased but $-\Delta f/\Delta R$ remained constant, for example, this change would be attributed to the viscosity change, rather than the mass change.

The evaporation of 1,2-DCE led to a $-\Delta f/\Delta R$ value of approximately 5.5, which indicates that the solvent adsorbed onto the electrode. Figure 2.9c shows changes of Δf and ΔR as a function of time after the dropping of BF2DBMb in 1,2-DCE solution. The $-\Delta f/\Delta R$ value was maintained at 5.5 from just after dropping until 70 s, which is comparable to that in 1,2-DCE solvent. From 70 to 86 s, $-\Delta f/\Delta R$ temporarily increased to 9.2 at 84 s and then recovered to 5.5 until 112 s. Finally, the $-\Delta f/\Delta R$ value increased to 9.2 from 114 to 134 s.

Crystallization occurs in the monomer molecular assemblies via the formation of the liquid-like cluster state with amorphous property, proposed by the two-step nucleation model, as described in the previous section. It is expected that the mechanical

property will change from a viscous fluid to elastic media during the crystallization, that is, the $-\Delta f/\Delta R$ value will increase after crystallization together with the fluorescence color change from orange to blue. In the early state after the dropping, the $-\Delta f/\Delta R$ value indicates a viscous fluid owing to a large amount of solvent, which is considered to be due to the adhesion of the solvent to the substrate surface. This indicates that the molecule is dispersed in the solution and has a large amount of solvent attached to the substrate surface. The peak shape at 84 s of the $-\Delta f/\Delta R$ value is considered to be due to the artifact caused by the adhesion of the aggregated amorphous state to the Au electrode, because Δm also increased rapidly at the same time. The fluorescence color of the droplet at 84 s was orange, suggesting the formation of the amorphous phase. The $-\Delta f/\Delta R$ value from 91 to 111 s was the same as that from 0 to 80 s, suggesting that the amorphous state has a similar viscosity as the solution. The sudden rise of $-\Delta f/\Delta R$ at 111 s is ascribed to the transition to the elastic crystals.

We have reconsidered and proposed the schematic representation of the evaporative crystallization process combined with the two-step nucleation model and the present experimental results in terms of the viscoelastic properties, as shown in Fig. 2.10. Just after the dropping onto a substrate, the solute molecules exist in a monomeric state. With the elapse of time for the solvent evaporation, the monomer molecules aggregate with each other. The condensed monomer molecules form an amorphous state with an optically isotropic and viscous fluid; then, it adsorbs onto the substrate, which corresponds to a liquid-like cluster. The monomer molecules in the solvent are further adsorbed onto the amorphous state by solvent evaporation because the Δm continually increases with time. It is also found that in the amorphous phase observed in the QCM measurement a solvent-containing state most probably exists during the evaporative crystallization stage based on the viscoelastic properties of the amorphous phase. It is suggested that the difference between the amorphous state and the liquid-like cluster state originates from the presence of the solvent in the aggregate.

In previous reports, the relationship between the liquid-like cluster and amorphous state was only based on the fluorescence color. The results of the polarized optical images and QCM measurements indicate that the liquid-like cluster as an intermediate observed during the evaporative crystallization has high viscosity, despite the

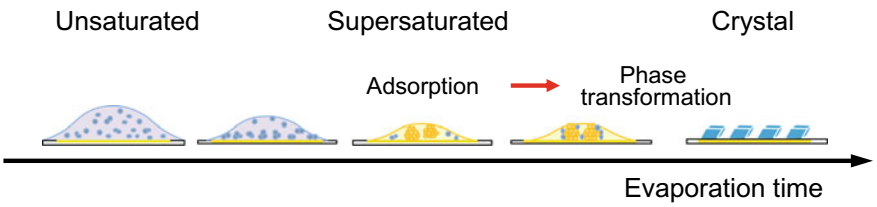

Fig. 2.10 Schematic of the evaporative crystallization of BF_2DBMb based on polarized optical images and viscoelastic measurements. From [31]. Reprinted with permission from Chemical Society of Japan

similar emission of the amorphous solid. The result of the two-step mass changes suggests that the liquid-like cluster has a finite size and then undergoes the phase transition to a crystal with desolvation during growth.

2.4 Molecular Assembling Probed by Aggregation-Induced Emission

Over the past decade, there have been many reports on aggregation-induced (or enhanced) emission (AIE or AIEE) in organic molecules [40], even though the fluorescence quantum yield is low in solution, as reported by Hong et al. [41]. AIEE enables selective detection of the assembly dynamics for aggregates and crystals. Here, for the first time, we apply AIEE to the dynamics of crystal formation. Specifically, we use a cyanostilbene derivative [1-cyano-*trans*-1,2-bis-(4′-methylbiphenyl)-ethylene (CN-MBE; Fig. 2.11)] for AIEE, as reported by An et al. [42]. Using a fluorescence microscope, we characterized the spectral and intensity changes of CN-MBE emission in solution during solvent evaporation [43, 44].

The absorption and fluorescence spectra of CN-MBE in solution and in nanoparticles were reported previously [42]. To suppress molecular rotation and aggregation for the observation monomer fluorescence, spectra of cast films of CN-MBE in PMMA were measured as a function of CN-MBE concentration (a polymer matrix in dilute conditions). Figure 2.12 plots normalized fluorescence spectra from 330-nm excitation of these films cast from DCE solutions. At concentrations <0.1 mol%, peak emission was observed at 440 nm, with a shoulder at 420–430 nm. At increased concentrations, the fluorescence peak shifts to 470 nm and narrows. Aggregate species were observed with the fluorescence microscope at concentrations >1.0 mol%. Thus, the spectral shift and narrowing of the fluorescence originated from CN-MBE J-aggregates, according to the previous report [42]. To identify the emissive species at lower concentrations, excitation spectra of the CN-MBE/PMMA films were acquired, indicating a broad excitation spectrum at 355 nm for concentrations <0.1 mol% is most likely a combination of the planar and twisted conformers that coexist in the films as a monomer.

To confirm AIEE in the increased fluorescence intensity during crystal formation, we acquired fluorescence microscope images during solvent evaporation from 5.0×10^{-3} mol dm^{-3} CN-MBE in a DCE droplet (Fig. 2.13). During the initial 75 s, no emission was observed from the droplet. A violet-blue feature first appeared after 90 s.

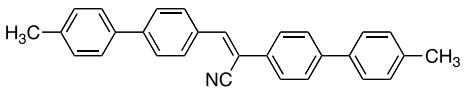

Fig. 2.11 Molecular structure of CN-MBE

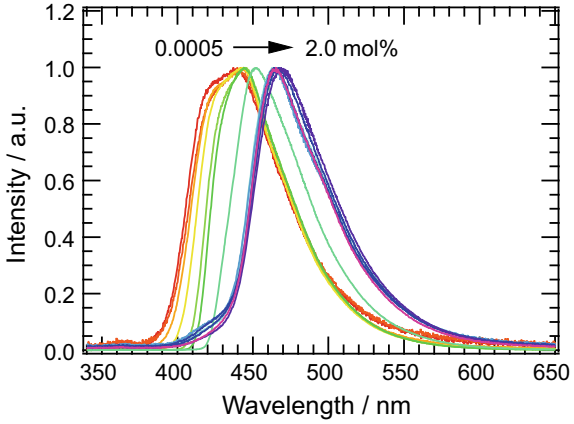

Fig. 2.12 Fluorescence spectra of CN-MBE in PMMA films as a function of concentration (excitation at 330 nm). Reproduced from Ref. [43] by permission of The Royal Society of Chemistry

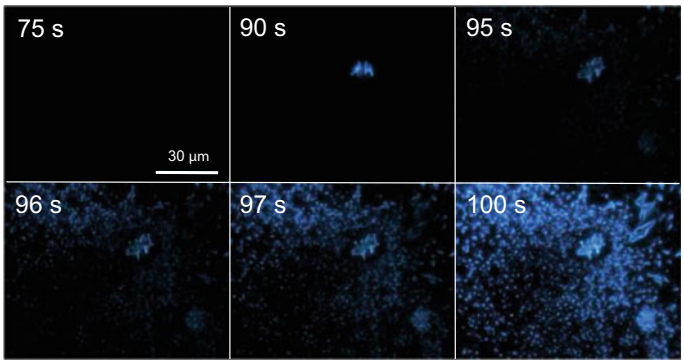

Fig. 2.13 Fluorescence microscope images as a function of time for 5.0×10^{-3} mol dm^{-3} CN-MBE in a DCE droplet during solvent evaporation. Reproduced from Ref. [43] by permission of The Royal Society of Chemistry

More features appeared over time, aggregated around the initial feature and accompanying the increased fluorescence intensity, until the completion of the evaporation at 100 s. These images indicated that CN-MBE emission in the solution phase was very weak. The polarization microscopy images were obtained with crossed Nicol polarizers, indicating the crystal formation. These observations suggest that AIEE allows us to follow crystal formation by changes in the fluorescence intensity. We can thus characterize the dynamics of organic crystal formation by the fluorescence intensity changes.

To investigate the molecular dynamics of crystal formation, fluorescence spectra were acquired during solvent evaporation for droplets of 5.0×10^{-3} mol dm^{-3} CN-MBE in DCE (Fig. 2.14a). As above, the fluorescence intensity was weak just after

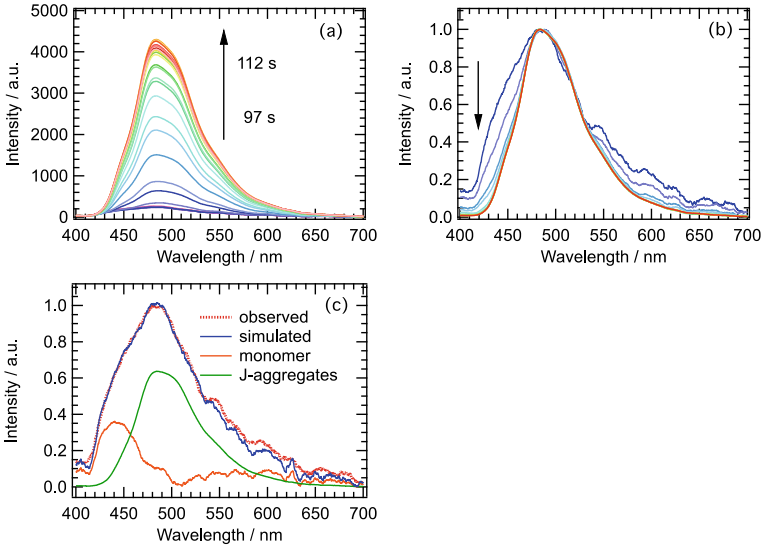

Fig. 2.14 Fluorescence spectral changes (**a**) and normalized spectra (**b**) of 5.0×10^{-3} mol dm^{-3} CN-MBE in a DCE droplet during solvent evaporation as a function of time. **c** The observed spectra after 97 s and simulated spectra from summation of the relative abundance of the planar conformational monomer and the J-aggregates by least-square fitting. Reproduced from Ref. [43] by permission of The Royal Society of Chemistry

the drop was formed. With time, the fluorescence intensity gradually increased by a factor of 100; normalized spectra are shown in Fig. 2.14b. After 97 s, the peak emission was at 480 nm, with a shoulder at 440 nm. Other peaks that originate from the monomer structure are observed at 443, 474, and 505 nm. The spectra became narrower with time, especially over 410–450 nm, as the solvent completely evaporated, confirmed by microbalance. After 112 s, the spectra are identical to those in Fig. 2.12, suggesting that solvent evaporation results in the formation of molecular assemblies owing to increasing concentrations of CN-MBE.

The fluorescence spectra were analyzed as a function of concentration as shown in Fig. 2.14c. We assumed that the spectra are from two species: a planar conformational monomer and J-aggregates. The spectrum of J-aggregates was from CN-MBE crystals. The spectrum of the planar conformational monomer was calculated from the difference between observed spectra at different time intervals. The observed spectra at each time were reproduced by nonlinear least squares fitting of the summation of emission from the planer monomer and J-aggregates.

Figure 2.15 shows a plot of the time evolution of the total fluorescence intensity of CN-MBE and the relative abundance of J-aggregates in a DCE droplet during solvent evaporation. The total fluorescence intensity significantly and monotonically increased after 98 s and became constant after 110 s. The relative abundance of the J-aggregates increased after 97 s and became constant (0.97) after 102 s. Therefore, the rate of J-aggregate formation is faster than the increase in total fluorescence intensity,

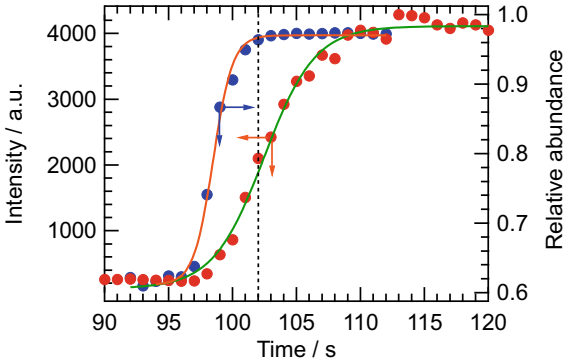

Fig. 2.15 Change in fluorescence intensity (red circles) and relative abundance of J-aggregate (blue circles) of CN-MBE as a function of time. The solid line is a curve fit based on the sigmoidal function (see main text). Reproduced from Ref. [43] by permission of The Royal Society of Chemistry

indicating a time lag for the increase in fluorescence intensity for J-aggregates. The time at which a constant fraction of J-aggregates is reached (102 s) appears to coincide with the half maximum of the total fluorescence intensity (dashed vertical line as shown in Fig. 2.15). As mentioned above, the total fluorescence intensity is probably attributable to the amount of CN-MBE crystals, which implies that fluorescence spectral and intensity changes reflect crystal nuclei formation and crystal growth. This phenomenon was observed not only in the solvent evaporation process, but also for the water fraction dependence of the nanoparticle formation for CN-MBE, which supports our findings.

On the basis of classical nucleation theory, the time evolution of CN-MBE fluorescence spectra during solvent evaporation can be used to model droplet growth [45, 46]. Initially, the concentration in solution was relatively low; thus, an equilibrium state was established between the monomer and J-aggregates. The J-aggregates begin from the smallest cluster of two monomers formed via intermolecular interactions. This small cluster is unstable because of the unfavorable surface free energy and dissociates before crystal formation. As the concentration increases by solvent evaporation, there are aggregates (concentration fluctuations) in supersaturated solutions. As apparent in Fig. 2.15, the abundance of J-aggregates during solvent evaporation indicates the formation of subcritical clusters. In general, the nucleus formation rate J is given by the Arrhenius reaction rate equation: $J = A\exp(-\Delta G/k_{\mathrm{B}}T)$, where k_{B} is Boltzmann's constant, A is the pre-exponential factor, and ΔG is the Gibbs energy of cluster formation. Because of the energy barrier, critical nuclei formation is a competition between growth and dissolution. Therefore, the time lag between the J-aggregate abundance, and the total fluorescence intensity indicates that the growth from J-aggregates to crystal nuclei is the rate-determining step of nucleation. Whether nuclei formation occurs depends on whether there is classical nucleation theory or not, although clearly only in the present results.

Amyloid fibril formation has been probed with thioflavin T (ThT) fluorescent dye [47], which is essentially nonfluorescent in solution [48]. An interaction with, or binding to, the amyloid fibril results in fluorescence enhancement; thus, ThT is a powerful tool for studying the kinetics of fibril formation, which is analogous to

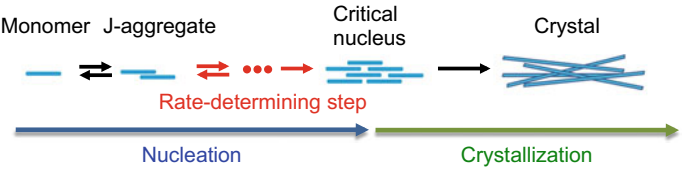

Fig. 2.16 Schematic of CN-MBE crystal formation based on changes in fluorescence spectra. Reproduced from Ref. [43] by permission of The Royal Society of Chemistry

the organic crystal formation. We can use the fibrillation kinetics to model the initial stage of CN-MBE crystal formation. A sigmoidal function can be used to obtain an estimate of the time required for aggregation to level off [49],

$$I = I_{\text{base}} + \frac{I_{\max}}{1 + \exp[-k(t_{\text{half}} - t)]} \tag{2.4}$$

where I is fluorescence intensity, I_{base} and $I_{\max}$ are, respectively, the fluorescence intensity before and after the change, k is the apparent rate constant for the growth, and t_{half} is the time to half of maximal fluorescence. The time evolution of the fluorescence intensity and the relative abundance of J-aggregates were well reproduced by Eq. 2.1. The larger values of k and t_{half} for growth of the J-aggregates relative to those for the fluorescence intensity strongly support the notion that J-aggregates act as precursors for crystal nuclei. The solvent dependence for the time evolution depends on the kinetic values associated with the boiling point and polarity of solvents, although it did not depend on the sigmoidal behavior. It is suggested that the molecular assembly kinetics mainly govern the increase in the local concentration of the droplets. The initial stages of crystal nuclei and crystal formation are schematically depicted in Fig. 2.16.

2.5 Summary

The present method allows crystal formation to be observed using a conventional optical detection system under ambient conditions, making it attractive to study the control of polymorphism of organic emissive materials with multiple emissive states or colors depending on their phase, such as mechanofluorochromic materials.

The study has clearly confirmed that the two-step nucleation model is based on the fluorescence color change. The intermediate state, such as the liquid-like cluster, is an important indicator of polymorphic expression, the origin of which will be key to understanding. The present method has low requirements for experimental equipment because the crystal formation can be observed using a conventional optical detection system under the ambient atmosphere, especially the control of polymorphism for organic emissive materials with multiple emissive states or color depending on the

phase such as mechanofluorochromic molecules. The method represents a direct visualization of Ostwald's rule of stages during the phase change of organic molecular solids, including the inhomogeneous phenomena.

Acknowledgements The authors thank Mr. Jun-ichi Fujimori, Ms. Yukino Suzuki, Ms. Mai Saigusa, and Prof. Naoki Kanayama (Shinshu University); Dr. Mitsuo Hara and Prof. Takahiro Seki (Nagoya University); and Dr. Ryohei Yasukuni, and Prof. Marc Lamy de la Chapelle (Paris 13 University) for their support for the experiment and kind discussion. We also thank Dr. Kennosuke Itoh (Shinshu University) for the NMR measurements. This work was partly supported by the Nanotechnology Platform Program, by JSPS KAKENHI Grants Numbers JP21750021, JP15H01081, JP17H05253, JP19H02686, by the Iketani Science and Technology Foundation, and by the JGC-S Scholarship Foundation.

References

1. Wolde, P.R., Frenkel, D.: Enhancement of protein crystal nucleation by critical density fluctuations. Science **277**, 1975–1978 (1997)
2. Erdemir, D., Lee, A.Y., Myerson, A.S.: Nucleation of crystals from solution: classical and two-step models. Acc. Chem. Res. **42**, 621–629 (2009)
3. Vekilov, P.G.: The two-step mechanism of nucleation of crystals in solution. Nanoscale **2**, 2346–2357 (2010a)
4. Schwoerer, M., Wolf, H.C.: Organic Molecular Solids. Wiley-VCH, Weinheim, Germany (2007)
5. Ye, X., Liu, Y., Lv, Y., Liu, G., Zheng, X., Han, Q., Jackson, K.A., Tao, X.: In situ microscopic observation of the crystallization process of molecular microparticles by fluorescence switching. Angew. Chem. Int. Ed. **54**, 7976–7980 (2015)
6. Tran, V.L., Genot, V., Audibert, J.F., Prokazov, Y., Turbin, E., Zuschratter, W., Kim, H.J., Jung, J., Park, S.Y., Pansu, R.B.: Nucleation and growth during a fluorogenic precipitation in a micro-flow mapped by fluorescence lifetime microscopy. New J. Chem. **40**, 4601–4605 (2016)
7. Zheng, C., Zang, Q., Nie, H., Huang, W., Zhao, Z., Qin, A., Hu, R., Tang, B.Z.: Fluorescence visualization of crystal formation and transformation processes of organic luminogens with crystallization-induced emission characteristics. Mater. Chem. Front. **2**, 180–188 (2018)
8. Halik, M., Wenseleers, W., Grasso, C., Stellacci, F., Zojer, E., Barlow, S., Bredas, J.L., Perry, J.W., Marder, S.R.: Bis(dioxaborine) compounds with large two-photon cross sections, and their use in the photodeposition of silver. Chem. Commun. 1490–1491 (2003)
9. Cogne-Laage, E., Allemand, J.F., Ruel, O., Baudin, J.B., Croquette, V., Blanchard-Desce, M., Jullien, L.: Diaroyl(methanato)boron difluoride compounds as medium-sensitive two-photon fluorescent probes. Chem. Eur. J. **10**, 1445–1455 (2004)
10. Ono, K., Yoshikawa, K., Tsuji, Y., Yamaguchi, H., Uozumi, R., Tomura, M., Taga, K., Saito, K.: Synthesis and photoluminescence properties of BF2 complexes with 1,3-diketone ligands. Tetrahedron **63**, 9354–9358 (2007)
11. Zhang, G.Q., Lu, J.W., Sabat, M., Fraser, C.L.: Polymorphism and reversible mechanochromic luminescence for solid-state difluoroboron avobenzone. J. Am. Chem. Soc. **132**, 2160–2162 (2010)
12. Zhang, G.Q., Singer, J.P., Kooi, S.E., Evans, R.E., Thomas, E.L., Fraser, C.L.: Reversible solid-state mechanochromic fluorescence from a boron lipid dye. J. Mater. Chem. **21**, 8295–8299 (2011)
13. Samonina-Kosicka, J., DeRosa, C.A., Morris, W.A., Fan, Z.Y., Fraser, C.L.: Dual-emissive difluoroboron naphthyl-phenyl beta-diketonate polylactide materials: effects of heavy atom placement and polymer molecular weight. Macromolecules **47**, 3736–3746 (2014)

14. Sakai, A., Tanaka, M., Ohta, E., Yoshimoto, Y., Mizuno, K., Ikeda, H.: White light emission from a single component system: remarkable concentration effects on the fluorescence of 1,3-diaroylmethanatoboron difluoride. Tetrahedron Lett. **53**, 4138–4141 (2012)
15. Sakai, A., Ohta, E., Yoshimoto, Y., Tanaka, M., Matsui, Y., Mizuno, K., Ikeda, H.: Novel fluorescence domain "excited multimer" formed upon photoexcitation of continuously-stacked diaroylmethanatoboron difluoride molecules with fused π-orbital in crystals. Chem. Eur. J. **21**, 18128–18137 (2015)
16. Sagawa, T., Ito, F., Sakai, A., Ogata, Y., Tanaka, K., Ikeda, H.: Substituent-dependent backward reaction in mechanofluorochromism of dibenzoylmethanatoboron difluoride derivatives. Photochem. Photobiol. Sci. **15**, 420–430 (2016)
17. Ito, F., Sagawa, T.: Quantitative evaluation of thermodynamic parameters for thermal back-reaction after mechanically induced fluorescence change. RSC Adv. **3**, 19785–19788 (2013)
18. Zhang, G., Chen, J., Payne, S.J., Kooi, S.E., Demas, J.N., Fraser, C.L.: Multi-emissive difluoroboron dibenzoylmethane polylactide exhibiting intense fluorescence and oxygen-sensitive room-temperature phosphorescence. J. Am. Chem. Soc. **129**, 8942–8943 (2007)
19. Ito, F., Suzuki, Y., Fujimori, J., Sagawa, T., Hara, M., Seki, T., Yasukuni, R., de la Chapelle, M.L.: Direct visualization of the two-step nucleation model by fluorescence color changes during evaporative crystallization from solution. Sci. Rep. **6**, 22918 (2016)
20. Galer, P., Korosec, R.C., Vidmar, M., Sket, B.: Crystal structures and emission properties of the BF2 Complex 1-Phenyl-3-(3,5-dimethoxyphenyl)-propane-1,3-dione: multiple chromisms, aggregation- or crystallization-induced emission, and the self-assembly effect. J. Am. Chem. Soc. **136**, 7383–7394 (2014)
21. Schenning, A., Benneker, F.B.G., Geurts, H.P.M., Liu, X.Y., Nolte, R.J.M.: Porphyrin wheels. J. Am. Chem. Soc. **118**, 8549–8552 (1996)
22. Knezic, D., Zaccaro, J., Myerson, A.S.: Nucleation induction time in levitated droplets. J. Phys. Chem. B **108**, 10672–10677 (2004)
23. Hughes, C.E., Harris, K.D.M.: A technique for in situ monitoring of crystallization from solution by solid-state C-13 CPMAS NMR spectroscopy. J. Phys. Chem. A **112**, 6808–6810 (2008)
24. Hughes, C.E., Williams, P.A., Keast, V.L., Charalampopoulos, V.G., Edwards-Gau, G.R., Harris, K.D.M.: New in situ solid-state NMR techniques for probing the evolution of crystallization processes: pre-nucleation, nucleation and growth. Faraday Discuss. **179**, 115–140 (2015)
25. Harano, K., Homma, T., Niimi, Y., Koshino, M., Suenaga, K., Leibler, L., Nakamura, E.: Heterogeneous nucleation of organic crystals mediated by single-molecule templates. Nat. Mater. **11**, 877–881 (2012)
26. Garetz, B.A., Matic, J., Myerson, A.S.: Polarization switching of crystal structure in the nonphotochemical light-induced nucleation of supersaturated aqueous glycine solutions. Phys. Rev. Lett. **89**, 175501 (2002)
27. Vekilov, P.G.: Nucleation. Cryst. Growth Des. **10**, 5007–5019 (2010b)
28. Guo, C., Wang, J., Li, J., Wang, Z., Tang, S.: Kinetic Pathways and mechanisms of two-step nucleation in crystallization. J. Phys. Chem. Lett. **7**, 5008–5014 (2016)
29. Zhang, T.H., Liu, X.Y.: How does a transient amorphous precursor template crystallization. J. Am. Chem. Soc. **129**, 13520–13526 (2007)
30. Tsarfati, Y., Rosenne, S., Weissman, H., Shimon, L.J.W., Gur, D., Palmer, B.A., Rybtchinski, B.: Crystallization of organic molecules: nonclassical mechanism revealed by direct imaging. ACS Cent. Sci. **4**, 1031–1036 (2018)
31. Ito, F., Saigusa, M., Kanayama, N.: Chem. Lett in press (2019)
32. Lu, F.N., Jang, K., Osica, I., Hagiwara, K., Yoshizawa, M., Ishii, M., Chino, Y., Ohta, K., Ludwichowska, K., Kurzydlowski, K.J., Ishihara, S., Nakanishi, T.: Supercooling of functional alkyl-p molecular liquids. Chem. Sci. **9**, 6774–6778 (2018)
33. Ariga, K., Endo, K., Aoyama, Y., Okahata, Y.: QCM analyses on adsorption of gaseous guests to cast films of porphyrin-resorcinol derivatives. Colloids Surf. A **169**, 177–186 (2000)

34. Lakowicz, J.R.: Radiative decay engineering: biophysical and biomedical applications. Anal. Biochem. **298**, 1–24 (2001)
35. Ito, F., Ohta, R., Yokota, Y., Ueno, K., Misawa, H., Nagamura, T.: Near-infrared fluorescence enhancement by regularly arranged gold nanoblocks. Chem. Lett. **39**, 1218–1219 (2010)
36. Sauerbrey, G.: Verwendung von Schwingquarzen zur Wägung dünner Schichten und zur Mikrowägung. Zeitschrift für Physik **155**, 206–222 (1959)
37. Kanazawa, K.K., Gordon, J.G.: Frequency of a quartz microbalance in contact with liquid. Anal. Chem. **57**, 1770–1771 (1985)
38. Muramatsu, H., Tamiya, E., Karube, I.: Computation of equivalent circuit parameters of quartz crystals in contact with liquids and study of liquid properties. Anal. Chem. **60**, 2142–2146 (1988)
39. Kubono, A., Akiyama, R.: Viscoelastic analysis in the formation of organic thin films. Mol. Cryst. Liq. Cryst. **445**, 213–222 (2006)
40. Tang, B.Z., Qin, A.: Aggregation-Induced Emission: Fundamentals. Wiley, United Kingdom (2013)
41. Hong, Y.N., Lam, J.W.Y., Tang, B.Z.: Aggregation-induced emission. Chem. Soc. Rev. **40**, 5361–5388 (2011)
42. An, B.K., Kwon, S.K., Jung, S.D., Park, S.Y.: Enhanced emission and its switching in fluorescent organic nanoparticles. J. Am. Chem. Soc. **124**, 14410–14415 (2002)
43. Ito, F., Fujimori, J.I.: Fluorescence visualization of the molecular assembly processes during solvent evaporation via aggregation-induced emission in a cyanostilbene derivative. CrystEngComm **16**, 9779–9782 (2014)
44. Ito, F., Fujimori, J., Oka, N., Sliwa, M., Ruckebusch, C., Ito, S., Miyasaka, H.: AIE phenomena of a cyanostilbene derivative as a probe of molecular assembly processes. Faraday Discuss. **196**, 231–243 (2017)
45. Davey, R.J., Schroeder, S.L.M., ter Horst, J.H.: Nucleation of organic crystalsa molecular perspective. Angew. Chem. Int. Ed. **52**, 2166–2179 (2013)
46. Okutsu, T.: Photochemically-induced crystallization of protein. J. Photochem. Photobiol. C **8**, 143–155 (2007)
47. Buxbaum, J.N., Linke, R.P.: A molecular history of the amyloidoses. J. Mol. Biol. **421**, 142–159 (2012)
48. Stsiapura, V.I., Maskevich, A.A., Kuzmitsky, V.A., Uversky, V.N., Kuznetsova, I.M., Turoverov, K.K.: Thioflavin T as a molecular rotor: fluorescent properties of Thioflavin T in solvents with different viscosity. J. Phys. Chem. B **112**, 15893–15902 (2008)
49. Nielsen, L., Khurana, R., Coats, A., Frokjaer, S., Brange, J., Vyas, S., Uversky, V.N., Fink, A.L.: Effect of environmental factors on the kinetics of insulin fibril formation: elucidation of the molecular mechanism. Biochemistry **40**, 6036–6046 (2001)

Chapter 3
Anti-solvent Crystallization Method for Production of Desired Crystalline Particles

Hiroshi Takiyama

Abstract Anti-solvent crystallization is widely used in the pharmaceutical industry from the viewpoint of the ambient temperature operating condition and high yield production. In the anti-solvent crystallization, the quality control of crystalline particles is necessary. Since polymorphism phenomena affect dissolution property, productivity, and bioavailability, it is important to control polymorph formation. The consideration of the solution addition methods to control polymorph in anti-solvent crystallization is engineering challenge. In this chapter, the operation design and/or operating strategies to obtain crystalline particles with the desired polymorph are described. The ternary phase diagram is proposed to control polymorphs. In order to determine both the anti-solvent addition rate and a temperature profile, the temperature-dependent solid–liquid equilibrium (ternary phase diagram) is necessary. By using this operation design and the simulation, the required polymorph is successfully obtained in the anti-solvent crystallization. The proposed operation design method by using the operation point trajectory is effective for controlling crystal quality in the anti-solvent crystallization.

Keywords Anti-solvent crystallization · Ternary phase diagram · Polymorphism · Pharmaceuticals

3.1 Introduction

Crystal products are widely found in pharmaceutical, food, fine chemicals, agrichemicals, cosmetic, and many other industries. Crystallization is the process of formation of ordered three-dimensional molecular array (crystal) from solution, melt, or gas. This process has been used as a method to produce crystalline particles and as a way to separate and purify the desired component. There are many types of crystallization. In each type, the solubility of solute is reduced by lowering the temperature

H. Takiyama (✉)
Department of Chemical Engineering, Tokyo University of Agriculture and Technology (TUAT), Tokyo, Japan
e-mail: htakiyam@cc.tuat.ac.jp

M. Sakamoto and H. Uekusa (eds.), *Advances in Organic Crystal Chemistry*,
https://doi.org/10.1007/978-981-15-5085-0_3

(cooling crystallization), removing the solvent (evaporative crystallization), the addition of anti-solvent (anti-solvent/drowning-out crystallization), activating a reaction (reaction crystallization), and sublimation of solute (vapor crystallization). As in most industrial crystallization processes, polymorph, crystal morphology, and size are important qualities of crystal products. These qualities can have a huge impact on downstream processes. Fluidity, granularity, and compressibility of crystals may differ due to the polymorph, morphology, and size. Hence, solid–liquid separation characteristics, washing and drying process, tableting operation will be affected. Eventually, the time of process, purity, and cost of the products will also be affected. In addition, solubility of crystals also varies with crystal polymorph, morphology, and size. This causes significant effects on the bioavailability and safety of medicine in pharmaceutical field. Therefore, it is crucial to control the crystal polymorph, morphology and size. In anti-solvent crystallization, when anti-solvent or solvent mixture is added into the crystallizer, the solubility of the solute will be reduced, and supersaturation which acts as the driving force of crystallization is generated. Since this method can be carried out in ambient temperature, it is suitable for the production or separation of heat-sensitive materials.

Polymorphism means that a compound has two or more crystal structures. Differences in crystal structures cause changes in physicochemical properties. In the pharmaceutical industry, it is necessary to control polymorphs because of their differences in bioavailability. There are many papers on the effects of operation factors such as solvent and solution concentration. In particular, polymorphic crystallization is affected by solvents, different polymorphs can be obtained from solutions with different solvents. In the manufacture of pharmaceuticals, anti-solvent crystallization is widely used from the viewpoint of high yield production. However, it is difficult to select the suitable operating conditions for controlling polymorph formation in anti-solvent crystallization because a particular polymorph may precipitate at limited temperatures and in limited solvent compositions.

Much effort has been devoted to determine the influence of operating conditions on crystal polymorph in anti-solvent crystallization, such as feeding rate, feed and bulk concentration, agitation rate, and so on. It was found out that the operating conditions have strong effects on the qualities of crystalline particles. Therefore, if the relationship between crystal polymorph and operating conditions can be clarified, we can easily determine the operating conditions and design the optimum method to obtain desired crystal polymorph.

3.2 Anti-solvent Crystallization

3.2.1 Theory and Characteristics

In anti-solvent crystallization, supersaturation (driving force) is produced by adding anti-solvent or solvent mixture into a solution. This will reduce the solubility of the

solute in the solution and crystal will be produced. This crystallization process is often used especially in pharmaceutical industry.

The characteristics of anti-solvent crystallization are described as follows [1]:

(a) Operation at ambient temperature
This crystallization method is operated at ambient temperature and it is not necessary to heat up or cool down the crystallizer in order for crystallization. This will have huge benefits in terms of cost and expenditure. Additionally, it is suitable for crystallization of heat-sensitive materials such as biomaterial and pharmaceutical products. Moreover, crystallization of soluble materials whose solubility is weak in temperature dependency can be carried out too.

(b) High yield in productivity
Just by adding the solution, supersaturation will be generated and crystal will be produced within a shorter period of time. Besides that, in the case where there is still solute dissolved in solution, adding more anti-solvent will help in the solute recovery process.

(c) Unique product quality
Compared to cooling crystallization, wide attainability of supersaturation can be achieved. With higher supersaturation, nucleation rate will increase and fine crystals can be easily produced. However, with the generation of more fine crystals, crystals will agglomerate and there will be difficulty in solid–liquid separation process.

3.2.2 Ternary Phase Diagram

In order to further understand the anti-solvent crystallization process, it is easier to use a ternary phase diagram. Considering a solute dissolved at an arbitrary temperature. The solubility curve is shown in a ternary phase diagram as in Fig. 3.1. E (solute)–B (original solvent)–A (anti-solvent) system is considered. Solution A is the anti-solvent-rich solution and solution B is the original solvent-rich saturated solution. When solution A and B with mass m_A and m_B are mix together the mass ratio will become $m_A : m_B = \alpha:\beta$ from the principle of lever rule, and the apparent mix solution will be at point M. Since solution M is supersaturated, crystals will be generated and the composition of the solution will move to point S which is the equilibrium point.

Concentration difference, ΔC can be express as

$$\Delta C = C_0 - C^* \tag{3.1}$$

C^* represents the equilibrium concentration. Saturation ratio, S and Supersaturation ratio, σ can be written as

$$\ln\frac{C_0}{C^*} = \ln S = \ln\left(1 + \frac{(C_0 - C^*)}{C^*}\right) = \ln\left(1 + \frac{\Delta C}{C^*}\right) = \ln(1+\sigma) \cong \sigma \tag{3.2}$$

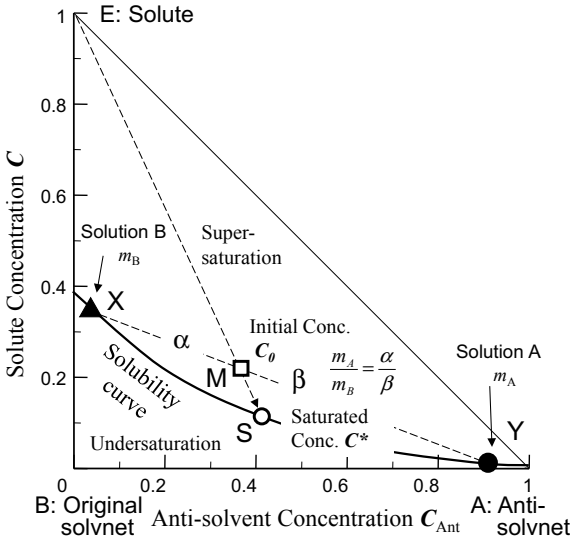

Fig. 3.1 Definition of anti-solvent crystallization using ternary phase diagram

3.3 Crystal Polymorph

Polymorphism means the phenomenon in which the same compound shows two or more crystal structures. In the case of the organic substances, the network structure of the hydrogen bond is different in every polymorph [2]. The characterization of polymorph is possible by X-ray powder diffraction (XRD) and thermal analysis. If the crystallization of each polymorph is not controlled, various problems of production or quality occur.

(1) Stability [3]:
Transformation from a metastable polymorph to a stable polymorph occurs, and crystalline qualities are not guaranteed.
(2) Industrial characteristics:
Solid–liquid separation performance changes because crystal morphology also changes.
(3) Bioavailability [4]:
Since the solubility, shape, density, etc. change bioavailability change as the result.

When crystal polymorph is produced selectively, it is very important to consider supersaturation change. For example, when crystallization material has two polymorphs, the precipitation behavior of the polymorph in a solution can be explained as Fig. 3.2 (monotropic system in which solubility does not cross). Metastable Form I deposits and solution concentration becomes the point *Q* with the growth of Form I. The solution state of the point *Q* is saturation for Form I, however, the solution state

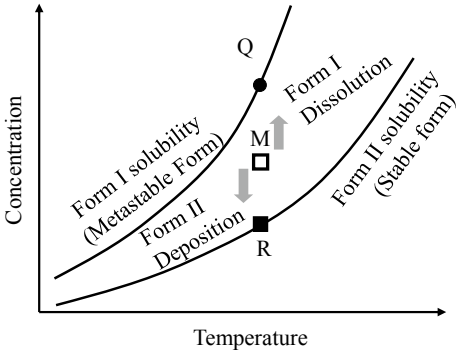

Fig. 3.2 Solution-mediated polymorph transformation

is supersaturation condition for Form II. If the nucleation of Form II occurs here, crystallization of Form II starts and solution concentration decreases. Since, the solution becomes undersaturated for Form I, Form I which already deposited dissolves. Therefore, in the region between solubility curves, solution-mediated transformation occurs as shown in Fig. 3.3.

Anti-solvent crystallization method is also important for the control of crystal polymorph [5] and morphology [6, 7]. Then, let's consider the operation of anti-solvent crystallization in which an operation point (solution concentration in ternary phase diagram) does not exceed the solubility of metastable form in ternary phase diagram. The example is explained in Fig. 3.4. If a pure anti-solvent is added in the solution (point *S*), the solution composition moves to the right along the straight line

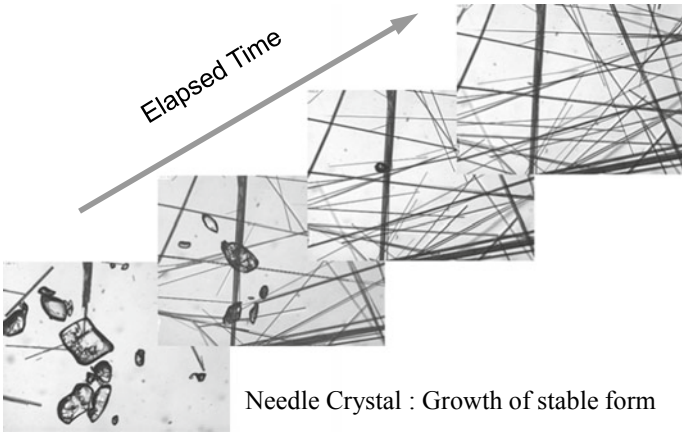

Fig. 3.3 Changes in polymorph crystals during solution-mediated polymorph transformation

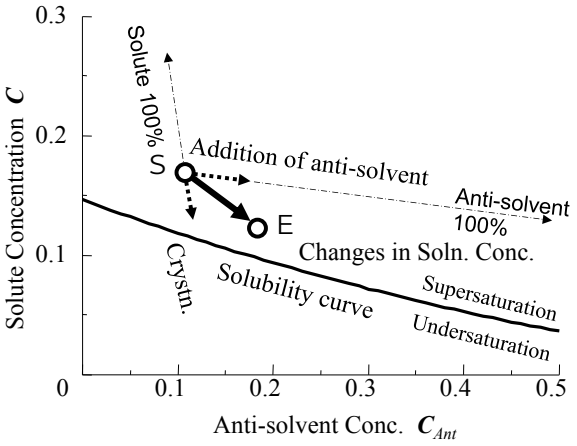

Fig. 3.4 Operation point for controlling polymorphism in anti-solvent crystallization

passing through the anti-solvent apex. Then, crystals deposit and solution composition move downward along the straight line which connects the apex of solute. Finally, solution composition moves in the direction of the lower right (point *E*). In this way, the traveling rate of operation point (solution composition) is decided by the addition rate of an anti-solvent, and the deposition rate of crystals [8, 9]. That is, the trajectory of operation point on a phase diagram is decided by the addition rate of an anti-solvent, and the deposition rate of crystals. Therefore, an operation design can be achieved if the solubility of the three-component system [10] is known in polymorph control of anti-solvent crystallization [5].

3.4 Controlling Polymorphism in Anti-solvent Crystallization

In order to select the suitable operating conditions for controlling polymorph formation in anti-solvent crystallization is difficult because a particular polymorph may precipitate at limited temperature and solvent composition [11, 12]. The crystallization behavior of polymorphous crystals depends on the anti-solvent addition rate and the initial concentration of the solution in the anti-solvent crystallization [7]. These phenomena were explained with operation point trajectory in phase diagram in which the stability regions of each polymorph were described. So it is necessary to determine the operating conditions such as anti-solvent feed rate for controlling polymorph formation. If several kinds of polymorph crystals precipitate and the target polymorph crystal is the stable form, the solvent-mediated transformation of metastable polymorph crystals must be completely suppressed in order to avoid contamination. To obtain only desired stable polymorph, it is required not to be precipitated metastable polymorph crystals. In the anti-solvent crystallization,

solubility profiles are essential data for crystallization operation design to selectively isolate the target polymorph. By using solubility data, operation strategies were designed [13], and the anti-solvent was added at controlled rates as reflected by the changes in the solubility curves. In such a way the operating conditions should be designed to obtain the target polymorph with consideration of solubility.

3.4.1 Operation Design of Anti-solvent Crystallization

Indomethacin (IMC)–Acetone (original solvent)–Heptane (anti-solvent) is a target system in this chapter. There are several polymorphs and solvates in IMC [14, 15]. Two polymorphs (α-form and γ-form) were mainly handled this study chapter. The solubility of each polymorph was measured in detail by using pure α-form and γ-form crystals. Temperature and composition of mixed solvent (acetone and heptane) were changed as the experimental conditions. The stable and metastable polymorph solubilities were determined by measuring solution concentration during solution-mediated transformation. From the experimental results, the ternary phase diagram of IMC–acetone–heptane system was prepared based on the mass fraction.

In the anti-solvent crystallization for IMC, supersaturation was generated by adding heptane (anti-solvent) and the crystals were precipitated. Operation strategy for controlling polymorph formation based on ternary phase diagram is shown in Fig. 3.5 as a rectangular triangle diagram. Figure 3.5 is the part of ternary phase diagram. In order to perform anti-solvent crystallization in the operation area where only a certain polymorphism (γ-form was a target polymorph in this study) deposits, it is necessary to control the feed rate of heptane according to the deposition rate of γ-form. If α-form crystals deposit in the solution, it is difficult to agitate the slurry because agglomerated α-form crystals have cotton-like shape. By the consideration of a ternary phase diagram [16], an operation point leaves from a solubility curve by addition of heptane. According to ternary phase diagram, when the anti-solvent is fed to the solution, an operation point moves to $w_{\mathrm{H}} = 1.0$ by using lever rule along with the line *A*. When the crystals are deposited, an operation point closes to solubility curve along the line *B* by using lever rule. Finally, an operation point moves toward resultant vector of anti-solvent addition rate and crystal deposition rate. An operation point becomes higher supersaturation by anti-solvent addition and then an operation point approaches a solubility curve by precipitation of IMC. Hence, the operation point can pass through a specific solution concentration range which does not exceed the solubility of α-form (undesired polymorph) by choosing the optimal anti-solvent feed rate suitably.

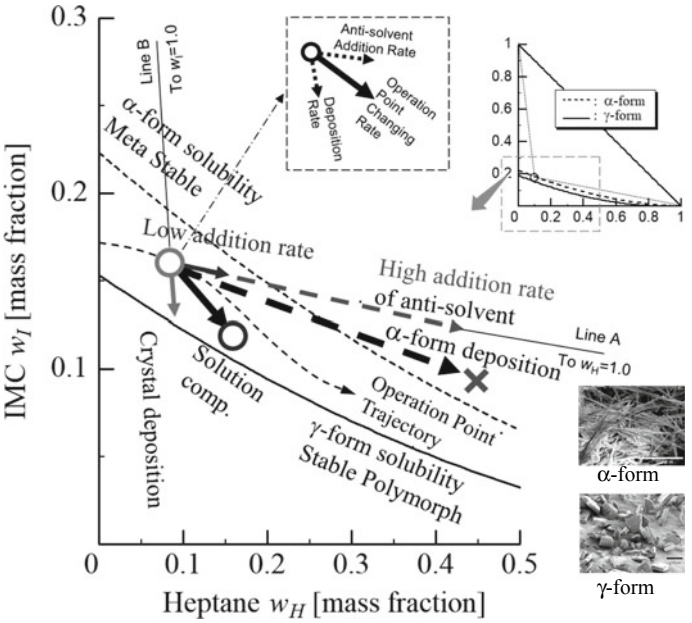

Fig. 3.5 Operation strategy for controlling polymorphism in IMC anti-solvent crystallization

3.4.2 Simulation Model for Operation Point Trajectory

In order to determine suitable anti-solvent feed rate, the anti-solvent crystallization model for calculating the operation point during crystallization was proposed. The assumptions of this operation model for seeding type anti-solvent crystallization are as follows.

(1) The shape of crystal (γ-form) does not change.
(2) The supersaturation of a solution is consumed with growth of γ-form seed crystals.

The growth rate expressed the difference of solution concentration as a driving force (Eqs. 3.3 and 3.4).

$$\frac{\mathrm{d}W}{\mathrm{d}t} = K\Phi_{\mathrm{s}}\left(\frac{W}{\Phi_s \rho_{\mathrm{c}}}\right)^{2/3} \rho_{\mathrm{L}}\left(w - w^*\right)^m \tag{3.3}$$

$$\frac{\mathrm{d}W}{\mathrm{d}t} = K_{\mathrm{g}}^{'}(W)^{2/3}\left(w - w^*\right)^m \tag{3.4}$$

Growth rate constant K'_{g} and the growth order m were computed by optimization calculation from the solution concentration change of preliminary γ-form crystal precipitation experiments.

The IMC concentration change of the solution was predicted from the simulation result. The operation model is as follows.

$$\frac{\mathrm{d}W}{\mathrm{d}t} + \frac{\mathrm{d}M}{\mathrm{d}t} = P_{\mathrm{H}} \tag{3.5}$$

$$\frac{\mathrm{d}W}{\mathrm{d}t} + M\frac{\mathrm{d}w}{\mathrm{d}t} + w\frac{\mathrm{d}M}{\mathrm{d}t} = 0 \tag{3.6}$$

$$w_{\mathrm{H}}(t) = \frac{\int_0^t P_{\mathrm{H}}\mathrm{d}t}{Mw + M_0 - M_0 w_0 + \int_0^t P_{\mathrm{H}}\mathrm{d}t} \tag{3.7}$$

Equation (3.5) is total mass balance of semi-batch operation for anti-solvent crystallization. Equation (3.6) is IMC component mass balance and Eq. (3.7) is heptane composition in the solution at time t.

3.4.3 *Simulation Results Under the Condition of Isothermal*

The solution concentration (operation point) simulation which changed the feed rate of anti-solvent during crystallization was carried out, and the results of solution concentration change are shown in Fig. 3.6. The results obtained under the condition of three different feed rates are compared. Operating period until the solution composition w_H reaches 0.4 is shown in Table 3.1.

Under the conditions of feed rate $P_{\mathrm{H}} = 0.01$, an operation point does not exceed the solubility of α-form (undesired polymorph). However, operating period became long. On the other hand, when the feed rate is fast (for example, $P_{\mathrm{H}} = 0.1$), the

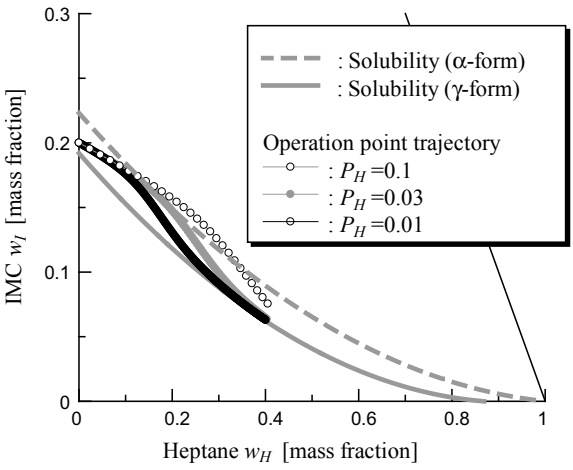

Fig. 3.6 Changes in solution concentration and operation point depending on anti-solvent feed rate ($\boldsymbol{w_{\mathrm{H}}} <$ 0.4)

Table 3.1 Comparison of operating period (crystallizer volume = 1000 mL, w_H = 0.4)

P_H (g/s)	Operating period (h)
0.01	4.2
0.03	1.4
0.1	0.4

operation point exceeds the solubility of α-form. From the simulation using the proposed model, the anti-solvent feed rate conditions that an operation point does not exceed the solubility of α-form can be decided.

3.4.4 Operation Strategies of Anti-solvent Addition Rate

From the simulation results, when anti-solvent composition of mixed solution increased, it was clear that the driving force generated by addition of anti-solvent was consumed immediately. From these results, it is possible to increase the feed rate of anti-solvent in the latter half of anti-solvent crystallization operation, and it is expected that operating period can be shortened. Based on the result of $P_H = 0.03$, the simulation result under the conditions in which the feed rate of the anti-solvent is made to increase gradually according to solvent composition is shown in Fig. 3.7. The feed rate was changed from 0.02 g/s to 1.0 g/s (Profile-A: $P_H = 0.02$; $0 < t <$ 4200 s, $P_H = 0.06$; $4200 < t < 5100$ s, $P_H = 1.0$; $5100 < t < 5400$ s). According to the simulation result, an operation point does not exceed the solubility of α-form.

Under Profile-A condition, the anti-solvent crystallization was carried out by using 1000 mL crystallizer. From the comparison between simulation and experimental results, the simulation results for solution concentration were good agreement with

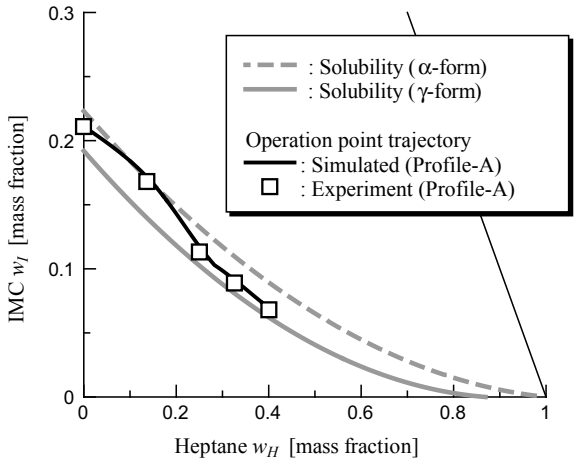

Fig. 3.7 Comparison between simulation and experimental results (Profile-A)

experimental results (Fig. 3.7). As the experimental result under Profile-A condition, the product crystal identified to be γ-form.

3.4.5 *Operation Strategies of Solution Addition Method*

In order to establish a production method of the target polymorph in the anti-solvent crystallization, the simulation model was proposed [5] to determine anti-solvent feed rate based on the ternary phase diagram. The stability of the polymorph of indomethacin (IMC) crystal in the solution changed not only with temperature but with the composition of the mixed solvent. And the design strategy of anti-solvent crystallization was proposed. It was reported that the modulation operation is effective for the improvement of crystal quality. The temperature modulated operation [17] was effective for improvement of crystal size distributions. So, the crystal quality may be further improved by integrating some crystallization operations. In the case of anti-solvent crystallization, desired crystal polymorphism may be achieved by integrating with solution addition method and temperature change operation.

Three kinds of anti-solvent addition methods were carried out. The anti-solvent addition rates in each experiment were determined by the simulation. Method A is the method that an anti-solvent is added at the constant flow rate. Method B is the method that the addition rate of anti-solvent increases in three stages. Method C is the method that an anti-solvent is added intermittently at the constant rate. The experimental conditions are summarized in Table 3.2.

Table 3.2 Experimental conditions and results in isothermal anti-solvent crystallization

Run	Method	Anti-solvent		Batch time (h)	Yield (%)	Polymorph
		Addition rate (g/min)	Addition period (min)			
1	A	0.726	120	2	29	γ-form
2	A	2.46	120	2	63	α- and γ-form
3	A	3.68	120	2	77	α- and γ-form
4	B	0.726 2.40 4.90	70 (0 $-$ 70) 30 (70 $-$ 100) 20 (100 $-$ 120)	2	58	γ-form
5	C	3.60	100 (20 min intermission)	2	59	α- and γ-form
6	C	2.46	110 (10 min intermission)	2	63	γ-form

3.4.5.1 Method A (Constant Addition Rate)

In Run 1, precipitation of α-form was not observed during the experiment. It became clear that γ-form can be selectively obtained from this result by using an anti-solvent addition rate with which solution composition does not approach the solubility of α-form.

In Run 2 and Run 3, α-form deposited during the experiment (Table 3.2). In order to obtain γ-form in stability, there is an anti-solvent addition rate that does not exceed the solubility curve of α-form. It is confirmed that it is important to control the solution composition in the operation area where only γ-form deposits using the ternary phase diagram and the simulation. However, under the conditions of a constant addition rate, the batch operation time becomes long.

3.4.5.2 Method B (Gradual Change of Addition Rate)

It was understood that a crystal growth rate constant K'_g becomes large with anti-solvent (heptane) composition (Fig. 3.8). Using the nature of this crystallization phenomenon, if an anti-solvent addition rate increases gradually, the batch operation time will be shortened. Then, the endpoint of Method A and Method B (Run 4) were compared by the simulation. The results of the solution composition trajectory are shown in Fig. 3.9.

Under the same batch time condition, the endpoint of Method A (Run 1) is $w_H = 0.29$ (yield 29%) and Method B (Run 4) is $w_H = 0.52$ (yield 58%), respectively. In this way, when Method B is used, it is expected that the yield can increase even in the same batch operation time. From the experimental result of Run 4, γ-form was selectively obtained in 2 h after the experiment start-up (Table 3.2).

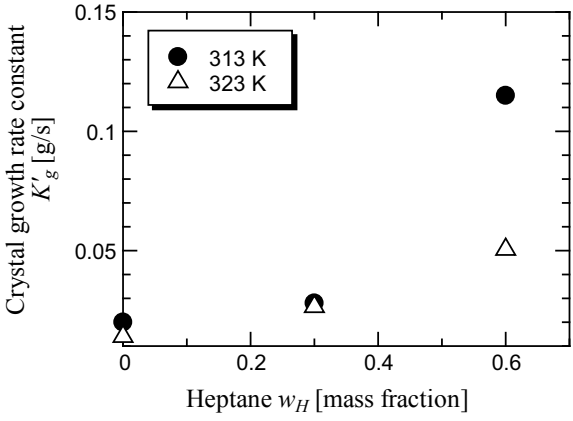

Fig. 3.8 Anti-solvent composition dependence crystal growth rate constant K'_g at 313 and 323 K

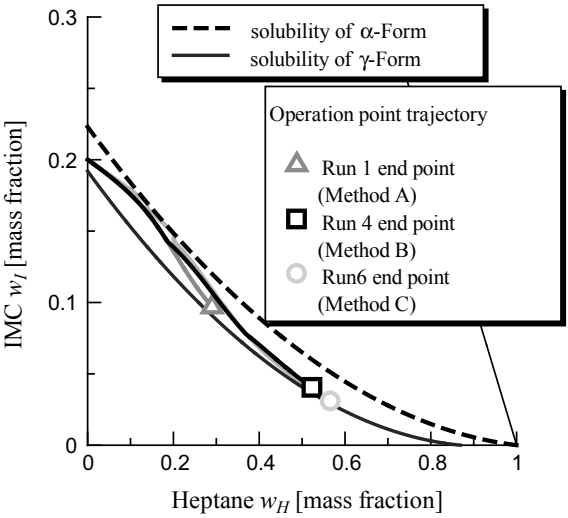

Fig. 3.9 Solubility curves for α-form and γ-form, and solution composition trajectories of Method A (Run 1), Method B (Run 4) and Method C (Run 6)

3.4.5.3 Method C (Intermittent Anti-solvent Addition)

In order to shorten batch operation time, it is necessary to supply an anti-solvent at a high addition rate. However, the existence of local supersaturation near the anti-solvent addition position is a problem under this operating condition. If the crystallization is carried out by using the lower addition rate than the critical rate at which the accumulation of α-form occurs by local supersaturation, and in the operation region in which solution composition does not exceed the solubility of α-form, it is considered that γ-form can be obtained selectively. In the early stage of Run 5, the plate-like crystal (γ-form) deposited. However, in the middle stage of Run 5, the cotton-like crystal deposited in large quantities. In Run 6, although the cotton-like crystal deposited in the middle of the experiment, the crystals which suspended at the end of batch operation time became only γ-form (Fig. 3.9).

3.4.5.4 Analysis of Precipitated Crystal and Existence of A′-Form

The cotton-like crystal deposited in the middle stage of the experiment not only under the condition of Method C but also under the condition with which does not exceed the solubility of α-form. There is a report that solvate deposits in crystallization of IMC from an acetone solution. When the precipitated crystal was analyzed in detail, the cotton-like crystal was the solvate of acetone. Therefore, if the solubility of solvate (α'-form) is not taken into consideration, γ-form cannot be obtained selectively. The solubilities of each polymorph are shown in Fig. 3.10.

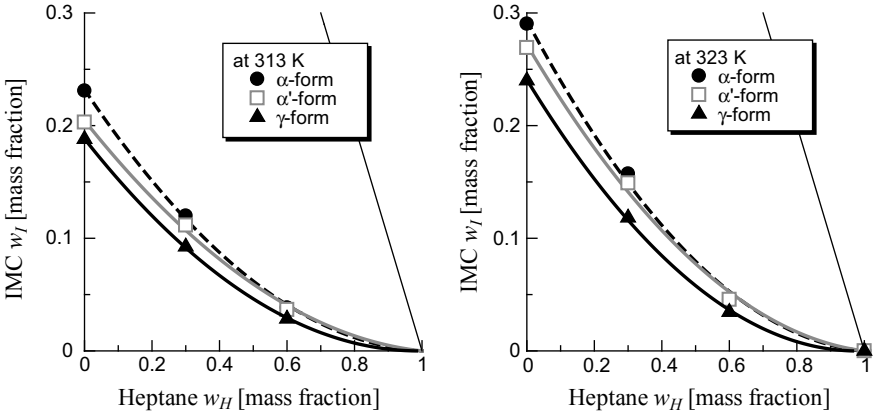

Fig. 3.10 Solubility curves of three kinds of IMC polymorph (α-form, α'-form and γ-form) at 313 and 323 K

3.4.5.5 Proposed Method D (Anti-solvent Crystallization with a Particular Temperature Profile)

If the operation point trajectory is maintained in the range between γ-form and α'-form solubility, a batch operation time becomes long under isothermal conditions. From the results of operation point trajectories, if the solution is heated when operation point approaches close to the solubility of α- or α'-form, it is possible to eliminate the limitation of the anti-solvent addition rate. In order to realize the anti-solvent crystallization incorporating heating operation, the temperature-dependent ternary phase diagram (Fig. 3.10) is necessary.

It is necessary to accelerate the anti-solvent addition rate in the early stages of an experiment for batch operation time shortening. Then, if the temperature-dependent solubility is applied, the increase in an addition rate is possible. As for the solubility of IMC in this system, temperature dependency becomes small in the region where heptane composition is high (Fig. 3.10). So, the increase in the addition rate in early stages of a batch operation time is the efficient crystallization method. Furthermore, since the deposition rate became accelerating in the high heptane composition region, it was considered that crystallization could be carried out without exceeding the solubility of α'-form. The experimental conditions are shown in Table 3.3.

In Run 7, linear heating was carried out from 313 to 333 K. The experimental result is shown in Fig. 3.11. Only γ-form was obtained without solution composition which exceeds the solubility of α'-form. However, the crystallization yield decreases, since the temperature of the end of operation becomes high when heating operation is incorporated. In this ternary system, a deposition rate increases with heptane concentration. If this crystallization phenomenon is used, recovery of yield is possible by incorporating cooling operation in the latter half of a batch operation time.

Table 3.3 Experimental conditions and results of Method D

Run	Method	Anti-solvent addition rate (g/min)	Batch time (h)	Temperature profile (K)	Final poly	Yield (%)
7	D	2.70	2	From 313 to 333	γ-form	27
8	D	2.70	2	From 313 to 323 and from 323 to 313	γ-form	65

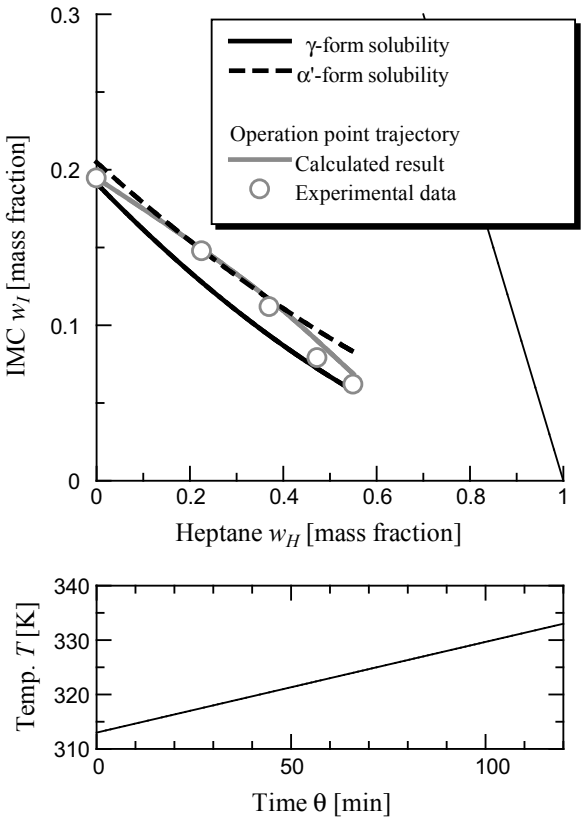

Fig. 3.11 Solubility curves for α'-form and γ-form in the ternary phase diagram and operation point trajectories of Method D (Run 7), and temperature profile of Run 7

In Run 8, the solution was heated by 10 K/h, and solution temperature was kept at 323 K for 30 min, and then it was cooled by 20 K/h for the last 30 min of a batch operation time (Fig. 3.12). Actual solution composition could be maintained in the region between α'-form and γ-form, and γ-form was obtained selectively. Thus, the particular temperature operation integrating the suitable temperature change was

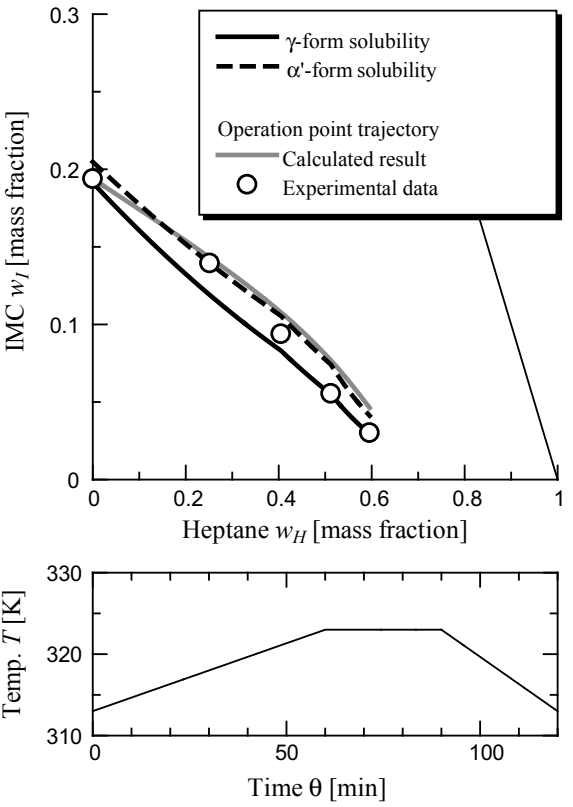

Fig. 3.12 Solubility curves for α'-form and γ-form in the ternary phase diagram and operation point trajectories of Method D (Run 8), and the particular temperature profile of Run 8

carried out for anti-solvent addition crystallization, and desired γ-form was able to be obtained in a short time with a certain level of yield.

3.5 Summary

The operation design of anti-solvent crystallization based on ternary phase diagram is proposed and the polymorphism precipitation phenomenon is discussed. The stability of the polymorph crystal in the solution changes not only with temperature but with the composition of the mixed solvent. The modeling of the crystallization operation for determining the optimal anti-solvent feed rate was carried out by using the ternary phase diagram, and the operation strategy for considering control of polymorph formation was proposed.

In the isothermal anti-solvent crystallization experiment, stable form is able to be selectively obtained by using the anti-solvent addition rate determined with the phase diagram. However, the solubility difference between metastable and stable

form is narrow. Therefore, if the operation point trajectory should not exceed the solubility of metastable form, the batch operation time becomes long by the limitation of anti-solvent addition rate. Then, by incorporating heating operation in anti-solvent crystallization, it becomes possible to increase an anti-solvent addition rate. Moreover, when the particular temperature operation is integrated into anti-solvent crystallization, target polymorph is successfully obtained with high yield compared with isothermal conditions.

References

1. Takiyama, H.: Supersaturation operation for quality control op crystalline particles in solution crystallization. Advanced Powder Tech. **23**, 273–278 (2012)
2. Slavin, P.A., Sheen, D.B., Shepherd, E.E.A., Sherwood, J.N., Feederb, N., Docherty, R., Milojevic, S.: Morphological evaluation of the γ-polymorph of indomethacin. J. Crystal Growth. **237–239**, 300–305 (2002)
3. Morissette, S.L., Almarsson, O., Peterson, M.L., Remenar, J.F., Read, M.J., Lemmo, A.V., Ellis, S., Cima, M.J., Gardner, C.R.: High-throughput crystallization: polymorphs, salts, co-crystals and solvates of pharmaceutical solids. *Adv. Drug Delivery Rev.*, **56**, 275–300 (2004)
4. Singhal, D., Curatolo, W.: Drug polymorphism and dosage form design: a practical perspective. Adv. Drug Deliv. Rev. **56**, 335–347 (2004)
5. Takiyama, H., Minamisono, T., Osada, Y., Matsuoka, M.: Operation design for controlling polymorphism in the anti-solvent crystallization by using ternary phase diagram. Chem. Eng. Res. Des. **88**, 1242–1247 (2010)
6. Holmback, X., Rasmuson, A.C.: Size and morphology of benzoic acid crystals produced by drowning-out crystallisation. J. Crystal Growth **198**(199), 780–788 (1999)
7. Kitamura, M., Sugimoto, M.: Anti-solvent crystallization and transformation of thiazoled-erivative polymorphs-I: effect of addition rate and initial concentrations. J. Crystal Growth **257**, 177–184 (2003)
8. Galan, O., Grosso, M., Baratti, R., Romagnoli, J.A.: Stochastic approach for the calculation of anti-solvent addition policies in crystallization operations: An application to a bench-scale semi-batch crystallizer. Chem. Eng. Sci. **65**, 1797–1810 (2010)
9. Sheikhzadeh, M., Trifkovic, M., Rohani, S.: Real-time optimal control of an anti-solvent isothermal semi-batch crystallization process. Chem. Eng. Sci. **63**, 829–839 (2008)
10. Taboada, M.E., Graber, T.A., Asenjo, J.A., Andrews, B.A.: Drowning-out crystallisation of sodium sulphate using aqueous two-phase systems. J. Chromatogr. B **743**, 101–105 (2000)
11. Borissova, A., Dashova, Z., Lai, X., Roberts, K.J.: Examination of the semi-batch crystallization of benzophenone from saturated methanol solution via aqueous antisolvent drowning-out as monitored in-process using ATR FTIR spectroscopy. *J. Crystal Growth Des.*, **4**, 1053–1060 (2004)
12. Chang, S.M., Kim, J.M., Kim, I.H., Shin, D.M., Kim, W.S.: Agglomeration control of L-Ornithine aspartate crystals by operating variables in drowning-out crystallization. Ind. Eng. Chem. Res. **45**, 1631–1635 (2006)
13. Wang, J., Loose, C., Baxter, J., Cai, D., Wang, Y., Tom, J., Lepore, J.: Growth promotion by H_2O in organic solvent—selective isolation of a target polymorph. J. Crystal Growth **283**, 469–478 (2005)
14. Masuda, K., Tabata, S., Kono, H., Sakata, Y., Hayase, T., Yonemochi, E., Terada, K.: Solid-state 13C NMR study of indomethacin polymorphism. Int. J. Pharm. **318**, 146–153 (2006)
15. Slavin, P.A., Sheen, D.B., Shepherd, E.E.A., Sherwood, J.N., Feeder, N., Docherty, R., Milojevic, S.: Morphological evaluation of the γ-polymorph of indomethacin. J. Crystal Growth **237–239**, 300–305 (2002)

16. Takiyama, H., Otsuhata, T., Matsuoka, M.: Morphology of NaCl crystals in drowning-out precipitation operation. Chem. Eng. Res. Des. **76**, 809–814 (1998)
17. Takiyama, H., Shindo, K., Matsuoka, M.: Effects of undersaturation on crystal size distribution in cooling type batch crystallization. J. Chem. Eng. Japan **35**, 1072–1077 (2002)

Chapter 4
Crystal Nucleation of Proteins Induced by Surface Plasmon Resonance

Tetsuo Okutsu

Abstract The crystallization of lysozyme and ribonucleaseA was induced using photochemical reactions triggered by surface plasmon resonance of gold nanostructures. The tryptophan residues of the protein are radicalized by the enhanced electric field induced by surface plasmon resonance. This radical reacts in the protein molecule to produce a reaction intermediate in which a nearby tyrosine residue is radicalized. This reaction intermediate reacts with another protein to form a dimer linked by tyrosine residues. Since this dimer is covalently bonded, it is stable without decomposition. With this as a nucleus, it grows into a crystal. An enhanced electric field induced by surface plasmon resonance of gold nanostructures was used to radicalize amino acids in proteins. Surface plasmon resonance induced by visible light radicalizes amino acids by the same mechanism as multiphoton absorption. When a metastable solution of lysozyme and ribonucleaseA was dropped on the substrate on which the gold nanostructure was constructed, and surface plasmon resonance of the gold nanostructure was induced, crystals precipitated.

Keywords Surface plasmon resonance · Protein crystallization · Lysozyme · RibonucleaseA · Gold nanostructure

4.1 Introduction

Experiments to crystallize proteins are important in the fields of drug discovery and structural biology. In the field of drug discovery, we elucidate the structure of target proteins that cause diseases. Based on the information of its structure, molecules that exactly fit the protein, i.e., drugs, are designed and synthesized. In the field of structural biology, studies are being made to elucidate functions from protein structures. In these fields, in order to determine the structure of a protein, X-ray crystallography is carried out after crystallizing the protein [1]. In Japan, synchrotron radiation facilities such as SPring-8 have been built, and the technology of crystal

T. Okutsu (✉)
Division of Molecular Science Graduate School of Science and Technology, Gunma University, 1-5-1 Tenjin-cho, Kiryu-shi, Gunma-ken 376-8515, Japan
e-mail: okutsu@gunma-u.ac.jp

M. Sakamoto and H. Uekusa (eds.), *Advances in Organic Crystal Chemistry*,
https://doi.org/10.1007/978-981-15-5085-0_4

structure analysis has been advanced. At the same time, advances in science and technology to make crystals are desired.

Crystal growth of proteins is carried out by researchers in the field of drug discovery and biology using experience and intuition based on information in the literature and data base. On the other hand, basic research on crystal growth of proteins has been made from the viewpoint of crystal growth science regarding nucleation and growth mechanism [2]. In addition, researchers specializing in crystal growth have come into the business of crystallizing proteins for drug discovery [3].

There are several reasons why protein crystallization is more difficult than small-molecule substances. First, although proteins have large molecular weight, they aggregate with small intermolecular force such as van der Waals force and hydrogen bond, and therefore they have the property of being hard to crystallize. Protein is a colloidal particle with charge repulsion, and when it crystallizes, salting out cancels the charge and causes mild aggregation to crystallize. If the charge is roughly canceled, it will easily become an amorphous precipitate. Second, proteins have large molecular anisotropy and no symmetry. For this reason, there is a problem that when incorporated into the crystal phase, the crystal phase is entered only when approaching in a specific direction. Therefore, even in a supersaturation, small clusters are easily separated, so it is difficult to form a critical nucleus, and a supersaturated solution with a concentration many times that of the solubility still exists. Research to obtain protein crystals is to address these issues.

In recent years, as a method of crystal growth, a phenomenon that induces crystallization by the perturbation of light has been found and noted [4]. The action of light is roughly divided into physical perturbations and methods using chemical actions. Research using physical perturbations has been developed with a focus on groups in the United States and Osaka University. The Osaka University group has successfully commercialized protein crystallization as a venture business [5].

Our group has found the phenomenon of crystallization using chemical perturbation of light, and we have been working on elucidating its mechanism [6]. The crystallization of proteins induced by photochemical reactions is described. The appearance of the initial stage of crystal growth is shown in Fig. 4.1 by a model of ball gathering.

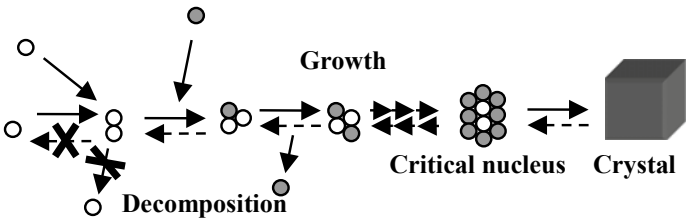

Fig. 4.1 Protein nucleation process and photoinduced crystallization mechanism. In the process of crystal nucleation, small aggregates below the critical nucleus are unstable and easily decomposed. Crystal nucleation is promoted by forming dimers that do not break covalent bonds through photochemical reactions

Two molecules meet and a bimolecular cluster is formed by intermolecular force due to hydrogen bonding or van der Waals force. Small clusters are unstable and do not grow spontaneously, but they grow spontaneously when they grow larger than the critical radius. In the case of a molecule such as a protein, even if the degree of supersaturation is large, the small clusters are often unstable and nucleation does not occur.

Imagine adding a stable bimolecular cluster bound covalently to the solution. The bimolecular cluster was the most unstable and easily dissociated, making it difficult to grow into a trimolecular cluster. However, if the bimolecular cluster is stable, it is easy to grow and a critical nucleus is easily formed. The protein crystallization method triggered by a photochemical reaction is to create a stable protein dimer in the system.

4.2 Photochemical Reaction of Proteins

Next, the relationship between the photochemical reaction of proteins and the mechanism of crystallization will be described. Figure 4.2 shows the chemical reactions that occur in proteins. First, the Trp residue absorbs light and becomes an excited state. At this time, a reaction intermediate in which the nitrogen atom on the five-membered ring is radicalized is generated [7, 8]. Then the radical undergoes a hydrogen abstraction reaction from the OH group of the neighboring Tyr residue, and the Tyr residue is radicalized. This radicalized protein has a long lifetime and reacts with other ground state proteins between collisions Tyr residues, and finally a protein dimer bound between Tyr–Tyr is formed [9].

The formation of this dimer can be observed by electrophoresis. The formation of the Tyr–Tyr bond can be confirmed by the characteristic fluorescence generated by the Tyr–Tyr bond. In hen egg-white lysozyme, dimers linked by Tyr^{53}–Tyr^{53} are generated. This dimer was found to resemble the arrangement of neighboring molecules in the crystal. It is thought that the dimer bonded at Tyr^{53}–Tyr^{53} grows into a crystal nucleus as a template. Nucleation by a similar mechanism has been shown using ribonucleaseA as a protein without thaumatin and Trp residues [10].

Fig. 4.2 Mechanism of photochemical reaction of protein. First, an excited state of tryptophan residue (Trp) is generated and radicalized. The radical transfer reaction proceeds in the molecule, and finally a reaction intermediate protein in which the tyrosine residue (Tyr) is radicalized is generated. This radical reacts to produce a protein dimer bonded between tyrosine, which functions as a template to grow into the crystal nucleus

In this study, we examined a method for inducing crystallization by photochemical reaction using a method that is not directly photoexcited amino acids of proteins [11, 12]. Protein was photoexcited using light of a wavelength at which the protein does not absorb. As a method for causing such photoexcitation, the reaction was induced with a reaction field based on a strong light-molecule coupling field constructed on a crystallization vessel. Proteins always have the problem of denaturation when exposed to ultraviolet light with light absorption. In order to examine the practical application of photoinduced crystallization, it is necessary to limit the amount of light to be irradiated to the minimum amount necessary for nucleation. In other words, it is necessary to carry out with as little light as possible. Excitation using a strong photo-molecular coupling field investigated in this study is equivalent to excitation by multiphoton absorption. Therefore, light absorption is a phenomenon that rarely occurs and excitation efficiency is extremely low. This is the same as using extremely weak light when excited by light absorption by one photon. The reaction field by the strong light-molecule coupling field was constructed in a commercially available crystallization vessel.

4.3 Reaction Field Using Light-Molecular Strong Coupling Field

The light-molecule strong coupling field used in this study is explained [13]. The light-molecule strong coupling field has a function of giving the influence of the electric field of light more strongly to the molecule. In this study, localized plasmon resonance was used as a strong light-molecule coupling field. In this field, chemical reaction of molecules was promoted. Brus et al. predicted that the reaction would theoretically be accelerated [14], Harris et al. reported that the aromatic photolysis reaction was promoted near the surface of silver nanoparticles [15].

Studies on reactions using multiphoton absorption by nonlinear optical phenomena using the electric field enhancement effect of plasmons are also progressing. For example, it is known that simultaneous two-photon absorption occurs when light having a high photon density. It has been also reported that simultaneous two-photon absorption is induced even when the plasmon-enhanced electric field by the steady light of the lamp [16, 17]. In this study, we investigated photoinduced crystallization that induces localized plasmon resonance by multiphoton absorption of visible light using gold nanostructures.

In this study, a checkerboard-like gold nanostructure and a gold-deposited film were used as a strong photo-molecular coupling field. Figure 4.3 shows a schematic diagram of the gold nanostructure. The gold nanostructure is a 100 nm × 100 nm, 40 nm-high gold nanostructure island aligned on a glass substrate at intervals of 200 nm. This structure was constructed in an area of 1 mm × 1 mm by electron beam drawing. Gold nanostructures were created in collaboration with a group of

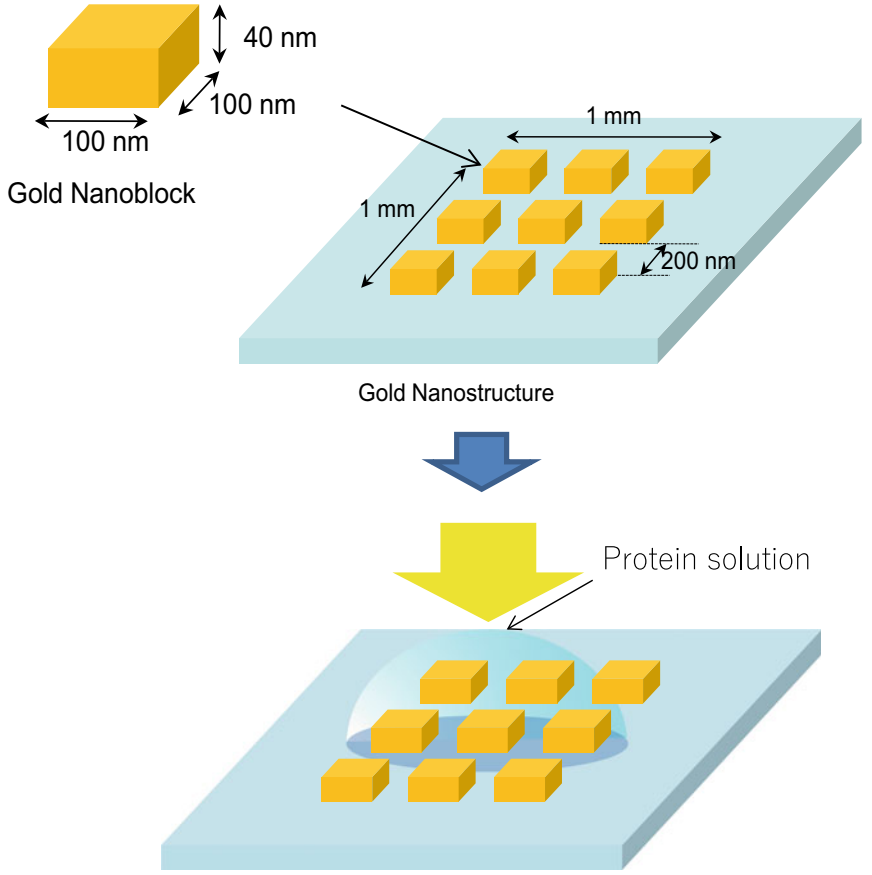

Fig. 4.3 Reaction field using plasmon resonance using photon-molecule strong coupling field with gold nanostructure

Prof. Hiroaki Misawa, Institute for Electrochemical Research, Hokkaido University. A 300 W Xe lamp was used as the irradiation light source.

4.4 Crystallization Experiment by Localized Plasmon Excitation

An experiment was carried out in which a protein solution was dropped on the gold nanostructure and irradiated with light. A supersaturated solution having a concentration three times the solubility was used as the protein solution. The crystallization experiment at this degree of supersaturation is at the boundary of whether or not

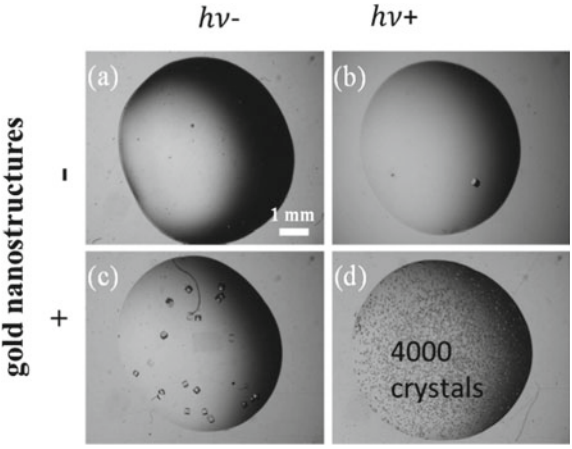

Fig. 4.4 Results of lysozyme crystallization experiment. Experimental results for the presence or absence of gold nanostructures and the presence or absence of light irradiation are shown. The appearance frequency of crystals increased remarkably in the presence of gold nanostructure and light irradiation

crystal nuclei appear spontaneously, and is a condition suitable for determining the effect of light-induced crystallization.

The presence or absence of gold nanostructures and the presence or absence of light irradiation on the protein solution on the substrate were compared. Figures 4.4a–d show photographs of the experimental results. Figures 4.4a–c are control experiments in which the protein solution was dropped onto a substrate without a gold nanostructure. (a) is without light irradiation and (c) is the result with light irradiation. No crystal appeared in (a), and one crystal appeared in (c). Since the solution used in this experiment is a solution having a boundary condition of "whether or not crystals appear spontaneously", variations occur in several appearance ranges depending on the droplets. (b) and (d) are experimental results on a substrate with a gold nanostructure. (b) shows the experimental results without light irradiation, and (d) shows the experimental results with light irradiation. In the experiment of (b), dozens of crystals appeared. This result can be said that the number of crystals appeared significantly increased compared to the experiments (a) and (c). In (d) about 4000 crystals appeared in the solution. Light-induced crystallization due to plasmon excitation of the gold nanostructure was confirmed. In the experiment of (b), the light of the Xe lamp was not applied, but the experiment was carried out under room light with a fluorescent lamp, and it is considered that crystals appeared due to the effect of the light of the fluorescent lamp, not the Xe lamp.

4.5 Reaction Field Construction and Crystallization Experiments with Gold-Sputtered Substrates

In the previous section, crystallization experiments were carried out using nanostructures. However, the construction of this nanostructure requires a long time. For example, it takes 20 h to create the 1 mm × 1 mm substrate shown in Fig. 4.3. It is

impossible for practical use to construct this nanostructure in a protein crystallization vessel. Localized plasmon resonance has been reported to occur on incompletely deposited metal films. In this study, we examined the effect of protein crystallization promotion by inducing plasmon resonance by thinly sputtered gold.

A sputtered gold film was thinly formed on a glass substrate. A gold sputtering apparatus for electron microscope (JEOL JFC-1500) used for preparation of SEM observation sample was used for the sputtered film preparation. The sample was prepared so that the thickness of the sputter was adjusted to 0–60 nm. Figure 4.5 shows the absorption spectrum of the sputtered film. An absorption peak appeared at 560 nm on the 10 nm thick substrate. This can be interpreted as that local plasmon resonance occurred because gold was in an island shape at the initial stage of sputtered deposition and had a structure similar to that of gold nanoparticles. As the thickness of the sputtered film was increased, the localized plasmon resonance at 560 nm disappeared, and broad absorption appeared at 500–1000 nm. This absorption is called gap mode plasmon resonance and is a characteristic spectrum of plasmon resonance caused by a film defect. Crystallization experiments were carried out with this substrate.

A protein solution was dropped using a crystallization vessel on which the gold thin film was sputtered, and visible light was irradiated. The crystallization experiment used a metastable state of supersaturation 3 ribonucleaseA solution. The experiment was carried out at a film thickness of 20 nm. The results are shown in Fig. 4.6. Crystals appeared under the condition of gold evaporation and light irradiation. From this result, we confirmed the effect of promoting crystallization when exciting localized plasmon in a thin and incompletely deposited film.

This method does not care about the problem of denaturation caused by excessive light and can obtain the effect of promoting crystallization without changing the experimental method conventionally carried out by researchers in the field of drug discovery. I think that it is useful.

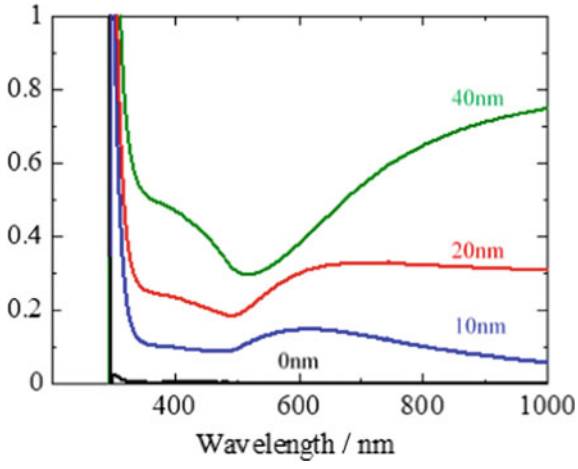

Fig. 4.5 Absorption spectrum of gold-sputtered thin film. The plasmon resonance of gold particles is visible at a film thickness of 10 nm, but gap mode absorption appears at a film thickness of 20 nm

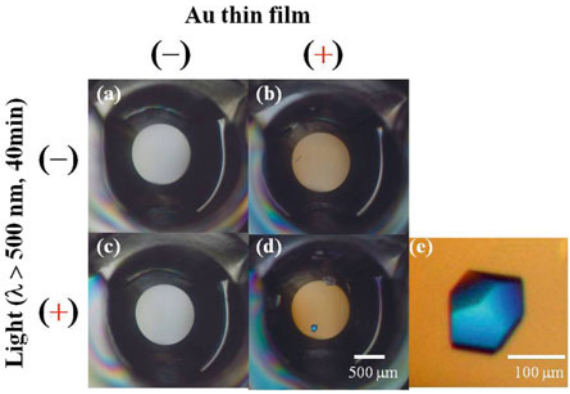

Fig. 4.6 Results of crystallization experiments on a sputtered gold substrate using ribonucleaseA. Crystals appeared under conditions of both gold sputtering and light irradiation

4.6 Future Prospective

Our recent experiments have found that crystallization is induced by a mechanism other than photochemical reactions. The enhanced electric field induced by surface plasmon resonance is said to have the same effect as optical tweezers. It has been suggested that the effect of optical tweezers may trap proteins and concentrate them locally, causing crystallization. We plan to study the phenomenon that protein crystallization is induced by this photophysical mechanism.

References

1. McPherson, A.: Preparation and Analysis of Protein Crystals. Krieger Publishing Company, Malabar, Florioda (1989)
2. Sugiyama, S., Maruyama, M., Sazaki, G., Hirose, M., Adachi, H., Takano, K., Murakami, S., Inoue, T., Mori, Y., Matsumura, H.: Growth of protein crystals in hydrogels prevents osmotic shock. J. Am. Chem. Soc. **134**, 5786–5789 (2012)
3. Sugiyama, S., Kashiwagi, K., Kakinouchi, K., Tomitori, H., Kanai, K., Murata, M., Adachi, H., Matsumura, H., Takano, K., Murakami, S., Inoue, T., Mori, Y., Igarashi, K.: Crystallization and preliminary crystallographicstudies of PotA, a membrane-associated ATPase of the spermidine-preferential uptake system in *Thermotoga maritima.* Acta Cryst. **F70**, 738–741 (2014)
4. Okutsu, T.: Light-induced crystal growth. J. Jpn. Assoc. Crystal Growth **38**, 160–160 (2011a)
5. Yoshikawa, H., Murai, Y., Sugiyama, S., Adachi, H., Matsumura, H., Inoue, T., Murakami, S., Takano, K., Mori, Y.: J. Jpn. Assoc. Crystal Growth **38**, 161–168 (2011)
6. Okutsu, T.: J. Jpn. Assoc. Crystal Growth **38**, 177–182 (2011b)
7. Grossweiner, L.I., Kaluskar, A.G., Baugher, J.F.: Flash photolysis of enzymes. Int. J. Radiat. Biol. **29**, 1–16 (1976)
8. Grossweiner, L.I., Usui, Y.: Sensitivity of chick embryos to ultraviolet radiation during early embryogenesis. Photochem. Photobiol. **13**,195–214 (1971)
9. Hashimoto, S.: Lysozyme dimer formation on lysozyme oxidation with Br 2 as studied by fluorescence evolution. Int. J. Radiat. Biol. **41**, 303–314 (1982)
10. Furuta, K., Horiuchi, H., Hiratsuka, H., Okutsu, T.: Photochemically induced nucleation of ribonucleaseA enhanced by a stable protein dimer produced from the photochemical reaction of Tyr residual groups. Crystal Growth Des. **8**, 1886–1889 (2008)

11. Haruta, S., Misawa, H., Ueno, K., Yokota, Y., Uehara, H., Hiratsuka, H., Horiuchi, H., Okutsu, T.: Protein crystallization induced by strong photons–molecules coupling fields photochemical reaction. J. Photochem. Photobiol. A: Chem. **221**, 268–272 (2011)
12. Tawa, K., Haruta, S., Okutsu, T., Nishii, J.: Photochemically induced crystallization of proteins accelerated on two-dimensional gold gratings. Jpn. J.Appl. Phys. (JJAP), **51,** 06FK09 (2012)
13. Okamoto, T., Kajikawa, K.: Plasmonics Kodansha (2010)
14. Nitzan, A., Brus, L.E.: Theoretical model for enhanced photochemistry on rough surfaces. J Chem. Phys. **75**, 2205 (1981)
15. Goncher, G.M., Persons, C.A., Harris, C.B.: Photochemistry on rough metal surface. J. Phys. Chem. **88**, 4200–4209 (1984)
16. Ueno, K., Juodkazis, S., Shibuya, T., Yokota, Y., Mizeikis, V., Sasaki, K., Misawa, H.: Nanoparticle plasmon-assisted two-photon polymerization induced by incoherent excitation source. J. Am. Chem. Soc. **130**, 6928–6929 (2008)
17. Tsuboi, Y., Shimizu, R., Shoji, T., Kitamura, N.: Near-ifrared continuous-wave light driving a two-photon photochromic reaction with the assistance of localized surface plasmon. J. Am. Chem. Soc. **131**, 12623–12627 (2009)

Chapter 5
Control of Crystal Size Distribution and Polymorphs in the Crystallization of Organic Compounds

Koichi Igarashi and Hiroshi Ooshima

Abstract Many of organic compounds, such as pharmaceuticals and chemicals, are produced as crystals. Controlling the characteristics of these crystal products with good reproducibility is essential for crystallization of organic compounds. There are various characteristics to be controlled, such as grain size and distribution, crystal polymorphism, crystal habit, and purity, but grain size and crystal polymorphism are particularly essential characteristics. In order to control them, the authors have developed several new crystallizers. This chapter highlights some recent crystallizers to produce organic crystals with high quality.

Keywords Crystal property · Size distribution · Polymorphs

5.1 Introduction

5.1.1 Crystallization of Organic Compounds

Crystallization is one of the important unit operations of separation and purification processes widely used in the production of pharmaceuticals, chemical products, foods, etc. Since the product substance is recovered as a solid-state, solid–liquid separation is possible by filtration, and the subsequent separation operation becomes easy. Also, since the molecules are regularly arranged in the crystal, the products with a high-purity can be obtained. The crystallization is generally considered to be a low energy consuming process in the unit operation.

Generally, the drugs contain an active pharmaceutical ingredient (API) as a solid (crystal), so crystallization is an important process. In particular, since the quality of the API crystal as the final product also affects the drug efficacy in the body, special care must be taken to control various crystal properties. For example, in the

K. Igarashi (✉)
Graduate School of Engineering, Osaka City University, Osaka, Japan
e-mail: igarashi@osaka-cu.ac.jp

H. Ooshima
Kansai Chemical Engineering Co. Ltd., Amagasaki, Hyogo, Japan

M. Sakamoto and H. Uekusa (eds.), *Advances in Organic Crystal Chemistry*,
https://doi.org/10.1007/978-981-15-5085-0_5

production process of API, the crystallizations are performed to separate the target substance from raw materials or by-products at each step of the synthesis route, which involves multiple steps. Care must be taken to improve yield and purity at each step. It is because desired crystal characteristics may not be obtained due to the influence of a small amount of raw material and by-products contained in crystals.

When the crystallization is performed in the manufacture of pharmaceuticals, it is necessary to control various crystal characteristics to produce the desired crystals with good reproducibility. There are various crystal characteristics to be controlled, such as particle size, particle size distribution, crystal polymorphism, purity, shape, and crystallinity. If control of such characteristics insufficient, the subsequent operability and quality may be significantly affected. Therefore, it is important to clarify the causal relationship between the crystallization conditions and the characteristics of the obtained crystals and to control the crystal characteristics based on the theory [1, 2].

5.1.2 Crystal Properties to Be Controlled

5.1.2.1 Crystal Size and Crystal Size Distribution

Crystal size and size distribution are one of the critical characteristics to be controlled in the crystallization process. In industrial crystallization, depending on the purpose, a large crystal may be desired, or a small crystal may be desired.

When importance is attached to solid–liquid separation in the filtration, uniform and large crystals without small crystals are desired because unwanted fine crystals can cause clogging of the filtration device. If it is difficult to obtain large crystals and there is a problem in the filterability due to generation of fine particles, preparation of agglomerates of the desired size by aggregation the micro crystals are attempted.

On the contrary, small crystals are often desired. When the size of the crystal is large, the gap between the crystals becomes wide, and the amount of the crystal that can be put in a specific container is reduced. When paying attention to the transportation of products, smaller crystals are advantageous because of their higher bulk density. Furthermore, in recent years, the number of poorly water-soluble pharmaceuticals has increased, and in order to improve the solubility, it is necessary to make fine crystals.

5.1.2.2 Polymorphs

In the crystal, the molecules are regularly arranged and bonded by appropriate intermolecular interactions. In the crystal, molecules at each point in the lattice have the same conformation. There may be one or more regular arrangements for a substance, and crystals with different structures are called crystal polymorphs.

Some compounds incorporate solvent molecules in the crystals, and such crystals are called solvates or pseudo polymorphs. Nowadays, solvates have also been considered as one of the polymorphs [3]. In the solvate crystal, not only the interaction between the solute molecules but also the interaction via the solvent molecule exists. So the solvent molecule should play an important role in crystal formation. Many hydrates are also found in the pharmaceutical products, and one-third of drugs registered in the European Pharmacopoeia is hydrate form.

Control of crystal polymorphism is crucial because different crystal structures have different solubility and stability in the same substance [4]. Particularly in drug substance, the dissolution properties of crystals may affect the pharmacokinetics of drugs, and a technique for reliably producing a particular crystal polymorph is required.

5.1.3 Crystallization Technics

Some oils are crystallized by melt crystallization, but many organic compounds are generally crystallized from the solution. There are various methods for crystallization from a solution. Cooling crystallization is the most common method. When the solution containing a given amount of solute is cooled via the outer jacket of the crystallization vessel or the cooling coil inserted inside, the solution becomes supersaturated. Thereafter, the crystal appears via nucleation and growth. The amount of crystals obtained can be estimated by the feed concentration and the solubility at the final cooling temperature. Therefore, the cooling crystallization is advantageous when crystallizing a substance having a high-temperature dependence of solubility.

When the solubility does not change much with temperature, or when the solubility at low temperatures is high, the amount of solute recovered by cooling crystallization may be small. In such a case, a method other than cooling should be selected. For example, in order to generate supersaturation, the solvent composition is changed. The additional solvent is added to the solution to reduce solubility. We need to select such an appropriate solvent so that the solvent and the solution should be miscible. Usually, in the crystallization of hydrophilic compounds, water is used as a good solvent, and an organic solvent is used as an antisolvent. Conversely, water is used as an antisolvent for the crystallization of poorly water-soluble compounds.

What should be taken care of in the drowning out crystallization is that when the crystallization is performed from a condition where the concentration of the initial solution is excessively high, liquid–liquid phase separation often occurs without precipitation of crystals. Liquid–liquid phase separation is a phenomenon in which solute molecules exist in a liquid state with a super-high concentration, and in many cases, precipitation of crystals does not occur. It is because even if the concentration is very high, the solution contains a solvent with high affinity and is stable in the solution state. Moreover, since the viscosity is high due to the high concentration, nucleation is suppressed kinetically. On the other hand, there are some examples in which particle size control is attempted using liquid–liquid separation phenomena.

Drowning out crystallization is an effective method selected next to cooling crystallization, but the cost of the solvent used for that cannot be ignored. When repeatedly using a solvent, two or more solvents must be separated to pure solvents again by distillation or the like.

Evaporation of solvent is also used for crystallization of highly water-soluble compounds like sugars and amino acids. It is the simple method, but changes in various phenomena such as the thermal stability of the solute and the increase in viscosity due to concentration must be estimated in advance.

In any case, in crystallization from a solution, the solution should be supersaturated by a suitable method, and induce crystallization.

5.2 Production of Crystals with a Large and Narrow Size Distribution Using Internal Fines Dissolver [5]

5.2.1 Introduction

As mentioned above, industrial crystallization is expected to produce solids having not only a particular composition but also a desired crystal size distribution (CSD), because CSD often determines handling and many end-use properties. A product with unimodal and narrow size distribution and large mean size is often desired.

It is well known that CSD is dependent on the primary nucleation, growth kinetics, and also on secondary nucleation that is mainly caused by a collision between crystals and the impeller in the crystallizer.

We have proposed a novel crystallizer. The crystallizer, named as WWDJ-batch crystallizer, is equipped with a double-deck jacket and Wall Wetter™, which is a slurry sprinkler. The structure of the crystallizer is quite simple, as shown below. It is easy to wash and clean the inside of the vessel. This is a severe demand in the production of pharmaceuticals. The crystallizer allowed the batch production of large crystals with a narrow crystal size distribution (CSD) through the selective dissolution of fine crystals that progresses simultaneously with crystallization.

In this section, we describe the production of the large crystals of glycine with a narrow CSD using the WWDJ-batch crystallizer.

5.2.2 Apparatus

The WWDJ (Wall Wetter/Double-deck Jacket) batch crystallizer is illustrated in Fig. 5.1a. The crystallizer is a cylindrical glass vessel with a round bottom, covered with a double-deck jacket. The working volume of this crystallizer is 1.7 L. The crystallizer was equipped with a four-blade propeller. It was also equipped with a

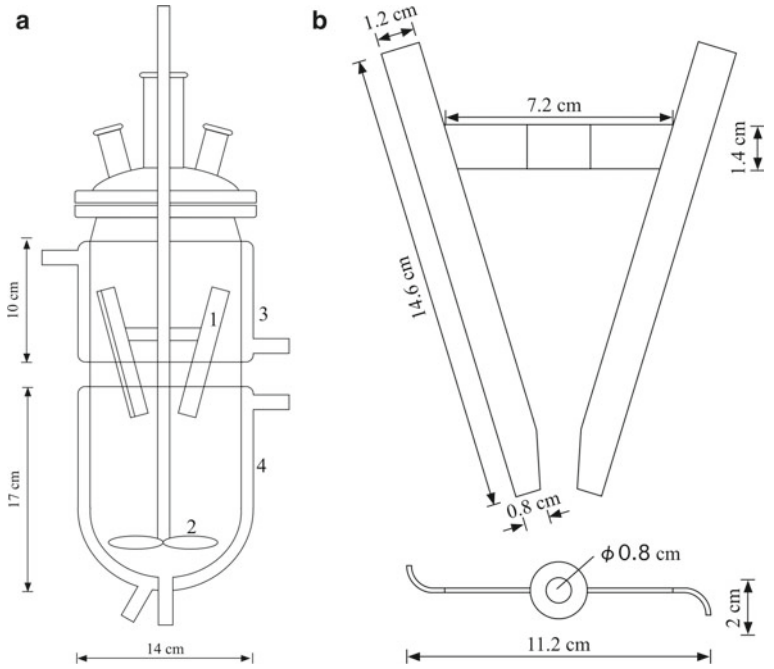

Fig. 5.1 Schematic diagrams of the WWDJ-crystallizer (**a**) and Wall-wetter™ (**b**)

Wall Wetter [6] that is a slurry sprinkler, namely a device specially designed for sprinkling slurry or a solution on the wall of the crystallizer headspace.

The Wall Wetter adopted in this study comprised two-channel bars with a J-shaped cross-section, as shown in Fig. 5.1b. The device was fixed to the agitation shaft at a given angle. The slurry was raised along the channel by centrifugal force and sprinkled on the upper wall, then fell down the wall. During the fall, it can be expected that crystals dissolve partially so that fine crystals disappear if the upper jacket temperature is higher than that of the lower jacket. The surviving large crystals are also expected to grow further, at the expense of fine crystals, after returning to the lower crystallization phase.

5.2.3 Crystallization of Glycine Using WWDJ-Crystallizer

The cooling crystallization of glycine was carried out using WWDJ-crystallizer. First, the temperatures of the upper and lower jackets of the WWDJ-crystallizer were adjusted to 55.6 °C. An aqueous solution (1.7 L) of 250 mg/mL glycine was prepared at 70 °C and then quickly introduced into the crystallizer. After the solution temperature reached 55.6 °C, the solution was cooled at a constant cooling speed, 10 °C/h, where the final temperature of the solution and lower jacket were set at 25 °C

and 10.3 °C, respectively. The upper jacket temperature was not changed during the crystallization. The temperature difference between the slurry falling down the upper wall and the slurry in the lower crystallization part, that is the driving force of the dissolution of fine crystals, was set at 7 °C.

Figure 5.2 shows a change in the temperature of the glycine solution during crystallization. Open symbols indicate for WWDJ-operation, and closed symbols indicate for conventional operation (control experiment). The crystallization temperature was controlled from 55.6 to 25 °C along with the same profile for these two crystallizers.

After the crystallization, we recovered the crystals obtained from both crystallizers and compared the crystal size distribution (CSD). Figure 5.3a shows the comparison of CSD. In the conventional crystallizer, a broad CSD with two peaks was observed. The smaller peak may be partially caused by the attrition of crystals with the propeller. On the other hand, in the WWDJ-crystallizer, the large crystals with a narrow CSD were obtained. Notably, small crystals less than 500 μm were well removed by the dissolution of fine particles. Figure 5.3b shows cumulative CSD. The 50% value of the cumulative CSD, L50, of glycine crystals obtained using WWDJ-crystallizer was 950 μm, compared with 460 μm in the conventional crystallizer not using the Wall Wetter. These results show that the WWDJ-crystallizer is useful for the production of large crystals with a narrow CSD.

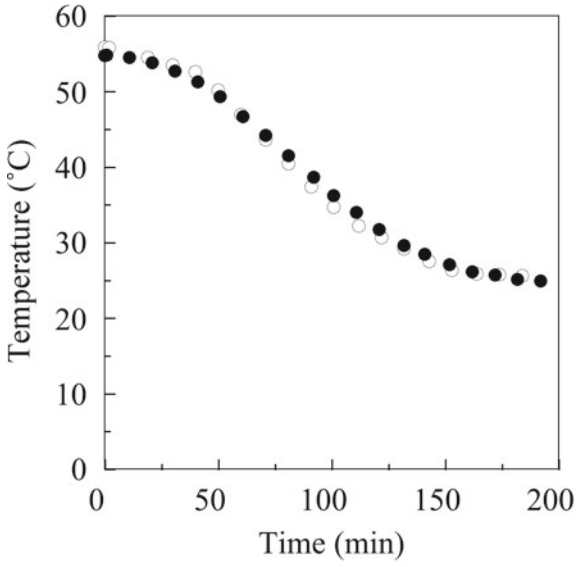

Fig. 5.2 Changes in the temperature of the glycine solution for WWDJ operation (open symbols) and conventional operation (closed symbols)

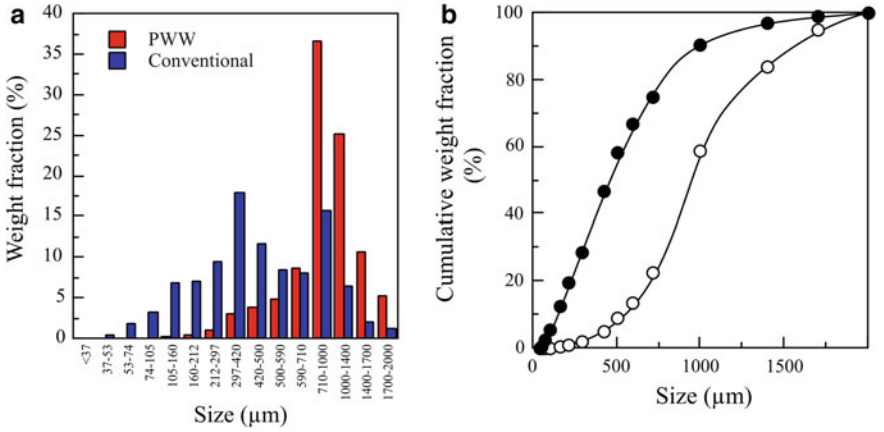

Fig 5.3 The comparison of crystal size distribution of glycine crystals obtained by WWDJ crystallizer and conventional crystallizer. **a** histogram, **b** cumulative distribution

5.3 Control of Crystal Size Distribution Using a mL-Scale Continuous Crystallizer Equipped with a High-Speed Agitator [7]

5.3.1 Introduction

As described above, hardly water-soluble drugs are increasing [8, 9]. In such a case, smaller crystals have an advantage on dissolution property. Small particles are expected to increase the dissolution rate because of their large specific surface area. However, it is not easy to produce such fine particles. The birth of crystal is the result of the nucleation process. Therefore, the number of crystals obtained is determined by the frequency of nucleation events. In order to obtain a large number of small crystals, the nucleation event must be intensely accelerated. In addition, excessive growth must be suppressed after nucleation. For this purpose, it is necessary to prevent the crystals from staying in the crystallization vessel for a long time.

In this section, we propose a new crystallizer that overcomes these problems, namely "mL-scale continuous crystallizer." The crystallizer is a small-size continuous crystallizer, and the particles after crystallization are quickly discharged from the crystallizer. In addition, a high-speed stirrer provides vigorous shearing to promote nucleation.

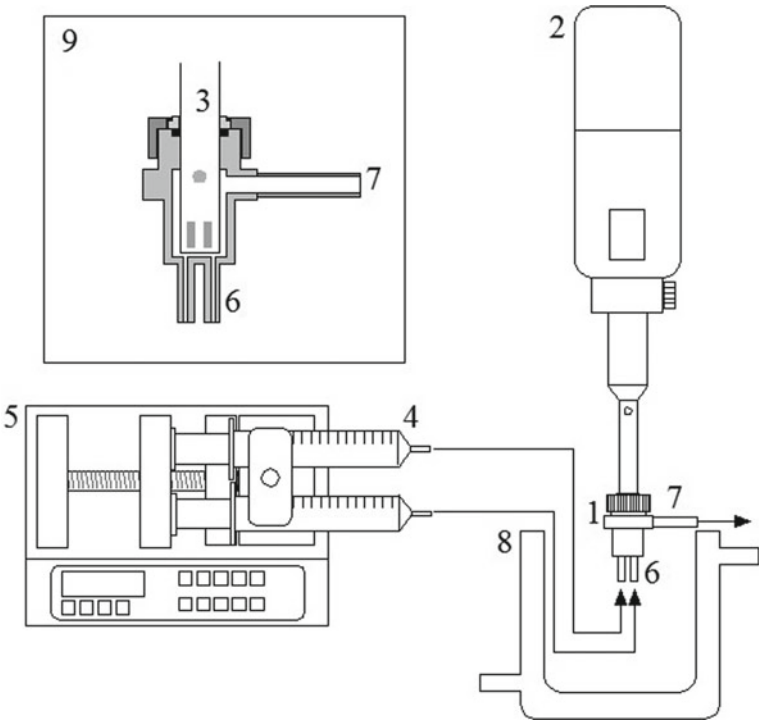

Fig. 5.4 Schematic diagrams of the mL-scale crystallizer. 1. Mixing vessel, 2. high speed agitator, 3. dispersing element, 4. plastic syringes, 5. syringe pump, 6. inlet tubes, 7. outlet tube, 8. glass vessel with an water jacket, and 9. enlarged illustration of the mixing vessel

5.3.2 Apparatus

Figure 5.4 shows a schematic diagram of the mL-scale crystallizer. The crystallizer is composed of a stainless-steel vessel, a high-speed agitator (Ultra-turrax T25 homogenizer, IKA), and a syringe pump (IC3210, KD Scientific). The maximum rotation speed of homogenizer is 24,000 rpm. An agitation shaft is inserted from the top of the vessel and fixed by a screw lid and O-ring. The solute solution and the antisolvent are supplied from two inlet tubes by the syringe pump and intensely mixed with the agitator. The void volume of the crystallizer is 0.9 mL, respectively. The slurry is recovered from an outlet tube at the side of the vessel.

5.3.3 Crystallization of Glycine and Alanine Crystals

Amino acids, glycine, and alanine, were crystallized using the mL-crystallizer. The initial concentration of L-alanine and glycine were 166 mg/mL and 250 mg/mL,

respectively. Methanol was used as an antisolvent. The solution and methanol were injected into the crystallizer by a syringe pump. The flow rate of a solution/methanol mixture was set to 1.6, 16, and 160 mL/min. These flow rates correspond to 33, 3.3, and 0.33 s of the average residence time τ, respectively.

Figure 5.5 presents SEM images of glycine crystals. The shorter the residence time, the smaller crystals were obtained. The size of crystals was measured from the SEM images. Figure 5.6 presents the size distribution of glycine crystals on the basis of the long axis length. The peak shifted to smaller size with a decrease of residence time. The recovery yield was higher at a short residence time rather than a long residence time as shown in Table 5.1. At the residence time of 0.33 and 3.3 s, the yield was 100%, but at $\tau = 33$ s the yield was decreased to 93%. The fact that the crystal yield was 100% at short residence times indicated that the smaller size of crystals obtained at those residence times was not caused by insufficient nucleation and crystal growth due to the short residence time.

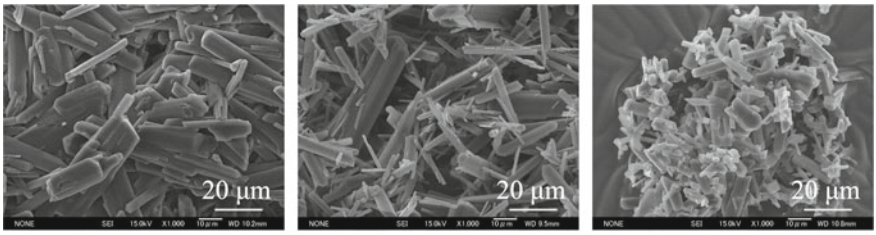

Fig. 5.5 SEM images of the glycine crystals

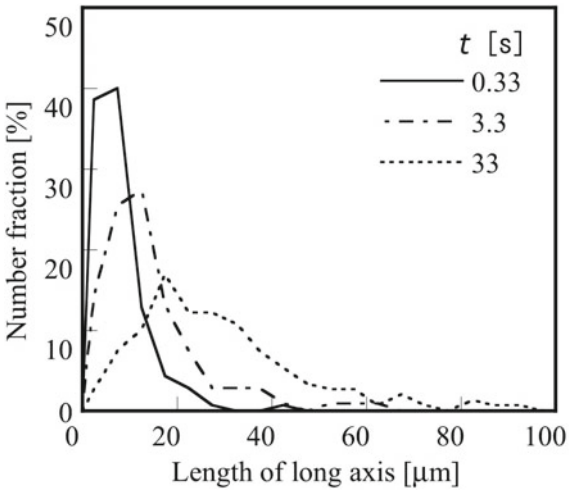

Fig. 5.6 Size distribution of the glycine crystals on the basis of the long axis length

Table 5.1 Yields of glycine and L-alanine crystals obtained at different residence time

Methanol composition (%)	Average residence time, τ (s)	
	3.3	33
50	α	α
78	β	α
91	β	$\alpha + \beta$

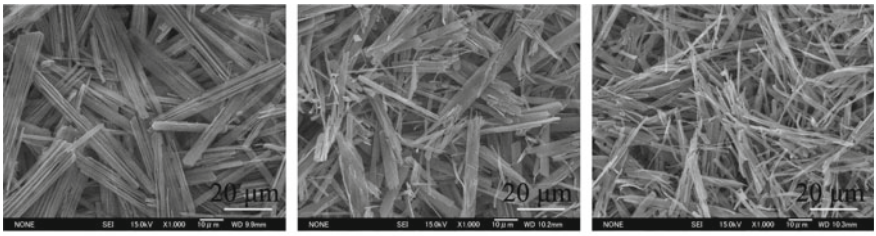

(a) $\tau = 33$ s (b) $\tau = 3.3$ s (c) $\tau = 0.33$ s

Fig. 5.7 SEM images of the alanine crystals

Figure 5.7 presents SEM images of the crystals of L-alanine obtained at various residence times. The crystals were needle-like and those were bundled. The typical shape of a L-alanine crystal is prismatic [10], which can be obtained by cooling crystallization. In the present poor solvent crystallization, needle-like crystals were obtained. However, since the XRD pattern for the needle-like crystals was the same as that of the prismatic crystals (data not shown), the difference of shape was not due to polymorphism. The crystals obtained at $\tau = 33$ s were thick and easy to cleave. The crystals obtained at short residence time were thin.

In the present study, the homogenizer was used for agitation. There is some fear of breakage of crystals by high-speed mixing. Therefore, we checked the influence of agitation for the crystal size and shape. 0.84 g of L-alanine crystals of 65 μm in average size was suspended in 17 mL of saturated solution of L-alanine. The suspension was agitated by the homogenizer at 24,000 rpm for 10 min. After that, the crystals were recovered and observed by SEM. The shape and size of obtained crystals were almost the same as those of the original crystals. Therefore, we concluded that crystals with a size of less than at least 65 μm in average size were not broken by short (second time-scale) high-speed agitation.

Figure 5.8 shows size distributions on the basis of the long axis length. At $\tau = 0.33$ and 3.3 s, the size of crystals was small and the distribution was narrow. A broad distribution was obtained at $\tau = 33$ s. In a long mean residence time, some crystals may stay in the crystallizer for long time and the supplied supersaturation may be used for the growth of resident crystals, resulting in broad size distribution. The short residence time should be advantageous to produce small crystals with a narrow size distribution.

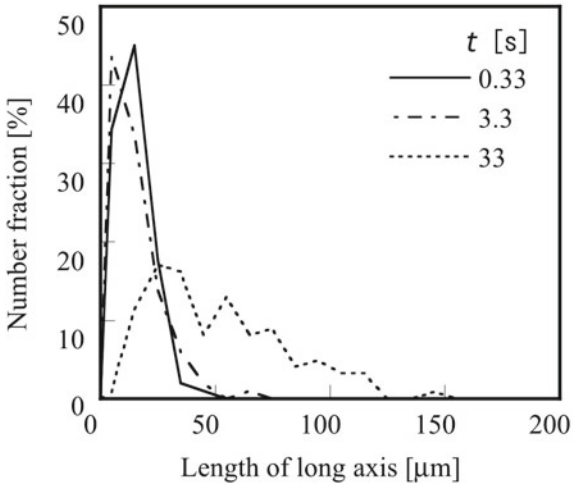

Fig. 5.8 Size distribution of the alanine crystals on the basis of the long axis length

5.3.4 Control of Polymorph by Changing Mixing Ratio of Glycine Solution and Poor Solvent Methanol

The experimental results shown above were obtained by poor solvent crystallization where equal volume of the solution and methanol were mixed. The solubility changes with the composition of solvent and the supersaturation also change with those mixing ratios. Then, we investigated the effect of mixing ratio of the solution and poor solvent methanol on the crystallization of L-alanine. The mixing ratio of methanol was changed by using different size of plastic syringes to 50, 78, and 91%. The residence time was fixed to 3.3 s. Figure 5.9 presents the SEM images of L-alanine crystals. The size of crystals became small with an increase in the methanol composition. The supersaturation ratio was 3.1 at 50% methanol and 9.8 at 91% methanol. The high supersaturation resulted in micronization of crystals.

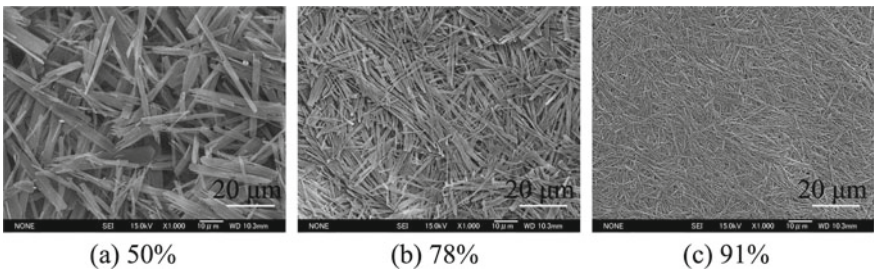

Fig. 5.9 SEM images of the alanine crystals

Three types of polymorphs have been reported for glycine. In cooling crystallization from the aqueous solution, metastable α-form and stable γ-form are obtained. On the other hand, it is known that needle-like β-form is precipitated from an aqueous alcohol solution. The β-form is the most unstable of the three polymorphs and is known to change to metastable α-form by solvent-mediated transformation in solution.

The polymorphs of the obtained crystals were identified by XRD. Figure 5.10 shows XRD profiles of glycine crystals obtained with different methanol compositions. The average residence time τ is 3.3 s. It can be seen that there is a difference in the XRD pattern between the methanol composition of 50% and the others. The α-form of glycine has characteristic peaks that are not found in other polymorphs at $2\theta = 14.8°$, 29.2°, 29.9°. In addition, the peaks peculiar to β-form appear at 17.9°, 33.8°, and 34.4°. From the results, it was found that α-form was obtained at 50% methanol, and β-form was obtained at 73 and 91% (Table 5.2).

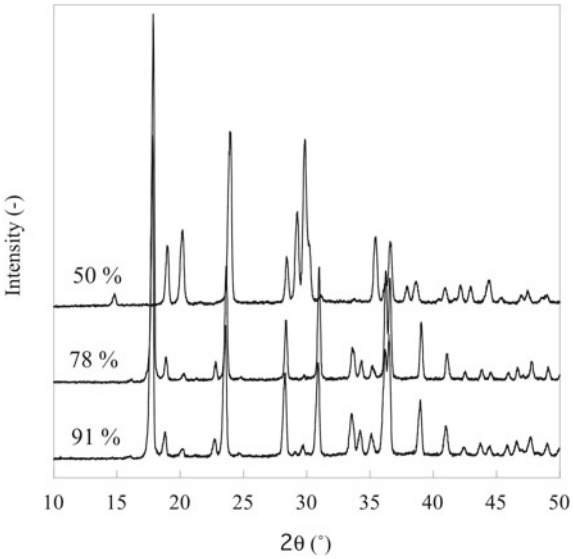

Fig. 5.10 XRD profiles of glycine crystals obtained with different methanol composition

Table 5.2 Summary of polymorphs of the glycine crystals obtained at different methanol composition and residence time

Residence time τ (s)	Yield of crystals (%)	
	Glycine	L-alanine
0.33	102	87.2
3.3	101	89.1
33	92.5	98.8

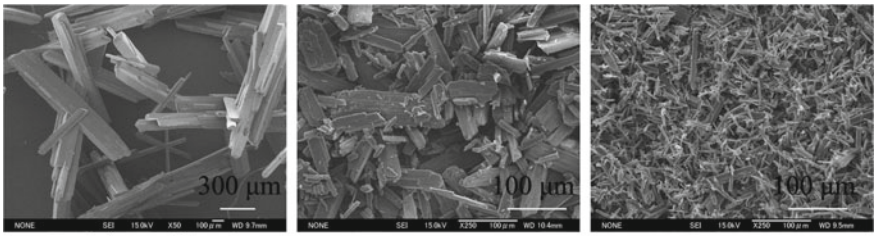

Fig. 5.11 SEM images of glycine crystals obtained by using three different crystallizers

In general, obtaining metastable crystals is not as easy as obtaining stable crystals. It is necessary to suppress the nucleation of the stable form and recover the metastable form quickly before the transformation.

In the antisolvent crystallization of glycine, if the purpose is to obtain metastable β form selectively, the metastable crystals should be recovered quickly. Since the mL-scale crystallizer performs continuous crystallization with a residence time of seconds order, it is possible to recover successfully the desired polymorph before the transformation.

5.3.5 Comparison of Crystallizer Performance Between Conventional Crystallizers and the Present Continuous mL-Scale Crystallizer

In order to compare the performance of the mL-crystallizer with those of conventional crystallizers, the product crystals were compared. As conventional crystallizers, we chose a semi-batch crystallizer and a MSMPR type crystallizer having 64-times volume of the present mL-scale continuous crystallizer. Figure 5.11 presents SEM images of glycine crystals obtained by using three different crystallizers. In the semi-batch crystallization, large crystals were obtained. It was suggested that glycine supplied was consumed for the growth of crystals produced in the early stage of crystallization. In the continuous crystallization operated at the mean residence time of 11.5 min, small crystals were obtained, compared with those obtained by the semi-batch crystallization. Crystals obtained by using the continuous mL-crystallizer were much smaller and more homogeneous in size than the former two.

5.4 Summary

In recent years, demand for development of continuous crystallizer especially in the fields of pharmaceutical crystallization. In order to obtain crystals with uniform

physical properties, the tubular flow type is more advantageous than the stirred tank type which a residence time distribution. However, since the tubular type crystallizer is not sufficiently stirred, a very long apparatus must be manufactured. Therefore, the continuous oscillated baffled crystallizer (COBC), in which the tube is separated into multiple compartments, is attracting attention. This section introduced a device for obtaining large crystals and a small crystallizer for obtaining small crystals. In the future, more sophisticated crystallizers will be developed.

References

1. Haleblia, J., Mccrone, W.: Pharmaceutical applications of polymorphism. J. Pharm. Sci. **58**, 911 (1969)
2. Haleblian, J.K.: Characterization of habits and crystalline modification of solids and their pharmaceutical applications. J. Pharm. Sci. **64**, 1269–1288 (1975)
3. Brittain, H.G.: Polymorphism in Pharmaceutical Solids, 2nd edn. Informa Healthcare (2009)
4. Aguiar, A.J., Krc, J., Kinkel, A.W., Samyn, J.C.: Effect of polymorphism on absorption of chloramphenicol from chloramphenicol palmitate. J. Pharm. Sci. **56**, 847 (1967)
5. Ooshima, H., Igarashi, K., Sasaki, Y., Azuma, M., Noda, H.: Production of large crystals of glycine with a narrow size distribution using WWDJ-batch crystallizer. Chem. Eng. Trans. **1**, 981–986 (2002)
6. Noda, H., Yamaji, H., Kuratani, N., Mukaida, T., Ohuchi, M.: Challenge to a precess revolution. Wall Wetter. Kagaku Kougaku **63**, 295–296 (1999)
7. Igarashi, K., Yamanaka, Y., Azuma, M., Ooshima, H.: Control of crystal size distribution using a mL-scale continuous crystallizer equipped with a high speed agitator. J. Chem. Eng. Jpn. **45**, 28–33 (2012)
8. Bittner, B., Mountfield, R.J.: Intravenous administration of poorly soluble new drug entities in early drug discovery: the potential impact of formulation on pharmacokinetic parameters. Curr. Opin. Drug Discov. Devel. **5**, 59–71 (2002)
9. Kakran, M., Sahoo, N.G., Li, L., Judeh, Z., Wang, Y., Chong, K., Loh, L.: Fabrication of drug nanoparticles by evaporative precipitation of nanosuspension. Int. J. Pharm. **383**, 285–292 (2010)
10. Lechuga-Ballesteros, D., & Rodríguez-Hornedo, N. (1995). Effects of molecular structure and growth kinetics on the morphology of l-alanine crystals. *International Journal of Pharmaceutics, 115*(2), 151–160.

Chapter 6
Managing Thermal History to Stabilize/Destabilize Pharmaceutical Glasses

Kohsaku Kawakami

Abstract Vitrification is a powerful methodology for improving the dissolution of poorly soluble drugs. Thus, amorphous dosage forms are sometimes employed in the pharmaceutical industry for enhancing their oral absorption, for which the dissolution process plays an important role. Amorphous structures change with time because of their non-equilibrium property, and this impacts their physical stability. Thus, assurance of their physical stability can be challenging during their development. Amorphous properties are significantly influenced by their thermal history. Here, the influence of thermal history on the crystallization behavior of pharmaceutical glasses is discussed with emphasis on possible nucleation, relaxation, decrease in free volume, etc., during the thermal treatment. Factors that enhance crystallization such as mechanical stress and moisture sorption are also discussed.

Keywords Pharmaceutical glass · Crystallization · Nucleation · Thermal history · Relaxation

6.1 Introduction

In the pharmaceutical industry, poorly soluble candidates frequently survive screening studies, hence there is a need to increase their solubility. Amorphous solids, because of their high energy state, may be employed for this purpose [1–4]. Amorphous drugs are usually stabilized in the form of solid dispersion, and polymeric excipients are added for improving solid-state stability and dissolution.

Crystallization tendency is compound dependent [5]. Many research groups have assessed crystallization tendency by applying a cooling/reheating cycle to the melt using differential scanning calorimetry (DSC). The classification criteria proposed by Taylor et al. are as follows [6]:

K. Kawakami (✉)
International Center for Materials Nanoarchitectonics, National Institute for Materials Science, 1-1 Namiki, Tsukuba 305-0044, Ibaraki, Japan
e-mail: kawakami.kohsaku@nims.go.jp

M. Sakamoto and H. Uekusa (eds.), *Advances in Organic Crystal Chemistry*,
https://doi.org/10.1007/978-981-15-5085-0_6

Class 1: Compounds that crystallize during cooling from the melt at 20 °C/min.
Class 2: Compounds that do not crystallize during the cooling mentioned above but crystallize during subsequent heating at 10 °C/min.
Class 3: Compounds that do not crystallize during the cooling/heating cycle mentioned above.

Determination of a critical cooling rate that inhibits crystallization was also introduced as an alternative way by, Rades et al., to assess the crystallization tendency [7].

Class 1: Compounds that crystallize at a cooling rate of 750 °C/min.
Class 2: Compounds that crystallize at ca. 10–20 °C/min.
Class 3: Compounds that do not crystallize at a cooling rate of 2 °C/min.

Despite having different definitions, both these classifications provide similar results. The difference in class 1 and 2 compounds is likely to have originated from the degree of difference in nucleation and crystal growth temperatures, whereas the greater stability of class 3 compounds seems to be due to the strong intermolecular interactions [5, 8].

Isothermal crystallization is practically more significant than the non-isothermal one for pharmaceutical applications. Under careful investigations, the initiation time for crystallization of class 1 and 2 compounds can be summarized as a function of T_g/T, where T_g and T are the glass transition and storage temperature, respectively (Fig. 6.1) [9, 10]. Although the class 3 compounds have higher stability, their worst case of stability agreed with that of class 1 and 2 compounds [11]. This result indicates that crystallization is basically governed by molecular mobility. Strong molecular interactions result in higher stability. However, it must be emphasized that this result was obtained after very careful investigation, where the glass samples were prepared by quenching the melts in DSC pans, and then subjected to isothermal storage as they were. Crystallization of practical glasses, for which disturbance factors including mechanical stress are applied during preparation, cannot be interpreted in such a simple manner. These details will be discussed later.

Thermal history is one of the least important factors in many crystallization studies but it has a significant effect on crystallization behavior. Due to their non-equilibrium nature, amorphous solids undergo relaxation to obtain a more stable state. Nucleation may proceed as well but it is difficult to detect it directly. The influence of thermal history on glass stability is discussed below.

6.2 Effect of Cooling Rate on the Properties of Quenched Glass

When glasses are prepared by quenching, their stability is influenced by the cooling rate. Figure 6.2a, b show reversing and non-reversing heating curves of probucol glass obtained by cooling the melt [12]. The effect of the cooling rate was observed at 20,

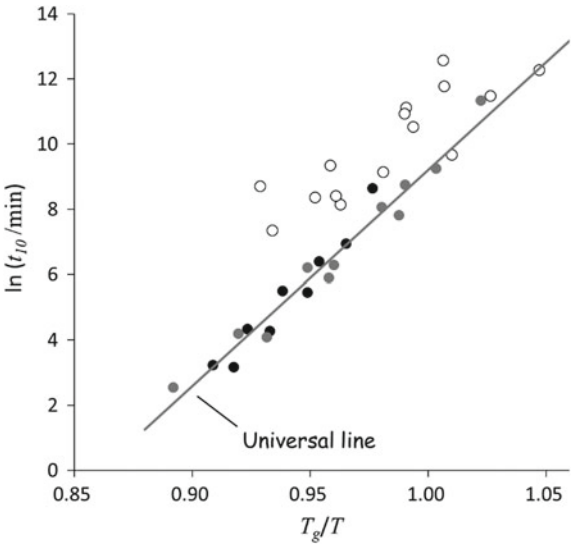

Fig. 6.1 Initiation time for crystallization (time to reach 10% of crystallinity, t_{10}, min) as a function of T_g/T [9, 10]. The glass samples were prepared by quenching the melts in DSC, and the samples were subjected to the isothermal storage as they were. Closed (black), gray, and open (white) symbols represent class 1 (tolbutamide, chlorpropamide), 2 (acetaminophen, nifedipine, phenobarbital), and 3 (indomethacin, ritonavir, loratadine, probucol) compounds, respectively. The universal line is the best fit for class 1 and 2 compounds

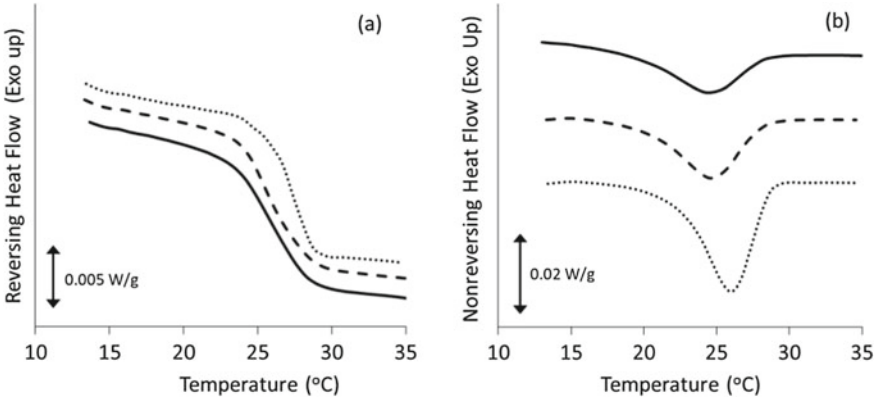

Fig. 6.2 Reversing (**a**) and non-reversing (**b**) heat flow curves of quenched probucol glass prepared by different cooling rates: 20 °C/min (solid), 1 °C/min (break), 0.1 °C/min (dotted). In the measurements, the samples were heated in modulation mode at 2 °C/min with a 60 s period and 0.5 °C amplitude

1, and 0.1 °C/min in the T_g region. There was an increase in T_g and the heat capacity difference, ΔC_p, between the supercooled liquid and the glass, on decreasing the cooling rate. Growth of the enthalpy recovery peak was observed with a decrease in the cooling rate, which can be explained by the relaxation that proceeds during cooling. Figure 6.3 summarizes the effect of the cooling rate, q, on T_g, ΔC_p, and the relaxation enthalpy, ΔH. The influence of the cooling rate was insignificant when it was larger than 5 °C/min. T_g increased by ca. 2.5 °C on decreasing the cooling rate from 5 °C/min to 0.05 °C/min.

Table 6.1 shows the summary of the slopes of the best fit lines for pharmaceutical glasses along with their thermodynamic and structural properties [12]. The T_g of curcumin, itraconazole, and probucol was the most affected by the cooling rate. The ΔC_p of curcumin, ritonavir, and ibuprofen was significantly influenced, although the correlation was not high for this. Effect on ΔH was very significant for ritonavir, procaine, and curcumin. Properties of ibuprofen and loratadine glasses were less sensitive to the cooling rate.

It is interesting to examine which structural and/or thermodynamic parameters correlate the most with sensitivity to the cooling rate. The impact of the cooling rate

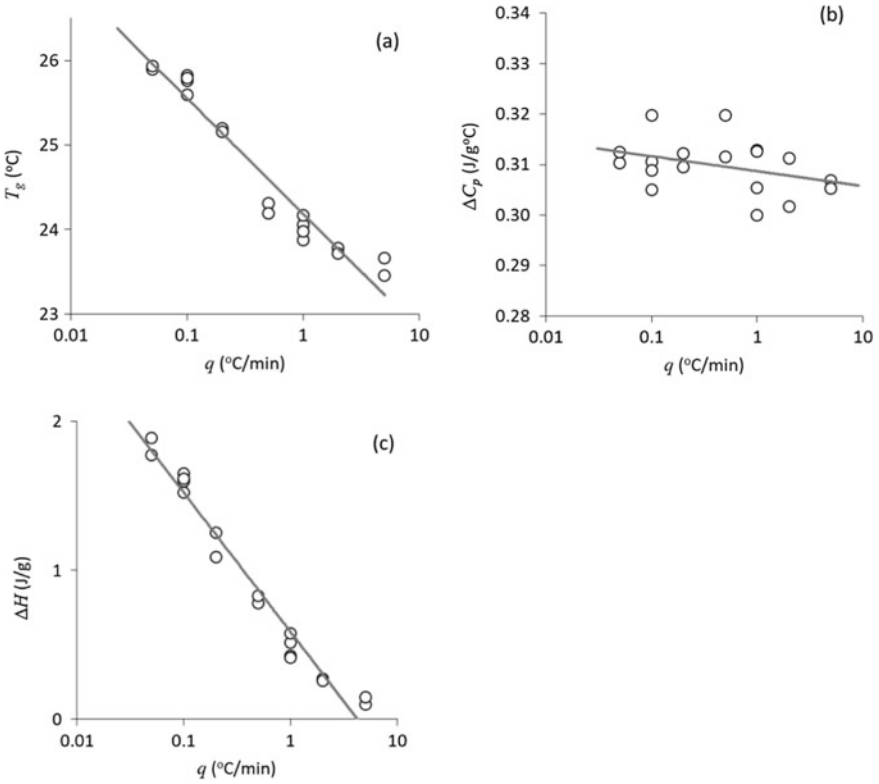

Fig. 6.3 Effect of the cooling rate, q, on **a** T_g, **b** ΔC_p, and **c** ΔH for quenched probucol glass

Table 6.1 Slopes of the best fit lines for pharmaceutical glasses with their thermodynamic and structural properties

Compounds	Molecular weight (Da)	T_g (°C)[a]	ΔC_p (J/g °C)[b]	T_m (°C)	ΔH_m (J/mol)	m_{DC}	m_{DT_g}	H_{donor}	H_{accept}	Rotatable bonds	Slope for T_g-q	Slope for ΔC_p-q	Slope for ΔH-q
Clotrimazole	344.8	26.8	0.330	141	33.3	91	63	0	1	4	0.398	0.00625	0.662
Curcumin	368.4	61.9	0.517	182	50.1	79	87	2	6	8	0.261	0.00095	0.291
Fenofibrate	360.8	−22.0	0.434	80	33.0	73	82	0	3	7	0.477	0.00215	0.668
Ibuprofen	206.3	−46.7	0.362	76	26.5	51	75	1	2	4	0.515	0.00197	0.568
Indomethacin	357.8	43.3	0.417	161	37.6	67	85	1	4	4	0.594	0.00128	0.406
Itraconazole	705.6	54.9	0.428	168	57.6	126	125	0	9	11	0.394	0.00303	0.510
Ketoconazole	531.4	41.9	0.405	147	52.9	118	97	0	6	7	0.414	0.00314	0.550
Ketoprofen	254.3	-5.6	0.471	95	28.3	61	67	1	3	4	0.337	0.00499	0.624
Loratadine	382.9	33.8	0.295	134	27.3	78	72	0	2	2	0.199	0.00593	0.281
Probucol	516.8	23.8	0.298	126	34.2	60	138	2	2	8	0.509	0.00243	0.987
Procaine	236.3	−42.2	0.655	61	26.2	129	90	1	3	7	0.412	0.00525	0.872
Ribavirin	244.2	52.6	0.707	168	45.7	96	70	4	7	3	0.732	0.00657	0.749
Ritonavir	721.0	45.7	0.470	122	65.3	75	86	4	6	18	0.696	0.00212	0.559

T_g: glass transition temperature, ΔC_p: heat capacity difference at T_g, T_m: melting temperature, ΔH_m: melting enthalpy, m_{DC}: fragility determined by extrapolation of the configurational entropy to the Kauzmann temperature, m_{DT_g}: fragility determined from the ramp rate dependence of T_g, H_{donor}: number of hydrogen bond donor, H_{accept}: number of hydrogen bond acceptor

[a]Onset temperature, cooled at 20 °C/min and heated at 10 °C/min

[b]Cooled at 20 °C/min and heated at 10 °C/min

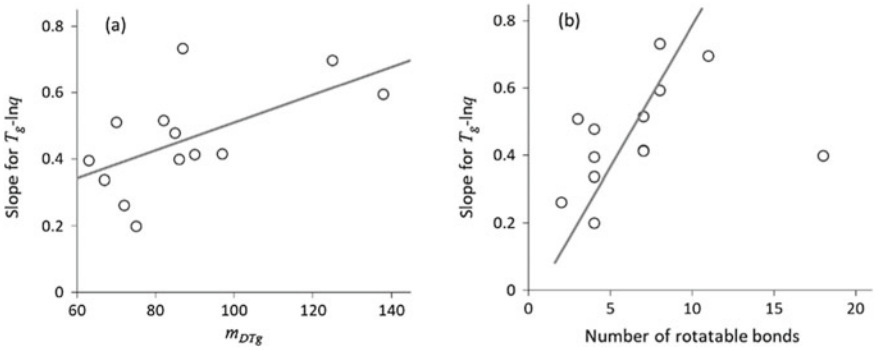

Fig. 6.4 **a** Relationship between the slope for the T_g-ln$q$ fitting and m_{DT_g}. **b** Relationship between the slope for the T_g-ln$q$ fitting and the number of rotatable bonds. The outlying data point was for ritonavir glass. Figures are adopted from Ref. [12] with permission of American Chemical Society.

on the change in T_g correlated the most with m_{DT_g}, the fragility [13, 14] determined from the ramp rate dependence of T_g [14, 15], as shown in Fig. 6.4a. Efficient stabilization of fragile glass by slow cooling seems to be a reasonable observation because the volume and viscosity of the fragile glass have a strong temperature dependence in the T_g region. Correlation was also found between the number of rotatable bonds and the impact of the cooling rate on T_g with an outlying data point for ritonavir glass (Fig. 6.4b). The exceptional behavior of ritonavir glass appeared to be because of stabilization by four hydrogen bonds per molecule [16], which possibility suppresses the molecular motion despite the presence of many rotatable bonds. Moreover, its large molecular weight may also play a partial role in stabilization. Correlation between the number of rotatable bonds and the increase in T_g also seems to be reasonable because high molecular flexibility based on many rotatable bonds should help in effective condensation during cooling.

6.3 Sub-T_g Annealing to Stabilize Glass Structure

The initiation time for crystallization of ritonavir glass obeys Arrhenius rule between 45 and 60 °C as shown in Fig. 6.5. However, it does not crystallize at 40 °C, in violation of the Arrhenius rule [17]. This observation can be partially explained by the suppression of the molecular mobility below T_g. However, this extreme behavior indicates the presence of a stabilization mechanism in the glass structure at 40 °C, slightly below T_g.

Isothermal crystallization of ritonavir glass was found to be retarded significantly by applying preannealing at 40 °C beforehand [17]. Figure 6.6 shows the isothermal crystallization behavior of ritonavir glass at 60 °C and the effect of preannealing at

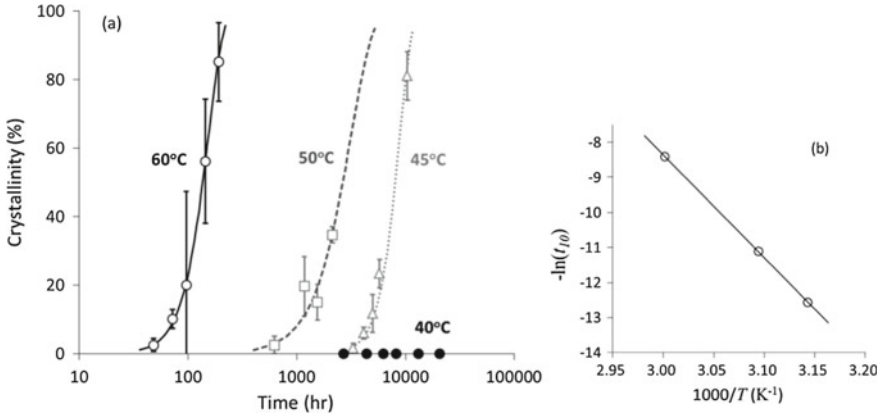

Fig. 6.5 **a** Change in the crystallinity of ritonavir glass as a function of time. The storage temperature is indicated in the Figure. The data were fitted to Avrami-Erofeev equation. **b** The Arrhenius plot of induction time of crystallization of ritonavir glass. The data acquired at 45, 50, and 60 °C were plotted. Figures are adopted with modification form Ref. [17] with permission of American Chemical Society

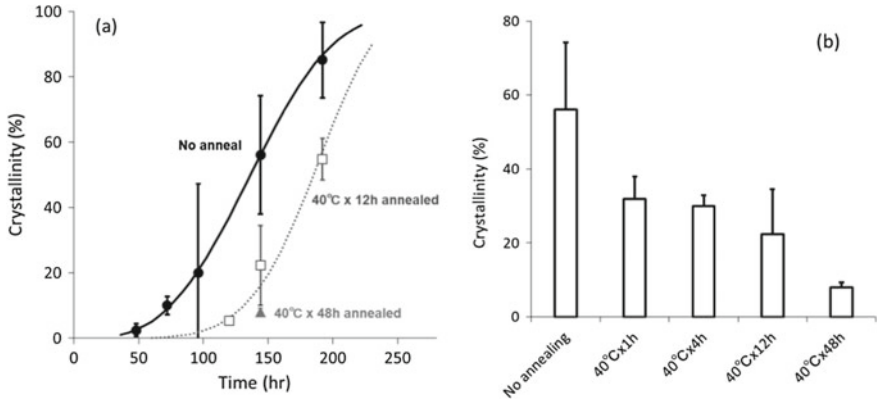

Fig. 6.6 **a** Change in crystallinity of ritonavir glass as a function of time at 60 °C. The "No anneal" data coincides with the "60 °C" data in Fig. 6.5a. Also presented are the crystallization data for ritonavir glass, which was preannealed at 40 °C before the storage at 60 °C as indicated. The data were fitted to Avrami-Erofeev equation. **b** Effect of preannealing time at 40 °C on subsequent isothermal crystallization study at 60 °C for 6 days. The crystallinity after storage at 60 °C is presented. Notably, no crystallization occurred during preannealing at 40 °C. Figures are adopted with modification form Ref. [17] with permission of American Chemical Society

40 °C on the subsequent crystallization study at 60 °C. Crystallinity of intact ritonavir glass reached 58% during annealing at 60 °C for 6 days. However, crystallization was obviously retarded by preannealing at 40 °C. When preannealing was performed for 2 days, the crystallinity after storage at 60 °C for 6 days was only 8% (Fig. 6.6b).

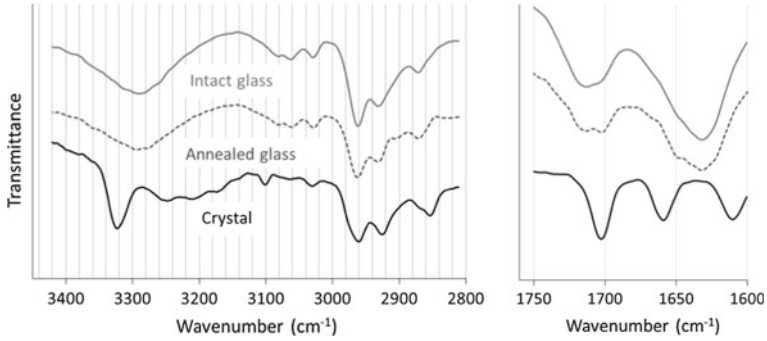

Fig. 6.7 FT-IR spectra of ritonavir crystal, intact glass, and annealed glass at 40 °C for 28 days. Figures are adopted with modification form Ref. [17] with permission of American Chemical Society

The changes in the molecular interactions during annealing at 40 °C were observed using FT-IR spectra (Fig. 6.7) [17]. In the spectrum of the crystalline ritonavir, the sharp peak at 3320 cm^{-1} corresponded to carbamate N–H stretching, which formed weak hydrogen bonds with amide C=O. The broad peaks in the range 3250–3100 cm^{-1}, were attributed to the N–H stretching bands of ureido and amide groups, which formed weak hydrogen bonds (N–H$\cdots$O). The peak around 3100 cm^{-1} corresponded to the O–H stretching band of hydroxyl group with intermediate hydrogen bond strength. The spectrum of the intact glass had a monomodal broad peak attributed to the N–H stretching around 3200–3450 cm^{-1}, but the O–H stretching shifted from 3100 to 3080 cm^{-1}, suggesting that hydrogen bonding was weaker for N–H than for O–H, in glass when compared to the crystal. The acceptors of the hydrogen bonds illustrated these changes more clearly in hydrogen bonds. In the crystalline solid, hydrogen bonds were formed with strong acceptors of C=O in carbamate groups (1702 cm^{-1}), ureido groups (1658 cm^{-1}) and amide groups (1613 cm^{-1}). In the intact glass, the left C=O peak shifted to a higher wavenumber (1712 cm^{-1}) with a shoulder at 1702 cm^{-1}, suggesting that most of the C=O (carbamate) were free from hydrogen bonds or had only weak hydrogen bonding in the glass. The right peak and the middle peak approached each other and formed a broad peak at 1630 cm^{-1}, indicating that the hydrogen bonding with the C=O (amide) became weaker whereas that with the C=O (ureido) became stronger than in the crystal. These observations were in agreement with the pair-distribution function analysis, which proved reduction in the free volume during annealing. Thus, the physical stabilization of the ritonavir glass during annealing at 40 °C was ascertained to be because of the change in the hydrogen-bonding pattern and reduction in the free volume.

6.4 Nucleation During Low-Temperature Storage to Promote Crystallization

The optimum nucleation temperature, i.e., the temperature where the nucleation rate becomes maximum, is usually located well below the optimum crystal growth temperature. Thus, low-temperature storage can influence the physical stability of the glasses. Figure 6.8 shows the DSC heating curves of celecoxib melt, and dependence of the cold crystallization on the target temperature of cooling, T_L [18]. When the melt was cooled to −20 °C, a crystallization exotherm was found in the heating curve. However, crystallization was not investigated when $T_L = 0$ °C. Generally, celecoxib glass is expected to crystallize during heating in the DSC measurement [5]. This analysis suggested that the optimum nucleation temperature was below 30 °C.

Thus, isothermal annealing was applied at the low-temperature region for the celecoxib glass after quenching to find the optimum nucleation temperature [18]. If nucleation proceeds during this annealing, then subsequent crystallization should be promoted. The cold crystallization did not show reproducibility even under identical annealing conditions because of the stochastic property of the nucleation of celecoxib glass. Figure 6.9a illustrates the probability of crystallization after annealing for 1 h at various temperatures, T_a. Crystallization was confirmed to be reproducible when T_a was lower than −10 °C, but the probability of crystallization decreased with increasing temperature. The least probability was at 50 °C and then increased again. The high probability of crystallization at low temperatures can be attributed to the high probability of nucleation, whereas appearance of the minimum probability was likely to be because of rapid crystal growth above 60 °C. The probability of crystallization even after annealing for 1 h at 30 °C was ca. 56%. Therefore, the

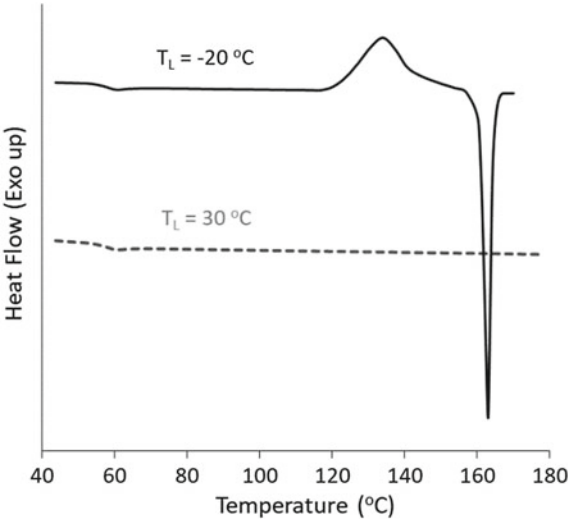

Fig. 6.8 DSC heating curves of quenched celecoxib glass . After the melting, the sample was cooled at approximately 50 °C/min to T_L, and then reheated at 10 °C/min. Figure is adopted with modification form Ref. [18] with permission of Elsevier

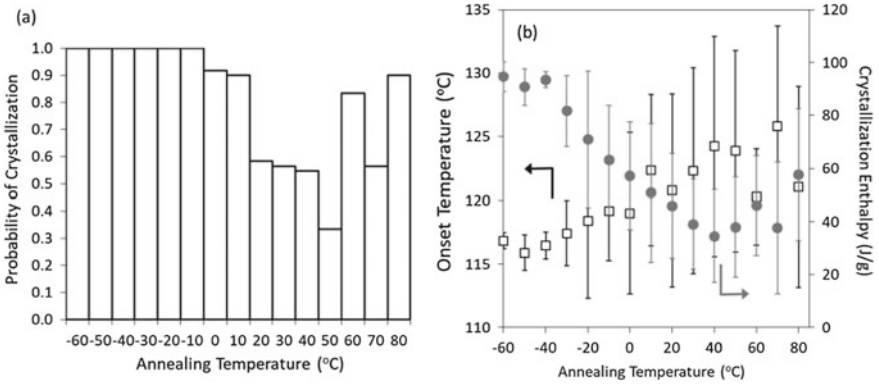

Fig. 6.9 **a** Probability of cold crystallization of quenched celecoxib glass during reheating as a function of annealing temperature (for 1 h). **b** Onset temperature of cold crystallization and crystallization enthalpy of celecoxib glass after 1 h annealing as a function of annealing temperature. Figures are adopted with modification form Ref. [18] with permission of Elsevier

failure in the cold crystallization of celecoxib glass, which was cooled to 30 °C, where the temperature was maintained only for 30 s, was convincing.

Figure 6.9b shows the effect of T_a on the onset temperature and enthalpy of cold crystallization. The crystallization enthalpy was nearly constant at $T_a = -60$, -50, and -40 °C (94 J/g), which agreed with the literature value for form III. Thus, crystallization was regarded as almost completed after the annealing at these temperature conditions. The enthalpy of crystallization decreased with increase in T_a to a minimum value of 34 J/g at $T_a = 40$ °C and then increased again above 40 °C. This trend is consistent with the crystallization probability shown in Fig. 6.9a. The crystallization onset obtained a minimum value at -50 °C and then increased when annealed at a higher temperature. The optimum nucleation temperature was observed to be below -40 °C, whereas the optimum temperature for crystal growth appeared to be above 80 °C. In the annealing study where the annealing time was shortened to 5 min and the temperature interval narrowed to 5 °C the optimum nucleation temperature was observed to be -50 °C. This observation indicated that comprehension of the nucleation temperature is extremely important for evaluating physical stability of glasses.

6.5 Mechanical Activation of Glasses

According to Fig. 6.1, glass stability can be conveniently summarized as a function of T_g/T under well-regulated conditions. However, the stability of practical glasses can be different from those presented in Fig. 6.1, because it is influenced by various

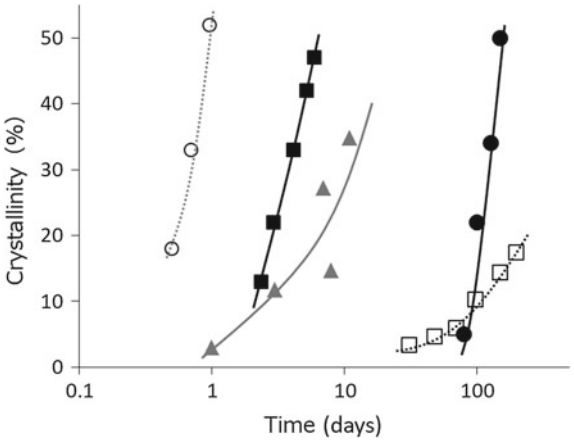

Fig. 6.10 Isothermal crystallization of indomethacin glasses at 30 °C under dried condition. (○) Quenched and milled. Crystallized to form γ [24]. (■) Quenched and milled. Crystallized to form α [25]. (▲) Quenched and cryomilled. Crystallized to mixture of forms α and γ [5]. (●) Quenched. Crystallized to form γ [26]. (□) Quenched and stored in DSC pan. Crystallized to form α which contains small amount of form γ [5]. Figure is adopted with modification form Ref. [5]

physical stresses. Sometimes cracks formed during quenching [19] or even transferring to different containers [20] are suspected to be triggers for crystallization. Strong mechanical stresses such as milling and compression are known to have a significant impact on physical stability. Figure 6.10 presents a comparison of the isothermal crystallization behavior of melt-quenched indomethacin glasses at 30 °C with and without milling before storage [5]. Unless milling was performed, the quenched glass remained in an amorphous state for more than one month. However, for milled glass, crystallization was initiated within a day. This comparison clearly indicates the significance of milling on crystallization behavior, which was most likely due to the increase in surface area and mechanical activation. Notably, the resultant crystal form was not identical in these examples, which might be due to the differences in their impurity profiles.

Compression is also known to affect crystallization kinetics. The effect of compression pressure on crystallization of sucrose glass using isothermal microcalorimetry was studied [21]. Initiation time for crystallization was hardly affected below 0.5 MPa; however, crystal growth was enhanced with an increase in pressure. The crystallization onset was shortened at 2.5 MPa, indicating that condensation of glass structure can promote nucleation. A similar observation was made by Ayenew et al., where cold crystallization of indomethacin glass was enhanced by compression at ca. 43.7 MPa [22]. Enhancement of isothermal crystallization of etoricoxib was observed by Rams-Baron et al. after compression at 300 MPa [23]. However, the acceleration in crystallization was not observed when the drug was mixed with polyvinylpyrrolidone (PVP). This indicated that excipients were an effective physical barrier for inhibiting pressure-induced nucleation.

6.6 Impact of Moisture Sorption on Crystallization

Crystallization is frequently accelerated by moisture sorption, because the solvent can act as a plasticizer. The degree of acceleration may be explained by the decrease in T_g. Figure 6.11a shows that T_g of freeze-dried ritonavir glass was lowered by storage under humid atmosphere [11]. Figure 6.11b illustrates the t_{10} of the ritonavir glass stored under both dry and humid conditions. As discussed earlier, quenched ritonavir glass was more stable than that expected from the universal line. However, t_{10} of the freeze-dried glass could be found on the universal line, most likely because the crystallization was enhanced by an increase in the surface area. The t_{10} for the ritonavir glass stored under humid condition was also found on the universal line, indicating that T_g/T can be regarded as a controlling parameter even for the glass with the plasticizer.

The impact of moisture sorption is sometimes more significant than that anticipated from change in T_g. Figure 6.1 shows the physical stability data of nifedipine glass acquired after careful experimentation. In this experiment, crystalline powder of nifedipine was dried in a vacuum oven at 50 °C and stored in a desiccator with silica gel prior to usage. Then, the dried powder was loaded into a hermetically sealed pan under a dried nitrogen atmosphere and subjected to the melt-quench process in DSC. All these steps have a significant impact on the stability of the nifedipine glass, although changes in the moisture levels during these treatments are insignificant. In this case, the bulk T_g does not work for the prediction of the physical stability, rather the T_g of the surface molecules appears to be more important.

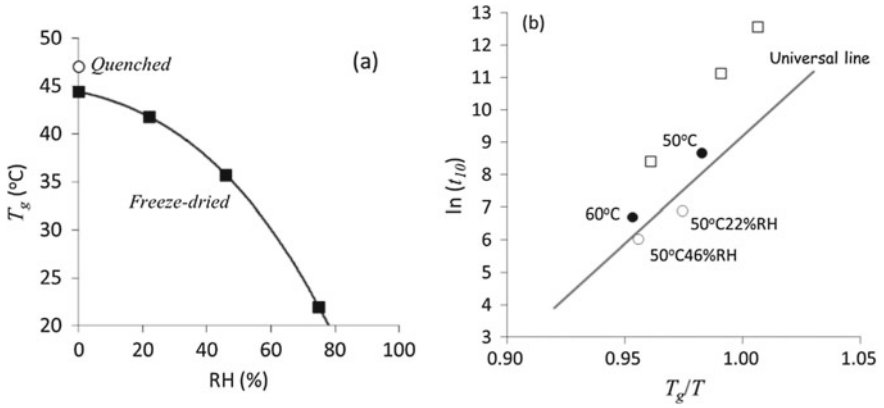

Fig. 6.11 **a** Effect of storage relative humidity (RH) on T_g (onset values) of the freeze-dried ritonavir glass. T_g of the quenched glass is also presented. **b** t_{10} of Ritonavir glass as a function of T_g/T. (□) quenched glass, (●) freeze-dried glass stored under dry condition, (○) Freeze-dried glass stored under humid condition. The storage temperature and humidity for the freeze-dried glasses are indicated in the Figure. Figures are adopted with modification form Ref. [11] with permission of Elsevier

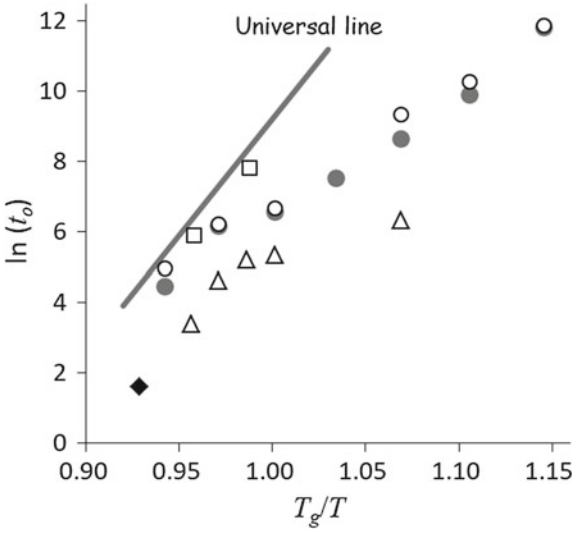

Fig. 6.12 Onset crystallization time (to, min) of nifedipine glass as a function of T_g/T. (□) After the pretreatment (see text), quenched in a hermetically sealed pan [9]. (○) Quenched in sealed DSC pan without pretreatment [5]. (●) Quenched in DSC pan [28]. (△) Quenched on glass slides. Crystallization was evaluated using polarized light microscopy. Cracked glasses were excluded from the analysis [27]. (◆) Quenched in DSC pan [29]. All the literature data were recalculated using the T_g value of 45.5 °C. The definition of onset crystallization time, which is analogous to t_{10}, is slightly different depending on literature, but its impact is ignorable in this analysis. Figure is adopted with modification form Ref. [5]

Therefore, the data for nifedipine crystallization found in the literature were generally faster than that expected from the universal line. Figure 6.12 presents the onset of crystallization times of nifedipine glasses found in various sources [5]. The data obtained after adhering to the careful treatment mentioned above were on the universal line. However, the crystallization was much faster for the glasses loaded in normally sealed pans without such pretreatment. Studies using polarized light microscopy by Bhugra et al. were performed very carefully, where cracked glasses were eliminated from the analysis [27] because they could enhance crystallization. However, the crystallization was much faster presumably because the glasses were not completely protected from the atmosphere outside.

6.7 Formulation Stability

The discussion so far was mainly focused on one-component pharmaceutical glass prepared by the melt-quench procedure. However, practical amorphous formulations are not manufactured by melt-quenching and contain other components such as hydrophilic polymers. The most representative manufacturing methods including

spray-drying, freeze-drying, and hot-melt extrusion. The glasses produced by spray- and freeze-drying have large surface areas. Those obtained from hot-melt extrusion are subjected to milling during the formulation process. Thus, the practical amorphous formulations are anticipated to be unstable compared to the melt-quenched glasses. On the other hand, the polymeric excipients typically included in amorphous formulations are expected to retard the crystallization of the drug molecules because of two reasons: steric hindrance between the drug molecules and low crystallization tendency of the polymeric excipients.

Figure 6.13 compares the various onset crystallization times of binary amorphous solid dispersions (ASDs) reported in the literature [5]. As an overall trend, the universal line seems to be valid even for the binary formulations. Comparison of nifedipine/PVP ASDs from three different sources indicates that milling promotes nucleation. However, the presence of polymeric excipients appears to stabilize the ASDs, most likely because of steric hindrance and interaction with the drug. The observations from Sanofi-Aventis compounds are very useful from a practical viewpoint since the ASDs were prepared by spray-drying. Stability of these ASDs was slightly lower but roughly on the universal line regardless of absence/presence of the moisture. Thus, accelerated physical stability testing may be possible for ASDs based on this information.

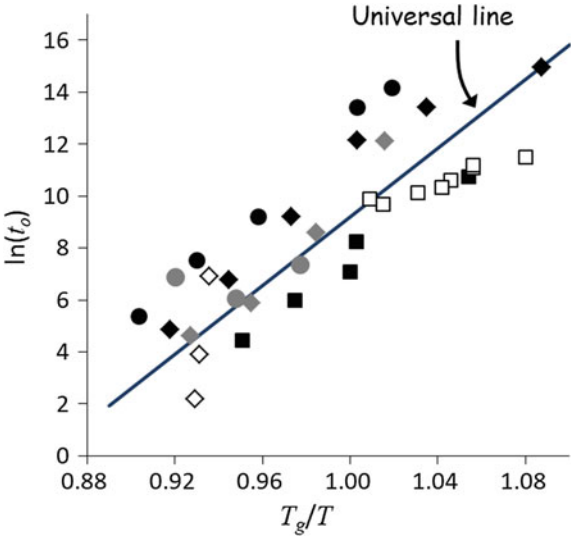

Fig. 6.13 Onset crystallization time (t_o, min) of binary ASDs as a function of T_g/T. (◆, ◆, ◇) Nifedipine/PVP ASDs prepared by melt-quench [30, 31] followed by milling [29], respectively. (●, ●) Phenobarbital/PVP ASDs prepared by melt-quench [30, 31]. (■, □) Sanofi-Aventis compound/Hydroxypropyl methylcellulose phthalate ASDs prepared by spray-drying stored under dried and humid conditions, respectively [32]. The definition of onset crystallization time, which is analogous to t_{10}, depends on literature, but the difference is ignorable in this analysis. Figure is adopted with modification form Ref. [5]

6.8 Summary

Crystallization experiments frequently face reproducibility problems. Sometimes it is unavoidable because of the stochastic property of nucleation, but other cases may be explained by the difference in thermal history of the materials. In this chapter, influence of thermal history on physical stability (crystallization) was discussed with many examples. When the glass is prepared by the quench cooling, the target (minimum) temperature of the cooling process is usually not provided in the literature. However, it may have a great impact on the crystallization behavior. Ideally, optimal nucleation and crystal growth temperatures should be comprehended to control the crystallization behavior of the glass. The crystallization tendency of the compounds, though it is not discussed in this chapter, must also be comprehended well. The cooling rate also has significant importance in determining the glass property. The relevance of chemical structure to the sensitivity of the glass property on thermal history requires more understanding. In addition to thermal history, the importance of other factors such as surface area, mechanical stress, and sorption of trace amount of moisture needs to be recognized.

Although there is no doubt that the amorphous state is quite useful in the pharmaceutical field, its practical use is relatively limited, partially because of difficulty in its handling. Storage of ASDs under freezing temperature sounds appropriate for the long-term, but it is not true in some cases as observed for celecoxib glass in this chapter. Since the current crystallization theory was developed with inorganic compounds in mind, its application to crystallization of small organics requires attention, where the structure is maintained by various strong and weak interactions such as covalent and noncovalent binding forces. Further understanding of this field should enable more frequent use of the amorphous state for practical products.

References

1. Kawakami, K.: Modification of physicochemical characteristics of active pharmaceutical ingredients and application of supersaturatable dosage forms for improving bioavailability of poorly absorbed drugs. Adv. Drug Deliv. Rev. **64**, 480–495 (2012)
2. Paudel, A., Worku, Z.A., Meeus, J., Guns, S., Van den Mooter, G.: Manufacturing of solid dispersions of poorly soluble drugs by spray drying: formulation and process considerations. Int. J. Pharm. **453**, 253–284 (2013)
3. Kawakami, K.: Theory and practice of supersaturatable formulations for poorly soluble drugs. Ther. Deliv. **6**, 339–352 (2015)
4. Singh, A.: Spray drying formulation of amorphous solid dispersions. Adv. Drug Deliv. Rev. **100**, 27–50 (2016)
5. Kawakami, K.: Crystallization tendency of pharmaceutical glasses: relevance to compound properties, impact of formulation process, and implications for design of amorphous solid dispersions. Pharmaceutics **11**, 202 (2019)
6. Baird, J.A., van Eerdenbrugh, B., Taylor, L.S.: A classification system to assess the crystallization tendency of organic molecules from undercooled melts. J. Pharm. Sci. **99**, 3787–3806 (2010)

7. Blaabjerg, L.I., Lindenberg, E., Löbmann, K., Grohganz, H., Rades, T.: Glass forming ability of amorphous drugs investigated by continuous cooling and isothermal transformation. Mol. Pharm. **13**, 3318–3325 (2016)
8. Kawakami, K.: Supersaturation and crystallization: non-equilibrium dynamics of amorphous solid dispersions for oral drug delivery. Expert Opin. Drug Deliv. **14**, 735–743 (2017)
9. Kawakami, K., Harada, T., Miura, K., Yoshihashi, Y., Yonemochi, E., Terada, K., Moriyama, H.: Relationship between crystallization tendencies during cooling from melt and isothermal storage: toward a general understanding of physical stability of pharmaceutical glasses. Mol. Pharm. **11**, 1835–1843 (2014)
10. Kawakami, K., Ohba, C.: Crystallization of probucol from solution and the glassy state. Int. J. Pharm. **517**, 322–328 (2017)
11. Kawakami, K.: Surface effects on the crystallization of ritonavir glass. J. Pharm. Sci. **104**, 276–279 (2015)
12. Kawakami, K.: Ultraslow cooling for the stabilization of pharmaceutical glasses. J. Phys. Chem. B **123**, 4996–5003 (2019)
13. Angell, C.A.: Relaxation in liquids, polymers and plastic crystals—strong/fragile patterns and problems. J. Non-Cryst. Solids **131–133**, 13–31 (1991)
14. Crowley, K.J., Zografi, G.: The use of thermal methods for predicting glass-former ability. Thermochim. Acta **380**, 79–93 (2001)
15. Kawakami, K., Harada, T., Yoshihashi, Y., Yonemochi, E., Terada, K., Moriyama, H.: Correlation between glass forming ability and fragility of pharmaceutical compounds. J. Phys. Chem. B **119**, 4873–4880 (2015)
16. Bauer, J., Spanton, S., Henry, R., Quick, J., Dziki, W., Porter, W., Morris, J.: Ritonavir: an extraordinary example of conformational polymorphism. Pharm. Res. **18**, 859–866 (2001)
17. Tominaka, S., Kawakami, K., Fukushima, M., Miyazaki, A.: Physical stabilization of pharmaceutical glasses based on hydrogen bond reorganization under sub-Tg temperature. Mol. Pharm. **14**, 264–273 (2017)
18. Kawakami, K.: Nucleation and crystallization of celecoxib glass: impact of experience of low temperature on physical stability. Thermochim. Acta **671**, 43–47 (2019)
19. Descamps, M., Dudognon, E.: Crystallization from the amorphous state: nucleation-growth decoupling, polymorphism interplay, and the role of interfaces. J. Pharm. Sci. **103**, 2615–2628 (2014)
20. Bhugra, C., Shmeis, R., Pikal, M.J.: Role of mechanical stress in crystallization and relaxation behavior of amorphous indomethacin. J. Pharm. Sci. **97**, 4446–4458 (2008)
21. Kawakami, K., Miyoshi, K., Tamura, N., Yamaguchi, T., Ida, Y.: Crystallization of sucrose glass under ambient conditions: evaluation of crystallization rate and unusual melting behavior of resultant crystals. J. Pharm. Sci. **95**, 1354–1363 (2006)
22. Ayenew, Z., Paudel, A., Rombaut, P., Van den Mooter, G.: Effect of compression on non-isothermal crystallization behaviour of amorphous indomethacin. Pharm. Res. **29**, 2489–2498 (2012)
23. Rams-Baron, M., Pacult, J., Jedrzejowska, A., Knapik-Kowalczuk, J., Paluch, M.: Changes in physical stability of supercooled etoricoxib after compression. Mol. Pharm. **15**, 2969–3978 (2018)
24. Crowley, K.J., Zografi, G.: Cryogenic grinding of indomethacin polymorphs and solvates: assessment of amorphous phase formation and amorphous phase physical stability. J. Pharm. Sci. **91**, 492–507 (2002)
25. Otsuka, M., Kaneniwa, N.: A kinetic study of the crystallization process of noncrystalline indomethacin under isothermal conditions. Chem. Pharm. Bull. **36**, 4026–4032 (1988)
26. Andronis, V., Zografi, G.: Crystal nucleation and growth of indomethacin polymorphs from the amorphous state. J. Non-Cryst. Solids **271**, 236–248 (2000)
27. Bhugra, C., Shmeis, R., Krill, S.L., Pikal, M.J.: Prediction of onset of crystallization from experimental relaxation times. II. Comparison between predicted and experimental onset times. J. Pharm. Sci. **97**, 455–472 (2008)

28. Aso, Y., Yoshioka, S., Kojima, S.: Relationship between the crystallization rates of amorphous nifedipine, phenobarbital, and flopropione, and their molecular mobility as measured by their enthalpy relaxation and 1H NMR relaxation times. J. Pharm. Sci. **89**, 408–416 (2000)
29. Kothari, K., Ragoonanan, V., Suryanarayanan, R.: The role of polymer concentration on the molecular mobility and physical stability of nifedipine solid dispersions. Mol. Pharm. **12**, 1477–1484 (2015)
30. Aso, Y., Yoshioka, S., Kojima, S.: Molecular mobility-based estimation of the crystallization rates of amorphous nifedipine and phenobarbital in poly(vinylpyrrolidone) solid dispersions. J. Pharm. Sci. **93**, 384–391 (2004)
31. Caron, V., Bhugra, C., Pikal, M.J.: Prediction of onset of crystallization in amorphous pharmaceutical systems: phenobarbital, nifedipine/PVP, and phenobarbital/PVP. J. Pharm. Sci. **99**, 3887–3900 (2010)
32. Greco, S., Authelin, J.R., Leveder, C., Segalini, A.: A practical method to predict physical stability of amorphous solid dispersions. Mol. Pharm. **29**, 2792–2805 (2012)

Part II
Structure and Design of Crystals

Chapter 7
Supramolecular, Hierarchical, and Energetical Interpretation of Organic Crystals: Generation of Supramolecular Chirality in Assemblies of Achiral Molecules

Mikiji Miyata and Seiji Tsuzuki

Abstract Recent progress in personal computers and computational methods has enabled us to practically perform quantitative evaluation of intermolecular interaction energies of organic molecules consisting of more than one hundred carbon atoms using density functional theory (DFT) calculations with dispersion correction. The calculations prompted us to make a systematic method for defining dimeric molecular assemblies in organic crystals. Based on *Z*-matrix involving dummy atoms, we designed a rectangular triangle model where a molecule positions through three kinds of rotations. This model clarified generation of position-dependent chirality along an axis. Symmetry operations, such as translation, two-fold rotation, two-fold helix, and so on, connect the identical triangles to generate position-dependent supramolecular chirality of the assemblies. The intermolecular interaction energies of the dimers evaluated by the supermolecule method depend on assemble modes of the dimers, leading us to the interpretation for hierarchical structures in crystals as well as generation of supramolecular chirality from achiral molecules in the crystals.

Keywords DFT calculations · Dispersion correction · Position-dependent chirality · Supramolecular chirality · Intermolecular interaction energy · Hierarchical structures · Chiral crystallization

M. Miyata (✉)
The Institute of Scientific and Industrial Research, Osaka University, 8-1 Mihogaoka, Ibaraki 567-0047, Osaka, Japan
e-mail: miyata@mls.eng.osaka-u.ac.jp

S. Tsuzuki
Research Center for Computational Design of Advanced Functional Materials (CD-FMat), National Institute of Advanced Industrial Science and Technology (AIST), 1-1-1 Umezono, Tsukuba 305-8568, Ibaraki, Japan
e-mail: s.tsuzuki@aist.go.jp

M. Sakamoto and H. Uekusa (eds.), *Advances in Organic Crystal Chemistry*,
https://doi.org/10.1007/978-981-15-5085-0_7

7.1 Introduction

Organic crystals are analyzed by using a large amount of reflection data according to X-ray crystallography which bases on symmetry theory in mathematics [1]. This indicates that the analysis has no relation to interaction energies among molecules. Substantially, the crystals are formed due to intermolecular interactions among organic molecules [2]. Conventionally, such interaction energies have been calculated with powerful supercomputers using high-level ab initio calculations by specialists in quantum chemistry. This mainly comes from the fact that a large basis set and electron correlation correction are necessary for an accurate evaluation of the dispersion interactions. Therefore, an accurate evaluation of the dispersion energies demands a vast amount of computational resources, introducing much difficulty to understand energetic aspect of organic crystals [3–5].

However, recent progresses in personal computers and computational methods give us a challenging time to overcome this difficulty as for the evaluation of the dispersion energies. Namely, new personal computers with multicore CPU perform rapid calculations for intermolecular interactions of organic molecules with more than a hundred carbons using dispersion-corrected DFT method [6]. Therefore, the interaction energies between two neighbored molecules in crystals can be briefly evaluated. Gaussian is one of the well-known ab initio molecular orbital and DFT calculation program [7]. GaussView is graphical user interface (GUI) program for Gaussian [8]. We can easily evaluate intermolecular interaction energies between molecules in organic crystals using Gaussian and GaussView programs.

Such a change would introduce the third stage of our studies on organic crystal chemistry (Fig. 7.1). In the first stage, on the basis of space group [1], we classified crystal structures (Fig. 7.1a) [9, 10]. In the second stage, according to the Cambridge Structural Database and its graphics Mercury [11], we devoted to two subjects about organic crystals (Fig. 7.1b) [12, 13]. The one is supramolecular chirality of two-fold helical (or screw) molecular assemblies, and the other is hierarchical structures through bundles of the assemblies. The former indicates a difference between space geometry and space group [14–16]. For example, two-fold helical assemblies are discriminable in handedness from an anisotropic view. In contrast, from an isotropic view of space group, two-fold helical operations form identical assemblies by both clockwise and anticlockwise rotations.

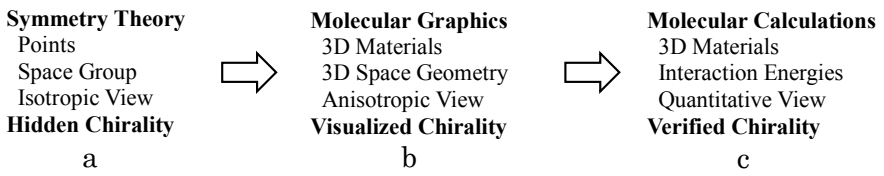

Fig. 7.1 Three stages for understanding generation of supramolecular chirality in crystal structures from viewpoints of symmetry theory (**a**), molecular graphics (**b**), and molecular calculations (**c**)

The other subject deals with hierarchical structures of organic crystals, such as 1D columns, 2D layers, 3D stacked layers [16–18]. For example, the preferred two-fold helical columns with three-axial chirality construct chiral layers, which are stacked to give chiral crystals. According to such a bundling model, chiral crystals are briefly defined as follows. Only right- or left-handed two-fold helices are bundled to form the corresponding right- or left-handed crystals, respectively.

It is considered that these two subjects demand any quantitative expressions in mathematics (Fig. 7.1c). It is noteworthy that the above-mentioned Gaussian program uses *Z*-matrix and permits dummy atoms for defining geometries of organic molecules [5]. Accordingly, positions of any atoms of a molecule can be defined by three parameters which determine distances between atoms, angles formed by three atoms, and dihedral angles. Significantly, the last dihedral angles are suitable for determining chirality, since the four points for defining the dihedral angles enable us to determine handedness of chirality. Likewise, the above-mentioned hierarchical structures demand any quantitative explanation from an energetical viewpoint. The Gaussian program serves as an excellent tool for providing interaction energies between molecules.

We aim to solve two challenging problems, generation of supramolecular chirality and hierarchical structures in organic crystals. This chapter deals with (i) a rectangular triangle model by using *Z*-matrix and dummy atoms for positioning molecules, (ii) generation of supramolecular chirality in molecular assemblies on the basis of three kinds of rotations along an axis, and (iii) generation of hierarchical structures on the basis of interaction energies between neighbored molecules in organic crystals. As described below, the solution has come from an elucidation of three kinds of rotations of a molecule at the fixed point along an axis.

7.2 Rectangular Triangle Unit with a Molecule

7.2.1 Connection Model of a Rectangular Triangle and a Molecule

Z-matrix defines the position of an atom ($C4$) by using the positions of preceding three atoms ($C3$, $C2$, $C1$), as shown in Fig. 7.2a. Firstly, the parameter $B3$ determines the distance between $C4$ and $C3$; secondly, the parameter $A2$ determines the angle formed by $C4$, $C3$, and $C2$; and thirdly, the parameter $D1$ determines the dihedral (torsion) angle formed by $C4$, $C3$, $C2$, and $C1$ with the direction from $C4$ to $C1$ ($C4 \rightarrow C3 \rightarrow C2 \rightarrow C1$). Such a dihedral angle is possible to take a sign of either plus (right) or minus (left), prompting us to discriminate the chirality and its handedness. Figure 7.2b shows a *Z*-matrix description for the Gaussian program.

In addition to real atoms, we may employ dummy atoms that enable us to freely design assemblies of points, including lines, polygons, polyhedrons, and so on. Figure 7.2c shows an example of a rectangular triangle with three dummy atoms

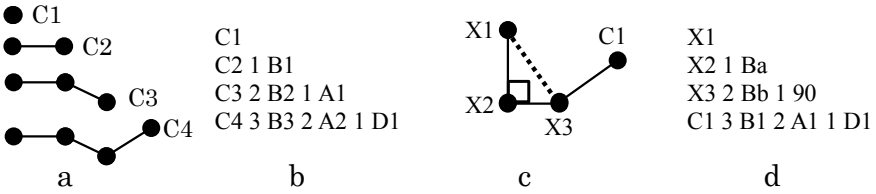

Fig. 7.2 Definition of the position of atom ($C4$) based on the distance ($B3$) from $C3$, the angle ($A2$) formed by $C4$, $C3$ and $C2$, as well as a dihedral (torsion) angle ($D1$) defined by $C4$, $C3$, $C2$ and $C1$ (**a**), Z-matrix for an assembly of four carbon atoms (**b**), a rectangular triangle as an assembly of three dummy atoms and a carbon atom connected to the third dummy atom (**c**), and its Z-matrix (**d**)

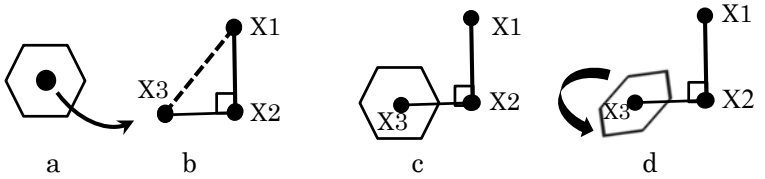

Fig. 7.3 A benzene molecule with a dummy atom (**a**), a rectangular triangle composed of three dummy atoms (**b**), the dummy atom of benzene and the dummy atom $X3$ are overlapped (**c**), and any movements of the molecule around the center (**d**)

($X1, X2, X3$). This model suggests that the fourth real atom is connected to the third dummy atom $X3$ which serves as a root for connecting any molecule (Fig. 7.2d).

Z-matrix provides multiple ways to define the structure of organic molecule and any others. Figure 7.3 shows an example of a benzene molecule. Figure 7.3a depicts the molecule with a dummy atom which was put on the center of benzene. Figure 7.3b displays a rectangular triangle composed of three dummy atoms. The dummy atom at the center of benzene and the $X3$ are overlapped (Fig. 7.3c).

7.2.2 Relation to a Unit Cell of a Crystal

The above-mentioned connection induced us to design a triangle model which simulates a steric situation of a molecule in organic crystals. Thus, a perpendicular line ($X1$–$X2$) in Fig. 7.3c functions as a unit axis for a two-fold rotation or helix in a unit cell of a crystal. Another horizontal line ($X2$–$X3$) corresponds to a distance between the axis and the center of a molecule. Namely, $X3$ serves as a root for positioning the molecule.

It is necessary to use real parameters for understanding the above-mentioned triangle. One takes an example of benzene. The main lattice parameters for its crystal with space group $P2_1/c$ are summarized in Fig. 7.4. The distance between $X1$ and

Benzene
Monoclinic
Space group $P2_1/c$

a:5.417, b:5.376. c:7.532
a Ba=b=5.376
Bb=c/4=1.883
Bc=a=5.417

α:90, β:110, γ:90
b Ae =α=90
Af1=β=110
Af2=180-β=70
Ag=γ=90

Rotations along b-axis
c x(φ): 20 y(ψ): 30 z(ω): 27

d Angles for z-matrix
Bond angles
Ax: 20 Ay: 30 Az: 90
Dihedral angles
Dx: -90; -90; +90; +90
Dy: +90; +90; -90; -90
Dz: -27 ; +27; -27; +27

Fig. 7.4 Relation between lattice parameters and *Z*-matrix of a benzene crystal. Parameters of distances (**a**) and angles (**b**) for a unit cell and a triangle. Three kinds of rotations along *b*-axis (**c**). Bond and dihedral angles for *Z*-matrix (**d**)

*X*2 (Ba) is 5.376 Å which corresponds to a unit length of *b*-axis, while one between *X*2 and *X*3 (Bb) is 1.883 Å which does to the one-fourth length of *c*-axis. These Ba and Bb are available for *Z*-matrix in Fig. 7.2d.

In this way, the triangle model is related to the crystal structure, but one problem remains. In spite of a fixed orientation to the axis in Fig. 7.3c, molecular graphics mostly displays diverse orientations in crystals. At last, we reached an idea that such a difference derives from any rotations of the molecule toward the axis (Fig. 7.3d). The next section describes how to simulate the rotations.

7.2.3 Positioning for Three Kinds of Rotations

The earth rotates around the sun (Fig. 7.5a). In daily life, we sit on a rotating chair at a desk and rotate in various ways (Fig. 7.5b). This movement can be simplified as rotations around three axes of a facial plate (Fig. 7.5c).

Mathematically, the rotations of the plate can be combined with the triangle. First of all, a point of a plate (***o***) is overlapped with the *X*3 of the rectangular triangle. Next, like our body on a chair, the plate can rotate at the *X*3 around three axes (x, y, z). In order to define each rotation angle (φ, ψ, ω), we employ the corresponding unit vectors (***x***, ***y***, ***z***) (Fig. 7.6a), which are expressed by three additional dummy

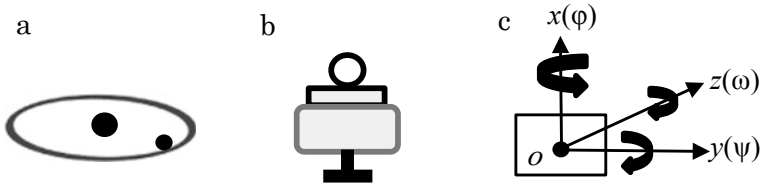

Fig. 7.5 Rotations of a material around other material or axes, the earth around the sun (**a**), a person on a rotating chair at a desk (**b**), and a facial plate towards three axes (**c**)

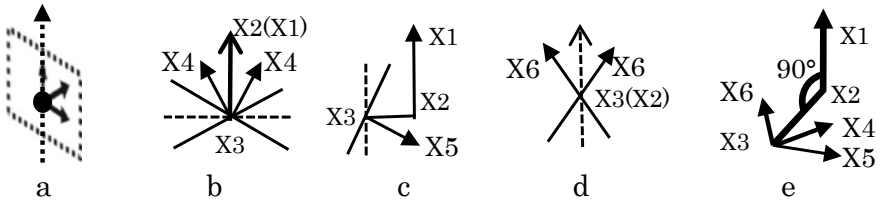

Fig. 7.6 Three kinds of rotations of a facial plate with the corresponding three unit vectors (**a**), a unit vector $\boldsymbol{x}$ as an over-view (**b**), $\boldsymbol{y}$ as a side-view (**c**), $\boldsymbol{z}$ as a front-view (**d**) for denoting three rotation angles, and dummy atoms ($X4$, $X5$, $X6$) connected with the dummy atom $X3$ of the rectangular triangle ($X1$, $X2$, $X3$) (**e**)

atoms ($X4$, $X5$, $X6$) (Fig. 7.6b–d). These dummy atoms are connected to the above-mentioned triangle ($X1$, $X2$, $X3$) (Fig. 7.6e). The $X3$ serves as a root of the vectors, and the $X4$, $X5$, and $X6$ function for determining bond angles and dihedral angles of Z-matrix in the following way.

The first vector $\boldsymbol{x}$, which is perpendicular to the plate, rotates around the x-axis by an angle (φ) and is denoted as the $X4$ (Fig. 7.6b). The rotational direction is right (clockwise) or left (anticlockwise) to the axis $X3$–$X2$ of the triangle. The second vector $\boldsymbol{y}$, which is perpendicular to both x-axis and y-axis, rotates around the y-axis by an angle (ψ) and is denoted as the $X5$ (Fig. 7.6c). This corresponds to a tilt forward to the axis $X1$–$X2$. The third vector $\boldsymbol{z}$, which is perpendicular to the vector $\boldsymbol{y}$, indicates a rotation around the z-axis by an angle (ω) and is denoted as the $X6$ (Fig. 7.6d). This angle corresponds to the right (clockwise) or left (anticlockwise) rotation from the x-axis and is fully described as a dihedral angle in the next section.

In organic crystals, the amount of each angle is restricted much smaller than 90°, since the molecule touches to the axis $X1$–$X2$ on both sides. Their angles (φ, ψ, ω) are roughly measured by using a semicircular protractor on display for molecular graphics. Figure 7.4 includes their values for benzene crystal.

7.2.4 Position-Dependent Chirality

The additional dummy atoms ($X4$, $X5$, $X6$) require bond angles (Ax, Ay, Az) and dihedral angles (Dx, Dy, Dz) for Z-matrix. The results are summarized in Fig. 7.7, where you see four sets of three bond angles and three dihedral angles.

Figure 7.7a shows a clockwise or right-handed rotation (R) of $X4$ with a bond angle of $Ax(\varphi)$. Such a horizontal rotation yields a constant dihedral angle $Dx(X4 \rightarrow X3 \rightarrow X2 \rightarrow X1)$ with $-90°$. The subsequent tilt rotations of $X5$ with a bond angle of $Ay(\psi)$ ($0 < \psi < 90$) yield a constant dihedral angle $Dy(X5 \rightarrow X3 \rightarrow X4 \rightarrow X2)$ with $+90°$ (Fig. 7.7b). So, chiral isomers with $(-90, +90)$ are recognized as (R)-isomers.

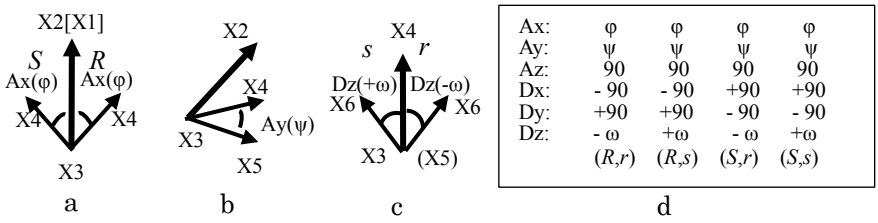

Fig. 7.7 Combination of angles formed by three atoms and dihedral angles for three kinds of rotations. Right-slide (*R*) or left-one (*S*) from the axis *X*2–*X*3 (*X*4, *Ax*) (**a**), tilt to the axis *X*2–*X*3–*X*4 (*X*5, *Ay*) (**b**), right-rotation (*r*) or left-one (*s*) from *X*3–*X*4 (*X*6, A*z*) (**c**), and four combinations of the angles generated from three kinds of rotations on *X*3 (**d**)

In contrast, there exists an anticlockwise or left-handed rotation (*S*) of *X*4 with a bond angle of $Ax(\varphi)$. Such rotations yield a dihedral angle $Dx(X4 \rightarrow X3 \rightarrow X2 \rightarrow X1)$ with $+90°$, followed by the subsequent tilt rotations of *X*5 having a constant dihedral angle $Dy(X5 \rightarrow X3 \rightarrow X4 \rightarrow X2)$ with $-90°$. So, chiral isomers (+90, −90) are recognized as (*S*)-isomers.

Furthermore, the third rotation of *X*6, which has a defined angle $Az(X6\text{–}X3\text{–}X5)$ with $+90°$, yields a dihedral angle $Dz(X6 \rightarrow X3 \rightarrow X5 \rightarrow X4)$ with a value of either $-\omega$ or $+\omega$ (Fig. 7.7c), indicating generation of chiral (*r*)- or (*s*)-isomers, respectively. In this way, we discriminate four sets of bond angles and dihedral angles as (*R*, *r*), (*R*, *s*), (*S*, *r*), and (*S*, *s*) (Fig. 7.7d).

At last, we reached the novel idea that the triangle rotation model makes clear the existence of four stereoisomers. We term this chirality as position-dependent chirality, since the chirality depends on a position of a molecule toward an axis. This finding leads us to specify their *Z*-matrix by use of six dummy atoms involving (*X*1, *X*2, *X*3) for the triangle and (*X*4, *X*5, *X*6) for the three kinds of rotations (Fig. 7.8).

(*R*,*r*) a	(*R*,*s*) b	(*S*,*r*) c	(*S*,*s*) d
X1	X1	X1	X1
X2 1 Ba	X2 1 Ba	X2 1 Ba	X2 1 Ba
X3 2 Bb 1 90	X3 2 Bb 1 90	X3 2 Bb 1 90	X3 2 Bb 1 90
X4 3 1.0 2 φ 1 -90	X4 3 1.0 2 φ 1 -90	X4 3 1.0 2 φ 1 90	X4 3 1.0 2 φ 1 90
X5 3 1.0 4 ψ 2 90	X5 3 1.0 4 ψ 2 90	X5 3 1.0 4 ψ 2 -90	X5 3 1.0 4 ψ 2 -90
X6 3 1.0 5 90 4 -ω	X6 3 1.0 5 90 4 ω	X6 3 1.0 5 90 4 -ω	X6 3 1.0 5 90 4 ω

Fig. 7.8 *Z*-matrix expression of position-dependent chiral isomers (*R*, *r*) (**a**), (*R*, *s*) (**b**), (*S*, *r*) (**c**) and (*S*, *s*) (**d**) by using the rectangular triangle and rotation model with an organic molecule. Three rotation angles (φ, ψ, ω) can be measured on molecular graphics

a (*R*,*r*)-Isomer

```
X1
X2 1 Ba
X3 2 Bb 1 90
X4 3 1.0 2 φ 1 -90
X5 3 1.0 4 ψ 2 90
X6 3 1.0 5 90 4 -ω
C1 3 R1 5 90 6 0
C2 3 R1 5 90 6 60
C3 3 R1 5 90 6 120
C4 3 R1 5 90 6 180
C5 3 R1 5 90 6 240
C6 3 R1 5 90 6 300
H1 3 R2 5 90 6 0
H2 3 R2 5 90 6 60
H3 3 R2 5 90 6 120
H4 3 R2 5 90 6 180
H5 3 R2 5 90 6 240
H6 3 R2 5 90 6 300

R1 1.394
R2 2.475
```

b (*R*,*s*)-Isomer

```
X1
X2 1 Ba
X3 2 Bb 1 90
X4 3 1.0 2 φ 1 -90
X5 3 1.0 4 ψ 2 90
X6 3 1.0 5 90 4 ω
C1 3 R1 5 90 6 0
C2 3 R1 5 90 6 60
C3 3 R1 5 90 6 120
C4 3 R1 5 90 6 180
C5 3 R1 5 90 6 240
C6 3 R1 5 90 6 300
H1 3 R2 5 90 6 0
H2 3 R2 5 90 6 60
H3 3 R2 5 90 6 120
H4 3 R2 5 90 6 180
H5 3 R2 5 90 6 240
H6 3 R2 5 90 6 300

R1 1.394
R2 2.475
```

c (*S*,*r*)-Isomer

```
X1
X2 1 Ba
X3 2 Bb 1 90
X4 3 1.0 2 φ 1 90
X5 3 1.0 4 ψ 2 -90
X6 3 1.0 5 90 4 -ω
C1 3 R1 5 90 6 0
C2 3 R1 5 90 6 60
C3 3 R1 5 90 6 120
C4 3 R1 5 90 6 180
C5 3 R1 5 90 6 240
C6 3 R1 5 90 6 300
H1 3 R2 5 90 6 0
H2 3 R2 5 90 6 60
H3 3 R2 5 90 6 120
H4 3 R2 5 90 6 180
H5 3 R2 5 90 6 240
H6 3 R2 5 90 6 300

R1 1.394
R2 2.475
```

d (*S*,*s*)-Isomer

```
X1
X2 1 Ba
X3 2 Bb 1 90
X4 3 1.0 2 φ 1 90
X5 3 1.0 4 ψ 2 -90
X6 3 1.0 5 90 4 ω
C1 3 R1 5 90 6 0
C2 3 R1 5 90 6 60
C3 3 R1 5 90 6 120
C4 3 R1 5 90 6 180
C5 3 R1 5 90 6 240
C6 3 R1 5 90 6 300
H1 3 R2 5 90 6 0
H2 3 R2 5 90 6 60
H3 3 R2 5 90 6 120
H4 3 R2 5 90 6 180
H5 3 R2 5 90 6 240
H6 3 R2 5 90 6 300

R1 1.394
R2 2.475
```

Fig. 7.9 *Z*-matrix of a benzene molecule in its crystal on the basis of the rectangular triangle and three kinds of rotations. Four position-dependent isomers; (*R*, *r*)-isomer (**a**), (*R*, *s*)-isomer (**b**), (*S*, *r*)-isomer (**c**), and (*S*, *s*)-isomer (**d**)

7.2.5 Z-Matrix of a Molecule with Position-Dependent Chirality in Crystals

Now, one can write down the *Z*-matrix for any organic molecules in crystals by using the triangle and three kinds of rotations. The necessary parameters (distances, angles, and dihedral angles) are acquired from the known crystal parameters as well as the measured rotation angles on graphics. As described in the next section, the latter angles are determined by comparison of bond distances due to Mercury [11] and GaussView [8] more exactly than by a semicircular protractor on display. Figure 7.9 denotes an example of a benzene molecule which belongs to space group $P2_1/c$. The measured angles (φ, ψ, ω) are available in Fig. 7.4.

7.3 Bimolecular Assembly with Connection of the Triangle Units

7.3.1 Connection of Two Rectangular Triangles Through Symmetry Operations

Two rectangular triangular units are connected by using dummy atoms in various ways. Regular structures of dimers in crystals owe to symmetry operations. It is noteworthy that translation operation derives from translation of a cell unit of crystals,

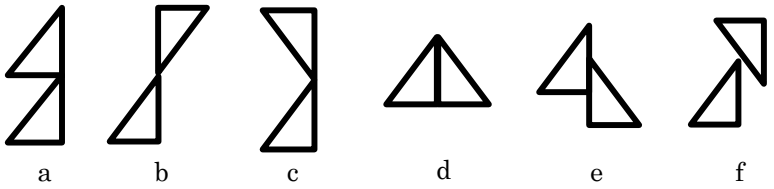

Fig. 7.10 Various overlaps of two triangular triangles: two points (**a**–**c**), two points and two lines (**d**, **e**), and a point and a line onto a glide plane (**f**)

resulting in 1D columnar assemblies which serve as fundamental architecture in organic crystals. Figure 7.10 exemplifies various overlaps of points and lines. The one is an overlap of two points. Figure 7.10a–c depict translation, inversion, and reflection, respectively. The other is an overlap of two lines composed of two points, yielding two-fold rotation (Fig. 7.10d) and two-fold helix (Fig. 7.10e). Figure 7.10f illustrates an overlap on a glide plane.

7.3.2 Connection of Molecules with Position-Dependent Chirality

We consider a triangle with a molecule involving three kinds of rotations. The resulting four stereoisomers of (*R*, *r*), (*R*, *s*), (*S*, *r*), and (*S*, *s*) are possible to combine together for dimers. Among them, the same stereoisomers of (*R*, *r*) or (*S*, *s*) are assembled by symmetry operations, such as translation, two-fold rotation, and two-fold helix along an axis to yield a chiral (*R*, *r*)(*R*, *r*)- or (*S*, *s*)(*S*, *s*)-dimer (and vice versa).

On the other hand, an enantiomer of (*R*, *r*) and (*S*, *s*) is assembled by symmetry operations, such as inversion at one point, reflection on a mirror plane, reflection on a mirror with one-half translation to yield an achiral (*R*, *r*)(*S*, *s*)-dimer. The other enantiomer of (*R*, *s*) and (*S*, *r*) is possibly combined to yield an achiral (*R*, *s*)(*S*, *r*)-dimer.

In principle, another diastereomeric (*R*, *r*)(*R*, *s*)-dimer, (*S*, *s*)(*S*, *r*)-dimer, (*R*, *r*)(*S*, *r*)-dimer as well as (*S*, *s*)(*R*, *s*)-dimer are possible. Symmetry operations do not express these diastereomeric dimers, and probably we can observe these dimers as two independent molecules in crystals. More detailed research is necessary for discussing these dimers.

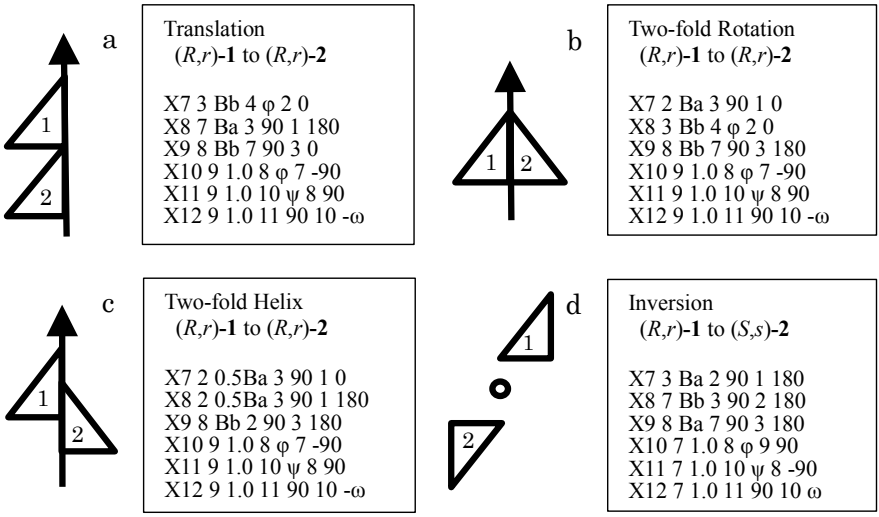

Fig. 7.11 Connection of two triangular triangles with symmetry operations: translation (**a**), two-fold rotation (**b**), two-fold helix (**c**) along an identical axis, and inversion (**d**) through a point

7.3.3 Connection of Molecules Along Identical Axes

These assemble methods have the corresponding *Z*-matrix. The first triangle has the same six dummy atoms (*X*1 to *X*6) as the ones in Fig. 7.8, while the second triangle has additional six dummy atoms (*X*7 to *X*12). The representative four kinds of the dimers (only *X*7 to *X*12) are illustrated in Fig. 7.11. *Z*-matrix has a rule to specify each atom or dummy atom through a completely arranged number from the first one. These expressions by *Z*-matrix in Fig. 7.11 start from the number 1 for the first dummy atom *X*1 and go to the number 12 for the last dummy atom *X*12.

7.3.4 Connection of Molecules Along Separated Axes

Next, we consider other cases that the lines (*X*1–*X*2) of the triangles are separated from each other. The above-mentioned examples in Fig. 7.11 belong to the identical cases, while those in Fig. 7.12 to the separated ones. The latter is observed in stacking of layers as mentioned later.

The other dimers through reflection on a mirror as well as glide plane can be expressed in a similar way to give us achiral dimers, leading us to the world of achiral assemblies in comparison with one of chiral ones.

At last, we obtain whole *Z*-matrix of four kinds of benzene dimers. Three examples of them are shown in Fig. 7.13.

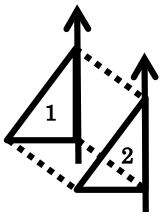

a

Translation
(*R*,*r*)-**1** to (*R*,*r*)-**2**

X7 1 Bc 2 90 3 Af1
X8 7 Ba 1 90 2 0
X9 8 Bb 7 90 1 -Af2
X10 9 1.0 8 φ 7 -90
X11 9 1.0 10 ψ 8 90
X12 9 1.0 11 90 10 -ω

b

Two-fold helix
(*R*,*r*)-**1** to (*R*,*r*)-**2**

X7 2 Bc 1 90 3 Af1
X8 7 0.5Ba 2 90 1 180
X9 8 Bb 7 90 2 -Af1
X10 9 1.0 8 φ 7 -90
X11 9 1.0 10 ψ 8 90
X12 9 1.0 11 90 10 -ω

Fig. 7.12 Connection of two triangular triangles with symmetry operations: translation (**a**) and two-fold helix (**b**) through the separating axes

(*R*,*r*)(*R*,*r*)-Dimer
through translation

X1
X2 1 Ba
X3 2 Bb 1 90
X4 3 1.0 2 Ax 1 -90
X5 3 1.0 4 Ay 2 90
X6 3 1.0 5 90 4 Dzr
C1 3 R1 5 90 6 0 0 1
C2 3 R1 5 90 6 60 0 1
C3 3 R1 5 90 6 120 0 1
C4 3 R1 5 90 6 180 0 1
C5 3 R1 5 90 6 240 0 1
C6 3 R1 5 90 6 300 0 1
H1 3 R2 5 90 6 0 0 1
H2 3 R2 5 90 6 60 0 1
H3 3 R2 5 90 6 120 0 1
H4 3 R2 5 90 6 180 0 1
H5 3 R2 5 90 6 240 0 1
H6 3 R2 5 90 6 300 0 1
X7 3 Bb 4 Ax 2 0
X8 2 Ba 3 90 1 180
X9 20 Bb 19 90 3 0
X10 21 1.0 20 Ax 19 -90
X11 21 1.0 22 Ay 20 90
X12 21 1.0 23 90 22 Dzr
C7 21 R1 23 90 24 0 0 2
C8 21 R1 23 90 24 60 0 2

(Abbreviated)

R1 1.394
R2 2.475
Ba 5.376
Bb 1.883
Ax 20
Ay 30
Dzr -27

a

(*R*,*r*)(*R*,*r*)-Dimer
through two-fold helix

X1
X2 1 Ba
X3 2 Bb 1 90
X4 3 1.0 2 Ax 1 -90
X5 3 1.0 4 Ay 2 90
X6 3 1.0 5 90 4 Dzr
C1 3 R1 5 90.0 6 0 0 1
C2 3 R1 5 90.0 6 60 0 1
C3 3 R1 5 90.0 6 120 0 1
C4 3 R1 5 90.0 6 180 0 1
C5 3 R1 5 90.0 6 240 0 1
C6 3 R1 5 90.0 6 300 0 1
H1 3 R2 5 90.0 6 0 0 1
H2 3 R2 5 90.0 6 60 0 1
H3 3 R2 5 90.0 6 120 0 1
H4 3 R2 5 90.0 6 180 0 1
H5 3 R2 5 90.0 6 240 0 1
H6 3 R2 5 90.0 6 300 0 1
X7 2 Ba2 3 90 1 0
X8 2 Ba2 3 90 1 180
X9 20 Bb 19 90 3 180
X10 21 1.0 20 Ax 19 -90
X11 21 1.0 22 Ay 20 90
X12 21 1.0 23 90 22 Dzr
C7 21 R1 23 90 24 0 0 2
C8 21 R1 23 90 24 60 0 2

(Abbreviated)

R1 1.394
R2 2.475
Ba 5.376
Ba2 2.688
Bb 1.883
Ax 20
Ay 30
Dzr -27

b

(*R*,*r*)(*S*,*s*)-Dimer
through inversion

X1
X2 1 Ba
X3 2 Bb 1 90.0
X4 3 1.0 2 Ax 1 -90
X5 3 1.0 4 Ay 2 90
X6 3 1.0 5 90 4 Dzr
C1 3 R1 5 90 6 0 0 1
C2 3 R1 5 90 7 60 0 1
C3 3 R1 5 90 8 60 0 1
C4 3 R1 5 90 9 60 0 1
C5 3 R1 5 90 10 60 0 1
C6 3 R1 5 90 11 60 0 1
H1 3 R2 5 90 7 0 0 1
H2 3 R2 5 90 8 0 0 1
H3 3 R2 5 90 9 0 0 1
H4 3 R2 5 90 10 0 0 1
H5 3 R2 5 90 11 0 0 1
H6 3 R2 5 90 12 0 0 1
X7 3 Ba 2 90 1 180
X8 19 Bb 3 90 2 180
X9 20 Ba 19 90 3 180
X10 19 1.0 20 Ax 21 90
X11 19 1.0 22 Ay 20 -90
X12 19 1.0 23 90 22 Dzs
C7 19 R1 23 90 24 0 0 2
C8 19 R1 23 90 25 60 0 2

(Abbreviated)

R1 1.394
R2 2.475
Ba 5.376
Bb 1.883
Ax 20
Ay 30
Dzr -27
Dzs 27

c

Fig. 7.13 *Z*-matrix of benzene dimers together with a rectangular triangle and three kinds of rotations: dimers with symmetry operation, such as translation (**a**), two-fold helix (**b**), inversion (**c**)

```
%nprocshared=4
%chk=Benzene(Rr)(Rr)Dimer(trala-column).chk
#p b3lyp/6-311g(d,p) empiricaldispersion=gd3 counterpoise=2

Benzene(Rr)(Rr)Dimer(trala-column) (DFT)(GD3)(6-311G**)

0 1 0 1 0 1
```

Fig. 7.14 Example of input file for Gaussian calculations

7.4 Intermolecular Interaction Energy Calculations by Gaussian Program

7.4.1 Methods of DFT Calculations

Intermolecular interaction energies were calculated using Gaussian 16 W [7]. The B3LYP functional and 6-311G** basis set were used for the DFT calculations with Grimme's D3 dispersion correction [19]. The basis set superposition error (BSSE) [20] was corrected for all the interaction energy calculations using the counterpoise method [21]. Figure 7.14 shows an example of input file for the calculation of the interaction energy of an (*R*, *r*)(*R*, *r*)-dimer of benzene with translation (trala) for symmetry operation. The contents of Figs. 7.13 and 7.14 are merged according to the defined procedure to yield the final input file of the Gaussian program for calculating the intermolecular interaction energies of neighbored molecules in organic crystals.

7.4.2 Dependence of the Interaction Energies on Rotation Parameters

In order to evaluate effects of various parameters, we checked two distances of triangles as well as three kinds of rotations in the case of benzene crystal with space group $P2_1/c$ (Fig. 7.4). The former is exactly obtained by crystal lattice parameters, while the latter angles of rotations are roughly measured on display by GaussView [8] and Mercury [11]. Namely, we check the distances between atoms in the designed structures by GaussView and those in crystal structures by Mercury with changes of the rotation values. Among many values, we employ the most suitable ones.

The interaction energies may naturally depend on the rotation angles. For an example, Table 7.1 displays the energy changes of an (*R*, *r*)(*R*, *r*)-dimer of benzene obtained through two-fold helix symmetry operation. The angles of $Ax(\varphi)$, $Ay(\psi)$, and $Dzr(-\omega)$ were changed with a range of 10°. Each minimum value approximately lies in $Ax(\varphi) = 18, Ay(\psi) = 26, Dzr(-\omega) = -29$, which are somewhat different from the set of values (20, 30, −27) in Fig. 7.4. This suggests that crystal structures are

Table 7.1 Interaction energies (kcal/mol) of (*R*, *r*)(*R*, *r*)-dimer of benzene through two-fold helix symmetry operation on dependence of a set of rotation angles (φ, ψ, ω) for $Ax(\varphi)$, $Ay(\psi)$, and $Dzr(-\omega)$ in *Z*-matrix of Fig. 7.13b

(12, 30, 27) −2.31	(20, 22, 27) −2.41	(20, 30, 21) −1.99
(14, 30, 27) −2.34	(20, 24, 27) −2.44	(20, 30, 23) −2.15
(16, 30, 27) −2.35	(20, 26, 27) −2.44	(20, 30, 25) −2.25
(18, 30, 27) −2.35	(20, 28, 27) −2.40	(20, 30, 27) −2.32
(20, 30, 27) −2.32	(20, 30, 27) −2.32	(20, 30, 29) −2.33
(22, 30, 27) −2.22	(20, 32, 27) −2.19	(20, 30, 31) −2.30

constructed to increase the stabilization by interactions with many molecules in the crystal.

7.4.3 *One Molecule Surrounded by Twelve Neighbored Molecules*

A spherical material is generally surrounded by other twelve ones, termed as the closest packing structure [22, 23]. Organic crystals may keep the same principle in spite of non-spherical shape of molecules. Namely, one organic molecule is surrounded by twelve neighbored organic molecules. Figure 7.15a shows an example of benzene crystal which belongs to monoclinic, space group $P2_1/c$ [39]. Figure 7.15b depicts centroids of the molecules, indicating that a center molecule (**0**) is surrounded by twelve neighbored molecules through symmetry operations as follows (Fig. 7.15c). The translation operations transfer two equal molecules to the

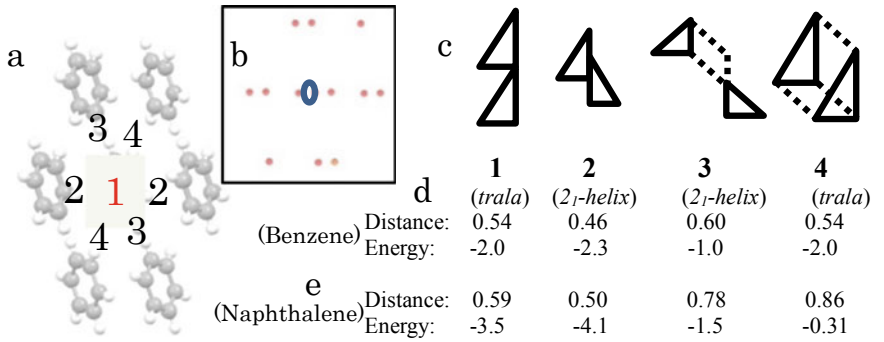

Fig. 7.15 A center molecule (hidden **0**) surrounded by twelve neighbored molecules (**a**) and their centroids (**b**) through symmetry operations such as translation (trala) (**1**), two-fold helix (**2**) and (**3**), translation (**4**). Distances (nm) between centroids of molecules and interaction energies (kcal/mol) for benzene (**d**) and naphthalene (**e**)

directions of up-and-down (**1**) and front-and-back (**4**), yielding totally four neighbored molecules. On the other hand, each of four two-fold helix operations (**2**, **2**, **3**, **3**) transfer two equal molecules per a helical axis, yielding totally eight ones. In case of this space group $P2_1/c$, translation and reversion provide the same neighbored molecules. Of course, case by case, we need to check distances and contacts between the neighbored molecules, since organic molecules possess diverse structures.

7.4.4 Intermolecular Distances and Interaction Energies

It is known that the dispersion force is mainly responsible for the attraction between aromatic compounds without substituents [24, 25]. Therefore, the interaction energies approximately depend on distances between neighbored molecules. Figure 7.15d contains the distances between centroids of the neighbored molecules as well as their interaction energies by using $(\varphi, \psi, \omega) = (20, 30, 27)$. It is reasonable that the operations (**1**, **2**) along the identical axes afford more energies than those (**3**, **4**) along the separated axes. Further separations of the molecules lead to the energies less than −0.5 kcal/mole.

This relation is observed in naphthalene [39] more clearly than in benzene [39] (Fig. 7.15e). The interaction energies for naphthalene is calculated by using $(\varphi, \psi, \omega) = (33, 21, 12)$. It is notable that the energies by operations (**1**, **2**) in naphthalene are about two times more as compared to those in benzene. This means that the energies of dispersion force increase with increasing carbon numbers of organic molecules, when the intermolecular distances are almost equal.

It is generally considered that organic molecules are possible to have more dispersion energies with increasing carbon atoms. Accordingly, when neighbored molecules are closely located through the operations of translation (**1**) and two-fold helix (**2**) along the identical axis, they acquire maximal energies. In the case of pentacene, the energies amount to more or less −10 kcal/mol in the translation and two-fold helix along the axes, whose values are almost comparable or more to those of hydrogen bonds.

7.5 Hierarchical Structures and Interaction Energies

7.5.1 1D Column Surrounded by Six Columns

It is noteworthy that the conventional symmetry operations do not include translation itself, but the crystal units repeatedly transfer a molecule to yield translation assemblies. Such assemblies along an identical axis can exhibit short intermolecular distances, and obtain a large amount of interaction energies. Therefore, the following three ideas may be introduced, as illustrated in Fig. 7.16 regarding anthracene [39].

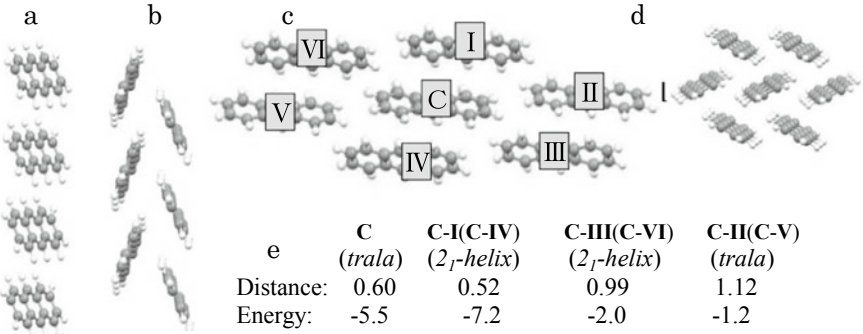

e	**C** (*trala*)	**C-I(C-IV)** (2_1-*helix*)	**C-III(C-VI)** (2_1-*helix*)	**C-II(C-V)** (*trala*)
Distance:	0.60	0.52	0.99	1.12
Energy:	-5.5	-7.2	-2.0	-1.2

Fig. 7.16 Anthracene crystal (monoclinic, $P2_1/a$) consisting of 1D columnar assemblies. Column (**C**) by translation (trala) along crystallographic *b*-axis (**a**), column (**C-I**) by two-fold helix along *b*-axis (**b**), central column (**C**) surrounded by six neighbored columns (**I** to **VI**) as viewed down *b*-axis (**c**), another translation column as viewed down *c*-axis (**d**), Distances (nm) between centroids of the molecules and interaction energies (kcal/mol) by using (φ, ψ, ω) = (28, 23, 6) (**e**)

Firstly, the translation operations yield a one-dimensional (1D) column along an identical axis with a preferential amount of energies (Fig. 7.16a). Secondly, combinations of the translation with two-fold helix operations produce the most amount of interaction energies among various combinations to give the strongest 1D columns (Fig. 7.16b). Thirdly, one of the columns (**C**) is surrounded by six neighbored columns (**I** to **VI**) (Fig. 7.16c). Such a columnar model plays a key role for understanding organic crystals in comparison with the known spherical model of inorganic crystals.

7.5.2 2D Layers: Alignment of Columns by Maximal Interaction Energies

The resulting columns are bundled with other columns in parallel or anti-parallel through symmetry operations such as translation, two-fold helix, inversion and so on, to afford two-dimensional (2D) layers. In the case of anthracene (Fig. 7.16c), the centered column (**C**) forms three kinds of 2D layered alignments (**I-C-IV**, **II-C-V**, **III-C-VI**). Among them, the layer **I-C-IV** is the strongest, because it has a minimal intermolecular distances (0.60 nm (**C**), 0.52 nm (**C-I** or **C-IV**)) and maximal interaction energies (−5.5 kcal/mol (**C**), −7.2 kcal/mol (**C-I** or **C-IV**)) by using (φ, ψ, ω) = (28, 23, 6) (Fig. 7.16e).

It is generally considered that a combination of the columns with maximal interaction energies makes the most preferential layer among the above-mentioned three kinds of layers.

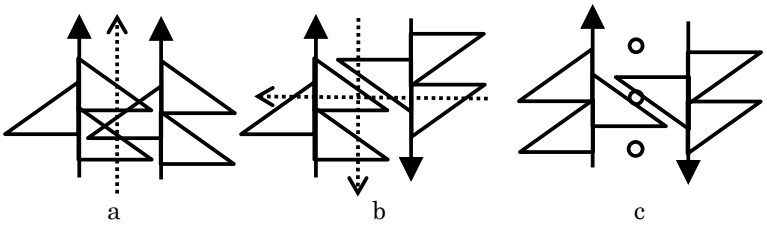

Fig. 7.17 Three kinds of stacking for 2D layers consisting of two-fold helix 1D columns through symmetry operations of translation (**a**), two-fold helix (**b**), inversion (**c**), as their side-views of the 2D layers by using the rectangular triangle models. Broken arrows depict two-fold helix axes, while circles do inversion centers between layers

7.5.3 3D Stacked Layers Related to Space Group of Crystals

The layers are also stacked in various ways. The simplest way is observed by translation of the 2D layers in the monoclinic $P2_1/c$ crystals of benzene, naphthalene and anthracene. This is exemplified as the side-view of the stacked layer in anthracene (Fig. 7.16d). It should be mentioned that parallel or perpendicular two-fold helix operation between two layers forms stacked layers with the same or reverse direction with space group $P2_1/c$ (Fig. 7.17a) or $P2_12_12_1$ (Fig. 7.17b), respectively. In contrast, inversion operation between two layers induces the racemic stacked layers in anti-parallel (Fig. 7.17c).

In addition, these layers can slide each other between the layers, explaining the angles of lattice parameters which are apart from 90° between crystallographic axes. Namely, one directional sliding corresponds to monoclinic crystals, while two directional one does to triclinic crystals.

7.6 Supramolecular Chirality and Handedness in Crystals

7.6.1 Chiral Assemblies Composed of Identical Isomers

Supramolecular chirality [26, 27] is an important subject for understanding chiral materials in universe [28, 29]. Position-dependent chirality clearly indicates that identical molecules yield chiral assemblies through symmetry operations, including translation, two-, three-, four-, or six-fold rotation and helix. For example, (*R*, *r*)-isomers produce a 1D chiral column through translation. Such columns are bundled to a 2D chiral layer, and further the layers are stacked to a 3D chiral crystal through the operations. Simply, they are termed as right-handed (*R*, *r*)-column, (*R*, *r*)-layer, (*R*, *r*)-crystal (and vice versa).

In 2007, we reported that a two-fold helical molecular assembly of benzene exhibits right- or left-handedness [30, 31]. This was responsible for 3D geometry on

display by molecular graphics Mercury. Thus, a side-view of a face affords a line. So, two-fold helical assembly of the faces composes an assembly of the lines. When the lines in front exhibit right-tilt alignment along the two-fold helical axis, the helical assembly is right-handed (and vice versa). Now, such a visual and qualitative description has developed to a quantitative one according to three kinds of rotations along a two-fold helical axis. These rotations bring about position-dependent chirality, explaining the well-known fact that supramolecular chirality generates in molecular assemblies composed of achiral molecules [32]. We can say that the conventional idea focused on molecular chirality, but did not on supramolecular chirality in crystals.

7.6.2 Achiral Assemblies of Enantiomeric and Diastereomeric Isomers

A combination of racemic (*R*, *r*)- and (*S*, *s*)-isomers forms an achiral (*R*, *r*)(*S*, *s*)-dimer through inversion, reflection or glide operation. The operations are repeated to form achiral 1D columns, which align toward achiral 2D layers, and further achiral 3D crystals.

The diastereomeric (*R*, *r*)(*R*, *s*)- or (*S*, *s*)(*S*, *r*)-dimer may be observed in organic crystals. For example, pentacene [39] form crystals which belong to space group *P*-1. It can be seen on display by Mercury that their dimers have parallel and *T*-type arrangements, indicating the same ω values of the rotations around *z*-axis in Fig. 7.5(c). As a result, the two-fold helix operations disappear and only inversion operations remain. Namely, pentacene employs (φ, ψ, ω) = (16, 28, 22) for three rotation angles and forms four kinds of position-dependent chiral isomers with (*Dx*, *Dy*, *Dz*) as follows; (−90, 90, −22) for (*R*, *r*), (−90, 90, 22) for (*R*, *s*), (90, −90, −22) for (*S*, *r*) and (90, −90, 22) for (*S*, *s*) (see Fig. 7.7d).

7.6.3 Diverse Diastereomers Regarding Position-Dependent Chirality

In principle, it is possible that diastereomeric isomers are combined to yield other achiral dimers, including an enantiomeric (*R*, *s*)(*S*, *r*)-dimer, a diastereomeric (*R*, *r*)(*S*, *r*)- or (*S*, *s*)(*R*, *s*)-dimer. Symmetry operations do not describe these dimers, and probably one might observe these dimers as two independent molecules in crystals.

It should be mentioned once more that the tilt rotation along *y*-axis in Fig. 7.5c is limited to forward tilt ($0° < \psi < 90°$) in this article. If necessary, this can be extended to backward tilt or reclination. This extension would make the discussion more complex than that mentioned above.

7.7 Chiral Crystallization of Achiral Molecules

7.7.1 New Understanding for Chiral Crystallization

From an isotropic viewpoint of symmetry theory, symmetry operations such as translation, two-fold rotation and two-fold helix do not enable us to discriminate handedness of the resultant assemblies. Nevertheless, from an anisotropic viewpoint, such assemblies exhibit chirality and handedness according to 3D space geometry by molecular graphics [14–16]. Furthermore, the latter anisotropic insight led us to the hierarchical structures in organic crystals [16–18] as well as the linkage between molecular and supramolecular chirality [33, 34].

The present article describes a new understanding for chiral crystallization of achiral molecules, telling that the triangle method reasonably explains generation and handedness of supramolecular chirality of the assemblies on the basis of position-dependent chirality. It still remains unclear to elucidate a relationship between molecular structures and space group of their crystals. Hereafter one can find the relation throughout a series of relative compounds, including polycyclic aromatic compounds, chalcones, and so on.

It is noteworthy that chiral crystallization forms an equimolar amount of (*R*)- and (*S*)-crystals. Their separation needs another insight. Recent crystal engineering presents a great possibility for their separation [35, 36].

7.7.2 Connection of Organic Molecules via Their Centroids

Benzene, naphthalene and anthracene are achiral organic molecules with intramolecular inversion points (Fig. 7.18a), producing no chiral crystals. However, achiral molecules without such inversion points have a great potential to undergo the chiral crystallization. Instead of the points, centroids of organic molecules are briefly determined by the graphics Mercury, and useful for connecting the *X*3 of the triangles.

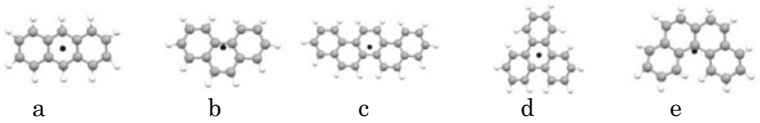

Fig. 7.18 Achiral molecules with an inner inversion center; anthracene (**a**), instead with a centroid; phenanthrene (**b**), picene (**c**), triphenylene (**d**), and benzo[c]phenanthrene (**e**)

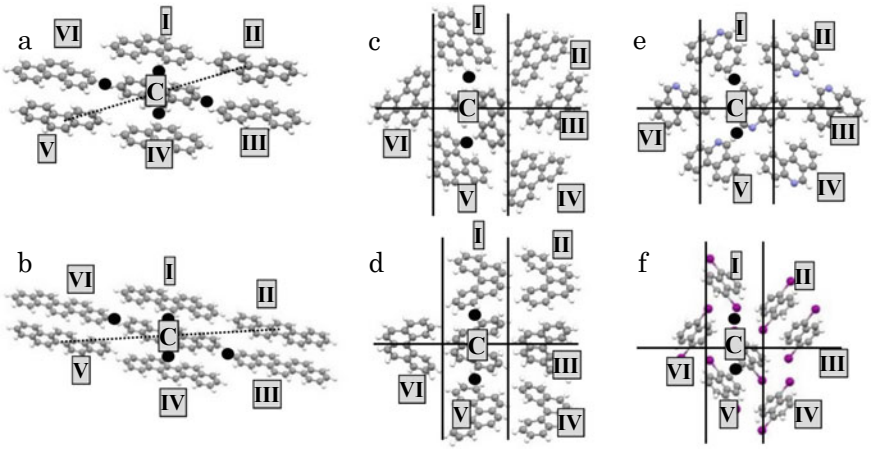

Fig. 7.19 Chiral crystals with space group $P2_1$; phenanthrene (**a**) and picene (**b**), with space group $P2_12_12_1$; triphenylene (**c**), benzo(c)phenanthrene (**d**), phenanthridine (**e**) and 1,5-diiodonaphthalene (**f**). The central column (**C**) is surrounded by six columns (**I** to **VI**). Symmetry operation; two-fold helix ((●) and (–)), translation (· · ·)

7.7.3 Examples of Chiral Crystallization of Achiral Molecules

We continue a research for resolving a relation between molecular and crystal structures. Among them, three examples of polycyclic aromatic compounds are described below.

The first example focuses on chiral crystals which belong to monoclinic, $P2_1$. Phenanthrene [39] has a centroid in the middle ring (Fig. 7.18b), where the dummy atom $X3$ is connected like anthracene. Figure 7.19a shows its (R, r)-crystal. The centered translation (R, r)-column (**C**) is surrounded by six (R, r)-columns (**I** to **VI**). The columnar alignment (**I**-**C**-**IV**) constitutes a preferential 2D (R, r)-layer, which is stacked by translation to yield a 3D (R, r)-crystal. This hierarchical structure is the same as that of anthracene. The preferential layer comes from different intermolecular distances (0.68, 0.51, 0.53 nm for **C**, **C**-**I**, **C**-**IV** compared to 0.95, 1.03 nm for **C**-**II**, **C**-**III**). Figure 7.19b involves another example of the achiral molecule without the inversion center, called picene (Fig. 7.18c) [39]. One can see the same hierarchical structure as phenanthrene.

The second examples deal with crystals which belong to orthorhombic, $P2_12_12_1$. Triphenylene (Fig. 7.18d) [39] is illustrated in Fig. 7.19c. The centered translation column (**C**) is surrounded by six columns (**I** to **VI**), and the main layer is (**I**-**C**-**V**) instead of (**I**-**C**-**IV**). The difference lies in two kinds of two-fold helical axes between the layers, causing a rotation by 180° between the layers. The axis perpendicular to the layers ascribes to steric and electronic complementarity between the neighbored molecules. Figure 7.19d involves another example of the achiral molecule,

called benzo(c)phenanthrene (Fig. 7.18e) [39], which displays the same hierarchical structure.

Thirdly, substituted aromatic compounds (orthorhombic, $P2_12_12_1$) are employed. Phenanthridine [39] involves nitrogen at 6-position. The nitrogen functions for a connection of 1D translation column through hydrogen bonds to form a preferential 2D layer, which is stacked with two-fold helix operation (Fig. 7.19e). In addition, 1,5-diiodonaphthalene [39] has iodine for halogen bonds (Fig. 7.19f). The translation columns are combined by halogen bonds.

7.8 Conclusions and Perspectives

It has been found that supramolecular chirality of molecular assemblies in organic crystals is attributable for position-dependent chirality. We designed a rectangular triangle model attached with a molecule, enabling us to evaluate a position of organic molecules through three kinds of rotations toward an axis. The combination of the rotations leads us to four kinds of isomers with position-dependent chirality. The isomers are combined through symmetry operations, including translation, two-fold rotation, two-fold helix, and so on, to construct the corresponding molecular assemblies with supramolecular chirality.

Z -matrix, which is used for the Gaussian program, enables us to describe such a triangle model, leading to the evaluation of intermolecular interaction energies between neighbored molecules in organic crystals. The resulting interaction energies explain the hierarchical structures involving 1D columns, 2D layers, and 3D layer-stacked crystals, prompting us to understand space group of crystals as well as chiral crystallization of achiral molecules.

Dispersion energies contribute to such hierarchical structures. Basically, short distances between neighbored molecules play a key role in determining the columns and the layers. Hopefully, this research prompts us to elucidate the relation between molecular structures and space group of crystals, to dissolve various hidden chirality [37, 38], and to overcome diversity of organic compounds.

References

1. Hahn, T. (ed.): International Tables for Crystallography. Space-Group Symmetry, vol. A. Kluwer Academic Publishers, London (1983, 1st edn.), (2002 5th edn.)
2. Dunitz, J.K., Gavezzotti, A.: How molecules stick together in organic crystals: weak intermolecular interactions. Chem. Soc. Rev. **38**, 2622 (2009)
3. Stone, A.J.: The Theory of Intermolecular Forces, 2nd edn. Oxford University Press, Oxford (2013)
4. Beran, G.J.O., Nanda, K.: Predicting organic crystal lattice energies with chemical accuracy. J. Phys. Chem. Lett. **1**, 3480 (2010)

5. Tsuzuki, S.: Intermolecular Forces of Organic Molecules: Analysis of Intermolecular Interaction Energy by Ab Initio Molecular Orbital Calculations. University of Tokyo Press, Tokyo (2015)
6. Kigure, S., Omachi, H., Shinohara, H., Okada, S.: Nano-Saturn: energetics of the inclusion process of C_{60} into cyclohexabiphenylene. J. Phys. Chem. C **119**, 8931–8936 (2015)
7. Gaussian 16, Revision A.01, Frisch, M.J., Trucks, G.W., Schlegel, H.B., Scuseria, G.E., Robb, M.A., Cheeseman, J.R., Scalmani, G., Barone, V., Petersson, G.A., Nakatsuji, H., Li, X., Caricato, M., Marenich, A.V., Bloino, J., Janesko, B.G., Gomperts, R., Mennucci, B., Hratchian, H.P., Ortiz, J.V., Izmaylov, A.F., Sonnenberg, J.L., Williams-Young, D., Ding, F., Lipparini, F., Egidi, F., Goings, J., Peng, B., Petrone, A., Henderson, T., Ranasinghe, D., Zakrzewski, V. G., Gao, J., Rega, N., Zheng, G., Liang, W., Hada, M., Ehara, M., Toyota, K., Fukuda, R., Hasegawa, J., Ishida, M., Nakajima, T., Honda, Y., Kitao, O., Nakai, H., Vreven, T., Throssell, K., Montgomery Jr., J.A., Peralta, J.E., Ogliaro, F., Bearpark, M.J., Heyd, J.J., Brothers, E.N., Kudin, K.N., Staroverov, V.N., Keith, T.A., Kobayashi, R., Normand, J., Raghavachari, K., Rendell, A.P., Burant, J.C., Iyengar, S.S., Tomasi, J., Cossi, M., Millam, J.M., Klene, M., Adamo, C., Cammi, R., Ochterski, J.W., Martin, R.L., Morokuma, K., Farkas, O., Foresman, J.B., Fox, D.J.: Gaussian, Inc., Wallingford CT (2016)
8. GaussView, Version 6.1, Dennington, R., Keith, T.A., Millam, J.M.: Semichem Inc., Shawnee Mission, KS (2016)
9. Miyata, M., Sada, K.: In: Lehn, J.-M. (ed.) Comprehensive Supramolecular Chemistry. Solid State Supramolecular Chemistry: Crystal Engineering, vol. 6, p. 147. Pergamon, Oxford (1996)
10. Miyata, M., Sada, K., Yoswathananont, N.: In: Atwood, J.L., Steed, J.W. (eds.) Encyclopedia of Supramolecular Chemistry, vol. 1, p. 441. Marcel Dekker, New York (2004)
11. Cambridge Structural Database and Mercury: https://www.ccdc.cam.ac.uk/.
12. Miyata, M., Tohnai, N., Hisaki, I.: Crystalline host–guest assemblies of steroidal and related molecules: diversity, hierarchy, and supramolecular chirality. Acc. Chem. Res. **40**, 694 (2007)
13. Miyata, M., Tohnai, N., Hisaki, I.: Supramolecular chirality in crystalline assemblies of bile acids and their derivatives; three-axial, tilt, helical, and bundle chirality. Molecules **12**, 1973 (2007)
14. Hisaki, I., Sasaki, T., Tohnai, N., Miyata, M.: Supramolecular-tilt-chirality on twofold helical assemblies. Chem. Eur. J. (Concept) **18**, 10066 (2012)
15. Miyata, M., Tohnai, N., Hisaki, I., Sasaki, T.: Generation of supramolecular chirality around twofold rotational or helical axes in crystalline assemblies of achiral components. Symmetry (Open Access) **7**, 1914 (2015)
16. Miyata, M., Hisaki, I.: In: Tamura, R., Miyata, M. (eds.) Advances in Organic Crystal Chemistry, Chapter 19, p. 371. Springer, Tokyo, Japan (2015)
17. Hisaki, I., Sasaki, T., Tohnai, N., Miyata, M.: Multipoint approximation method for handedness determination of two-fold helical assemblies and their bundles. J. Synth. Org. Chem. Jpn. **70**, 908 (2012)
18. Sasaki, T., Ida, Y., Tanaka, A., Hisaki, I., Tohnai, N., Miyata, M.: Chiral crystallization by non-parallel face contacts on the basis of three-axially asymmetric twofold helices. CrystEngComm **15**, 8237 (2013)
19. Grimme, S., Antony, J., Ehrlich, S., Krieg, H.: A consistent and accurate ab initio parametrization of density functional dispersion correction (DFT-D) for the 94 elements H-Pu. J. Chem. Phys. **132**, 154104 (2010)
20. Ransil, B.J.: Studies in molecular structure. IV. Potential curve for the interaction of two helium atoms in single-configuration LCAO MO SCF approximation. J. Chem. Phys. **34**, 2109 (1961)
21. Boys, S.F., Bernardi, F.: The calculation of small molecular interactions by the differences of separate total energies. Some procedures with reduced errors. Mol. Phys. **19**, 553 (1970)
22. Glusker, J.P., Trueblood, K.N.: Crystal Structure Analysis: A Primer, 3rd edn. Oxford University Press, Oxford (2010)
23. Bennett, D.W.: Understanding Single-Crystal X-Ray Crystallography. Wiley-VCH, Weinheim (2010)

24. Tsuzuki, S., Honda, K., Uchimaru, T., Mikami, M., Tanabe, K.: Origin of attraction and directionality of the π/π interaction: model chemistry calculations of benzene dimer interaction. J. Am. Chem. Soc. **124**, 104–112 (2002)
25. Tsuzuki, S., Honda, K., Uchimaru, T., Mikami, M.: High-level ab initio computations of structures and interaction energies of naphthalene dimers: origin of attraction and its directionality. J. Chem. Phys. **120**, 647 (2004)
26. Lehn, J.M.: Supramolecular Chemistry: Concepts and Perspectives. VCH, Weinheim (1995)
27. Desiraju, G.R.: The Crystal as a Supramolecular Entity. Wiley, Chichester (1995)
28. Gardner, M.: The New Ambidextrous Universe. W. H. Freeman and Company, New York (1999)
29. Hegstrom, R.A., Kondepudi, D.K.: Sci. Am. **262**, 108 (1990)
30. Tanaka, A., Hisaki, I., Tohnai, N., Miyata, M.: Supramolecular tilt chirality derived from symmetrical benzene molecules: handedness of the 2_1 helical assembly. Chem. Asian J. **2**, 230 (2007)
31. Hisaki, I., Sasaki, T., Sakaguchi, K., Liu, W.T., Tohnai, N., Miyata, M.: Right- and left-handedness of 2_1 symmetrical herringbone assemblies of benzene. Chem. Commun. **48**, 2219 (2012)
32. Matsuura, T., Koshima, H.: J. Synth. Org. Chem. Jpn. **56**, 268/466 (1998)
33. Sasaki, T., Hisaki, I., Miyano, T., Tohnai, N., Morimoto, K., Sato, H., Tsuzuki, S., Miyata, M.: Linkage control between molecular and supramolecular chirality in 2_1-helical hydrogen-bonded networks using achiral components. Nat. Commun. **4**, 1787/1–7 (2013)
34. Miyata, M.: Supramolecular chirality generated in organic crystals: stereochemical course for conglomerates. J. Synth. Org. Chem. Jpn. **75**, 503 (2017)
35. Viedma, C.: Chiral symmetry breaking during crystallization: complete chiral purity induced by nonlinear autocatalysis and recycling. Phys. Rev. Lett. **94**, 065504 (2005)
36. Sakamoto, M., Mino, T., Yoshida, Y.: Asymmetric synthesis using crystal chirality. J. Synth. Org. Chem. Jpn. **75**, 509 (2017)
37. Sasaki, T., Ida, Y., Hisaki, I., Yuge, T., Uchida, Y., Tohnai, N., Miyata, M.: Characterization of supramolecular hidden chirality of hydrogen-bonded networks by advanced graph set analysis. Chem. Eur. J. **20**, 2478 (2014)
38. Sasaki, T., Miyata, M.: Characterization of hidden chirality: two-fold helicity in β-strands. Symmetry (Open Access) **11**, 499 (2019)
39. Cambridge Structural Database (Compound name, Identifier, Deposition Number): (Benzene, BENZEN04, 1108753), (Naphthalene, NAPHTA15, 233928), (Anthracene, ANTCEN, 1103062), (Phenanthrene, PHENAN04, 1232369), (Pentacene, PENCEN, 1230799), (Picene, ZZZOYC01, 1319885), (Triphenylene, TRIPHE, 1275702), (Benzo(c)phenanthrene, BZPHAN, 1118394), (Phenanthridine, PHENAT02, 1232381), (1,5-Diiodonaphthalene, NIFHAM, 647708)

Chapter 8
Relationship Between Atomic Contact and Intermolecular Interactions: Significant Importance of Dispersion Interactions Between Molecules Without Short Atom–Atom Contact in Crystals

Seiji Tsuzuki

Abstract Intermolecular interactions in crystals of polycyclic aromatic molecules, *n*-hexane, and hexamine were analyzed by dispersion-corrected DFT calculations. The origin of the attraction and the relationship between short atom–atom contact and magnitude of attraction were discussed. The calculations show that the dispersion interactions are the primary source of the attraction between adjacent molecules in the crystals. The strong attraction by the dispersion interactions often exists between adjacent molecules in the crystals, even if the adjacent molecules do not have short atom–atom contact. Although intermolecular interactions in crystals have been discussed based on the presence or absence of atom–atom contact at short distances, our analysis shows that it is often dangerous to discuss the intermolecular interactions in crystals solely based on crystal structures.

Keywords Intermolecular interaction · DFT calculations · Dispersion interaction · Short atom–atom contact · Crystal structure

8.1 Introduction

The intermolecular interactions control the arrangement of molecules in organic crystals and greatly affect the physicochemical properties of the organic crystals. For this reason, detailed information on intermolecular interactions is increasingly required in the development of organic materials. With regard to the structures of organic crystals, a huge amount of data obtained by crystal structure analysis has been accumulated. On the other hand, it is not easy to directly elucidate the nature (magnitude, directionality and origin of attraction) of the intermolecular interactions between molecules in crystals solely by experimental methods. For this reason, until now, intermolecular interactions in organic crystals have often been discussed

S. Tsuzuki (✉)
National Institute of Advanced Industrial Science and Technology, Tsukuba 305-8568, Ibaraki, Japan
e-mail: s.tsuzuki@aist.go.jp

M. Sakamoto and H. Uekusa (eds.), *Advances in Organic Crystal Chemistry*,
https://doi.org/10.1007/978-981-15-5085-0_8

based on the presence or absence of atomic contact at short distances (contact at interatomic distances less than the sum of the van der Waals radii). Recently, high-level ab initio molecular orbital calculations and dispersion-corrected DFT (density functional theory) calculations can evaluate intermolecular interaction energies in organic crystals sufficiently accurately. Recently reported calculations show that strong attraction owing to the dispersion interactions often exists between molecules in crystals which do not have short atom–atom contact. For example, in crystals of polycyclic aromatic molecules such as thienoacenes [1], strong attraction owing to dispersion interactions exist between adjacent molecules which do not have short atom–atom contacts. Here, the intermolecular interactions in the crystals of polycyclic aromatic molecules, *n*-hexane, and hexamine analyzed by dispersion-corrected DFT calculations are shown. They are compared with HF calculations which cannot evaluate the dispersion interactions to estimate the contribution of the dispersion interactions to the attraction. We also point out the danger of the discussion on intermolecular interactions in organic crystals based solely on the presence or absence of contact of atoms at short distances.

8.2 Intermolecular Interactions

There exist several intermolecular interactions which have different origins between interacting molecules [2]. The intermolecular interactions classified by physical origins are shown in Table 8.1. The intermolecular interactions can be classified into two groups. The first one is long-range interactions, which have their origin in Coulomb interactions. The long-range interactions can work even when molecules are well separated. The second one is short-range interactions, which have their origin in interactions between molecular orbitals. The short-range interactions only work at short distances where the overlap of molecular orbitals is significant. The electrostatic, that is the Coulomb interaction between the static charge distributions of molecules, the induction, that is the attraction due to induced polarization, and the dispersion, that is the attraction due to the correlated motion of electrons, are the

Table 8.1 Intermolecular interactions

Intermolecular interactions	Feature
Long-range interactions (*Coulombic interactions*, $E \sim R^{-n}$)	
Electrostatic	Attraction or repulsion, directional
Induction (polarization)	Attraction
Dispersion (van der Waals attraction)	Attraction
Short-range interactions (*overlap of molecular orbitals*, $E \sim \exp(\alpha R)$)	
Exchange-repulsion	Strong repulsion at short distance
Charge-transfer	Attraction

long-range interactions. The magnitude of the energies of the long-range interactions are proportional to some inverse power of the intermolecular distance, and therefore, the energies of the long-range interactions decrease slowly with the increase of the intermolecular distance. On the other hand, the exchange-repulsion, that is the strong repulsion at short distance, and the charge-transfer, that is the attraction due to the interactions between molecular orbitals, are the short-range interactions. Since the energies of the short-range interactions are approximately proportional to the overlap integral, they decrease rapidly as the intermolecular distance increases. For this reason, the short-range interactions do not work at long distance.

The classification of intermolecular interactions by structural features is also often used. Typical intermolecular interactions classified by structural features are shown in Fig. 8.1. When a hydrogen atom bonded to an electronegative atom (oxygen, nitrogen, etc.) is in contact with another electronegative atom or π-electron system and there exists attraction between them, the interaction is called hydrogen bond. When aromatic rings are in contact and there exists attraction, the interaction is called π/π interaction. The contact between C-H bonds and aromatic rings is often observed in organic crystals and the interaction between C-H bond and aromatic ring is called CH/π interaction. Further, it is known that there exists strong attraction between halogen atom such as iodine or bromine and Lewis base, the interaction is called halogen bond.

The classification of intermolecular interactions by structural features has many problems, although it is widely used to discuss intermolecular interactions due to the abundance of crystal structure data. For example, the structure of CH/π interaction is similar to the structure of π hydrogen bond between water and benzene. For this reason, it was believed that the CH/π interaction was weak hydrogen bond and its properties were similar to hydrogen bonds [3]. However, high-level ab initio calculations revealed that the nature of the CH/π interactions is completely different form hydrogen bonds [4, 5]. The major source of the attraction in hydrogen bonds is the highly directional electrostatic interactions, and therefore, hydrogen bonds have

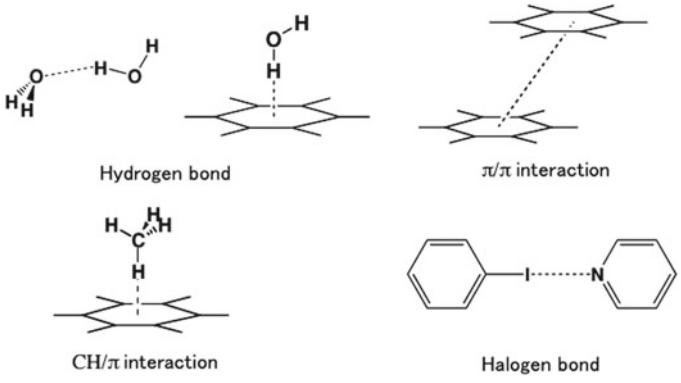

Fig. 8.1 Intermolecular interactions classified by structural feature

strong directionality. On the other hand, the major source of the attraction in the CH/π interactions is the dispersion interactions. The contribution of the electrostatic interaction is very small. Therefore, the directionality of the CH/π interactions is very weak. The directionality of hydrogen bonds is important for controlling orientation of molecules in crystals and supermolecules [6]. The weak directionality of the CH/π interactions suggests that the CH/π interactions are difficult to play important roles in controlling arrangement of molecules in molecular assemblies as in the cases of hydrogen bonds. Another example is the interactions between benzene and aromatic cations. The structure of the benzene-*N*-methylpyridinium complex is similar to the structure of the π-stacked benzene dimer. But the nature of the interactions in the benzene-*N*-methylpyridinium complex is completely different from that in the benzene dimer [7]. The interactions in the benzene-*N*-methylpyridinium complex are significantly stronger than that in the benzene dimer owing to the strong electrostatic and induction interactions. On the other hand, the dispersion interactions are the major source of the weak attraction in the benzene dimer.

8.3 Calculation of Intermolecular Interaction Energy

The energies of molecules and dimers obtained by molecular orbital calculations and DFT calculations are the stabilization energies by the formation of molecules and dimers from isolated nuclei and electrons. Therefore, the intermolecular interaction energy (E_{int}) can be obtained by subtracting the sum of the energies of monomers ($E_{\mathrm{A}} + E_{\mathrm{B}}$) from the energy of dimer (E_{AB}) as shown in Eq. 8.1. This method for the calculation of intermolecular interaction energy is called supermolecule method. Since the intermolecular interaction energy calculated by the supermolecule method is overestimated by the basis set superposition error (BSSE), the BSSE is corrected by the counterpoise method.

$$E_{\mathrm{int}} = E_{\mathrm{AB}} - (E_{\mathrm{A}} + E_{\mathrm{B}}) \tag{8.1}$$

Ab initio molecular orbital calculation is an approximation, although it does not use any empirical parameter based on experimental measurements. The level of approximation is mainly determined by the choice of basis set and electron correlation correction procedure used for the calculation. Molecular orbital is described as a linear combination of gauss functions located on atoms of the molecule in ab initio molecular orbital calculation. The set of gauss functions (basis function) is called as basis set. The accuracy of the calculated intermolecular interaction energy strongly depends on the number and the angular flexibility of gauss functions used for the calculation. The calculated intermolecular interaction energy also depends strongly on the choice of electron correlation correction procedure. Therefore, sufficiently large basis set and electron correlation correction by a proper method are necessary for an accurate evaluation of intermolecular interaction energy. Figure 8.2 shows the intermolecular interaction energies calculated for the slipped-parallel benzene

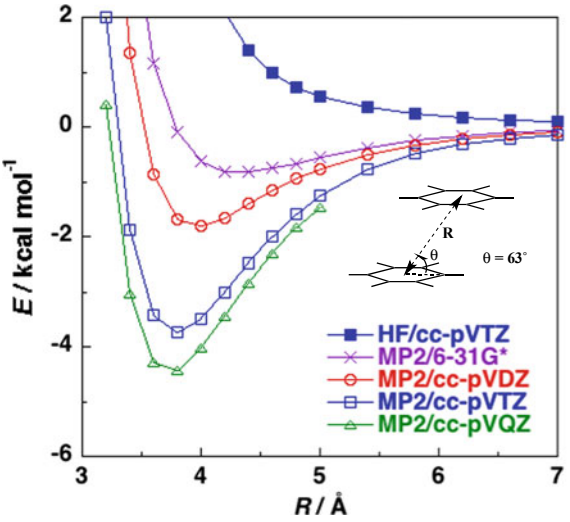

Fig. 8.2 Effects of basis set on calculated interaction energy for benzene dimer

dimer at HF and MP2 levels using several basis sets. The HF level interaction energy potential does not have a potential minimum, while the attraction is calculated when the electron correlation is corrected by the MP2 method, which clearly shows that the primary source of the attraction in the benzene dimer is the dispersion interactions. The dispersion interactions have their origin in electron correlation, and therefore, HF calculation cannot evaluate the dispersion interactions. The magnitude of the attraction calculated by the MP2 method depends strongly on the basis set. Small basis sets such as the 6-31G* basis set underestimates the attraction significantly compared with large basis sets such as the cc-pVQZ basis set. Figure 8.3 shows the calculated interaction energies for the slipped-parallel benzene dimer by the HF, MP2

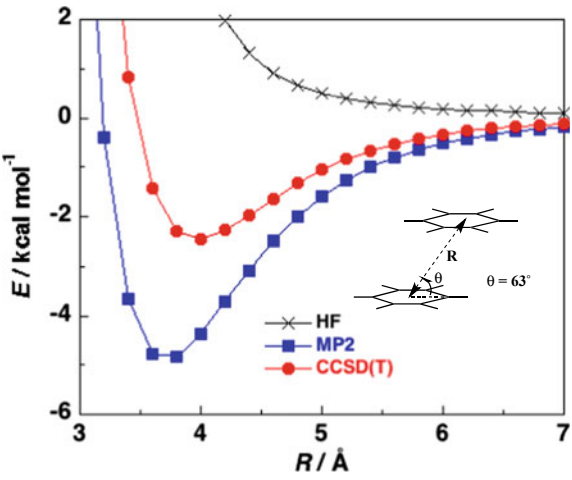

Fig. 8.3 Effects of electron correlation correction on calculated interaction energy for benzene dimer. MP2 and CCSD(T) interaction energies are the estimated interaction energies at the basis set limit

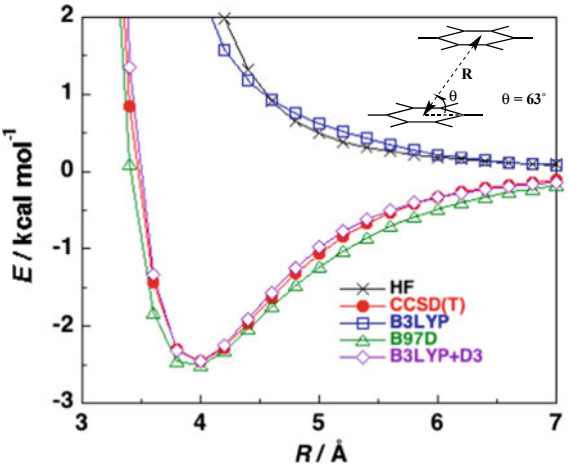

Fig. 8.4 Comparison of interaction energies calculated for benzene dimer using dispersion-corrected DFT methods with those obtained by HF and CCSD(T) methods

and CCSD(T) methods. The MP2 and CCSD(T) level interaction energies are the estimated interaction energies at the basis set limit. The MP2 method overestimates the attraction compared with more accurate CCSD(T) method.

The DFT calculations do not require large computation time compared with ab initio calculations. The required computational time for DFT calculations are proportional to the cubic of the number of basis functions. On the other hand, the computational time for MP2 and CCSD(T) calculations are proportional to the 5th and 7th power of the number of basis functions, respectively. For this reason, the DFT calculations of large molecules are relatively easy. However, the DFT calculations using functionals such as B3LYP [8] cannot evaluate the attraction by the dispersion interactions as shown in Fig. 8.4. The intermolecular interaction potential calculated for the slipped-parallel benzene dimer using the B3LYP functional does not have a minimum as in the case of the HF level potential. For this reason, the dispersion-corrected DFT methods have been developed. The energy of dispersion interactions is corrected by empirical parameters in the dispersion-corrected DFT methods. In calculations using functionals such as B97D [9], the dispersion-corrected calculations are performed. It is also possible to carry out B3LYP calculations with Grimme's D3 dispersion correction [10] (B3LYP + D3). The calculated interaction energies by the dispersion-corrected DFT methods are often close to those obtained by high-level ab initio calculation (CCSD(T) calculation using a large basis set near the basis set limit). The comparison of the calculated interaction energies using B97D and B3LYP + D3 methods with those obtained by the CCSD(T) method is shown in Fig. 8.4.

8.4 Intermolecular Interactions of Naphthalene

Herringbone structures are often observed in the crystals of polycyclic aromatic molecules such as the crystal of naphthalene as shown in Fig. 8.5. A naphthalene molecule interacts strongly with six adjacent molecules in the crystal. Two adjacent molecules are π-stacked and arranged in parallel orientation. The remaining four adjacent molecules are molecules in adjacent π-stacked columns and arranged in tilted T-shape configuration. The short atom–atom contact less than the sum of van der Waals radii is shown by arrows in Fig. 8.5. Short atom–atom contact exists between adjacent molecules in tilted T-shape configuration. On the other hand, there is no short contact between adjacent molecules arranged in parallel.

The interaction energies between adjacent naphthalene molecules in the crystal (E_{B97D}) calculated by the dispersion-corrected DFT method (B97/6-311G**) are shown in Table 8.2. The interaction energy with the tilted T-shape adjacent molecule was calculated as −4.83 kcal/mol. The magnitude of the attraction is close to the

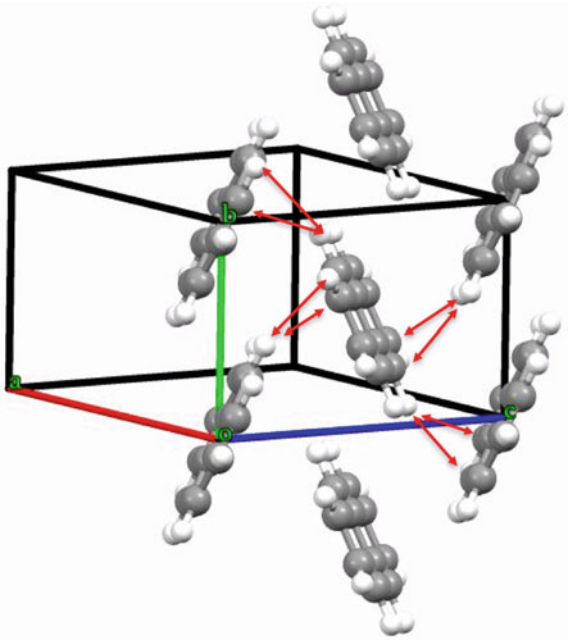

Fig. 8.5 Crystal structure of naphthalene

Table 8.2 Intermolecular interaction energies between adjacent naphthalene molecules in crystal. Energy in kcal mol^{-1}

	E_{B97D}	E_{HF}	E_{disp}
Tilted T-shape	−4.83	3.31	−8.14
Parallel	−3.62	0.41	−4.03

hydrogen bond of water dimer (about −5 kcal/mol). The interaction energy with parallel adjacent molecule was calculated as −3.62 kcal/mol. These results show that there exists strong attraction not only between the tilted T-shape adjacent molecules, but also between the parallel adjacent molecules, although there is no short atom–atom contact between the parallel adjacent molecules.

The HF level (HF/6-311G**) interaction energies (E_{HF}) between the tilted T-shape adjacent molecules and between the parallel adjacent molecules are 3.31 and 0.41 kcal/mol, respectively, as summarized in Table 8.2. The HF method cannot evaluate the dispersion interactions, therefore the contributions of the dispersion interactions (E_{disp}) can be estimated approximately by subtracting E_{HF} from E_{B97D} as shown in Eq. 8.2.

$$E_{disp} = E_{B97D} - E_{HF} \tag{8.2}$$

The contributions of the dispersion interactions (E_{disp}) calculated for the interactions between the tilted T-shape and parallel adjacent molecules are −8.14 and −4.03 kcal/mol, respectively (Table 8.2). The contributions of the dispersion interactions are significant. The calculated positive values of E_{HF} suggest that the contributions of the electrostatic interactions to the attractions are not large, since the attraction by the electrostatic interactions can be evaluated by the HF calculations. These calculations show that the dispersion interactions are the major source of the attraction between adjacent naphthalene molecules in the crystal. Although there is no short atom–atom contact between parallel adjacent molecules, there exists strong attraction by the dispersion interactions. This indicates that the strong attraction between parallel adjacent molecules due to the dispersion interactions will be overlooked, if the intermolecular interactions in the crystal are discussed based solely on the presence of short atom–atom contact in crystals.

8.5 Intermolecular Interactions of Other Polycyclic Aromatic Molecules

Not only in the crystal of naphthalene, but also in the crystals of other polycyclic aromatic molecules, there exist strong attraction between adjacent molecules. The intermolecular interaction energies between parallel adjacent molecules in the crystals of anthracene, tetracene, pentacene, and pyrene (Fig. 8.6) were calculated by the dispersion-corrected DFT method (B97D/6-311G**) and by HF method (HF/6-311G**) The calculated interaction energies (E_{B97D} and E_{HF}) are summarized in Table 8.3. Although there is no short atom–atom contact between the parallel adjacent molecules in these crystals, there exists strong attraction.

As the number of aromatic rings increases, the magnitude of the intermolecular interaction (E_{B97D}) increases. The intermolecular interaction energy between parallel adjacent pentacene molecules is −9.68 kcal/mol, and that for parallel adjacent pyrene

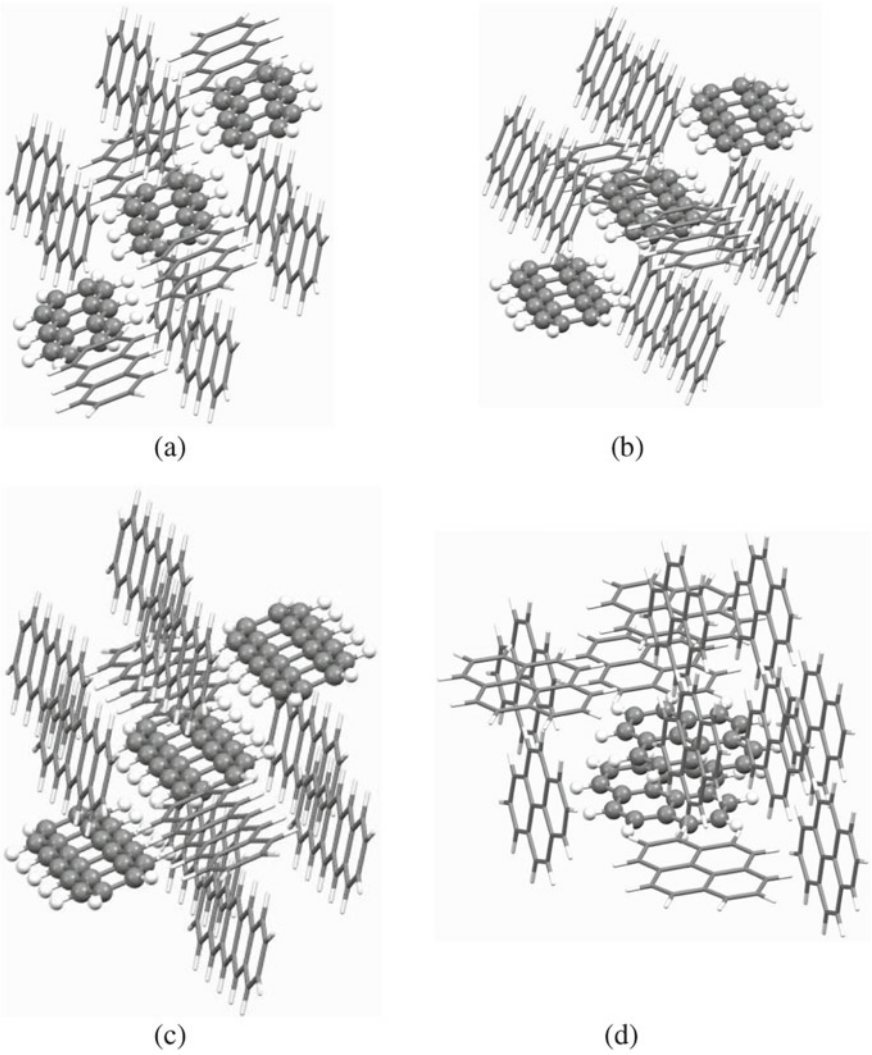

Fig. 8.6 Crystal structures of **a** anthracene; **b** tetracene; **c** pentacene; **d** pyrene. Parallel adjacent molecules in crystals are shown in ball and stick model

Table 8.3 Intermolecular interaction energies between parallel adjacent molecules in crystals of polycyclic aromatic molecules. Energy in kcal mol^{-1}

	E_{B97D}	E_{HF}	E_{disp}
Naphthalene ($P2_1/c$)	−3.62	0.41	−4.03
Anthracene ($P2_1/a$)	−5.25	0.17	−5.42
Tetracene (P^-1)	−7.55	0.56	−8.11
Pentacene (P^-1)	−9.68	1.61	−11.29
Pyrene ($P2_1/a$)	−12.06	15.63	−27.69

molecules is −12.06 kcal/mol. They are about the double of the hydrogen bond of the water dimer. The calculated E_{disp} show that the strong dispersion interactions exist between parallel adjacent molecules in the crystals. The analysis of the intermolecular interactions in the crystals of polycyclic aromatic molecules also shows that it is dangerous to discuss the intermolecular interactions in crystals solely based on the presence or absence of short atom–atom contact.

8.6 Intermolecular Interactions of *n*-hexane

The arrangement of *n*-hexane molecules in the crystal is shown in Fig. 8.7a. The long axes of *n*-hexane are aligned in parallel in the crystal. The molecular arrangement seen from the C-axis direction of the crystal is shown in Fig. 8.7b. The calculated intermolecular interaction energies in three pairs of adjacent molecules arranged in parallel in the crystal are shown in Table 8.4. Although there is no short atom–atom contact between any parallel adjacent molecules, there exists considerable attraction between parallel adjacent molecules. The calculated intermolecular interaction energy (E_{B97D}) between molecules A and B is −5.19 kcal/mol, which is nearly identical to the interaction energy of hydrogen bond in water dimer. The calculated E_{disp} shows that the strong dispersion interactions are responsible for the attraction. The analysis of the intermolecular interactions in the *n*-hexane crystal also indicates that the strong attraction owing to the dispersion interactions exists between molecules without short atom–atom contact.

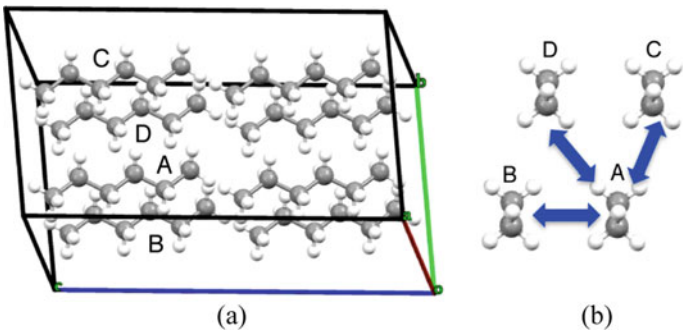

Fig. 8.7 Crystal structure of *n*-hexane

Table 8.4 Intermolecular interaction energies between adjacent *n*-hexane molecules in crystal. Energy in kcal mol^{-1}

	E_{B97D}	E_{HF}	E_{disp}
A-B	−5.19	3.06	−8.25
A-C	−2.87	1.73	−4.60
A-D	−2.04	0.93	−2.97

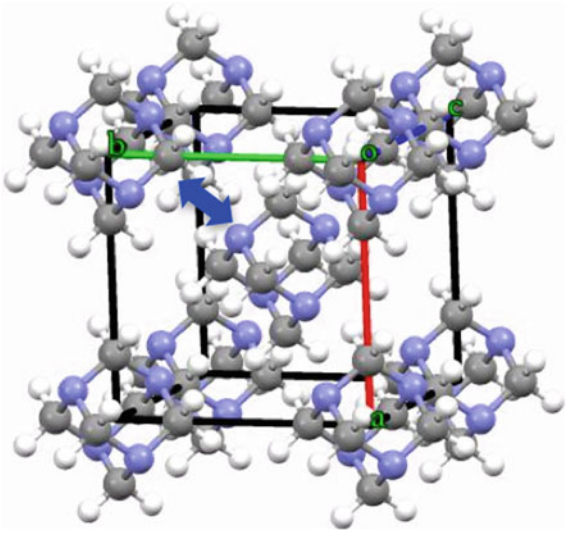

Fig. 8.8 Crystal structure of hexamine

Table 8.5 Intermolecular interaction energies between adjacent hexamine molecules in crystal. Energy in kcal mol^{-1}

	E_{B97D}	E_{HF}	E_{disp}
Hexamine	−4.64	0.31	−4.95

8.7 Intermolecular Interactions of Hexamine

The arrangement of hexamine molecules in the crystal is shown in Fig. 8.8. There is no short atom–atom contact between adjacent molecules in the hexamine crystal. However, there exists significant attraction between adjacent molecules. The adjacent molecule pair indicated by arrow in Fig. 8.8 has the strongest interaction. The intermolecular interaction energy (E_{B97D}) calculated for this pair is −4.64 kcal/mol as shown in Table 8.5. The calculated E_{disp} shows that the dispersion interactions are again responsible for the strong attraction.

8.8 Why Strong Attraction Exists Between Molecules Without Short Atom–Atom Contact?

Analysis of intermolecular interactions in the crystals of organic molecules shows that the strong attraction caused by the dispersion interactions exists between adjacent molecules in crystals, even if there is no short atom–atom contact. Therefore, the question arises why strong attraction owing to the dispersion interactions exists

between adjacent molecules without short atom–atom contact. Intermolecular interactions in crystals have been discussed mainly based on the presence or absence of short atom–atom contacts in crystals. The short atom–atom contact is observed mainly in the cases where single atom of one molecule is in contact with an atom or atoms of another molecule such as the interactions of hydrogen bonds and halogen bonds. By comparing with hydrogen bonds, we would like to discuss the reason why short atom–atom contact is not observed between adjacent molecules even when there exist strong dispersion interactions.

The interatomic distance between adjacent molecules is determined by the balance between attractive and repulsive interactions acting between molecules. In hydrogen bonds and halogen bonds, the major source of the attraction is the electrostatic interactions, and therefore, strong attraction due to the electrostatic interactions acts between positively charged atoms (hydrogen bond or halogen bond donor) and negatively charged atoms (hydrogen bond or halogen bond acceptor). The structure of the hydrogen bonded cluster of methanol dimer is shown in Fig. 8.9a. The equilibrium distance between the hydrogen atom of the donor molecule and the oxygen atom of the acceptor molecule is determined by the balance between the attractive electrostatic interactions and the exchange-repulsion interactions. The distance between the hydrogen atom and the oxygen atom needs to be considerably short to increase the repulsive interactions that can balance the strong attraction by the electrostatic interactions, since only one hydrogen atom and one oxygen atom can contribute to the repulsion. For this reason, in the cases of hydrogen bonds and halogen bonds, the short atom–atom contact between adjacent molecules is necessary when strong attraction exists between molecules.

The dispersion interaction has its origin in molecular polarization. For this reason, the dispersion interactions between molecules with large polarizabilities are strong. The polarizability of molecule composed of a large number of atoms is large, since the polarizability of molecule is approximately the sum of the polarizabilities of the atoms constituting the molecule. In hydrocarbons, carbon atoms are mainly responsible for the dispersion interactions, since the polarizability of hydrogen atoms is small. The dispersion interactions between one carbon atom and one carbon atom are small. For example, the intermolecular interaction energy of methane dimer is

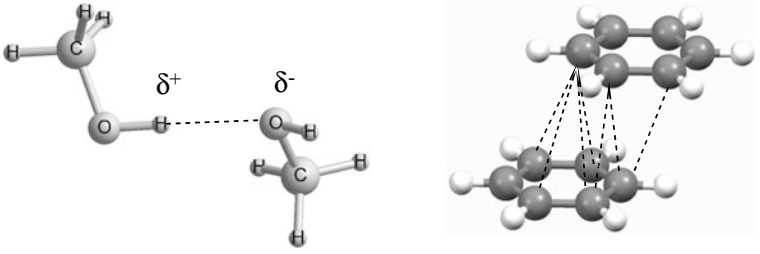

Fig. 8.9 Attraction in hydrogen bonded complex and dispersion-dominated complex

about −0.5 kcal/mol [11]. On the other hand, a number of carbon atoms interact at distances close to the sum of the van der Waals radii in the crystals of polycyclic aromatic molecules and saturated hydrocarbon molecules (Fig. 8.9b), so that the strong dispersion interactions exist between adjacent molecules. In this case, the attractive interaction between each atom pair is weak, so the attractive interaction can be balanced with exchange-repulsion even when the atoms do not contact at short distance less than the sum of the van der Waals radii. For this reason, no short atom–atom contact is observed, even if strong attraction owing to the dispersion interactions exists between adjacent molecules.

8.9 Importance of Dispersion Interactions in Organic Crystals

The dispersion interactions are famous as the origin of the weak attraction between rare gas atoms. For this reason, it is often misunderstood that the dispersion interactions between organic molecules are also weak. However, the analysis of intermolecular interactions shows that the strong dispersion interactions exist between adjacent molecules in the organic crystals. The polarizabilities of organic molecules are significantly large compared with rare gas atoms such as neon and argon. For this reason, the strong dispersion interactions exist between adjacent molecules in the organic crystals.

The structures of organic crystals also suggest the importance of the dispersion interactions for the stabilization of the crystals. The crystal structure of water (Fig. 8.10a) is characterized by large vacant space. The highly directional electrostatic interactions are the major source of the attraction (hydrogen bond) between water molecules. Hydrogen bonds have strong orientation dependence owing to the large contributions of the electrostatic interactions. For this reason, neighboring molecules have to locate at specific positions advantageous to increase the attraction by the highly directional electrostatic interactions for the stabilization of water

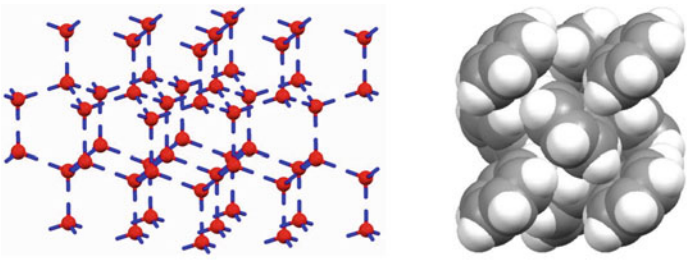

Fig. 8.10 Crystal structure of water and benzene

crystal. Therefore, the water crystal has large vacant space, which is not advantageous for the stabilization by the dispersion interactions.

On the other hand, the crystal structure in which the vacant space is reduced and the average intermolecular distance is shortened like the benzene crystal in Fig. 8.10b is advantageous for the stabilization of the crystal, if the major source of the attraction between adjacent molecules in the crystal is the dispersion interactions. Most of organic crystals have structures which have few vacant spaces. This result suggests that the dispersion interactions are the primary source of attraction in most of organic crystals.

8.10 Summary

Ab initio molecular orbital calculations and dispersion-corrected DFT calculations are becoming powerful methods for studying intermolecular interactions in organic crystals. We can obtain detailed information on the intermolecular interactions in crystals (magnitude and origin of attraction). The intermolecular interactions in crystals have been mainly discussed based on the presence or absence of atom–atom contact at short distances. However, analysis of intermolecular interactions in organic crystals show that the strong attraction by the dispersion interactions often exists between adjacent molecules in crystals, even if adjacent molecules do not have short atom–atom contact. The analysis shows that we should remember the significant importance of the dispersion interactions in organic crystals and the danger to discuss the intermolecular interactions in crystals solely based on crystal structures. The analysis of intermolecular interactions in crystals by theoretical calculations is important for understanding structures and properties of organic crystals.

References

1. Tsuzuki, S., Orita, H., Sato, N.: Intermolecular interactions of oligothienoacenes: do S···S interactions positively contribute to crystal structures of sulfur-containing aromatic molecules? J. Chem. Phys. **145**, 174503 (2016)
2. Stone, A.J.: The Theory of Intermolecular Forces, 2nd edn. Oxford University Press, Oxford (2013)
3. Nishio, M., Hirota, M., Umezawa, Y.: The CH/π Interaction. Wiley-VCH, New York (1998)
4. Tsuzuki, S., Honda, K., Uchimaru, T., Mikami, M., Tanabe, K.: The magnitude of the CH/π interaction between benzene and some model hydrocarbons. J. Am. Chem. Soc. **112**, 3746–3753 (2000)
5. Tsuzuki, S., Fujii, A.: Nature and physical origin of CH/π interaction: significant difference from conventional hydrogen bonds. Phys. Chem. Chem. Phys. **10**, 2584–2594 (2008)
6. Desiraju, G.R., Steiner, T.: The Weak Hydrogen Bond (Oxford University Press, New York, 1999)
7. Tsuzuki, S., Mikami, M., Yamada, S.: Origin of attraction, magnitude, and directionality of interactions in benzene complexes with pyridinium cations. J. Am. Chem. Soc. **129**, 8656–8662 (2007)

8. Becke. A.D.: Density-functional thermochemistry. III. The role of exact exchange. J. Chem. Phys. **98**, 5648–5652 (1993)
9. Grimme, S.: Semiempirical GGA-type density functional constructed with a long-range dispersion correction. J. Comp. Chem. **27**, 1787–1799 (2006)
10. Grimme, S., Antony, J., Ehrlich, S., Krieg, H.: A consistent and accurate ab initio parameterization of density functional dispersion correction (DFT-D) for the 94 elements H-Pu. J. Chem. Phys. **132**, 154104 (2010)
11. Tsuzuki, S., Uchimaru, T., Tanabe, K., Kuwajima, S.: Refinement of nonbonding interaction potential parameters for methane on the basis of the pair potential obtained by MP3/6-311G(3d,3p)-level *ab initio* molecular orbital calculations: the anisotropy of H/H interaction. J. Phys. Chem. **98**, 1830–1833 (1994)

Chapter 9
Pharmaceutical Multicomponent Crystals: Structure, Design, and Properties

Okky Dwichandra Putra and Hidehiro Uekusa

Abstract Multicomponent crystals, which include cocrystals and salts, have been of great interest to the pharmaceutical field owing to their ability to be used as an alternative solid form of drugs with better physicochemical properties compared to their corresponding parent drugs and as a potential source for patents and research opportunities. Although multicomponent crystal formation was originally seen to only improve the solubility and dissolution rate profiles of drug molecules, it has also shown potential applications in overcoming other problems, such as hygroscopicity, poor tabletability, instability, and bitter taste. This chapter highlights some multicomponent crystal applications that tackle common unfavorable physicochemical properties of drugs in the pharmaceutical field. The multicomponent crystal design has been covered with regard to the relation between the crystal structure and physicochemical properties. The study cases presented in this chapter emphasize the structural aspect of multicomponent crystals to provide a molecular-level understanding of the physicochemical property changes accompanying multicomponent crystal formation.

Keywords Multicomponent crystals · Cocrystal · Salt · Physicochemical properties · Crystal structure · Design

O. D. Putra · H. Uekusa (✉)
Department of Chemistry, Tokyo Institute of Technology, Ookayama 2-12-1, Meguro-ku, Tokyo, Japan
e-mail: uekusa@chem.titech.ac.jp

O. D. Putra
e-mail: dwichandraputra@yahoo.com

M. Sakamoto and H. Uekusa (eds.), *Advances in Organic Crystal Chemistry*,
https://doi.org/10.1007/978-981-15-5085-0_9

9.1 Introduction

9.1.1 Solid Active Pharmaceutical Ingredients (APIs)

Active pharmaceutical ingredients (APIs) are classified in numerous ways, based on the existing pharmaceutical disciplines. In general, APIs can be classified based on their chemical nature, source, target organ, therapeutic uses, physiological system, physical effect, phase, etc. [1]. In this chapter, we will focus on the classification that is based on the phase system. In the pharmaceutical field, APIs can be grouped into three phases: solid, liquid, and gas (i.e., nitrous oxide) [2, 3]. APIs are most commonly formulated in the solid-state, in which their physical and chemical stabilities are typically better. Moreover, solid-state preparation of APIs is more practical due to ease of handling, processing, and packaging during the various stages of drug development and preparation [4, 5].

The study of solid APIs involves many scientific disciplines because many phenomena influence the physicochemical properties of solid APIs: stability, hygroscopicity, dissolution rate, color, etc. [6–10]. Solid APIs can generally be classified as amorphous and crystalline solids. Crystalline solids include polymorphs, hydrates, solvates, cocrystals, and salts, as shown in Fig. 9.1 [11]. The classification of crystalline solid API evolves continuously, allowing each type of crystalline solid to merge with other types, resulting in new subsets of crystalline solids, i.e., polymorphs of hydrates, hydrate cocrystals, hydrate salts, etc. [12–14].

Amorphous solids are defined as solid materials that lack a long-range order in their internal structure [15]. The molecules within an amorphous material exhibit liquid state disorder but solid rheological properties. There are various techniques to produce an amorphous solid, such as spray drying, freeze-drying, grinding, melt extrusion, melt quenching, and co-precipitation [16]. A molecule in amorphous form is in a higher energy state compared to its crystalline counterpart [17]. This can be

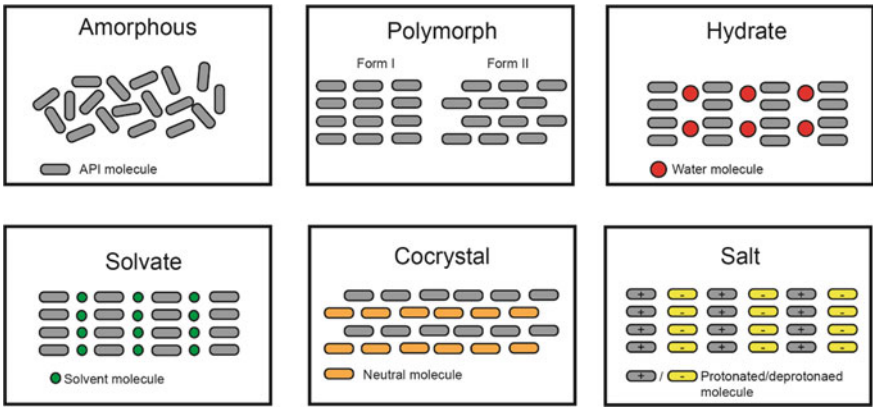

Fig. 9.1 Simplified illustration of solid APIs

exploited in pharmaceutical applications to increase the solubility of problematic APIs. However, from a thermodynamic point of view, the amorphous state of a solid is unstable and has the tendency to convert to its low-energy and more stable crystalline form over time [18]. Therefore, the number of successful products available in this solid form in the market is still limited.

Most marketed APIs, therefore, consist of crystalline solids. In contrast with amorphous solids, crystalline materials consist of minimal building blocks called unit cells that contain all the structural features and symmetry elements of the crystal and are repeated regularly in three-dimensional space [19]. Furthermore, API crystalline molecules are typically amenable to form multiple crystal forms known as polymorphs [20]. Organic molecules, including APIs, generate polymorphic crystals through two mechanisms. The first mechanism leads to so-called packing polymorphs, in which molecules with relatively rigid conformations can be assembled into different three-dimensional structures. The second mechanism occurs when a flexible molecule bends into different conformations to subsequently be packed into alternative crystal structures [21]. Some polymorphic APIs have mixed mechanisms and exhibit different packing and conformational polymorphs [22].

API crystalline molecules can also exist as multicomponent crystals by incorporating other molecules into the crystal lattice. “Pseudopolymorph” is the widely accepted term for crystals with solvent molecules incorporated into their lattice [23–25]. Hydrates are crystalline solid adducts that contain water molecules and are known as the largest class of pseudopolymorps [4]. If a crystalline solid accommodates another solvent molecule than water, the solvate terminology is generally used [26]. If a multicomponent crystal contains two components, both of them solid in ambient conditions, the multicomponent crystal can further be classified as cocrystal and salt [27]. Cocrystals are generally defined as crystalline materials comprising two or more neutral molecules in the same crystal lattice [27]. Contrarily, a salt is formed if any part of an API gives or receives a proton to or from another molecule [28]. Polymorphic, pseudopolymorphic, cocrystal, and salt states have quickly evolved from being relative obscure to widely studied crystal forms in the context of pharmaceutical science and engineering [12, 13].

When APIs form multicomponent crystals, the driving force is typically a molecular synthon, such as a hydrogen bond, π-π interaction, or halogen bond, which involves supramolecular chemistry [28]. To put this in the pharmaceutical science context, the study of multicomponent crystal APIs, particularly their physicochemical properties relevant to clinical performance and long-term stability, represents an important aspect in drug discovery and development. In the past decade, pharmaceutical multicomponent crystals have emerged as promising tools for solid formulation testing during drug discovery and development, as their design can profoundly influence their physicochemical properties. Pharmaceutical multicomponent crystals offer massive opportunities for research topics and patent development, as well as for functional materials applications. The number of research projects and patent applications in the multicomponent crystal field should, therefore, be unsurprising.

9.1.2 Challenges of Solid APIs

In the pharmaceutical industry, one of the bottlenecks in the discovery and development of APIs is the optimization of drug product performance by pre-formulation research [29, 30]. The goal of pre-formulation research is to provide optimized APIs featuring suitable physiological profiles that can later be formulated into pharmaceutical dosage forms [31, 32]. As mentioned before, APIs are most commonly formulated in solid form, i.e., tablets, capsules, and granules, because the chemical stability is superior to that of a solution. Furthermore, solid-state dosage forms provide more practical processing, packaging, handling, and allow, for most patients, the preferred choice of drug intake, oral delivery.

Solid APIs are generally used for dosage forms intended for oral delivery. It should be noted that oral delivery typically requires the dissolution of active ingredients at the absorption site, while avoiding precipitation during gastrointestinal transit, until complete absorption [33]. Unfortunately, about 40% of marketed drugs and almost double the percentage of drug candidates are thought to have solubility issues in oral administration [34, 35]. Meanwhile, many solid APIs exhibit other unfavorable physicochemical properties, such as hygroscopicity, [36] brittleness, [37] and chemical instability, [38] which become a problem during manufacturing and storage. In general, low solubility and stability pose a serious threat for candidate APIs by preventing the drug from reaching minimum therapeutic concentrations in the biological system [39–41].

Moreover, some drugs exhibit more than one unfavorable physicochemical property, creating the need for an ultimate simultaneous solution. Hygroscopicity is considered an unfavorable physicochemical property, which leads to increased production costs. By far, the biggest challenge posed hygroscopicity is the extra effort required to dry the APIs during processing and then before packaging. The judicious use of production rooms with controlled humidity and sealed packaging systems is advisable in many cases [42]. Brittleness is another hostile physicochemical property that is mostly related to processing bulk APIs. Difficulties due to brittleness often arise during milling, filling, and compaction, due to the poor mechanical properties of bulk powders [43]. The physicochemical properties of insolubility and chemical instability are strongly negatively related to the safety, quality, and efficacy of APIs [44, 45].

Some approaches that tackle these unfavorable physicochemical properties can be divided into formulation, particle engineering, and crystal engineering (Fig. 9.2). In formulation, an API is combined with other substances or excipients to optimize the physicochemical properties, therapeutic potential, safety, and stability of the final dosage form. The formulation of the drug also covers the processing methods and devices, and the packaging [46]. Particle engineering involves the methodology used to obtain the optimal particle size, size distribution, morphology, and surface characteristics. Particle engineering can cover all aspects that modify the morphology and surface behavior of a drug, with or without the addition of excipients [47, 48].

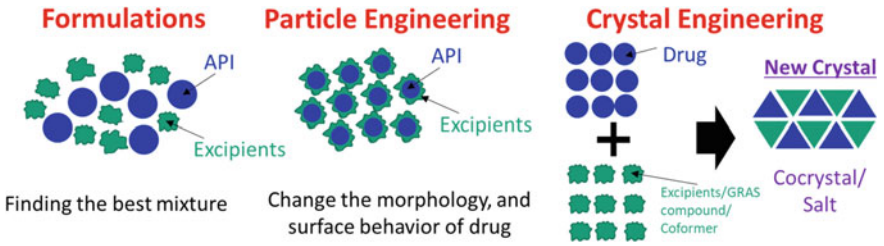

Fig. 9.2 Schematic illustration of formulation, particle engineering, and crystal engineering to produce and deliver an API with suitable physicochemical properties

The latter is crystal engineering which is a popular terminology for multicomponent crystal formations. Crystal engineering in the pharmaceutical field utilizes non-covalent interaction, such as hydrogen and halogen bonds, and π-π interactions, to create a new crystal structure containing APIs and coformer that can be a typical excipient or other generally recognized as safe (GRAS) compounds. Pharmaceutical scientists, crystallographers, and solid-state chemists have taken advantages of crystal engineering to remedy deficiencies of different nature of APIs. The next sub-chapter provides some interesting examples of design and formation of multicomponent crystal in the pharmaceutical field which overcome the unfavorable physicochemical properties of solid APIs.

9.2 Structural Design and Investigation of Physicochemical Alteration in Pharmaceutical Multicomponent Crystals

9.2.1 Solubility Improvement by Layered Structure Formation

Solubility improvement is arguably the most common topic in multicomponent crystal research, reflected not only by a large number of publications and patents but also by the fact that multicomponent crystals can alter the solubility of problematic APIs. In this review, we emphasize the benefits of solubility improvement by layered structure formation. Particularly, the structural origin of the improved solubility of the epalrestat cocrystal will be described briefly.

Epalrestat (EPR, Scheme 9.1 left) is an aldose reductase inhibitor used for the treatment of diabetic neuropathy [49]. Marketed EPR formulations are known to have low bioavailability. In addition, EPR, which is a class II molecule, according to the Biopharmaceutical Classification System (BCS), exhibits poor solubility and a slow dissolution rate [50]. Therefore, the solubility and dissolution rate reasonably constitutes the rate-limiting step of its bioavailability. The solid-state properties of EPR have been widely investigated; EPR exists in five known polymorphic forms

Scheme 9.1 Chemical structure of EPR (left) and CAF (right)

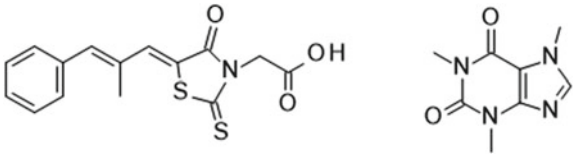

and several crystalline solvates, and it is commercially available in the form I EPR [51–57].

EPR has a carboxylic acid moiety in its molecular structure, which can potentially be employed as a supramolecular synthon. From an analysis of the Cambridge Structural Database (CSD), caffeine (CAF, Scheme 9.1 right) might be particularly suited to act as a promising coformer in the formation of a neutral cocrystal. Moreover, CAF is widely used as the coformer, when trying to avoid proton transfer, since its ionization is only limited to strong acids. A search in the CSD also reveals promising neutral cocrystal structure reports, resulted from the interaction between compounds containing carboxylic acid moieties and CAF.

The preparation of the cocrystal involved several cocrystal screening methods such as liquid-assisted grinding, neat grinding, ball milling, and solvent evaporation. The above-mentioned single-phase cocrystal can be prepared by ethanol liquid-assisted grinding. However, to grow a single crystal, we used methanol as a solvent in the solvent evaporation technique. All cocrystals in this method were prepared by mixing EPR and CAF in a 1:1 molar ratio. The powder diffraction patterns from both the liquid-assisted grinding and solvent evaporation technique were the same as the simulated powder diffraction pattern, indicating that these methods led to a pure phase (Fig. 9.3).

The EPR–CAF cocrystal generated a triclinic crystal system with the space group *P*-1. An asymmetric unit contains a CAF molecule and an EPR molecule. The CAF molecule was refined to be disordered around a non-crystallographic two-fold axis through O4–C16–C20 with the occupancy of the major part determined at 0.518(5). The extensive hydrogen bonding between the EPR and CAF molecules created a layered structure. Further, only one conventional hydrogen bond, between the oxygen atom (O3) in EPR's carboxylic acid and the oxygen atom (O4) in the CAF molecule was observed. The other two hydrogen bonds (C2–H$\cdots$O and C5–H$\cdots$O2) connected an EPR molecule with two adjacent EPR molecules and were considered unconventional weak hydrogen bonds. These interactions resulted in a layered structure, perpendicular to the c-axis, as illustrated in Fig. 9.4. In this architecture, the EPR layer was sandwiched between two CAF layers.

The solubility change through cocrystallization is particularly important in this case, as EPR is classified as a class II drug, according to BCS. We predict that the poor aqueous solubility of EPR, in general, maybe due to its high molecular weight (319.04 g mol^{-1}) and the lack of a functional group that can interact with a solvent molecule. Therefore, the equilibrium solubility and intrinsic dissolution rate of EPR and its cocrystal were evaluated.

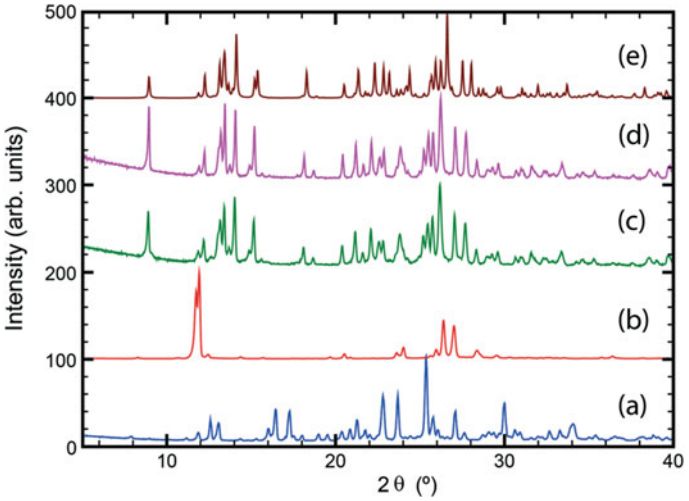

Fig. 9.3 The PXRD pattern of **a** EPR, **b** CAF, EPR–CAF from **c** the liquid-assisted grinding technique, **d** the solvent evaporation technique, and **e** simulation from single-crystal data. Reproduced from Ref. [58] with permission from the Royal Society of Chemistry

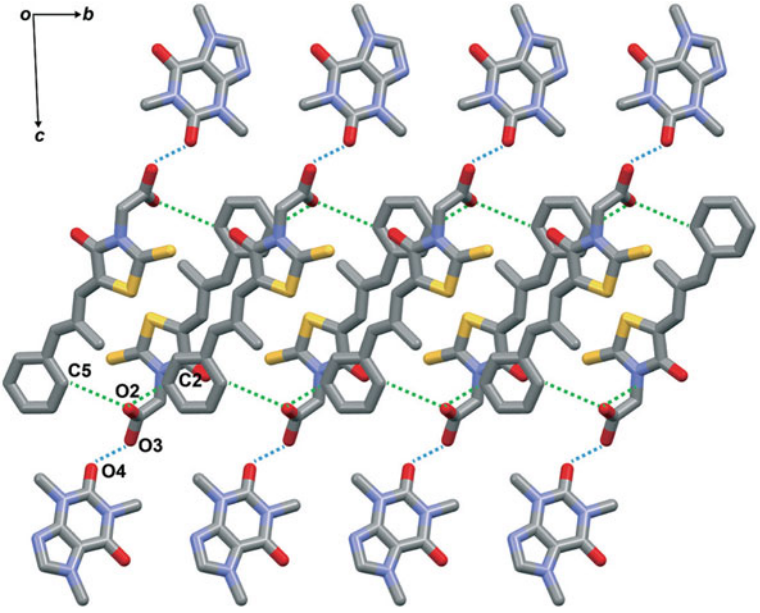

Fig. 9.4 Layered structure, resulted from the interaction between EPR–CAF and EPR–EPR. The hydrogen atoms and minor component molecules are omitted for clarity. Reproduced from Ref. [58] with permission from the Royal Society of Chemistry

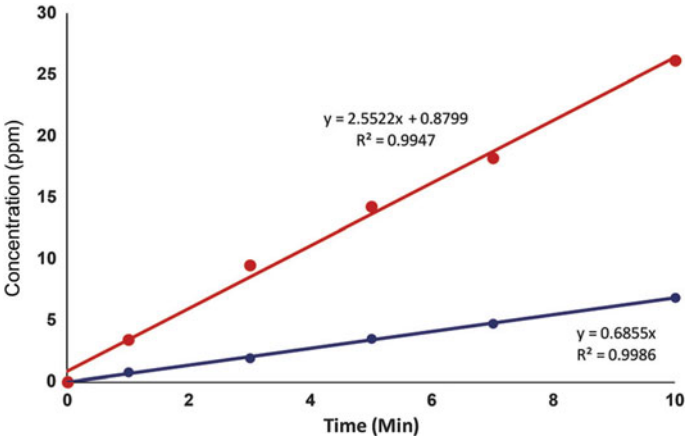

Fig. 9.5 Intrinsic dissolution rate curves of EPR (blue) and EPR–CAF (red). Reproduced from Ref. [58] with permission from the Royal Society of Chemistry

The equilibrium solubility of EPR, CAF, and EPR–CAF were 2.956, 33.280, and 4.557 mg L^{-1}, respectively. The equilibrium solubility of the cocrystal was almost twice as that of the pure drug. This result needed to be reinforced by the kinetic behavior of EPR, represented by the dissolution rate. Intrinsic dissolution tests were conducted for tablets of each material to avoid the influence of particle orientation, agglomeration during dissolution, and particle size variability. As shown in Fig. 9.5, the intrinsic dissolution rate of the cocrystal is almost four times that of raw EPR. Close PXRD pattern examinations of residues remaining after solubility and dissolution rate experiments indicate that no EPR–CAF to EPR phase dissociation occurred. Furthermore, no significant pH change was detected before and after the solubility and dissolution rate experiments.

The improvement in solubility and intrinsic dissolution rate can be explained by the molecular arrangement of the cocrystal. As previously mentioned, a layered structure is formed by alternate arrangements of EPR and CAF molecules, wherein a layer of EPR molecules resides in the channel formed between two layers of CAF molecules. This configuration, in contrast to an extended chain structure, only composed of EPR molecules in raw form with a strong hydrogen bond, predictably facilitates the improvement in solubility and dissolution by facilitating contact with the solvent. When the more soluble conformer is in contact with the solvent it dissolves and the only interaction between EPR–CAF is broken ($E_{int} = -27.45$ kJ mol^{-1}); consequently, the chain consisting of EPR molecules is exposed to the solvent media. Since the EPR molecules within the chain have weak interactions (E_{int} of C2–H2$\cdots$O2 $= -2.30$ kJ mol^{-1} and E_{int} of C5–H5$\cdots$O2 $= -2.61$ kJ mol^{-1}), the EPR will dissolve more easily, leading to increased solubility. The proposed mechanism suggests that the internal arrangement of molecules in a crystal lattice plays an important role in tuning the physicochemical properties of solid forms. It should also be noted that here, the EPR–CAF cocrystal, being

more soluble and having a faster dissolution, enables possible EPR dose reductions in future applications. In addition, from a pharmacological point of view, the dose of CAF in this cocrystal will not exceed the maximum daily intake (200 mg per day) for a diabetic patient [58].

9.2.2 Simultaneous Modulation of Hygroscopicity and Solubility of APIs by Drug-Drug Multicomponent Crystal Formation

Hygroscopicity or the stability of solid APIs to water vapor is a major concern for the pharmaceutical industry. The conversion of an API into a wet powder could bring undesired physicochemical properties and difficulties for both drug storage and processing. The preparation of new multicomponent crystals, cocrystals, and salts alike has been widely reported to prevent API hydrate formation. The potential of multicomponent crystals containing drug combinations to offer physicochemical properties superior to the parent drugs has been investigated [59, 60]. This family of crystals, besides providing technological advantages, also offers improved pharmacological effects and patient compliance [61]. These are likely the most important advantages of drug-drug multicomponent crystals over single drug and nondrug multicomponent crystals.

A screening of marketed combination drug formulations yielded the combination of non-insulin-dependent diabetes mellitus (NIDDM) drugs metformin (MET, Scheme 9.2 right) and gliclazide (GLI, Scheme 9.2 left). MET is a blood glucose-normalizing derivative of guanidine, and GLI is a potent oral hypoglycaemic agent for the long-term treatment of diabetes mellitus. MET and GLI are effective in the treatment of NIDDM in both single and combined therapies. Recently, combination oral therapies have become widely used and clinically needed. Indeed, the combination of MET and GLI offers better control of blood glucose and lipid index, major concerns in the treatment of diabetes [62].

Unfortunately, both MET and GLI exhibit unfavorable physicochemical properties. The base form of MET is a hygroscopic powder. Attempts to overcome this hygroscopicity, through special treatment during the manufacturing process and the use of a closed packaging system, are expensive and may increase the cost of the drug [63]. Therefore, in order to avoid hygroscopicity, MET is found on the market as a hydrochloride salt [64]. In addition, GLI, a class II molecule, according to the Biopharmaceutical Classification System, exhibits low solubility [65].

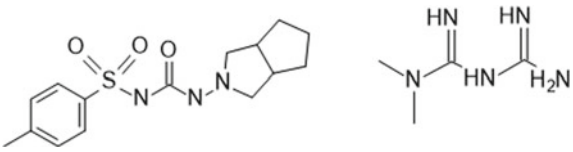

Scheme 9.2 Chemical structure of GLI (right) and MET (left)

The single-phase multicomponent crystal of MET and GLI could be obtained from liquid-assisted grinding and ball milling. However, the solvent evaporation technique was used to grow single crystals. Surprisingly, "halo" peaks were observed in the powder pattern of the GLI and MET mixture after the ball milling experiment. After milling for 24 h, the crystals were amorphized. These amorphized powders were stored for one month without any physical treatment. After 4 weeks, the amorphous powder transformed into a multicomponent crystal of GLI-MET, as shown in Fig. 9.6f and g. The amorphous phase, well known as energetically unstable has the ability to turn to the crystalline phase during storage. It is interesting that all three techniques successfully form the same multicomponent crystal instead of different crystal growth mechanisms (Fig. 9.6).

Single-crystal X-ray analysis reveals that the GLI-MET multicomponent crystal is a salt. A proton transfer was reasonable because ΔpK_a was greater than 3. The intermolecular interactions in the MET-GLI crystal are shown in Fig. 9.7. The MET molecules formed a centrosymmetric dimer structure through two N8–H···N6 hydrogen bonds (Fig. 9.7, right). MET also interacted with three GLI molecules via relatively strong hydrogen bonds. The interaction between MET and the first GLI molecule was formed by the $N5^+$–H···O(1) carbonyl hydrogen bond. Charge transfer-mediated hydrogen bonds in $N5^+$–H···N3 − connected MET to the second GLI molecule. An additional hydrogen bond in the N7–H···O2 sulfonyl stabilized the interaction with the second GLI molecule. N7 formed bifurcated hydrogen bonds

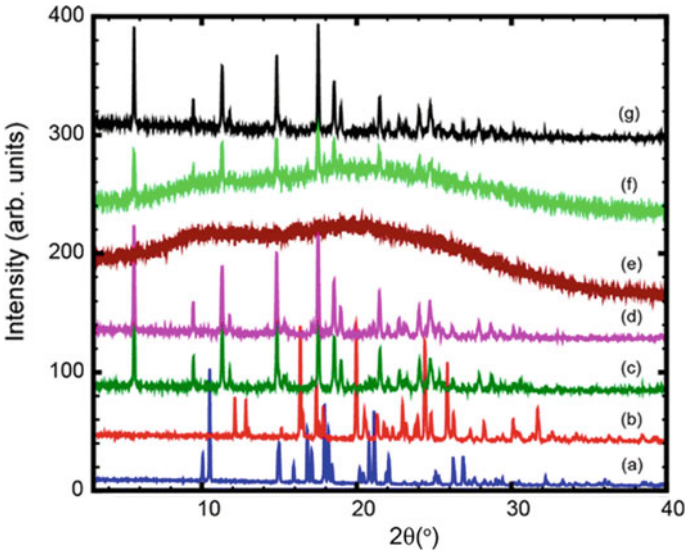

Fig. 9.6 PXRD patterns of **a** GLI, **b** MET, MET-GLI from **c** liquid-assisted grinding, **d** solvent evaporation, **e** ball milling, **f** 2 weeks after ball milling, and **g** 4 weeks after ball milling. Reprinted (adapted or reprinted in part) with permission from [66]. Copyright 2011 American Chemical Society

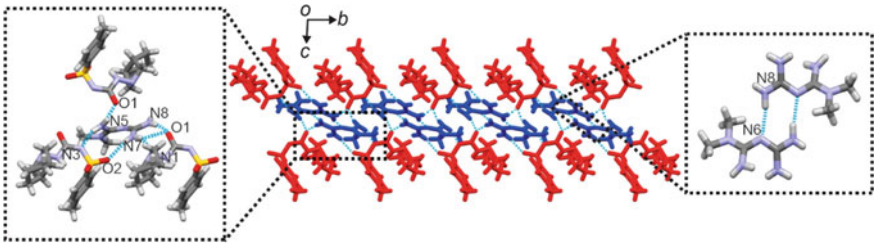

Fig. 9.7 Infinite one-dimensional (1D) hydrogen bond chain of the MET-GLI crystal along the *a*-axis (blue for MET and red for GLI). Insets show the detailed interaction between MET-MET (right) and MET-GLI (left) presented in default color according to the different elements. Blue-dashed lines indicate hydrogen bonds. Reprinted (adapted or reprinted in part) with permission from [66]. Copyright 2011 American Chemical Society

through N7–H···N1 and N7–H···O1 carbonyl with the third GLI molecule. The hydrogen bond in the N8–H···O1 carbonyl also contributed to the interaction with the third GLI molecule.

In the hydrogen-bonding analysis, all donor and acceptor moieties of the hydrogen bonds in MET actually formed hydrogen bonds with both MET and GLI molecules. Such characteristic hydrogen-bonding ability indicated that MET can act as a promising coformer during the formation of multicomponent crystals. Based on the intermolecular interactions described above, a continuous hydrogen bond chain could be observed along the *a*-axis, in which the MET molecules were sandwiched between GLI molecules.

The physicochemical evaluation started with dynamic vapor sorption (DVS) analysis of the multicomponent crystal and the individual intact materials (Fig. 9.8). During the tests, the relative humidity (RH) did not exceed 80% because the MET powder exhibited a considerable hygroscopicity. MET started to absorb atmospheric water from 60% RH and became deliquescent at higher values. However, the GLI powder crystals were stable at RH values up to 80% with no significant amount of water being absorbed. This result is in agreement with the low water solubility of GLI, aspect that is not soluble in water and hence not hygroscopic.

Interestingly, multicomponent crystals of MET-GLI were present as a non-hygroscopic powder. The water uptake at an RH of 80% was only 3.3%, which corresponded to surface water. The reduced hygroscopicity of the multicomponent crystals as compared with MET alone could be explained by the crystal structure. As shown in Fig. 9.7, MET was located in the channel formed by GLI molecules; thus, the GLI molecules, which were less hydrophilic, protected MET and formed hydrogen bonds to close potential hydrogen-bonding sites. Thus, it is reasonable to conclude that the multicomponent crystals of MET-GLI showed lower hygroscopicity than MET.

As shown in Fig. 9.8d, the multicomponent crystals enabled a significantly higher dissolution rate than GLI alone and consistently higher released drug amounts at

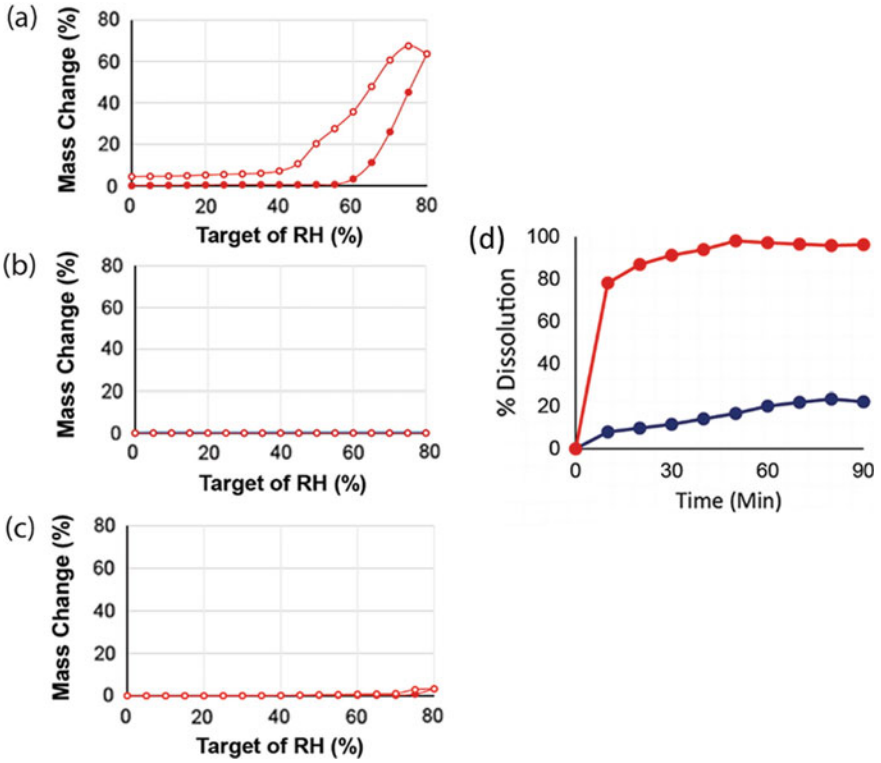

Fig. 9.8 DVS charts of **a** MET, **b** GLI, and **c** MET-GLI. The solid and open symbols represent absorption and desorption, respectively. **d** Dissolution rate of GLI (blue) and MET-GLI (red) in acidic medium (pH = 1.2). Reprinted (adapted or reprinted in part) with permission from [66]. Copyright 2011 American Chemical Society

each dissolution time, reaching a maximum value of nearly 100%. Whereas MET-GLI dissolved rapidly, reaching equilibrium after 40 min, pure GLI maintained a slow rate from the beginning of the experiment, achieving equilibrium after 70 min.

Surprisingly, we observed desirable hygroscopicity and solubility changes at the same time, despite the general coincidence of these physicochemical properties, difficult to reconcile simultaneously because these factors are contradictory. In many cases, the hygroscopicity of a substance can be reduced by decreasing its solubility and vice versa. The above-mentioned work presents a remarkable exception where the hygroscopicity can be reduced but by channel formation, the solubility can be maintained.

The physicochemical property changes are strongly related to the superficial molecular configuration of materials. As shown in Fig. 9.9a, the dominant crystal face (001) was hydrophobic, with the exception of side faces (010) and (100), which provided access to the hydrophilic MET channel. The hydrophobic frame

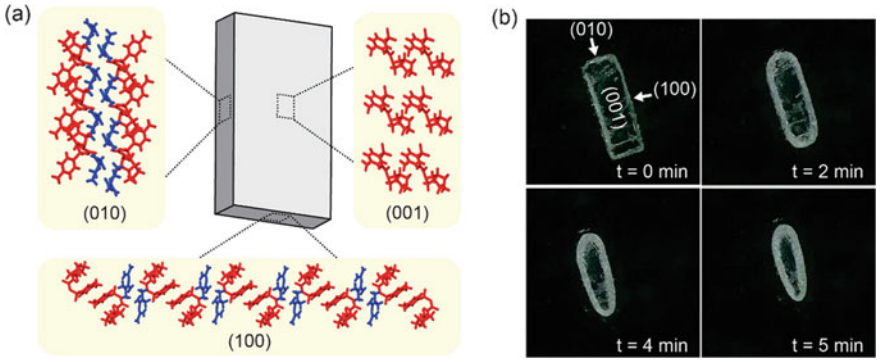

Fig. 9.9 **a** Calculated crystal morphology and packing view of each face of MET-GLI. MET (hydrophilic compound) and GLI (hydrophobic compound) are drawn in blue and red, respectively. **b** Microscopic visualization of single crystals of MET-GLI from the (001) face direction during the solubility experiment. Reprinted (adapted or reprinted in part) with permission from [66]. Copyright 2011 American Chemical Society

could reduce the probability of water vapor contact with the hydrophilic MET, thus eventually reducing the hygroscopicity of the multicomponent crystals.

The channel structures of the hydrophilic side faces could play an important role in solubility improvement, owing to the molecular characteristics of the surface. Furthermore, the direct observation of a single crystal's shape variation during solubilization offered reasonable evidence for underlying structure–solubility relationships. As illustrated in Fig. 9.9b, the crystal shrunk along the direction of hydrophilic faces (010) and (100), indicating that the solvent gradually penetrated and extracted molecules from those surfaces. Moreover, a loss of face transparency suggested solubilization, as observed in the (010) and (100) faces. On the other hand, the dominant (001) face appeared transparent during this observation, suggesting that no significant solubilization occurred on this face [66].

9.2.3 Improving Mechanical Properties

The most convenient and arguably the most common pharmaceutical dosage form is the tablet. One of the most important aspects of tablet preparation is the evaluation of mechanical properties. This is particularly important for APIs that constitute a large portion of the tablet [67]. The mechanical properties of APIs can also affect the overall formulation design and manufacturing strategies [68].

In many cases, poor API mechanical properties can be overcome by the addition of excipients such as lactose or microcrystalline cellulose that improve tabletability. However, this strategy can be considered a curative remedy for tablet brittleness instead of an improvement to the mechanical properties of APIs themselves. The crystal engineering strategies are an alternative way of addressing poor

compaction behavior that overcomes the root of poor mechanical properties itself, the arrangement of API molecules within the crystal structure [69].

This section presents the study case of desloratadine (DES, Scheme 9.3 left), a derivative of loratadine used to treat allergic rhinitis, urticaria, and inflammation. Pharmacologically, DES is a selective H_1 histamine receptor inverse agonist [70]. DES exhibits poor mechanical characteristics, manifested by capping during tablet compression and results in drug processing difficulties [71].

DES has pyridine and piperidine rings that can enable many potential intermolecular interactions with mildly acidic carboxylic acids. Therefore, the screening targeted generally recognized as safe (GRAS) compounds containing carboxylic acid moieties. The attempts to prepare a multicomponent crystal of DES used highly efficient cocrystal generating methods, such as liquid-assisted grinding, slurry mixing, dry milling, and solvent evaporation techniques.

Surprisingly, in the PXRD analysis of potential single-phase crystals, only benzoic acid (BA, Scheme 9.3 right) generated a pattern change, which indicates that a new phase could have been obtained. The new, purely single-phase DES-BA multicomponent crystal was prepared using the solvent evaporation method, aided by a rotary evaporator; conversely, liquid-assisted grinding, slurry mixing, and dry milling were not successful. Notably, the utilization of a rotary evaporator was essential for avoiding the formation of a fat-based suspension. As illustrated in Fig. 9.10, no trace of DES or BA impurities is observable. Moreover, the experimental and calculated

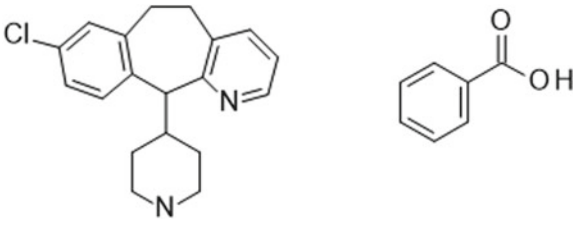

Scheme 9.3 Chemical structure of DES (left) and BA (right)

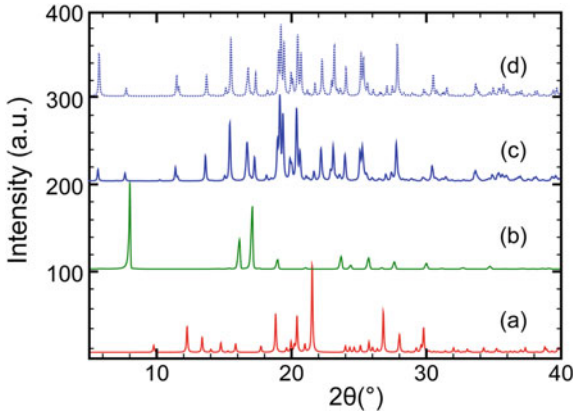

Fig. 9.10 The PXRD patterns of **a** DES, **b** BA, and DES-BA from **c** experimental and **d** simulation data from a single crystal. Reprinted from [72]. Copyright 2012, with permission from Elsevier

PXRD patterns are similar, indicating the absence of significant amounts of impurities. It should be noted here that the differences between the experimental and simulated powder patterns, in this case, might be caused by experimental factors such as differences in temperature and preferred orientation.

Single-crystal structure analysis revealed that the DES-BA multicomponent crystal is a salt. The crystal structure of DES-BA is constructed both by conventional N–H···O and unconventional C–H···O hydrogen bonds. The charge-assisted hydrogen bonds of N2–H···O1 and N2–H···O2 connect DES and BA along the *c*-axis. Therefore, each DES molecule is hydrogen-bonded to two neighboring BA molecules, and conversely, each BA molecule is hydrogen-bonded to two DES molecules. The outcome of these interactions is a layered structure formed by one-dimensional chain structures. The weak hydrogen bond of C17–H···N1 stabilizes this layered structure by connecting DES molecules within the chain (Fig. 9.11a). One layered structure is connected to two other adjacent layered structures through the C13–H···O1 and C18–H···O2 weak hydrogen bonds, as illustrated in Fig. 9.11b, c. These weak hydrogen bonds form slip planes, parallel to the dominant crystal face (001), and

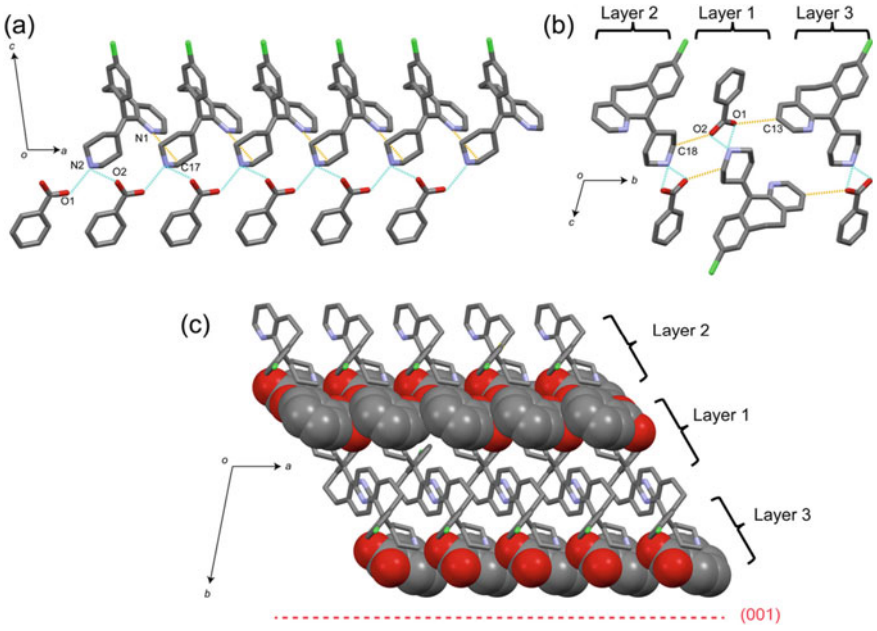

Fig. 9.11 Molecular packing motifs in the crystal showing **a** a layered structure formed by a one-dimensional chain hydrogen bond between DES-BA along the c-axis, and **b** the interaction among layered structures. **c** The packing view along the c-axis shows the existence of slip planes parallel to (001). DES and BA are drawn in capped stick and space fill settings in (**c**), respectively. The conventional NH···O and unconventional CH···O hydrogen bonds are drawn as blue and orange dashed lines, respectively. Hydrogen atoms are omitted for clarity. Reprinted from [72]. Copyright 2012, with permission from Elsevier

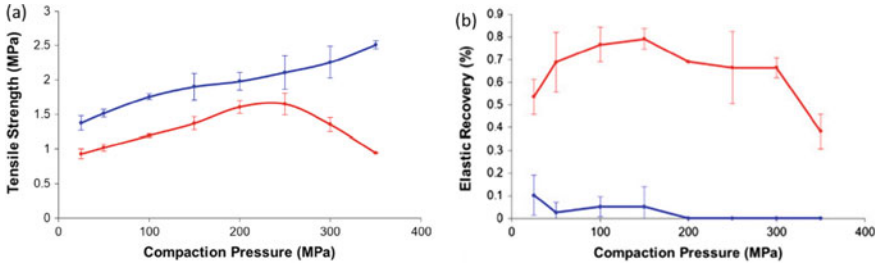

Fig. 9.12 **a** Tabletability profiles and **b** elastic recovery as a function of compaction pressure of DES (red) and DES-BA (blue). Reprinted from [72]. Copyright 2012, with permission from Elsevier

are considerably important for the tabletability of the DES-BA salt multicomponent crystal.

The tabletability profiles of DES and DES-BA as a function of compaction pressures between 25 and 350 MPa are shown in Fig. 9.12a. The tensile strength of the DES tablet was lower than that of the DES-BA tablet: it started at ~0.9 MPa at a 25 MPa compaction pressure, maintained ~1.6 MPa at a 250 MPa compaction pressure, and decreased at compaction pressures higher than 250 MPa. The tensile strength of DES tablets was poor (<1 MPa) at compaction pressures below 150 MPa. However, DES can form a relatively suitable tablet at compaction pressures between 150 and 250 MPa. Surprisingly, DES-BA generated better tabletability profiles than DES. DES-BA could be made into a suitable tablet until 350 MPa, which is the highest compaction pressure employed in this study. Furthermore, a tensile strength above 2 MPa could be attained at compaction pressures exceeding 200 MPa. It should be noted that a minimum tensile strength of 2 MPa has been proposed for ensuring the integrity of a pharmaceutical tablet. Therefore, a DES-BA formulation will probably have no substantial tabletability problems—even at high compaction pressures.

The elasticity-plasticity profiles of DES and DES-BA were investigated afterward. Plasticity and elasticity are defined by the elastic recovery in this case. The profiles of elastic recovery under different compression pressures are presented in Fig. 9.12b. The elastic recovery of DES gradually increased up to a compaction pressure of 150 MPa and decreased at higher compaction pressures. Therefore, an elastic recovery depletion tendency was observed in DES with increasing compaction pressures. We predicted that corrugated or interlocked hydrogen-bonded structures in the DES parent drug were responsible for the depletion of elastic recovery. By comparing the elastic recoveries of DES and DES-BA, the novel multicomponent crystal reported in this study is considerably more plastic than the parent drug; this may suggest that a DES-BA tablet has lower porosity and is stronger than a DES tablet for the same compaction pressures.

A tendency for capping was observed in the DES tablet if the compaction pressure was increased above 250 MPa (Fig. 9.13a). Such profiles are called ‘over-compaction’

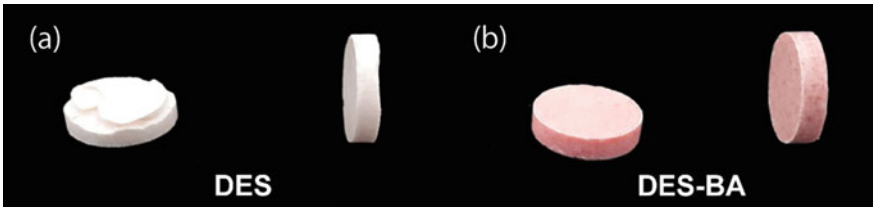

Fig. 9.13 Tablet overview of **a** DES and **b** DES-BA after applying a compaction pressure of 350 MPa. Reprinted from [72]. Copyright 2012, with permission from Elsevier

profiles due to the elastic deformation of DES. However, neither capping nor lamination tendency was observed in the DES-BA multicomponent crystal, as illustrated in Fig. 9.13b.

The fact that DES-BA exhibited better tabletability profiles than DES can be understood from a structural point of view. Therefore, it is very useful to compare the crystal structures of DES and DES-BA. As illustrated in Fig. 9.14, the crystal structure of DES shows a corrugated, hydrogen-bonded chain structure containing only one weak CH···N hydrogen bond. Due to its rigidity, this structure possibly responds less to plastic deformation stress. In contrast with DES, the existence of a layered structure and of a slip plane parallel to (001) possibly provides an enhanced ability to form a tablet. As previously demonstrated, layered structures enable substantial tabletability improvements in many pharmaceutical multicomponent crystals. In addition, the existence of a slip plane, which is only composed of weak CH···O hydrogen bonds, might also facilitate shearing and possibly allows the layered structure to easily slide. These features can eventually lead to improved durability during the compaction-induced plastic deformation [72].

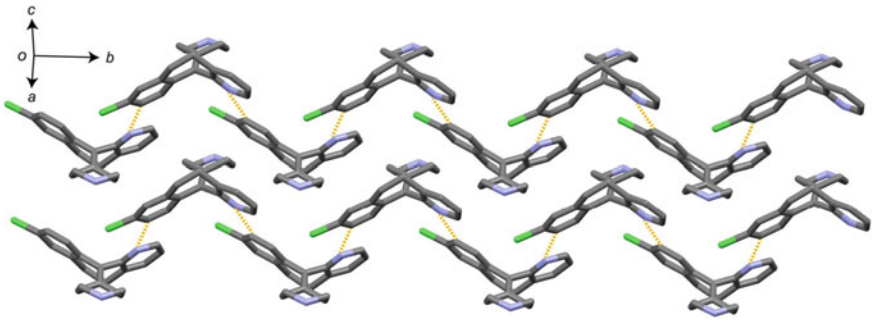

Fig. 9.14 Corrugated, hydrogen-bonded chain structure in DES parent drugs. The hydrogen atoms are omitted for clarity. The crystal structure was obtained from Cambridge Structural Database (REFCODE: GEHXEX). Reprinted from [72]. Copyright 2012, with permission from Elsevier

9.2.4 *Improving Photostability by Preventing Tautomerization*

Although many drugs successfully surmount the long development process, many of them still have chemical stability problems. It is suggested that these drugs are still present in the market due to their pharmacological importance. Drugs that pose stability problems usually require a strict control strategy in their design and development stages. Chemical instability is considered an ominous feature, which not only leads to drug ineffectiveness but also endangers the patient through potentially toxic decomposition products [73]. Therefore, chemical instability is a subject of increased concern for the pharmaceutical industry.

Numerous studies described the benefits of cocrystals in overcoming the stability problems of APIs. A common strategy for producing pharmaceutical cocrystals utilizes the so-called pK_a rule, [74] which states that a neutral cocrystal is generated instead of an ionic salt when the difference between the pK_a of a base and that of its conjugate is negative or at least as low as possible. However, the proton transfer is sometimes unavoidable, even in systems with a low ΔpK_a (<1) [45, 75]. An alternative approach features the use of a zwitterionic coformer to avoid the proton transfer between drug molecules. Since the proton donor and acceptor sites of zwitterionic molecules are already deprotonated and protonated, respectively, such coformers cannot participate in the proton transfer between drug molecules. They consequently enable the formation of zwitterionic cocrystals, a less explored type of cocrystals compared to molecular or ionic types [76]. In this context, we were particularly interested in betaine (BET, Scheme 9.4 right), a naturally occurring zwitterionic compound. This compound is widely distributed in nature as a metabolite of choline and is found in sugar beet and marine animals such as crabs and shrimp, thereby being an acceptable coformer candidate for the formation of API-containing cocrystals [77].

Herein, epalrestat (EPR, Scheme 9.4 left), an aldose reductase inhibitor used in diabetic neuropathy, was used as a model drug due to its photoinstability [53]. The photosensitivity of EPR manifests through *E,Z* to *Z,Z* isomerization upon exposure to light easily occurring even in ambient light irradiation (Fig. 9.15). Although an earlier study attempted to tackle EPR's photosensitivity problem by cocrystallization and salt formation, it ended unsuccessfully [78].

The preparation of equimolar zwitterionic cocrystals involved methods such as liquid-assisted grinding, slurry mixing, dry milling, and solvent evaporation. However, PXRD pattern changes were only observed in the liquid-assisted grinding and solvent evaporation techniques, with peaks of BET remaining present in both

Scheme 9.4 Chemical structure of EPR (left) and BET (right)

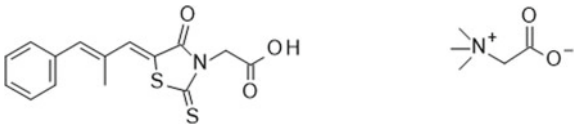

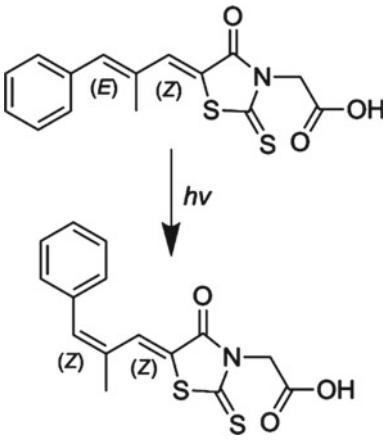

Fig. 9.15 Photoisomerization of EPR accounting for its photoinstability. Reprinted (adapted or reprinted in part) with permission from [79]. Copyright 2011 American Chemical Society

cases. Therefore, further attempts to obtain pure cocrystals were only conducted using the above two techniques and a 2:1 EPR/BET molar ratio. As illustrated in Fig. 9.16, no raw material peaks were observed under these conditions, indicating the formation of a new phase. In addition, the new PXRD patterns matched well with the simulated ones, suggesting high sample purity. The minor differences between

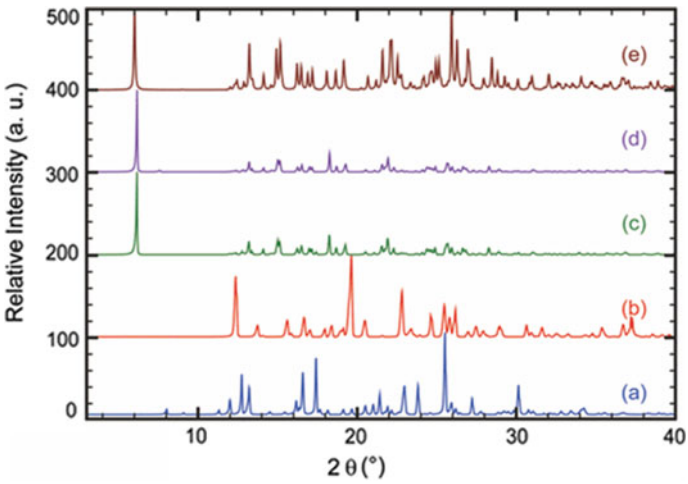

Fig. 9.16 PXRD patterns of **a** EPR, **b** BET, and EPR–BET obtained by **c** liquid-assisted grinding and **d** solvent evaporation. **e** Simulated single-crystal pattern of EPR–BET. Reprinted (adapted or reprinted in part) with permission from [79]. Copyright 2011 American Chemical Society

the experimental and simulated PXRD patterns were ascribed to the preferred orientation effect. As expected, the utilization of a zwitterionic coformer preserved the neutrality of EPR molecules.

The EPR–BET cocrystal structure was supported by complicated intermolecular interactions (Fig. 9.17a). From all the hydrogen bonds, two strong, charge-assisted bonds connected the carboxylate group of a BET molecule with the moieties of two EPR molecules (EPR I and II) via the O3–H···O8(−) and O6–H···O7(−) interactions (the blue, dashed lines in Fig. 9.17a). Notably, the O3···O8 and O6···O7 distances equaled 2.550(2) and 2.573(2) Å, respectively, being shorter than the O···O distances in common hydrogen bonds (∼2.74 Å). Abundant weak hydrogen bonds (the orange, dashed lines in Fig. 9.3a) further connected EPR I and BET molecules (C6–H···O8 and C34–H···O1) and EPR II and BET molecules (C16–H···O8 and C32–H···O5). The BET molecules were interconnected by weak C35–H···O8 hydrogen bonds in the (001) plane. The EPR I molecules were also joined by weak C2–H···O2 and C5–H···O2 hydrogen bonds. Finally, C1–H···O5 hydrogen bonds connected the EPR

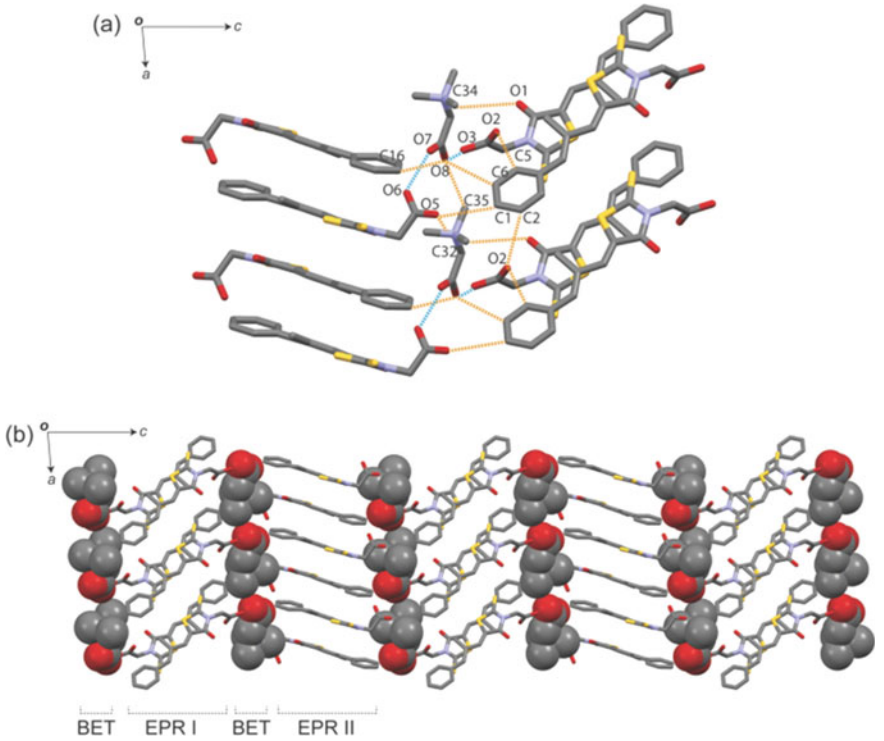

Fig. 9.17 Hydrogen bond architecture **a** and molecule packing **b**, viewed along the *b*-axis of a zwitterionic EPR–BET cocrystal, with blue and orange lines representing conventional and unconventional hydrogen bonds, respectively. In the packing view, the BET molecules are rendered in a space-filling view, with hydrogen atoms omitted for clarity. Reprinted (adapted or reprinted in part) with permission from [79]. Copyright 2011 American Chemical Society

I and EPR II molecules via $x + 1$, y, z symmetry operations. The above hydrogen bonds resulted in a layered structure (Fig. 9.17b) with alternately arranged EPR I, BET, and EPR II molecules, stacked along the a-axis.

Photoinstability is one of the greatest, not yet successfully tackled challenges of the pharmaceutical field. Solid-state EPR is stable in the dark, but undergoing *E,Z* to *Z,Z* isomerization even when exposed to ambient light. From a crystal engineering viewpoint, zwitterionic cocrystals should provide a good opportunity to overcome this problem, since the zwitterionic coformer is expected to form strong, charge-assisted hydrogen bonds with the EPR molecules, stabilizing their conformation, a phenomenon, however not yet observed in other EPR cocrystals and salts. Therefore, BET was selected as a coformer due to its inherent ability to form charge-assisted hydrogen bonds.

The photostability of zwitterionic EPR cocrystals was qualitatively examined by ^{1}H NMR measurements aimed at detecting the *E,Z* to *Z,Z* photoisomerization. In addition, to reduce experimental conditions interference, the samples were prepared less than 5 min before the NMR spectra acquisition. As illustrated in Fig. 9.18, solid-state EPR underwent *E,Z* to *Z,Z* isomerization after a 24 h irradiation at 6000 lx, indicated by the appearance of new peaks in the ^{1}H NMR spectra (see the small black dots corresponding to the Z,Z isomer). This isomerization induced a color change

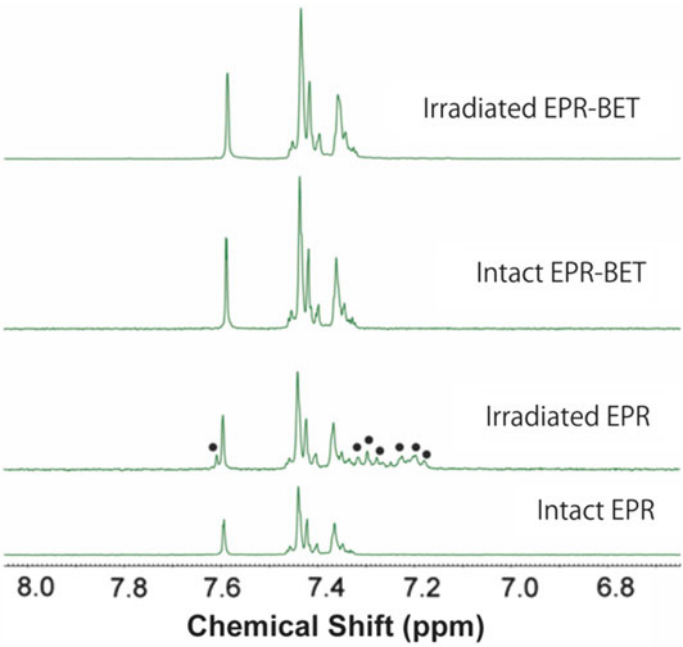

Fig. 9.18 1H NMR spectra of EPR and EPR–BET before and after irradiation, with black dots indicating peaks of the *Z,Z* EPR isomer. Reprinted (adapted or reprinted in part) with permission from [79]. Copyright 2011 American Chemical Society

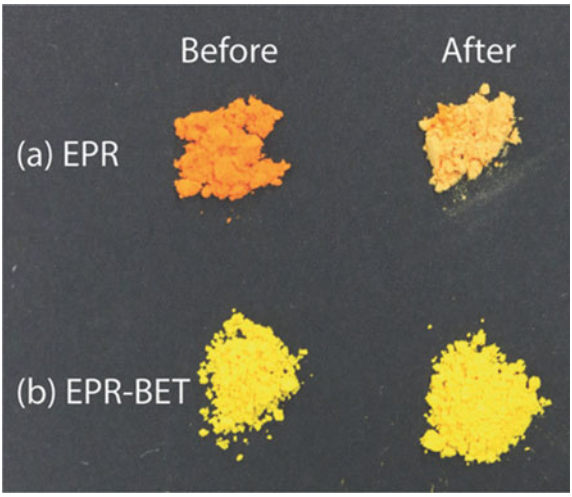

Fig. 9.19 Visual appearance of **a** EPR and **b** EPR–BET, before and after irradiation. Reprinted (adapted or reprinted in part) with permission from [79]. Copyright 2011 American Chemical Society

from orange to pale yellow (Fig. 9.19a), as previously reported. [79] Under the same conditions, the EPR–BET cocrystal exhibited no isomerization, also indicated by the absence of the above-mentioned color change (Fig. 9.19b).

The observed photosensitivity was attributed to intermolecular interaction changes dependent on the reaction cavity size. It is generally known that (depending on their number and strength) intermolecular interactions constrain the EPR molecules in the lattice and prevent their *E,Z* to *Z,Z* isomerization. As described above, the EPR and BET molecules in the cocrystal were connected by numerous hydrogen bonds, including two strong O···O hydrogen bonds ($D_{O\cdots O}$ = 2.550(2) and 2.573(2) Å) and many other weak bonds (EPR–EPR and EPR–BET). These bonds were expected to restrain the EPR molecules and therefore prevent their isomerization.

The photostability improvement can also be deducted from the "reaction cavity" concept: the space around a reactive group in a crystal structure [80] influences the probability of a solid-state reaction. Herein, the reaction cavity was characterized for both the whole EPR molecule and its olefin part, reflecting molecular mobility.

It should be noted that the intact form I EPR crystal contained two different EPR molecules, EPR A and EPR B. The calculated reaction cavity volumes of EPR A, EPR B, (from the intact-crystal EPR form I) EPR I, and EPR II (from the EPR–BET cocrystals) were 103.4, 108.6, 84.1, and 85.5 $Å^3$, respectively (Fig. 9.20). Unsurprisingly, the reaction cavities of the cocrystal EPR were considerably smaller (by ~30 $Å^3$) than those of the intact-crystal EPR. In addition, the olefin reaction cavity volumes of the EPR A, EPR B, EPR I, and EPR II equaled 26.6, 18.0, 15.0, and 17.3 $Å^3$, respectively, with cocrystal values also being smaller than those of EPR form I crystals. The above-mentioned reaction cavity decrease correlated with the limitation of *E,Z* to *Z,Z* isomerization; smaller reaction cavities limited the molecular motion and therefore hindered isomerization [79].

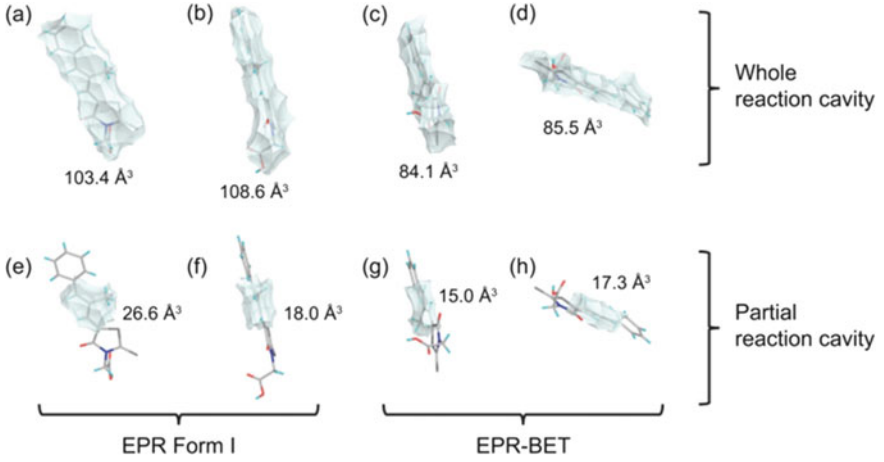

Fig. 9.20 Whole **a**–**d** and partial **e**–**h** reaction cavities (drawn as blue translucent spaces) of EPR molecules. EPR form I comprised EPR A (**a** and **e**) and EPR B (**b** and **f**) molecules and EPR–BET cocrystals contained EPR I (**c** and **g**) and EPR II (**d** and **f**) molecules. Reprinted (adapted or reprinted in part) with permission from [79]. Copyright 2011 American Chemical Society

9.2.5 Taste Masking of Bitter Drugs by Utilizing Artificial Sweeteners as Coformers

In the early days, it was believed that bitter-tasting drugs were more curable. However, bitter drugs are inconvenient nowadays, especially for pediatric and geriatric patients [81]. Several proposed solutions for the bitter taste of APIs involved cyclodextrin derivates, [82] or polymer encapsulation methods [83]. Crystal engineering also offers an answer to the bitter taste problem, by cocrystallization or salt formation, with sweeteners acting as coformers [84].

Benexate (BEX, Scheme 9.5 left), a defensive type anti-ulcer agent, was used as a model compound in the following study case. BEX's defensive effects on the gastric mucosa have been demonstrated by the promotion of prostaglandin synthesis, protein secretion, and blood flow stimulation in the gastrointestinal tract [85]. This drug is marketed as a hydrochloride salt (BEX–HCl) and is part of an inclusion complex with β-cyclodextrin. The hydrochloride salt was originally meant to improve the

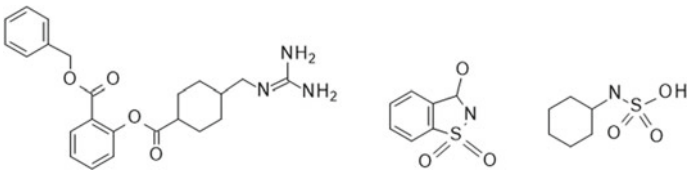

Scheme 9.5 Chemical structure of BEX (left), SAC (middle), and CYM (right)

low solubility of BEX, but that proved to be insufficient due to the high molecular weight of BEX–HCl (molecular weight = 445.93 g mol^{-1}). Later, BEX–HCl was complexed with β-cyclodextrin, aiming to improve its solubility and to reduce the bitter taste [86, 87].

From the crystal engineering perspective, BEX is both an interesting and challenging compound because it has two major problems: bitter taste and low solubility. To date, no new reported salt structure could tackle these unfavorable characteristics of BEX. Therefore, we explored artificial sweeteners that can be used as salt coformers for naturally overcoming the native unpleasant taste of BEX. Artificial sweeteners have been reported to improve the solubility and dissolution rate of several drugs, including quinine, haloperidol, mirtazapine, pseudoephedrine, lamivudine, risperidone, sertraline, venlafaxine, zolpidem, amlodipine, and piroxicam [88]. This implies that artificial sweeteners are also potentially applicable to BEX's low solubility issue.

The preparation of novel salts involved an anion exchange reaction between the chloride anion and the saccharinate (SAC, Scheme 9.5 middle) or cyclamate (CYM, Scheme 9.5 right) anion; therefore, the sodium salts of those sweeteners were chosen. Notably, other coformers used in either salt or acidic form failed to form new solid products. As illustrated in Fig. 9.21, no raw material trace was observed through this method, indicating the formation of new phases. Benexate-saccharinate (BEX–SAC,) and benexate-cyclamate (BEX–CYM,) were produced alongside a sodium chloride byproduct from the anion exchange reaction. However, BEX–SAC, and BEX–CYM could easily be separated from sodium chloride by filtration since these salts precipitated before sodium chloride, which was retained in solution. This method effectively produced pure BEX–SAC and BEX–CYM with high yields (>95%). The purities of the BEX–SAC and BEX–CYM salts were confirmed by the considerable agreement between experimental and simulated PXRD patterns and by the absence of raw material peaks. The difference between the experimental and simulated PXRD patterns was acceptable and attributed to the preferred orientation effect.

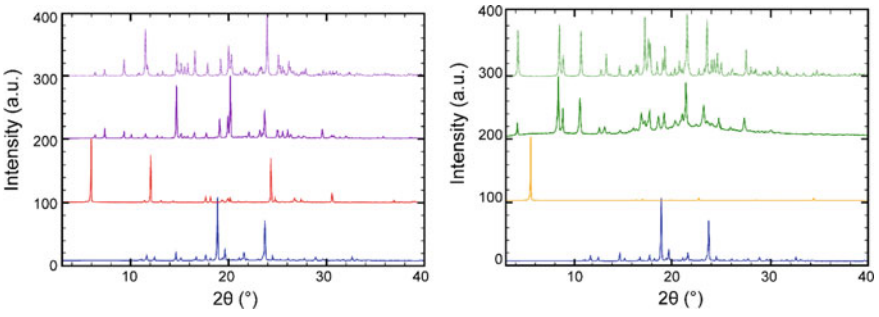

Fig. 9.21 PXRD patterns of benexate hydrochloride (BEX–HCl) (blue), sodium saccharinate (red), benexate-saccharinate (BEX–SAC) (purple), sodium cyclamate (yellow), and benexate-cyclamate (BEX–CYM) (green). The solid and dashed lines represent the experimental and simulated PXRD patterns, respectively. Reprinted from [89] by the author(s) licensed under CC BY 4.0

Other attempts employing high salt formation methods and the same conformer and solvent system, such as slurry mixing, co-grinding, and dry milling failed, resulting in sticky, amorphous solids.

After the anion exchange reaction that yielded BEX–SAC and BEX–CYM, we were able to isolate single crystals from the reaction flask and perform single-crystal X-ray structure. The single-crystal structure analysis revealed an asymmetric BEX–SAC unit that contained one cationic benexate, one anionic saccharinate, and one water molecule. Similarly, an asymmetric BEX–CYM unit contained one cationic benexate and one anionic cyclamate molecule. Therefore, BEX–SAC and BEX–CYM existed as monohydrate and ansolvate/anhydrous crystals, respectively.

The crystal structure of BEX–SAC contained complicated hydrogen bonds, as illustrated in Fig. 9.22. One set of cationic benexate and anionic saccharinate were bound by a charge-assisted hydrogen bond, $N2^{+}$–H···N4 − and a conventional hydrogen bond, N1–H···O5, which enclosed a R_2^2 (8) hydrogen bond loop. An additional weak hydrogen bond, C20–H···O5 stabilized this interaction. Two symmetrical N2–H···O6 hydrogen bonds connected two sets of one cationic benexate and one anionic saccharinate. These hydrogen bonds constructed an R_4^4 (20) loop around the center of symmetry, as shown in Fig. 9.22a. Figure 9.22b illustrates the one-dimensional (1D) chain structure built by connecting each pair of cationic benexate and anionic saccharinate sets along the (110) plane, with intercalated water molecules. The N3–H···O8 hydrogen bonds with two different symmetric operations ($x + 1$, y, $z + 1$ and $-x + 2$, $-y$, $-z + 1$) played important roles in building this 1D chain structure. 1D chains were connected to each other via O8–H···O4 and

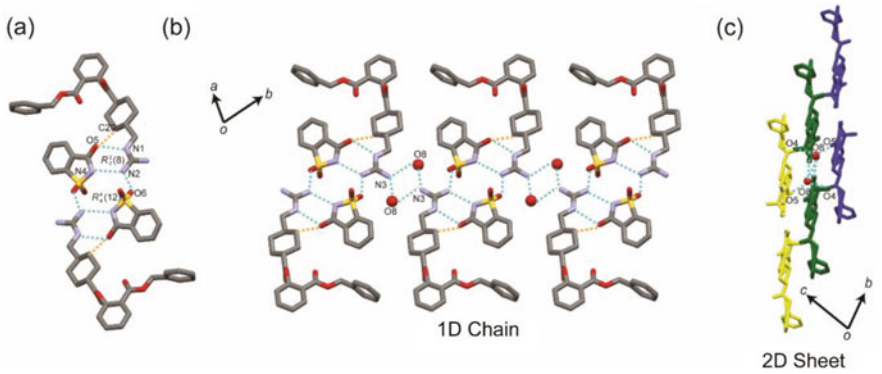

Fig. 9.22 The hydrogen bond architecture of the BEX–SAC crystal. **a** The interaction involving two sets of cationic benexate and anionic saccharinate molecules and water constructs. **b** 1D chain structure parallel to the (110) plane. **c** 2D sheet structure composed of 1D chains (represented by different colors) that interact with each other to form (**c**) a 2D sheet structure. Conventional and non-conventional hydrogen bonds are drawn by dashed blue and orange lines, respectively. Hydrogen atoms have been omitted for clarity. The oxygen atoms from water molecules are drawn in ball-setting. Reprinted from [89] by the author(s) licensed under CC BY 4.0

O8–H···O5 hydrogen bonds, leading to a two-dimensional (2D) sheet structure, as illustrated in Fig. 9.22c.

The crystal structure of BEX–CYM also contained intricate hydrogen-bond networks. Conventional (N–H···N and N–H···O) and unconventional (C–H···O and C–H···N) hydrogen bonds were observed in the crystal. The N3 atom of the guanidine radical in the benexate molecule formed three hydrogen bonds: N3–H3A···N4, N3–H3A···O6, and N3–H3B···O7, including bifurcated hydrogen bonds. The other N atoms of the guanidine moiety in the benexate molecule also interacted with O6 from the cyclamate anion to form N1–H···O6 and N2–H···O6 hydrogen bonds. These hydrogen bonds formed a 1D chain structure along the *b*-axis (Fig. 9.23a). The

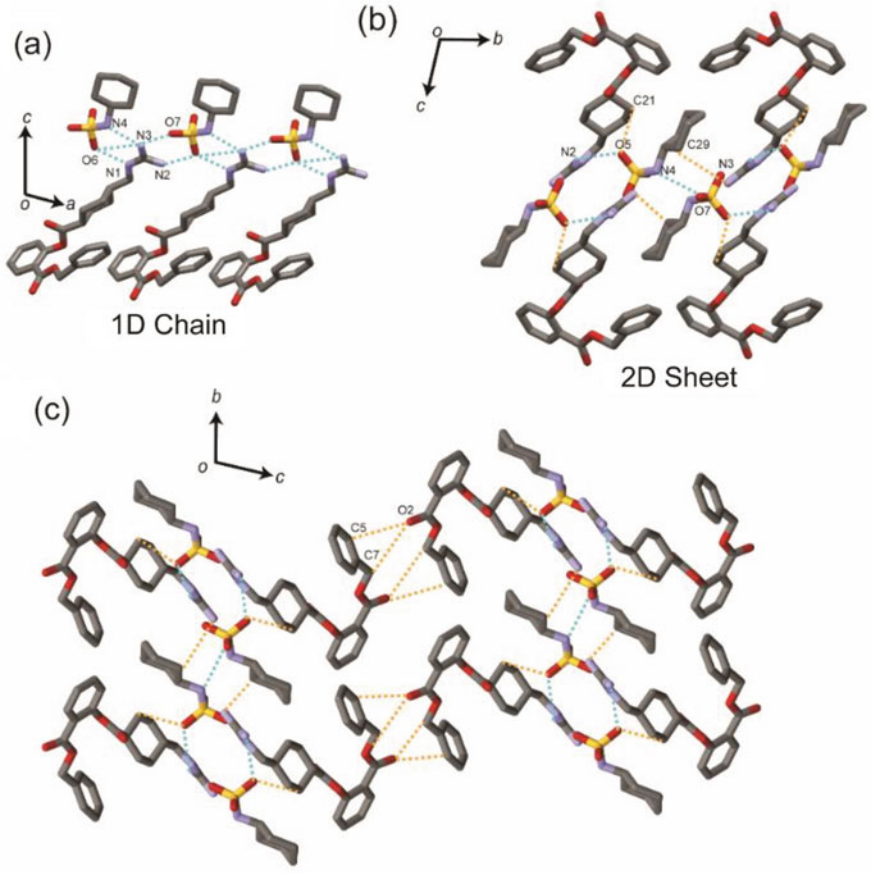

Fig. 9.23 **a** 1D chain and **b** 2D sheet structures of the BEX–CYM crystal. **c** The 2D sheet structure is stacked along the a-axis through C5–H···O2 and C7–H···O2 hydrogen bonds. Conventional and non-conventional hydrogen bonds are drawn by dashed blue and orange lines, respectively. Hydrogen atoms have been omitted for clarity. Reprinted from [89] by the author(s) licensed under CC BY 4.0

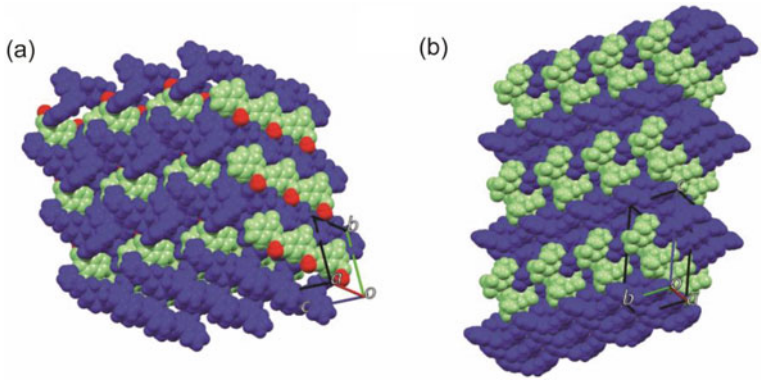

Fig. 9.24 Packing view of **a** BEX–SAC and **b** BEX–CYM. All molecules are rendered in a space-filling setting. Cationic benexate, anionic salt coformer, and water molecules are colored in dark blue, light green, and red, respectively. Reprinted from [89] by the author(s) licensed under CC BY 4.0

hydrogen bonds N2–H···O5 and N4–H···O7 along with the weak hydrogen bonds C29–H···N3 and C21–H···O5 connected two adjacent 1D chains. This is hereafter defined as the 2D sheet structure of BEX-CYM (Fig. 9.23b). These 2D sheet structures were stacked through C5–H···O2 and C7–H···O2 hydrogen bonds along the *a*-axis, as illustrated in Fig. 9.23c.

Despite the hydrogen bond network differences between BEX–SAC and BEX–CYM, these crystals shared something in common. As shown in Fig. 9.24, the packing motifs of BEX–SAC and BEX–CYM showed local layered-like structures composed of alternate arrangements between cationic benexate molecules and coformer molecules. Water molecules were also involved in the formation of a local layered-like structure in BEX–SAC.

In these two cases, it is expected that the BEX–SAC, and BEX–CYM formulations provide a sweeter taste than BEX–HCl due to the inherent sweetness of the anion molecules in these crystals. Notably, the sweetness level of cyclamate and saccharine is approximately 30–50 and 300 times higher than that of sucrose, respectively [90].

The solubility of BEX–HCL reached 104.42 ± 27.60 μg/mL. All the new solid forms presented in this study displayed improved solubility. The solubility of BEX–SAC and BEX–CYM was 512.16 ± 22.06 and 160.53 ± 14.52 μg/mL, respectively (Fig. 9.25a). This means a solubility increase of 5 and 1.5 times, respectively, relative to the marketed form of BEX. In agreement with the solubility results, the intrinsic dissolution rate showed a similar trend with BEX–SAC and BEX–CYM exhibiting improved dissolution rates of around 5 and 2 times higher than that of BEX–HCL, respectively (Fig. 9.25b). All solid forms maintained their molecular structures at the end of the solubility and dissolution rate experiments, as confirmed by PXRD measurements.

We related the solubility and dissolution rate improvement to the molecular arrangement in the crystal structure. As mentioned above, the overall packing features

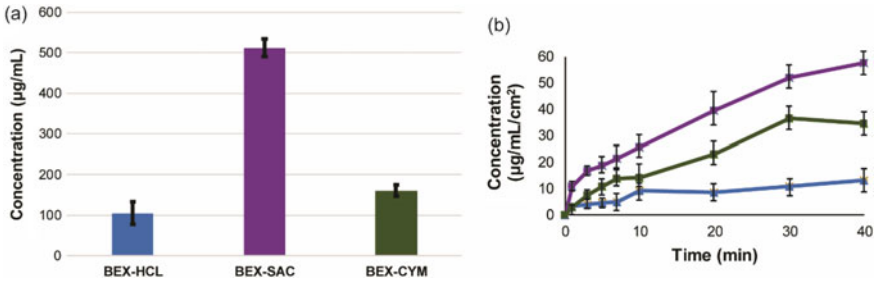

Fig. 9.25 **a** The solubility and **b** intrinsic dissolution rate of BEX–HCl (blue), BEX–SAC (purple), and BEX–CYM (green). Solubility and dissolution rate experiments were conducted in triplicate. Reprinted from [89] by the author(s) licensed under CC BY 4.0

of BEX–SAC, and BEX–CYM displayed local layered-like structures composed of an alternate arrangement between cationic benexate and coformer molecules. This local layered-like structure facilitated a structural collapse during dissolution by propagating a breach in the interaction between the drug and the salt coformer. This mechanism has been proposed in studies aimed at improving the solubility of insoluble drugs. Given the improved solubility and dissolution rate profiles observed in these novel BEX salts, a likely bioavailability improvement of BEX could also be observed if these solid forms are chosen for further development [89].

9.3 Conclusion

The use of multicomponent crystals is a new trend in pharmaceutical crystal engineering. They not only provide solutions to unfavorable physicochemical properties but also for the research and patent opportunities offered by new pharmaceutical solids. Multicomponent crystals have gained increasing interest and scientific value due to the possibility to deduct the physicochemical property changes from the multicomponent crystal structure. In this chapter, some examples that showcase the potential applications of multicomponent crystals in combatting common physicochemical difficulties faced in the pharmaceutical field are presented. Solution to unfavorable physicochemical properties, such as insolubility, hygroscopicity, tabletability, drug instability, and bitter taste, indicates the potential benefits of multicomponent crystals in pharmaceutical drug development.

References

1. Goodman, L.S., Gilman, A., Hardman, J.G., Gilman, A.G., Limbird, L.E.: Goodman and Gilmans's the Pharmacological Basis of Therapeutics. McGraw-Hill, New York (1996)
2. Brittain, H.G.: Polymorphism in Pharmaceutical Solids. Informa, New York (2009)

3. Lynn, E.J., Walter, R.G., Harris, L.A., Dendy, R., James, M.J.: Nitrous oxide: it's a gas. Psychedelic Drugs **5**, 1–7 (1972)
4. Vippagunta, S.R., Brittain, H.G., Grant, D.J.W.: Crystalline solids. Adv. Drug. Deliv. Rev. **48**, 3–26 (2001)
5. Shan, N., Zawarotko, M.J.: The role of cocrystals in pharmaceutical science. Drug Discov. Today **13**, 440–446 (2008)
6. Byrn, S.R., Pfeiffer, R.R., Stephenson, G., Grant, D.J.W., Gleason, W.B.: Solid-state pharmaceutical chemistry. Chem. Mater. **6**, 1148–1158 (1994)
7. Cheney, M.L., Weyna, D.R., Shan, N., Hanna, M., Wojtas, L., Zawarotko, M.J.: Supramolecular architectures of meloxicam carboxylic acid cocrystals, a crystal engineering case study. Cryst. Growth Des. **10**, 4401–4413 (2010)
8. Sun, C.C., Hou, H.: improving mechanical properties of caffeine and methyl gallate crystals by cocrystallization. Cryst. Growth Des. **8**, 1575–1579 (2008)
9. Chen, S., Guzei, I.A., Yu, L.: New polymorphs of ROY and new record for coexisting polymorphs of solved structures. J. Am. Chem. Soc. **127**(27), 9881–9885 (2005)
10. Yu, L.: Polymorphism in molecular solids: an extraordinary system of red, orange, and yellow crystals. Acc. Chem. Res. **43**, 1257–1266 (2010)
11. Bryn, S., Pfeiffer, R., Ganey, M., Hoiberg, C., Poochikian, G.: Pharmaceutical solids: a strategic approach to regulatory considerations. Pharm. Res. **12**, 945–954 (1995)
12. Aitipamula, S., Banerjee, R., Bansal, A.K., Biradha, K., Cheney, M.L., Choudhury, A.R., Desiraju, G.R., et al.: Polymorphs, salts, and cocrystals: what's in a name? Cryst. Growth Des. **12**, 2147–2152 (2012)
13. Grothe, E., Meekes, H., Vlieg, E., ter Horst, J.H., de Gelder, R.: Solvates, salts, and cocrystals: a proposal for a feasible classification system. Cryst. Growth Des. **16**, 3237–3243 (2016)
14. Kavanagh, O.N., Croker, D.M., Walker, G.M., Zaworotko, M.J.: Pharmaceutical cocrystals: from serendipity to design to application. Drug Discov. Today **24**, 796–804 (2019)
15. Hancock, B.C., Zografi, B.: Characteristics and significance of the amorphous state in pharmaceutical systems. J. Pharm. Sci. **86**, 1–12 (1997)
16. Hancock, B.C., Parks, M.: What is the true solubility advantage for amorphous pharmaceuticals? Pharm. Res. **17**, 397–404 (2000)
17. Grohganz, H., Lobman, K., Priemel, P., Jensen, K.T., Graeser, K., Rades, T.: Amorphous drugs and dosage forms. J. Drug. Del. Sci. Tech. **23**, 403–408 (2013)
18. Sibik, J., Lobmann, K., Zeitler, T., Rades, J.A.: Predicting crystallization of amorphous drugs with terahertz spectroscopy. Mol. Pharm. **12**, 3062–3068 (2015)
19. Datta, S., Grant, D.J.W.: Crystal structures of drugs: advances in determination, prediction and engineering. Nat. Rev. Drug Discov. **3**, 42–57 (2004)
20. Bernstein, J.: Polymorphism in Molecular Crystals. Clarendon, Oxford (2002)
21. Morissette, S.L., Almarsson, O., Peterson, M.L., Remenar, J.F., Read, M.J., Lemmo, A.V., Ellis, S., Cima, M.J., Gardner, C.R.: High-throughput crystallization: polymorphs, salts, co-crystals and solvates of pharmaceutical solids. Adv. Drug. Deliv. Rev. **56**, 275–300 (2004)
22. Hilfiker, R.: Polymorphism in the Pharmaceutical Industry. Wiley, Weinheim (2006)
23. Seddon, K.R.: Pseudopolymorph: a polemic. Cryst. Growth Des. **4**, 1087–1087 (2004)
24. Bernstein, J.: …And another comment on pseudopolymorphism. Cryst. Growth Des. **5**, 1661–1662 (2005)
25. Putra, O.D., Pettersen, A., Lill, S.O.N., Umeda, D., Yonemochi, E., Nugraha, Y.P., Uekusa, H.: Capturing a new hydrate polymorph of amodiaquine dihydrochloride dihydrate via heterogeneous crystallization. Cryst. Eng. Commun. **2019**(21), 2053–2057 (2019)
26. Healy, A.M., Worku, Z.A., Kumar, D., Madi, A.M.: Pharmaceutical solvates, hydrates and amorphous forms: a special emphasis on cocrystals. Adv. Drug Deliv. Rev. **117**, 25–46 (2017)
27. Vioglio, P.C., Chierotti, M.R., Gobetto, R.: Pharmaceutical aspects of salt and cocrystal forms of APIs and characterization challenges. Adv. Drug Deliv. Rev. **117**, 86–110 (2017)
28. Desiraju, G.R., Vittal, J.J., Ramanan, A.: Crystal Engineering: A Textbook. World Scientific, Singapore (2011)

29. Baghel, S., Cathcart, H., O'Reilly, N.J.: Polymeric amorphous solid dispersions: a review of amorphization, crystallization, stabilization, solid-state characterization, and aqueous solubilization of biopharmaceutical classification system class II drugs. J. Pharm. Sci. **105**, 2527–2544 (2016)
30. Almarsson, O., Vadas, E.B.: Molecules, materials, medicines (M3): linking molecules to medicines through pharmaceutical material science. Cryst. Growth. Des. **15**, 5645–5647 (2015)
31. Daousani, C., Macheras, P.: Biopharmaceutic classification of drugs revisited. Eur. J. Pharm. Sci. **82–87**, 82–87 (2016)
32. Butler, J.M., Dressman, J.B.: The developability classification system: application of biopharmaceutics concepts to formulation development. J. Pharm. Sci. **99**, 4940–4954 (2010)
33. Khadka, P., Ro, J., Kim, H., Kim, I., Kim, J.T., Kim, H., Cho, J.M., Lee, J.: Pharmaceutical particle technologies: an approach to improve drug solubility, dissolution and bioavailability. Asian J. Pharm. Sci. **9**, 304–316 (2014)
34. Kawabata, Y., Wada, K., Nakatani, M., Yamada, S., Onoue, S.: Formulation design for poorly water-soluble drugs based on biopharmaceutics classification system: basic approaches and practical applications. Int. J. Pharm. **420**, 1–10 (2011)
35. Onoue, S., Yamada, S., Chan, H.K.: Nanodrugs: pharmacokinetics and safety. Int. J. Nanomed. **9**, 1025–1037 (2014)
36. Newman, A.W., Reutzel-Edens, S.M., Zografi, G.: Characterization of the "hygroscopic" properties of active pharmaceutical ingredients. J. Pharm. Sci. **97**, 1047–1059 (2008)
37. Sun, C.C., Grant, D.J.W.: Improved tableting properties of p-hydroxybenzoic acid by aater of crystallization: a molecular insight. Pharm. Res. **21**, 382–386 (2004)
38. Zu, B., Wang, J., Zhang, Q., Zu, B., Wang, J., Zhang, Q., Mei, X.: Improving dissolution and photostability of vitamin K3 via cocrystallization with naphthoic acids and sulfamerazine. Cryst. Growth Des. **16**, 483–492 (2016)
39. Song, J.X., Yan, Y., Yao, J., Chen, J.M., Lu, T.B.: Improving the solubility of lenalidomide via cocrystals. Cryst. Growth Des. **14**, 3069–3077 (2014)
40. Geng, N., Chen, J.M., Li, Z.J., Jiang, L., Lu, T.B.: Approach of cocrystallization to improve the solubility and photostability of tranilast. Cryst. Growth Des. **13**, 3546–3553 (2013)
41. Good, D.J., Rodríguez-Hornedo, N.: Solubility advantage of pharmaceutical cocrystals. Cryst. Growth Des. **9**, 2252–2264 (2009)
42. Visalakshi, N.A., Mariappan, T.T., Bhutani, H., Singh, S.: Behavior of moisture gain and equilibrium moisture contents (EMC) of various drug substances and correlation with compendial information on hygroscopicity and loss on drying. Pharm. Dev. Tech. **10**, 489–497s (2005)
43. Sun, C.C., Grant, D.J.W.: Influence of crystal structure on the tableting properties of sulfamerazine polymorphs. Pharm. Res. **18**, 274–280 (2001)
44. Gupta, D., Bhatia, D., Dave, B., Sutariya, V., Gupta, S.V.: Salts of therapeutic agents: chemical, physicochemical, and biological considerations. Molecules **23**, 1719 (2018)
45. Putra, O.D., Yoshida, T., Umeda, D., Gunji, M., Uekusa, H., Yonemochi, E.: Crystallographic analysis of phase dissociation related to anomalous solubility of irsogladine maleate. Cryst. Growth Des. **16**, 6714–6718 (2016)
46. Tovey, G.D.: Pharmaceutical Formulation: The Science and Technology of Dosage Forms. The Royal Society of Chemistry, Croydon (2018)
47. Iacocca, R.G., Burcham, C.L., Hilden, L.R.: Particle engineering: a strategy for establishing drug substance physical property specifications during small molecule development. J. Pharm. Sci. **99**, 51–75 (2010)
48. Chattoraj, S., Sun, C.C.: Crystal and particle engineering strategies for improving powder compression and flow properties to enable continuous tablet manufacturing by direct compression. J. Pharm. Sci. **107**, 968–974 (2018)
49. Ramirez, M.A., Borja, N.L.: Epalrestat: an aldose reductase inhibitor for the treatment of diabetic neuropathy. Pharmacotherapy **28**, 646–655 (2008)
50. Steel, J.W., Faulds, D., Goa, K.L.: Epalrestat. a review of its pharmacology, and therapeutic potential in late-onset complications of diabetes mellitus. Drugs Aging **3**, 532–555 (1993)

51. Swapna, B., Suresh, K., Nangia, A.: Color polymorphs of aldose reductase inhibitor epalrestat: configurational, conformational and synthon differences. Chem. Commun. **52**, 4037–4040 (2016)
52. Igarashi, R., Nagase, H., Furuishi, T., Endo, T., Tomono, K., Ueda, H.: Crystal structure of epalrestat non-solvate. X-Ray Struct. Anal. Online **29**, 23–24 (2013)
53. Ishida, T., In, Y., Inoue, M., Ueno, Y., Tanaka, C., Hamanaka, N.: Structural elucidation of epalrestat (ONO-2235), a potent aldose reductase inhibitor, and isomerization of its double bonds. Tetrahedron Lett. **30**, 959–962 (1989)
54. Nagase, H., Kobayashi, M., Ueda, H., Furuishi, T., Gunji, M., Endo, T., Yonemochi, E.: Crystal structure of an epalrestat dimethanol solvate. X-Ray Struct. Anal. Online **32**, 7–9 (2016)
55. Ishida, T., In, Y, Inoue, M., Tanaka, C., Hamanaka, N.: Conformation of (Z)-3-carboxymethyl-[(2E)-2-methyl-3-phenylpropenylidene]rhodanine (epalrestat), a potent aldose reductase inhibitor: X-ray crystallographic, energy calculational, and nuclear magnetic resonance Studies. J. Chem. Soc. Perkin Trans. **2**(2), 1085–1091 (1990)
56. Umeda, D., Putra, O.D., Gunji, M., Fukuzawa, K., Yonemochi, E.: Epalrestat tetrahydrofuran monosolvate: crystal structure and phase transition. Acta Crystallogr. E Cryst. Commun. **73**, 941–944 (2017)
57. Putra, O.D., Umeda, D., Fukuzawa, K., Gunji, M., Yonemochi, E.: A New solvate of epalerstat, a drug for diabetic neuropathy. Acta Crystallogr. E Cryst. Commun. **73**, 1264–1267 (2017)
58. Putra, O.D., Umeda, D., Nugraha, Y.P., Furuishi, T., Nagase, H., Fukuzawa, K., Uekusa, H., Yonemochi, E.: Solubility improvement of epalrestat by layered structure formation via cocrystallization. Cryst. Eng. Commun. **19**, 2614–2622 (2017)
59. Umeda, Y., Fukami, T., Furuishi, T., Suzuki, T., Makimura, M., Tomono, K.: Molecular complex consisting of two typical external medicines: intermolecular interaction between indomethacin and lidocaine. Chem. Pharm. Bull. **55**, 832–836 (2007)
60. Wang, J., Yu, Q., Dai, W., Mei, X.: Drug-drug co-crystallization presents a new opportunity for the development of stable vitamins. Chem. Commun. **52**, 3572–3575 (2016)
61. Bangalore, S., Kamalakkannan, G., Parkar, S., Messerli, F.H.: Fixed-dose combinations improve medication compliance: a meta-analysis. Am. J. Med. **120**, 713–719 (2007)
62. Vilar, L., Canadas, V., Arruda, M.J., Arahata, C., Agra, R., Pontes, L., Montenegro, L., Vilar, C.F., Silva, L.M., Albuquerque, J.L., Gusmão, A.: Comparison of metformin, gliclazide MR and rosiglitazone in monotherapy and in combination for type 2 diabetes. Arq. Bras. Endocrinol. Metabol. **54**, 311–318 (2010)
63. Jakobsen, D.F., Frokjaer, S., Larsen, C., Niemann, H., Buur, A.: Application of isothermal microcalorimetry in preformulation. I. hygroscopicity of drug substances. Int. J. Pharm. **156**, 67–77 (1997)
64. Childs, S.L., Chyall, L.J., Dunlap, J.T., Coates, D.A., Stahly, B.C., Stahly, G.P.: A metastable polymorph of metformin hydrochloride: isolation and characterization using capillary crystallization and thermal microscopy techniques. Cryst. Growth Des. **4**, 441–449 (2004)
65. Putra, O.D., Yonemochi, E., Uekusa, H.: Isostructural multicomponent gliclazide crystals with improved solubility. Cryst. Growth Des. **16**, 6568–6573 (2016)
66. Putra, O.D., Furuishi, T., Yonemochi, E., Terada, K., Uekusa, H.: Drug-drug multicomponent crystals as an effective technique to overcome weaknesses in parent drugs. Cryst. Growth Des. **16**, 3577–3581 (2016)
67. Tye, C.K., Sun, C.C., Amidon, G.E.: Evaluation of the effects of tableting speed on the relationships between compaction pressure, tablet tensile strength, and tablet solid fraction. J. Pharm. Sci. **94**, 465–472 (2005)
68. Patel, S., Kaushal, A.M., Bansal, A.K.: Compression physics in the formulation development of tablets. Crit. Rev. Ther. Drug Carrier Syst. **23**, 1–65 (2006)
69. Bag, P.P., Chen, M., Sun, C.C., Reddy, C.M.: Direct correlation among crystal structure, mechanical behaviour and tabletability in a trimorphic molecular compound. CrystEngComm **14**, 3865–3867 (2012)
70. Canonica, G.W., Blaiss, M.: Antihistaminic, anti-inflammatory, and antiallergic properties of the nonsedating second-generation antihistamine desloratadine: a review of the evidence. World Allergy Organ. J. **4**, 47–53 (2011)

71. Kumar, B.V.S., Kale, S.A., Choudhari, R.B., Pradhan, N.S.C.: Novel crystalline forms of desloratadine and processes for their preparation. Patent US2007/0135472A1 (2006)
72. Ainurofiq, A., Mauludin, R., Mudhakir, D., Umeda, D., Soewandhi, S.N., Putra, O.D., Yonemochi, E.: Improving mechanical properties of desloratadine via multicomponent crystal formation. Eur. J. Pharm. Sci. **111**, 65–72 (2018)
73. Tao, W., Chen, J., Lu, T., Ma, L.: Phenazopyridine cocrystal and salts that exhibit enhanced solubility and stability. Cryst. Growth Des. **12**, 3144–3152 (2012)
74. Stanton, M.K., Bak, A.: Physicochemical properties of pharmaceutical co-crystals: a case study of ten AMG 517 co-crystals. Cryst. Growth Des. **8**, 3856–3862 (2008)
75. Putra, O.D., Yoshida, T., Umeda, D., Higashi, K., Uekusa, H., Yonemochi, E.: Crystal structure determination of dimenhydrinate after more than 60 years: solving salt-cocrystal ambiguity via solid-state characterizations and solubility study. Cryst. Growth Des. **16**, 5223–5229 (2016)
76. He, H., Huang, Y., Zhang, Q., Wang, J., Mei, X.: Zwitterionic cocrystals of flavonoids and proline: solid-state characterization, pharmaceutical properties, and pharmacokinetic performance. Cryst. Growth Des. **16**, 2348–2356 (2016)
77. Maeno, Y., Fukami, T., Kawahata, M., Yamaguchi, K., Tagami, T., Ozeki, T., Suzuki, T., Tomono, K.: Novel pharmaceutical cocrystal consisting of paracetamol and trimethylglycine, a new promising cocrystal former. Int. J. Pharm. **473**, 179–186 (2014)
78. Swapna, B., Nangia, A.: Epalrestat-cytosine cocrystal and salt structures: attempt to control E,Z→Z,Z isomerization. Cryst. Growth Des. **17**, 3350–3360 (2017)
79. Putra, O.D., Umeda, D., Nugraha, Y.P., Nango, K., Yonemochi, E., Uekusa, H.: Simultaneous improvement of epalrestat photostability and solubility via cocrystallization: a case study. Cryst. Growth Des. **18**, 373–379 (2018)
80. Ohashi, Y., Tomotake, Y., Uchida, A., Sasada, Y.: Crystalline-state reaction of cobaloxime complexes by X-ray exposure. 13. A stepwise structure analysis of the concerted process of racemization. J. Am. Chem. Soc. **108**, 1196–1202 (1986)
81. Couplands, J.N., Hayes, J.E.: Physical approaches to masking bitter taste: lessons from food and pharmaceuticals. Pharm. Res. **31**, 2921–2939 (2014)
82. Del Valle, E.M.M.: Cyclodextrins and their uses: a review. Process Biochem. **38**, 1033–1046 (2004)
83. Thakral, S., Thakral, N.K., Majumdar, D.K.: Eudragit: a technology evaluation. Expert Opin. Drug Deliv. **10**, 131–149 (2013)
84. Wang, C., Hu, S., Sun, C.C.: Expedited development of a high dose orally disintegrating metformin tablet enabled by sweet salt formation with acesulfame. Int. J. Pharm. **532**, 435–443 (2017)
85. Iwasaki, T., Matsunaga, K.: Nitric oxide-associated vasorelaxing effect of an anti-ulcer agent, benexate hydrochloride betadex. Drug. Dev. Res. **36**, 13–19 (1995)
86. Hori, Y., Odaguchi, K., Jyoyama, H., Yasui, K., Mizui, T.: Differential effect of benexate hydrochloride betadex on prostaglandin levels in stomach and inflammatory sites in rats. Jpn. J. Pharmacol. **72**, 183–190 (1996)
87. Muranushi, N., Yoshida, M., Kinoshita, H., Hirose, F., Fukuda, T., Doteuchi, M., Yamada, H.: Studies of benexate CD: effect of inclusion compound formation on the antiulcer activity of benexate, the effective ingredient of benexate CD. Folia Pharmacol. Jpn. **91**, 377–383 (1988)
88. Banarjee, R., Bhatt, P.M., Ravindra, N.V., Desiraju, G.R.: Saccharin Salts of Active Pharmaceutical Ingredients, Their Crystal Structure, and Increased Water Solubilities. Cryst. Growth Des. **5**, 2299–2309 (2005)
89. Putra, O.D., Umeda, D., Fujita, E., Haraguchi, T., Uchida, T., Yonemochi, E., Uekusa, H.: Solubility improvement of benexate through salt formation using artificial sweetener. Pharmaceutics **10**(64) (2018)
90. Cattopadhyay, S., Raychaudhuri, U., Chakraborty, R.: Artificial sweeteners—a review. J. Food Sci. Technol. **51**, 611–621 (2014)

Chapter 10
The Design of Porous Organic Salts with Hierarchical Process

Norimitsu Tohnai

Abstract Porous organic materials have attracted significant attention due to their design flexibility and functional versatility. Recently, a new and widely applicable strategy for the efficient construction of versatile porous organic materials using organic salts containing triphenylmethylamine (TPMA) and sulfonic acids was reported. Combinations of TPMA and sulfonic acids with polyaromatic moieties represent a new class of porous structures consisting of diamondoid networks, termed diamondoid porous organic salts (*d*-POS) herein. In a *d*-POS, the TPMA and sulfonic acid assemble into stable tetrahedral supramolecular clusters through charge-assisted hydrogen bonding, representing the initial building blocks. These clusters subsequently accumulate via π-π interactions between polyaromatic moieties, such that the d-POS is generated. As a result of the significant steric hindrance associated with such clusters, the diamondoid network cannot build a highly interpenetrating structure, resulting in the formation of continuous open channels. It should be noted that the extent of interpenetration in the diamondoid networks can be controlled by adjusting the bulkiness of the clusters by changing the sulfonic acid. Anthracene-2-sulfonic acid (2-AS) builds a three-fold structure with one-dimensional channels, while pyrene-1-sulfonic acid produces a two-fold structure with two-dimensional channels. In addition, organic salts composed of TPMA and 2-AS also provide polymorphic structures depending on the ratio of pores to template molecules and the template species. These structures demonstrate the stability and flexibility of *d*-POS materials.

Keywords Organic salt · Charge-assisted hydrogen bond · Porous structure · Diamondoid network · Crystal engineering

N. Tohnai (✉)
Department of Applied Chemistry, Graduate School of Engineering, Osaka University, Yamadaoka 2-1, Suita, Osaka 565-0871, Japan
e-mail: tohnai@chem.eng.osaka-u.ac.jp

M. Sakamoto and H. Uekusa (eds.), *Advances in Organic Crystal Chemistry*,
https://doi.org/10.1007/978-981-15-5085-0_10

10.1 Introduction

The construction of porous structures using small organic compounds is of significant interest, and this technique has a wide range of applications related to gas and molecular storage [1] as well as the fabrication of template response materials, including chemical sensors [2]. Recently, the strategic construction of porous structures, such as metal–organic frameworks (MOFs) [3] and covalent-organic frameworks (COFs) [4], has attracted attention because such techniques provide efficient synthetic strategies and molecular compatibility. These structures are generated via the formation of either coordination or covalent bonds and thus are robust. However, organic porous structures held together by weak non-covalent bonds are also an attractive alternative, due to their processing advantages and good workability [5]. As an example, porous structures can be designed based on organic ammonium sulfonate salts [6]. Organic salt systems comprising two components allow systematic structural design simply by varying the combination of materials. In addition, ammonium sulfonate ion pairs generate strong intermolecular hydrogen bonding and electrostatic interactions. Over the past 20 years, Ward et al. have studied a variety of porous structures based on guanidine and disulfonic acids [7]. In these structures, two-dimensional hydrogen-bonded sheets containing guanidinium and sulfonate ions are connected by disulfonate pillars to produce a grid-like structure with one-dimensional open channels. Our own group has previously reported the preparation of organic structures consisting of sulfonic acids and aliphatic amines, termed porous organic salts (POSs) [8]. As an example, biphenyl-4,4′-disulfonic acid and aliphatic primary amines can be employed to build a POS with a layered network via charge-assisted hydrogen bonding [8a]. The size and shape of the void spaces in such materials can be readily adjusted simply by changing the amine. These POS systems are expected to provide tunable substances with highly versatile functions due to the variety of possible combinations of sulfonic acids and amines.

Herein, a new and efficient strategy for building porous structures with diamondoid networks is proposed, using the POS approach. The construction of such structures is attractive not only as a means of obtaining highly symmetric, well-shaped networks, but also because these materials can provide high stiffness, good stability, and large voids. Since the first report of a stable organic diamondoid network of tetrahedral tetracarboxylic acid derivatives in 1988 by Ermer, [9] several porous materials utilizing similar single tetrahedral molecules as building blocks have been prepared [10]. However, it is still difficult to achieve the desired diversity in such structures using this conventional strategy. This is because the structural design of the diamondoid network often restricts the molecular configuration to a tetrahedral shape that cannot be further modified. In addition, these diamondoid networks tend to form highly interpenetrating structures [11], in which void spaces are smaller or absent due to the use of “non-bulky” building blocks. To overcome these problems, a supramolecular-based hierarchical strategy is proposed, in which tetrahedral supramolecules formed by simple molecules are employed as

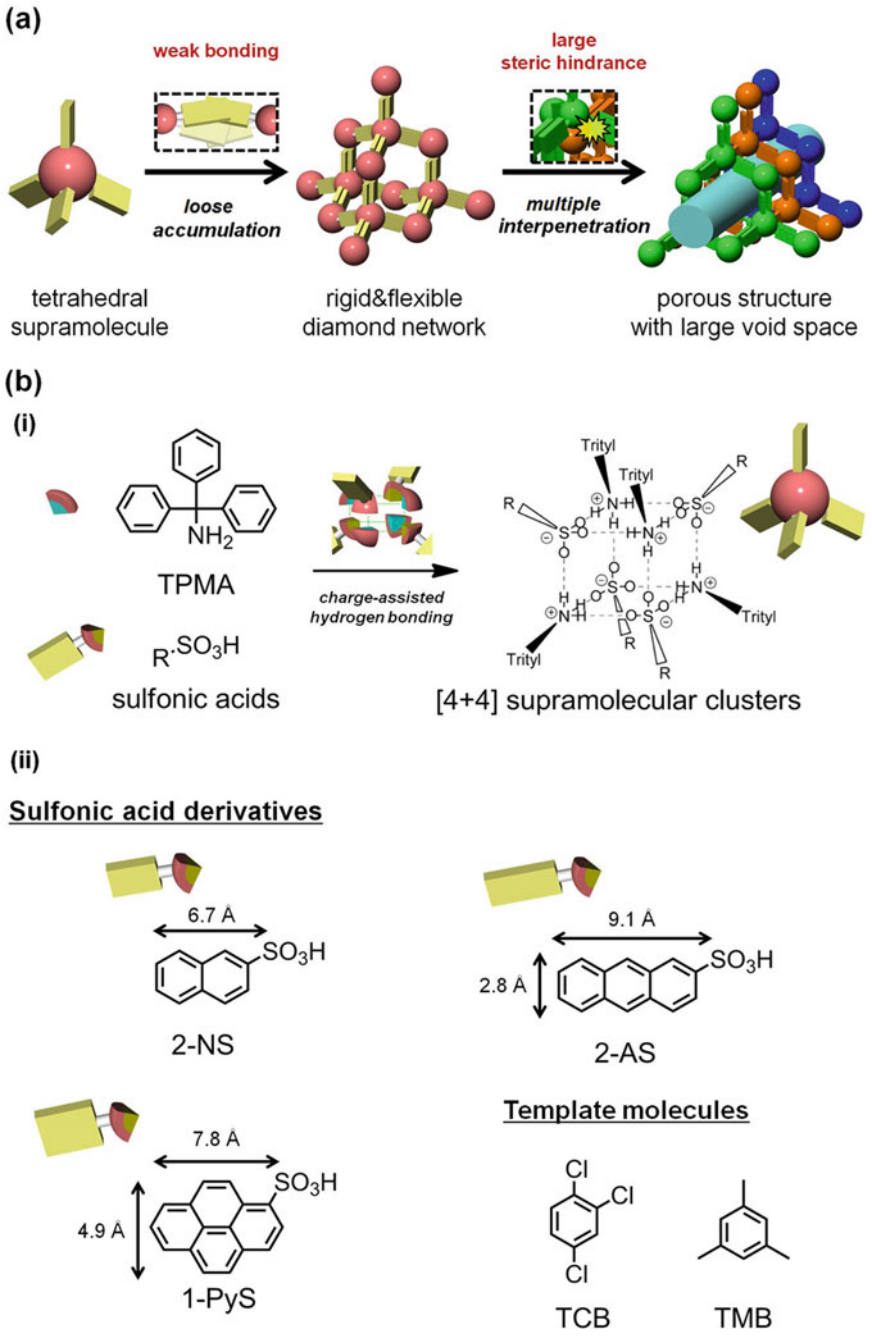

Fig. 10.1 **a** Proposed supramolecular-based hierarchical strategy. **b** [4 + 4] supramolecular cluster constructed of TPMA and sulfonic acid derivatives (i) and chemical structures of sulfonic acid derivatives and template molecules (ii). The distances are defined between a carbon or sulfur atom and any carbon atoms

building blocks for fabrication of the diamondoid network (Fig. 10.1a). Tetrahedral supramolecules are expected to act as sterically bulky nodes that prevent the diamondoid network from forming a highly interpenetrating structure. Previously, a specific type of supramolecule was also reported, termed a [4 + 4] supramolecular cluster. This compound was made of organic salts comprising triphenylmethylamine (TPMA) and monosulfonic acid derivatives (Fig. 10.1b, i). Within these clusters, the sulfonic acid derivatives are always arranged in tetrahedra as a result of cubic charge-assisted hydrogen bonding. Specific tetrahedral supramolecular clusters were designed that combined TPMA and monosulfonic acid derivatives with polycyclic aromatic moieties to produce diamondoid networks. In these substances, the long aromatic moieties protruding in the tetrahedral direction also function as a supramolecular adhesive that connects clusters via π-π interactions [12], thus generating not only rigid but also flexible (amphoteric) diamondoid networks and porous structures. These amphoteric structures are expected to provide more static and dynamic responses to external stimuli than are obtained with some flexible MOFs [2b, c, 3c]. Furthermore, the size, shape, and functionality of the clusters are dependent on the specific sulfonic acid derivative employed. In the present work, three different sulfonic acid derivatives were combined with TPMA: naphthalene-2-sulfonic acid (2-NS, 1), anthracene-2-sulfonic acid (2-AS, 2) [13], and pyrene-1-sulfonic acid (1-PyS, 3) [14] (Fig. 10.1b, ii). Organic salts containing either 2-AS or 1-PyS were used to construct diamondoid networks and interpenetrated porous structures containing aromatic molecules as templates. Interestingly, the degree of interpenetration of these diamondoid networks can be controlled by adjusting the bulkiness of the clusters, resulting in the formation of voids with various sizes and dimensions. In addition, the 2-AS diamondoid network changes structure depending on the ratio of pores to template molecules and the type of template.

10.2 Hierarchical Construction of d-POSs

The organic salts made by combining 2-AS and TPMA in the present work were recrystallized from a mixture of ethanol and nonpolar solvents such as aromatic hydrocarbons and appeared as yellow crystals. Single crystals suitable for single X-ray crystallographic analysis were obtained by recrystallization from a mixture of ethanol and 1,2,4-trichlorobenzene (TCB) [15]. This crystallographic analysis established that the crystals had a porous structure based on a diamondoid network, and so the materials produced in this work are generally referred to herein as diamondoid POSs (*d*-POSs) (specifically, *d*-POS-2a, Fig. 10.2a). Figure 10.2c illustrates the manner in which the *d*-POS-2a structure was built hierarchically, starting with 2-AS and TPMA (Fig. 10.2c). In the first step, the 2-AS and TPMA are assembled into [4 + 4] supramolecular clusters due to the effects of charge-assisted hydrogen bonding. The length of the hydrogen bond between the oxygen atom of the 2-AS and the nitrogen atom of the TPMA ranged from 2.735 to 2.863 Å (Fig. 10.3a). These hydrogen bonds produced a cubic network. However, because the anthracenyl

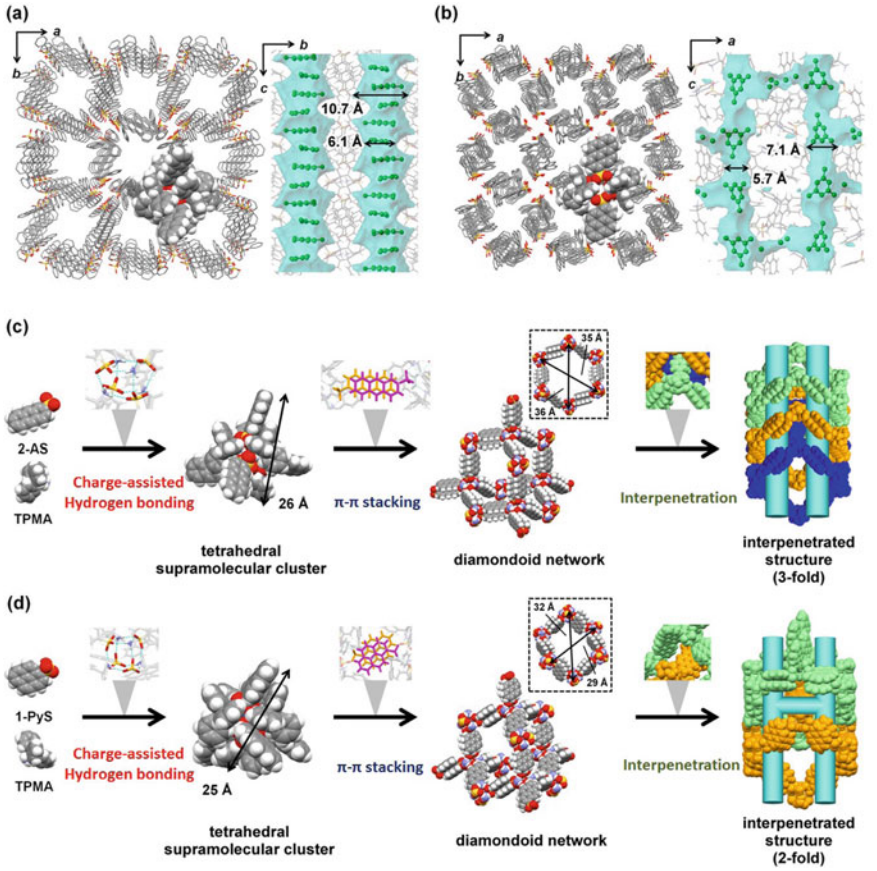

Fig. 10.2 Crystal structures of *d*-POSs. Top view and void space of d-POSs **a** composed of 2-AS and TPMA including TCB (***d*-POS-2a**) and **b** 1-PyS and TPMA including TMB (***d*-POS-3**). In the top view, template molecules are omitted for clarity. In the sky-blue-colored void space, template molecules are represented by green balls and sticks. Hydrogen atoms are omitted for clarity except in the space-filling model of a cluster. Hierarchical interpretation of **c *d*-POS-2a** and **d *d*-POS-3**. In the diamondoid networks and interpenetrated structures, triphenylmethyl groups are omitted for clarity. The independent diamondoid networks are indicated by orange, green, and blue

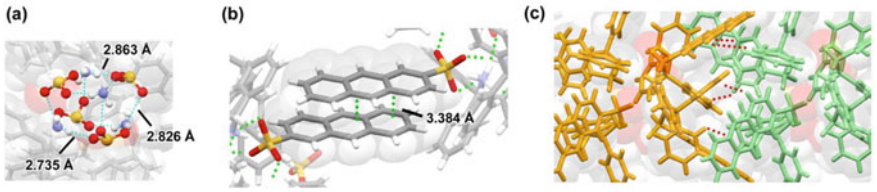

Fig. 10.3 **a** Cubic-like hydrogen bonding network in the tetrahedral supramolecular cluster. **b** π-π stacking manners between the clusters in *d*-POS-2a. **c** Close up view between the clusters in different diamondoid networks. Red lines represent CH-π intercluster contacts

group is much longer than the triphenylmethyl group, the cluster is tetrahedral and the maximum distance between the sulfur and carbon atoms is 9.1 Å (Figs. 10.1b and 10.2c). The maximum distance between the adjacent sides of the tetrahedral cluster in this structure is approximately 26 Å. Subsequently, the anthracenyl groups undergo π-π stacking and serve as linkers to arrange the clusters into a diamondoid network (Fig. 10.2c) in which the average distance between the aromatic moieties is 3.384 Å (Fig. 10.3b). This network contains very large voids associated with 35 × 36 Å hexagonal windows and three independent diamondoid networks penetrate one another to fill such voids. Nevertheless, the interpenetrating structure still possesses one-dimensional (1D) voids containing TCB molecules from the recrystallization solvent that act as template molecules (Fig. 10.2c, a, right). The bulkiness of the supramolecular clusters at the tetrahedral nodes plays an important role in creating the voids, and the diameter of the spherical core covered with triphenylmethyl groups in the clusters is approximately 16 Å. This bulkiness leads to significant steric hindrance between the nodes that prevents the formation of highly interpenetrating structures and inhibits complete filling of the voids (Fig. 10.3c). Calculations using the PLATON/VOID software package established that the void volume was 30% [16], the maximum void area was 10.7 × 10.7 Å, and the minimum was 6.1 × 6.1 Å (Fig. 10.2a, right). Each void was found to contain four TCB molecules per cluster. Interestingly, these template molecules were arranged almost parallel to one another (Fig. 10.2a, right, and Fig. 10.4), with a distance between adjacent molecules of 3.930 Å. The template molecules also adjusted the arrangement in the void space based on CH-Cl contact, while the void surfaces were covered by the aromatic rings. The effective CH-Cl contact between the template molecule and the wall contributes significantly to the specific parallel arrangement. Highly interpenetrating structures are generally considered undesirable because they tend

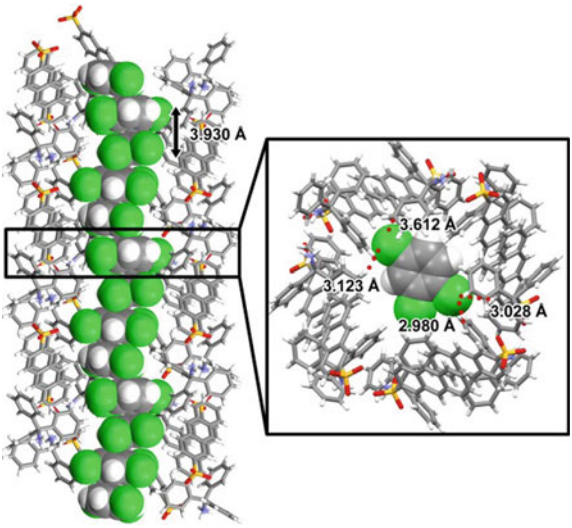

Fig. 10.4 1D array of the template molecules in the *d*-POS-2a

to reduce the void volume. However, in this material, the characteristic arrangement of template molecules is confined by the 1D voids formed by three interpenetrating diamondoid networks. This 1D molecular array could result in unique properties such as polarization performance and anisotropic charge conduction [17].

10.3 Structural Diversification of *d*-POSs with Variations in the Sulfonic Acid

Similar to the organic salt containing 2-AS, organic salts composed of 1-PyS and TPMA also formed a *d*-POS-2 type material through a similar hierarchical process (Fig. 10.2b, d). Single crystals for X-ray crystallographic analysis were obtained by recrystallization from a mixture of ethanol and 1,3,5-trimethylbenzene (TMB). According to X-ray analysis, the 1-PyS and TPMA also formed tetrahedral supramolecular clusters through charge-assisted hydrogen bonding (Fig. 10.2d), with a maximum distance between adjacent sides of the clusters of approximately 25 Å. The clusters were arranged in a diamondoid network by π-π stacking between the pyrenyl groups and the resulting diamondoid network also contained large voids with 29 × 32 Å hexagonal windows, leading to an interpenetrating structure. However, it should be noted that, unlike the three-fold interpenetration associated with the *d*-POS-2a, only two independent diamondoid networks penetrate one another in this material. Therefore, there are 2D voids in the porous structure (Fig. 10.2b, right). The 1D voids having a maximum space of 7.1 × 5.1 Å and a minimum space of 5.7 × 5.7 Å are connected by small orthogonal channels, and the calculated air gap volume is 29%. The TMB molecules from the recrystallization solvent were contained in the primary 1D voids and acted as templates. These void differences arise from variations in the shapes and sizes of the substituents in the sulfonic acid derivatives. The maximum distance between the sulfur and carbon atoms in 1-PyS is 7.8 Å, which is slightly less than that in 2-AS (Fig. 10.1b, ii). Therefore, the hexagonal windows in the *d*-POS-3 diamondoid network were smaller than the hexagonal windows in the *d*-POS-2a. In contrast, the width of 1-PyS is greater than that of 2-AS, and the maximum distances between any two carbon atoms in these compounds were 4.9 and 2.8 Å, respectively (Fig. 10.1b, ii). Therefore, 1-PyS and TPMA form more sterically bulky clusters than 2-AS and TPMA, preventing interpenetration more effectively (Fig. 10.2d). These results show that the relative ratio of the cluster core diameter to the polycyclic aromatic length has a significant effect on the avoidance of highly interpenetrating structures. When the polyaromatic group is short and wide, the relative proportion of the cluster cores increases. As a result, the resulting tetrahedral clusters exhibit increased steric hindrance and there is reduced interpenetration in the diamondoid network. In contrast, the organic salt composed of 2-NS and TPMA did not form a porous structure with a diamondoid network (Fig. 10.5). This difference can be attributed to the naphthyl groups of the 2-NS molecules (in which the maximum distance between sulfur and carbon atoms is 6.7 Å), which are too short

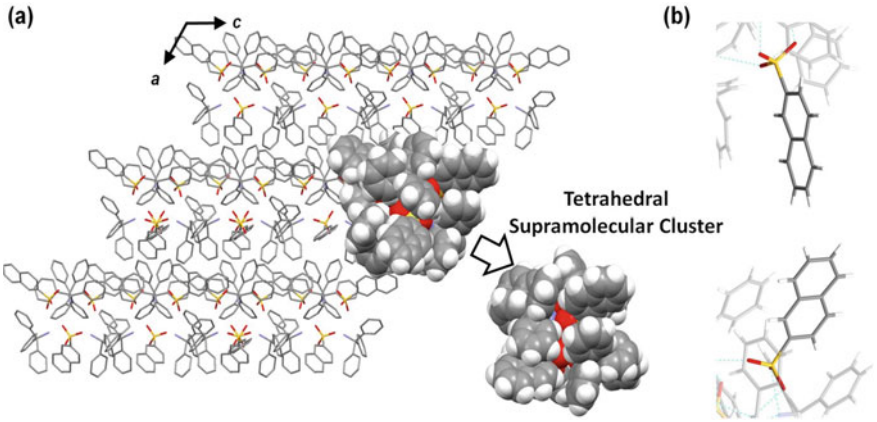

Fig. 10.5 Crystal structure composed of 2-NS and TPMA. **a** Top view of the structure. Hydrogen atoms are omitted for clarity except in the space-filling model of one supramolecular cluster. **b** Location of the naphthyl groups between neighboring clusters in the structure

to protrude from the cluster toward the tetrahedron and that do not undergo π-π interactions between themselves. Thus, the clusters form a close-packed structure without a diamondoid network. These results show that selecting the appropriate sulfonic acid derivative allows ready adjustment of the networks and the degree of interpenetration.

10.4 Structural Diversification of *d*-POSs Depending on Template Molecules

Interestingly, the diamondoid network also exhibits structural flexibility depending on the type and amount of template molecule. A typical example is the aforementioned organic salt composed of 2-AS and TPMA. The organic salt also gave two other pseudopolymorphic crystals, *d*-POS-2b and *d*-POS-2c, upon recrystallization from a mixture of ethanol and TMB. The *d*-POS-2b was obtained by slow recrystallization, while *d*-POS-2c was primarily obtained by rapid recrystallization. X-ray crystallographic analysis demonstrated that these crystals were composed of *d*-POS structures containing TMB molecules from the recrystallization solvent in 1D voids, where they served as template molecules (Fig. 10.6a, b). The *d*-POS-2b contained indented 1D voids with a maximum cross-section of 10.6 × 9.6 Å and a minimum of 4.5 × 3.0 Å (Fig. 10.6c). The void volume was determined to be 29% per unit cell using the PLATON/VOID software. In contrast, the *d*-POS-2c contained relatively straight 1D voids (Fig. 10.6d) having a maximum void size of 11.2 × 9.9 Å and a minimum size of 6.5 × 6.0 Å. Compared to the *d*-POS-2b, the voids in the *d*-POS-2c were slightly larger and had no pockets, while accounting for 36% of

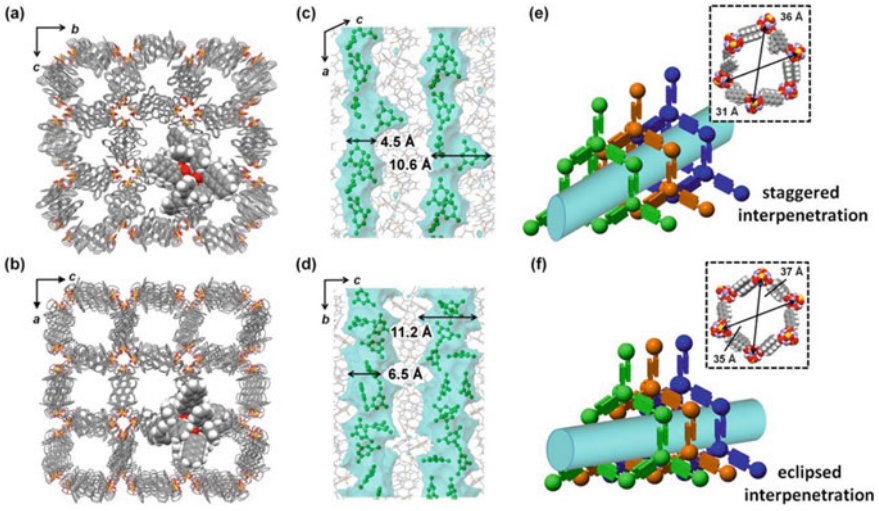

Fig. 10.6 Crystal structures of *d*-POSs composed of 2-AS and TPMA including TMB. Top view of **a *d*-POS-2b** and **b *d*-POS-2c**. In the top view, guest molecules and hydrogen atoms are omitted for clarity except for in the space-filling model of one supramolecular cluster. Visualization of the void space in **c *d*-POS-2b** and **d *d*-POS-2c**. Void spaces are indicated in sky blue, and guest molecules are represented by green sticks. Hydrogen atoms of the guests are omitted for clarity. Schematic representation of the interpenetration manners of the diamondoid networks in **e *d*-POS-2b** and **f *d*-POS-2c**

the unit cell volume. These materials were built up through the same hierarchical process as described above. That is, three independent diamondoid networks could be obtained, having the same topology and interpenetrating porous structures. These results indicate that stable diamondoid networks could be formed regardless of the template. However, the shape and size of the diamondoid networks were significantly different: the *d*-POS-2b and *d*-POS-2c diamondoid networks had 31 × 36 and 35 × 37 Å hexagonal windows (Fig. 10.6e, f, inset). This expansion and contraction of the diamondoid network is related to the template ratio. Specifically, the *d*-POS-2b incorporated three template molecules per cluster, while the *d*-POS-2c contained four. In addition, the template species also affected the structure of the diamondoid network. The *d*-POS-2c had hexagonal window that were slightly larger than the window in the material containing TCB molecules, even though both samples had the same template ratio (Fig. 10.2a, c). This difference may have occurred because TMB is slightly larger than TCB. These results demonstrate that the diamondoid networks were stable and flexible in response to changes in the template molecule. Such behavior is clearly different from that of conventional diamondoid networks based on strong interactions such as covalent bonds. The flexibility of the present diamondoid networks is derived not only from the malleability of the cluster conformations, but also from the ability of the π-π stacking orientation between the clusters to change. The interpenetration of the networks is also tunable (Fig. 10.7). These

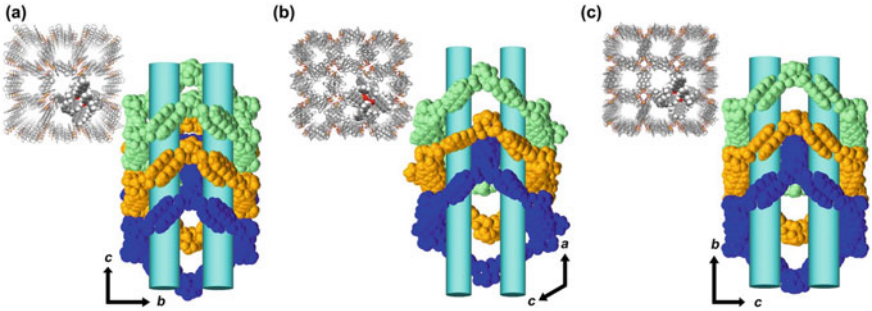

Fig. 10.7 Interpenetration manners of **a** ***d*-POS-2a**, **b** ***d*-POS-2b** and **c** ***d*-POS-2c**. The independent diamondoid networks are indicated by blue, green and orange, respectively. The blue tubes indicate the void spaces. Triphenylmethyl groups are omitted for clarity

phenomena are ascribed to the surprising stability and reproducibility of the cubic hydrogen-bonded network. As demonstrated in the previous work, this network is always formed regardless of the sulfonic acid derivative that is employed [18]. Therefore, the π-π stacking is affected by the template molecule that is used, potentially providing voids with varying shapes and sizes. The flexibility of these structures increases the degree of inclusion that is possible and renders the porous structure sensitive to external stimuli.

10.5 Structural Transformation of *d*-POSs on Template Release

To further assess the porosity of these *d*-POS materials, structural stability during template release was investigated, and thermogravimetric analysis (TGA) of *d*-POS-2a to c single crystals showed different template release profiles (Fig. 10.8). The first peak in each TGA plot is associated with the release of template molecules from the *d*-POS. The second peak, above 200 °C, occurs in conjunction with a significant mass loss, and indicates the decomposition of the host framework components. As shown in Fig. 10.8a, the *d*-POS-2a completed the release of TCB template molecules before 100 °C, after which there was no mass loss up to 200 °C. The *d*-POS-2c produced the same TMB template release profile as the *d*-POS-2a. Conversely, the *d*-POS-2b TGA data indicate a gradual mass loss that continues until decomposition of the structural components above 200 °C. These differences can likely be attributed to variations in void shapes. The voids in the *d*-POS-2b had protruding pockets that were able to incorporate template molecules, while the voids in the *d*-POS-2a and *d*-POS-2c did not have this ability. These pockets would presumably allow the structure to hold the template molecules more steadily, leading to a gradual release at higher temperatures.

As shown in Fig. 10.9, powder X-ray diffraction (PXRD) analyses confirmed the high degree of crystallinity of these crystals even after template release. PXRD data

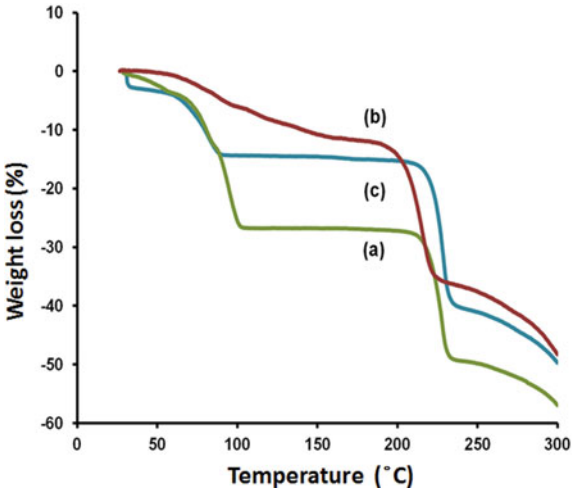

Fig. 10.8 TGA data of the d-POSs: **a *d*-POS-2a**, **b *d*-POS-2b**, and **c *d*-POS-2c**

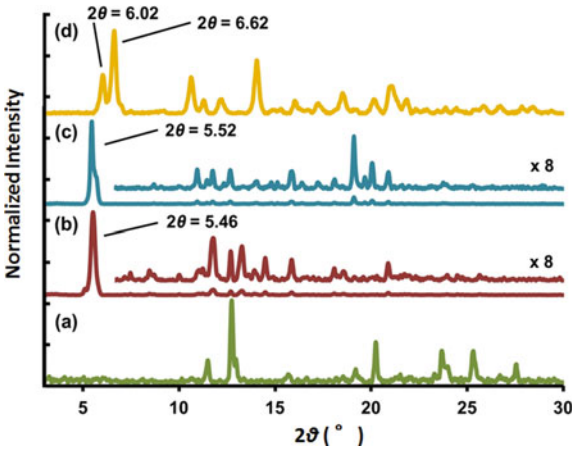

Fig. 10.9 PXRD patterns of the *d*-POSs: **a *d*-POS-2a**, **b *d*-POS-2b**, **c *d*-POS-2c** and **d *d*-POS-2b** after guest release

also showed that each *d*-POS was transformed to the same structure upon template release. Prior to release, the PXRD patterns for the *d*-POS-2b and *d*-POS-2c contain single sharp peaks at $2\theta = 5.46°$ ($d = 16.2$ Å) and 5.52° ($d = 16.0$ Å), respectively, corresponding to the distances between channels. These peaks disappear and two new peaks appear at 6.02° ($d = 14.7$ Å) and 6.62° ($d = 13.3$ Å) after the template release, indicating anisotropic shrinkage of the structure. Considering the shrinkage of the distance between channels (approximately 1.5–3.0 Å), the molecular arrangements and unit cells of the converted structures were not determined from the PXRD patterns, but it is believed that voids were present in the converted structures. These results indicate that these materials have potential applications in both molecular and gas storage.

10.6 Conclusion

In summary, a supramolecular-based hierarchical strategy was employed to build a new class of porous structures with diamondoid networks, termed diamondoid porous organic salts. Sterically hindered tetrahedral clusters prevent the excessive interpenetration of the diamondoid network and produce a porous structure. In addition, these diamondoid networks are easily adjusted by changing the sulfonic acid derivative, allowing control of the degree of interpenetration and number of voids. Moreover, the flexible accumulation of clusters provides flexibility and stability to the diamondoid network. The proposed strategy makes it possible to build organic porous structures with various functions. Tetrahedral clusters are evidently an excellent platform for arranging a wide range of organic molecules into tetrahedral shapes, even when the organic molecules themselves do not have a tetrahedral structure. This ability contributes to easy structural changes and functionalization of porous materials. As an example, the introduction of polycyclic aromatic groups into a porous structure could result in fluorescence properties depending on the template molecule employed. Furthermore, the porosity (size, shape, stability, etc.) of such materials can be controlled by selecting specific combinations of the two components. The extension of this strategy to other sulfonic acid derivatives has been actively investigated in order to construct unique functional organic porous structures.

References

1. (a) Sozzani, P., Bracco, S., Comotti, A., Ferretti, L., Simonutti, R.:Angew. Chem. Int. Ed. **44**, 1816−1820 (2005); (b) Mastalerz, M., Oppel, I.M.: Angew. Chem. Int. Ed. **51**, 5252−5255 (2012); (c) Yang, W., Greenaway, A., Lin, X., Matsuda, R., Blake, A., Wilson, C., Lewis, W., Hubberstey, P., Kitagawa, S., Champness, N., Schroder, M.: J. Am. Chem. Soc. **132**, 14457−14469 (2010); (d) Sudik, A.C., Millward, A.R., Ockwig, N.W., Coté, A.P., Kim, J., Yaghi, O.M.: J. Am. Chem. Soc. **127**, 7110−7118 (2005); (e) Furukawa, H., Yaghi, O.M.: J. Am. Chem. Soc. **131**, 8875−8883 (2009); (f) Tsue, H., Ishibashi, K., Tokita, S., Takahashi, H., Matsui, K., Tamura, R.: Chem. Eur. J. **14**, 6125−6134 (2008)
2. (a) Lu, Z.Z., Zhang, R., Li, Y.Z., Guo, Z.J., Zheng, H. G.: J. Am.Chem. Soc. **133**, 4172−4174 (2011); (b) Takashima, Y., Martinez, V.M., Furukawa, S., Kondo, M., Shimomura, S., Uehara, H., Nakahama, M., Sugimoto, K., Kitagawa, S.: Nat. Commun., 2−8 (2011); (c) Yanai, N., Kitayama, K., Hijikata, Y., Sato, H., Matsuda, R., Kubota, Y., Takata, M., Mizuno, M., Uemura, T., Kitagawa, S.: Nat. Mater. **10**, 787−793 (2011)ss
3. (a) Yaghi, O.M., O'Keeffe, M., Ockwing, N.W., Chae, H.K., Eddaoudi, M., Kim, J.: Nature **423**, 705−714 (2003); (b) Horike, S., Shimomura, S., Kitagawa, S.: Nat. Chem. 1, 695−704 (2009); (c) Farha, O.K., Hupp, J.T.: Acc. Chem. Res. **43**, 1166−1175 (2010)
4. (a) Coté, A.P., Benin, A.I., Ockwig, N.W., Matzger, A.J., O'Keeffe, M., Yaghi, O.M.: Science **310**, 1166−1170 (2005); (b) El-Kaderi, H.M., Hunt, J.R., Mendoza-Cortés, J.L., Côté, A.P., Taylor, R.E., O'Keeffe, M., Yaghi, O.M.: Science **316**, 268−272 (2007)
5. (a) Holst, J.R., Trewin, A., Cooper, A.I.: Nat. Chem. **2**, 915−920 (2010); (b) Tian, J., Thallapally, P.K., McGrail, B.P.: Cryst. Eng. Commun. **14**, 1909−1919 (2012)
6. (a) Su, X., Guo, D.S., Liu, Y.: Cryst. Eng. Commun. **12**, 947−952 (2010); (b) Leverd, P.C., Berthault, P., Lance, M., Nierlich, M.: Eur. J. Org. Chem., 133−139 (2000)

7. (a) Russell, V.A., Evans, C.C., Li, W.J., Ward, M.D.: Science **276**, 575−579 (1997); (b) Holman, K.T., Pivovar, A.M., Ward, M.D.: Science, **294**, 1907−1911 (2001); (c) Holman, K.T., Pivovar, A.M., Swift, J.A., Ward, M.D.: Acc. Chem. Res. **34**, 107−118 (2001)
8. (a) Mizobe, Y., Miyata, M., Hisaki, I., Tohnai, N.: Chem. Lett. **36**, 280−281 (2007); (b) Mizobe, Y., Miyata, M., Hisaki, I., Hasegawa, Y., Tohnai, N.: Org. Lett. **8**, 4295−4298 (2006); (c) Mizobe, Y., Hinoue, T., Miyata, M., Hisaki, I., Hasegawa, Y., Tohnai, N.: Bull. Chem. Soc. Jpn. **80**, 1162−1172 (2007)
9. (a) Ermer, O.: J. Am.Chem. Soc. **110**, 3747–3754 (1988); (b) Ermer, O., Eling, A.: Angew. Chem. Int. Ed. Eng. **27**, 829–833 (1988)
10. (a) Brunet, P., Simard, M., Wuest, J.D.: J. Am.Chem. Soc. **113**, 4696–4698 (1991); (b) Jones, K.M.E., Mahmoudkhani, A.H., Chandler, B.D., Shimizu, G.K.H.: Cryst. Eng. Commun. **8**, 303–305 (2006); (c) Uribe-Romo, F.J., Hunt, J.R., Furukawa, H., Klöck, C., O'Keeffe, M., Yaghi, O.M.: J. Am. Chem. Soc. **131**, 4570–4571 (2009)
11. (a) Reddy, D.S., Dewa, T., Endo, K., Aoyama, Y.: Angew. Chem. Int. Ed. **39**, 4266–4268 (2000); (b) Metrangolo, P., Meyer, F., Pilati, T., Proserpio, D.M., Resnati, G.: Chem. Eur. J. **13**, 5765–5772 (2007)
12. Desiraju, G.R.: Angew. Chem. Int. Ed. Engl. **34**, 2311–2327 (1995)
13. Acquavella, M.F., Evans, M.E., Farraher, S.W., Nèvoret, C.J., Abelt, C.J.: J. Org. Chem. **59**, 2894−2897 (1994)
14. Menger, F.M., Whitesell, L.G.: J. Org. Chem. **52**, 3793–3798 (1987)
15. CCDC 880742 (***d*-POS-1a**), 880741 (***d*-POS-2**), 881390 (***d*-POS-1b**), 881391 (***d*-POS-1c**) contain the supplementary crystallographic data. These data can be obtained free of charge from The Cambridge Crystallographic Data Centre via www.ccdc.cam.ac.uk/data_request/cif
16. Spek, A.L.: Acta Crystallogr. Sect. D **65**, 148–155 (2009)
17. Hertzach, T., Budde, F., Weber, E., Hulliger, J.: Angew. Chem. Int. Ed. **41**, 2281–2284 (2002)
18. Tohnai, N., Mizobe, Y., Doi, M., Sukata, S., Hinoue, T., Yuge, T., Hisaki, I., Matsukawa, Y., Miyata, M.: Angew. Chem. Int. Ed. **46**, 2220–2223 (2007)

Chapter 11
Layered Hydrogen-Bonded Organic Frameworks as Highly Crystalline Porous Materials

Ichiro Hisaki, Qin Ji, Kiyonori Takahashi, and Takayoshi Nakamura

Abstract Porous molecular crystals (PMCs) with well-defined, self-standing pores have been attracted much attention due to significant functionality provided by selective and reversible inclusion of certain chemical species into the pores. PMCs constructed through preorganized hydrogen bonds (H-bonds) are specifically called as hydrogen-bonded organic frameworks (HOFs). For recent two decades, HOFs have been intensively explored. HOFs are frequently obtained as single crystals, which is convenient to reveal the structure–property relationship. Their regenerable and reusable features are also appealing. However, HOFs are relatively fragile, and their designing strategy needs to be more considered compared with other porous frameworks because of weakness of H-bonds. Regarding this, we have demonstrated that C_3-symmetric π-conjugated molecules (C_3PIs) possessing *o*-bis(4-carboxyphenyl)benzene moieties in their periphery give layered frameworks composed of isostructural H-bonded hexagonal networks (H-HexNets) and that the frameworks can effectively provide stable, robust, multifunctional HOFs with permanent porosity. The frameworks also can work as a platform to achieve very unique alignment of functional molecules such as C_{60}. Our strategy for constructing functional HOFs contributes to developing a new field of porous organic materials.

Keywords Porous molecular crystal · Hydrogen-bonded organic framework · π-conjugated molecule · Carboxylic acid · Permanent porosity

I. Hisaki (✉) · K. Takahashi · T. Nakamura
Research Institute for Electronic Science, Hokkaido University, N20W10, Sapporo, Hokkaido 001-0020, Japan
e-mail: hisaki@chem.es.osaka-u.ac.jp

I. Hisaki · Q. Ji · K. Takahashi · T. Nakamura
Graduate School of Environmental Science, Hokkaido University, N10W5, Sapporo, Hokkaido 060-0810, Japan

Present Address:
I. Hisaki
Graduate School of Engineering Science, Osaka University, 1-3 Machikaneyama, Toyonaka, Osaka 560-8531, Japan

M. Sakamoto and H. Uekusa (eds.), *Advances in Organic Crystal Chemistry*,
https://doi.org/10.1007/978-981-15-5085-0_11

11.1 Introduction: Porous Molecular Crystals

Porous molecular crystals (PMCs) are crystalline materials with permanent porosity constructed from discrete organic molecules through reversible non-covalent intermolecular interactions. A pioneering work, for example, is of tris-*o*-phenylenedioxycyclotriphosphazene (TPP) [1–3]. Although PMCs are closely related to organic inclusion crystals [4], an important feature of PMCs is that they have self-standing pores (i.e., permanent porosity) that can accommodate various and/or specific guest molecules reversibly. PMCs have recently attracted renewed attention from viewpoint of applications such as selective gas storage/separation, catalysis, chemical sensing, drug delivery, and optoelectronics [5–8].

Specifically, PMCs that are formed via hydrogen bonds (H-bonds) are often called as hydrogen-bonded organic frameworks (HOFs) [9–13], which was introduced by Chen [14]. Although several names and acronyms to describe PMCs constructed through H-bonding can be found in the literature, we call such PMCs as HOFs in this chapter. Typical merits of HOFs are as follows:

- HOFs are frequently obtained as single crystals via a simple solution process due to the reversible nature of H-bonds, which enables to determine the precise crystal structures by single-crystal X-ray diffraction (SXRD).
- HOFs do not need metal species for framework construction, allowing lightweight and environmentally friendly porous materials.
- HOFs have ability to restore its original crystallinity by reannealing.

However, such intrinsic properties of HOFs simultaneously cause the following problems:

- HOFs tend to collapse when solvent molecules are removed from voids to activate the porous structures.
- HOFs are difficult to predesign: Even if building block molecules are preorganized thoughtfully, the porous HOFs are not always produced as designed.
- The H-bonding moieties of building blocks are often trapped by polar solvent molecules used for recrystallization, preventing formation of porous networked frameworks.

Therefore, we need solve these kinds of dilemmas.

An important point to construct stable HOFs with permanent porosity is to combine non-covalent intermolecular interactions such as π/π interactions with H-bonds, because a H-bond alone is too weak to maintain low-density porous materials, compared with a dative or covalent bond. Fortunately, significant progress in the field has resulted in the production of excellent HOFs with permanent porosity, thermal and chemical durability, and functionality [15–41]. Some typical molecular skeletons and supramolecular synthons are listed in Fig. 11.1. For construction of predesigned molecular architectures, the appropriate selection of both a supramolecular synthon (directionality and multiplicity of H-bonding) and molecular skeletons (geometry, size, rigidity, planarity, symmetry, and functionality) to satisfy both H-bonds, and

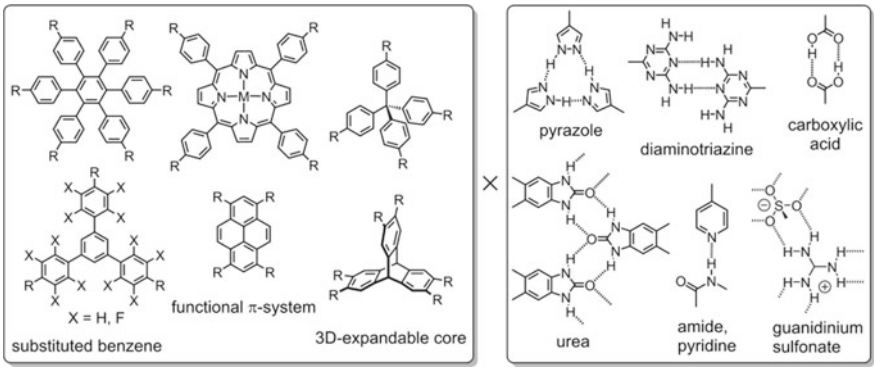

Fig. 11.1 Some examples of molecular skeletons and supramolecular synthons providing HOFs with permanent porosity

the additional interactions is important. Furthermore, it is remarkable that Cooper, Day, and co-workers recently introduced "energy–structure–function maps" built by combining computational crystal structure prediction with property prediction [42, 43]. The maps describe the possible structures and properties that are available to a candidate molecule and can accelerate development of new functional HOFs.

11.2 Hydrogen-Bonding Motifs

11.2.1 Networked Structures Connected by Carboxylic Acid Dimers

A H-bonded dimer of carboxy groups is one of the simplest and the most classical molecular glues to make molecular assemblies [44–46]. Meanwhile, the dimer has still been a suitable supramolecular synthon to construct exotic supramolecular architectures, because of the following two features: facile synthesis of derivatives with carboxy groups and its high directional H-bond formation. Particularly, the latter feature enables one to design supramolecular network motifs, combined with geometrically well-defined molecular platforms, as shown in Fig. 11.2.

It is well known that Marsh and Duchamp demonstrated in 1969 that trimesic acid yielded a waved H-bonded honeycomb network, which was then interpenetrated to yield a non-porous crystal [47]. It was in 1987 that layered honeycomb structures of trimesic acid with 1D inclusion channels were constructed by Herbestein and co-workers through template crystallization [48].

Carboxylic acid-based HOFs with permanent porosity have started to be reported intensively since around 2015. Some remarkable examples are described as follows

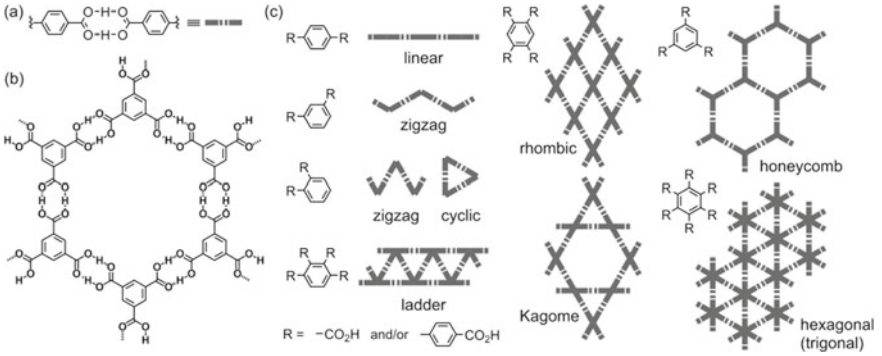

Fig. 11.2 **a** Carboxylic acid dimer, the simplest supramolecular synthon. **b** Honeycomb network of trimesic acid reported by Marsh and Duchamp. **c** Possible H-bonded networked structures composed of carboxy- and/or carboxyphenyl-substituted benzene derivatives

(Fig. 11.3). Rowsell, Zentner, and co-workers demonstrated that 1,3,5-tris(4-carboxyphenyl)benzene (**1**) yielded porous crystals **tcpb** with interpenetrated honeycomb sheets [28]. Tris(4-carboxyphenyl)amine (**2**) gave 3D networked porous framework (**HOF-11**) with Brunauer–Emmett–Teller surface area (SA_{BET}) of 687 m^2g^{-1} [29, 30]. Comotti, Sozzani, and co-workers reported dynamic gas sorption behavior of **TCF-1** and-**2** composed of **3a** and **3b**, respectively [38]. Wu, Yuan, and co-workers reported biphenyl derivative **4** gave 3D networked porous framework (**HOF-TCBP**), which exhibits SA_{BET} of 2066 m^2g^{-1} [31]. Liu, Cao, and co-workers applied pylene derivative **5** to construct HOF (**PFC-1**) with SA_{BET} of 2122 m^2g^{-1} and demonstrated proof-of-concept for chemo and photodynamic therapy [34]. Hisaki, Douhal, and co-workers demonstrated construction of highly stable, single-crystalline, isostructural HOFs (**CPHAT** and **CBPHAT**) with SA_{BET} of 649 m^2g^{-1} and 1288 m^2g^{-1} based

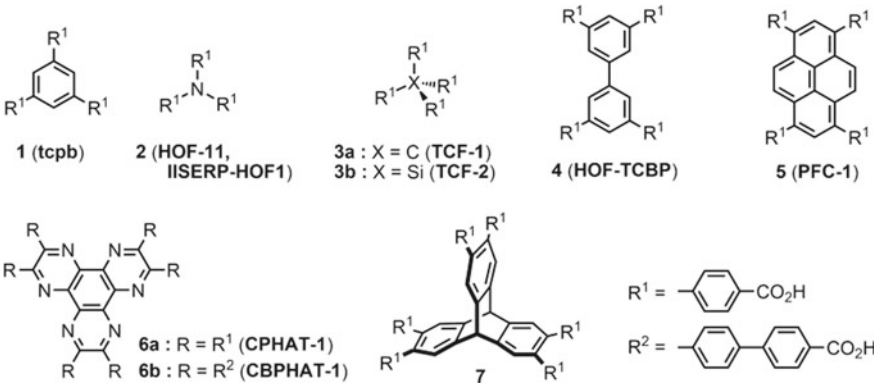

Fig. 11.3 Some examples of building blocks providing stable 2D- or 3D-networked HOFs with permanent porosity. Acronyms in parentheses denote HOF's names constructed from the corresponding building blocks

on shape-fitted docking strategy with hexaazatriphenylene (HAT) derivatives **6a**, **b** [32, 33, 41]. Stoddart and co-workers reported that triptycene derivative **7** provided interpenetration polymorphs of H-bonded networks [39].

It is remarkable that reported building blocks contain carboxyphenyl groups instead of carboxy groups. This is probably because such building-block molecules can easily synthesized by metal-catalyzed cross-coupling reactions between aryl groups such as Suzuki–Miyaura reaction [49]. Moreover, introduction of carboxyphenyl groups into π-conjugated skeleton improves solubility of the molecule into solvents compared with those directly bonded by carboxy groups [50, 51]. The phenylene group also acts as a spacer to generate pores [52]. However, systematic construction of carboxylic-acid-based HOFs is still challenging.

In connection with this, we have proposed that C_3-symmetric π-conjugated building blocks (C_3PIs) possessing three *o*-bis(4-carboxyphenyl)benzene moieties in periphery of the core can systematically provide isostructural H-bonded hexagonal networks (H-HexNets) with multiple void spaces, and that the HexNets are stacked without interpenetration to give porous layered assembly of H-HexNets (LA-H-HexNets). This working hypothesis to achieve formation of H-HexNet-based layered HOF is summarized in Fig. 11.4. C_3-symmetric, rigid, planar cores with sides of two different lengths are applied for the central part of C_3PIs. Such C_3PIs enable the formation of a planar 2D H-HexNet motif with multivoid spaces. Moreover, the size and shape of the void can be varied by changing the side length of the C_3PIs. The peripheral *o*-bis(4-carboxyphenyl)benzene moieties can form a H-bonded triangular porous motif, so-called phenylene triangle (PhT) motif to network the C_3PI. The PhT motif was first observed in a crystal of hexakis(4-carboxyphenyl)benzene reported by Kobayashi and co-workers in 2000 [53].

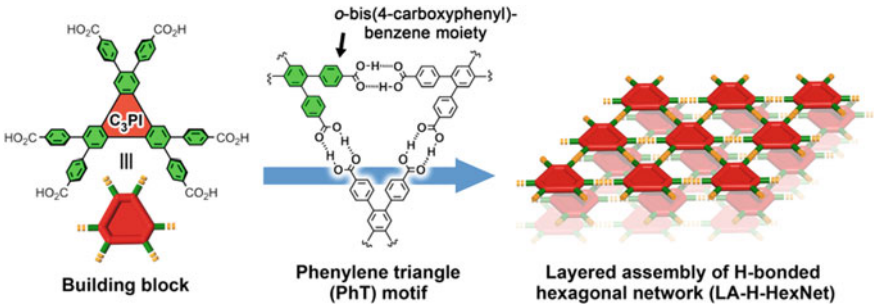

Fig. 11.4 Schematic representation for construction of layered assembly of hydrogen-boned hexagonal networks (LA-H-HexNet) with planar C_3-symmetric π-conjugated molecules (C_3PIs) via formation of a cyclic hydrogen-bonded motifs, so-called phenylene triangle (PhT) motif

11.2.1.1 Phenylene Triangle (PhT)

As described above, the PhT motif is a key structure for H-HexNet-based layered HOFs. To confirm whether the PhT is a robust H-bonding motif in crystals, *o*-bis(4-carboxyphenyl)benzene (**8a**), 4,5-dibromo-1,2-bis(4-carboxyphenyl)benzene (**8b**), and 1,2,3,4-tetrakis(4-carboxyphenyl)benzene (**9**) were crystallized from a mixed solution of DMF, 1,2,4-trichlorobenzene (124TCB) and 1,3,5-trichlorobenzene (135TCB) at 50 °C. Pristine **8a** yields zigzag-shaped 1D H-bonded chain as in the case of the corresponding *meta*- and *para*-substituted derivatives. Brominated derivative **8b**, on the other hand, forms the PhT through H-bonding between the carboxy groups (Fig. 11.5a). The PhT of **8b** possesses a triangular void with a side of ca. 12.5 Å and diameter of ca. 9.7 Å, in which 124TCB and/or 135TCB molecules are accommodated. Threefold CH/Br intermolecular interactions (H···Br distances: 2.79–2.96 Å, C–H–Br angles: 144–167°) afford formation of the PhT motif, instead of a zigzag chain. Similarly, **9** forms the PhT motif to give a ladder-type porous network structure (Fig. 11.5b). These results indicate that, although the pristine unit does not always form the PhT motif, geometrically or electrostatically well-organized derivatives can form the PhT motif [54].

It is unignorable that the PhT motif exhibits the specific structural feature originated from conformation of the *o*-terphenyl moiety as described below. The PhT includes conformational frustration. The two peripheral phenylene groups in the *ortho*-position prefer to incline in the same direction (*P* or *M*) to avoid steric repulsion between them (Fig. 11.6a). Therefore, although we have not observed the PhT motif with three frustrated dimers because of its instability (Fig. 11.6b), the motif

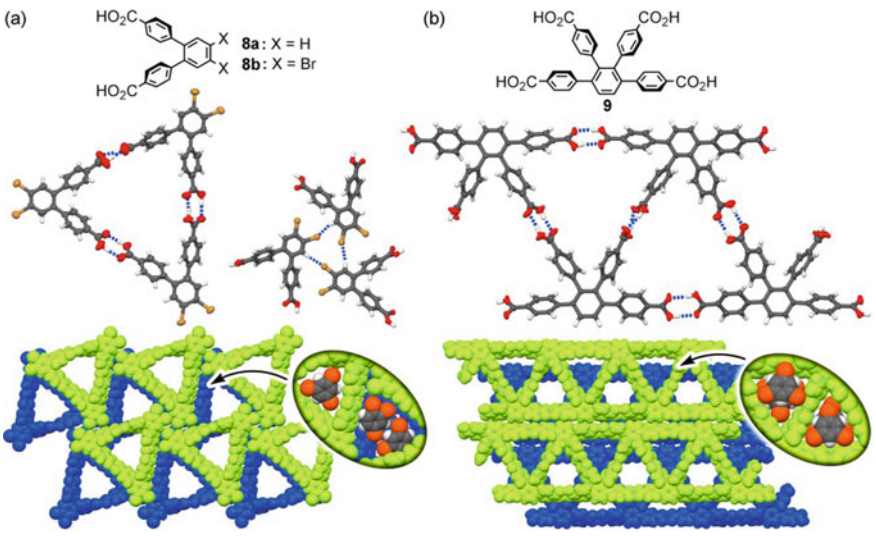

Fig. 11.5 Crystal structures and H-bonded PhT motifs formed by *o*-bis(4-carboxyphenyl)benzene analogues **a 8b**, **b 9**

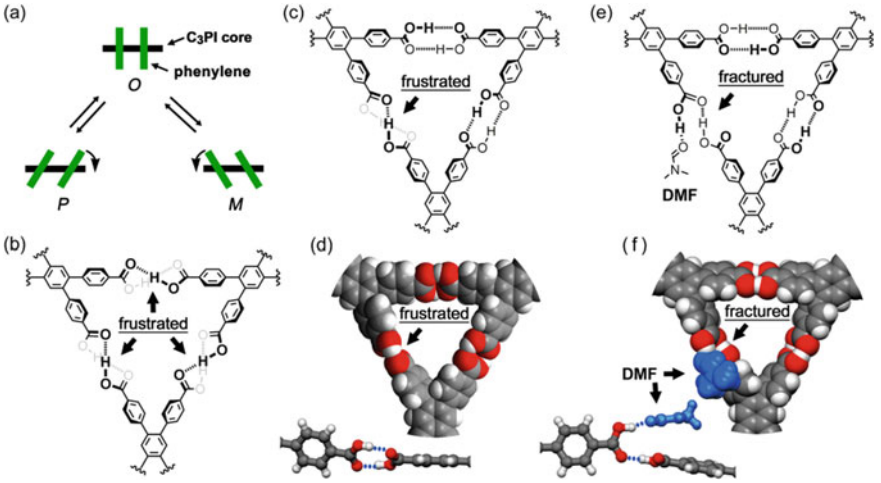

Fig. 11.6 Geometrical feature of PhT motif. **a** Cooperative incline of the peripheral phenylene groups. Chemical structures of **b** PhT with three frustrated dimers, **c** PhT with one frustrated dimer, and **e** PhT with one fractured dimer by insertion of DMF molecules. Selected crystal structures of **d** frustrated and **e** fractured PhT observed in crystals of **T18**

normally includes at least one conformationally frustrated H-bonded carboxy dimer (Fig. 11.6c, d), except for the case that the all phenylene groups are in the orthogonal conformation as in the case of Kobayashi's structure [53]. The conformationally frustrated part is sometimes trapped by polar solvent molecule such as DMF through H-bonding to form "truncated catemer"-type dimer to release the distortion (Fig. 11.6e, f) [54].

11.3 Construction of HOFs Based on Hexagonal Network

Based on the idea described above, C_3PIs possessing three *o*-bis(4-carboxyphenyl)benzene moiety were designed and synthesized (Fig. 11.7). Recrystallization of the compounds was performed by slow evaporation of a mixed solution of a highly polar solvent such as DMF and a high-boiling aromatic solvent such as 124TCB or methyl benzoate (MeBz) at relatively high temperature (50–120 °C), yielding single crystals suitable for SXRD analysis. It is noteworthy that crystallization at relatively low temperature such as at 30 °C results in formation of solvate crystals, in which some of carboxy groups make H-bonds with solvent molecules, preventing formation of completely networked LA-H-HexNet structures.

In the following part, crystal structures and properties of their LA-H-HexNets are described.

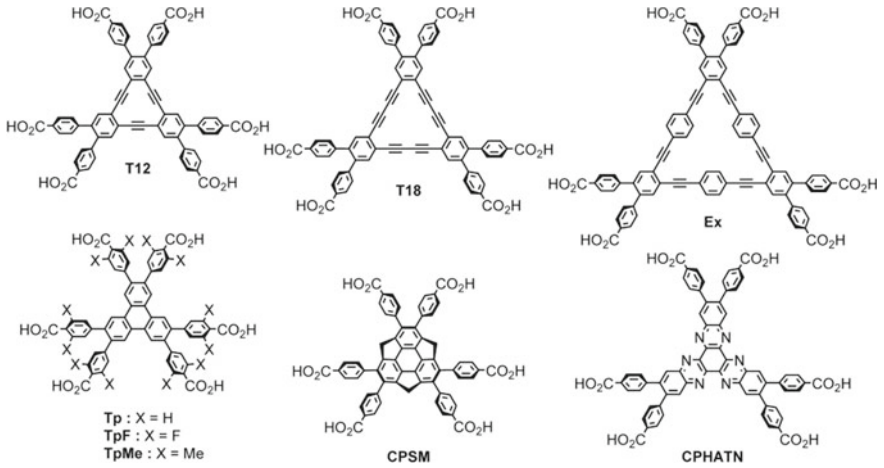

Fig. 11.7 C_3PIs applied to construct HOFs

11.3.1 A Series of Cyclic π-Conjugated Systems with Different Sizes of Macrocycles

C_3PIs **Tp**, **T12**, **T18**, and **Ex** give H-HexNets structures via complemental H-bonding between the carboxy groups (Fig. 11.8a–d) [55]. In the H-HexNet sheet, three kinds of pores are formed. Void I has width of approximately 8 Å is formed within the PhT motif. Void II has a non-regular hexagonal-shaped aperture. Its dimension is varied depending on the size of the core of C_3PIs: The longer sides of void II are the same (15.8 Å) in the four systems, while the shorter sides have various lengths ranging from 2.0 to 11.4 Å. Void III is inherent pores located at the center of the cyclic compounds. The H-HexNet sheets stack without interpenetration to give porous LA-H-HexNets (**Tp-1**, **T12-1**, **T18-1**, and **Ex-1**, respectively). Although the molecules give isostructural H-HexNets sheets, stacking manner of the H-HexNets depends on the molecular structures (Fig. 11.8e–h). The void ratio of **Tp-1**, **T12-1**, **T18-1**, and **Ex-1** calculated by PLATON software with probe radius of 1.2 Å is 54%, 41%, 58%, and 59%, respectively. Aromatic solvent molecules used for recrystallization are accommodated in the voids. The neighbored H-HexNet layers are stacked by weak interactions such as face-to-face (π/π), face-to-edge (CH/π), and CH/O interactions. These weak interlayer interactions, as well as rotational flexibility of the peripheral phenylene rings, allow **Tp** to yield at least four polymorphs of LA-H-HexNets including **Tp-1** [56].

To investigate the structural changes upon removal of solvent molecules from the void space, crystalline bulks of **Tp-2Ds**, **T12-1**, **T18-1**, and **Ex-1** were subjected to varied temperature (VT)-PXRD measurements as shown in Fig. 11.9, where **Tp-2Ds** denotes the crystalline bulk of LA-H-HexNet of **Tp** because it includes either or both of two polymorphic forms **Tp-1** and **Tp-2**. The pattern of the as-formed crystals at first showed almost no recognizable peaks, due to significantly low electron

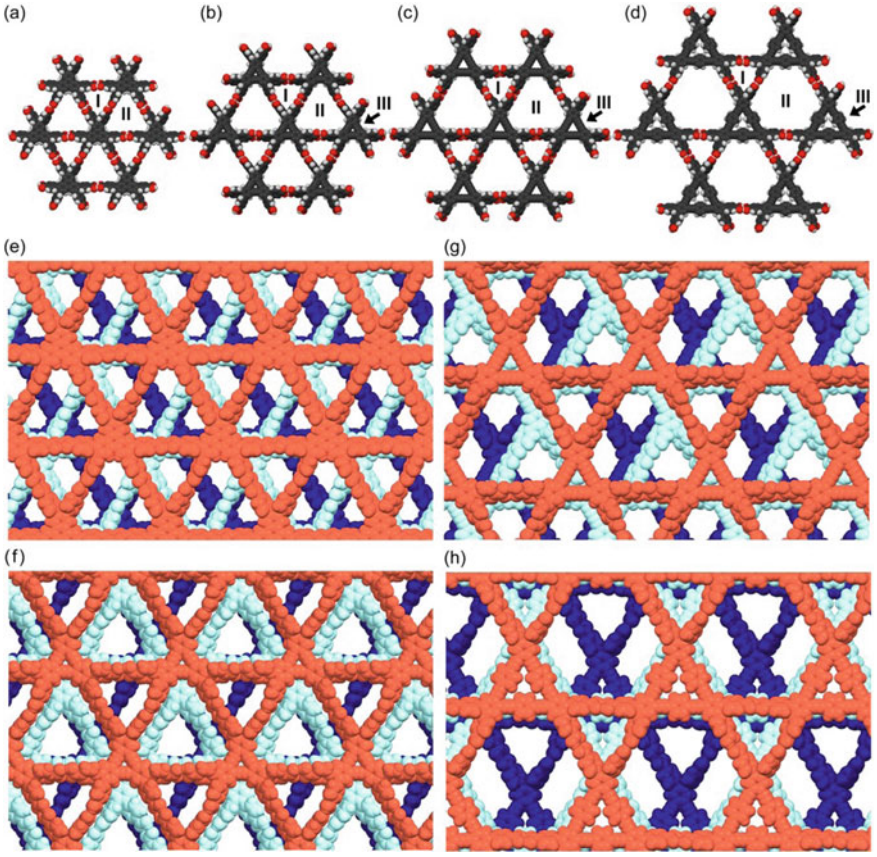

Fig. 11.8 Crystal structures of LA-H-HexNets: **a**, **e Tp-1**, **b**, **f T18-1**, **c**, **g T18**, **d**, **h Ex-1**. **a**–**d** H-HexNet sheet. **e**–**h** Packing diagrams of stacked neighboring three layers. Solvent molecules accommodated in the voids are omitted for clarity

diffraction contrast provided by the low density H-HexNet frameworks composed of no metal but low-weight elements and highly disordered solvent molecules within the frameworks. However, the diffraction peaks became unambiguous upon heating as the solvent molecules were removed. **Tp** and **T18** showed PXRD pattern changes in two or three steps, indicating formation of intermediate phases. After completing removal of the solvents, the materials still exhibit obvious PXRD patterns, which are not in agreement with the original patterns of the solvate crystals, indicating that crystal structure of LA-H-HexNets changes to other crystalline forms upon desolvation. Further increase of the temperature revealed that frameworks of **Tp**, **T12**, **T18**, and **Ex** decomposed at 323 °C, 360 °C, 242 °C, and 249 °C, respectively.

By using PXRD pattern after desolvation, we attempted to identify the crystal structures of activated forms and successfully estimated or solved the reasonable

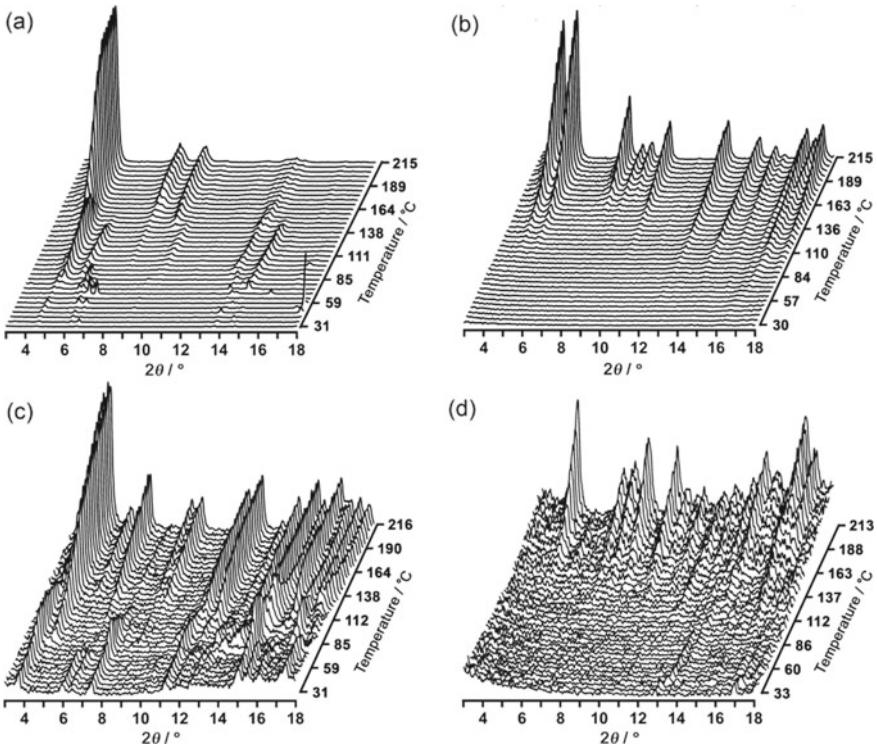

Fig. 11.9 Changes of PXRD ($Cu_{K\alpha}$) patterns of **a Tp-2Ds**, **b T12-1**, **c T18-1**, and **d Ex-1** upon heating from ambient temperature to ca. 215 °C. Temperature was increased at the rate of 1 °C min^{-1}. Patterns were recorded from 3° to 18° of 2θ with the scan rate of 3° min^{-1}. Each scan has a temperature gradient of ca. 5 °C. Since the as-formed crystal of **Tp** includes either or both of two polymorphic forms, the crystalline bulk was referred as **Tp-2Ds**

structures for **Tp-apo** and **T12-apo** by using the crystal structure prediction technique and powder X-ray analysis including the Rietveld refinement, respectively. The activated structures are shown in Fig. 11.10.

It is noteworthy that **Tp-apo** crystal retains a layered structure of H-HexNet sheets with permanent porosity. The adjacent **Tp** cores are stacked with larger overlap compared with **Tp-1** and triangular channels with a diameter of ca. 8.5 Å run along the *c* axis. The void ratio calculated by PLATON software with probe radius of 1.2 Å is 33%. Similarly, **T12-apo** retains a layered structure of HexNet sheets, although H-bonded moieties are partly deformed. **T12** cores are overlapped with an interplanar distance of ca. 3.2 Å through π/π interactions. One-dimensional (1D) channel with a triangular cross section with width of 8.8 Å and branched small voids with a diameter of 2.8 Å are formed. The void ratio of **T12-apo** is calculated to be 38%.

Activation of LA-H-HexNets was conducted by immersing the as-formed crystalline powders into benzene for overnight at room temperature, followed by lying under vacuum condition (0.2 kPa) for 1 day at 40–100 °C, providing HOFs with

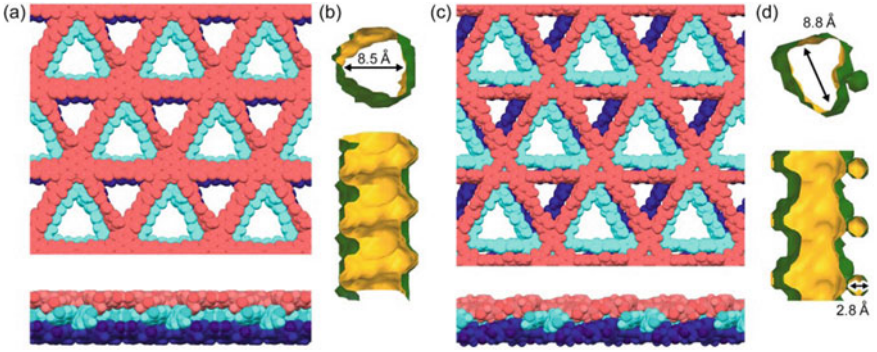

Fig. 11.10 Crystal structures of **a Tp-apo** and **c T12-apo** provided by the crystal structure prediction approach and the Rietveld refinement based on PXRD pattern, respectively. Visualized surface of void channels of **b Tp-apo** and **d T12-apo**

permanent porosity (**Tp-apo**, **T12-apo**, **T18-apo**, and **Ex-apo**). **Tp-apo** and **T12-apo** show a type-I N_2 sorption isotherm at 77 K with an uptake of 187 cm^3g^{-1} and 85.4 cm^3g^{-1}, respectively. Similarly, **Tp-apo** has a type-I sorption isotherm with an uptake of 194 cm^3g^{-1}. SA_{BET} was calculated to be 788 m^2g^{-1}. The SA_{BET} of **T12-apo** was also calculated based on the CO_2 sorption isotherm to be 557 m^2g^{-1}. Although **T18-apo** and **Ex-apo** also absorbed N_2 and CO_2, the details are not shown because of their ambiguous structures.

Interestingly, **T12-apo** shows a two-stepped sorption isotherm with hysteric behavior for CO_2 at 195 K. *In situ* PXRD measurements disclosed that **T12-apo** experiences up to four kinds of crystalline forms (states 1–4) reversibly during CO_2 absorption–desorption process at 195 K (Fig. 11.11) [57]. Although these crystal structures have not been determined precisely, the observed PXRD patterns indicate that the layered structure of the original framework of **T12-apo** changes by distorting the network, slipping of the H-HexNet layers, and/or increasing in the interlayer distance (states 1–4 shown in Fig. 11.11c). These results indicate that layered organic crystals might be more flexible than those previously considered. The results can aid the construction of soft porous crystalline materials.

The H-bonded low-density framework is also demonstrated to be capable of applying as a platform to accomplish an isolated arrangement of finite-numbered clusters of C_{60} molecules. Crystallization of **T18** in the presence of C_{60} gave two types of inclusion crystals **T18-C_{60}-1** and **-2** (Fig. 11.12). Interestingly, void II in **T18-C_{60}-2** accommodates two C_{60} molecules at its corners, and the resulting dimeric array of C_{60} is isolated from the adjacent dimers by the H-HexNet framework. The distance between the centroids of the nearest two C_{60} molecules is 11.2 Å and that between the second nearest two molecules is 15.12 Å. The isolated C_{60} pair observed in the present system is a unique type of C_{60} array. Namely, the present system is regarded as the smallest crystalline system of an finite-number-isolated array of C_{60} and the first example of an isolated C_{60} dimeric pair within a well-defined, H-bonded, low-density framework. These results imply that the present LA-H-HexNet can be

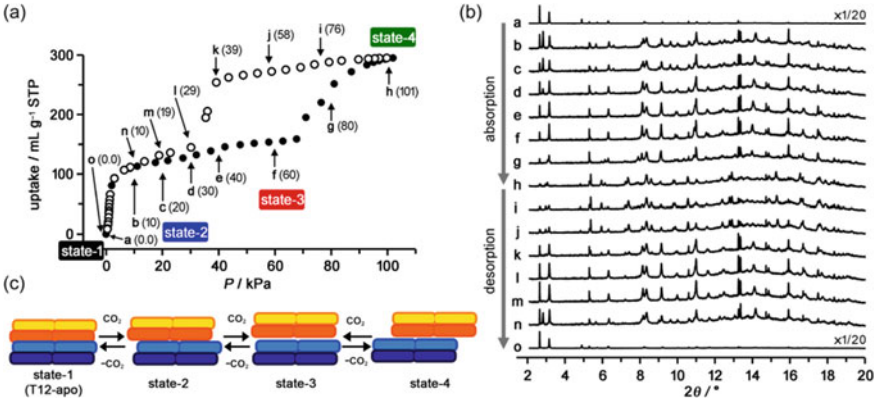

Fig. 11.11 Structural changes of **T12-apo** upon CO_2 sorption at 195 K. **a** CO_2 sorption isotherm, where solid and open symbols denote absorption and desorption processes, respectively. **b** in situ PXRD ($\lambda = 1.000$ Å) patterns of **T12-apo** under a CO_2 adsorption–desorption process at 195 K. Patterns **a**–**o** are recorded under conditions **a**–**o** in the isotherm (**a**). Pressure (/kPa) that the pattern was recorded at is shown in the parentheses. **c** Proposed structural changes including slippage, expansion, and deformation of the layered structure

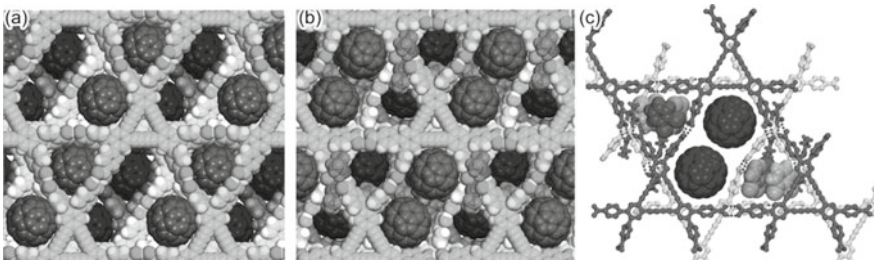

Fig. 11.12 Crystal structures of **a T18-C_{60}-1**, **b T18-C_{60}-2**, and **c** lattice unit of **T18-C_{60}-2**

applied as a platform to align functional molecules, aiming to developing such as artificial photosynthetic systems [58].

11.3.2 Sterically Hindered Hydrogen-Bonding Systems

As described in Sect. 11.2, the peripheral carboxyphenyl groups in the building block molecules are not in coplanar with but twisted against a plane of the central core (Fig. 11.6). This twisted conformation plays a role in stacking ways of the H-HexNets to give layered structures. To explore further effects of twisted conformation of the peripheral groups, triphenylene derivatives (**TpMe** and **TpF**) with substituents (Me or F) in the *ortho*-positions of the carboxy groups were designed and synthesized

[59]. The substitution is expected to force the carboxy and phenylene groups to be twisted (Fig. 11.13), and therefore, to change molecular arrangements and properties of the resultant networked crystals.

Although computational calculation revealed that both substituent groups −F and −Me at the *ortho*-positions had no effects on binding energy of H-bonded dimerization (~15 kcal/mol), the substituents made the both carboxy and phenylene groups twisted, resulting increase of variability of the peripheral conformation. As shown in Fig. 11.14a–c, **TpMe** gave three polymorphs that exhibit different peripheral conformations and stacking manners of the H-HexNet layers. On the other hand, **TpF** yielded one crystalline form (Fig. 11.14d–f). However, in the crystals both carboxy and difluorophenylene groups are highly disordered. These observations indicate that introduction of the substituents on the *ortho*-position results high degree of freedom on the peripheral conformation, which results in generation of polymorphs in the case of larger substituent (i.e. **TpMe**), while in the case of smaller substituent (i.e. **TpF**), the single form with highly disordered local structures yields. Thermal stability and permanent porosity are drastically changed by the substituents even the both crystals have quite similar LA-H-HexNet structures. Regarding thermal stability of the LA-H-HexNets, the framework of **Tp** decomposes at 323 °C, while those of **TpF** and **TpMe** at 301 °C and 155 °C, respectively. Especially, the framework of **TpF** tends to lose its crystallinity as heating. Activation of **TpF** and **TpMe** was performed by solvent exchanging with benzene followed by heating up to 100 °C to yield porous materials **TpF-1a** and **TpMe-1a**, respectively, although their crystallinity was relatively low. SA_{BET} of **TpF-1a** and **TpMe-1a** was determined by CO_2 sorption isotherms at 195 K to be 561 m^2g^{-1} and 219 m^2g^{-1}, respectively. Only **TpF-1a** shows selective sorption of CO_2 over N_2.

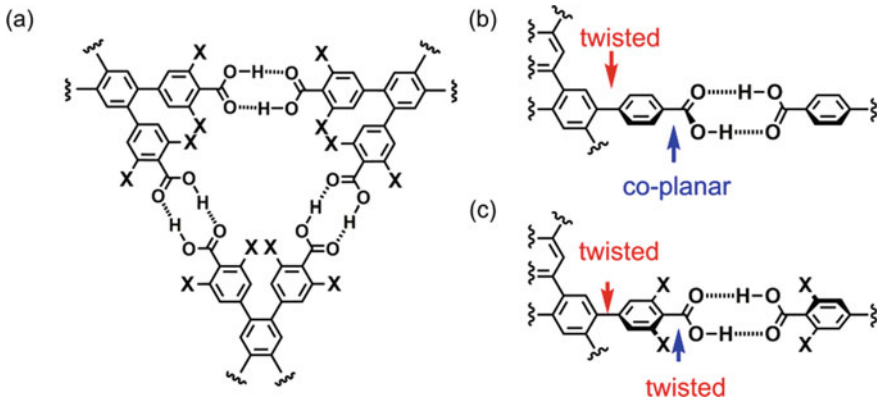

Fig. 11.13 **a** Sterically crowded PhT motif. Conformation of peripheral carboxyphenyl group, **b** without and **c** with substituents at the *ortho*-positions of the carboxy group

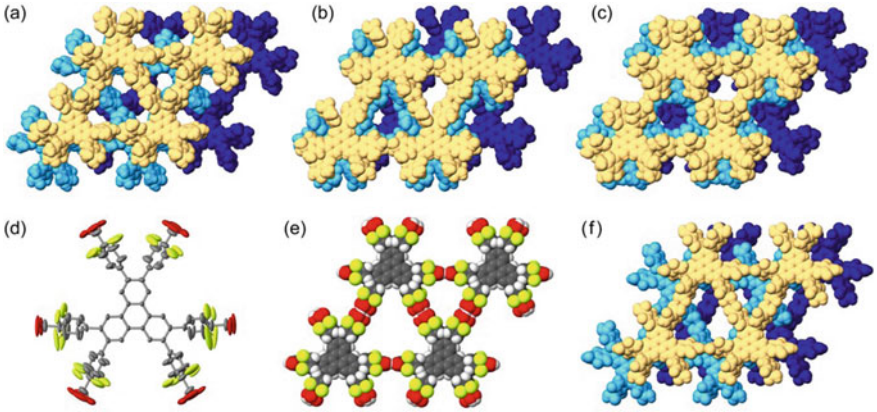

Fig. 11.14 Crystal structures of three polymorphs of **TpMe** (Top) and **TpF-1** crystal (bottom). **a TpMe-1**, **b TpMe-2**, **c TpM-3**. **d** Molecular structure of **TpF** with anisotropic displacement ellipsoids with 50% probability. **e** Rhombic motif of **TpF-1** with local disorder. **f** Layered framework, which is drawn with one of the disordered structures for clarity reason. Solvent molecules accommodated in the voids are omitted for clarity

11.3.3 Bowl-Shaped C_3PI: A Sumanene Derivative

Former sections describe that planar C_3PIs, such as the triphenylene derivative (**Tp**), form porous H-HexNet structures and that the H-HexNet sheet stacks without interpenetration to give crystalline porous layered frameworks [56]. On the other hand, a periodic 2D framework composed of non-planar π-conjugated molecules is also attractive because such a framework with curved and bumpy surface is expected to show unique electronic, chemical, or physical properties originating from the curved π-system. Furthermore, it also can provide useful information how curved building blocks achieve fully networked layered assemblies. Keeping this in mind, we planned to construct a H-bonded 2D framework by using the C_3-symmetric buckybowl, sumanene [60].

CPSM gives three types of crystals, two of which are revealed to have H-bonded HexNet structures (Fig. 11.15). In crystal **CPSM-1**, all carboxy groups of **CPSM** form a H-bonded dimer, and the molecules are connected via the PhT motif, giving a waved H-HexNet sheet with a periodicity of 35.3 Å along the *b* axis due to an alternate alignment of bowl-up and bowl-down buckybowls. Because of geometrically mismatched unfavorable H-bonds, two carboxyphenyl groups bend outward and the bowl becomes shallower: The bowl depth (BD) is 0.985 Å, which is smaller than optimized pristine sumanene (1.11 Å) [61]. Void within and between the waved H-HexNet sheets are filled by solvent molecules, and the void ratio is calculated to be 63% by PLATON software with probe radius of 1.2 Å.

In crystal **CPSM-2**, the molecule forms a hamburger-like dimer possessing internal void with volume of 140 $Å^3$ by interdigitating peripheral phenylene groups. The dimers are connected through a trefoil knot shaped H-bonding motif to form

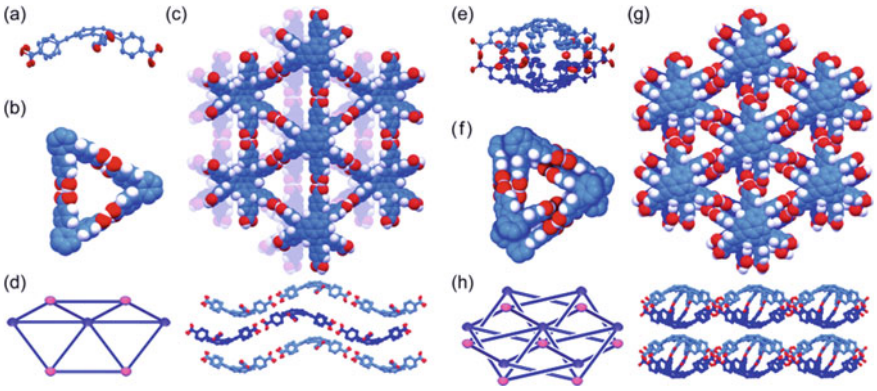

Fig. 11.15 Crystal structures of H-bonded networks **CPSM-1** (**a**–**d**) and **CPSM-2** (**e**–**g**). **a**, **e** Side view of **CPSM** molecule and dimer, respectively. **b**, **f** H-bonded motifs: PhT and trefoil knot, respectively. **c**, **g** Selected packing diagram. **d**, **h** Topological illustration of the networked structures

a 2D HexNet bilayer. The six peripheral carboxy groups of **CPSM** are capable of forming H-bonds without severe geometrical mismatch: The BD is 1.15 Å. The total void ratio is calculated to be 48%. Regarding network topology, **CPSM-1** has a six-connected two-dimensional uninodal *hxl* net. **CPSM-2** also has a six-connected two-dimensional network, while the topology of the network has been hitherto unknown (Fig. 11.15d, h).

Crystal structures composed of **CPSM** have less contact between the neighboring layers, compared with **Tp-1**, due to their bumpy surfaces. This inspires us to explore whether the crystals can be deformed by compression. The single crystals of **CPSM-1** and **CPSM-2** were subjected to X-ray diffraction analysis under high-pressure conditions. Although **CPSM-1** lost its crystallinity under high pressure, crystal **CPSM-2** kept its single crystallinity and showed significant anisotropic changes of the cell parameters upon addition of isotropic hydrostatic fluid pressure. The crystallographic *c* axis of **CPSM-2** under 970 MPa was shortened by 11.0% compared with that under ambient pressure, while the other parameters showed subtle changes (Fig. 11.16a). These changes were irreversible and the shrunk cell remained after release of the pressure. SXRD analysis at 970 MPa revealed that the bilayered H-HexNet sheets slipped in a deeply offset stacking fashion and that interlayer distance became shorter. As shown in Fig. 11.16b, c, two contacted **CPSM** molecules (I and II) are slipped along their curved surfaces, resulting in shrinkage of interlayer distance and decrease of overlap between **CPSM** cores. Such a dynamic behavior between non-planar sheets is hitherto unknown and can provide new insights into 2D-networked architectures based on non-planar π-conjugated systems.

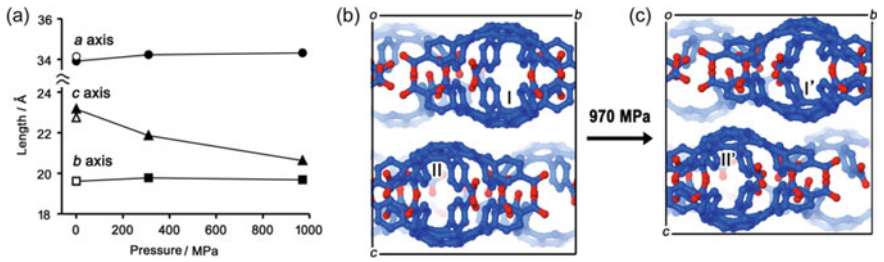

Fig. 11.16 Anisotropic structural changes of **CPSM-2** crystal under 970 MPa. **a** Changes in the unit cell upon increasing pressure. Open symbols refer the cell parameters obtained from SXRD analysis conducted at −120 °C under ambient pressure. Closed symbols refer those obtained from SXRD analysis conducted at ambient temperature with varying pressure. Molecular packing, **b** under ambient pressure at −120 °C and **c** under 970 MPa at 20 °C

11.3.4 Nitrogen-Incorporated C_3PI: A Hexaazatrinaphthylene Derivative

Introducing nitrogen atoms into polycyclic aromatic hydrocarbons is capable of altering frontier orbital levels and of interacting and coordinating with cationic species such as metal ions, proton, and other organic cations. Therefore, HOFs composed of such N-hetero-π-conjugated molecules are expected to show multi-functionality. Regarding this, we planned to construct LA-H-HexNets with a hexaazatrinaphthylene derivative **CPHATN** possessing carboxyphenyl substituents [62].

CPHATN forms the PhT motif via H-bonding of carboxy groups to give a H-HexNet sheet, which then stacks without interpenetration to give a LA-H-HexNet **CPHATN-1(124TCB)** (Fig. 11.17a, b). It is noteworthy that carboxy groups form no H-bond with the basic pyrazine moieties, which remains non-bonded in the crystal and play a role for acid responsiveness as described later. The framework has 1D channels with width of 6.2 Å, in which 124TCB molecules used for crystallization are accommodated. A void ratio calculated by PLATON software with probe radius of 1.2 Å was 26%.

TG analysis of **CPHATN-1(124TCB)** showed weight loss of 22% up to ca. 250 °C, indicating that the framework contains 124TCB with a host–guest ratio of 1:2 (calc. 25%) and solvent molecules were completely removed at around this temperature (Fig. 11.18a). VT-PXRD experiments of as-formed crystalline bulk of **CPHATN-1(124TCB)** were subsequently carried out as shown in Fig. 11.18b. The initial patterns at around room temperature are not clear as in the case of other systems described in Fig. 11.9. Upon heating, peaks started to appear at 83 °C and slightly shifted to wider angle up to 114 °C, indicating subtle shrinkage of the crystallographic cell. Subsequently, the peak intensity increased as heating, reached plateau at ca. 250 °C, and remained up to 360 °C, indicating that the framework is extremely stable and rigid enough to retain the porous structure at high temperature. SXRD analysis of the activated framework, **CPHATN-1a**, gave almost the same crystal

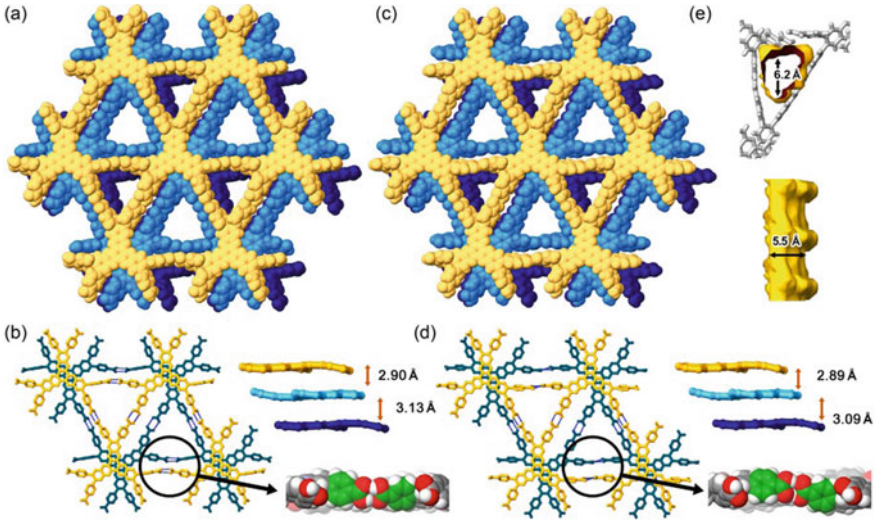

Fig. 11.17 Crystal structures of as-formed solvate **CPHATN-1(124TCB)** (**a**, **b**) and activated form **CPHATN-1a** (**c**–**e**), solved by SXRD analysis. **a**, **c** Stacked three layers of H-HexNet sheets. **b**, **d** Relative orientation of the stacked layers, where structural changes upon activation were observed in the conformationally frustrated carboxylic acid dimers in circles. **e** Visualized surface of the void

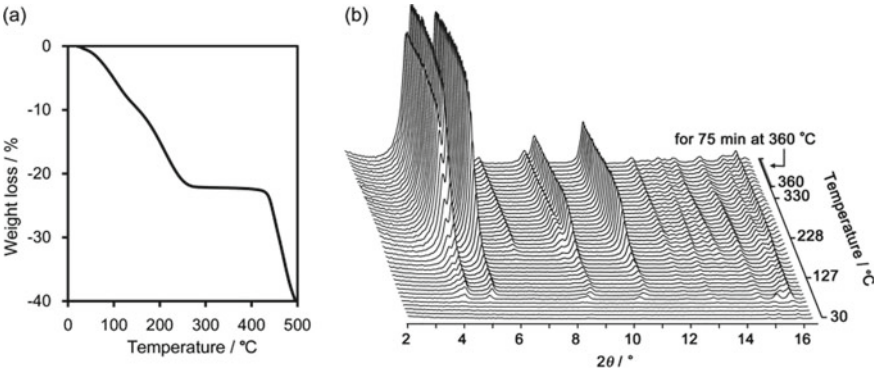

Fig. 11.18 Thermal behavior of **CPHATN-1(124TCB)**. **a** TG analysis. **b** VT-PXRD pattern changes upon heating from room temperature to 360 °C

structure, in which conformationally frustrated dimer was slightly deformed when compared with the structure of **CPHATN-1(124TCB)** as shown in Fig. 11.17c, d. The void is slightly shrunk from 26 to 20%. SA_{BET} was estimated based on N_2 sorption isotherm at 77 K to be 379 m^2g^{-1}.

Interestingly, **CPHATN-1a** changes its color from yellow to reddish-brown when exposed to both 37%-HCl aqueous solution and HCl vapor (Fig. 11.19a). Its fluorescence also can be switched OFF or ON in presence or removing of the acid. These

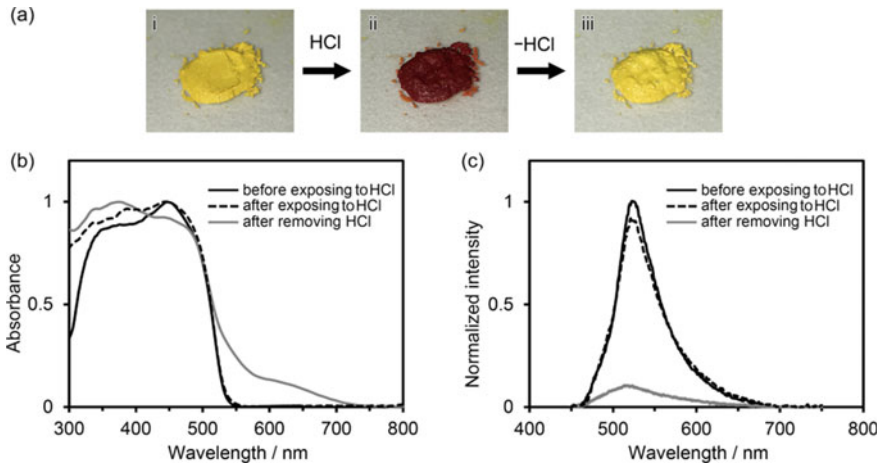

Fig. 11.19 HCl responsive color changes of **CPHATN-1a**. **a** Photographs of the crystalline bulk (i) before experiment, (ii) after 37%-HCl was dropped on, and (iii) after removing HCl by heating at 150 °C for 30 min. **b** Absorption and **c** emission spectral changes of the crystalline bulk upon exposure to HCl atmosphere for 40 min and after removing HCl by leaving in air for 48 h

changes are reversible. The absorption spectrum exhibits a new band at 500–600 nm upon the exposure (Fig. 11.19b). Simultaneously, the emission band at 539 nm is strongly quenched (Fig. 11.19c). These observations clearly indicate the sensitivity of this HOF to HCl vapors and explain in terms of interactions between the protons and basic nitrogen atoms incorporated in the HATN core. Removal of HCl from the HOF resulted in recover of the original absorption and emission spectra. This is, to our knowledge, the first example of HOFs with external stimuli responsiveness in color and emission. The present results would open a door to develop a new porous materials with stimuli responsiveness.

11.4 Conclusion

It has been regarded that a H-bond is too weak interaction to apply for construction of supramolecular architectures possessing self-standing large pores. Such concernment, however, is about to be gone away. It is getting easy to construct HOFs with permanent porosity by introducing secondary interacting moieties capable of forming well-fitted intermolecular contacts to support the H-bonded networks, in addition to suitable selection of supramolecular synthons and molecular skeleton, namely H-bonding moieties that allow highly directional H-bonds with predictable manners and rigid molecular skeletons with exclusive degree of conformational freedom. As examples of such designed HOFs, we described LA-H-HexNets

composed of C_3-symmetric π-conjugated molecules (C_3PIs) possessing three *o*-bis(4-carboxyphenyl)benzene moieties in the periphery. Thanks to the triangular H-bonded motif named phenylene triangle (PhT), C_3PIs can form isostructural H-HexNet sheets, which further stack via secondary intermolecular interactions such as a π/π interaction to give layered HOFs. Moreover, we revealed that even bowl-shaped C_3PI form H-bonded, 2D networked structures, in which all of carboxy groups satisfied through formation of H-bonded dimer. These results can make us realize promising potentials of HOFs. Once the construction ways of HOFs have been established, the properties and functionality of HOFs begin to be investigated. As reported by Cooper and Day, high-throughput exploration for development of functional porous materials is becoming possible by combining with theoretical calculation and robotics [63]. We hope that we would report multifunctional HOFs in the near future.

References

1. Allcock, H.R., Siegel, L.A.: Phosphonitrilic compounds. III. Molecular inclusion compounds of tris(*o*-phenylenedioxy)phosphonitrile trimer. J. Am. Chem. Soc. **86**, 5140–5144 (1964)
2. Sozzani, P., Comotti, A., Simonutti, R., Meersmann, T., Logan, J.W., Pines, A.: A porous crystalline molecular solid explored by hyperpolarized xenon. Angew. Chem. Int. Ed. **39**, 2695–2698 (2000)
3. Sozzani, P., Bracco, S., Comotti, A., Ferretti, L., Simonutti, R.: Methane and carbon dioxide storage in a porous van der Waals crystal. Angw. Chem. Int. Ed. **44**, 1816–1820 (2005)
4. Atwood, J.L., Davies, J.E.D., MacNicol, D.D. (eds.): Inclusion Compounds, vol. 1–3. Academic Press, London (1984)
5. Barbour, L.J.: Crystal porosity and the burden of proof. Chem. Comm. 1163–1168 (2006)
6. Tian, J., Thallapally, P.K., McGrail, B.P.: Porous organic molecular materials. CrystEngComm **14**, 1909–1919 (2012)
7. Mastalerz, M.: Permanent Porous materials from discrete organic molecules—towards ultra-high surface areas. Chem. Eur. J. **18**, 10082–10091 (2012)
8. Atwood, J.L., Barbour, L.J., Jerga, A.: Storage of methane and freon by interstitial van der Waals confinement. Science **296**, 2367–2369 (2002)
9. Adach, T., Ward, M.D.: Versatile and resilient hydrogen-bonded host frameworks. Acc. Chem. Res. **49**, 2669–2679 (2016)
10. Lu, J., Cao, R.: Porous organic molecular frameworks with extrinsic porosity: a platform for carbon storage and separation. Angew. Chem. Int. Ed. **55**, 9474–9480 (2016)
11. Luo, J., Wang, J.-W., Zhang, J.-H., Lai, S., Zhong, D.-C.: Hydrogen-bonded organic frameworks: design, structures and potential applications. Zhong, CrystEngComm **20**, 5884–5898 (2018)
12. Lin, R.-B., He, Y., Li, P., Wang, H., Zhou, W., Chen, B.: Multifunctional porous hydrogen-bonded organic framework materials. Chen. Chem. Soc. Rev. **48**, 1362–1389 (2019)
13. Hisaki, I., Chen, X., Takahashi, K., Nakamura, T.: Designing hydrogen-bonded organic frameworks (HOFs) with permanent porosity. Angew. Chem. Int. Ed. **58**, 11160–11170 (2019)
14. He, Y., Xiang, S., Chen, B.: A microporous hydrogen-bonded organic framework for highly selective C_2H_2/C_2H_4 separation at ambient temperature. J. Am. Chem. Soc. **133**, 14570–14573 (2011)
15. Maly, K.E., Gagnon, E., Maris, T., Wuest, J.D.: Engineering hydrogen-bonded molecular crystals built from derivatives of hexaphenylbenzene and related compounds. J. Am. Chem. Soc. **129**, 4306–4322 (2007)

16. Yang, J., Dewal, M.B., Profeta, S., Smith Jr., M.D., Li, Y., Shimizu, L.S.: Origins of selectivity for the [2 + 2] cycloaddition of α, β-unsaturated ketones within a porous self-assembled organic Framework. J. Am. Chem. Soc. **130**, 612–621 (2008)
17. Comotti, A., Bracco, S., Distefano, G., Sozzani, P.: Methane, carbon dioxide and hydrogen storage in nanoporous dipeptide-based materials. Chem. Commun. 284–286 (2009)
18. Yang, W., Greenaway, A., Lin, X., Matsuda, R., Blake, A.J., Wilson, C., Lewis, W., Hubberstey, P., Kitagawa, S., Champness, N.R., Schröder, M.: Exceptional thermal stability in a supramolecular organic framework: porosity and gas storage. J. Am. Chem. Soc. **132**, 14457–14469 (2010)
19. Mastalerz, M., Oppel, I.: Rational construction of an extrinsic porous molecular crystal with an extraordinary high specific surface area. Angew. Chem. Int. Ed. **51**, 5252–5255 (2012)
20. Luo, X.-Z., Jia, X.-J., Deng, J.-H., Zhong, J.-L., Liu, H.-J., Wang, K.-J., Zhong, D.-C.: A microporous hydrogen-bonded organic framework: exceptional stability and highly selective adsorption of gas and liquid. J. Am. Chem. Soc. **135**, 11684–11687 (2013)
21. Lü, J., Perez-Krap, C., Suyetin, M., Alsmail, N.H., Yan, Y., Yang, S., Lewis, W., Bichoutskaia, E., Tang, C.C., Blake, A.J., Cao, R., Schröder, M.: A robust binary supramolecular organic framework (SOF) with high CO_2 adsorption and selectivity. J. Am. Chem. Soc. **136**, 12828–12831 (2014)
22. Comotti, A., Bracco, S., Yamamoto, A., Beretta, M., Hirukawa, T., Tohnai, N., Miyata, M., Sozzani, P.: Engineering switchable rotors in molecular crystals with open porosity. J. Am. Chem. Soc. **136**, 618–621 (2014)
23. Chen, T.-H., Popov, I., Kaveevivitchai, W., Chuang, Y.-C., Chen, Y.-S., Daugulis, O., Jacobson, A.J., Miljanić, O.Š.: Thermally robust and porous noncovalent organic framework with high affinity for fluorocarbons and CFCs. Nat. Commun. **5**, 5131 (2014)
24. Tian, J., Zhou, T.-Y., Zhang, S.-C., Aloni, S., Altoe, M.V., Xie, S.-H., Wang, H., Zhang, D.-W., Zhao, X., Liu, Y., Li, Z.-T.: Three-dimensional periodic supramolecular organic framework ion sponge in water and microcrystals. Nat. Commun. **5**, 5574 (2014)
25. Li, P., He, Y., Zhao, Y., Weng, L., Wang, H., Krishna, R., Wu, H., Zhou, W., O'Keeffe, M., Han, Y., Chen, B.: A rod-packing microporous hydrogen-bonded organic framework for highly selective separation of C_2H_2/CO_2 at room temperature. Angew. Chem. Int. Ed. **54**, 574–577 (2015)
26. Wang, H., Li, B., Wu, H., Hu, T.-L., Yao, Z., Zhou, W., Xiang, S., Chen, B.: A flexible microporous hydrogen-bonded organic framework for gas sorption and separation. J. Am. Chem. Soc. **137**, 9963–9970 (2015)
27. Yadav, V.N., Comotti, A., Sozzani, P., Bracco, S., Bonge-Hansen, T., Hennum, M., Görbitz, C.H.: Microporous molecular materials from dipeptides containing non-proteinogenic sesidues. Angew. Chem. Int. Ed. **54**, 15684–15688 (2015)
28. Zentner, C.A., Lai, H.W.H., Greenfield, J.T., Wiscons, R.A., Zeller, M., Campana, C.F., Talu, O., FitzGerald, S.A., Rowsell, J.L.C.: High surface area and Z' in a thermally stable 8-fold polycatenated hydrogen-bonded framework. Chem. Commun. **51**, 11642–11645 (2015)
29. Nandi, S., Chakraborty, D., Vaidhyanathan, R.: A permanently porous single molecule H-bonded organic framework for selective CO_2 capture. Chem. Commun. **52**, 7249–7252 (2016)
30. Yang, W., Wang, J., Wang, H., Bao, Z., Zhao, J.C.-G., Chen, B.: Highly interpenetrated robust microporous hydrogen-bonded organic framework for gas separation. Cryst. Growth Des. **17**, 6132–6137 (2017)
31. Hu, F., Liu, C., Wu, M., Pang, J., Jiang, F., Yuan, D., Hong, M.: An ultrastable and easily regenerated hydrogen-bonded organic molecular framework with permanent porosity. Angew. Chem. Int. Ed. **56**, 2101–2104 (2017)
32. Hisaki, I., Ikenaka, N., Gomez, E., Cohen, B., Tohnai, N., Douhal, A.: Hexaazatriphenylene-based hydrogen-bonded organic framework with permanent porosity and single-crystallinity. Chem. Eur. J. **23**, 11611–11619 (2017)
33. Hisaki, I., Suzuki, Y., Gomez, E., Cohen, B., Tohnai, N., Douhal, A.: Docking strategy to construct thermostable, single-crystalline, hydrogen-bonded organic framework with high surface area. Angew. Chem. Int. Ed. **57**, 12650–12655 (2018)

34. Yin, Q., Zhao, P., Sa, R.-J., Chen, G.-C., Lü, J., Liu, T.-F., Cao, R.: An ultra-robust and crystalline redeemable hydrogen-bonded organic framework for synergistic chemo-photodynamic therapy. Angew. Chem. Int. Ed. **57**, 7691–7696 (2018)
35. Yamagishi, H., Sato, H., Hori, A., Sato, Y., Matsuda, R., Kato, K., Aida, T.: Self-assembly of lattices with high structural complexity from a geometrically simple molecule. Science **361**, 1242–1246 (2018)
36. Hashim, M.I., Le, H.T.M., Chen, T.-H., Chen, Y.-S., Daugulis, O., Hsu, C.-W., Jacobson, A.J., Kaveevivitchai, W., Liang, X., Makarenko, T., Miljanić, O.Š., Popovs, I., Tran, H.V., Wang, X., Wu, C.-H., Wu, J.I.: Dissecting porosity in molecular crystals: influence of geometry, hydrogen bonding, and [π···π] stacking on the solid-state packing of fluorinated aromatics. J. Am. Chem. Soc. **140**, 6014–6026 (2018)
37. Gomez, E., Gutierrez, M., Cohen, B., Hisaki, I., Douhal, A.: Single crystal fluorescence behavior of a new HOF material: potential candidate for a new LED. J. Mater. Chem. C **6**, 6929–6939 (2018)
38. Bassanetti, I., Bracco, S., Comotti, A., Negroni, M., Bezuidenhout, C., Canossa, S., Mazzeo, P.P., Marchil, L., Sozzani, P.: Flexible porous molecular materials responsive to CO_2, CH4 and Xe stimuli. J. Mater. Chem. A **6**, 14231–14239 (2018)
39. Li, P., Li, P., Ryder, M.R., Liu, Z., Stern, C.L., Farha, O.L., Stoddart, J.F.: Interpenetration isomerism in triptycene-based hydrogen-bonded organic frameworks. Angew. Chem. Int. Ed. **58**, 1664–1669 (2019)
40. Han, B., Wang, H., Wang, C., Wu, H., Zhou, W., Chen, B., Jiang, J.: Postsynthetic metalation of a robust hydrogen-bonded organic framework for heterogeneous catalysis. J. Am. Chem. Soc. **141**, 8737–8740 (2019)
41. Gomez, E., Suzuki, Y., Hisaki, I., Moreno, M., Douhal, A.: Spectroscopy and dynamics of a HOF and its molecular units: remarkable vapor acid sensing. J. Mater. Chem. C **7**, 10818–10832 (2019)
42. Pulido, A., Chen, L., Kaczorowski, T., Holden, D., Little, M.A., Chong, S.Y., Slater, B., McMahon, D.P., Bonillo, B., Stackhouse, C.J., Stephenson, A., Kane, C.M., Clowes, R., Hasell, T., Cooper, A.I., Day, G.M.: Functional materials discovery using energy-structure-function maps. Nature **543**, 657–666 (2017)
43. Day, G.M., Cooper, A.I.: Energy–structure–function maps: cartography for materials discovery. Adv. Mater. 1704944 (2017)
44. Desiraju, G.R.: Supramolecular synthons in crystal engineering—a new organic synthesis. Angew. Chem. Int. Ed. Engl. **34**, 2311–2327 (1995)
45. Ivasenko, O., Perepichka, D.F.: Mastering fundamentals of supramolecular design with carboxylic acids common lessons from X-ray crystallography and scanning tunneling microscopy. Chem. Soc. Rev. **40**, 191–206 (2011)
46. Moulton, B., Zawarotko, M.J.: From molecules to crystal engineering: supramolecular isomerism and polymorphism in network solids. Chem. Rev. **101**, 1629–1658 (2001)
47. Duchamp, D.J., Marsh, R.E.: The crystal structure of trimesic acid (benzene-1,3,5-tricarboxylic acid). Acta Crystallogr. B **25**, 5–19 (1969)
48. Herbstein, F.H., Kapon, M., Reisner, G.M.: Catenated and non-catenated inclusion complexes of trimesic acid. J. Inclusion Phenom. **5**, 211–214 (1987)
49. Miyaura, N., Suzuki, A.: Palladium-catalyzed cross-coupling reactions of organoboron compounds. Chem. Rev. **95**, 2457–2483 (1995)
50. Hisaki, I., Sakamoto, Y., Shigemitsu, H., Tohnai, N., Miyata, M., Seki, S., Saeki, A., Tagawa, S.: Superstructure-dependent optical and electrical properties of an unusual face-to-face, π-stacked, one-dimensional assembly of dehydrobenzo[12]annulene in the crystalline state. Chem. Eur. J. **14**, 4178–4187 (2008)
51. Hisaki, I., Senga, H., Sakamoto, Y., Tuzuki, S., Tohnai, N., Miyata, M.: Specific interaction between chloroform and the pockets of triangular annulene derivatives providing symmetry carry-over crystallization. Chem. Eur. J. **15**, 13336–13340 (2009)
52. Hisaki, I., Senga, H., Shigemitsu, H., Tohnai, N., Miyata, M.: Construction of 1D π-stacked superstructures with inclusion channels through symmetry-decreasing crystallization of discotic molecules of C_3 symmetry. Chem. Eur. J. **17**, 14348–14353 (2011)

53. Kobayashi, K., Shirasaka, T., Horn, E., Furukawa, N.: Two-dimensional hexagonal hydrogen-bonded network with triangle-like large cavities: hexakis(4-carboxyphenyl)benzene. Tetrahedron Lett. **41**, 89–93 (2000)
54. Hisaki, I., Nakagawa, S., Tohnai, N., Miyata, M.: A C_3-symmetric macrocycle-based, hydrogen-bonded, multiporous hexagonal network as a motif of porous molecular crystals. Angew. Chem. Int. Ed. **54**, 3008–3012 (2015)
55. Hisaki, I., Nakagawa, S., Ikenaka, N., Imamura, Y., Katouda, M., Tashiro, M., Tsuchida, H., Ogoshi, T., Sato, H., Tohnai, N., Miyata, M.: A series of layered assemblies of hydrogen-bonded, hexagonal networks of C_3-symmetric π-conjugated molecules: a potential motif of porous organic materials. J. Am. Chem. Soc. **138**, 6617–6628 (2016)
56. Hisaki, I., Ikenaka, N., Tohnai, N., Miyata, M.: Polymorphs of layered assemblies of hydrogen-bonded hexagonal networks caused by conformational frustration. Chem. Commun. **52**, 300–303 (2016)
57. Hisaki, I., Nakagawa, S., Suzuki, Y., Tohnai, N.: CO_2 sorption of layered hydrogen-bonded organic framework causes reversible structural changes involving four different crystalline states under ambient pressure. Chem. Lett. **47**, 1143–1146 (2018)
58. Hisaki, I., Nakagawa, S., Sato, H., Tohnai, N.: Alignment of paired molecules of C_{60} within a hexagonal platform net-worked through hydrogen bonds. Chem. Commun. **52**, 9781–9784 (2016)
59. Hisaki, I., Ikenaka, N., Tsuzuki, S., Tohnai, N.: Sterically crowded hydrogen-bonded hexagonal network frameworks. Mater. Chem. Front. **2**, 338–346 (2018)
60. Hisaki, I., Toda, H., Sato, H., Tohnai, N., Sakurai, H.: A hydrogen-bonded hexagonal buckybowl framework. Angew. Chem. Int. Ed. **56**, 15294–15298 (2017)
61. Sakurai, H., Daiko, T., Sakane, H., Amaya, T., Hirao, T.: Structural elucidation of sumanene and generation of Its benzylic anions. J. Am. Chem. Soc. **127**, 11580–11581 (2005)
62. Hisaki, I., Suzuki, Y., Gomez, E., Ji, Q., Tohnai, N., Nakamura, T., Douhal, A.: Acid responsive hydrogen-bonded organic frameworks. J. Am. Chem. Soc. **141**, 2111–2121 (2019)
63. Greenaway, R.L., Santolini, V., Bennison, M.J., Alston, B.M., Pugh, C.J., Little, M.A., Miklitz, M., Eden-Rump, E.G.B., Clowes, R., Shakil, A., Cuthbertson, H.J., Armstrong, H., Briggs, M.E., Jelfs, K.E., Cooper, A.I.: High-throughput discovery of organic cages and catenanes using computational screening fused with robotic synthesis. Nat. Commun. **9**, 2849 (2018)

Chapter 12
Kinetic Assembly of Porous Coordination Networks Leads to Trapping Unstable Elemental Allotropes

Hiroyoshi Ohtsu, Pavel M. Usov, and Masaki Kawano

Abstract Kinetic assembly is an important method for obtaining desired materials in chemical synthesis and material sciences. However, the application of this strategy to porous coordination networks has been limited. We highlight the kinetic assembly of porous coordination networks, which promote the production of interactive pore sites. These sites can activate or stabilize different guest molecules. The properties of interactive pores are exemplified by iodine chemisorption and small sulfur encapsulation. Using the interactive feature of these pores, we were able to trap small sulfur allotropes, such as S_2, cyclo-S_3, bent-S_3, and S_6, demonstrating their importance for the stabilization of unusual elemental species. Furthermore, several reactive elemental allotropes could also be incorporated into the interactive pores. Herein, we address the important aspects of creating interactive pore sites by kinetic assembly of porous coordination networks and present detailed case-by-case studies of small allotrope encapsulation.

Keywords Porous coordination network · Kinetic assembly · Unstable small sulfur species · Elemental allotropes

12.1 Introduction

12.1.1 Scope of the Book Chapter

The kinetic assembly method for the coordination network formation is introduced in this chapter. This method is not common in coordination network chemistry, despite it having a great capacity to create functional materials. Furthermore, the kinetically assembled networks enabled us to successfully trap and visualize unstable elemental allotropes.

H. Ohtsu · P. M. Usov · M. Kawano (✉)
Tokyo Institute of Technology, Tokyo, Japan
e-mail: mkawano@chem.titech.ac.jp

M. Sakamoto and H. Uekusa (eds.), *Advances in Organic Crystal Chemistry*,
https://doi.org/10.1007/978-981-15-5085-0_12

12.1.2 Kinetically Controlled Network Formation

Kinetic control of chemical reactions is a critical tool to produce desired products in chemical synthesis and material sciences. Diamond, one of the carbon allotropes, is less stable than graphite, which means that it is a metastable state. However, because of the large activation energy required to transform diamond to graphite, it remains as a stable crystalline solid under ambient conditions. This is a typical example of kinetically stabilized phase found in nature. Many researchers have used kinetic control to direct reactions along alternative pathways to produce desired products. In particular, in organic syntheses, kinetic control (or resolution) is often crucial to selectively obtain only one specific molecule and limit side reactions [1]. Biological systems use kinetically trapped states in living cells to sustain their function. For example, the protein folding can be finely tuned through kinetically guided assembly [2, 3]. Furthermore, the synthesis of inorganic materials, such as zeolites, is typically carried out under kinetic control [4, 5].

In addition, kinetic assembly was used to change the morphology of materials to create functional nanostructures via weak intermolecular interactions [6–8]. For example, the complexation of perylene tetracarboxylate (PTC) with Ni^{2+} displays selective kinetic/thermodynamic assembly depending on reaction temperatures. The coordinating amphiphile, PTC, has a planar conjugated skeleton. At temperatures below 25 °C, the intermolecular coordination between PTC and Ni^{2+} extends the coordinating system along the long axis of PTC, resulting in a microbelt structure several micrometers in length. However, PTC in this coordination mode is not planar, therefore, the system cannot minimize its energy via π–π stacking, indicating that it is a kinetic product. In contrast, at temperatures above 60 °C, PTC–Ni undergoes intramolecular coordination where the ligand adopts a planar conformation, facilitating π–π stacking. Consequently, it can be concluded that PTC–Ni self-assembles into much shorter nanorods under thermodynamic conditions. The two morphologies exhibit vastly differing electronic properties. The kinetically assembled microbelts have excellent electronic conductivity [6]. In another example, kinetic control was used to obtain various metal phenolic network (MPN) films. For this purpose, temporal and spatial control of MPN growth by promoting self-correction of the coordinating building blocks through oxidation-mediated network assembly was utilized [7]. The formation and growth mechanisms were investigated and used to engineer films with microporous structures and continuous gradients. These results show that morphological structure control by kinetic assembly is a promising strategy for producing functional materials.

However, for coordination networks, also known as coordination polymers (CPs) or metal–organic frameworks (MOFs), kinetic control has not been commonly employed in their synthesis [9–23]. Normally, the networks are synthesized under harsh conditions that lead to thermodynamically stable crystalline structures. For example, solvothermal reactions, which are carried out in a solvent close to or above its boiling point, and often under autogenous pressure, produce network single crystals. Some of the most thermally stable materials reported, such as MOF-5, HKUST-1,

MIL-101, and UiO-66 [24] are obtained using this technique. These types of synthesis are classified as thermodynamic assembly because the final product, including the solvent and adducts, represents a global energy minimum on the reaction coordinate landscape. In contrast, kinetic assembly traps metastable states during crystallization before equilibrium is reached, which requires much faster formation rates. The kinetic products tend to form polycrystalline powders rather than single crystals suitable for single-crystal structure analysis. As a result, the kinetic network formation has not been widely explored because of the difficulty of ab initio structure determination of crystalline powders by X-ray diffraction.

There are several examples of the kinetic assembly of coordination networks [4, 25–31]. The Cd-based network, [Cd(bpy)(bdc)] (bpy = 4,4′-bipyridine, bdc = 1,4-benzenedicarboxylate) can be generated as a single non-interpenetrating net by kinetic control at low temperature or high concentration. Whereas an interpenetrating network is obtained under thermodynamic control at high temperature or low concentration [25]. The interpenetration creates more stable structures relative to their non-interpenetrating analogues due to increase of crystal density and reduction of void space. Therefore, an increase in the degree of interpenetration tends to stabilize network structures. The consequence of this behavior is the increase of the accessible pore space inside the kinetically assembled networks, which could be beneficial for several applications, such as gas storage and separation. However, the fine balance between stability and porosity needs to be carefully controlled to achieve the desired material. Recently, this concept was applied to the synthesis of Fe-bpdc (bipy = biphenyl-4,4′-dicarboxylate) MOFs [26].

Other methods for the control of reaction pathways during coordination polymer synthesis have been reported. The most common approach is simply changing the reaction temperature to produce different network polymorphs. Cheetham et al. reported that they could obtain five structures from an identical starting mixture of $Co(OH)_3$ and succinic acid by running the reaction at five different temperatures [32]. In another example, a one-dimensional (1D) coordination polymer was formed by kinetical trapping of the reaction mixture of ZnI_2 and pyrimidine [33]. These results highlight the tendency of kinetically assembled networks to contain larger internal voids and exhibit lower density [34–39].

Another important feature of kinetic assembly is the creation of interactive sites within the structure [40, 41]. Since this process halts the network formation before it can reach a thermodynamic equilibrium by trapping metastable intermediate states, the resultant structures could contain “under-reacted” sites. In contrast, the thermodynamic structures typically have minimal latent reactivity and therefore are comparatively inert.

Figure 12.1 shows the schematic difference between thermodynamic and kinetic assemblies. In the former situation, the coordinating groups on the linkers and open sites around the coordination sphere of metal centers are fully paired up. Whereas in the latter case, some connecting sites remain unoccupied, resulting in pore environments that can interact with guest molecules.

In the following section, we will describe how interactive pores can be obtained by kinetic assembly and discuss their applications. In particular, we will demonstrate the

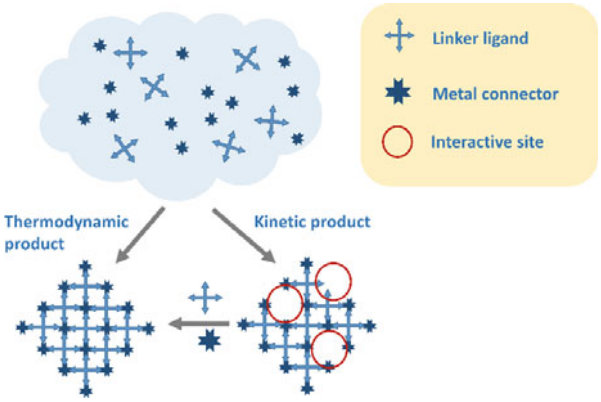

Fig. 12.1 Example of kinetic and thermodynamic assemblies of coordination networks. Reproduced by permission of The Royal Society of Chemistry

use of interactive sites inside networks to stabilize and crystallographically visualize highly reactive elemental allotropes.

12.1.3 Kinetic Assembly of Coordination Networks Using Zn Units

Kinetic assembly facilitates properties that are useful for creating functional materials, such as interactive pore sites and open non-interpenetrating structures. We developed the rapid synthetic method for kinetically controlled assembly of coordination networks [42]. This approach involves simple mixing of metal precursors (nodes) and organic ligands (linkers) in solution, which results in instantaneous reaction and network crystallization. In our first attempts, we used 2,4,6-tri(4-pyridyl)-1,3,5-triazine (TPT; Fig. 12.2) as a tridentate ligand.

When a nitrobenzene/methanol solution containing TPT was mixed with a methanol solution of $ZnBr_2$, a crystalline powder composed of micrometer-sized (<10 μm) uniform particles precipitated instantly (~30 s). The PXRD pattern of the crystalline powder indicated that the formation of a coordination network had occurred. The crystal structure was determined by ab initio PXRD analysis, which determined that it had the molecular formula of $[(ZnBr_2)_3(TPT)_2]$ and was isostructural with a related ZnI-based network, $[(ZnI_2)_3(TPT)_2]$. The structure of the iodide analogue contained a large flexible channel capable of reversible guest uptake and release in the crystalline state (Fig. 12.2) [42].

The structure of the kinetically assembled network was different from a polymorph formed under thermodynamic control. The thermodynamic network obtained by the layer diffusion method, $[(ZnBr_2)_3(TPT)_2]$, had 1D channels formed by π–π stacking of TPT (Fig. 12.2, left). This material exhibited a greater number of

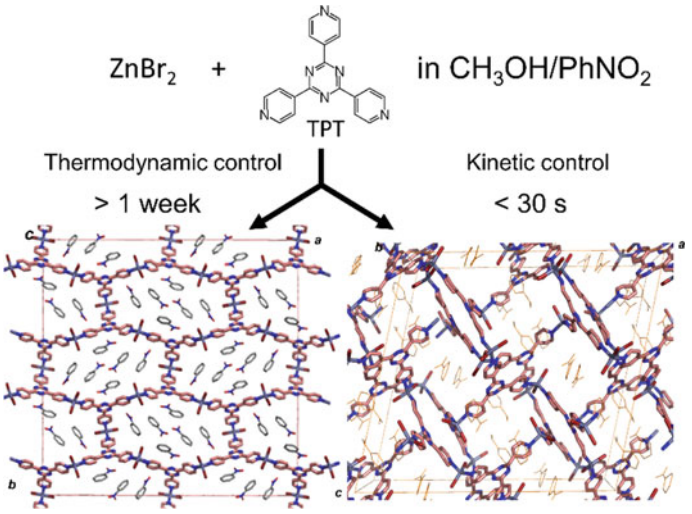

Fig. 12.2 Kinetic and thermodynamic control of network formation from $ZnBr_2$ and TPT. Reproduced by permission of The Royal Society of Chemistry

intramolecular interactions in its structure than the kinetic analogue. The thermodynamic/kinetic product assignment of these structures is consistent with their synthetic procedures—rapid crystallization resulted in a kinetic material, whereas the slower thermally equilibrated reaction gave the thermodynamic network. Moreover, the rapidly precipitated product can be converted to the more stable network by heating the crystalline powder, as determined by PXRD and differential scanning calorimetry (DSC), which provides additional evidence for the relative stabilities of the two materials. The PXRD measurements showed that the phase transformation of kinetically assembled network to the thermodynamic analogue occurred at 553 K. The DSC curve of the kinetical product showed an exothermic peak (40.10 kJ/mol) centered at 553 K, which was about three times larger than that for the other network. These results indicate that the rapidly synthesized network is a metastable state. Therefore, this type of synthetic method is convenient for producing kinetic phases. However, because the resultant products are often isolated as microcrystalline powders, ab initio PXRD analysis is the most suitable structure determination method for kinetically assembled coordination networks.

The rapid precipitation method was also applied with ZnI_2 metal connector. When a nitrobenzene/methanol solution of TPT was mixed with a methanol solution of ZnI_2, a crystalline powder quickly appeared. The crystal structure determined by ab initio PXPD analysis showed that it consisted of doubly interpenetrating 10,3-nets with the formula $[(ZnI_2)_3(TPT)_2]$ [43, 44]. In the network, the Zn atom is coordinated by two nitrogen atoms from TPT linkers and two iodides. This type of structure has been reported previously [42].

The interpenetrating network obtained under kinetic control, $[(ZnI_2)_3(TPT)_2]$, exhibited an unusual crystalline-to-amorphous-to-amorphous-to-crystalline (CAAC)

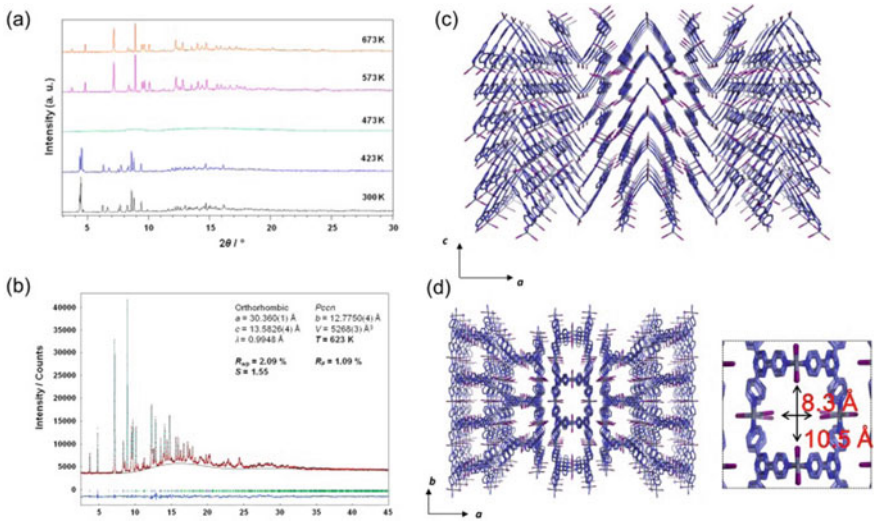

Fig. 12.3 **a** PXRD patterns of the kinetically assembled, interpenetrating network $[(ZnI_2)_3(TPT)_2]$ at different temperatures. It shows a crystalline-to-amorphous phase transition at 473 K and an amorphous-to-crystalline phase transition at 573 K. (Middle) **b** Rietveld refinement of the saddle network. **c**, **d** Crystal structures of the saddle network, $[(ZnI_2)_3(TPT)_2]$ with pore dimensions. Reproduced with permission of the American Chemical Society

phase transition upon heating [44–46]. The metastable state was converted to more stable states with increasing temperature. The microcrystals of the kinetic interpenetrating network were heated from 300 to 673 K and monitored by in situ synchrotron PXRD and TG-DSC. The diffraction showed crystalline-to-amorphous and amorphous-to-crystalline phase transitions at 473 and 673 K, respectively (Fig. 12.3a). Recently, we found that there are in fact two distinct amorphous phases occurring between the initial and final crystalline states. Therefore, the entire transformation sequence was denoted as CAAC phase transition. These types of transitions are rare in porous coordination networks. The closest related example was observed in some zeolitic imidazole frameworks (ZIFs), which underwent a two-step CAC transition [47–49].

The new crystalline state obtained by heating of the amorphous phase was different from the initial network structure and was thermally stable up to 673 K. The crystal structure was unambiguously determined by ab initio PXRD analysis, which showed that it has retained the molecular formula of $[(ZnI_2)_3(TPT)_2]$ (Fig. 12.3). In this new network, two TPT ligands are connected through two ZnI_2 units forming a "saddle" structure, which extended along the *b*-axis as 1D chains, thus, it was denoted as a "saddle network" (Fig. 12.3a–d). Adjacent chains are held together by intermolecular π–π interactions between stacked pyridyl and triazine rings along the *c*-axis giving rise to non-interpenetrating 1D channels with the dimensions of 6.2 × 8.5 Å. Due to its high thermal and structural stability, the saddle network could be used to encapsulate

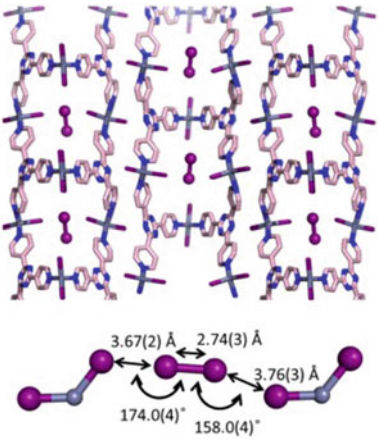

Fig. 12.4 (Top) Crystal structure of I_2-encapsulating saddle network, $I_2@[(ZnI_2)_3(TPT)_2]$. (Bottom) Interaction of the guest I_2 with the ZnI pore sites. Reproduced by permission of The Royal Society of Chemistry

guests by liquid–solid and gas–solid inclusion reactions. The isostructural network, $[(ZnBr_2)_2(ZnCl_2)(TPT)_2]$, was obtained by the solid–liquid interface reaction [50].

The structural transformation in the CAAC phase transition involves unlocking of the initial interpenetrating (10,3)-*b* network and its rearrangement into a 1D chain. First, guest removal and shrinking of the network occurs, followed by the opening of the 3D nets through cleavage of coordination bonds. After the chain rearrangement and the bond re-formation, the saddle network is obtained.

This type of thermal annealing can produce highly crystalline materials that are commonly used as ceramics and zeolites. This method was also applied to ZIF networks. When ZIF-4 ($[Zn(im)_2]$, im = imidazolate) was heated at 573 K, it changed to an amorphous phase, and further heating at 673 K produced another crystalline ZIF polymorph with different topology. The structure of the amorphous phase was a SiO_2 glass-like structure confirmed by pair distribution function analysis [47].

An important feature of the saddle structure is that the terminal iodide coordinating to Zn(II) faces into the pore (Fig. 12.3a–d). A guest molecule that enters the channel could interact with these iodide sites. For example, iodine can be physisorbed into the network, facilitated by halogen–halogen interactions (Fig. 12.4) [51]. The near-linear geometry between the network iodide and the guest I_2 molecules indicates a typical halogen–halogen interaction between positive (σ-hole) and negative sites (unpaired electrons) [52].

12.1.4 Interactive Pores in the Saddle Structure

Because the pores in the saddle network are decorated with terminal iodide groups creating interactive sites, they can be used for host-guest related applications, such as I_2 encapsulation. Due to this feature, the open structure was expected to function as a crystalline molecular flask, which could be used to monitor chemical reactions

directly by X-ray analysis [53–61]. Therefore, we decided to use the crystalline powder of this network for this role and selectively trap metastable and reactive species [62].

The small sulfur allotropes, S_n ($n < 6$), are unstable and cannot be isolated from the allotrope mixture either in the gas phase or in a solid Ar matrix [63–65]. These sulfur species are highly reactive and readily condense into heavier allotropes under ambient conditions. Therefore, their structures cannot be determined directly by X-ray diffraction. To overcome this issue, we trapped these unstable species inside a crystal matrix using the crystalline molecular flask method. We used interactive pore sites in the saddle porous coordination network, $[(ZnI_2)_3(TPT)_2]$, where the pore facing iodide groups could interact with the guest sulfur atoms and stabilize the reactive species.

Sulfur was encapsulated in the saddle network structure by vapor diffusion at 533 K under vacuum for 6 h. Under these conditions, the gaseous sulfur and the host network were fully equilibrated. After this treatment, the pale-yellow network powder turned bright yellow accompanied by change in the PXRD pattern. The changes in the peak positions and their relative intensities suggested that sulfur was successfully encapsulated into the network pores (Fig. 12.5).

Herein, we describe the structure determination procedure for the sulfur species, which were identified by ab initio PXRD analysis. After sulfur encapsulation, the crystal system of the network changed from *P*ccn with $a = 30.690$ Å, $b = 12.775$ Å, $c = 13.5826$ Å to *P*n with $a = 30.690$ Å, $b = 6.595$ Å, $c = 12.824$ Å, $\beta = 91.558°$. The structure of the sulfur-encapsulating network was solved by ab initio PXRD analysis using synchrotron data. First, the structure was solved using the model of the original network and several combinations of individual sulfur atoms to obtain the initial structural information about the possible sulfur allotropes. All solutions showed the presence of a S_3 moiety inside the pore of the coordination network. Using a S_3 model obtained from rotational spectroscopy experiments, [66] the ab initio PXRD analysis was repeated. The structure was further refined by the Rietveld method using the S_3-encapsulating model with soft restraints for the geometrical parameters.

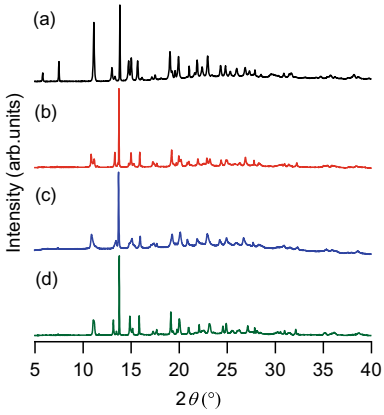

Fig. 12.5 RXPD pattern of the saddle network, **a** before sulfur encapsulation, **b** S_3-encapsulating network, **c** S_6-encapsulating network, and **d** sulfur polymer-encapsulating network. Reproduced with permission of the American Chemical Society

The good agreement between the experimental and calculated diffraction patterns indicated that the structure was correct. The X-ray diffraction analysis and elemental analysis revealed that discreet S_3 species were selectively trapped in the network pores (Fig. 12.6).

This example represents the first crystal structure determination of a reactive sulfur allotrope smaller than S_6. The open-triangle C_{2v} structure of the observed S_3 agreed well with structures obtained by rotational spectroscopy [66]. The sulfur molecule in the pore was disordered over two positions. Notably, the short interatomic distances between sulfur and iodide in the major component of S_3 were 3.1 and 3.3 Å, which were considerably shorter than the sum of their van der Waals radii (3.8 Å), indicating a strong interaction between them (Fig. 12.7). It was postulated that this interaction enabled the encapsulation and stabilization of, otherwise, reactive S_3 molecule.

The presence of S_3 in the pores was additionally confirmed spectroscopically from the characteristic shoulder peak in the vibrational spectrum at about 680 cm^{-1}, which corresponds to the S_3 asymmetric stretching. The encapsulated sulfur species exists in a neutral state, which was determined by the assignment of IR peaks and lack of a signal in the electron spin resonance spectrum.

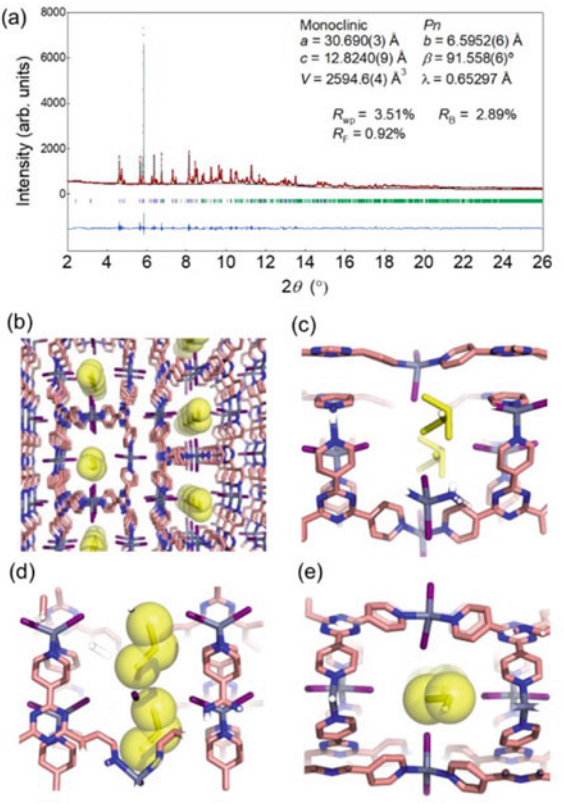

Fig. 12.6 Ab initio PXPD analysis of the S_3-encapsulating network. **a** Rietveld refinement and **b**–**e** crystal structure of the S_3-encapsulating network. Reproduced with permission of the American Chemical Society

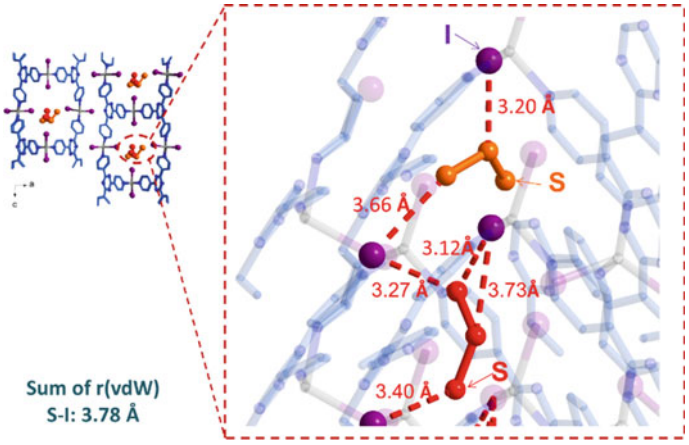

Fig. 12.7 Interaction of S_3 with interactive pore sites. The distances between S and I show important interactions. Reproduced by permission of The Royal Society of Chemistry

The S_3 encapsulated in the pores was remarkably stable because of the interaction with the pore facing iodide sites (Fig. 12.7). The PXRD pattern of the S_3-encapsulating network powder did not change significantly over 3 months of the exposure to ambient atmosphere. Thermogravimetric analysis of the host-guest material showed a weight decrease at temperatures above 500 K, which indicated that sulfur evaporation from the pores occurred at higher temperatures. Furthermore, the S_3 molecule inside the network was found to be inert to photo-irradiation oxidation conditions. These results further highlight the remarkable stabilization of the S_3, an analogue of ozone, inside the interactive pores of the saddle network.

Nevertheless, the encapsulated S_3 exhibited a unique reactivity. When the crystalline network powder was heated with NH_4Cl at 473 K for 6 h under vacuum, the PXRD pattern changed, indicating a structural transformation. The crystal structure determined by ab initio PXRD analysis showed that there were now 0.5 S_6 molecules in each pore (Figs. 12.5 and 12.8). The product of this transformation was six-membered rings with a chair conformation, which is characteristic of discrete S_6 molecules [63]. This result suggests that the S_3 in the pores dimerized to produce S_6 as follows:

$$S_3 + S_3 \rightarrow S_6$$

In the crystal structure, the encapsulated S_6 also interacts with network iodide as evidenced in the interatomic distances between sulfur and iodide (3.1 and 3.4 Å), which are shorter than the sum of their van der Waals radii (3.8 Å). The close proximity between S_6 and iodide indicates the presence of strong host–guest interaction, similar to the S_3. S_6 itself cannot enter the pore from outside because the diameter of the opening aperture is too small. Therefore, the only way to encapsulate S_6 is a ship-in-a-bottle approach [67] starting from smaller sulfur allotropes, like S_3.

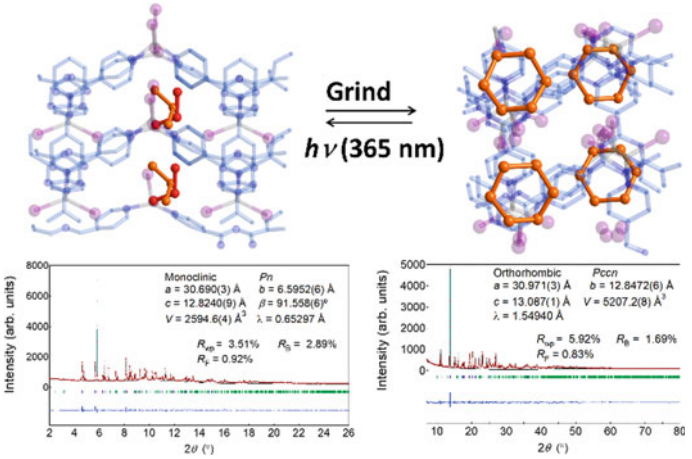

Fig. 12.8 Ab initio XRPD snapshots of the transformation of S_3 to S_6. Reproduced by permission of The Royal Society of Chemistry

However, the S_3 dimerization could not be achieved by simple heating, and NH_4Cl was required to catalyze the transformation. NH_4Cl is an impurity remaining from the ligand synthesis and acts as proton donor (Scheme 12.1) [68]. It is proposed that the hydrogen-bonding brings the sulfur trimers closer together allowing for cyclization to take place. Furthermore, the same structural transformation could be induced by mechanical action when grinding the S_3-encapsulating network powder, indicating the flexibility of the saddle structure.

Interestingly, this transformation could be reversed by excitation at 365 nm, fully recovering the starting S_3 molecules. This result indicates that inside the pore, S_3 is more stable toward light irradiation than S_6 (Fig. 12.8).

Overall, the interactivity of the pores was the key for efficient trapping of small sulfur allotrope and its conversion, helping to uncover the chemistry of these rare sulfur species.

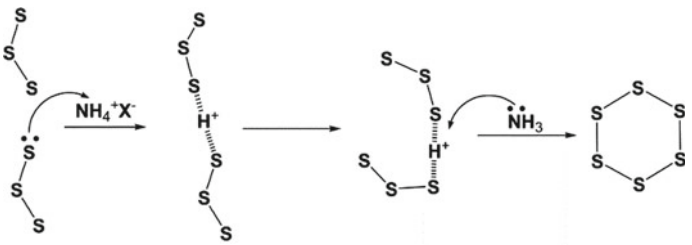

Scheme 12.1 Transformation of $2S_3$ to S_6 catalyzed by NH_4Cl

12.1.5 *Encapsulation of Reactive Molecules, P_4 and Br_2*

In addition, we used the saddle network to capture and stabilize other reactive elemental species, namely P_4, also known as white phosphorous, and Br_2 [69, 70]. Phosphorus tetramer was encapsulated into the pores using phosphorus vapor created by heating red phosphorus. The P_4 trapping was confirmed by X-ray diffraction, as shown in Fig. 12.9. This species was stabilized by weak interaction with the pore walls and was stable under air at 300 K. This means that this network can be used as a versatile P_4 container. The removal and re-trapping processes could be repeated, which is important for the molecular flask reusability. The presence of interactive sites inside the coordination network was demonstrated to be, once again, crucial for efficient trapping and release of reactive species. As a result, chemically and thermally robust porous networks can be used as facile and reusable reagent containers.

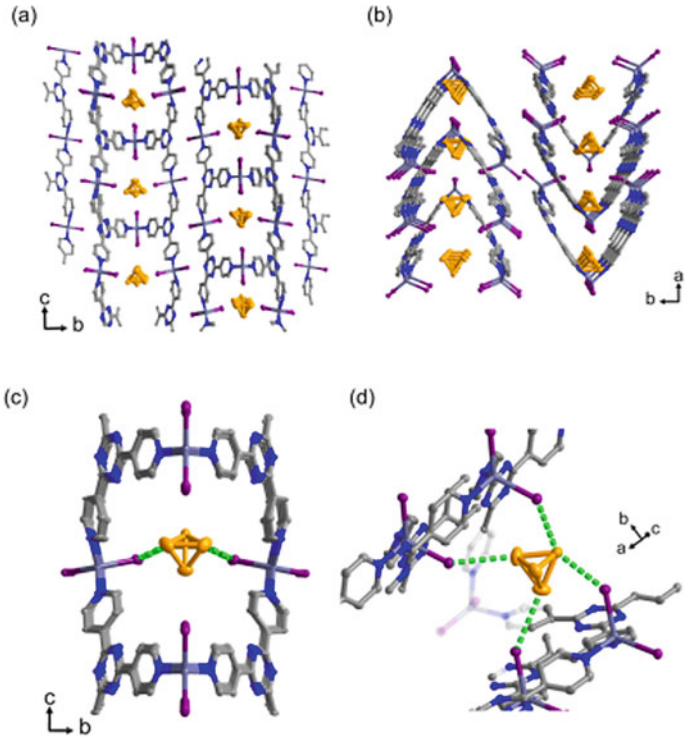

Fig. 12.9 Crystal structures (ORTEP plots, 50% probability) of single-crystal P_4@network **1** at 100 K: **a** view along *b*-axis, **b** view along *c*-axis, **c** pore description green dotted lines show interactions, **d** interaction between P_4 and iodides. Color codes: C, gray; N, blue; P, orange; Zn, pale-blue; and I, purple. Reproduced by permission of The Royal Society of Chemistry

12.1.6 Br_2 Encapuslation

To further investigate the trapping ability of the saddle network, we performed bromine encapsulation to determine whether Br_2 can be safely stored inside [70]. During this investigation, it was found that instead of just simply encapsulating Br_2 through physisorption, the oxidation of coordinated iodide had occurred, producing I_2. Furthermore, this reaction caused the displacement of iodide by bromide in the coordination sphere of Zn(II), giving rise to the ZnBr-based network containing I_2 as a guest:

$$\left[(ZnI_2)_3(TPT)_2\right] + 3Br_2 \rightarrow \left[(ZnBr_2)_3(TPT)_2(I_2)\right] + 2I_2$$

The new structure was confirmed by ab initio PXRD analysis (Fig. 12.10). The trapped I_2 showed strong interactions with the pore of the ZnBr network.

Additional evidence for the presence of I_2 inside the network was provided by Raman spectroscopy [71–73]. The Raman spectrum showed sharp peaks at 174 and 194 cm^{-1}, corresponding to I_2 encapsulated in the pore and I_2 attached to the

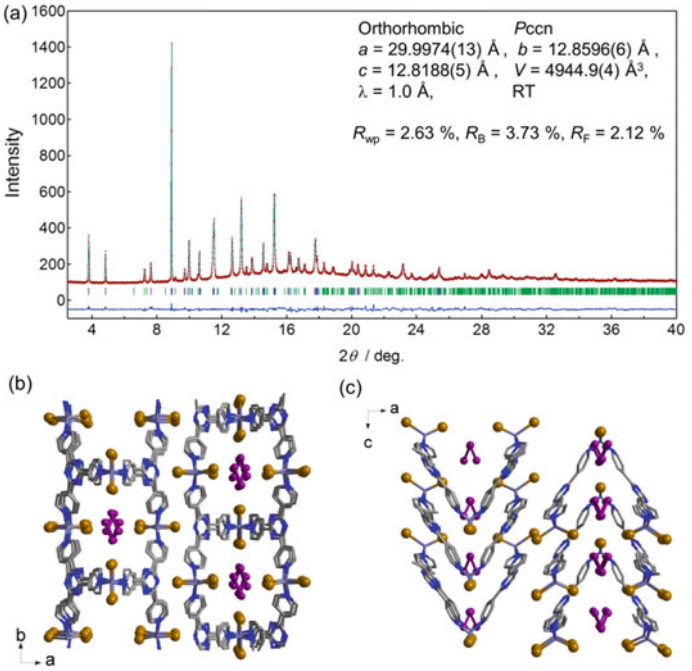

Fig. 12.10 Experimental (red), calculated (black), and difference (blue) PXRD profiles from the final Rietveld refinement of the I_2@$[(ZnBr_2)_3(TPT)_2]$. Crystal structure: **b** view along the *c*-axis. I_2 (occupancy 0.5) occupies two symmetrically related positions. **c** View along the *b*-axis. Color codes: C, gray; N, blue; Zn, pale-blue; I, purple; and Br, brown. Reproduced by permission of The Royal Society of Chemistry

surfaces of crystals, respectively. The presence of surface-confined iodine could not be avoided because the reaction produces two additional equivalents of I_2 which escapes the pores. The elemental analysis results determined the chemical formula of the network product to be $[(ZnBr_2)_3(TPT)_2(I_2)](I_{2\text{-surface}})_{0.67}$. The iodine loading was also quantified by TGA, which showed a two-step weight loss. The first step corresponds to desorption of I_2 from the particle surface, whereas the second one corresponds to the loss of I_2 from the pores. The overall weight decrease below 575 K was approximately 25.3%, which agrees with the total iodine content (24.6%) calculated from the molecular formula, $[(ZnBr_2)_3(TPT)_2(I_2)](I_{2\text{-surface}})_{0.67}$. The I_2 in the pore interacts with the Br^- sites of the network. The I···Br distance is 3.61 Å, which is shorter than the sum of the individual van der Waals radii of I and Br (3.75 Å) [74]. Also, the I–I–Br angle is 153° (non-linear), indicating mainly a π-type interaction combined with some contribution of σ-type interactions. The appearance of absorption band at 280 nm can be attributed to a strong charge-transfer interaction between Br^- and I_2. This band was not clearly observed in the $[(ZnI_2)_3(TPT)_2]$ network containing encapsulated I_2, indicating that only σ-type interactions occur between I^- sites of the network and the guest I_2. The brominated network shows significantly stronger affinity for I_2 because of the additional contribution of π-interactions which are absent in the iodine analogue.

This post-synthetic modification of the pore is due to the strong oxidative ability of Br_2. The oxidation potential of Br_2/Br^- redox couple is 1.087 V versus SHE, which is higher than that for the I_2/I^- couple, 0.54 V versus SHE. Therefore, the encapsulated of Br_2 readily oxidizes the constituent I^- to give I_2. This type of post-synthetic reaction is the first example of redox induced ligand transformation, which results in a network component replacement. The resulting pore modification enables the dramatic changes in the properties of interactive sites by switching from I^- to Br^-.

Furthermore, thermal treatment of the I_2 encapsulated ZnBr network led to the guest removal affording an activated structure. When the I_2 loaded $[(ZnBr_2)_3(TPT)_2]$ network was heated at 573 K, the powder turned white, which is a sign of the release of I_2 molecules from the pores. The ab initio PXRD structural analysis of the remaining white powder revealed it to be isostructural with the starting $[(ZnI_2)_3(TPT)_2]$ network (Fig. 12.11). The pore window of the bromine structure is 2.6 × 4.6 Å, which is larger compared to the iodide analogue because of the smaller ionic radius of Br^- relative to I^-. The halide replacement retained the overall saddle-type network structure and preserved the topology. The same structure could not be obtained starting directly from $ZnBr_2$ and TPT, either using a solution-phase synthesis or by crystallization from vapor. In both cases, the interpenetrating network was the predominant product. As a result, the only available synthetic route toward the $[(ZnBr_2)_3(TPT)_2]$ material is through oxidative encapsulation and ligand replacement with Br_2. The resultant bromide network was found to be stable up to 673 K under N_2, as confirmed by TGA measurements.

Due to the presence of Br^- ions as interactive pore sites, the trapping of Br_2 was attempted. For these experiments, the Br_2 vapor diffusion was also performed under the same conditions as those used for the Br_2 encapsulation into $[(ZnI_2)_3(TPT)_2]$.

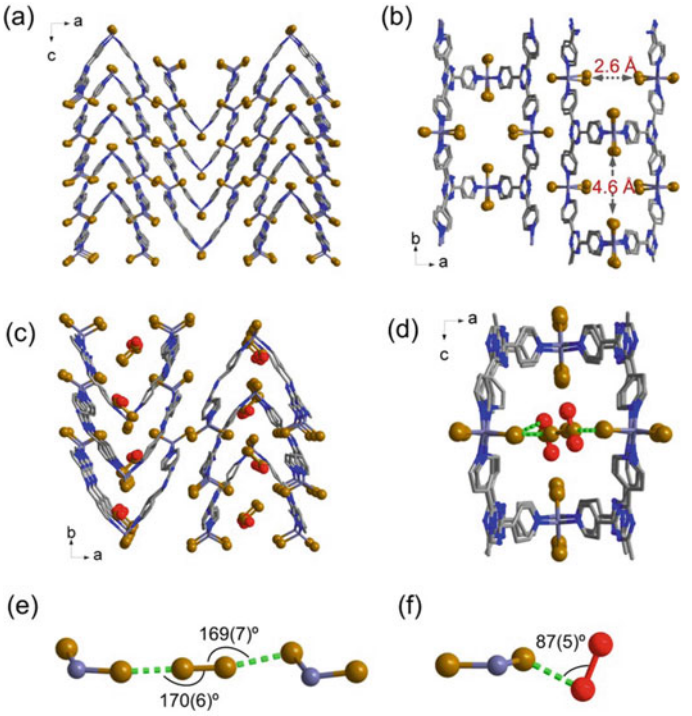

Fig. 12.11 Crystal structure of $[(ZnBr_2)_3(TPT)_2]$: **a** view along the *b*-axis, **b** view along the *c*-axis. Crystal structure of $Br_2@[(ZnBr_2)_3(TPT)_2]$: **c** view along the *c*-axis, **d** view along the *b*-axis. Green dotted lines show interactions. **e** Linear interactions between Br_2 and Br^- ions. **f** Perpendicular interactions between Br_2 and Br^- ions. Color codes: C, gray; N, blue; Zn, pale-blue; and Br, brown and red to distinguish disordered molecules. Reproduced by permission of The Royal Society of Chemistry

After the vapor exposure the bromide network powder changed color from white to yellow accompanied by the change in the PXRD pattern. The ab initio PXRD structural analysis of the resultant yellow powder revealed that the material has retained its basic ZnBr network structure while also incorporating the disordered Br_2 guests. These were physically adsorbed into the pore, strongly interacting with the network bromide groups. The observed Br$\cdots$Br distances were 3.44, 3.55, and 3.22 Å, shorter than the sum of the van der Waals radii of Br (3.70 Å). One of the disordered Br_2 molecules exhibits an almost linear geometry (Fig. 12.11e), which is an indication of σ-type halogen–halogen interaction. In contrast, the other disordered Br_2 assumes an almost perpendicular geometry (Fig. 12.11f), a telltale sign of a π-type interaction featuring an elongated Br_2 bond (2.38(14) Å) [75]. Therefore, both σ-hole and π-orbitals-based interactions can occur between the guest Br_2 and the host Br^-. These results highlight the diversity of halogen bonding types that are possible inside the interactive pores, which presents an opportunity to generate and study unusual polynuclear halide species that cannot exist outside.

12.1.7 Kinetic Assembly Using a Labile CuI Unit

The success of S_3 encapsulation prompted us to design materials that contain intrinsic interactivity within their pores using the principles of kinetic assembly. To produce coordination networks under kinetic control, we employed labile metal connectors. If a metal can readily exchange ligands under the reaction conditions, usually in solution, it may generate several species during network formation because of the presence of several intermediate metal complexes. In particular, labile multinuclear metal clusters could give rise to multiple species existing simultaneously in solution. However, in most metal ions the intermediate state geometries are predictable, which limits the number of easily accessible structures for the network metal connectors.

Therefore, to demonstrate the kinetic control for network formation, we decided to utilize labile metal connectors instead of commonly used metal ions [41, 76]. These were combined using a rigid, highly symmetric ligand to produce structurally robust networks. For this study, $[Cu_4I_4(PPh_3)_4]$ was selected as a suitable metal precursor, because its central Cu_4I_4 cubane core is kinetically labile in solution and can be readily converted into other copper iodide clusters [77, 78]. For the ligand, tetra-4-(4-pyridyl)phenylmethane (tppm) was used, which possesses all the required characteristics, namely structural rigidity, thermal stability, and tetrahedral symmetry. Upon heating a suspension of $[Cu_4I_4(PPh_3)_4]$ and tppm in DMSO in air at 453 K for 30 min, a homogenous colorless solution was obtained. Depending on the cooling rate, two kinds of network crystals could be obtained. Rapid cooling (ca. 20 K min^{-1}, kinetic assembly) exclusively produced yellow needles with the formula $[(CuI)_2(tppm)]$ in 99% yield. In contrast, slow cooling (ca. 3 K min^{-1}, thermodynamic assembly) resulted in the formation orange prisms with the formula $[(Cu_2I_2)(tppm)]$ in 95% yield. Although these two networks had the exact same chemical composition, their connectivity and topology were markedly different. Therefore, these materials could be considered as structural isomers (Fig. 12.12).

The single-crystal structure analysis of the kinetic isomer revealed that CuI helical chains bridged by tppm ligands formed a non-interpenetrating porous network along the *c*-axis, where each Cu(I) ion is coordinated by two nitrogen atoms of tppm ligand and two bridging iodide groups. The helical chain network has 1D channels with pore windows of 5.8 × 5.5 Å and a 35% void space (without solvent) in the unit cell volume. The most important feature of this structure is that the bridging iodide in the connecting cluster faces into the 1D channel, and therefore can act as interactive pore site (Fig. 12.12a, c, e).

The crystal structure analysis of the thermodynamic isomer on the other hand, revealed that it has a quadruply interpenetrating network consisting of Cu_2I_2 dimer units and tppm ligands. The structure is a 4,4-connected grid with the PtS topology if the Cu_2I_2 dimer units are considered as square-planar sites and the central carbon atom of tppm as a tetrahedral node. In addition, this network contains 1D channels with pore windows of 4.0 × 3.9 Å and a 22% void space in the unit cell volume. The iodide groups in the Cu_2I_2 dimer are obscured by tppm ligands from the interpenetrating nets, which is different from the kinetic structure. As a result, the channels

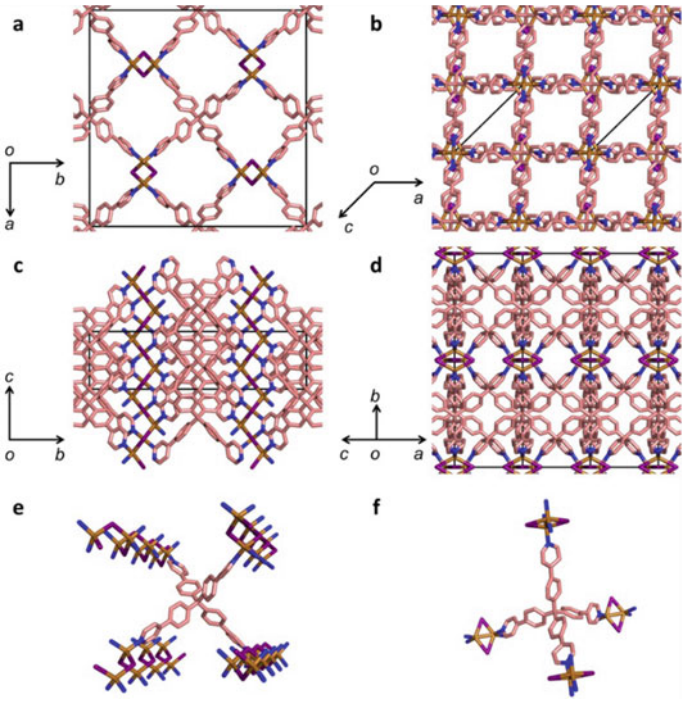

Fig. 12.12 Crystal structure of **a**, **c**, **e** kinetically assembled network, $[(CuI)_2(tppm)]$ and **b**, **d**, **f** thermodynamically assembled network isomer, $[(Cu_2I_2)(tppm)]$. Reproduced with permission of John Wiley and Sons

in the thermodynamic network are not decorated by the interactive iodide sites, and thus are relatively featureless (Fig. 12.12b, d, f).

The helical isomer can be converted to the dimer isomer by heating the powder in DMSO at 373 K for 1 day. This result confirms the kinetic nature of the helical network. On the other hand, the dimer network was found to be thermodynamically stable in a DMSO solution up to the decomposition temperature of DMSO.

The crystals of kinetic network exhibit higher stability in the solid state compared to solution. TGA showed that the decomposition temperatures of the two isomers were above 673 K under nitrogen atmosphere. More importantly, both networks crystals retained their crystallinity and porosity even after desolvation. It can be concluded that in solid state there is a very high energy barrier for the conversion of helical isomer into dimer structure. Due to this remarkable stability, the kinetic product could be suitable for practical solid-state applications.

To elucidate the properties of interactive pore sites, I_2 sorption experiments were performed on both solvated and desolvated networks. The sample crystallinity was retained after the I_2 exposure. Single-crystal structure analysis showed that the pores of the kinetic network encapsulated I_2 via chemisorption mechanism converting I^- groups in the connector units into linear I_3^- (Fig. 12.13a, b). In contrast, the ther-

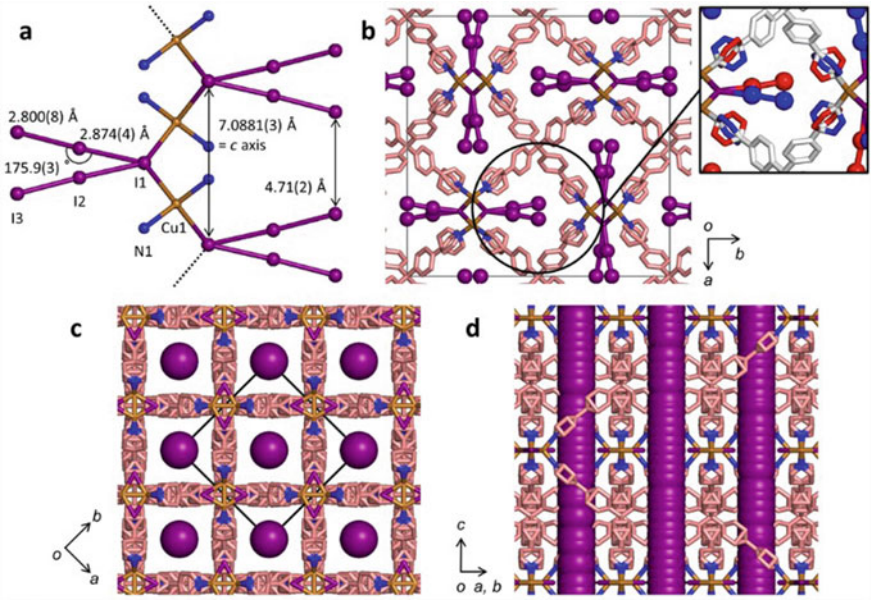

Fig. 12.13 Crystal structure of **a**, **b** chemisorption of I_2 (I_2@[$(CuI)_2$(tppm)]) and **c**, **d** physisorption of I_2 (I_2@[(Cu_2I_2)(tppm)]). Reproduced with permission of John Wiley and Sons

modynamic network only displayed physisorption of I_2 (Fig. 12.13c, d). The crystal structure analysis revealed that the I_2 molecules are arranged linearly along the 1D channels and are highly disordered, which is similar with I_2 physisorption in an organic zeolite and a phosphazene crystal [79, 80]. These results clearly demonstrate the importance of interactive pores in facilitating the chemical bond formation between bridging iodides and guest I_2.

Remarkably, even though I_2 formed chemical bonds with the pores of helical network, its desorption temperature was unexpectedly lower than for the physisorbed I_2 inside the dimer network. This behavior was attributed to the steric repulsion between adsorbed I_2 molecules and the framework backbone. In particular, the pyridyl ring rotation is expected to become more rapid with increasing temperature, which would cause the collisions with the I_3^- units leading to their displacement.

I_2 sorption was also investigated in solution by UV–Vis spectroscopy. The kinetics of I_2 sorption in cyclohexane solution revealed two distinct stages. Initially, a first-order sorption process is observed, suggesting physisorption, followed by a second-order sorption process, indicative of chemisorption.

The mechanism of kinetic network formation was investigated by nuclear magnetic resonance (NMR) spectroscopy. The NMR study revealed that oxygen is essential for the reaction. In anaerobic conditions, no network formation was detected. The NMR results helped to elucidate the mechanism. First, the PPh_3 group in the starting material, $[Cu_4I_4(PPh_3)_4]$, is removed by oxidation to produce

a vacant copper site and O = PPh_3. Second, DMSO rapidly occupies the coordinatively unsaturated site to generate a solvated CuI monomer at 453 K. Then, a tppm ligand coordinates to the resultant CuI monomer to generate the intermediate species, $[(CuI(DMSO)_2)_4(tppm)]$. The kinetic network can be crystallized from this intermediate complex by rapid cooling of the reaction mixture. The outlined kinetic assembly process is a powerful method for creating interactive pore sites in coordination networks.

12.1.8 S_2 Trapping in Thermodynamically Assembled Network

Because thermodynamic network has small pores, it can be particularly suitable for small sulfur allotrope encapsulation, similar to the studies described in Sect. 12.1.4. The small pore size cannot accommodate sulfur clusters larger than S_3, and it was expected to predominantly encapsulate disulfur, S_2. This favorable characteristic prompted us to conduct an in-depth study into sulfur encapsulation in the dimer network [81].

Sulfur was encapsulated from the gas phase by the kinetic trapping method, in which only sulfur vapor was present in the glassware while the network was kept at room temperature to create a temperature gradient (as described in Sect. 12.1.9).

X-ray structure analysis of the sulfur-containing network revealed that S_2 molecules were physisorbed at two different sites inside the channel: (i) Highly disordered along the length of the channel and (ii) within small cavities adjacent to the Cu_2I_2 units (Fig. 12.14).

Only the physisorption of S_2 was observed in the pore because of the steric hindrance around the iodide sites. The small size and linear shape of the 1D channels selectively trapped S_2 molecules and prevented further growth of larger sulfur allotropes. The presence of sulfur dimers in the network was confirmed by Raman spectroscopy at room temperature. A new band appeared at 728 cm^{-1} corresponding to the S_2 symmetric stretching mode. The encapsulated sulfur species remained stable inside the network up to 500 K because of the confinement effect of the pore.

The fact that the S_2 was detected in the pores implies that gas-phase sulfur incorporation in other porous networks proceeds predominantly via the sulfur dimers.

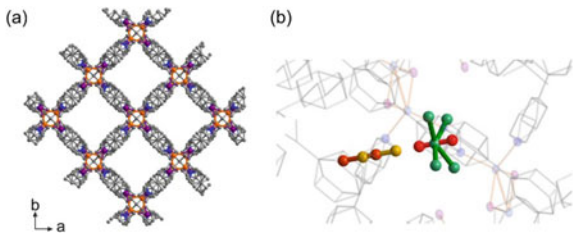

Fig. 12.14 Crystal structure of **a** desolvated CuI network, $[(Cu_2I_2)(tppm)]$ and **b** S_2-encapsulating $[(Cu_2I_2)(tppm)]$. Reproduced with permission of the International Union of Crystallography

This is consistent with the fact that the largest fraction of the gaseous sulfur is in its dimer state [65]. Therefore, S_3 encapsulation in the saddle $[(ZnI_2)_3(TPT)_2]$ network likely occurred via a ship-in-a-bottle cluster assembly. First, S_2 (disulfur) molecules enter the pores of the network and then are converted to S_3 (trisulfur) due to its higher stability. Since the encapsulation is conducted under the equilibrium conditions, it is difficult to determine the exact mechanism of disulfur molecule conversion. To observe these processes, the guest molecules should be kinetically trapped before the equilibrium state is reached. To achieve this, iodide sites could act as suitable interactive sites to capture small sulfur species and prevent their aggregation. To explore this possibility, we employed of kinetically assembled helical CuI network with interactive pores, as discussed in Sect. 12.1.7.

12.1.9 X-Ray Snapshots of the S_2 Conversion Inside an Interactive Pore

As mentioned in Sect. 12.1.4, pores lined up with interactive iodide sites could serve as efficient traps to stabilize and visualize small sulfur species. Furthermore, in Sect. 12.1.4, we also described sulfur encapsulation into the saddle ZnI network performed under equilibrium conditions. Elemental sulfur and the network powder were kept at 533 K under vacuum for 6 h to encapsulate sulfur gas. Because of the equilibrium conditions, it was difficult to determine the conversion mechanism before the sulfur species reached their equilibrium state inside the network pores. To overcome this limitation, kinetic trapping of small metastable sulfur allotropes was used to observe their conversion in the pore.

The CuI helical network was used for the trapping experiments due to the presence of interactive iodide sites where the sulfur transformation could occur. Unlike earlier encapsulation experiments, the sulfur trapping into the helical structure was carried out under kinetic conditions. Elemental sulfur and the desolvated network powder were placed at well-separated locations in a zig-zag glass tube, followed by sealing it under vacuum (~10^{-6} Torr). The sulfur side of the tube was heated to generate the sulfur vapor, while the network side was kept at the room temperature creating a sharp temperature gradient. This arrangement enabled the gaseous sulfur molecules to be trapped kinetically by the porous material. After the reaction was complete, single-crystal X-ray diffraction was performed on the resultant sample sequentially at 250, 300, 350, and again 250 K. The analysis of these diffraction patterns revealed the structure of transient small sulfur allotropes. The initial structure at 250 K showed the presence of two types of physisorbed guests in the network channels, S_2 and bent-S_3 species. Upon increasing the temperature to 300 K, the crystal structure analysis revealed the formation of cyclo-S_3 chemisorbed to the bridging iodide sites in addition to bent-S_3 and cyclo-S_3, both physisorbed in the channels. A theoretical investigation showed that the stronger interacting cyclo-S_3 species should be in its dicationic state, cyclo-S_3^{2+}. Further heating to 350 K resulted in the opening of the

cyclic trimers to give two kinds of bent-S_3 species, one still bound to the network iodide sites and the other physisorbed inside the pore.

From these X-ray diffraction experiments, a tentative reaction mechanism for the temperature-induced interconversion of sulfur species inside the helical CuI network is proposed. First, S_2 is kinetically trapped by rapid absorption into the pore and then partially transformed into bent-S_3 structure. Since the dimer was only detected at 250 K, it is a strong indicator that this allotrope is the starting point for the following conversion reactions. Second, on heating, S_2 converts to a number of trimeric species, namely chemisorbed cyclo-S_3^{2+} and physisorbed cyclo-S_3 and bent-S_3. After that, the cyclic forms underwent a ring opening to produce more stable bent-S_3 species (Fig. 12.15). Despite the kinetic nature of the experiments, the X-ray analysis results were generally reproducible.

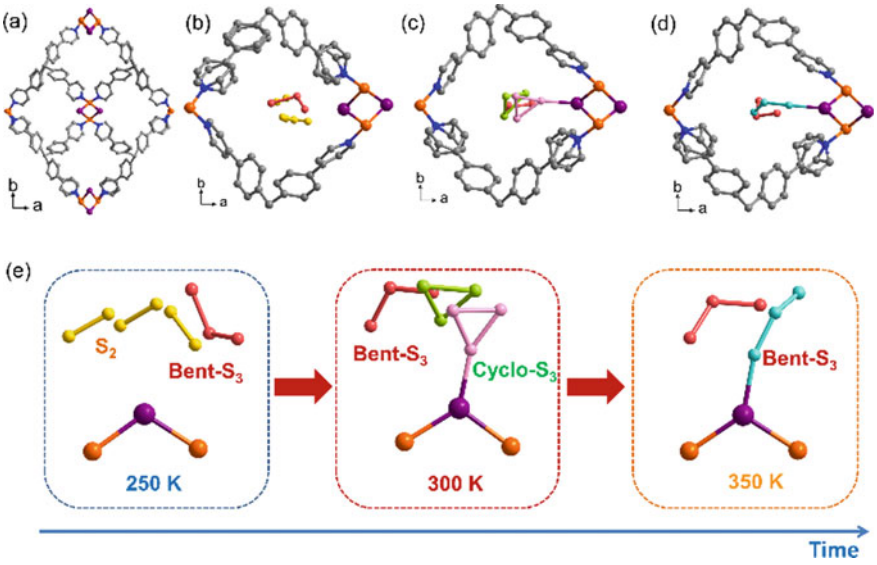

Fig. 12.15 Pore description in crystal structure of **a** the CuI helical network, $[(CuI)_2(tppm)]$, **b** helical network after sulfur encapsulation at 250 K, **c** 300 K and **d** 350 K. **e** The crystal structure of sulfur-encapsulating helical network showing parts of {CuI} unit and sulfur species. At 250 K, physisorbed S_2 and bent-S_3 were observed (left), at 300 K, chemisorbed cyclo-S_3^{2+}, physisorbed cyclo-S_3 and bent-S_3 were observed (middle), and at 350 K, bent-S_3 was observed. Blue arrow indicates the time course of the measurements showing molecular transformation mechanism from S_2 to bent-S_3 species. Atoms coloring: Cu, orange; I, purple, S, yellow, red, green, pink and cyan to distinguish disordered molecules. Reproduced with permission of the International Union of Crystallography

12.1.10 Identifying Cyclo-S_3 Species in the Pore

Theoretical calculations predicted that cyclo-S_3 is less stable than bent-S_3, yet energetically accessible. However, its experimental observation had never been reported before. Hoffman used DFT calculations to show that the neutral form of cyclo-S_3 is 5.6 to 9.3 kJ/mol less stable than bent-S_3, depending on the calculation method [82]. Therefore, the cyclic form was predicted to be a metastable state. Indeed, the interactive pores were able to temporarily trap cyclo-S_3 as an intermediate species. This result represents the first structure of a cyclic S_3 allotrope determined using single-crystal X-ray diffraction. The cyclo-S_3 was stabilized through a chemical bond formation to create an I-(cyclo-S_3^{2+}) complex. Furthermore, the dication of the cyclic trimer is the isoelectric state to a cyclo-SiS_2 molecule isolated by matrix isolation, supporting the possibility of cyclo-S_3^{2+} existence [83]. The structural analysis of the metastable sulfur allotrope trapped by the pore of the coordination network opens up new avenues for producing and characterizing unusual sulfur species.

12.1.11 Theoretical Investigation of Sulfur Allotropes in the Pores

The ability of interactive pore sites to trap and stabilize small sulfur allotropes was investigated using theoretical calculations. Since both physisorbed and chemisorbed S_2 species appeared in the same structure, the energetics of the chemisorption process and electronic spin changes were evaluated. To obtain this information, the energy of the $I^- \cdots S$–S complex was calculated.

In a triplet electronic state, the S_2 molecule is only physisorbed onto the iodide. The interaction energy of this intermolecular interaction was calculated to be −29.2 kJ/mol with the I–S bond order of 0.1294. As a result, this intermolecular interaction cannot be considered as a covalent bond and is more similar in strength to a halogen bond. The formation of this weakly interacting complex involves charge transfer from the iodide primarily to the furthest sulfur atom. The equilibrium distance for this interaction is 3.317 Å and the resultant species has a bent geometry with a $I \cdots S$–S angle of 127.5°.

On the other hand, in the singlet electronic state (Table 12.1 and Fig. 12.16), the S_2 molecule is chemisorbed onto the iodide. In the process, a covalent I–S bond is formed with a bond order of 0.9293 and the bond distance of 2.602 Å. The geometry of chemisorbed complex is also bent, with an I–S–S angle of 112.5°. In addition, there is a considerable charge transfer from the iodide to the sulfur atoms. The I–S–S Mulliken charges are −0.372, −0.144, and −0.484, respectively. The distant sulfur atom receives the highest negative charge. From these results, it can be concluded that a donor-acceptor bond forms between the iodide and the sulfur atom. However, the total energy gain in creating this intramolecular bond is only −19.4 kJ/mol, almost 10 kJ/mol less stabilizing than physisorption.

Table 12.1 Stability and key structural parameters for the optimized $I^{-}\cdots S_2$ complex in the triplet and singlet spin states

	$I^{-}\cdots S_2$	
Spin	Triplet	Singlet
Nature	Physisorption	Chemisorption
d(I–S) in Å	3.317	2.602
Wiberg I–S bond order	0.1943	0.9293

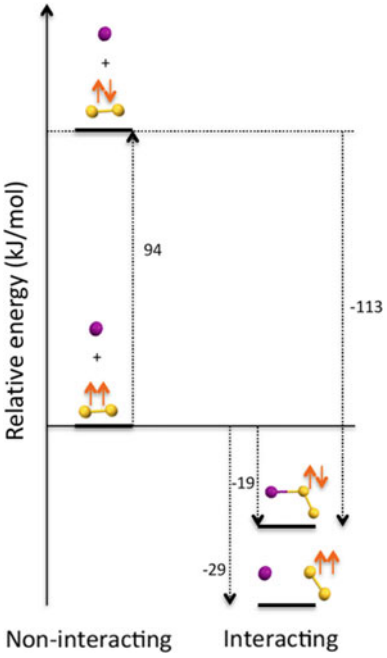

Fig. 12.16 Schematic of the stability of the interacting $I^{-}\cdots S_2$ with respect to the isolated species in the singlet and triplet spin states. Reproduced with permission of the International Union of Crystallography

Chemisorption is energetically less favorable than physisorption in this system because the triplet-to-singlet spin conversion is required for this process. The relative energies of the various (isolated, non-interacting, and interacting) systems are shown in Fig. 12.16.

In isolation, the triplet spin state of the S_2 molecule is considerably more stable than the singlet state by approximately 94 kJ/mol. Therefore, when the sulfur gas was produced for the encapsulation experiment, it likely mostly consisted of triplet dimers. In the presence of the iodide groups however, both the chemisorbed singlet and the physisorbed triplet states have similar energies. They differ by only 10 kJ/mol. With respect to the isolated S_2 triplet state, the singlet chemisorbed S_2 is only

19 kJ/mol more stable. In comparison, the singlet chemisorbed S_2 state is 113 kJ/mol more stable relative to its isolated form and is in the order of a covalent bond. These results unambiguously explain that the lower stability and generally weaker binding of the chemisorbed sulfur dimer compared to the physisorbed species is due to the energy of the spin transition. Therefore, the physisorption process is more favorable for S_2 encapsulation in the pores.

In addition, the reaction pathway from the physisorbed triplet S_2 to the chemisorbed singlet S_2 was examined. Figure 12.15 shows that the I–S bond formation process has an energy barrier of 15 kJ/mol. The transition state occurs at around $I^- \cdots S$ distance of 2.8 Å (Fig. 12.17).

Finally, the properties of the intermediate cyclo-S_3 species were calculated. The calculated structure of chemisorbed cylco-S_3^{2+} showed that the bond lengths in the sulfur-iodine complex were closely matching with those determined by the X-ray structure analysis without any geometrical constraints or restraints (Fig. 12.18).

Structural information is essential for understanding chemical reactions and material properties. However, the difficulty in determining the structures of intermediate

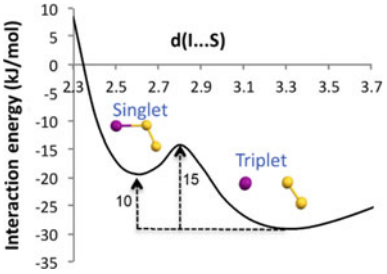

Fig. 12.17 Potential energy curve of the physisorption to chemisorption transition process of a molecule of S_2 onto an iodide atom in the gas phase. Reproduced with permission of the International Union of Crystallography

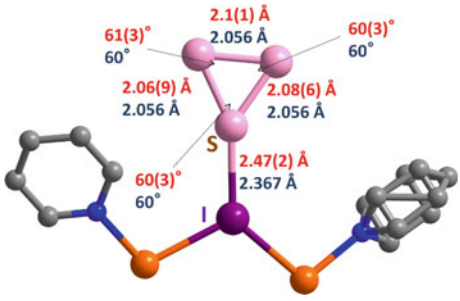

Fig. 12.18 Geometrical parameters from X-ray analysis and theoretical calculations for chemisorbed cyclo-S_3^{2+}. Red numbers refer to the values obtained from X-ray analysis, blue numbers refer to values obtained from the calculation of I-(cyclo-S_3^{2+}). Cu, orange; I, purple, and S, pink. Reproduced with permission of the International Union of Crystallography

and unstable species has hampered progress in their basic understanding. Herein, we demonstrated the advantages of using interactive pores to trap labile and unstable species and observe their reactivities by X-ray analysis. The representative example was the detection of metastable small sulfur allotropes and their interconversion for the first time inside the pores of the helical CuI network. Interactive pores used in these studies can be created by kinetic assembly of the coordination networks from their precursors. Application of this method to monitoring of catalytic transformations could lead to deeper understandings of their reaction mechanisms. These kinds of studies are crucial for the future design and development of novel functional materials.

12.1.12 Future Perspective

Self-assembly of coordination networks has been studied intensively by many researchers over the past quarter century. However, while the formation of kinetic side-products has been frequently noted, their detailed investigations have been scarce due to low stability and poor crystallinity. We demonstrated that kinetic assembly of porous coordination networks could be used to produce materials with interactive pore sites. The properties of these sites largely determine the possible applications of the kinetic materials.

One promising application for the interactive pore sites is trapping and visualization of unstable species. The range of potential unstable allotropes than can be targeted is broad and includes sulfur, phosphorus, and selenium among others. For example, in the case of phosphorus, only it is more widely known and a more stable form, P_4, was encapsulated in the interactive pores. However, there are still no examples of stabilization and visualization of elusive dimer, P_2, even though it is known to exist at high temperatures, and has the same electronic configuration as N_2. Therefore, this phosphorus allotrope could be a highly interesting candidate for the future encapsulation studies.

Another intriguing application is the control of transition states. If an interactive pore could behave like an enzyme pocket, it could be used to modulate transition states of various transformations. Achieving such degree of control could open up new reaction pathways that cannot be reached with the conventional methods. In addition, interactive sites could also function as active catalytic centers, if their interactions with a substrate lower the activation energy. Therefore, the design and construction of the desired interactive sites from suitable metal connectors and ligands could present and powerful approach for the development tailor-made catalysts. Some of the best catalytic systems in existence, natural enzymes, utilize interactive sites extensively in their functions. These systems enable unprecedented acceleration of otherwise difficult reactions, such as methane monooxygenase (MMO), which oxidizes methane to methanol. Our ultimate goal is to develop such bio-mimetic catalysts by utilizing interactive sites generated in kinetically assembled networks.

In this sense, the careful design of desired interactive sites is a key step toward building materials that mimic biological functions, particularly the ability to catalyze reactions under mild conditions. This task will be accomplished by the judicious development of multifunctional ligands, the selection of appropriate metal connectors, and tuning the reaction parameters. However, there are still many challenges that need to be addressed before the kinetically assembled coordination networks could come close to reaching such a formidable goal.

References

1. Dichtel, W.R., Miljanić, O.Š., Zhang, W., Spruell, J.M., Patel, K., Aprahamian, I., Heath, J.R., Stoddart, J.F.: Kinetic and thermodynamic approaches for the efficient formation of mechanical bonds. Acc. Chem. Res. **41**, 1750–1761 (2008)
2. Dickson, A., Brooks III, C.L.: Native states of fast-folding proteins are kinetic traps. J. Am. Chem. Soc. **135**, 4729–4734 (2013)
3. Hua, Q.X., Gozani, S.N., Chance, R.E., Hoffmann, J.A., Frank, B.H., Weiss, M.A.: Structure of a protein in a kinetic trap. Nat. Struct. Biol. **2**, 129–138 (1995)
4. Cheetham, A.K., Rao, C.N., Feller, R.F.: Structural diversity and chemical trends in hybrid inorganic–organic framework materials. Chem. Commun. **46**, 4780–4795 (2006)
5. Zhu, Y., Hua, Z., Zhou, J., Wang, L., Zhao, J., Gong, Y., Wu, W., Ruan, M., Shi, J.: Hierarchical mesoporous zeolites: direct self-assembly synthesis in a conventional surfactant solution by kinetic control over the zeolite seed formation. Chem. Eur. J. **17**, 14618–14627 (2011)
6. Wang, Y., Gao, X., Xiao, Y., Zhao, Q., Yang, J., Yan, Y., Huang, J.: Temperature dependent coordinating self-assembly. Soft Matter **11**, 2806–2811 (2015)
7. Zhong, Q.Z., Li, S., Chen, J., Xie, K., Pan, S., Richardson, J.J., Caruso, F.: Oxidation-mediated kinetic strategies for engineering metal-phenolic networks. Angew. Chem. Int. Ed. **58**, 12563–12568 (2019)
8. Michele, L.D., Varrato, F., Kotar, J., Nathan, S.H., Foffi, G., Eiser, E.: Multistep kinetic self-assembly of DNA-coated colloids. Nat. Commun. **4**, 2007 (2013)
9. Batten, S.R., Robson, R.: Interpenetrating nets: ordered, periodic entanglement. Angew. Chem. Int. Ed. **37**, 1460–1494 (1998)
10. Eddaoudi, M., Moler, D.B., Li, H., Chen, B., Reineke, T.M., O'Keefe, M., Yaghi, O.M.: Modular chemistry: secondary building units as a basis for the design of highly porous and robust metal–organic carboxylate frameworks. Acc. Chem. Res. **34**, 319–330 (2001)
11. Kitagawa, S., Kitaura, R., Noro, S.: Functional porous coordination polymers. Angew. Chem. Int. Ed. **43**, 2334–2375 (2004)
12. Kitagawa, S., Uemura, K.: Dynamic porous properties of coordination polymers inspired by hydrogen bonds. Chem. Soc. Rev. **34**, 109–119 (2005)
13. Bradshaw, D., Claridge, J.B., Cussen, E.J., Prior, T.J., Rosseinsky, M.J.: Design, chirality, and flexibility in nanoporous molecule-based materials. Acc. Chem. Res. **38**, 273–282 (2005)
14. Kawano, M., Fujita, M.: Direct observation of crystalline-state guest exchange in coordination networks. Coord. Chem. Rev. **251**, 2592–2605 (2007)
15. Férey, G.: Hybrid porous solids: past, present, future. Chem. Rev. **37**, 191–214 (2008)
16. Furukawa, H., Cordova, K.E., O'Keefe, M., Yaghi, O.M.: The chemistry and applications of metal-organic frameworks. Science **341**, 1230444 (2013)
17. Cook, T.R., Zheng, Y.R., Stang, P.J.: Metal-organic frameworks and self-assembled supramolecular coordination complexes: comparing and contrasting the design, synthesis, and functionality of metal-organic materials. Chem. Rev. **113**, 734–777 (2013)
18. Hoskins, B.F., Robson, R.: Infinite polymeric frameworks consisting of three dimensionally linked rod-like segments. J. Am. Chem. Soc. **111**, 5962–5964 (1989)

19. Hoskins, B.F., Robson, R.: Design and construction of a new class of scaffolding-like materials comprising infinite polymeric frameworks of 3D-linked molecular rods. A reappraisal of the zinc cyanide and cadmium cyanide structures and the synthesis and structure of the diamond-related frameworks $[N(CH_3)_4][Cu^{I}Zn^{II}(CN)_4]$ and Cu^{I}[4,4′,4″,4‴-tetracyanotetraphenylmethane]$BF_4 \cdot xC_6H_5NO_2$. J. Am. Chem. Soc. **112**, 1546–1554 (1990)
20. Fujita, M., Kwon, Y.J., Washizu, S., Ogura, K.: Preparation, clathration ability, and catalysis of a two-dimensional square network material composed of cadmium(II) and 4,4′-bipyridine. J. Am. Chem. Soc. **116**, 1151–1152 (1994)
21. Yaghi, O.M., Li, H.: Hydrothermal synthesis of a metal-organic framework containing large rectangular channels. J. Am. Chem. Soc. **117**, 10401–10402 (1995)
22. Kondo, M., Yoshitomi, T., Seki, K., Matsuzaka, H., Kitagawa, S.: Three-dimensional framework with channeling cavities for small molecules: $\{[M_2(4,4'\text{-bpy})_3(NO_3)_4] \cdot xH_2O\}_n$ (M = Co, Ni, Zn). Angew. Chem. Int. Ed. Engl. **36**, 1725–1727 (1997)
23. Riou, D., Serre, C., Férey, G.: Composite microporous compounds (MIL-n): II. Hydrothermal synthesis and ab initio resolution by X-ray powder diffraction of MIL-5: a vanadodiphosphonate with a three-dimensional neutral framework. J. Solid. State. Chem. **141**, 89–93 (1998)
24. Stock, N., Biswas, S.: Synthesis of metal-organic frameworks (MOFs): routes to various MOF topologies, morphologies, and composites. Chem. Rev. **112**, 933–969 (2012)
25. Zhang, J., Wojtas, L., Larsen, R.W., Eddaoudi, M., Zaworotko, M.J.: Temperature and concentration control over interpenetration in a metal–organic material. J. Am. Chem. Soc. **131**, 17040–17041 (2009)
26. Bara, D., Wilson, C., Mörtel, M., Khusniyarov, M.M., Ling, S., Slater, B., Sproules, S., Forgan, R.S.: Kinetic control of interpenetration in Fe-biphenyl-4,4′-dicarboxylate metal-organic frameworks by coordination and oxidation modulation. J. Am. Chem. Soc. **141**, 8346–8357 (2019)
27. Yang, S., Lin, X., Lewis, W., Suyetin, M., Bichoutskaia, E., Parker, J.E., Tang, C.C., Allan, D.R., Rizkallah, P.J., Hubberstey, P., Champness, N.R., Thomas, K.M., Blake, A.J., Schröder, M.: A partially interpenetrated metal–organic framework for selective hysteretic sorption of carbon dioxide. Nat. Mater. **11**, 710–716 (2012)
28. Yu, T., Wang, S., Li, X., Gao, X., Zhou, C., Cheng, J., Li, B., Li, J., Chang, J., Hou, H., Liu, Z.: Roles of temperature, solvent, M/L ratios and anion in preparing complexes containing a Himta ligand. CrystEngComm **18**, 1350–1362 (2016)
29. De, D., Neogi, S., Bharadwaj, P.K.: Stoichiometry controlled structural variation in three-dimensional Zn(II)–frameworks: single-crystal to single-crystal transmetalation and selective CO_2 adsorption. Cryst. Growth Des. **16**, 5238–5246 (2016)
30. Wee, L.H.H., Meledina, M., Turner, S., Van Tendeloo, G., Zhang, K., Rodriguez-Albelo, L.M., Masala, A., Bordiga, S., Jiang, J., Navarro, J.A.R., Kirschhock, C.E.A., Martens, J.A.: 1D–2D-3D transformation synthesis of hierarchical metal-organic framework adsorbent for multicomponent alkane separation. J. Am. Chem. Soc. **139**, 819–828 (2017)
31. Werner, J., Rams, M., Tomkowicz, Z., Runčevski, T., Dinnebier, R.E., Suckert, S., Näther, C.: Thermodynamically metastable thiocyanato coordination polymer that shows slow relaxations of the magnetization. Inorg. Chem. **54**, 2893–2901 (2015)
32. Forster, P.M., Burbank, A.R., Livage, C., Férey, G., Cheetham, A.K.: The role of temperature in the synthesis of hybrid inorganic–organic materials: the example of cobalt succinates. Chem. Commun. **4**, 368–369 (2004)
33. Näther, C., Bhosekar, G., Jess, I.: Preparation of stable and metastable coordination compounds: insight into the structural, thermodynamic, and kinetic aspects of the formation of coordination polymers. Inorg. Chem. **46**, 8079–8087 (2007)
34. Zhang, J.P., Huang, X.C., Chen, X.M.: Supramolecular isomerism in coordination polymers. Chem. Soc. Rev. **38**, 2385–2396 (2009)
35. Nagarkar, S.S., Chaudhari, A.K., Ghosh, S.K.: Role of temperature on framework dimensionality: supramolecular isomers of $Zn_3(RCOO)_8$ based metal organic frameworks. Cryst. Growth Des. **12**, 572–576 (2012)

36. Manna, B., Chaudhari, A.K., Joarder, B., Karmakar, A., Ghosh, S.K.: Dynamic structural behavior and anion-responsive tunable luminescence of a flexible cationic metal–organic framework. Angew. Chem. Int. Ed. **52**, 998–1002 (2013)
37. Bernini, M.C., de la Pena-O'Shea, V.A., Iglesias, M., Snejko, N., Gutiérrez-Puebla, E., Brusau, E.V., Narda, G.E., Illas, F., Monge, M.Á.: Thermodynamic and kinetic control on the formation of two novel metal-organic frameworks based on the Er(III) ion and the asymmetric dimethylsuccinate ligand. Inorg. Chem. **49**, 5063–5071 (2010)
38. Gándara, F., de la Pena-O'Shea, V.A., Illas, F., Snejko, N., Proserpio, D.M., Gutiérrez-Puebla, E., Monge, M.A.: Three lanthanum MOF polymorphs: insights into kinetically and thermodynamically controlled phases. Inorg. Chem. **48**, 4707–4713 (2009)
39. Dikhtiarenko, A., Serra-Crespo, P., Castellanos, S., Pustovarenko, A., Mendoza-Meroño, R., Garcia-Granda, S., Gascon, J.: Temperature-dependent supramolecular isomerism of lutetium-aminoterephthalate metal-organic frameworks: synthesis, crystallography, and physical properties. Cryst. Growth. Des. **16**, 5636–5645 (2016)
40. Martí-Rujas, J., Kawano, M.: Kinetic products in coordination networks: ab initio X-ray powder diffraction analysis. Acc. Chem. Res. **46**, 493–505 (2013)
41. Kitagawa, H., Ohtsu, H., Kawano, M.: Kinetic assembly of a thermally stable porous coordination network based on labile CuI units and the visualization of I_2 sorption. Angew. Chem. Int. Ed. **52**, 12395–12399 (2013)
42. Kawano, M., Haneda, T., Hashizume, D., Izumi, F., Fujita, M.: A selective instant synthesis of a coordination network and its ab initio powder structure determination. Angew. Chem. Int. Ed. **47**, 1269–1271 (2008)
43. Biradha, K., Fujita, M.: A springlike 3D-coordination network that shrinks or swells in a crystal-to-crystal manner upon guest removal or readsorption. Angew. Chem. Int. Ed. **41**, 3392–3395 (2002)
44. Ohara, K., Martí-Rujas, J., Haneda, T., Kawano, M., Hashizume, D., Izumi, F., Fujita, M.: Formation of a thermally stable, porous coordination network via a crystalline-to-amorphous-to-crystalline phase transition. J. Am. Chem. Soc. **131**, 3860–3861 (2009)
45. Martí-Rujas, J., Islam, N., Hashizume, D., Izumi, F., Fujita, M., Kawano, M.: Dramatic structural rearrangements in porous coordination networks. J. Am. Chem. Soc. **133**, 5853–5860 (2011)
46. Ohtsu, H., Bennett, T.D., Kojima, T., Keen, D.A., Niwa, Y., Kawano, M.: Amorphous–amorphous transition in a porous coordination polymer. Chem. Commun. **53**, 7060–7063 (2017)
47. Bennett, T.D., Goodwin, A.L., Dove, M.T., Keen, D.A., Tucker, M.G., Barney, E.R., Soper, A.K., Bithell, E.G., Tan, J.C., Cheetham, A.K.: Structure and properties of an amorphous metal-organic framework. Phys. Rev. Lett. **104**, 115503 (2010)
48. Bennett, T.D., Cheetham, A.K.: Amorphous metal-organic frameworks. Acc. Chem. Res. **47**, 1555–1562 (2014)
49. Bennett, T.D., Tan, J.C., Yue, Y., Baxter, E., Ducati, C., Terrill, N.J., Yeung, H.H.M., Zhou, Z., Chen, W., Henke, S., Cheetham, A.K., Greaves, G.N.: Hybrid glasses from strong and fragile metal-organic framework liquids. Nat. Commun. **6**, 8079 (2015)
50. Martí-Rujas, J., Matsushita, Y., Izumi, F., Fujita, M., Kawano, M.: Solid–liquid interface synthesis of microcrystalline porous coordination networks. Chem. Commun. **46**, 6515–6517 (2010)
51. Cavallo, G., Metrangolo, P., Milani, R., Pilati, T., Priimagi, A., Resnati, G., Terraneo, G.: The halogen bond. Chem. Rev. **116**, 2478–2601 (2016)
52. Resnati, G., Boldyreva, E., Bombicz, P., Kawano, M.: Supramolecular interactions in the solid state. IUCrJ **2**, 675–690 (2015)
53. Takaoka, K., Kawano, M., Ozeki, T., Fujita, M.: Crystallographic observation of an olefin photodimerization reaction that takes place via thermal molecular tumbling within a self-assembled host. Chem. Commun. **15**, 1625–1627 (2006)
54. Ohmori, O., Kawano, M., Fujita, M.: A two-in-one crystal: uptake of two different guests into two distinct channels of a biporous coordination network. Angew. Chem. Int. Ed. **44**, 1962–1964 (2005)

55. Ohmori, O., Kawano, M., Fujita, M.: Construction of biporous coordination networks via π−π interaction. CrystEngComm **7**, 255–259 (2005)
56. Kawano, M., Kawamichi, T., Haneda, T., Kojima, T., Fujita, M.: The modular synthesis of functional porous coordination networks. J. Am. Chem. Soc. **129**, 15418–15419 (2007)
57. Kawamichi, T., Kodama, T., Kawano, M., Fujita, M.: Single-crystalline molecular flasks: chemical transformation with bulky reagents in the pores of porous coordination networks. Angew. Chem. Int. Ed. **47**, 8030–8032 (2008)
58. Haneda, T., Kawano, M., Kawamichi, T., Fujita, M.: Direct observation of the labile imine formation through single-crystal-to-single-crystal reactions in the pores of a porous coordination network. J. Am. Chem. Soc. **130**, 1578–1579 (2008)
59. Kawamichi, T., Inokuma, Y., Kawano, M., Fujita, M.: Regioselecitive Huisgen cycloaddition within porous coordination networks. Angew. Chem. Int. Ed. **49**, 2375–2377 (2010)
60. Kawamichi, T., Haneda, T., Kawano, M., Fujita, M.: X-ray observation of a transient hemiaminal trapped in a porous network. Nature **461**, 633–635 (2009)
61. Inokuma, Y., Kawano, M., Fujita, M.: Crystalline molecular flasks. Nat. Chem. **3**, 349–358 (2011)
62. Ohtsu, H., Choi, W., Islam, N., Matsushita, Y., Kawano, M.: Selective trapping of labile S_3 in a porous coordination network and the direct X-ray observation. J. Am. Chem. Soc. **135**, 11449–11452 (2013)
63. Steudel, R., Eckert, B.: Solid sulfur allotropes. Top. Curr. Chem. **230**, 1–79 (2003)
64. Steudel, R., Steudel, Y., Wong, M.W.: Speciation and thermodynamics of sulfur vapor. Top. Curr. Chem. **230**, 117–134 (2003)
65. Meyer, B.: Elemental sulfur. Chem. Rev. **76**, 367–388 (1976)
66. McCarthy, M.C., Thorwirth, S., Gottlieb, C.A., Thaddeus, P., Gupta, H., Stanton, J.F.: Rotational spectroscopy and equilibrium structures of S_3 and S_4. J. Chem. Phys. **123**, 054326 (2005)
67. Ichikawa, M., Kimura, T., Fukuoka, A.: Stud. Surf. Sci. Catal. **60**, 335–342 (1991)
68. Maleki, B., Salehabadi, H.: Ammonium chloride; as a mild and efficient catalyst for the synthesis of some 2-arylbenzothiazoles and bisbenzothiazole derivatives. Eur. J. Chem. **4**, 377–380 (2010)
69. Choi, W., Ohtsu, H., Matsushita, Y., Kawano, M.: Safe P_4 reagent in a reusable porous coordination network. Dalton Trans. **45**, 6357–6360 (2016)
70. Ohtsu, H., Kawano, M.: Br_2 induced oxidative pore modification of a porous coordination network. Dalton Trans. **45**, 489–493 (2016)
71. Lang, J.P., Xu, Q.F., Yuan, R.X., Abrahams, B.F.: $\{[WS_4Cu_4(4,4'\text{-bpy})_4][WS_4Cu_4I_4(4,4'\text{-bpy})_2]\}_\infty$—an unusual 3D porous coordination polymer formed from the preformed cluster $[Et_4N]_4[WS_4Cu_4I_6]$. Angew. Chem. Int. Ed. **43**, 4741–4745 (2004)
72. Holzer, W., Murphy, W.F., Bernstein, H.J.: Resonance Raman effect and resonance fluorescence in halogen gases. J. Chem. Phys. **52**, 399–407 (1970)
73. Congeduti, A., Nardone, M., Postorino, P.: Polarized Raman spectra of a single crystal of iodine. Chem. Phys. **256**, 117–123 (2000)
74. Bondi, A.: van der Waals volumes and radii. J. Phys. Chem. **68**, 441–451 (1964)
75. El-Sheshtawy, H.S., Bassil, B.S., Assaf, K.I., Kortz, U., Nau, W.M.: Halogen bonding inside a molecular container. J. Am. Chem. Soc. **134**, 19935–19941 (2012)
76. Ohtsu, H., Kawano, M.: Kinetic assembly of coordination networks. Chem. Commun. **53**, 8818–8829 (2017)
77. Hathaway, B.J.: In: Wilkinson, G., Gillard, R.D., McCleverty, J.A. (eds.) Comprehensive Coordination Chemistry, vol. 5, pp. 533–774. Pergamon, Oxford (1987)
78. Ohara, K., Yamaguchi, K.: Cold-spray ionization mass spectrometric detection of a coordination oligomer. Anal. Sci. **28**, 635–637 (2012)
79. Allcock, H.R., Siegel, L.A.: Phosphonitrilic compounds. III. Molecular inclusion compounds of tris(o-phenylenedioxy)phosphonitrile trimer. J. Am. Chem. Soc. **86**, 5140–5144 (1964)

80. Hertzsch, T., Budde, F., Weber, E., Hulliger, J.: Supramolecular-wire confinement of I_2 molecules in channels of the organic zeolite tris(*o*-phenylenedioxy)cyclotriphosphazenephonitrile trimer. Angew. Chem. Int. Ed. **41**, 2281–2284 (2002)
81. Kitagawa, H., Ohtsu, H., Cruz-Cabeza, A.J., Kawano, M.: Isolation and evolution of labile sulphur allotropes via kinetic encapsulation in interactive porous networks. IUCrJ **3**, 232–236 (2016)
82. Flemming, B., Wolczanski, P.T., Hoffmann, R.: Transition metal complexes of cyclic and open ozone and thiozone. J. Am. Chem. Soc. **127**, 1278–1285 (2005)
83. Mück, L.A., Lattanzi, V., Throwirth, S., McCarthy, M.C., Gauss, J.: Cyclic SiS_2: a new perspective on the walsh rules. Angew. Chem. Int. Ed. **51**, 3695–3698 (2012)

Chapter 13
Creation of Organic-Metal Hybridized Nanocrystals Toward Nonlinear Optics Applications

Tsunenobu Onodera, Rodrigo Sato, Yoshihiko Takeda, and Hidetoshi Oikawa

Abstract Organic nanocrystals are occupied in an intermediate state between single molecule and the corresponding molecular crystal in a bulk state, which are fabricated in common by using the reprecipitation method. The crystal size is in the range of several tens nanometer to sub-micrometer. In particular, linear optical properties such as excitonic absorption spectrum and fluorescence emission spectrum are evidently dependent on crystal size, owing to thermally soften nanocrystal lattice with increasing specific surface area. Core–shell-type hybridization between organic nanocrystals and novel metal nanoparticles is of too much interest in current material science. In this chapter, creation of polydiacetylene nanocrystal fibers hybridized with gold nanoparticles will be introduced in details toward nonlinear optics applications. Polydiacetylene is typically one-dimensional π-conjugated polymer, and one of the most promising organic nonlinear optical materials. It is expected that nonlinear optical properties would be enhanced because of peculiar optoelectronic interaction between exciton in polydiacetylene and localized surface plasmon resonance effect in gold nanoparticles.

Keywords Polydiacetylene · Nanocrystal fiber · Nonlinear optical property · Exciton · Localized surface plasmon resonance

T. Onodera · H. Oikawa (✉)
Institute of Multidisciplinary Research for Advanced Materials (IMRAM), Tohoku University, Katahira 2-1-1, Aoba-ku, Sendai 980-8577, Japan
e-mail: hidetoshi.oikawa.e8@tohoku.ac.jp

R. Sato · Y. Takeda
Hydrogen Materials Engineering Group, Center for Green Research on Energy and Environmental Materials, National Institute for Materials Science (NIMS), Sakura 3-13, Tsukuba 305-0003, Japan

M. Sakamoto and H. Uekusa (eds.), *Advances in Organic Crystal Chemistry*,
https://doi.org/10.1007/978-981-15-5085-0_13

13.1 Introduction

13.1.1 Scopes of Hybridized Nanomaterials

Hybridization and/or hybrid on nanometer to sub-micrometer scales, for example, typically polymer blends (polymer alloys), and polymer composites containing inorganic fillers, is one of the most important molecule design concepts and the interesting topics in current materials science and technology [1]. In these hybridized systems, the domain size of each component and its three-dimensional distribution in a polymer matrix would determine mainly the final properties and function, accompanied with selection and combinations of component materials [2]. As a result, the resulting physicochemical properties would become additive and/or intermediate state in the hybridized materials. Especially, organic–inorganic hybridized materials like polymer composites are of too much interest [3], because of emergence of unique nanostructure, and of enhancement of noble physical properties and excellent functions, due to peculiar couplings and interactions at an interface between organic and inorganic components [4].

On the contrary, "hybridized nanomaterials" is on nanometer scale in overall size, and should be essentially different from above-mentioned hybridized materials [5]. The hybridized nanomaterials are in common comprised from metal nanoparticles (NPs) [6], semiconductor quantum dots (SQDs) [7], and magnetic (or inorganic oxides) NPs [8], and have recently attached great attention and interest on nanoscience and nanotechnology. These kinds of NPs themselves provide characteristic properties, e.g., localized surface plasmon resonance (LSPR) [6], quantum confinement effect [7], giant magneto resistive effect [8], and extraordinary polarization field induced by high refractive index [9]. In addition, π-conjugated organic and polymer nanocrystals (NCs) are also one of the candidate components in hybridized nanomaterials [10–12].

13.1.2 Organic and Polymer Nanocrystals

Organic and polymer NCs (hereinafter, called organic NCs) are a kind of molecule crystals, and are occupied at an intermediate state between single molecule and the corresponding bulk crystals [10–12]. Organic NCs are usually fabricated by means of so-called reprecipitation method and its developed and/or improved processes, and the crystal size is located in the range between several tens nanometer and sub-micrometers. For example, the acetone (good solvent) solution of diacetylene (DA) monomer is quickly injected into vigorously stirred water medium as a poor solvent, and then the formed DA NCs are solid-state polymerized to convert DA to polydicetylene (PDA) by UV-irradiation [13]. Here, PDA is a typical one-dimensional π-conjugated polymer, and is one of the most promising organic nonlinear optical

(NLO) materials having high third-order NLO susceptibility and ultra high speed optical response [14, 15].

As a result, one can successfully obtain well-defined PDA NCs dispersed in an aqueous medium [10–12]. The morphology such as crystal size and shape of organic NCs is controlled experimentally by changing reprecipitation conditions: selection of good and poor solvents, concentration and injected amount, injection rate, temperature and stirring rate of poor medium, addition of surfactant, and so on. Organic NCs provide some interesting linear optical properties and function [10–12]. For example, the excitonic absorption peak (EAP) positions are continuously blue-shifted with decreasing crystal size in the case PDA NCs [16], whereas the fluorescence emission peak positions measured with near-field scanning optical microspectroscopy (NSOM) are also blue-shifted in the case of perylene NCs as the crystal size is reduced [17]. These kinds of optical shift are due to thermally soften nanocrystal lattice induced by the increase in specific surface area in small-sized organic NCs, i.e., reduction of optoelectronically inter-molecular interaction in nanocrystal lattice [18]. In addition, the layered thin films have been finely prepared by utilizing negative surface potential of PDA NCs, and then the third-order NLO susceptibility was multiplied apparently with the number of layers toward optoelectronic and/or photonic device applications [10, 11].

13.1.3 Organic-Metal Hybridized Nanocrystals

So far, PDA core-silver (Ag) shell-type hybridized NCs have been fabricated successfully by establishing visible-light-driven photocatalytic reduction method [19], and were characterized carefully with scanning electron microscope (SEM), transmission electron microscope (TEM) with electron diffraction (ED) pattern, powder X-ray diffraction (XRD) pattern, and electron probe X-ray microanalyzer (EPMA).

In fact, the aqueous solution of $AgNO_3$ and NH_3 was added into PDA NCs dispersion liquids, and then visible (Vis) light was irradiated at a given interval. As a result, it was confirmed that Ag NPs (ca. 10 nm in size) as Ag shell were selectively deposited only on the surface of PDA NCs as a core. The extinction spectrum showed the interesting features, that is, the red-shift and broadening of LSPR peaks from Ag shell, and also red-shifted EAP of PDA core. The former is caused by imhomogeneous distribution in size and the dephasing effect of LSPR, and the later is due to changes of dielectric environment in the surrounding PDA core. The necessitated condition is that the redox potential of metal ion should be located between conduction band (CB) and valence band (VB) of PDA core [18]. Probably, the excited electron at CB would reduce metal ion effectively, and the formed metal NPs are selectively adsorbed only on the surface of PDA core with negative surface potential. In addition, the size and deposition density of the resulting metal NPs were influenced considerably by the relationship between redox potential of metal ion and work function of metal NPs [18, 19]. Actually, one can deposit Ag NPs on the surface of PDA core, being independent of morphology (size and shape) of PDA core [19]. The present concept of formation

mechanism could be basically applied to produce the other kinds of hybridized NCs such as polyalkylthiophene (PAT) core-platinum (Pt) hybridized NCs [20].

On the other hand, Ag core-PDA shell-type hybridized NCs were also produced by using co-reprecipitation and microwave-irradiation method [21]. In this case, the acetone solution of DA monomer was quickly injected into an aqueous dispersion liquid of Ag NPs, and then DA NCs as a shell were formed well on the surface of Ag NPs as a core. DA shell was converted to PDA shell by UV-irradiation.

In this chapter, a new type of hybridized PDA nanocrystal fibers (NCFs) [22] as a core with gold (Au) NPs as a shell have been created, and nanostructural correlation of optical properties will be discussed in detail. Interestingly, silica thin layer was introduced experimentally between PDA core and Au shell so as to possibly control LSPR effect from Au NPs [23].

13.2 Hybridized Polydiacetylene Nanocrystal Fibers

13.2.1 Preparation of PDA Nanocrystal Fibers

As described in the previous 13.1.2, it is possible to control the morphology of organic NCs by suitably optimizing the reprecipitation conditions. In the case of PDA NCs, the crystal size decreases in general with decreasing the concentration of injected DA-acetone solution [10–12]. On the other hand, the added surfactant and temperature of poor medium would affect remarkably the shape [22]. Actually, the formation of PDA NCFs was confirmed by SEM (JEOL: JSM-6700F) observation (Fig. 13.1). The two kinds of surfactants (SDS: sodium dodecyl sulfate, and CTAB: hexadecyl trimethyl ammonium bromide) were employed and added to DA-acetone solution in advance, and subsequently the injection was performed at the elevated temperature (60 °C) of water medium. The typical diameter is ca. 30–50 nm and the counter length is more than several μm in any resulting PDA NCFs. On the other hand, only PDA NCs were produced around and/or below at room temperature, even though the surfactants were co-existed.

The formation mechanism of PDA NCFs is speculated as follows [10–12]. Probably, amorphous NPs of DA is formed at the initial stage just after injection at the elevated temperature. These amorphous DA NPs are stabilized by the added surfactants, and then the delay in nanocrystallization would occur in individual amorphous DA NPs. Meanwhile, amorphous DA NPs are crystallized to form DA NCs with the elapsed time. At the next stage, already-formed DC NCs may act as a nucleus and/or a kind of substrate, and then another amorphous DA NPs are adsorbed on the facet surface of DA NCs. The adsorbed DA NPs are immediately crystallized through homo-epitaxial-like crystal growth. Consequently, this repetition process could provide one-dimensional DA NCFs, which are solid-state polymerized as usual to produce PDA NCFs. The crystal lattice structure of PDA NCFs was the same as that of PDA NCs by the measurements with powder XRD patterns (Bruker: D8

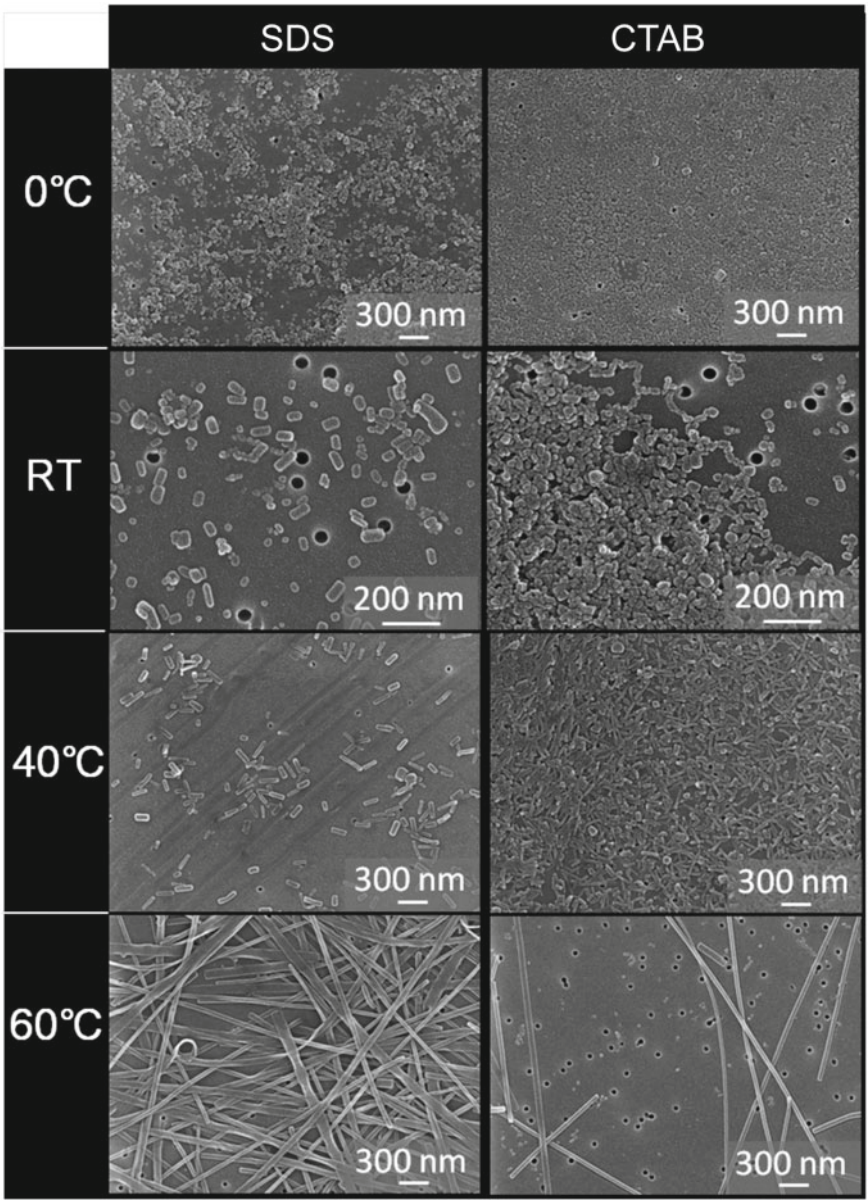

Fig. 13.1 SEM images of PDA NCs and PDA NCFs prepared at various temperatures, when the surfactants, SDS and/or CTAB, were added to acetone solution of DA in the reprecipitation method

ADVANCE) [22]. The surface potential of PDA NCFs is −40 to −60 mV, and PDA NCFs are dispersed stably for half a year in water medium. However, the dispersion stability was not so good in the case of CTAB.

The oriented thin films of PDA NCFs were fabricated easily by means of so-called convective assembly method, which order parameter determined experimentally by the dichroic ratio was high and about 0.87 [22].

13.2.2 Silica Coating of PDA Nanocrystal Fibers

The surface of PDA NCFs was coated with silica layer by using so-called sol–gel method [24], and this layer is much important to control optoelectronic interaction at the interface in the resulting hybridized NCFs [23]. A given amount of EtOH (ethanol), NH_3, and TEOS (tetraethyl orthosilicate) was added to PDA NCFs dispersion liquid, and then the mixed dispersion liquid was stirred for one hour at room temperature. The small-sized silica NPs were formed at the initial stage and adsorbed locally on the surface of PDA NCFs. After one hour, PDA NCFs were fully coated with silica layer (Fig. 13.2).

The optoelectronic interaction of exciton and LSPR at the interface is intensively dependent on the thickness of silica layer [23, 25, 26]. Namely, it is so important to possibly control the thickness with below 10 nm. However, the thickness of silica layer is estimated to be about 50 nm in Fig. 13.2c, since the diameter of PDA NCFs is 30 nm to 50 nm (Fig. 13.1). However, the trial use of much small amount of TEOS added was unexpectedly ineffective. So, the affinity between surface of PDA NCFs and silica layer has been further improved by employing cationic surfactant (CTAB) and neutral polymer (PEG: polyethylene glycol, $M_w = 3000$) as well as anionic surfactant (SDS). Namely, the sol–gel reaction proceeded under the co-existences of SDS, CTAB, and PEG in PDA NCFs dispersion liquid.

As a result, CTAB was much better to improve the affinity between PDA NCFs and silica layer as shown in SEM images (Fig. 13.3). That is to say, PDA NCFs were almost coated homogeneously with silica layer, when CTAB was used, compared with SDS and PEG. SDS is anionic surfactant, and was not adsorbed enough on

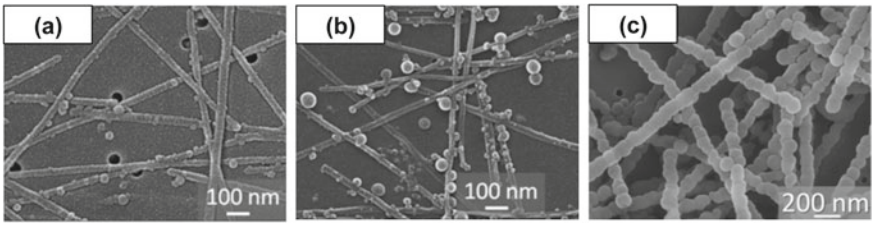

Fig. 13.2 SEM images of silica-coated PDA NCFs by means of sol–gel method. The coating times are **a** 30 min, **b** 40 min, and **c** 60 min

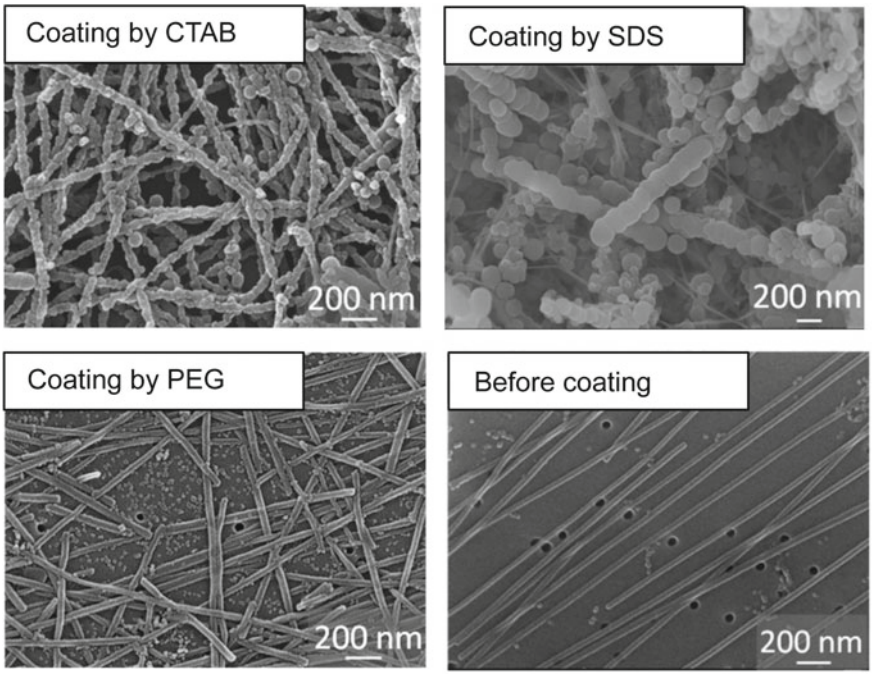

Fig. 13.3 SEM images of silica-coated PDA NCFs fabricated by using various surfactants (CTAB and SDS) and neutral polymer (PEG)

the surface of PDA NCFs, due to electrostatic repulsive interaction. PEG is probably adsorbed somewhat on PDA NCFs. It may be, however, difficult that the formed silica NPs would approach and adsorb subsequently on the surface of PDA NCFs, owing to steric hindrance or conformational repulsion along PEG chains. On the contrary, cationic CTAB may electrostatically interact effectively with both PDA NCFs and silica NPs because of the formation of well-defined bilayer structure having positive charge at both surface sides [27].

Besides the amount of added TEOS and suitably selected CTAB, reaction temperature (Fig. 13.4) and the mixture ratio of water and EtOH (Fig. 13.5) were also experimentally important factors.

These SEM images (Fig. 13.4) show the ones without purification by filtration. Namely, one can see un-adsorbed silica NPs as well as silica-coated PDA NCFs, and discuss qualitatively the temperature effect in the present sol–gel process [24]. The size of silica NPs became smaller with increasing temperature. So, it would be possible to relatively reduce the thickness of silica layer at high temperature.

These SEM images (Fig. 13.5) also exhibit the ones before purification by filtration in order to qualitatively investigate the effect of mixed solvents. The morphology of silica-coated PDA NCFs was changed and influenced remarkably at the various

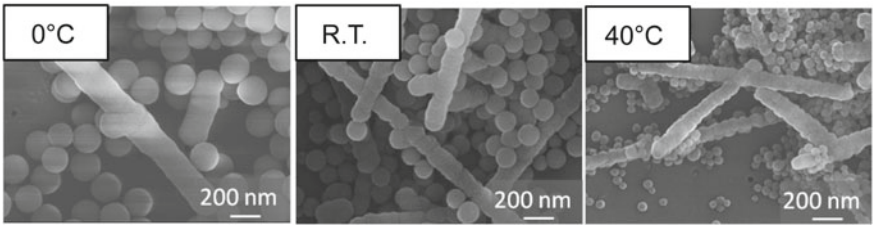

Fig. 13.4 SEM images of silica-coated PDA NCFs prepared at various reaction temperatures, when CTAB was used

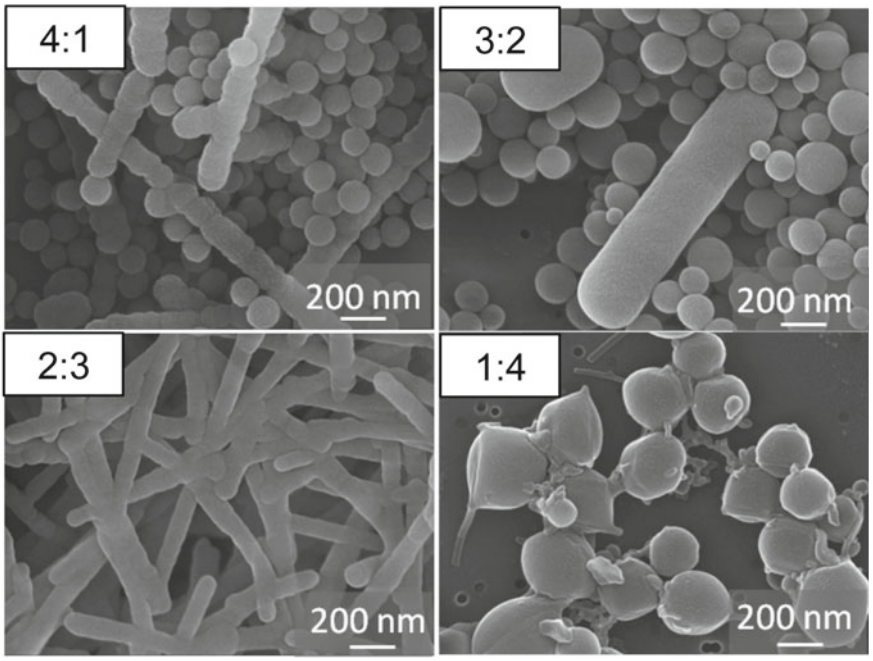

Fig. 13.5 SEM images of silica-coated PDA NCFs fabricated at the different mixture ratios of EtOH and water, EtOH: water = 4:1 to 1:4, when CTAB was also used

ratios of mixed EtOH and water. In common, EtOH added represses the rate of sol–gel reaction [24]. In addition, the critical micelle concentration (CMC) of CTAB in water medium (0.9 mM at 25 °C) is so different from that in EtOH (240 mM at 25 °C) [27]. Probably, these factors strongly affect the thickness of silica layer in the present case. Unexpectedly, it was confirmed from SEM observation that silica-coated PDA NCFs were partially connected each other, when the concentration of CTAB added was more than 10 mM.

Consequently, the silica-coating condition has been optimized successfully so as to fulfill the formation of silica layer with about or below 10 nm in thickness

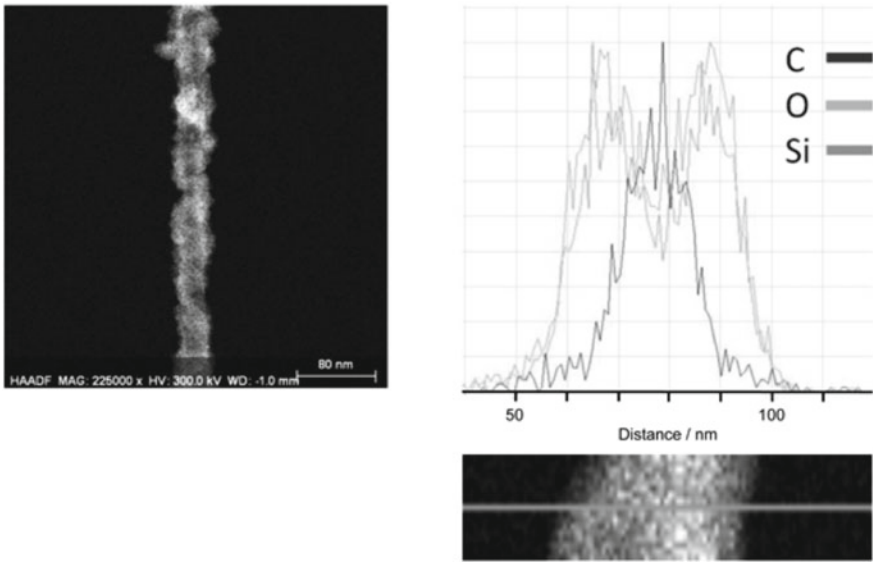

Fig. 13.6 HAADF-STEM image of silica-coated PDA NCFs (left), and the corresponding cross-section profile of elementary mapping (right). C: carbon, O: oxygen, and Si: silicon

on the basis above-mentioned experimental results. Actually, the obtained silica-coated PDA NCFs were characterized precisely with high-angle annular dark field scanning TEM (HAADF-STEM: Titan 80–300 with Image Corrector) observation and the corresponding cross-section profile of elementary mapping (Fig. 13.6). The distributions of oxygen and silicon are almost overlapped in the experimental errors, and the thickness of silica layer is estimated to be about 10 nm. This thickness is approximately comparable with the three-dimensional space distribution in enhanced photoelectric field of LSPR induced at the surrounding noble metal NPs [6, 28, 29], which would be deposited and hybridized on the surface of silica-coated PDA NCFs at the next hybridization step. So far, the emission enhancement of fluorescent dyes induced by LSPR effects has been investigated extensively, depending on thickness of dielectric insulator such as silica layer [25, 26].

13.2.3 Hybridization of PDA Nanocrystal Fibers

PDA core-Ag shell-type hybridized NCs have been fabricated as described in the previous Sect. 13.1.3. The hybridization of silica-coated PDA NCFs as a core and gold (Au) NPs as a shell will be discussed in this sub-section. The LSPR peak of Au NPs ($\lambda_{Au,\,LSPR}$ = ca. 500–550 nm) [30] is close to the EAP of PDA (PDA bulk crystal, PDA NCs, and PDA NCFs) ($\lambda_{PDA,\,EAP}$ = ca. 600–700 nm, including phonon-side band) [10–12]. So, the strong and peculiar optoelectronic interactions

would be emerged at the core–shell interface [31], rather than Ag NPs ($\lambda_{Ag,\ LSPR}$ = ca. 390–400 nm). This would expectedly lead to the enhancement of NLO properties [32], which is due to typically so-called excitation enhancement [23]. The surface of silica-coated PDA NCFs was further modified chemically by using silane-coupling agent (APTES: 3-aminopropyltriethoxysilane), so that amino-functional groups introduced on the surface of silica layer could control the adsorption amounts of Au NPs [33, 34]. After adding Au nano-seed (2–3 nm in size), aqueous solution of Au ion (Au^{3+}) added was reduced mildly by using reducing agent of formaldehyde (HCHO). Here, Au nano-seed was prepared by mixing an aqueous solution containing a given amount of tetrachloroauric (III) acid ($H[AuCl]_4$), sodium hydroxide (NaOH), and tertakis(hyroxymethyl)phosphonium chloride (THPC) [35]. On the other hand, aqueous solution of Au^{3+} was obtained by the incubating the mixture of $H[AuCl]_4$ aq. and potassium carbonate (K_2CO_3) aq. under dark condition at ca. 5 °C for three days [33]. Furthermore, the previously Pt-sputtered filter substrate was employed, when hybridized PDA NCFs was characterized with SEM observation without using the conventional Pt-sputtering treatment. One can clearly observe the deposited Au NPs, because Au NPs are distinguished from Pt NPs on the filter substrate.

Au NPs have been finely deposited on the surface of amino-terminated silica-coated PDA NCFs, that is, PDA NCFs hybridized with Au NPs, and the deposition amount (or coverage ratio) of Au NPs was controlled and tuned successfully with increasing the injected amount of aqueous solution of Au^{3+} (Fig. 13.7). Interestingly, the size of the deposited Au NPs was not so changed, and only the deposition amount was multiplied. In addition, HAADF-STEM images and the corresponding profile

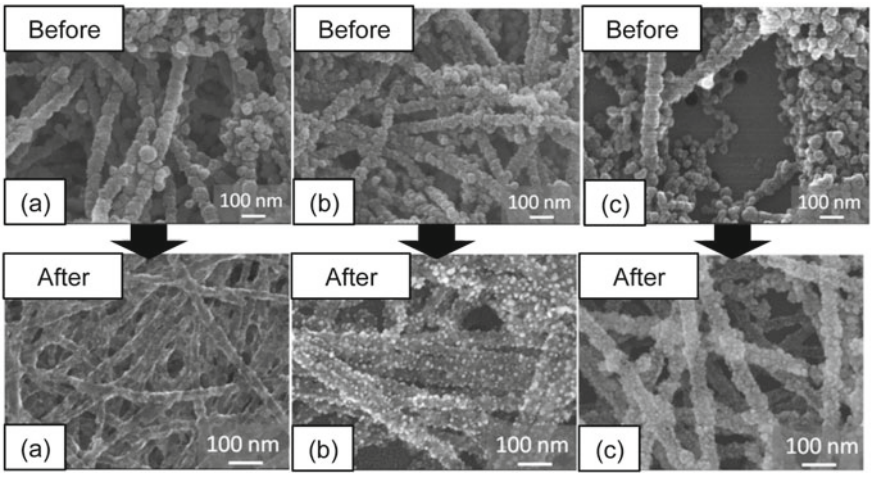

Fig. 13.7 SEM images before and after the deposition of Au NPs as a shell on the surface of amino-terminated silica-coated PDA NCFs. The deposition amounts of Au NPs increased from **a**–**c**, and the thickness of silica layer was about 10 nm in any case

of elementary mapping were also observed to further clarify the deposition nanostructure of Au NPs in hybridized PDA NCFs (Fig. 13.8). Au NPs were deposited randomly and almost isolated in the lower coverage ratio, whereas the Au NPs were densely located and connected partially with each other in the case of high coverage ratio.

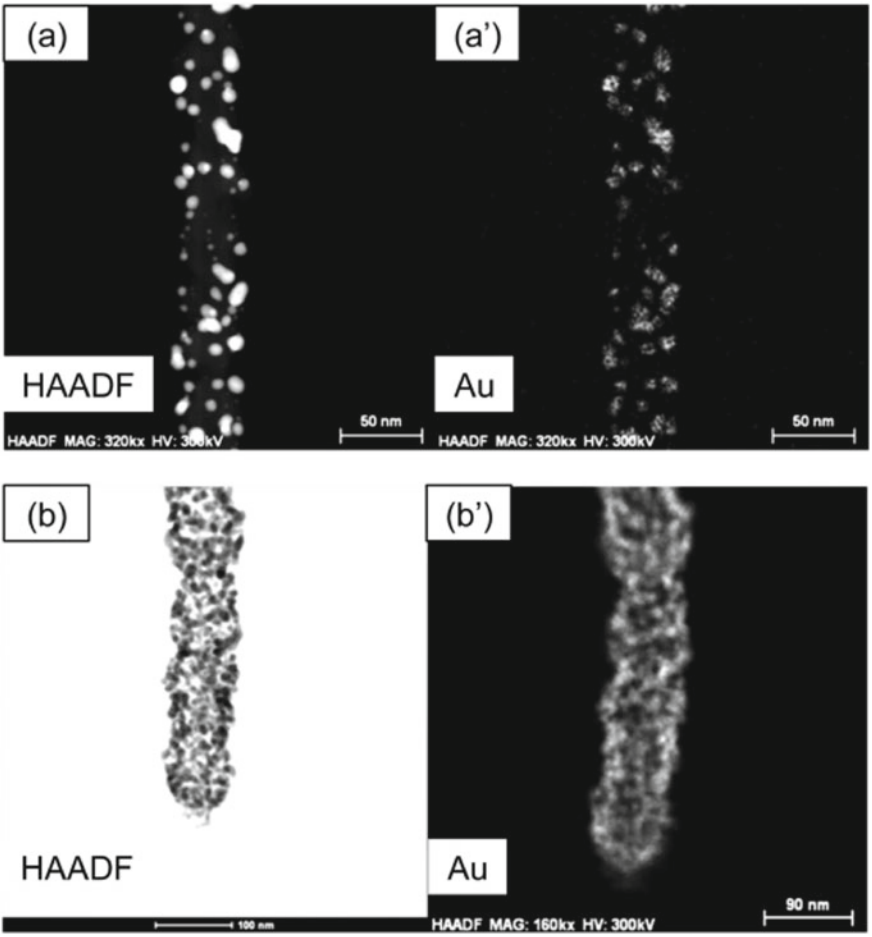

Fig. 13.8 HAADF images, (**a**) and (**b**), and the corresponding profiles of elementary mapping of Au, (**a'**) and (**b'**) for Au NPs as a shell deposited on the surface of amino-terminated silica-coated PDA NCFs in the cases of lower, (**a**) and (**a'**), and higher, (**b**) and (**b'**), coverage ratios

13.3 Optical Properties of Hybridized PDA Nanocrystal Fibers

13.3.1 Solid Thin Films and Linear Optical Properties

It is much important to fabricate well-defined solid thin films of PDA NCFs as well as hybridized PDA NCFs with highly optical quality in order to evaluate linear and nonlinear optical properties, and hybridized nanostructure correlations toward NLO devices applications. PDA NCFs- and/or hybridized PDA NCFs were loaded into polyvinyl alcohol (PVA, DP = 3100, degree of saponification = above 96%) matrix composites thin films in the present study. Actually, an aqueous dispersion liquid of PDA NCFs or hybridized PDA NCFs was mixed with PVA aq., and then water medium was evaporated quickly on a quartz substrate (KU1) around at 100 °C so as to possibly avoid aggregation and orientation. This fabrication process has the advantage to easily produce a large-area thin film without using a large amount of sample dispersion liquid in layer-by-layer method, etc.

The extinction spectra for PVA composites thin films of PDA NCFs or hybridized PDA NCFs were measured with UV–Vis absorption spectrometer (JASCO: V-570) (Fig. 13.9). The extinction spectrum of PVA composites thin film of PDA NCFs shows typically excitonic absorption peak ($\lambda_{PDA,\,EAP}$ = ca. 650 nm, phonon-side

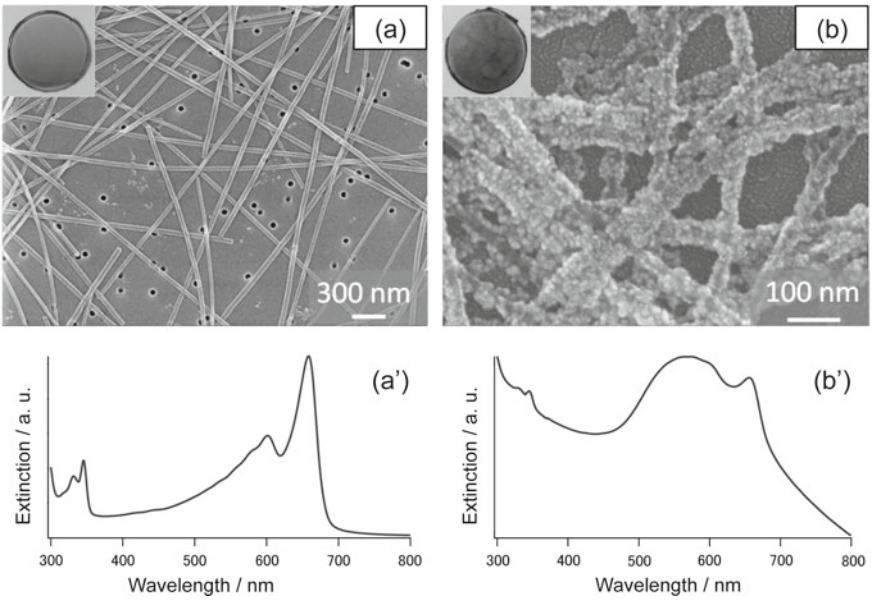

Fig. 13.9 SEM images of PDA NCFs (**a**) and hybridized PDA NCFs (**b**), and the corresponding extinction spectra of PVA composites thin film, (**a'**) and (**b'**). The real color of the photographs of both samples displayed in the insets of (**a**) and (**b**) are deep blue and deep black-violet, respectively

band around at 600–630 nm in wavelength). The baseline at above $\lambda = 700$ nm is almost zero. This fact suggests the resulting PVA composites thin film is transparent and highly optical quality with too much less scattering loss. On the other hand, one can see evidently the broad and intensively LSPR peak of deposited Au NPs in the extinction spectrum of hybridized PDA NCFs (($\lambda_{Au,\ LSPR}$ = ca. 500–550 nm) as well as EAP of PDA NCFs.

13.3.2 Pump-Probe Method to Measure Transient Transmission Spectrum for Evaluation of Third-Order NLO Properties

Third-order harmonic generation (THG) method [22] and Z-scan method [14, 18] are conventional techniques to evaluate third-order NLO properties, i.e., $\chi^{(3)}(\omega)$ value. However, the measurements are usually performed discontinuously at a specified wavelength. This is the drawback in these methods. In other words, it is so difficult to measure the wavelength dispersion of $\chi^{(3)}(\omega)$, which would surely bring about the difficulty for discussion about the correlation between $\chi^{(3)}(\omega)$ and nanostructure in the present hybridized systems. Recently, the experimental combination of pump-probe method and spectroscopic ellipsometry has been paid an attention, instead of the previous methods [36–39]. Namely, the wavelength dispersion of real and imaginary parts of $\chi^{(3)}(\omega)$ value is calculated from the difference in complex dielectric function, which is evaluated from experimentally determined wavelength dispersion of complex refractive index and transient transmission spectrum in the present measurement technique.

A pump-probe method was setup for the measurements of transient transmission spectrum (Fig. 13.10). Photo-degradation of PVA composites thin films has been checked from reproducibility of transient component.

13.3.3 Transient Transmission Spectra of PDA Nanocrystal Fibers and Hybridized PDA Nanocrystal Fibers

The transient transmission spectra for PDA NCFs and hybridized PDA NCFs have been measured successfully by using the pump-probe method as described in the previous sub-section (Fig. 13.11). The $\chi^{(3)}(\omega)$ value basically increases with the intensity of transient component, $(\Delta T + T)/T$ [36, 37].

The transient transmission peak appeared strongly at $\lambda = 630$–670 nm in any cases. Especially, the overall spectral shape in PDA NCFs corresponded to the extinction spectra (Fig. 13.9a). On the other hand, the value of $(\Delta T + T)/T$ unexpectedly became smaller than that of PDA NCFs, although the volume fraction of hybridized PDA NCFs is unclear exactly and not the same as that of PDA NCFs in PVA composites

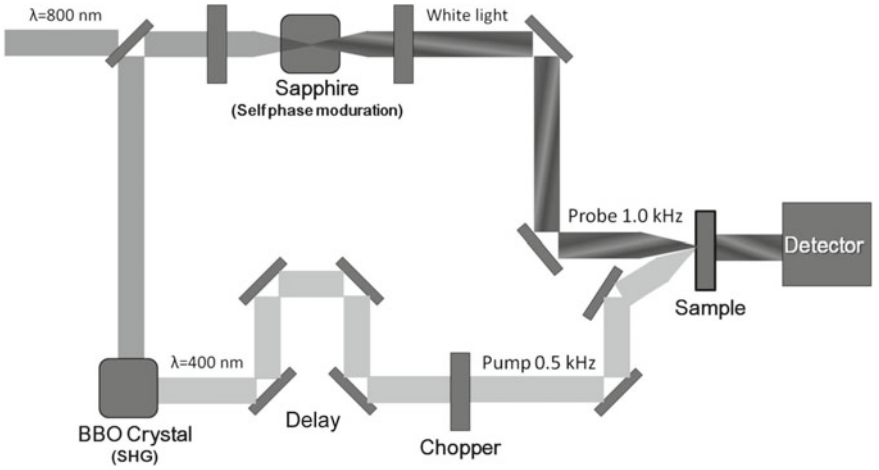

Fig. 13.10 Optical setup in the pump-probe method. Incident pump beam (λ = 800 nm, 130 fs, and 1 kHz) is launched from laser light source (Spectra-Physics, Inc., Mai-tai and Spitfire with BBO (β-BaB_2O_4) crystal for second harmonic generation (SHG)) consisted of Ti: sapphire laser (λ = 800 nm, 80 fs, 80 MHz, and above 15 nJ), regenerative amplifier [λ = 800, 130 fs, 1 kHz, and above 4 mJ), and Nd: YLF (1 kHz, and 20 W)]. The transient transmission spectrum of $SrTiO_3$ was measured to correct chirping of probe beam, and then the origin of time was revised at individual wavelength

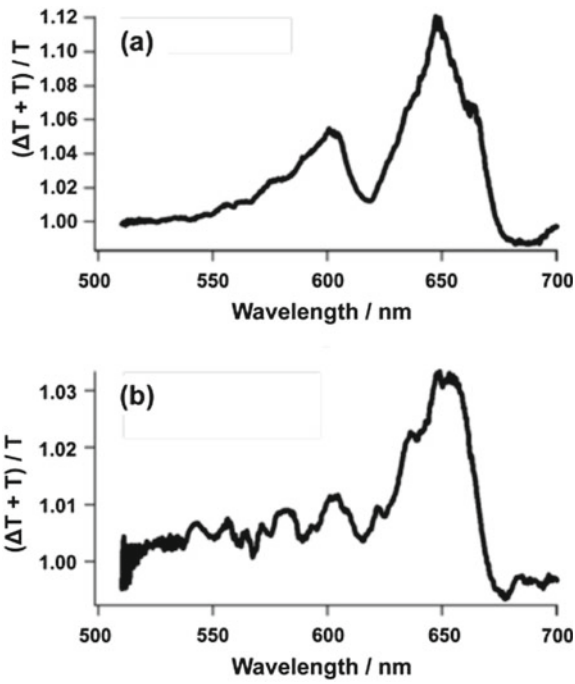

Fig. 13.11 Transient transmission spectra of **a** PDA NCFs and **b** hybridized PDA NCFs with lower coverage ratio of deposited Au NPs

thin film. There are essentially the two main reasons for reduction of $(\Delta T + T)/T$. One is the absorption of incident pump beam by deposited Au NPs (Fig. 13.9b), and the other scattering effect in the hybridized PDA NCFs. In other words, the deposition amount (or coverage ratio) of Au NPs was still excessive even in the case of hybridized PDA NCFs having lower coverage ratio. This fact would provide an important suggestion and guideline for material design of hybridized PDA NCFs. Probably, an extremely small amount of deposited Au NPs is enough to enhance $\chi^{(3)}(\omega)$ value, though no LSPR peak of Au NPs apparently appears in the extinction spectrum. In a word, one should control the deposition number and size of Au NPs, and avoid the aggregation by suitably selecting water-soluble polymers, improving surface modification, and by developing the fabrication processes.

13.4 Conclusions

Aiming at optoelectronic and/or photonic device applications, π-conjugated organic molecules and polymers are the promising NLO materials having high $\chi^{(3)}(\omega)$ value and rapid optical response. Especially, one-dimensional π-conjugated polymer, PDA, is of much interest, which is produced by solid-state polymerization in a crystal state. Morphologically-controlled PDA, that is, PDA NCFs are of great possible to fabricate the corresponding solid thin films, which are an assembled PDA NCFs and regarded as a kind of pseudo-bulk crystal of PDA. However, hybridization of PDA NCFs with noble metal NPs should be needed so as to further enhance $\chi^{(3)}(\omega)$ value. So, the basic fabrication processes, technical issues, and characterization have been investigated in details in this chapter.

The resulting core–shell-type hybridized PDA NCFs with Au NPs have silica layer as a dielectric layer between PDA NCFs as a core and Au NPs as s shell, which layer is important and effective for the purpose of controlling and tuning LSPR effect from Au NPs. Namely, the silica-coating conditions of PDA NCFs were optimized experimentally. Furthermore, the surface of silica layer was chemically modified by introducing amino-function moiety, and then the deposition efficiency of Au NPs was improved considerably.

The transient transmission spectra for PDA NCFs and hybridized PDA NCFs were measured successfully with the pump-probe method. These results and complex refractive index obtained by spectroscopic ellipsometry are fundamental data to preciously evaluate the wavelength dispersion of $\chi^{(3)}(\omega)$. It has become apparent that the deposition amounts of Au NPs were still excessive in the case of hybridized PDA NCFs. One should properly reduce the deposition amounts in the near future. To do so, "polydopamine" will be preferably used at the next objective stage [40], instead of amino-terminate silica layer. In addition, it should be necessary to produce well-defined solid thin films of hybridized PDA NCFs with too much low scattering loss by suitably selecting water-soluble polymers, in addition to PVA, and by optimizing the preparation processes.

Acknowledgements The authors especially thank to the late Professor Emeritus Hachiro Nakanishi in Tohoku University (TU, Japan), Prof. Hitoshi Kasai (IMRAM, TU, Japan), Mr. Y. Hayasaka (technical staff, The Electron Microscopy Center, IMR, TU, Japan), and M.Sc. Rie Chiba (Dept. of Chemistry, Graduate School of Sci., TU, Japan at that time) for their valuable scientific discussion and great experimental contributions.

References

1. Hur, K., Wiesner, U.: Design and applications of multiscale organic-inorganic hybrid materials derived from block copolymer self-assembly. Adv. Polym. Sci. **262**, 259–293 (2013)
2. Zhang, S., Pelligra, C.I., Feng, X., Osuji, C.O.: Direct assembly of hybrid nanomaterials and nanocomposites. Adv. Mater. **30**, 1705794-1–1705794-23 (2018)
3. Kango, S., Kalia, S., Thakur, P., Kumari, B., Pathania, D.: Semiconductor-polymer hybrid materials. Adv. Polym. Sci. **267**, 283–311 (2015)
4. Mai, Y.-W., Yu, Z.-Z.: Polymer Nanocomposites. Woodhead Publisher, Cambridge (2006)
5. Ni, W., Yang, Z., Chen, H., Li, L., Wang, J.: Coupling between molecular and plasmonic resonances in freestanding dye-gold nanorod hybrid nanostructures. J. Am. Chem. Soc. **130**, 6692–6693 (2008)
6. Loo, C., Lowery, A., Halas, N., West, J., Drezek, R.: Immunotargeted nanoshells for integrated cancer imaging and therapy. Nano Lett. **5**, 709–711 (2005)
7. Nomura, M., Kumagai, N., Iwamoto, S., Ota, Y., Arakawa, Y.: Laser oscillation in a strongly coupled single-quantum-dot-nanocavity system. Nat. Phys. **6**, 279–283 (2010)
8. Rodrigues, A.R.O., Gomes, I.T., Almeida, B.G., Araujo, J.P., Castanheira, E.M.S., Coutinho, P.J.G.: Magnetic liposomes based on nickel ferrite nanoparticles for biomedical applications. Phys. Chem. Chem. Phys. **17**, 18011–18021 (2015)
9. Kuznetsov, A.I., Miroshinichenko, A.E., Brongersma, M.L., Kivshar, Y.S., Luk'yanchuk, B.: Optically resonant dielectric nanostructures. Science, **354**, 2472-1–2472-8 (2016)
10. Oikawa, H., Kasai, H., Nakanishi, H.: Fabrication of organic microcrystals and their optical properties (Chap. 11), and Some applications of organic microcrystals (Chap. 12), In: *Anisotropic Organic Materials: Approaches to Polar Order*. ACS Symposium Series 798 (2001)
11. Nakanishi, H., Oikawa, H.: Reprecipitation method for organic nanocrystals (Chap. 2), Optical properties of polymer nanocrystals (Chap. 14), and Particle-based optical devices (Chap. 29). In: *Single Organic Nanoparticles, NanoScience and Technology*. Springer, Berlin (2003)
12. Oikawa, H., Masuhara, A., Kasai, H., Mitsui, T., Sekiguchi, T., Nakanishi, H.: Organic and polymer nanocrystals: their optical properties and function, in nanophotonics: integrating photochemistry, optics and nano/bio materials studies. Elsevier, Amsterdam (2004)
13. Wegner, G.: Solid-state polymerization mechanisms. Pure Appl. Chem. **49**, 443–454 (1997)
14. Matsuda, H., Molyneux, S., Kar, A.K., Wherrett, B.S., Okada, S., Nakanishi, H.: Third-order nonlinear optical properties of polydiacetylene crystal. J. Photopolym. Sci. Technol. **6**, 261–268 (1993)
15. Giorgetti, E., Margheri, G., Sottini, S., Chen, X., Cravino, A., Comoretto, D., Cuniberti, C., Dell'Erba, C., Dellepiane, G.: Linear and nonlinear characterization of polyDCHD-HS films. Synth. Met. **115**, 257–260 (2000)
16. Volkov, V.V., Asahi, T., Masuhara, H., Masuhara, A., Kasai, H., Oikawa, H., Nakanishi, H.: Size-dependent optical properties of polydiacetylene nanocrystals. J. Phys. Chem. B **108**, 7674–7680 (2004)
17. Oikawa, H., Mitsui, T., Onodera, T., Kasai, H., Nakanishi, H., Sekiguchi, T.: Crystal size dependence of fluorescence spectra from perylene nanocrystals evaluated by scanning near-field optical microspectroscop. Jpn. J. Appl. Phys. **42**, L111–L113 (2003)

18. Oikawa, H.: Hybridized organic nanocrystals for optically functional materials. Bull. Chem. Soc. Jpn **84**, 233–250 (2011)
19. Onodera, T., Oikawa, H., Masuhara, A., Kasai, H., Sekiguchi, T., Nakanishi, H.: Silver-deposited polydiacetylene nanocrystals produced by visible-light-driven photocatalytic reduction. Jpn. J. Appl. Phys. **46**, L336–L338 (2007)
20. Onodera, T., Ujita, J., Ishikawa, D., Masuhara, A., Kasai, H., Oikawa, H.: Hybridization of polydiacetylene core and metal shell. ECS Trans. **16**, 1–12 (2009)
21. Yokoyama, T., Masuhara, A., Onodera, T., Kasai, H., Oikawa, H.: Development of fabrication process for Ag/polydiacethylene (core/shell) hybridized nanocrystals. Synth. Met. **159**, 897–899 (2009)
22. Iimori, Y., Onodera, T., Kasai, H., Mitsuishi, M., Miyashita, T., Oikawa, H.: Fabrication of pseudo single crystalline thin films composed of polydiacetylene nanofibers and their optical properties. Opt. Mater. Exp. **7**, 2218–2223 (2017)
23. Naiki, H., Masuhara, A., Masuo, S., Onodera, T., Kasai, H., Oikawa, H.: Highly controlled plasmonic emission enhancement from metal-semiconductor quantum dot complex nanostructures. J. Phys. Chem. C **117**, 2455–2459 (2013)
24. Wang, X.D., Shen, Z.X., Sang, T., Cheng, X.B., Li, M.-F., Chen, L.-Y., Wang, Z.-S.: Preparation of spherical silica particles by Stöber process with high concentration of tetra-ethyl-orthosilicate. J. Colloid Interface Sci. **341**, 23–29 (2010)
25. Lakowicz, J.R.: Radiative decay engineering 1: Biophysical and biomedical applications. Anal. Biochem. **298**, 1–24 (2001)
26. Lakowicz, J.R., Shen, Y., D'Auria, S., Malicka, J., Fang, J., Gryczynski, Z., Gryczynski, I.: Radiative decay engineering 2. Effects of silver island films on fluorescence intensity, lifetimes, and resonance energy transfer. Anal. Biochem. **301**, 261–277 (2002)
27. Li, F., Li, G.Z., Wang, H.Q., Xue, Q.J.: Studies on cetyltrimethylammonium bromide (CTAB) micellar solution and CTAB reversed microemulsion by ESR and ^{2}H NMR. Colloids Surfaces A Physicochem. Eng. Aspects **127**, 89–96 (1997)
28. Jin, R.C., Cao, Y.W., Mirkin, C.A., Kelly, K.L., Schatz, G.C., Zheng, J.G.: Photoinduced conversion of silver nanospheres to nanoprisms. Science **294**, 1901–1903 (2001)
29. Murphy, C.J., Jana, N.R.: Controlling the aspect ratio of inorganic nanorods and nanowires. Adv. Mater. **14**, 80–82 (2002)
30. Chen, S.H., Wang, Z.L., Ballato, J., Foulger, S.H., Carroll, D.L.: Monopod, bipod, tripod, and tetrapod gold nanocrystals. J. Am. Chem. Soc. **125**, 16186–16187 (2003)
31. Sakamoto, N., Onodera, T., Dezawa, T., Shibata, Y., Oikawa, H.: Highly enhanced emission of visible light from core-dual-shell type hybridized nanoparticles. Part. Part. Syst. Charact. **34**, 1700258-1–1700258-8 (2017)
32. Neeves, A.E., Birnboim, M.H.: Composite structures for the enhancement of nonlinear-optical susceptibility. J. Opt. Soc. Am. B **6**, 787–796 (1989)
33. Nghiem, T.H.L., Le, T.N., Do, T.H., Vu, T.T.D., Do, Q.H., Tran, H.N.: Preparation and characterization of silica-gold core-shell nanoparticles. J. Nanopart. Res. **15**, 2091-1–2091-9 (2013)
34. Liang, Z.S., Liu, Y., Ng, S.S., Li, X.Y., Lai, L.H., Liu, S.Y.: The effect of pH value on the formation of gold nanoshells. J. Nanopart. Res. **13**, 3301–3311 (2011)
35. Shi, W.L., Sahoo, Y., Swihart, M.T., Prasad, P.N.: Gold nanoshells on polystyrene cores for control of surface plasmon resonance. Langmuir **21**, 1610–1617 (2005)
36. Sato, R., Momida, H., Ohnuma, M., Sasase, M., Ohno, T., Kishimoto, N., Takeda, Y.: Experimental dispersion of the third-order optical susceptibility of Ag nanoparticles. J. Opt. Soc. Am. B **29**, 2410–2413 (2012)
37. Sato, R., Ohnuma, M., Oyoshi, K., Takeda, Y.: Experimental investigation of nonlinear optical properties of Ag nanoparticles: effects of size quantization. Phys. Rev. B **90**, 1254171-1–1254171-6 (2014)
38. Sato, R., Ohnuma, M., Oyoshi, K., Takeda, Y.: Spectral investigation of nonlinear local field effects in Ag nanoparticles. J. Appl. Phys. **117**, 113101-1–113101-6 (2015)

39. Sato, R., Ishii, S., Nagao, T., Naito, M., Takeda, Y.: Broadband plasmon resonance enhanced third-order optical nonlinearity in refractory titanium nitride nanostructures. ACS Photonics **5**, 3452–3458 (2018)
40. Lee, H., Dellatore, S.M., Miller, W.M., Messersmith, P.B.: Mussel-inspired surface chemistry for multifunctional coating. Science **318**, 426–430 (2007)

Part III
Function

Chapter 14
Luminescent Crystal–Control of Excited-State Intramolecular Proton Transfer (ESIPT) Luminescence Through Polymorphism

Toshiki Mutai

Abstract Crystal polymorphism has a significant effect on the luminescence of materials. Using 2-(2′-hydroxyphenyl)imidazo[1,2-*a*]pyridine (HPIP) as the key compound, crystal structure-dependent luminescence, also known as polymorph-dependent luminescence (PDL), is described. HPIP shows excited-state intramolecular proton transfer (ESIPT) luminescence, which is quite efficient in the solid state, yet very weak in solution; it is mainly ascribed to the suppression of efficient radiationless decay via the S_0/S_1–conical intersection when the molecular conformation is fixed coplanar. The two polymorphic forms of the crystals display blue-green and yellow luminescence and can be interconverted via heat transfer between the two states. Three-color PDL (yellow, orange, and red) is observed in 6-cyano HPIP. The relationship between crystal structure and luminescence color was rationally explained by TD-DFT calculations using dimer models. It is remarkable, that this dimer model is reasonably supported by the femtosecond time-resolved transient absorption spectroscopy. These results will contribute to the understanding of structure–property relationships in solid-state luminescence at the molecular level and would further the design of new polymorph-dependent luminescent materials.

Keywords Luminescent crystal · Polymorph-dependent luminescence · Quantum chemical calculation · ESIPT · Fluorescence · Femtosecond time-resolved transient absorption spectroscopy

14.1 Introduction

Organic solid-state luminescent materials have garnered considerable interest in various areas of science including OLEDs [1, 2], sensors [3], solid lasers [4], near-infrared light sources [5], and so on [6, 7]. In most cases, the electronic properties of materials are controlled via synthetic modification of luminescent molecules.

T. Mutai (✉)
Department of Materials and Environmental Science, Institute of Industrial Science, The University of Tokyo, 4-6-1, Komaba, Meguro-ku, Tokyo 153-8505, Japan
e-mail: mutai@iis.u-tokyo.ac.jp

M. Sakamoto and H. Uekusa (eds.), *Advances in Organic Crystal Chemistry*,
https://doi.org/10.1007/978-981-15-5085-0_14

However, the luminescence of organic compounds is often quenched in the solid state, because the non-radiative deactivation pathway from the photoexcited state is enhanced through molecular interactions [8]. Common strategies to overcome this problem include the introduction of bulky groups [9–11] or design of non-planar structures [12–14] in order to avoid unfavorable molecular interactions. Therefore, these materials are primarily used as amorphous solids, and their luminescence is generally a reflection of that of a single molecule.

The luminescence of bulk solids is regulated not only by that of single molecules, but also by collective effects owing to the arrangement and interactions of small molecules. In other words, the luminescence of solid materials could be controlled by altering the molecular packing mode within the crystal structure, instead of by chemical modification.

Various examples of organic solid-state luminescent compounds have been developed in recent years. For example, aggregation-induced emission (AIE) [15, 16] is a phenomenon in which luminescence is enhanced rather than quenched by the aggregation of the molecules. In 2001, B. Z. Tang and co-workers reported [17] 1-methyl-1,2,3,4,5-pentaphenylsilole (Scheme 14.1a), which is non-luminescent in solution, exhibits remarkably enhanced emission (300 times) owing to the formation of nano-aggregates upon addition of a certain amount of a poor solvent. S. Y. Park and co-workers reported the enhanced luminescence of 1-cyano-*trans*-1,2-bis-(4′-methylbiphenyl)ethylene upon the formation of nanoparticles [18]. Tetraphenylethylene has also been a well-studied AIE-active core [19].

Most of AIE-active compounds are composed of two or more aromatic rings connected by a single bond or bonds. The aromatic rings can freely rotate in solution, and the excited state can be easily deactivated through thermal dissipation due to molecular rotation. In aggregates, where molecular rotation is suppressed, thermal deactivation is much less feasible and results in enhanced emission.

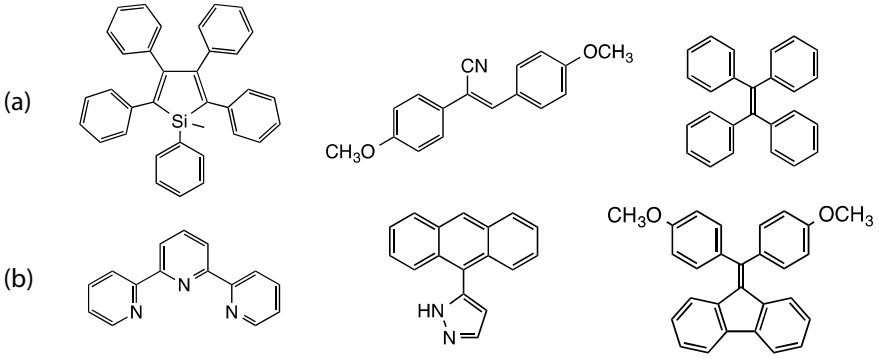

Scheme 14.1 **a** Molecules displaying aggregation-induced emission (AIE). From left to right: silole, 1-cyano-*trans*-1,2-bis-(4′-methylbiphenyl)ethylene, and tetraphenylethylene. **b** Molecules displaying polymorph-dependent luminescence (PDL). From left to right: 2,2′:6′,2″-terpyridine, 3-(9-anthryl)pyrazole, and di(*p*-methoxyphenyl)dibenzofulvene

14.1.1 Polymorph-Dependent Luminescence (PDL)

Controlling the luminescence of solid materials by changing or altering the polymorphs, i.e., different molecular packing modes in the crystalline phase of a specific compound resulting from a different arrangement of the molecules within the solid state, is called polymorph-dependent luminescence (PDL) (Scheme 14.2).

PDL has attracted considerable interest, because it can be used to modify the luminescence of materials and provides insight into the relationship between the molecular packing mode and bulk optical properties of said materials [20, 21]. Moreover, it may have applications in the development of new organic luminescent materials based on supramolecular chemistry. The most well-known is the stimuli–response emission, in which the emission properties are changed by external stimuli (heat, pressure, solvent vapor, and so on) without chemical modification.

The ability to tune the luminescence of materials by exploiting molecular packing has been studied extensively, and the number of reports on this subject has rapidly increased in recent years [22–28]. In these systems, alteration of inter-luminophore interactions [22–25] or packing-induced conformational changes of dye molecules [26–28] allows for the modulation of the luminescence.

One of the early examples of PDL-active molecules is 2,2′:6′,2″-terpyridine (tpy), which was reported in 2005 [29]; it is non-fluorescent in solution, but forms two polymorphic crystals, which show bright blue luminescence (quantum yield $\Phi \sim 0.2$) and very weak luminescence ($\Phi < 0.01$). Moreover, these two crystalline phases can be interconverted via heat-mode phase transfer, and the luminescence can be switched "on" or "off". The other example is 3-(9-anthryl)pyrazole [30], which exhibits different colored PDL, owing to differences in the intermolecular hydrogen bonding between the pyrazolyl units. The PDL of di(*p*-methoxyphenyl)dibenzofulvene [31] is also a noteworthy example, where the twisted conformation of the two anisole planes is responsible for the PDL.

However, the development of such systems remains a challenge because of the lack of effective mechanisms that can modulate the molecular packing and lead to different luminescence properties.

Detailed studies on the relationship between the molecular packing mode and luminescence have also garnered significant interest. Systems with multiple-color PDL are desirable in order to study structure–property relationships; however, most reports to date describe two-color systems [32, 33]. Systems exhibiting three or more luminescence colors are rare [30, 34, 35]. One of the reasons for this is the difficulty

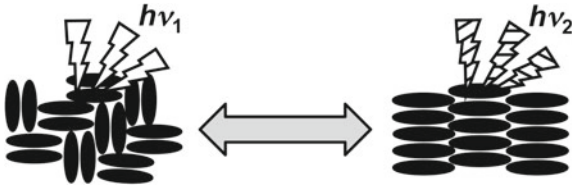

Scheme 14.2 Schematic representation of polymorph-dependent luminescence (PDL)

in preparing multiple polymorphic phases and obtaining appropriate crystal data, because some phases often have amorphous or microcrystalline states.

14.2 Molecular Design

14.2.1 Designing Polymorph-Dependent Luminescent Compound

The ability to (i) form polymorphic phases and (ii) transduce conformational changes and molecular interactions into altered luminescence is required for a molecule to display PDL. It would be interesting if the polymorphic phases could be interconverted by external stimuli, because it may lead to luminescence-switchable materials.

Our strategy to realize the above points is to introduce adequate flexibility in the molecular conformation, especially around the aromatic luminescent core. As shown in Scheme 14.2, two π-electronic planes connected by a covalent single bond are "moderately" fixed with a weaker hydrogen bond, so that various conformations and packing modes could be tolerated during crystallization.

The second strategy is to take advantage of a characteristic luminescence that stands on the intramolecular hydrogen bond: in this case, N···H–O. It has been demonstrated that the phenolic proton transfers to the nitrogen atom promptly after photoexcitation, which is termed excited-state intramolecular proton transfer (ESIPT), and the generated excited species is deactivated upon emitting low-energy light (see next section for details). ESIPT luminescence, especially in our system, is supposed to be susceptible to the molecular conformation and the effects of surrounding molecules; therefore, different ESIPT luminescence might be expected in different polymorphic phases.

14.2.2 Mechanism of ESIPT Luminescence

A photoinduced ESIPT [36] is reported to be a remarkably fast process (rate constant $k \approx 1 \times 10^{13}$ s^{-1}) [37, 38]. In the ground state, the acidities (pK_a) of phenolic–OH and hydrogen-bonded nitrogen are about 9 and 6, respectively; therefore, they may exist as an enol (N···H–O). Upon photoexcitation, the phenolic –OH becomes quite acidic ($pK_a \sim 2$) and the proton transfer to the nitrogen (ESIPT) and subsequent tautomerization to the keto form are promoted (Scheme 14.3) [39]. Emission from the keto form is characterized by a large Stokes shift (≈10,000 cm^{-1}), which enables long-wavelength fluorescence upon excitation with UV light. However, molecules which exhibit efficient ESIPT fluorescence are rather limited. The most studied

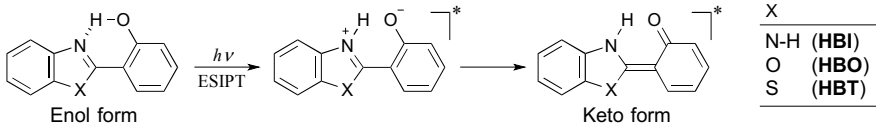

Scheme 14.3 Molecular structure of intramolecular hydrogen-bonded benzazoles (HBI, HBO, and HBT), and enol-to-keto tautomerization via ESIPT by photoexcitation

compounds to date are 2-(2′-hydroxyphenyl)benzimidazole (HBI) [33, 40–44], 2-(2′-hydroxyphenyl) benzoxazole (HBO) [45–48], 2-(2′-hydroxyphenyl)benzothiazole (HBT) [49–54], salicylideneaniline [55–57], and their analogs.

ESIPT luminescence in the solid state [33, 49, 58–61] is a significant topic, and there have been some recent reports of basic applications in electroluminescent devices [49, 62–66], as well as white luminescent materials [64–70].

14.2.3 2-(2′-Hydroxyphenyl)Imidazo[1,2-a]Pyridine (HPIP)

2-(2′-Hydroxyphenyl)imidazo[1,2-*a*]pyridine (HPIP, $\mathbf{1}_{\mathbf{Enol}}$; Scheme 14.4a) is an analog of HBI, i.e., isomeric heterocyclic system with varied heteroatom placement. The photoexcitation of HPIP similarly causes ESIPT, but contrary to the benzazoles mentioned above (HBI, HBO, and HBT), subsequent tautomerization to a typical keto form does not occur. Instead, HPIP proceeds to a zwitterionic IPT* emitting state ($\mathbf{1}_{\mathbf{IPT}}$*), which further forms a twisted conformation in a fluid solution.

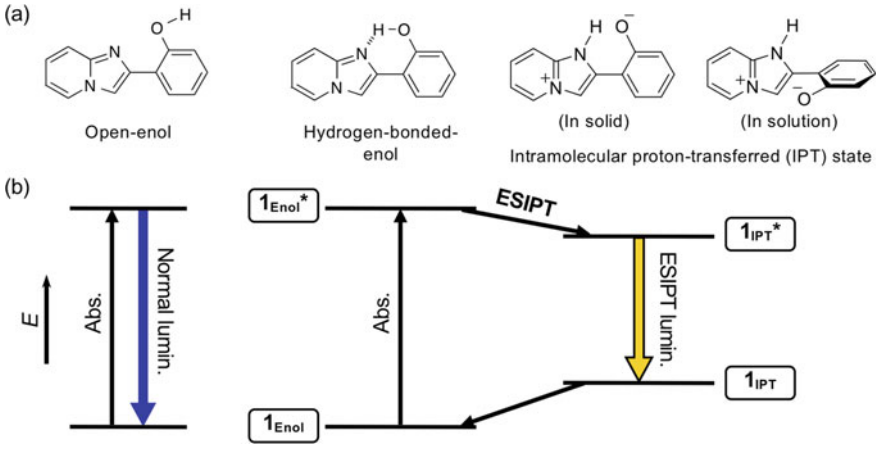

Scheme 14.4 **a** Molecular structure of 2-(2′-hydroxyphenyl)imidazo[1,2-*a*]pyridine (HPIP, **1**), and its open-enol, hydrogen-bonded enol ($\mathbf{1}_{\mathrm{Enol}}$), and intramolecular proton-transferred (IPT, $\mathbf{1}_{\mathrm{IPT}}$) forms. **b** Energy diagram of normal (left) and ESIPT (right) luminescence

As Douhal et al. reported [71, 72], HPIP exhibits ESIPT fluorescence ($\mathbf{1_{IPT}}^* \rightarrow \mathbf{1_{IPT}}$) [37, 38, 73] in nonpolar organic solutions, albeit with a low quantum yield ($\Phi =$ 0.01–0.08). The fluorescence appears at a significantly lower energy (~600 nm) than that of HBI (~480 nm), probably because of the decreased energy level of $\mathbf{1_{IPT}}^*$ and increased energy level of $\mathbf{1_{IPT}}$ owing to solvent rearrangement and/or conformational changes. This explanation is supported by the ESIPT fluorescence observed in rigid media. In a polymer matrix [74, 75] and frozen organic solution [61], where effects based on molecular motion are suppressed, the fluorescence is largely blue-shifted to ~520 nm.

In polar environments, where intramolecular hydrogen bonding is prevented, HPIP exists predominantly as the "open-enol" species and shows normal fluorescence (Scheme 14.4b).

14.3 Polymorph-Dependent Luminescence of HPIP

14.3.1 Overview

Two crystal polymorphs of HPIP (**1**) exhibit bright photoluminescence of different colors, blue-green and yellow, both of which are ESIPT luminescence. X-ray crystallographic analysis revealed different molecular conformations and packing in these two crystal polymorphs, and interconversion between the polymorphs can be realized via a heat-mode dry process.

Ab initio quantum chemical calculations were performed to investigate the enhanced ESIPT luminescence in the solid state.

14.3.2 Crystalline Polymorphism of HPIP

Slow and fast cooling of a heated aqueous ethanol solution of **1** gives polymorphic crystals **1-BG** and **1-Y**, respectively. In the infrared spectra of **1-BG** and **1-Y**, the O–H stretching band appears at around 3135 cm^{-1} in both crystals, indicating the intramolecular hydrogen bonding between the O–H and nitrogen (N1) in the imidazopyridine ring.

X-ray crystallographic analysis of **1-BG** (*Pbca*, $Z = 8$, Fig. 14.1) and **1-Y** ($P2_1/c$, $Z = 8$, Fig. 14.2) was performed at room temperature [76]. The asymmetric unit of **1-BG** and **1-Y** is composed of one and two molecules, respectively, and each molecule clearly participates in an intramolecular hydrogen bond (O–H···N1). The most notable conformational difference was the torsion angle θ (N1–C2–C1′–C2′) composed of the phenyl ring and the imidazopyridine ring. While the two aromatic rings are nearly coplanar ($\theta = -1.0°$ and 1.3°) in **1-Y**, a larger torsion angle was

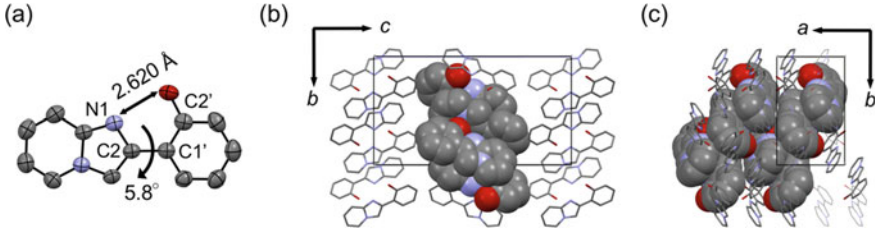

Fig. 14.1 **a** ORTEP drawing of molecular structure of **1** in crystal **1-BG**. **b** Molecular packing in **1-BG** viewed from *bc* (**b**) and *ab* (**c**) planes

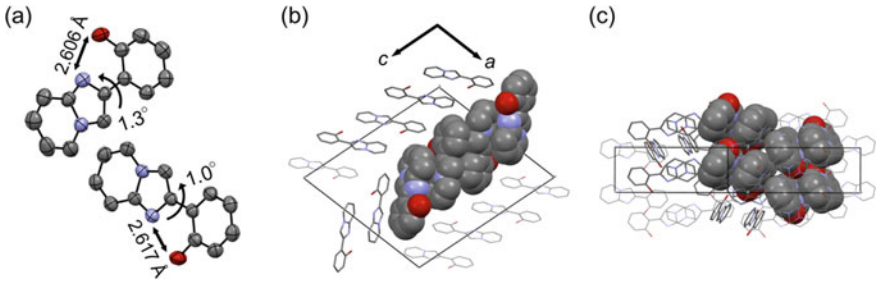

Fig. 14.2 **a** ORTEP drawing of molecular structure of **1** in crystal **1-Y**. **b** Molecular packing in **1-Y** viewed from *ac* (**b**) and (101) (**c**) planes

found in **1-BG** ($\theta = 5.8°$). The distance between O and N1, representing the length of the intramolecular hydrogen bond, showed only a slight difference (<0.02 Å).

In these crystals, two molecules are packed close enough to form a stacked pair in an antiparallel manner, and their inter-ring distances are the typical stacking distance of 3.4 Å. There is sufficient overlap between the stacked molecules in **1-BG** and **1-Y**. These molecular pairs are aligned in the edge-to-face mode in **1-BG** (Fig. 14.1b, c), or slipped edge-to-edge mode in **1-Y** (Fig. 14.2b, c).

14.3.3 Polymorph-Dependent Luminescence

The absorption spectra of **1-BG** and **1-Y** obtained by the diffuse reflectance method (Kubelka-Munk spectra) exhibited a maximum at around 340 nm (Fig. 14.3), which was close to that which is observed in a dilute THF solution. Upon excitation at 330 nm, **1-BG** and **1-Y** exhibited blue-green (496 nm) and yellow luminescence (529 nm), respectively. The luminescence quantum yields were considerably higher ($\Phi = 0.37$–0.50) compared to those in solution. An amorphous solid prepared by the freeze-dry method showed yellow luminescence, similar to that of **1-Y** (Table 14.1). The Stokes shift of the luminescence was large enough (9300–10,800 cm^{-1}) to be

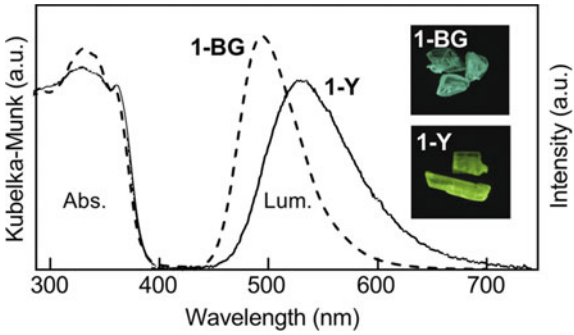

Fig. 14.3 Absorption and luminescence spectra of **1-BG** (dashed line) and **1-Y** (solid line). Modified from Mutai et al. [61] with permission from WIELY-VCH

Table 14.1 Absorption (Kubelka-Munk spectrum) and emission of **1** and MeOPIP in various solid states

	λ_{abs}/nm[a]	λ_{em}/nm (Φ)	τ/ns
*HPIP (**1**)*			
Crystal **1-BG**	339	496 (0.50)	5.91
Crystal **1-Y**	337	529 (0.37)	5.84
Amorphous	337	527 (0.39)	6.39
MeOPIP			
Powder	312	382 (0.24)	2.75

Modified from Mutai et al. [61] with permission from WIELY-VCH

well within the range of typical ESIPT fluorescence [39, 77]. Thus, ESIPT luminescence is dependent on the molecular packing mode in the solid state, probably because the emitting species has zwitterionic character, which is sensitive to the molecular conformation and field effects of surrounding molecules.

On the other hand, the 2′-methoxy derivative MeOPIP (Scheme 14.5), which does not form intramolecular hydrogen bonds, showed only blue, normal fluorescence (382 nm) in the solid state.

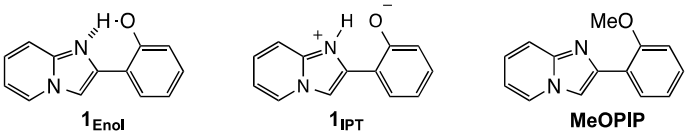

Scheme 14.5 Molecular structures of $\mathbf{1_{Enol}}$, $\mathbf{1_{IPT}}$, and MeOPIP

14.3.4 Thermal Properties and Luminescence Color Switching

Blue-green and yellow ESIPT luminescence is switchable by heat-mode control of the polymorphic states.

The thermal properties of both crystals will firstly be described. In the first differential scanning calorimetry (DSC) trace, **1-BG** showed an endothermic peak at the melting point (141 °C) (Fig. 14.4, left). On the other hand, **1-Y** and the amorphous solid displayed small peaks at around 131 °C, in addition to the melting peak at 141 °C; the former peaks were attributed to the phase transition of **1-BG**. When powdered crystals of **1-Y** or the amorphous solid were placed on a glass plate and heated at 135 °C for 1 min, the XRD pattern of the heated powder measured at the room temperature (Fig. 14.4d) was not the same as that of the starting crystal of **1-Y** (Fig. 14.4c) or the amorphous solid, but was comparable to that of **1-BG** (Fig. 14.4a). Accordingly, the luminescence turned from yellow to blue-green.

The resulting blue-green emitting powder was further heated above the melting point and kept at 150 °C for 1 min. Instant solidification of the heated material using ice cubes yielded a yellow-emitting solid, which showed only a vague XRD image, indicating that this solid was primarily amorphous.

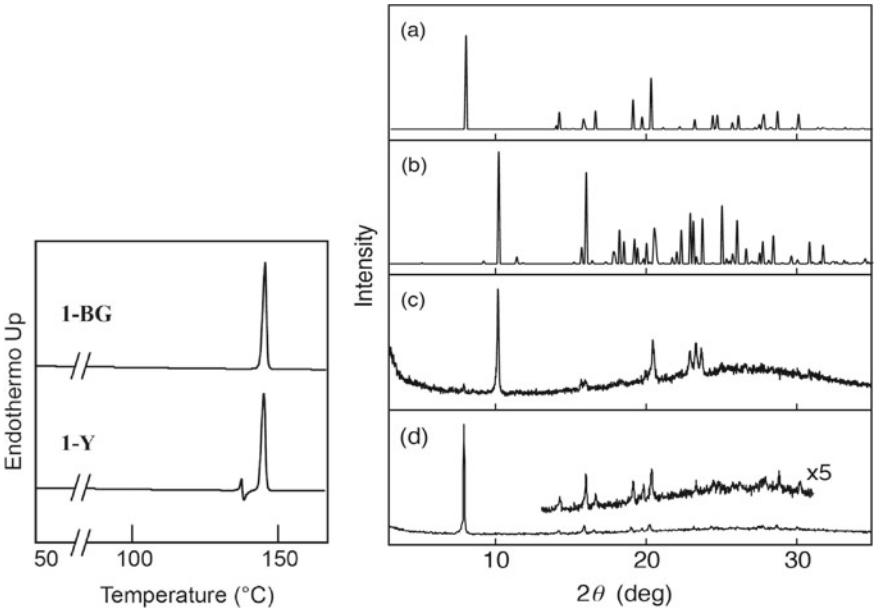

Fig. 14.4 Left: First-heating curves of DSC of **1-BG** and **1-Y**. Right: XRD profiles of **1-BG** (**a**) and **1-Y** (**b**) calculated from corresponding crystal structures, and the observed profiles of **1-Y** at room temperature (**c**) and after heating at 135 °C, 1 min (**d**). Modified from Mutai et al. [61] with permission from WIELY-VCH

Based on the above findings, we examined the repetitive-switching ability of the PDL of **1**. [Yellow → blue-green] Powdered crystals of **1-Y** were kept at 135 °C for 1 min, in order to convert them to the blue-green-emitting state. [Blue-green → yellow] Next, they were heated at 150 °C for 3 min and rapidly cooled, to generate the yellow-emitting state. Several color-switching cycles were successfully carried out, demonstrating that the color of the ESIPT luminescence of **1** could be interconverted via the heat-mode dry process.

14.3.5 Quantum Chemical Analysis

The luminescence property of **1** was further analyzed quantum chemically [78]. The ground-state geometries (S_0) of **1** were optimized using density functional theory (DFT) with the 6-31G(d,p) basis set in conjunction with the B3LYP functional. For the optimized S_0 geometries, the vertical excitation energies were evaluated with time-dependent (TD) DFT at the B3LYP/6-31+G(d,p) level of theory [79]. As a reference, the equation-of-motion with coupled-cluster singles and doubles (EOM-CCSD) method was performed to estimate the transition energies using the cc-pVDZ basis set [79]. The viability of the DFT calculations was verified by several higher-level methods. The quantitative vertical excitation energies including dynamical electron correlations were estimated by multi-state complete active-space second-order perturbation theory (MS-CASPT2) [80]. The singlet excited-state (S_1) geometries and energy profile as a function of torsion angle (θ) were evaluated by the complete active-space self-consistent field method (CASSCF) using the atomic natural orbital small basis set (CASSCF(6,6)/ANO-S) [80]. The fully relaxed S_1 potential energy surface (PES) was examined at the CASSCF(6,6)/ANO-S-MB (minimal base) level of theory.

14.3.6 S_0 and S_1 PES Scan Along the Central C-C Bond Torsion

In the ground state, the enol form (S_0-enol) was energetically stable than the IPT form (S_0-IPT) at all torsional angles (0–90°). The lowest-energy geometry in both states was the coplanar conformation, which could be due to the intramolecular hydrogen bond. The coplanar S_1-IPT form was more stable (32.5 kJ mol^{-1}) than the S_1-enol form, indicating that ESIPT could undergo from the enol form. The observed decay times of the ESIPT luminescence were 0.52 and 5.26 ns in fluid and frozen THF solutions, respectively. Because ESIPT is an extremely fast process (<1 ps) [81–83], the conversion from S_1-enol to S_1-IPT proceeds instantaneously.

The effects of torsion angle on the energy level of the S_1- and S_0-IPT state were evaluated. As shown in Fig. 14.5, an increase in the torsion angle from 0 to 45°

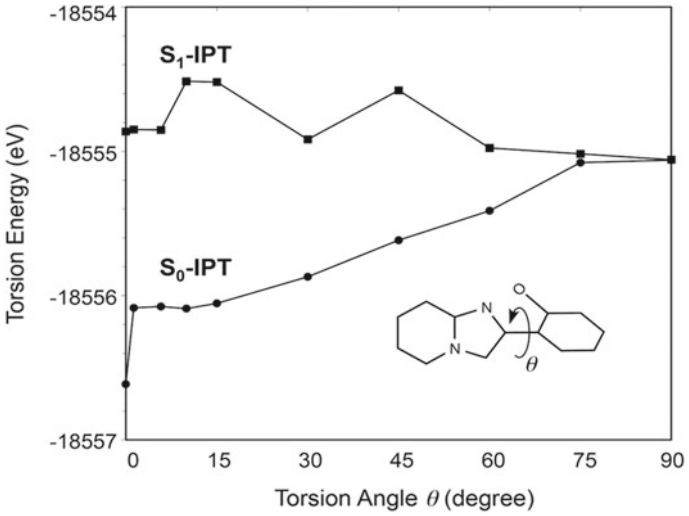

Fig. 14.5 S_0 and S_1 potential energy profiles for the enol and IPT forms at S_1-optimized geometries (CASSCF(6,6)/ANO-S). Adapted with permission from Shigemitsu et al. [78]. Copyright 2019 American Chemical Society

resulted in a relatively small change in the energy level of the S_1-IPT state with a small local minimum at around 30°, which then decreased gradually as the torsion angle increased beyond 45°. On the other hand, a monotonic elevation in the S_0-IPT energy level was observed as the torsion angle increased across the entire range examined (0 to 90°). The $S_0 \rightarrow S_1$ energy gap of the IPT form became sufficiently small at 60°, and the conical intersection (CI) was observed at 90°. In the CI model [84, 85], it acts as a "funnel" for an efficient deactivation to the ground state within a single vibrational period. Therefore, the S_0/S_1-CI facilitated the fast radiationless decay process of the excited state, which explains the low quantum yield of the ESIPT fluorescence in solution.

14.3.7 Enhanced Solid-State Luminescence of HPIP

HPIP **1** shows bright ESIPT luminescence not only in the crystalline form, but also in a dilute frozen solution and polymer matrices, whereas **1** shows weak luminescence in fluid solutions. The CASSCF study clearly demonstrated the presence of S_0/S_1-CI at $\theta = 90°$, where efficient radiationless decay coupled with the twisting motion of an excited molecule could proceed (Fig. 14.5). This can reasonably explain the weak emission in solution. In rigid media (i.e., frozen solvents and polymer matrices), molecules are fixed in the coplanar enol conformation. In both crystals, when the torsion angle θ was below 6°, the excited species could not reach the S_0/S_1-CI. Therefore, the fixation of molecules in the coplanar conformation should be the origin

of the observed emission enhancement. Suppression of the radiationless decay via the S_0/S_1-CI allows for emissive decay from the S_1-IPT to the S_0-IPT on a nanosecond timescale.

14.3.8 Polymorph-Dependent Luminescence Color of HPIP Crystals

From Fig. 14.5, it is apparent that the energy gap between the S_1-IPT and S_0-IPT states depends greatly on the torsion angle. Unless the energy gap becomes too small to induce efficient radiationless decay, or the torsion angle of the enol species is too large to block the ESIPT process, an increase in the torsion angle is expected to induce a redshift in the ESIPT luminescence. Notably, the potential energy of S_1-IPT has a small local minimum at around 30°, and the energy gap does not decrease monotonically as a function of torsion angle.

As shown in Fig. 14.3, there is a slight difference in the torsion angles in the two crystals: molecules in **1-BG** have a torsion angle of 5.8° and those of the two conformers, Y1 and Y2, in **1-Y** are 1.3° and –1.0°. Because the differences in the emission energies and torsion angles in **1-BG** and **1-Y** crystals are small, higher-level ab initio calculations, MS-CASPT2(10,9)/ANO-L methods, were applied in order to examine the effect of torsional conformation on the emission energy. Although the results suggested a slightly lower energy for Y1 in **1-Y**, there was no difference between **1-BG** and Y2. Because the estimation is based only on the conformational difference in a single molecule, it may be necessary to include the effects of surrounding molecules, as well as the degree of conformational freedom in the crystal [86–88].

14.4 Conclusions

Owing to the ESIPT mechanism, which generates environment-sensitive zwitterionic excited species, HPIP **1** shows distinct PDL, i.e., blue-green (**1-BG**) and yellow (**1-Y**). Moreover, reproducible switching of the PDL was achieved by heat-mode control of the molecular packing, which was reasonably supported by power XRD analysis and DSC measurements. Ab initio calculations suggested that a free S_1-IPT species could approach the S_0/S_1–CI coupled with the twisting motion of the central C–C bond, and return to the S_0-enol state without emitting light.

The enhanced emission of HPIP in the solid state can be explained by the following factors: (1) blocking S_1-IPT species ($\mathbf{1}_{\mathbf{IPT}}$*) from the twisting motion that reach the CI and efficient radiationless decay, and (2) inhibition of excimer formation, because of the unmatched energy state between $\mathbf{1}_{\mathbf{IPT}}$* and surrounding $\mathbf{1}_{\mathbf{Enol}}$ molecules.

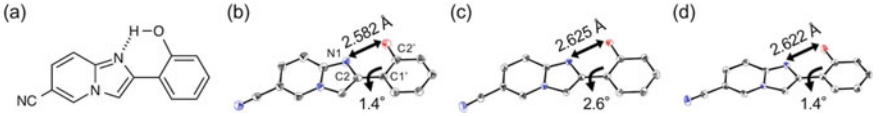

Fig. 14.6 Molecular structure of 6-cyano HPIP **2** (**a**), and ORTEP drawings of **2** in **2-Y** (**b**), **2-O** (**c**), and **2-R** (**d**)

14.5 Three-Color Polymorph-Dependent Luminescence

14.5.1 Overview

6-Cyano HPIP (**2**) (Fig. 14.6) forms three polymorphic crystals, which exhibit clearly different polymorph-dependent ESIPT luminescence (yellow, orange, and red) [89]. The effects of molecular packing on the ESIPT luminescence were studied by X-ray crystallographic analysis, quantum chemical calculations, and time-resolved transient absorption spectroscopy. TD-DFT calculations of the π-stacked dimer geometry extracted from each polymorphic crystal reasonably reproduced the luminescence energies. In addition, both the theoretical calculation and time-resolved measurement presented the similar result: interaction between the IPT* and neighbor enol species might be an important factor for PDL. The results give further insight into the relationship between luminescence and crystal structure and may contribute to the design of new PDL-active organic materials.

14.5.2 X-Ray Crystallographic Analyses of 2-Y, 2-O, and 2-R

The prismatic yellow-luminescent crystal **2-Y** and the platelet orange-luminescent crystal **2-O** were prepared separately by controlling the recrystallization conditions. Needle-like red-luminescent crystals of **2-R** were obtained manually from a mixture of polymorphic crystals.

In order to understand the role of molecular packing in PDL, X-ray crystallographic analyses of **2-Y**, **2-O**, and **2-R** were performed [90]. All crystals were monoclinic and had the same space group ($P2_1/n$, $Z = 4$) and nearly identical cell densities. Figure 14.6b-d shows ORTEP drawings of a molecule in the polymorphic crystals. The distance between the oxygen and nitrogen (N1) atoms was 2.582–2.625 Å, indicating the formation of an intramolecular hydrogen bond (O–H···N1). The small torsion angle between the two aromatic rings (θ(N1–C2–C1′–C2′) = 1.4–2.6°) confirmed the coplanar conformation.

On the other hand, the molecular packing in **2-Y**, **2-O**, and **2-R** was remarkably different, as illustrated in Figs. 14.7, 14.8, and 14.9, respectively. In **2-Y**, molecules form parallel-stacked columns, in which molecules are slip-stacked along the long axis with an interplanar distance of 3.38 Å (Fig. 14.7a). The fused imidazolyl moiety

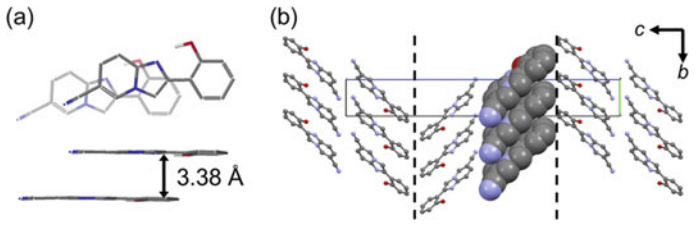

Fig. 14.7 Crystal structure of **2-Y**. Top and side views of the columnar packing (**a**) and molecular packing viewed from *bc* plane (**b**). Mutai et al. [89]—Reproduced by permission of The Royal Society of Chemistry

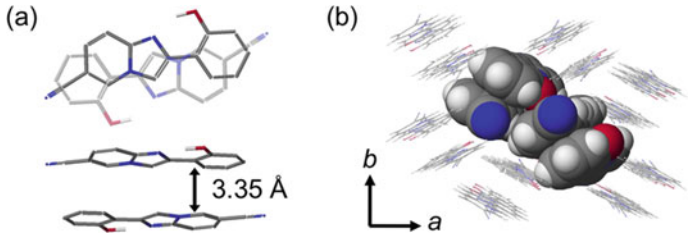

Fig. 14.8 Crystal structure of **2-O**. Top view of dimer (**a**) and molecular packing viewed from *ab* plane (**b**). Mutai et al. [89]—Reproduced by permission of The Royal Society of Chemistry

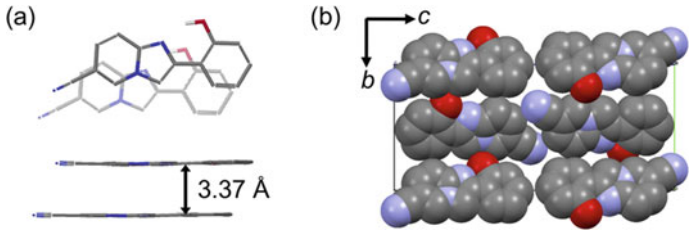

Fig. 14.9 Crystal structure of **2-R**. Top and side views of the columnar packing (**a**) and molecular packing viewed from *bc* plane (**b**). Mutai et al. [89]—Reproduced by permission of The Royal Society of Chemistry

overlaps with the phenyl moiety of the stacked molecule. The distance between an oxygen atom and the nearest nitrogen atom of a neighbor molecule is 3.64 Å, which ruled out the formation of an intermolecular hydrogen bond. As for the intercolumnar packing, every two columns aligned in an antiparallel fashion, to form a herringbone-like arrangement along the *c*-axis (Fig. 14.7b).

In **2-O**, antiparallel π–π stacked dimeric units formed with an interplanar distance of 3.35 Å (Fig. 14.8a). The imidazolyl moieties overlapped, and the phenyl moiety overlaid the fused pyridyl group. Neighboring dimeric units packed in an edge-to-face type arrangement (Fig. 14.8b), which was similar to that observed in **1-BG** (Fig. 14.1) [61].

Similar to **2-Y**, parallel slip-stacked columnar packing was observed in **2-R** (Fig. 14.9). The molecules were less slipped compared to **2-Y**, and the same aromatic moieties overlapped (Fig. 14.9a). Formation of an intermolecular hydrogen bond could also be ruled out because of the large distance (3.53 Å) between oxygen atoms and the nearest nitrogen atom of surrounding molecules. As for the intercolumnar packing, the adjacent columns aligned in an antiparallel manner along the *b*- and *c*-axes (Figs. 14.9b).

In the three polymorphic crystals, the molecular packing was remarkably different, whereas the conformation of the molecules was nearly identical. Therefore, the intermolecular interactions that vary according to the different molecular packing modes may be a dominant factor in the PDL of **2**.

14.5.3 Luminescence of 2-Y, 2-O, and 2-R

Figure 14.10 shows the luminescence spectra of the polymorphic crystals of **2-Y**, **2-O**, and **2-R** upon excitation at 330 nm. The luminescence decays of the three polymorphic crystals were reasonably fitted with a mono- or bi-exponential curve (Table 14.2). The weighted average lifetimes (τ_M) of **2-Y**, **2-O**, and **2-R** were 5.48, 5.51, and 2.26 ns, respectively, indicating singlet emission. The rate constants of the radiative (k_{em}) and non-radiative (k_{nr}) deactivations were within the ordinary values for a π–π* transition. The low quantum yield of **2-R** may be due to an efficient non-radiative deactivation pathway. Because the spectral data, Stokes' shift values, and luminescence lifetimes were similar to those observed in a poly(methyl methacrylate) (PMMA) matrix [74], where **2** exists as an isolated molecule, the luminescence of these crystals was considered to be ESIPT luminescence from single molecules.

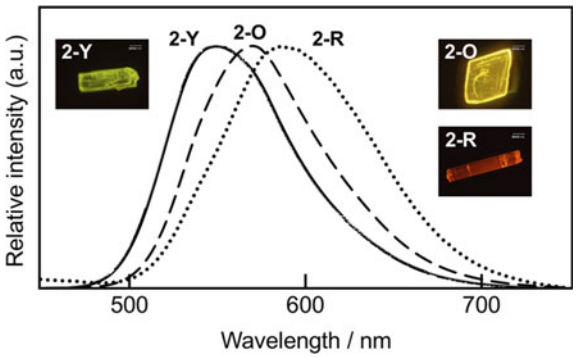

Fig. 14.10 Luminescence spectra of **2-Y** (solid line), **2-O** (broken line), and **2-R** (dotted line). Mutai et al. [89]—Reproduced by permission of The Royal Society of Chemistry

Table 14.2 Excitation and emission properties of polymorphic crystals of **2**

	λ_{ex}/nm	λ_{em}/nm (Φ)	τ_1/ns (A_1)	τ_2/ns (A_2)	χ^2	$k_{em}/10^7$ s^{-1}	$k_{nr}/10^8$ s^{-1}
2-Y	379	548 (0.49)	3.46 (0.18)	5.74 (0.82)	1.18	8.94	0.93
2-O	381	570 (0.25)	5.51 (1.00)	–	1.13	4.54	1.36
2-R	378	585 (0.10)	1.63 (0.93)	4.91 (0.07)	1.03	4.42	3.98
2[a]	351[b]	399,561 (0.13)	1.08 (0.53)	3.52 (0.47)	1.15	4.52	3.02

Mutai et al. [89]—Reproduced by permission of The Royal Society of Chemistry
[a]0.5 w% in poly(methyl methacrylate) (PMMA) matrix
[b]Maximum absorption wavelength

In contrast to the distinct luminescence colors, the excitation spectra were quite similar in shape and maximum wavelength, indicating that the light-absorption properties of **2** were not sensitive to molecular packing. Thus, differences in the molecular packing dominantly affected the electronic state of the IPT species and led to distinct ESIPT luminescence colors.

14.5.4 Heat-Mode Phase Transfer and Luminescence Color Switching

The thermal properties of the three polymorphs were examined by DSC. In the first-heating curve, **2-Y** showed only one endothermic peak at 247 °C, which corresponded to the melting point ($\Delta H = 31$ kJ mol^{-1}). On the other hand, **2-O** and **2-R** displayed a small endothermic peak around 190 °C ($\Delta H \approx 1$ kJ mol^{-1}) in addition to their melting peaks (247 °C). From optical microscopic observations, this thermal behavior was ascribed to a solid-solid phase transition, which was associated with a change in the luminescence color from orange (**2-O**) or red (**2-R**) to yellow.

When a microcrystalline powder of **2-O** was heated at 200 °C for 3 min and then cooled to the room temperature, the powder XRD pattern of the resultant solid was obviously different from that obtained before heating and was comparable to that of **2-Y**. It was therefore concluded that the small endothermic peak (190 °C) corresponded to the phase transition from **2-O** to **2-Y**. Although the XRD patterns of **2-R** before and after heating could not be obtained because of a microcrystalline sample shortage, it is reasonable to assume that **2-R** similarly undergoes a phase transfer to **2-Y** at 190 °C.

14.5.5 Theoretical Study on Polymorph-Dependent Luminescence

14.5.5.1 Accuracy of TD-DFT Calculations

In order to obtain a deeper understanding of the polymorph-dependent ESIPT luminescence of **2**, the ESIPT emission energies were evaluated using quantum chemical calculations. First, a series of computations, TD-DFT, CASSCF, and MS-CASPT2, were performed on the IPT form of the compound to validate the accuracies of the computed S_1–S_0 vertical transition energies. It was concluded that the TD-DFT level geometry optimization was sufficient to obtain an appropriate geometry of **2**, and the Coulomb-attenuated functional CAM-B3LYP [91] was in quantitative agreement with the S_1–S_0 gap obtained from the MS-CASPT2 calculations, whereas the B3LYP functional substantially underestimated the S_1–S_0 gap.

14.5.5.2 Calculation of ESIPT Luminescence Energy

Two-layer ONIOM models [92] were applied to the molecular clusters extracted from **2-Y**, **2-O**, and **2-R** in order to calculate the ESIPT state in different molecular aggregates. The effects of packing mode on ESIPT were taken into account through QM:MM calculations within the finite model. Each cluster model consisted of 17 molecules, in which one IPT species ($\mathbf{2_{IPT}}$) was surrounded with sixteen enol species ($\mathbf{2_{Enol}}$). The S_1 state of the center $\mathbf{2_{IPT}}$ was geometrically optimized at the TD-DFT(B3LYP)/6-31G(d) level of theory with fixed geometries of the surrounding $\mathbf{2_{Enol}}$ molecules calculated at the semiempirical PM3 level.

The single point $S_1 \rightarrow S_0$ emission energies were calculated at the TD(CAM-B3LYP)/6-31G(d). In the case of isolated monomer, optimized $\mathbf{2_{IPT}}$ without surrounding enols, the order of the computed emission energies (**2-O** < **2-R** < **2-Y**) did not coincide with the observed ESIPT luminescence (**2-R** < **2-O** < **2-Y**) (Table 14.3). On the other hand, when the π-stacked dimer geometries consisted of the optimized

Table 14.3 S_1–S_0 vertical energy (nm) of $\mathbf{2_{IPT}}$ for optimized geometry at TD(B3LYP)/6-31G(d):PM3 (1 $\mathbf{2_{IPT}}$+16 $\mathbf{2_{Enol}}$) ONIOM model

		Isolated model[a]		ONIOM model	
	Measured	Monomer	Dimer	Monomer	Dimer
2-Y	548	541.8	506.8	540.8	505.9
2-O	570	592.8	519.5	590.7	518.3
2-R	585	557.0	587.8	555.8	586.4
Non-stacked dimer (**2-O**)	–	–	567.4	–	565.1

Mutai et al. [89]—Reproduced by permission of The Royal Society of Chemistry
[a]Geometries extracted from the optimized 17-molecule ONIOM model

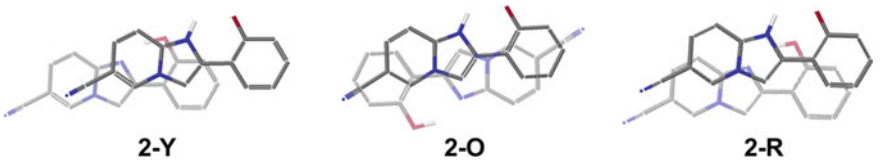

Fig. 14.11 π-stacked dimers composed of $\mathbf{2}_{IPT}$ (highlighted) and $\mathbf{2}_{Enol}$ (grayscale) of **2-Y**, **2-O**, and **2-R**

$\mathbf{2_{IPT}}$ and adjacent π-stacked $\mathbf{2_{Enol}}$ molecules (Fig. 14.11), the calculated emission energies were in accord with the observed ESIPT luminescence (Table 14.3). The calculations showed that the HOMO and LUMO existed on $\mathbf{2_{IPT}}$, indicating that the dimer models were suitable to simulate the ESIPT-type $S_1 \rightarrow S_0$ transition.

As a reference, the same TD-DFT calculation was also applied to the non-stacked dimer extracted from **2-O**. The computed energy was similar to that of the isolated monomer, suggesting that the difference in the energy of the π-stacked dimer models could be attributed to the effects of the π-stacking modes.

The emission energies of the clusters were further calculated using ONIOM models and were found to be virtually identical to the corresponding isolated models (Table 14.3). These results suggested that the quantum chemical interaction between $\mathbf{2_{IPT}}$ and π-stacked $\mathbf{2_{Enol}}$ contributed to the emission energies of the polymorphic crystals of **2**, while the effects of the surrounding enol molecules considered by the ONIOM models were limited.

14.5.6 Structure–Property Relationships in PDL

HPIP **1** has an intrinsic donor–acceptor nature due to the electron-rich and electron-deficient natures of phenyl and imidazopyridyl units, respectively (dipole moment of $\mathbf{1_{Enol}}$: 5.40 D). Therefore, antiparallel stacking, which cancelled the dipole effect, was predominantly observed in the crystals of **1** [61]. On the other hand, parallel and antiparallel stacking was observed in the crystals of **2**. DFT calculations showed that the dipole moment of $\mathbf{2_{Enol}}$ in the ground state was 1.66 D, which was much smaller than that of **1**. The weaker donor–acceptor nature of **2** may be the reason that antiparallel stacking was not essential to cancel the dipole effect and may also be why slipped-parallel stacking was allowed.

As for the proton-transferred emitting species, the dipole moments of the excited ($\mathbf{2_{IPT}}$*) and ground states ($\mathbf{2_{IPT}}$) were calculated to be 4.99 and 3.70 D, respectively, and were oriented in a high-angled manner (ca. 150°) (Fig. 14.12). This could be the reason for the polymorph dependence of the luminescence color. Alterations in the molecular packing mode, namely changes in the environment polarity, would cause different trends in the energy levels of the two IPT states, resulting in a variation in the energy gap. The calculated energy levels (E_{HOMO} and E_{LUMO}) of the π-stacked dimers were consistent with the above discussion. While the E_{HOMO} values increased

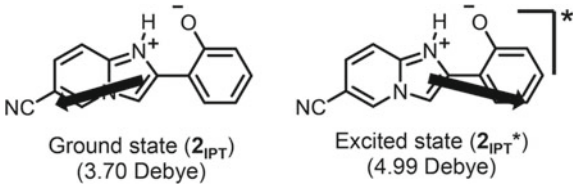

Fig. 14.12 Dipole moment in excited and ground states of IPT species of **2**. Mutai et al. [89]—Reproduced by permission of The Royal Society of Chemistry

in the order of **2-Y** < **2-O** < **2-R** ($\Delta E_{HOMO} = 0.36$ eV), those of E_{LUMO} increased in the order of **2-R** ~ **2-Y** < **2-O**, with a much smaller difference ($\Delta E_{LUMO} = 0.12$ eV).

14.5.7 Excited-State Dynamics in the Crystalline State

The excited-state dynamics of the PDL of **2** was further studied by means of a femtosecond pump-probe spectroscopic measurement [93]. By a femtosecond 400-nm pulse excitation of **2-Y**, **2-O**, and **2-R**, two processes with the decay time of <1 ps, which corresponds to the ESIPT ($\mathbf{2_{Enol}}^* \rightarrow \mathbf{2_{IPT}}^*$), and a slower process (11–45 ps) were observed before the radiative deactivation (2–8 ns).

In the case of **2-O**, the time-resolved profile of the transient absorbance was fitted with a triple-exponential function with lifetimes of 0.8 ± 0.3 ps (68%), 25 ± 5 ps (24%), and 5500 ps (8%). The third lifetime constant corresponding to the ESIPT emission was fixed to be 5500 ps. The shortest component (0.8 ps) was assigned to the ESIPT process ($\mathbf{2_{Enol}}^* \rightarrow \mathbf{2_{IPT}}^*$). In the crystalline solid, where molecules are densely packed, the twisting motion in the excited state is suppressed and the mutual interaction between excited-state and ground-state molecules should be easy. Therefore, we consider the 25 ps component to be the dynamics between the IPT* and enol species such as a heteroexcimer formation.

From the above discussion, the dynamics of the excited-state relaxation process of **2-O** is shown schematically in Fig. 14.13. Upon excitation of **2-O** by a fs 400 nm pulse, the $\mathbf{2_{Enol}}^*$ generated and the ESIPT took place with a time constant of 0.8 ps. Then the heteroexcimer between $\mathbf{2_{IPT}}^*$ and neighboring $\mathbf{2_{Enol}}$ species was formed with a time constant of 25 ps and deactivated with emission in a few nanoseconds.

In the case of **2-Y** and **2-R**, the time-resolved profiles show similar behaviors as **2-O**, while the time constants obtained by fitting with the triple-exponential function were different. The component due to ESIPT process is in the order **2-Y** (0.3 ps) < **2-R** (0.5 ps) < **2-O** (0.8 ps). The X-ray crystallographic analysis (Fig. 14.6) showed the distance between O and N1 as 2.582 Å (**2-Y**), 2.622 Å (**2-R**), and 2.625 Å (**2-O**), suggesting that the difference in the rate of ESIPT process might be related to the length of the intramolecular hydrogen bond (O–H···N1).

The rate of the heteroexcimer formation is in the order **2-R** (11 ps) < **2-O** (25 ps) < **2-Y** (45 ps). The excimer formation process might be affected by two factors: the

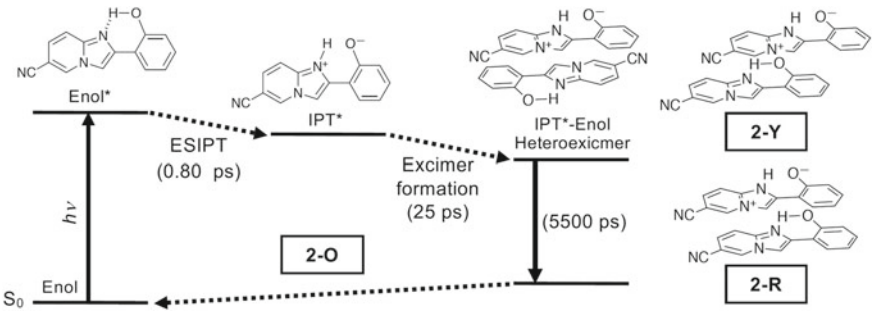

Fig. 14.13 Schematic diagram of ESIPT and subsequent relaxation processes of crystalline solid of **2**. Adapted with permission from Ishibashi et al. [93]. Copyright 2019 American Chemical Society

π–π interplanar distance and the longitudinal slippage of the dimeric unit. Because the interplanar π–π distances of the three polymorphs are nearly identical, the rate of the excimer formation would mainly depend on the longitudinal slippage (the overlap) of the π–π stacked dimeric unit as well as the small dihedral angle between the two aromatic rings (Fig. 14.6). The π–π overlap of dimer unit of **2-Y** was the smallest, resulting in the slowest excimer formation rate (45 ps). On the other hand, both **2-O** and **2-R** show larger π–π overlap, while the dihedral angle of **2-O** of the ground-state enol form was larger (2.6°) compared to that of **2-R** (1.4°). The less planarity of the molecule might result in the slower excimer formation time of **2-O** compared to **2-R**. From the above results, we can conclude that the difference in the molecular packings is somewhat capable of "controlling" the excimer formation.

14.6 Conclusion

In conclusion, the three-color, polymorph-dependent luminescence of 6-cyano HPIP (**2**) (**2-Y** (yellow), **2-O** (orange), and **2-R** (red)) was investigated. X-ray crystallographic analysis indicated a remarkable difference in the molecular packing, which should be a dominant factor in the polymorph-dependent ESIPT luminescence. Theoretical studies indicated that intermolecular interactions between π-stacked IPT and enol molecules may contribute to the emission energy of crystal polymorphs. The different directions of the dipole moments in the ESIPT and IPT states may be the reason for the sensitive polymorph-dependent luminescence color, as the energy level of the two states would shift differently with variations in the environment, resulting in changes in the energy gap. It is also remarkable that the excited-state dynamics of the three polymorphs elucidated by the femtosecond transient absorption and fluorescence lifetime measurements presented the consistent model with the quantum chemical simulations. Namely, between the rapid ESIPT (<1 ps) and the nanosecond

Scheme 14.6 Molecular structure of HPIP substituted at imidazopyridine (R^1) and phenyl (R^2) moieties

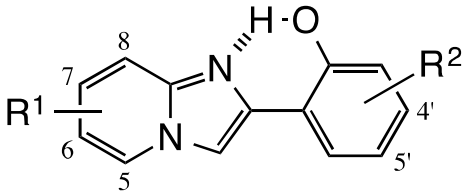

emissive decay processes, the heteroeximer formation process, whose rate is obviously dependent on the molecular packing mode (11–45 ps), is found. The result would open the way for detailed experimental analysis of the mechanism of PDL.

14.7 Other HPIP Derivatives

To date, various derivatives of HPIP have been synthesized, and the fluorescence of some derivatives has been reported [74]. Similar to **1** and **2**, the derivatives exhibited bright ESIPT fluorescence in a PMMA matrix ($\Phi = 0.1$–0.6), although they showed weak emission ($\Phi \approx 0.01$) in a THF solution. The introduction of electron-donating and electron-withdrawing groups onto the imidazopyridine moiety (R^1) caused blue and redshifts in the ESIPT fluorescence, respectively. On the contrary, substitution at the phenyl ring (R^2) shifted the ESIPT fluorescence in the opposite direction, i.e., electron-donating and electron-withdrawing groups caused red and blue shifts, respectively (Scheme 14.6).

Furthermore, some derivatives display polymorph-dependent ESIPT luminescence: for example, 6-bromo HPIP ($\lambda_{em} = 539$ and 575 nm), 5′-methyl HPIP ($\lambda_{em} = 521$ and 536 nm), and 6-chloro-5'-methyl HPIP ($\lambda_{em} = 541$ and 576 nm). On the other hand, polymorphism in aryl-substituted HPIPs has not been observed.

The luminescence of HPIP may be controlled by chemical modifications and supramolecular methods (polymorphism). Thus, HPIP could be a good model to evaluate the effects of substituents and polymorphism on solid-state luminescence.

14.8 Conclusions and Future Outlook

Crystal engineering toward the formation of polymorphic phases of luminophores is a powerful strategy for controlling the luminescence of molecular solids, and it may lead to new photofunctional materials.

Owing to ESIPT, HPIP **1** exhibits environment-sensitive zwitterionic excited species, which leads to PDL, i.e., blue-green (**1-BG**) and yellow (**1-Y**). Furthermore, 6-cyano HPIP **2** emits three-color PDL, i.e., yellow (**2-Y**), orange (**2-O**), and red (**2-R**). Switching luminescence color via heat-mode phase transfer indicates that ESIPT is a useful mechanism for converting information regarding molecular packing

into a significant change in luminescence. ESIPT luminescence of HPIP can also be controlled by common synthetic modifications, and the effects of substituents on luminescence can be reasonably explained by the calculated electronic configurations and energy levels of S_0-IPT and S_1-IPT states [36].

Theoretical studies of HPIP derivatives have presented valuable information on the electronic state of molecular crystals that may affect PDL. Femtosecond time-resolved measurement is also promising technique that will offer much clear and convincing experimental data for discussing the excited dynamics in crystals.

Thus, the remarkable polymorph dependence of the luminescence color demonstrates that ESIPT is a promising mechanism for packing-directed control of luminescence and will improve the understanding of the structure–property relationships observed in PDL. It should be possible to design a library of compounds based on the combination of conventional synthetic strategies and supramolecular chemistry (i.e., polymorph dependence).

Currently, the number of compounds that show PDL is still limited. Therefore, the development of a series of luminescent core-based PDL-active compounds should contribute to the understanding of crystal structure–luminescence relationships and may lead to the design of polymorphic materials displaying specific and desirable luminescence properties. These findings should also offer a novel design concept toward tunable organic luminescent solids and thus provide a roadmap for new functional materials.

Acknowledgements We thank Dr. Yasuhiro Shigemitsu at the Industrial Technology Center of Nagasaki (Japan) for the high level of quantum chemical calculations, and Prof. Tsuyoshi Asahi and Dr. Yukihide Ishibashi for the femtosecond pump-probe spectroscopic measurement. We also thank Emeritus Prof. Dr. Koji Araki at the Institute of Industrial Science, University of Tokyo.

References

1. Sasabe, H., Kido, J.: Multifunctional materials in high-performance OLEDs: challenges for solid-state lighting. Chem. Mater. **23**, 621–630 (2011)
2. Kamtekar, K.T., Monkman, A.P., Bryce, M.R.: Recent advances in white organic light-emitting materials and devices (WOLEDS). Adv. Mater. **22**, 572–582 (2010)
3. Yanai, N., Kitayama, K., Hijikata, Y., Sato, H., Matsuda, R., Kubota, Y., Takata, M., Mizuno, M., Uemura, T., Kitagawa, S.: Gas detection by structural variations of fluorescent guest molecules in a flexible porous coordination polymer. Nat. Mater. **10**, 787–793 (2011)
4. Samuel, I.D.W., Turnbull, G.A.: Organic semiconductor lasers. Chem. Rev. **107**, 1272–1295 (2007)
5. Qian, G., Wang, Z.Y.: Near-infrared organic compounds and emerging applications. Chem. -Asian J. **5**, 1006–1029 (2010)
6. Mishra, A., Bäuerle, P.: Small molecule organic semiconductors on the move: promises for future solar energy technology. Angew. Chem. Int. Ed. **51**, 2020–2067 (2012)
7. Zhao, Y.S., Fu, H., Peng, A., Ma, Y., Liao, Q., Yao, J.: Construction and optoelectronic properties of organic one-dimensional nanostructures. Acc. Chem. Res. **43**, 409–418 (2010)
8. Birks, J.B.: Photophysics of Aromatic Molecules. Wiley-Interscience, London (1970)

9. Moorthy, J.N., Natarajan, P., Venkatakrishnan, P., Huang, D.-F., Chow, T.J.: Steric Inhibition of π-stacking: 1,3,6,8-tetraarylpyrenes as efficient blue emitters in organic light emitting Diodes (OLEDs). Org. Lett. **9**, 5215–5218 (2007)
10. Qin, T., Zhou, G., Scheiber, H., Bauer, R.E., Baumgarten, M., Anson, C.E., List, E.J.W., Müllen, K.: Polytriphenylene dendrimers: a unique design for blue-light-emitting materials. Angew. Chem. Int. Ed. **47**, 8292–8296 (2008)
11. Li, B., Li, J., Fu, Y., Bo, Z.: Porphyrins with four monodisperse oligofluorene arms as efficient red light-emitting materials. J. Am. Chem. Soc. **126**, 3430–3431 (2004)
12. Li, M., Niu, Y., Zhu, X., Peng, Q., Lu, H.-Y., Xia, A., Chen, C.-F.: Tetrahydro[5]helicene-based imide dyes with intense fluorescence in both solution and solid state. Chem. Commun. **50**, 2993–2995 (2014)
13. Shimizu, M., Kaki, R., Takeda, Y., Hiyama, T., Nagai, N., Yamagishi, H., Furutani, H.: 1,4-bis(diarylamino)-2,5-bis(4-cyanophenylethenyl)benzenes: Fluorophores exhibiting efficient red and near-infrared emissions in solid state. Angew. Chem. Int. Ed. **51**, 4095–4099 (2012)
14. Shimizu, M., Takeda, Y., Higashi, M., Hiyama, T.: 1,4-Bis(alkenyl)-2,5-dipiperidinobenzenes: minimal fluorophores exhibiting highly efficient emission in the solid state. Angew. Chemie Int. Ed. **48**, 3653–3656 (2009)
15. Qin, A., Tang, B.Z. (eds.): Aggregation-Induced Emission: Fundamentals. Wiley, Chichester, UK (2014)
16. Mei, J., Hong, Y., Lam, J.W.Y., Qin, A., Tang, Y., Tang, B.Z.: Aggregation-induced emission: the whole is more brilliant than the parts. Adv. Mater. **26**, 5429–5479 (2014)
17. Luo, J., Xie, Z., Lam, J.W.Y., Cheng, L., Tang, B.Z., Chen, H., Qiu, C., Kwok, H.S., Zhan, X., Liu, Y., Zhu, D.: Aggregation-induced emission of 1-methyl-1,2,3,4,5-pentaphenylsilole. Chem. Commun. **381**, 1740–1741 (2001)
18. An, B.K., Kwon, S.K., Jung, S.D., Park, S.Y.: Enhanced emission and its switching in fluorescent organic nanoparticles. J. Am. Chem. Soc. **124**, 14410–14415 (2002)
19. Tong, H., Hong, Y., Dong, Y., Häussler, M., Lam, J.W.Y., Li, Z., Guo, Z., Guo, Z., Tang, B.Z.: Fluorescent "light-up" bioprobes based on tetraphenylethylene derivatives with aggregation-induced emission characteristics. Chem. Commun. 3705–3707 (2006)
20. Varughese, S.: Non-covalent routes to tune the optical properties of molecular materials. J. Mater. Chem. C **2**, 3499–3516 (2014)
21. Yan, D., Evans, D.G.: Molecular crystalline materials with tunable luminescent properties: from polymorphs to multi-component solids. Mater. Horiz. **1**, 46–57 (2014)
22. Yoon, S.J., Chung, J.W., Gierschner, J., Kim, K.S., Choi, M.G., Kim, D., Park, S.Y.: Multistimuli two-color luminescence switching via different slip-stacking of highly fluorescent molecular sheets. J. Am. Chem. Soc. **132**, 13675–13683 (2010)
23. Hinoue, T., Shigenoi, Y., Sugino, M., Mizobe, Y., Hisaki, I., Miyata, M., Tohnai, N.: Regulation of π-stacked anthracene arrangement for fluorescence modulation of organic solid from monomer to excited oligomer emission. Chem. Eur. J. **18**, 4634–4643 (2012)
24. Yamaguchi, S., Yoshikawa, I., Mutai, T., Araki, K.: Solid-state luminescence of tetraphenylpyrene derivatives: mechano/vapochromic luminescence of 1,3,6,8-tetra(4′-carboxyphenyl)pyrene. J. Mater. Chem. **22**, 20065 (2012)
25. Avobenzone, D., Zhang, G., Lu, J., Sabat, M., Fraser, C.L.: Polymorphism and reversible mechanochromic luminescence for solid-state. J. Am. Chem. Soc. **132**, 2160–2162 (2010)
26. Shida, T., Mutai, T., Araki, K.: Sterically induced polymorphism: ON–OFF control of excited-state intramolecular proton transfer (ESIPT) luminescence of 1-methyl-2-(2′-hydroxyphenyl)benzimidazole. CrystEngComm **15**, 10179–10182 (2013)
27. Luo, X., Li, J., Li, C., Heng, L., Dong, Y.Q., Liu, Z., Bo, Z., Tang, B.Z.: Reversible switching of the emission of diphenyldibenzofulvenes by thermal and mechanical stimuli. Adv. Mater. **23**, 3261–3265 (2011)
28. Li, Y.-X., Zhou, H.-B., Miao, J.-L., Sun, G.-X., Li, G.-B., Nie, Y., Chen, C.-L., Chen, Z., Tao, X.-T.: Conformation twisting induced orientational disorder, polymorphism and solid-state emission properties of 1-(9-anthryl)-2-(1-naphthyl)ethylene. CrystEngComm **14**, 8286–8291 (2012)

29. Mutai, T., Satou, H., Araki, K.: Reproducible on-off switching of solid-state luminescence by controlling molecular packing through heat-mode interconversion. Nat. Mater. **4**, 685–687 (2005)
30. Zhang, H.Y., Zhang, Z.L., Ye, K.Q., Zhang, J.Y., Wang, Y.: Organic crystals with tunable emission colors based on a single organic molecule and different molecular packing structures. Adv. Mater. **18**, 2369–2372 (2006)
31. Gu, X., Yao, J., Zhang, G., Yan, Y., Zhang, C., Peng, Q., Liao, Q., Wu, Y., Xu, Z., Zhao, Y., Fu, H., Zhang, D.: Polymorphism-dependent emission for Di(p-methoxylphenyl)dibenzofulvene and analogues: optical waveguide/amplified spontaneous emission behaviors. Adv. Funct. Mater. **22**, 4862–4872 (2012)
32. See for example, (a) Krishna, G.R., Kiran, M.S.R.N., Fraser, C.L., Ramamurty, U., Reddy, C.M.: The relationship of solid-state plasticity to mechanochromic luminescence in difluoroboron avobenzone polymorphs. Adv. Funct. Mater. **23**, 1422–1430 (2013); (b) Mikhlina, Y.A., Bolotin, B.M., Kuz'mina, L.G.: Relationship between the structure and luminescent properties for two crystal modifications of N-butyl-2-cyano-3-[4-(dimethylamino)phenyl]-2-propenamide. Crystallogr. Rep. **58**, 687–691 (2013); (c) Abe, Y., Karasawa, S., Koga, N.: Crystal structures and emitting properties of trifluoromethylaminoquinoline derivatives: thermal single-crystal-to-single-crystal transformation of polymorphic crystals that emit different colors. Chem. -Eur. J. **18**, 15038–15048 (2012); (d) Abe, Y., Karasawa, S., Koga, N.: Crystal structures and emitting properties of trifluoromethylaminoquinoline derivatives: thermal single-crystal-to-single-crystal transformation of polymorphic crystals that emit different colors. Chem. Eur. J. **18**, 15038–15048 (2012); (e) Kohmoto, S., Tsuyuki, R., Masu, H., Azumaya, I., Kishikawa, K.: Polymorphism-dependent fluorescence of 9,10-bis(pentafluorobenzoyloxy)anthracene. Tetrahedron Lett. **49**, 39–43 (2008)
33. Konoshima, H., Nagao, S., Kiyota, I., Amimoto, K., Yamamoto, N., Sekine, M., Nakata, M., Furukawa, K., Sekiya, H.: Excited-state intramolecular proton transfer and charge transfer in 2-(2′-hydroxyphenyl)benzimidazole crystals studied by polymorphs-selected electronic spectroscopy. Phys. Chem. Chem. Phys. **14**, 16448–16457 (2012)
34. Dong, Y., Xu, B., Zhang, J., Tan, X., Wang, L., Chen, J., Lv, H., Wen, S., Li, B., Ye, L., Zou, B., Tian, W.: Piezochromic luminescence based on the molecular aggregation of 9,10-Bis((E)-2-(pyrid-2-yl)vinyl)anthracene. Angew. Chem. Int. Ed. **51**, 10782–10785 (2012)
35. Luo, X., Zhao, W., Shi, J., Li, C., Liu, Z., Bo, Z., Dong, Y.Q., Tang, B.Z.: Reversible switching emissions of tetraphenylethene derivatives among multiple colors with solvent vapor, mechanical, and thermal stimuli. J. Phys. Chem. C **116**, 21967–21972 (2012)
36. Douhal, A., Lahmani, F., Zewail, A.H.: Proton-transfer reaction dynamics. Chem. Phys. **207**, 477–498 (1996)
37. Barbatti, M., Aquino, A.J.A., Lischka, H., Schriever, C., Lochbrunner, S., Riedle, E.: Ultrafast internal conversion pathway and mechanism in 2-(2′-hydroxyphenyl)benzothiazole: a case study for excited-state intramolecular proton transfer systems. Phys. Chem. Chem. Phys. **11**, 1406–1415 (2009)
38. Lochbrunner, S., Schultz, T., Schmitt, M., Shaffer, J.P., Zgierski, M.Z., Stolow, A.: Dynamics of excited-state proton transfer systems via time-resolved photoelectron spectroscopy. J. Chem. Phys. **114**, 2519–2522 (2001)
39. Ormson, S.M., Brown, R.G.: Excited state intramolecular proton transfer part 1: ESIPT to nitrogen. Prog. React. Kinet. **19**, 45–91 (1994)
40. Furukawa, K., Yamamoto, N., Nakabayashi, T., Ohta, N., Amimoto, K., Sekiya, H.: Changes in the electric dipole moments and molecular polarizabilities of enol and keto forms of 2-(2'-hydroxyphenyl)benzimidazole along the proton transfer reaction path in a PMMA film. Chem. Phys. Lett. **539–540**, 45–49 (2012)
41. Tsai, H.H.G., Sun, H.L.S., Tan, C.J.: TD-DFT study of the excited-state potential energy surfaces of 2-(2'-hydroxyphenyl)benzimidazole and its amino derivatives. J. Phys. Chem. A **114**, 4065–4079 (2010)
42. Henary, M.M., Wu, Y.G., Cody, J., Sumalekshmy, S., Li, J., Mandal, S., Fahrni, C.J.: Excited-state intramolecular proton transfer in 2-(2'-arylsulfonamidophenyl)benzimidazole derivatives: The effect of donor and acceptor substituents. J. Org. Chem. **72**, 4784–4797 (2007)

43. Ouyang, J., Ouyang, C., Fujii, Y., Nakano, Y., Shoda, T., Nagano, T.: Synthesis and fluorescent properties of 2-(1H-benzimidazol-2-yl)-phenol derivatives. J. Heterocycl. Chem. **41**, 359–365 (2004)
44. Das, K., Sarkar, N., Majumdar, D., Bhattacharyya, K.: Excited-state intramolecular proton transfer and rotamerism of 2-(2′-hydroxyphenyl) benzimidazole. Chem. Phys. Lett. **198**, 443–448 (1992)
45. Seo, J., Kim, S., Park, S., Park, S.Y.: Tailoring the excited-state intramolecular proton transfer (ESIPT) fluorescence of 2-(2′-Hydroxyphenyl)benzoxazole derivatives. Bull. Korean Chem. Soc. **26**, 1706–1710 (2005)
46. Chen, W., Twum, E.B., Li, L., Wright, B.D., Rinaldi, P.L., Pang, Y.: Rotational energy barrier of 2-(2′,6′-Dihydroxyphenyl)benzoxazole: a case study by NMR. J. Org. Chem. **77**, 285–290 (2012)
47. Ohshima, A., Momotake, A., Nagahata, R., Arai, T.: Enhancement of the large stokes-shifted fluorescence emission from the 2-(2′-hydroxyphenyl)benzoxazole core in a dendrimer. J. Phys. Chem. A **109**, 9731–9736 (2005)
48. Wang, H., Zhang, H., Abou-Zied, O.K., Yu, C., Romesberg, F.E., Glasbeek, M.: Femtosecond fluorescence upconversion studies of excited-state proton-transfer dynamics in 2-(2′-hydroxyphenyl)benzoxazole (HBO) in liquid solution and DNA. Chem. Phys. Lett. **367**, 599–608 (2003)
49. Ma, J., Zhao, J., Yang, P., Huang, D., Zhang, C., Li, Q.: New excited state intramolecular proton transfer (ESIPT) dyes based on naphthalimide and observation of long-lived triplet excited states. Chem. Commun. **48**, 9720–9722 (2012)
50. Yao, D., Zhao, S., Guo, J., Zhang, Z., Zhang, H., Liu, Y., Wang, Y.: Hydroxyphenylbenzothiazole based full color organic emitting materials generated by facile molecular modification. J. Mater. Chem. **21**, 3568–3570 (2011)
51. Mohammed, O.F., Luber, S., Batista, V.S., Nibbering, E.T.J.: Ultrafast branching of reaction pathways in 2-(2′-Hydroxyphenyl)benzothiazole in polar acetonitrile solution. J. Phys. Chem. A **115**, 7550–7558 (2011)
52. Rini, M., Dreyer, J., Nibbering, E.T.J., Elsaesser, T.: Ultrafast vibrational relaxation processes induced by intramolecular excited state hydrogen transfer. Chem. Phys. Lett. **374**, 13–19 (2003)
53. Frey, F., Laermer, T.: Elsaesser, Femtosecond studies of excited-state proton and deuterium transfer in benzothiazole compounds. J. Phys. Chem. **95**, 10391–10395 (1991)
54. Anthony, K., Brown, R.G., Hepworth, J.D., Hodgson, K.W., May, B., West, M.A.: Solid-state fluorescent photophysics of some 2-substituted benzothiazoles. J. Chem. Soc. Perkin Trans. **2**, 2111–2117 (1984)
55. Amimoto, K., Kawato, T.: Photochromism of organic compounds in the crystal state. J. Photochem. Photobiol. C Photochem. Rev. **6**, 207–226 (2005)
56. Mitra, S., Tamai, N.: Dynamics of photochromism in salicylideneaniline: a femtosecond spectroscopic study. Phys. Chem. Chem. Phys. **5**, 4647–4652 (2003)
57. Harada, J., Fujiwara, T., Ogawa, K.: Crucial role of fluorescence in the solid-state thermochromism of salicylideneanilines. J. Am. Chem. Soc. **129**, 16216–16221 (2007)
58. Kwon, J.E., Park, S.Y.: Advanced organic optoelectronic materials: harnessing excited-state intramolecular proton transfer (ESIPT) process. Adv. Mater. **23**, 3615–3642 (2011)
59. Seo, J., Kim, S., Lee, Y.S., Kwon, O.H., Park, K.H., Choi, S.Y., Chung, Y.K., Jang, D.J., Park, S.Y.: Enhanced solid-state fluorescence in the oxadiazole-based excited-state intramolecular proton-transfer (ESIPT) material: synthesis, optical property, and crystal structure. J. Photochem. Photobiol. A Chem. **191**, 51–58 (2007)
60. Chuang, W.-T., Hsieh, C.-C., Lai, C.-H., Lai, C.-H., Shih, C.-W., Chen, K.-Y., Hung, W.-Y., Hsu, Y.-H., Chou, P.-T.: Excited-state intramolecular proton transfer molecules bearing o-hydroxy analogues of green fluorescent protein chromophore. J. Org. Chem. **76**, 8189–8202 (2011)
61. Mutai, T., Tomoda, H., Ohkawa, T., Yabe, Y., Araki, K.: Switching of polymorph-dependent ESIPT luminescence of an imidazo[1,2-*a*]pyridine derivative. Angew. Chem. Int. Ed. **47**, 9522–9524 (2008)

62. Park, S., Park, J., Seo, S.H., Kim, S.Y.: Park, tetraphenylimidazole-based excited-state intramolecular proton-transfer molecules for highly efficient blue electroluminescence. Adv. Funct. Mater. **18**, 726–731 (2008)
63. Hu, Y., Zhang, Y., Liang, F., Wang, L., Ma, D., Jing, X.: Blue organic light-emitting diodes based on an oxadiazole-containing organic molecule exhibiting excited state intramolecular proton transfer. Synth. Met. **137**, 1123–1124 (2003)
64. Park, S., Ji, E.K., Se, H.K., Seo, J., Chung, K., Park, S.Y., Jang, D.J., Medina, B.M., Gierschner, J., Soo, Y.P.: A white-light-emitting molecule: frustrated energy transfer between constituent emitting centers. J. Am. Chem. Soc. **131**, 14043–14049 (2009)
65. Kim, S., Seo, J., Jung, H.K., Kim, J.-J., Park, S.Y.: White luminescence from polymer thin films containing excited-state intramolecular proton-transfer dyes. Adv. Mater. **17**, 2077–2082 (2005)
66. Chang, S.M., Tzeng, Y.J., Wu, S.Y., Li, K.Y., Hsueh, K.L.: Emission of white light from 2-(2′-hydroxyphenyl) benzothiazole in polymer electroluminescent devices. Thin Solid Films **477**, 38–41 (2005)
67. Shono, H., Ohkawa, T., Tomoda, H., Mutai, T., Araki, K.: Fabrication of colorless organic materials exhibiting white luminescence using normal and excited-state intramolecular proton transfer processes. ACS Appl. Mater. Interfaces. **3**, 654–657 (2011)
68. Tang, K.-C., Chang, M.-J., Lin, T.-Y., Pan, H.-A., Fang, T.-C., Chen, K.-Y., Hung, W.-Y., Hsu, Y.-H., Chou, P.-T.: Fine tuning the energetics of excited-state intramolecular proton transfer (ESIPT): white light generation in a single ESIPT system. J. Am. Chem. Soc. **133**, 17738–17745 (2011)
69. Sun, W., Li, S., Hu, R., Qian, Y., Wang, S., Yang, G.: Understanding solvent effects on luminescent properties of a triple fluorescent ESIPT compound and application for white light emission. J. Phys. Chem. A **113**, 5888–5895 (2009)
70. Chen, K.-Y., Hsieh, C.-C., Cheng, Y.-M., Lai, C.-H., Chou, P.-T.: Extensive spectral tuning of the proton transfer emission from 550 to 675 nm via a rational derivatization of 10-hydroxybenzo[h]quinoline. Chem. Commun. 4395–4397 (2006)
71. Douhal, A., Amat-Guerri, F., Acuna, A.U.: Photoinduced intramolecular proton transfer and charge redistribution in imidazopyridines. J. Phys. Chem. **99**, 76–80 (1995)
72. Douhal, A.: The involvement of rotational processes in the intramolecular proton-transfer cycle. Ber. Bunsenges. Phys. Chem. **102**, 448–451 (1998)
73. (a) Stasyuk, A.J., Banasiewicz, M., Cyrański, M.K., Gryko, D.T.: Imidazo[1,2-*a*]pyridines susceptible to excited state intramolecular proton transfer: one-pot synthesis via an Ortoleva-King reaction. J. Org. Chem. **77**, 5552–5558 (2012)
74. Mutai, T., Sawatani, H., Shida, T., Shono, H., Araki, K.: Tuning of excited-state intramolecular proton transfer (ESIPT) fluorescence of imidazo[1,2-*a*]pyridine in rigid matrices by substitution effect. J. Org. Chem. **78**, 2482–2489 (2013)
75. Douhal, A., Amat-Guerri, F., Acuña, A.U.: Probing nanocavities with proton-transfer fluorescence. Angew. Chemie Int. Ed. Eng. **36**, 1514–1516 (1997)
76. (a) Crystallographic data for **1-BG**: $C_{13}H_{10}N_2O$, $FW = 210.23$, Orthorhombic, *Pbca*, $a = 7.6560(2)$, $b = 12.1630(3)$, $c = 22.2380(5)$ Å, $V = 2070.80(9)$ Å^3, $Z = 8$, $d_{calcd} = 1.349$, $T = 298(2)$ K, 18651 measured and 2030 independent reflections, $R_1 = 0.0548$, w$R_2 = 0.1297$, $GOF = 1.104$. CCDC No.: 698144 (b) crystallographic data for **1-Y**: $C_{13}H_{10}N_2O$, $FW = 210.23$, Monoclinic, $P2_1/c$, $a = 18.2400(4)$, $b = 5.77300(10)$, $c = 20.3010(5)$ Å, $b = 108.1650(10)°$, $V = 2031.15(8)$ Å^3, $Z = 8$, $d_{calcd} = 1.375$, $T = 298(2)$ K, 18482 measured and 3733 independent reflections, $R_1 = 0.0624$, w$R_2 = 0.1732$, $GOF = 1.116$. CCDC No.: 698145
77. Khan, A.U., Kasha, M.: Mechanism of four-level laser action in solution excimer and excited-state proton-transfer cases. Proc. Natl. Acad. Sci. U. S. A. **80**, 1767–1770 (1983)
78. Shigemitsu, Y., Mutai, T., Houjou, H., Araki, K.: Excited-state intramolecular proton transfer (ESIPT) emission of hydroxyphenylimidazopyridine: computational study on enhanced and polymorph-dependent luminescence in the solid state. J. Phys. Chem. A **116**, 12041–12048 (2012)

79. Guallar, V., Moreno, M., Lluch, J.M., Amat-Guerri, F., Douhal, A.: H-atom transfer and rotational processes in the ground and first singlet excited electronic states of 2-(2′-Hydroxyphenyl)oxazole derivatives: experimental and theoretical studies. J. Phys. Chem. **100**, 19789–19794 (1996)
80. Organero, J.A., Moreno, M., Santos, L., Lluch, J.M., Douhal, A.: Photoinduced proton transfer and rotational motion of 1-Hydroxy-2-acetonaphthone in the S_1 state: a theoretical insight into its photophysics. J. Phys. Chem. A **104**, 8424–8431 (2000)
81. Fournier, T., Pommeret, S., Mialocq, J.-C., Deflandre, A.: Excited-state intramolecular proton transfer (ESIPT) and energy relaxation processes in hydroxyphenylbenzotriazole derivatives: a femtosecond laser study. In: De Schryver, F.C., De Feyter, S., Schweitzer, G. (eds.) Femtochemistry, pp. 323–333. Wiley-VCH, Weinheim, Germany (2001)
82. de Klerk, J.S., Bader, A.N., Ariese, F., Gooijer, C.: High-resolution fluorescence studies on excited-state intra- and intermolecular proton transfer. In: Geddes, C.D. (ed.) Reviews in Fluorescence, pp. 271–298. Springer, New York (2009)
83. Mitra, S., Tamai, N.: A combined experimental and theoretical study on the photochromism of aromatic anils. Chem. Phys. **246**, 463–475 (1999)
84. (a) Gentili, P.L., Ortica, F., Romani, A., Favaro, G.: Effects of proximity on the relaxation dynamics of flindersine and 6(5*H*)-Phenanthridinone. J. Phys. Chem. A **111**, 193–200 (2007); (b) Domcke, W., Yarkony, D.R., Köppel, H.: Conical Intersections: Electronic Structure, Dynamics & Spectroscopy, Advanced Series in Physical Chemistry. World Scientific, Singapore (2004); (c) Gustavsson, T., Improta, R., Markovitsi, D.: DNA/RNA: building blocks of life under UV irradiation. J. Phys. Chem. Lett. **1**, 2025–2030 (2010)
85. (a) Merchán, M., Serrano-Andrés, L.: Ultrafast internal conversion of excited cytosine via the lowest $\pi\pi^*$ electronic singlet state. J. Am. Chem. Soc. **125**, 8108–8109 (2003); (b) Ismail, N., Blancafort, L., Olivucci, M., Kohler, B., Robb, M.A.: Ultrafast decay of electronically excited singlet cytosine via a π,π^* to n_0,π^* state switch. J. Am. Chem. Soc. **124**, 6818–6819 (2002); (c) Blancafort, L., Cohen, B., Hare, P.M., Kohler, B., Robb, M.A.: Singlet excited-state dynamics of 5-Fluorocytosine and cytosine: an experimental and computational study. J. Phys. Chem. A **109**, 4431–4436 (2005); (d) Zgierski, M.Z., Fujiwara, T., Kofron, W.G., Lim, E.C.: Highly effective quenching of the ultrafast radiationless decay of photoexcited pyrimidine bases by covalent modification: photophysics of 5,6-trimethylenecytosine and 5,6-trimethyleneuracil. Phys. Chem. Chem. Phys. **9**, 3206–3209 (2007); (e) Paterson, M.J., Robb, M.A., Blancafort, L., DeBellis, A.D.: Theoretical study of benzotriazole uv photostability: ultrafast deactivation through coupled proton and electron transfer triggered by a charge-transfer state. J. Am. Chem. Soc. **126**, 2912–2922 (2004)
86. Fukunaga, H., Fedorov, D.G., Chiba, M., Nii, K., Kitaura, K.: Theoretical analysis of the intermolecular interaction effects on the excitation energy of organic pigments: solid state quinacridone. J. Phys. Chem. A **112**, 10887–10894 (2008)
87. Filhol, J.-S., Deschamps, J., Dutremez, S.G., Boury, B., Barisien, T., Legrand, L., Schott, M.: Polymorphs and colors of polydiacetylenes: a first principles study. J. Am. Chem. Soc. **131**, 6976–6988 (2009)
88. Wu, Q., Peng, Q., Niu, Y., Gao, X., Shuai, Z.: Theoretical insights into the aggregation-induced emission by hydrogen bonding: A QM/MM study. J. Phys. Chem. A **116**, 3881–3888 (2012)
89. Mutai, T., Shono, H., Shigemitsu, Y., Araki, K.: Three-color polymorph-dependent luminescence: crystallographic analysis and theoretical study on excited-state intramolecular proton transfer (ESIPT) luminescence of cyano-substituted imidazo[1,2-*a*]pyridine. CrystEngComm **16**, 3890–3895 (2014)
90. Crystallographic data for **2-Y**: $C_{14}H_9N_3O$, $FW = 235.24$, Monoclinic, $P2_1/n$, $a = 6.052(6)$, $b = 4.919(5)$, $c = 36.98(3)$ Å, $\beta = 94.155(4)°$, $V = 1098.0(17)$ Å^3, $Z = 4$, $d_{calcd} = 1.423$, $T = 113(2)$ K, 8137 measured and 2402 independent reflections, $R_1 = 0.0754$, w$R_2 = 0.2201$, $GOF = 0.938$. CCDC No.: 965203. Crystallographic data for **2-O**: $C_{14}H_9N_3O$, $FW = 235.24$, Monoclinic, $P2_1/n$, $a = 13.654(6)$, $b = 7.343(3)$, $c = 14.200(6)$ Å, $\beta = 130.054(2)°$, $V = 1089.8(8)$ Å^3, $Z = 4$, $d_{calcd} = 1.434$, $T = 113(2)$ K, 8291 measured and 2487 independent reflections, $R_1 = 0.0334$, w$R_2 = 0.0963$, $GOF = 1.097$. CCDC No.: 965204. Crystallographic

data for **2-R**: $C_{14}H_9N_3O$, $FW = 235.24$, Monoclinic, $P2_1/n$, $a = 3.8196(10)$, $b = 11.356(3)$, $c = 25.246(7)$ Å, $\beta = 93.1961(11)°$, $V = 1093.3(5)$ Å^3, $Z = 4$, $d_{calcd} = 1.429$, $T = 113(2)$ K, 8368 measured and 2479 independent reflections, $R_1 = 0.0591$, w$R_2 = 0.1328$, $GOF = 0.929$. CCDC No.: 965205

91. Yanai, T., Tew, D.P., Handy, N.C.: A new hybrid exchange–correlation functional using the Coulomb-attenuating method (CAM-B3LYP). Chem. Phys. Lett. **393**, 51–57 (2004)
92. Dapprich, S., Komáromi, I., Byun, K.S., Morokuma, K., Frisch, M.J.: A new ONIOM implementation in Gaussian98. Part I. The calculation of energies, gradients, vibrational frequencies and electric field derivatives. J. Mol. Struct. THEOCHEM **461–462**, 1–21 (1999)
93. Ishibashi, Y., Murakami, M., Araki, K., Mutai, T., Asahi, T.: Excited-state intramolecular proton-transfer process of crystalline 6-Cyano-2-(2′-hydroxyphenyl)imidazo[1,2-*a*]pyridine, as revealed by femtosecond pump-probe microspectroscopy. J. Phys. Chem. C **123**, 11224–11232 (2019)

Chapter 15
Solid-State Fluorescence Switching Using Photochromic Diarylethenes

Seiya Kobatake and Tatsumoto Nakahama

Abstract Solid-state fluorescence-switchable materials that show large changes in fluorescence intensities and/or colors in response to various external stimuli have attracted much attention in various applications, such as optical memories, display devices, and sensor materials. In particular, fluorescence switching using photochromic diarylethenes has been widely investigated because of the excellent performance of diarylethene with high thermal stabilities, high fatigue-resistant properties, and high reactivity in the solid states. Although many researchers investigated the fluorescence switching properties only in solution, the evaluation in solid states is essential for the practical applications. This chapter has focused on solid-state fluorescence switching behavior using diarylethene and reviewed the rational design and the properties for various types of the fluorescence-switchable materials.

Keywords Photochromism · Fluorescence switching · Diarylethene · Solid state

15.1 Introduction

Photochromic compounds that undergo a reversible transformation between two isomers having different absorption spectra upon photoirradiation have attracted much attention because various physicochemical properties, such as conductivity, fluorescence, and magnetism, can be modulated without any direct physical contact. Diarylethene is one of the most promising molecules exhibiting the excellent performance, with high thermal stabilities, high photocyclization quantum yields, and high fatigue-resistant properties compared to other photochromic compounds [1]. In addition, diarylethenes can undergo the photochromic reaction even in the solid states, such as polymer films and the crystalline phase. The reversible changes in the various physicochemical properties accompanying with the photochromic reaction of diarylethenes can be applied to optical memory media, various photoswitching devices, light-driven actuators, and so on.

S. Kobatake (✉) · T. Nakahama
Graduate School of Engineering, Osaka City University, 3-3-138 Sugimoto, Sumiyoshi-ku, Osaka 558-8585, Japan
e-mail: kobatake@a-chem.eng.osaka-cu.ac.jp

M. Sakamoto and H. Uekusa (eds.), *Advances in Organic Crystal Chemistry*,
https://doi.org/10.1007/978-981-15-5085-0_15

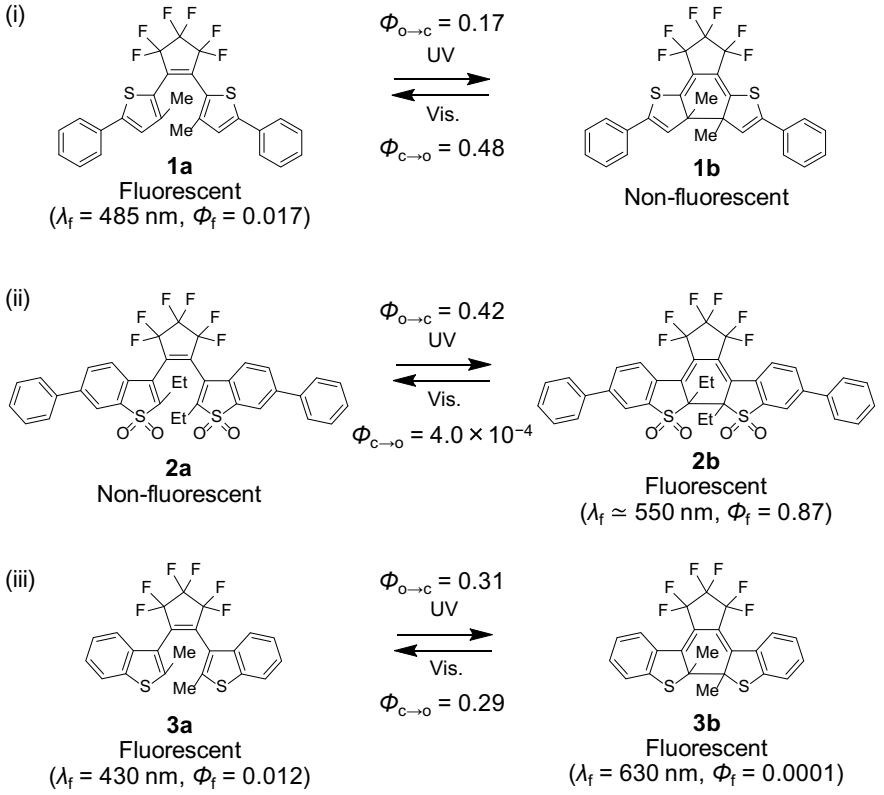

Fig. 15.1 Typical examples of diarylethenes exhibiting fluorescence (i) in the open-ring isomer, (ii) in the closed-ring isomer, and (iii) in both open- and closed-ring isomers

Some diarylethenes exhibit fluorescence in the open-ring form and/or the closed-ring form. As shown in Fig. 15.1, the fluorescent diarylethenes are classified into three types: diarylethenes exhibiting fluorescence (i) in their open-ring isomers (turn-off mode) [2–14], (ii) in their closed-ring isomers (turn-on mode) [15–20], and (iii) in both open- and closed-ring isomers [21–29]. Their fluorescence intensities or spectra change upon alternating irradiation with ultraviolet (UV) and visible light because the fluorescence properties between their open- and closed-ring forms are significantly different. In most cases, the fluorescent diarylethenes have quite low fluorescence quantum yield (Φ_f). It is not easy to design the fluorescent diarylethene with high Φ_f in addition to the high reactivities in photocyclization and photocycloreversion. To overcome this point, molecular systems combining diarylethenes and fluorophores by chemical bonding or mixing were proposed. In the systems, the fluorescence on/off switching accompanying with the photochromic reaction was accomplished. When diarylethene is in the open-ring form, the fluorophore exhibits fluorescence. On the other hand, when diarylethene is converted to the closed-ring form, the fluorescence is quenched. The processes are based on an energy transfer or intramolecular electron

transfer as described later. The fluorescence photoswitchable materials are one of the most promising systems for ultra-high density optical memories and display devices because the fluorescence signal can be detected even at a single-molecule level and the change can be visually observed by naked-eye.

Although various types of the fluorescent photoswitchable systems based on the photochromism of the diarylethene derivatives have been reported so far, most of the researchers have focused on their fluorescence switching behaviors only in solution. However, it is important to evaluate the fluorescence switching properties not only in the solution but also in the solid state for practical applications such as optical memories and display devices. Here, we have focused on the solid-state fluorescence photoswitching behavior using the diarylethenes and reviewed the progress and the development in this chapter. The researches on the fluorescence switching in solution are not described in detail here because many other excellent reviews reported previously will cover the results reported so far [1, 30–34].

15.2 Ultra-High Density Optical Memory

15.2.1 Fluorescence Photoswitching at a Single-Molecule Level

One of the advantages for fluorescence among various physicochemical properties is that the signal can be detected even at the single-molecule level. If a single molecule of diarylethene would work as one-bit memory, ultra-high density optical memory (1 Pbit/inch^2) could be realized. In this part, various researches for the ultra-high density optical memory are presented.

Irie and coworkers made an effort to realize the ultra-high density optical memory based on a photochromic reaction of the diarylethenes. First, they have tried to observe the fluorescence photoswitching at the single-molecule level using a diarylethene–fluorophore dyad **4a** that connects a fluorescent anthracene derivative to a photochromic diarylethene via a rigid adamantyl spacer (Fig. 15.2a) [35, 36]. The fluorescence intensity of **4a** reversibly changed upon irradiation with UV and visible light in toluene. When diarylethene is in the open-ring form, the fluorophore exhibits fluorescence. On the other hand, when diarylethene is converted to the closed-ring form, the fluorescence is quenched because of an energy transfer from the excited-state fluorophore to the diarylethene closed-ring form (Fig. 15.2b). The fluorescence photoswitching behavior at the single-molecule level was investigated using confocal microscopy in a Zeonex polymer film doped with the closed-ring form **4b**. Initially, the polymer film was non-fluorescent. Upon irradiation with visible light, the four fluorescent signals of **4a** could be detected as shown in Fig. 15.2c. The signals disappeared by irradiation with UV light. After that, the visible light irradiation recovered the fluorescence signals. Therefore, they accomplished that the fluorescence photoswitching can be controlled by alternating irradiation with UV and visible light at the

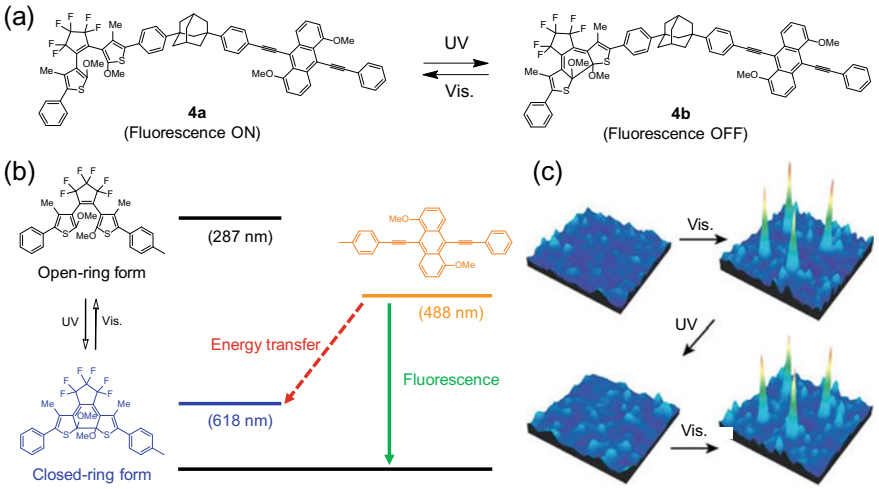

Fig. 15.2 **a** Molecular structure and **b** schematic illustration of fluorescence photoswitching by an energy transfer of diarylethene–fluorophore dyad **4a**, and **c** images of the single-molecular fluorescence photoswitching of four-individual diarylethenes. Reprinted by permission from Ref. [35]. Copyright 2002 Springer Nature

single-molecule level and provided the molecular design for the ultra-high density optical data storage.

However, the anthracene derivative as used above was decomposed after a few cycles of the fluorescence photoswitching. To realize the ultra-high density optical memory, the excellent fatigue resistance of the fluorophore is required. Here, the fluorophore moiety was replaced from the anthracene derivative to the perylenebisimide derivative having high photochemical stability, high Φ_f, and large molar extinction coefficient. The improved diarylethene–fluorophore dyad **5a** (Fig. 15.3a) exhibited the fluorescence photoswitching behavior even in the polymer film as well as **4a**. Dyad **5a** exhibited excellent photostability compared with **4a**. It was estimated that the photochromic performance of **5a** was kept after being excited around 10^6 times [37].

As a result of the improvement of the durability, a unique environmental effect on the photochromic reaction of dyads **5a** and **6a** at the single-molecule level was found [38]. Figure 15.3b–e shows on and off histograms observed for a single molecule **5a** in two kinds of polymer films. The histogram has an exponential shape in poly(*n*-butyl methacrylate) (PnBMA) with a low glass transition temperature (T_g) near room temperature, which indicates that the photocyclization/cycloreversion quantum yields are constant. On the other hand, the histograms of the exponential shape were not observed when T_g of the polymer is higher than room temperature like poly(methyl methacrylate) (PMMA). The result suggests that the quantum yields of the photochromic reaction are not constant and increase with an increase in the

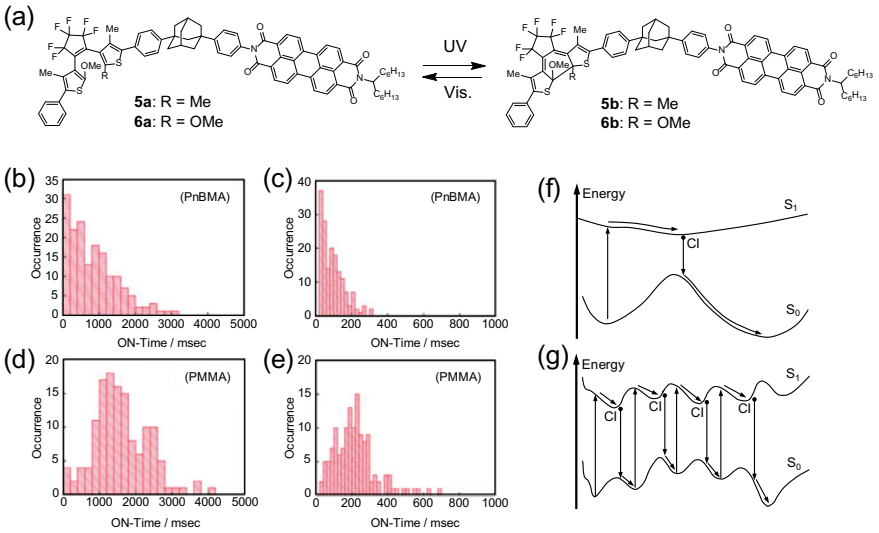

Fig. 15.3 **a** Molecular structures of diarylethene–fluorophore dyads **5a** and **6a**, **b–e** histograms of (**b**, **d**) on-time and (**c**, **e**) off-time in PnBMA (**b**, **c**) and PMMA (**d**, **e**) containing **5**, and (**f**, **g**) a schematic diagram of the potential energy surfaces of a diarylethene **f** in the gas phase and **g** in the polymer matrix. The histograms were constructed from the time trace of fluorescence intensity of **5** in the polymer matrixes irradiated with both 488 and 325 nm light. Reprinted with the permission from Ref. [38]. Copyright 2007 American Chemical Society

number of absorbed photons. The abnormal histograms can be explained by a multi-local minima model (Fig. 15.3f, g). The diarylethene molecule simply undergoes the photochromic reaction in the soft environment with low T_g. The rigid matrix with high T_g provides multilocal potential surfaces in the ground and excited states, which prevent the one-step photochromic reaction and require multistep photoexcitations to reach the final reaction process. The rigid matrix with high T_g leads to unique photochromic reaction behavior. However, it may complicate the fluorescence photoswitching behavior at the single-molecule level. The result revealed the importance of selecting a suitable matrix around the molecules to realize the ultra-high-density optical memory.

15.2.2 Fluorescence Photoswitching in Film Loaded with a Large Amount of Molecules

The fluorescence photoswitching at a single-molecule level in the previous part has shown the feasibility of ultra-high density optical memory. The photoswitching was performed in the polymer films loaded with a very small amount of the molecules. To realize the ultra-high density optical memory, it is necessary to demonstrate the

fluorescence photoswitching in the solid states loaded with a large amount of the molecules. However, most of the organic fluorophores become non- or very weak fluorescent with increasing concentration of the fluorophores due to concentration quenching, which is a serious problem for the application. To overcome this problem, Park and coworkers proposed to use cyanostilbene derivative as the fluorophore moiety [39]. Cyanostilbene is one of the molecules exhibiting aggregation-induced emission (AIE) [40–42]. The molecules having AIE characteristics exhibit weak or no emission in dilute solution but exhibit strong emission in the aggregated state. A diarylethene derivative bearing the cyanostilbene moiety (**7a**) (Fig. 15.4) also exhibited strong fluorescence with increasing concentration. The Φ_f values for **7a** increased from 0.00002 in dilute solution to 0.051 in nanoparticles fabricated by a reprecipitation method. The increased Φ_f value is due to the formation of J-aggregate. The fluorescence intensity of **7a** in the nanoparticles decreased accompanying with photocyclization of the diarylethene and almost quenched at the photostationary state (PSS) (fluorescence on/off contrast > 10). On the other hand, the photocyclization conversion at PSS was 35%, which suggests that the fluorescence photoswitching of the nanoparticles was affected by not only intramolecular energy transfer but also intermolecular energy transfer. The strong fluorescence intensity at on state and the reversible fluorescence photoswitching with high on/off contrast (>19) were observed even in the polymer film loaded with a large amount of **7a** (20 wt%).

Métivier, Nakatani, and coworkers have investigated the amplification effect of the fluorescence switching in polymer films doped with a diarylethene derivative and a BODIPY derivative that is one of the typical organic fluorophores [43]. They prepared two polymer films with different concentrations of the fluorophore, **PF-1** and **PF-2**. The concentration of the fluorophore in **PF-2** is 10 times higher than that in **PF-1**. Single molecules of the diarylethene closed-ring form could quench eight fluorophore molecules in **PF-2** and two fluorophore molecules in **PF-1**. The amplification effect of fluorescence quenching by the intermolecular energy transfer from the multiple fluorophores to the single diarylethene closed-ring form in polymers and nanoparticles was also investigated [44–46]. Thus, the increase of the

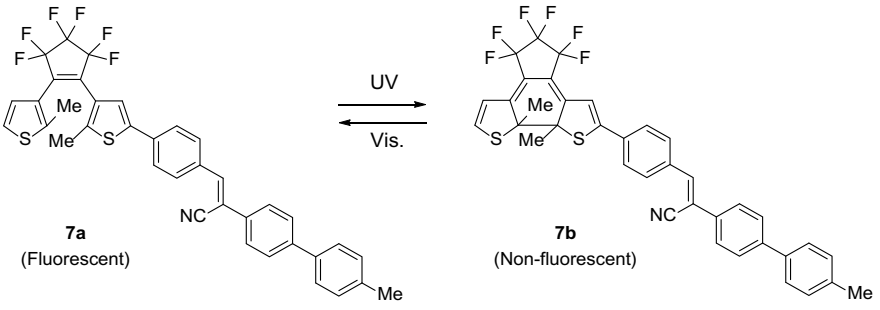

Fig. 15.4 Molecular structure of fluorescent photoswitchable diarylethene **7a**

concentration of the diarylethenes and the fluorophores results in more efficient fluorescence photoswitching when strong fluorescence of the fluorophore is observed even in high concentrations. However, a further increase in the number of doped molecules to the polymer film may cause problems such as a phase separation. Herein, a polymer bearing diarylethene and cyanostilbene moieties in the main chain were prepared and the fluorescence photoswitching behavior was investigated [47]. The neat polymer film exhibited strong fluorescence and the reversible fluorescence photoswitching with high on/off contrast (>10).

To achieve the high fluorescence on/off contrast and to suppress the undesired photoreaction on the readout, the absorption spectrum of the fluorophore is required to be separated from absorption peaks of both isomers of the diarylethene. A large overlap between the fluorescence spectrum of the fluorophore and the absorption spectrum of the diarylethene closed-ring form is also required. Park and coworkers succeeded in solving these points using a fluorophore (**DHBO**) that undergoes excited-state intramolecular proton transfer (ESIPT). As shown in Fig. 15.5a, **DHBO** enol form isomerizes to keto form through ESIPT process. As a result, **DHBO** keto form exhibited large Stokes-shifted fluorescence. Moreover, **DHBO** exhibits stronger fluorescence in the solid state ($\Phi_f = 0.1$) in comparison with that in chloroform

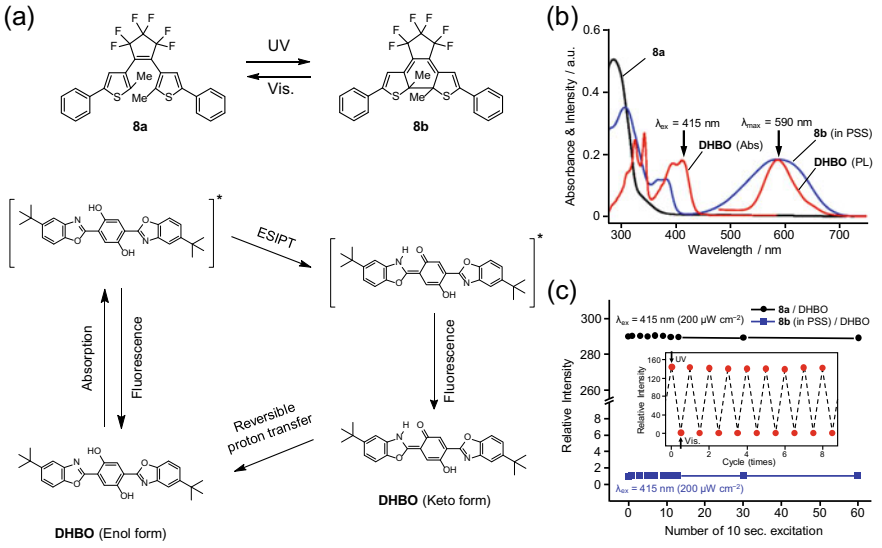

Fig. 15.5 **a** Molecular structures of **8a** and **DHBO**, and four-level excited-state intramolecular proton transfer (ESIPT) process of **DHBO**. **b** Absorption spectra of PMMA film loaded with **8a** in the open-ring form (black line) and in the PSS upon irradiation at 365 nm (blue line) and absorption and fluorescence spectra of PMMA film loaded with **DHBO** (red lines). **c** Non-destructive readout capabilities of **8a/DHBO**-loaded PMMA film in the open-form state (black lines, $\lambda_{ex} = 415$ nm, 200 μW cm^{-2}) and in the PSS upon irradiation at 365 nm (blue lines, $\lambda_{ex} = 415$ nm, 200 μW cm^{-2}). Inset shows the fluorescence photoswitching of the ESIPT fluorescence in **8a/DHBO**-loaded PMMA film. Reprinted with the permission from Ref. [48]. Copyright 2006 American Chemical Society

($\Phi_f = 0.02$). A pair of diarylethene **8a** and **DHBO** satisfies the essential spectral points for the efficient fluorescence switching (Fig. 15.5b). High on/off contrast fluorescence switching (fluorescence on/off contrast > 290), non-destructive readout, and the reversibility were accomplished as shown in Fig. 15.5c [48].

15.2.3 Three-Dimensional Fluorescence Recording

Previous studies have dealt with ultra-high-density optical memory in two-dimensional planes. If three-dimensional (3D) reading becomes possible, the capacity of the recording medium will be dramatically improved. Irie and coworkers demonstrated 3D erasable optical recording in a single crystal of a fluorescent diarylethene, 1,2-bis(3-methyl-2-thienyl)perfluorocyclopentene (**9a**) [2]. Figure 15.6a–h shows eight confocal laser scanning microscopic images of the recorded spots in the single crystal of **9a**. Diarylethene **9a** shows reversible turn-off mode fluorescence photoswitching even in the single crystal using an Ar ion laser (336–363 nm) and an Ar-Kr ion laser (488 nm). The recorded spots were detected as dark spots, and the size was approximately 200 nm in plane and 1.5 μm

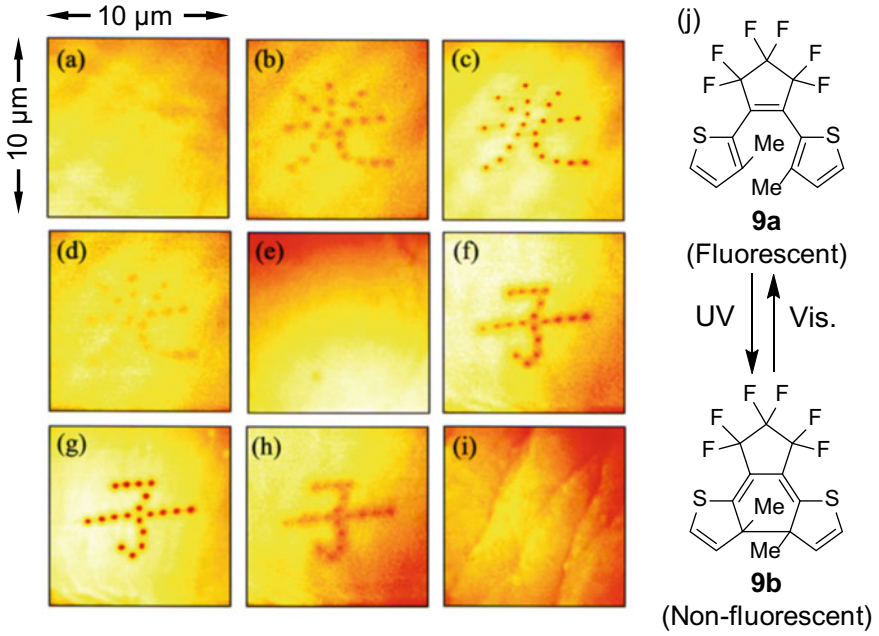

Fig. 15.6 **a–h** Sequence of eight confocal laser scanning microscopic images of the recorded spots in a single crystal of **9a**: image interval = 0.4 μm, **i** reflection mode confocal image of the crystal surface with 538 nm light, and **j** the molecular structure of diarylethene **9a**. Reprinted with the permission from Ref. [2]. Copyright © 2001 The Japan Academy

in depth, which corresponds to the recording density higher than 5 Tbit/cm^3. On the other hand, Belfield and coworkers accomplished 3D two-photon recording and two-photon fluorescence readout using polymer film containing a diarylethene and a fluorene derivative [49, 50]. Two layers separated by 50 μm in depth direction were written in the polymer film by two-photon absorption of 800 nm light. The fluorescence of the fluorene derivative was monitored for the readout.

15.2.4 Non-destructive Readout by Intramolecular Electron Transfer

The fluorescence quenching process as described above is based on the energy transfer from the excited fluorophore to the diarylethene closed-ring form or the photochromic reaction of the fluorescent diarylethene itself. However, such a readout process destroys the recording simultaneously with readout in the optical memory. Although the influence was minimized using very weak light for the readout and adopting the diarylethene derivatives with a quite low photocycloreversion quantum yield, they cannot lead to an essential solution. Here, the intramolecular electron transfer (IET) process was adopted to accomplish the complete non-destructive readout for the ultra-high density optical memory. The reduction and/or oxidation potential of the diarylethene can be altered upon the photochromic reaction. The changes in the redox potentials of the diarylethene activate or deactivate the pathways of the IET process between the diarylethene and fluorophore to the charge separation state. The radiative process of the excited fluorophore can be suppressed when the IET process occurs. The IET process makes it possible to separate the absorption spectra of both open- and closed-ring forms of the diarylethene and the fluorescence spectrum of the fluorophore. Several researchers have tried to design and synthesize various types of diarylethene–fluorophore dyads to achieve non-destructive readout in fluorescence photoswitching based on the IET process [51–55].

In 2011, Fukaminato and coworkers successfully demonstrated non-destructive fluorescence readout of a diarylethene–fluorophore dyad **10a** (Fig. 15.7a) in solution and at the single-molecule level based on the IET mechanism [56]. As shown in Fig. 15.7b, the fluorescence spectrum of the perylenebisimide derivative as the fluorophore moiety and the absorption spectra of the open- and closed-ring forms of the diarylethene moiety were completely separated. In addition, energy gaps for the charge separation in dichloromethane were calculated to be 1.23 and −8.55 kcal/mol for **10a** and **10b** by Rehm–Weller equation. It indicates that it is probable that the IET process takes place only for **10b** in the solution. As shown in Fig. 15.7c, only the Φ_f of the closed-ring form decreases with increasing the dielectric constant of the solvent. As predicted from this result, the fluorescence of dyad **10** can be reversibly switched by alternating irradiation with UV and visible light in polar solvents. In addition, the fluorescence intensities of the open- and closed-ring forms did not change even when irradiated with 532 nm light (2.5 mW/cm^2) for 2 h (Fig. 15.7d). These results

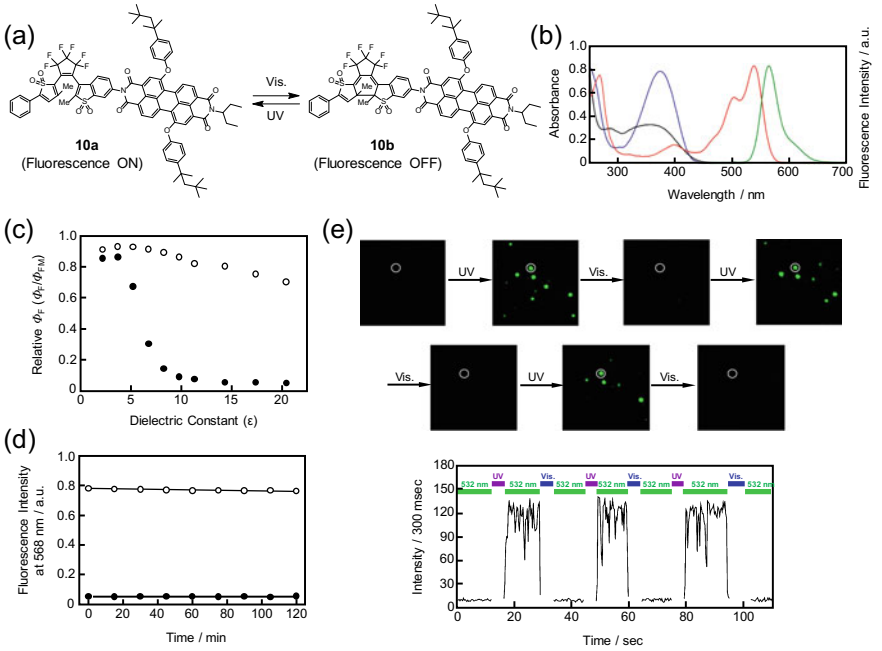

Fig. 15.7 **a** Molecular structure of the diarylethene–fluorophore dyad **10a**, **b** absorption and fluorescence spectra of each component of **10** in 1,4-dioxane: absorption spectra of the open-ring form and closed-ring form of the diarylethene moiety, and absorption and fluorescence spectra of the fluorophore moiety, **c** relative fluorescence quantum yields versus the dielectric constant for **10a** (open circle) and **10b** (closed circle), **d** change of fluorescence intensities at 568 nm under excitation at 532 nm of **10a** (open circle) and **10b** (closed circle) against irradiation time, and **e** single-molecule fluorescence photoswitching in a poly(methyl acrylate) (PMA) film containing **10b**: sequential wide-field fluorescence images of **10** embedded in the PMA film (upper) and the corresponding fluorescence intensity trajectory of a single molecule of **10**, represented as a white circle in the upper images. Reprinted with the permission from Ref. [56]. Copyright 2011 American Chemical Society

suggest that non-destructive fluorescence readout can be realized using dyad **10a**. They have investigated the fluorescence photoswitching and non-destructive fluorescence readout at the single-molecule level. Poly(methyl acrylate) (PMA), which was selected as a polar and soft polymer, loaded with **10b** was prepared. As shown in Fig. 15.7e, a non-destructive fluorescence readout based on the IET mechanism was successfully demonstrated even at the single-molecule level. To summarize the results so far, various attempts on the fluorescence photoswitching using the diarylethenes have been proposed and demonstrated. Their results will advance the realization of the ultra-high density optical memory.

15.3 Display Materials

15.3.1 Fluorescence Photomodulation Between Dual Colors

In the previous part, we reviewed various researches on the fluorescence on/off photoswitching in the solid states for the ultra-high density optical memory. On the other hand, multicolor fluorescent photomodulation materials that exhibit multiple distinguishable fluorescence signals are especially attractive due to their potential applications in flexible full-color displays and in next-generation lighting sources.

In 2012, efficient photoresponsive fluorescence color tuning has been demonstrated by combining two kinds of cyanostilbene derivatives having AIE characteristics, **CN-MBE** and **TPA-2CNMBE**, and diarylethene **8a** (Fig. 15.8a) [57]. A polymer (PMMA) film containing these three molecules was prepared. **CN-MBE** and **TPA-CNMBE** exhibited the violet-blue and orange-red fluorescence in PMMA film, respectively. When **8** was in the open-ring form, the orange-red fluorescence was observed because of the partial energy transfer from **CN-MBE** to **TPA-2CNMBE**. On the other hand, the fluorescence color significantly changed to violet-blue via white when **8a** was converted to **8b**. The result can be explained by the difference in

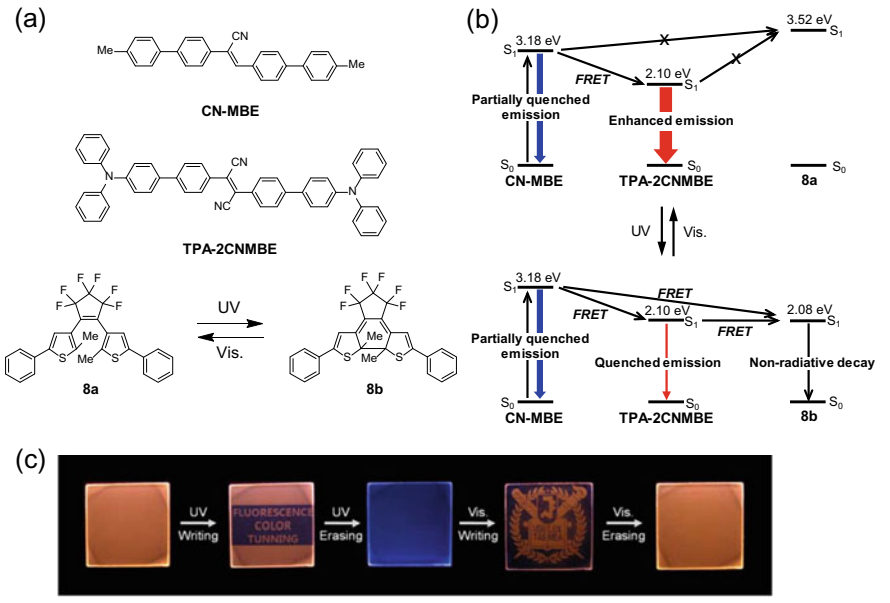

Fig. 15.8 **a** Molecular structures of **CN-MBE**, **TPA-2CNMBE**, and **8a**, **b** schematic illustration of the proposed FRET processes among **CN-MBE**, **TPA-2CNMBE**, and **8** after UV and visible light irradiation, and **c** photoresponsive reversible fluorescence images of a **CN-MBE/TPA-2CNMBE/8**-doped polymer film system. Reprinted with the permission from Ref. [57]. Copyright 2012 American Chemical Society

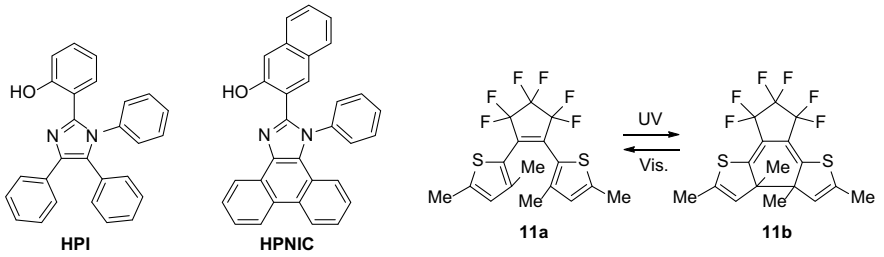

Fig. 15.9 Molecular structures of HPI, HPNIC, and **11a**

the energy transfer efficiency from two kinds of the fluorophores to **8b**. Figure 15.8b shows the energy level of **CN-MBE**, **TPA-2CNMBE**, and **8a/8b** calculated by time-dependent density functional theory (TD-DFT). The orange-red fluorescence of **TPA-2CNMBE** was largely quenched by **8b** in comparison with that of **CN-BME** because the energy level of **8b** was closer to that of **TPA-2CNMBE** than that of **CN-MBE**. Based on such a mechanism, the photoresponsive fluorescence color tuning between orange-red and violet-blue colors was achieved as shown in Fig. 15.8c.

However, this fluorescence color photomodulation involves a significant decrease of intensity on the overall fluorescence spectrum. To realize ideal color-specific photoswitching between multiple fluorescence colors, it is needed that fluorescence of one fluorophore can be selectively switched upon the photochromic reaction while other fluorophores are not affected by light irradiation. In addition, the energy transfer from one fluorophore to the others must be prohibited. The problems were solved using two types of ESIPT fluorophores: (2-(1,4,5-triphenyl-1H-imidazol-2-yl)phenol (**HPI**) and 3-(1-phenyl-1H-phenanthro[9,10-d]imidazol-2-yl)naphthalene-2-ol (**HPNIC**) (Fig. 15.9) [58]. The large Stokes-shifted fluorescence of **HPI** and **HPNIC** was observed because of the ESIPT process from enol form to keto form. The fluorescence maximum wavelength (λ_f) of **HPI** and **HPNIC** was 462 and 590 nm, respectively, while they have similar absorption maximum wavelength (λ_{abs}) (at 318 nm and 365 nm for **HPI** and **HPNIC**, respectively). Thus, there is almost no overlap between the absorption spectrum of **HPNIC** and the fluorescence spectrum of **HPI**, meaning that the energy transfer from excited **HPI** to **HPNIC** is negligible. As expected, a polymer film containing **HPI** and **HPNIC** (**HPI**:**HPNIC** = 1 wt%:1wt%) exhibited a dual peak fluorescence spectrum, which is almost the same as the fluorescence spectrum calculated by the simple addition of **HPI** and **HPNIC**. A diarylethene derivative, 1,2-bis(3,5-dimethyl-2-thienyl)perfluorocyclopentene (**11a**), whose color changes from colorless to yellow upon irradiation with UV light, was selected as the photochromic compound. The blue ESIPT fluorescence of **HPI** can be selectively switched by the photochromic reaction of **11a** because the absorption spectrum of **11b** overlaps with only the fluorescence spectrum of **HPI**. Three-component polymer film containing **HPI**, **HPNIC**, and **11a** shows white fluorescence at the initial state. Upon irradiation with UV light, the white fluorescence color was modulated to the orange by the selective quench of

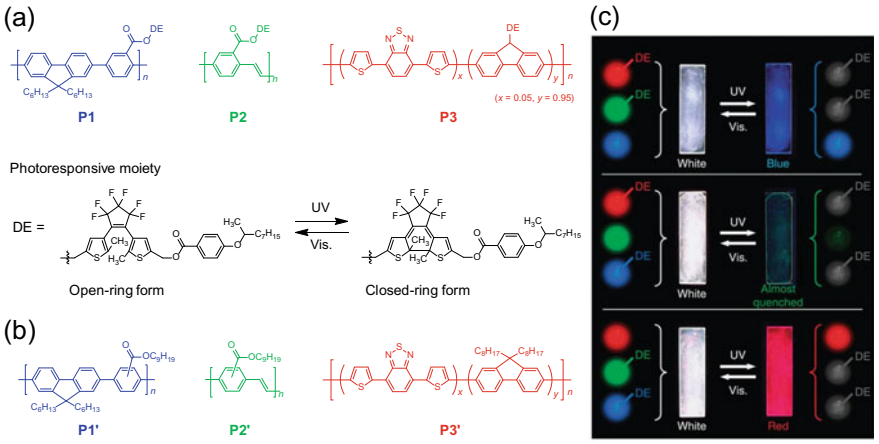

Fig. 15.10 (**a**, **b**) Chemical structures of **a** fluorescent photoswitchable polymers **P1**, **P2**, and **P3**, **b** fluorescent polymers (**P1′**, **P2′**, and **P3′**), and **c** photographs of fluorescent photoswitching between white and RGB in the mixture nanoparticle cast films: **P1′** + **P2** + **P3**, **P1** + **P2′** + **P3**, and **P1** + **P2** + **P3′** are the white-to-blue system, white-to-green system, and white-to-red system, respectively. Reprinted by permission from Ref. [59]. copyright 2014 Springer Nature

the blue fluorescence of **HPI**. The fluorescence color returned to white upon irradiation with visible light. Therefore, color-specific photoswitching between white and orange fluorescence colors was successfully demonstrated.

On the other hand, Akagi and coworkers reported another approach to construct the multicolor fluorescent photomodulation system [59]. Their concept is to mix several kinds of nanoparticles consisting of the fluorescent photoswitchable polymers. They synthesized the fluorescent photoswitchable aromatic conjugated polymers (**P1**, **P2**, and **P3**) having a diarylethene moiety at the side chains and the fluorescent aromatic conjugated polymers (**P1′**, **P2′**, and **P3′**), as shown in Fig. 15.10a, b. The nanoparticles consisting of the polymers fabricated by a reprecipitation method exhibited the blue (for **P1** and **P1′**), green (for **P2** and **P2′**), or red fluorescence (for **P3** and **P3′**) in water, respectively. The fluorescence of the nanoparticles consisting of **P1**, **P2**, or **P3** was quenched upon irradiation with UV light, and almost completely quenched at PSS (Fluorescence on/off contrast = 473.2, 850.7, and 98.9 for **P1**, **P2**, and **P3**). The high on/off contrast is ascribed to the large contribution of intermolecular energy transfer in the nanoparticles. A white fluorescence photoswitchable film was obtained by casting the solution mixing the three kinds of the nanoparticle solution at a molar ratio. The white fluorescence can be switched between the fluorescent and quenched states upon alternating irradiation with UV and visible light. In addition, the three components cast films containing two polymer nanoparticles having a diarylethene moiety and the other polymer nanoparticle without a diarylethene were fabricated. In these films, the energy transfer between individual nanoparticles was prohibited due to a long distance between the nanoparticles. Therefore, as shown in Fig. 15.10c, only two fluorescence colors were quenched upon irradiation with UV light, while

the other fluorescence was not altered. As a result, the color of the cast films was converted from white to blue, white to green, and white to red, respectively.

15.3.2 *Photo-Patternable Electroluminescence on Organic Light-Emitting Diode*

The rational designs of the fluorescent photoswitchable system enable not only the single fluorescence color on/off switching but also the fluorescence modulation between dual colors. Such materials have attracted much attention for the practical application such as organic light-emitting diodes (OLEDs), which are promising devices in flat-panel displays and in smart illumination technologies. The fabrication process of full-color OLED display consisting of RGB-emissive dyes is complicated and costly for fabricating large-area displays because the display must be selectively deposited precisely onto the substrates. Kawai and coworkers proposed the photo-patternable electroluminescence on OLEDs using diarylethene **12a** (Fig. 15.11a) [60]. The open-ring isomer **12a** is non-fluorescent, while the closed-ring isomer **12b** exhibits the orange fluorescence in the amorphous film. The photochromic reaction

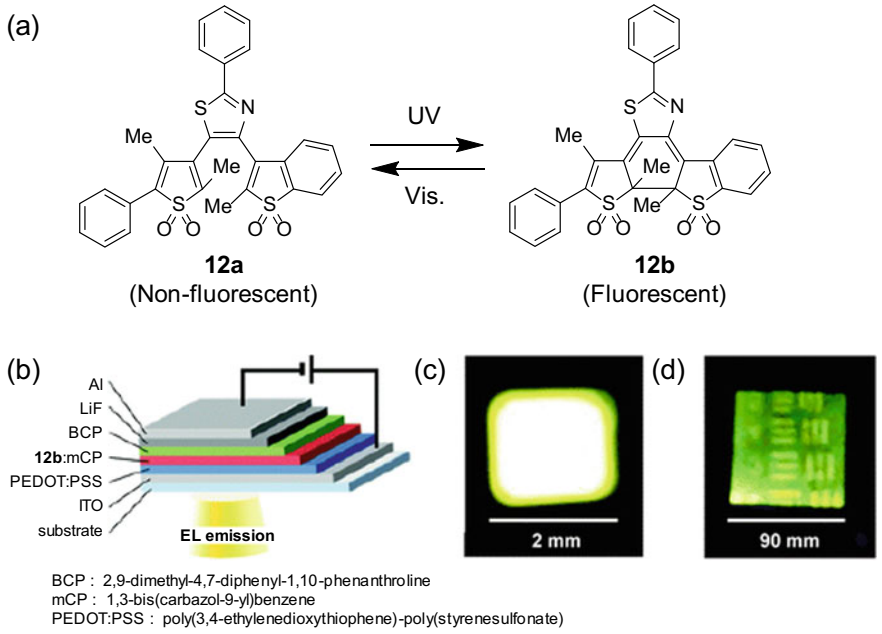

Fig. 15.11 **a** Molecular structure of diarylethene **12a**, **b** structure of bottom-emission type OLEDs using compound **12b** as a dopant on an emitting layer in the wet process, and (**c**, **d**) photographs of **c** yellow EL from the device and **d** patterned EL from the device. Reproduced from Ref. [60] by permission of The Royal Society of Chemistry

upon irradiation with UV and visible light can be undergone even in the amorphous film; thus, the amorphous film **12a** behaved as photo-patternable luminescence turn-on material. They fabricated a multilayer bottom-emission type OLED using **12b** as an emissive dopant in the emitting layer, as shown in Fig. 15.11b. The fabricated device with **12b** exhibited the yellow electroluminescence with an external quantum efficiency of 0.20% (Fig. 15.11c). In addition, patterned visible light irradiation on the device is area-selectively isomerized **12b** to **12a**, which results in the clear electroluminescence patterning as shown in Fig. 15.11d. The result shows the possibility of direct photo-patterning fabrication of full-color OLEDs using the fluorescent switchable system by the diarylethenes.

15.4 Crystalline State Fluorescence Behavior of Diarylethenes

15.4.1 High Contrast Fluorescence Photoswitching in Crystal

Crystals can be promising for the development of further efficient fluorescent photoswitchable materials because the molecules are regularly and very densely aggregated in the crystal. In this part, we introduce two topics, crystalline state turn-off and turn-on mode fluorescence photoswitching with high contrast and characteristics fluorescence behavior of inverse-type diarylethene in solid states.

As described above, 1,2-bis(3-methyl-2-thienyl)perfluorocyclopentene (**9a**) exhibits turn-off mode fluorescence switching accompanying with the photochromic reaction even in the single crystal (Fig. 15.6). However, the fluorescence on/off contrast is not high due to the low photoconversion yield in the single crystalline state. Fukaminato et al. designed a diarylethene derivative linked to the benzothiadiazole derivative (**13a**) (Fig. 15.12a) to obtain fluorescent diarylethene with efficient turn-off mode fluorescence photoswitching properties in the single crystal [61]. Each performance of the diarylethene and the fluorophore moieties in dyad **13a** can be carried out at a high level because they were separated by an ether bond. Initially, the single crystal of **13a** exhibited strong green fluorescence. Upon irradiation with area-selective UV light, the fluorescence intensity of the crystal was down to the background level. As shown in Fig. 15.12b, the size of the dark area gradually decreased toward the center with the recovery of the fluorescence upon irradiation with visible light. On the other hand, the fluorescence signal of quenched area in the PMMA film containing **13a** is uniformly recovered under irradiation with 438 nm light (Fig. 15.12c). The photocyclization conversion becomes high as the position is close to the center because UV light intensity has Gaussian distribution. The difference in the photocyclization conversion can be negligible in the PMMA film due to the small contribution of the intermolecular energy transfer. On the other hand, the

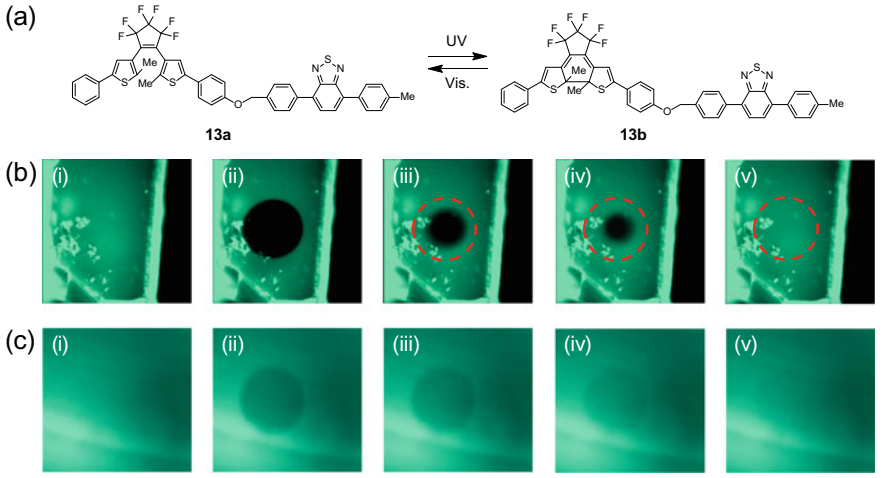

Fig. 15.12 **a** Molecular structure of diarylethene–fluorophore dyad **13a**, **b** fluorescence images under excitation with 438 nm light to the single crystal of **13a**, **c** a PMMA film containing **13a** (4 wt%); (i) before UV irradiation, (ii) after irradiation with 390 nm light, (iii)–(v) fluorescence recovery under excitation with 438 nm light. Reproduced from Ref. [61] by permission of The Royal Society of Chemistry

fluorescence intensity of the single crystal suddenly and largely changes upon irradiation with visible light, which is ascribed to the intermolecular energy transfer from a large number of the fluorophores to the small amount of diarylethene closed-ring forms in the crystal. The amplified intermolecular energy transfer process results in the high fluorescence on/off contrast and the fluorescence recovery behavior upon decreasing the size of the dark area.

On the other hand, Morimoto, Irie, and coworkers demonstrated high contrast fluorescence photoswitching in single crystals of diarylethene derivatives having benzothiophene *S*,*S*-dioxide at the aryl moieties (**14a**, **15a**) (Fig. 15.13) [62]. Diarylethenes **14a** and **15a** exhibit the reversible photochromic reaction and turn-on mode fluorescence photoswitching upon irradiation with UV and visible light in solution and in the single crystal. The single crystals emit no fluorescence when the diarylethenes are in their open-ring isomers. Upon irradiation with UV light, the crystals become fluorescent due to the generation of the fluorescent closed-ring forms. Thus, the single crystals underwent turn-on mode fluorescence photoswitching with high fluorescence on/off contrast.

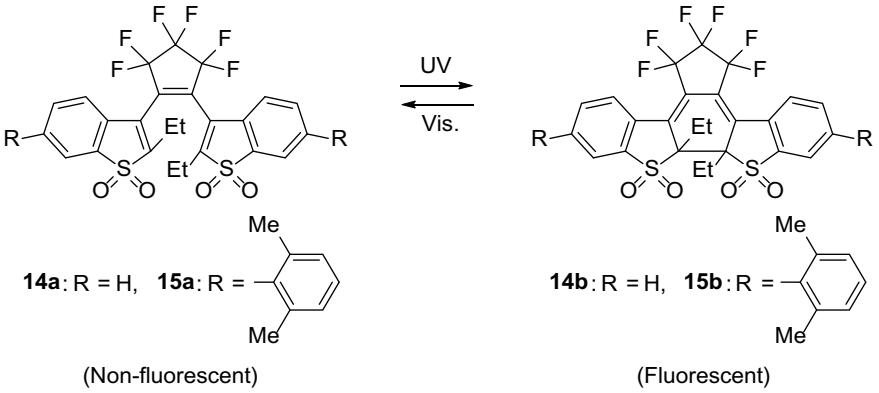

Fig. 15.13 Molecular structures of diarylethenes **14a** and **15a**

Fig. 15.14 Chemical structures of normal and inverse-type diarylethene derivatives

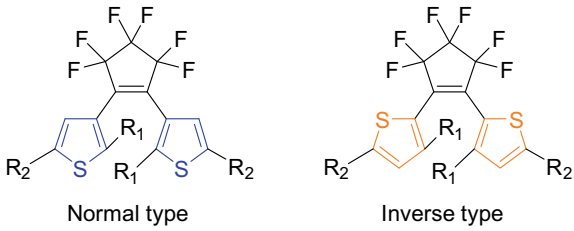

15.4.2 Characteristic Fluorescence Properties of Inverse-Type Diarylethenes in Crystal

Diarylethene derivatives can be categorized into two groups, a normal type and an inverse type, with respect to the orientation of the two aryl rings as shown in Fig. 15.14 [63]. The inverse-type diarylethenes are one of the typical fluorescent diarylethenes and show characteristic fluorescence and photochromic reaction behavior in the solid states. They have slightly red-shifted absorption spectra due to long π-conjugation compared with the normal-type diarylethenes and emit blue fluorescence in their open-ring forms [2, 3, 11–14]. The fluorescence intensity of the open-ring forms decreases upon irradiation with UV light. Upon irradiation with visible light, the fluorescence intensity returns to its initial one. As mentioned above, 1,2-bis(3-methyl-2-thienyl)perfluorocyclopentene (**9a**) exhibits turn-off mode fluorescence switching accompanying with the photochromic reaction even in the single crystal [2]. The fluorescence in the crystal is composed of short-lifetime component ($\lambda_f = 435$ nm, $\tau < 1.0$ ns) and the long lifetime component ($\lambda_f = 495$ nm, 1.0 ns $< \tau <$ 20 ns). Detailed analysis by time-resolved fluorescence measurement, X-ray crystallographic analysis, and polarized fluorescence measurements revealed that the short-lifetime component is ascribed to the monomer, and the aggregate formed by

the intermolecular interaction between two thiophene rings of neighboring molecules in the crystal have a longer lifetime and a longer λ_f compared with the monomer [3].

In 2005, Yu and coworkers found that an inverse-type diarylethene, 1,2-bis(4-methyl-2-(2-pyridyl)thiazolyl)perfluorocyclopentene (**16a**) (Fig. 15.15), exhibited stronger fluorescence around 500 nm ($\Phi_f = 0.20$) in the crystalline state compared with the solution ($\Phi_f = 0.005$) [11]. Diarylethene **16a** exists in the antiparallel conformation in crystal. The distance between the reactive carbons in the crystalline phase was 3.56 Å, which is sufficiently short for the photocyclization to take place in the crystalline phase [64]. However, the crystal did not show any photocyclization. Métivier and Nakatani et al. reported that the nanoparticles consisting of **16a** show the intermediate photocyclization reactivity and the Φ_f compared with the acetonitrile and in the crystal [12]. Based on the result, they assume that the conformational changes that are necessary for the photocyclization may be hindered when the environment around the diarylethene becomes rigid, such as in the crystal. Similar observation has been made for the other inverse-type diarylethene, 1,2-bis(3-methyl-5-phenyl-2-thienyl)perfluorocyclopentene (**1a**) as described in Fig. 15.16a [65]. Two polymorphic crystals of **1a**, crystals **1a-α** and **1a-β**, can be obtained by recrystallization from acetone and *n*-hexane solutions, respectively. Although all the diarylethene molecules in the crystals existed in the antiparallel conformation with the distances between the reactive carbons shorter than 4.2 Å, **1a** cannot undergo the photocyclization in the crystalline phase. However, the photocyclization of the diarylethene having the methyl groups (**11a**) instead of the phenyl groups can be observed even in crystal [66, 67]. On the other hand, the substitution of the methyl group to the methoxy group at the 3-position of thiophene rings (**17a**) also caused loss of the photocyclization reactivity in the crystal [68]. Miyasaka and coworkers revealed that the photocyclization quantum yield of **1a** decreases with an increase in the solvent viscosity in solution [63]. It can be concluded that specific substituents such as the phenyl and methoxy groups on the inverse-type diarylethenes may have some geometric or electronic effect prohibiting the photocyclization as the environment around the molecule becomes rigid although the reason and the mechanism are not clear yet.

In the viewpoint on the solid-state fluorescence properties, the inverse-type diarylethenes having the phenyl groups to R_2 positions have attractive solid-state

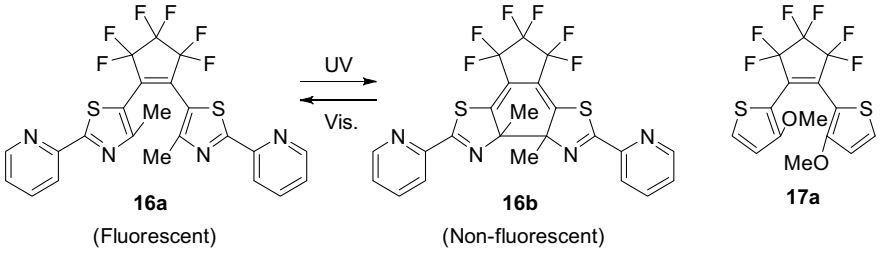

Fig. 15.15 Molecular structures of diarylethenes **16a** and **17a**

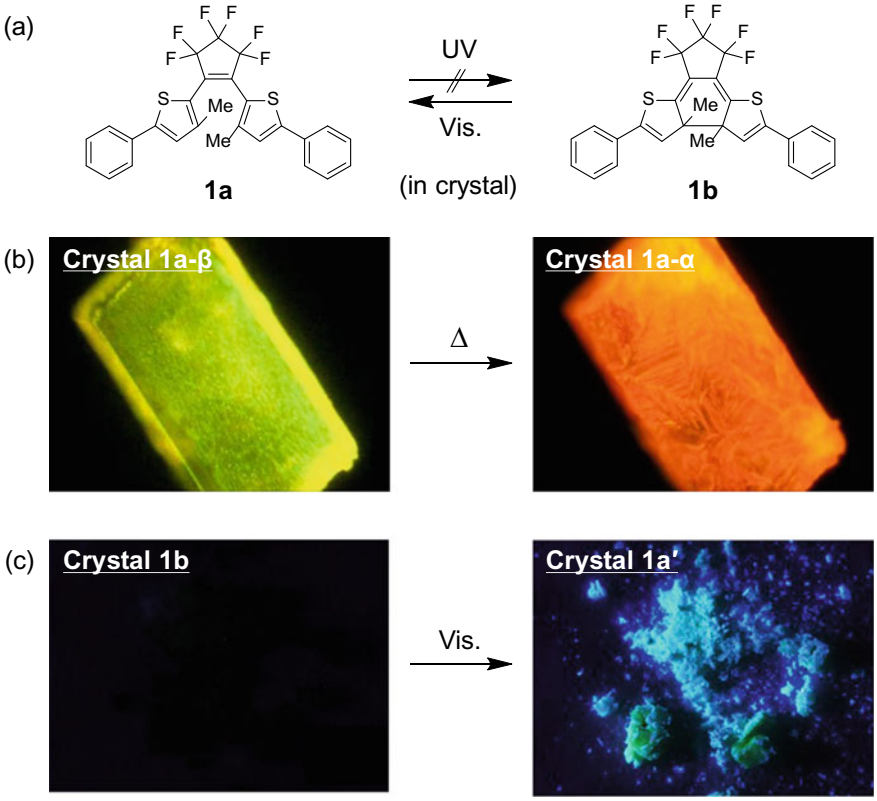

Fig. 15.16 **a** Molecular structure of inverse-type diarylethene **1a**, **b** optical microscopic photographs of crystal **1a-β** before and after heating at 50 °C for 80 min, and **c** optical microscopic photographs of crystal **1b** before and after irradiation with visible light. The photographs were observed under excitation with 365 nm light. Reprinted from Ref. [65]. Copyright 2017, with permission from Elsevier. Reprinted from Ref. [69]. Copyright 2018, with permission from The Chemical Society of Japan

fluorescence properties and can be expected as a new AIE molecular skeleton. As mentioned above, the crystal of **16a** exhibited stronger fluorescence compared with the solution [11, 12]. Additionally, both crystals **1a-α** and **1a-β** exhibited the largely red-shifted and stronger orange and yellow fluorescence ($\Phi_f = 0.52$ and 0.50 for crystals **1a-α** and **1a-β**) compared with the *n*-hexane ($\lambda_f = 480$ nm and $\Phi_f = 0.017$). Furthermore, the polymorphic phase transition from crystal **1a-β** that has one hexane molecule in the unit cell to crystal **1a-α** upon heating was found (Fig. 15.16b). In the phase transition process, the fluorescence color changed from yellow to orange via dark state because the phase transition includes the collapse of the β-crystalline phase accompanying the exclusion of the *n*-hexane molecules and the crystallization of the α-crystalline phase [65]. Crystals consisting of the closed-ring form (crystal **1b**) underwent the photocycloreversion upon irradiation with visible light. As shown

in Fig. 15.16c, the open-ring form crystal (crystal **1a′**) produced by the photocycloreversion exhibited green fluorescence that is a significant difference from those of crystals **1a-α** and **1a-β** [69]. Although the molecular geometry and intermolecular interactions in crystal **1a′** cannot be revealed due to the lack of crystallinity after the photocycloreversion, weaker intermolecular interactions in crystal **1a′** compared with crystals **1a-α** and **1a-β** may lead to the green fluorescence because the orange and yellow fluorescence of crystals **1a-α** and **1a-β** is ascribed to the intermolecular π-π interactions between the phenyl rings. Therefore, the introduction of steric substituents to the phenyl rings may modulate the intermolecular π-π interactions to result in a dramatic change in the solid-state fluorescence properties. As shown in Fig. 15.17a, b, inverse-type diarylethenes **18a-21a** having various alkyl chains at the *p*-position of phenyl rings exhibit the green fluorescence that is a similar color to that of crystal **1a′**. As expected, the molecules in crystals **18a-21a** have no π-π intermolecular interaction and only van der Waals interaction, which indicates that the alkyl chains prevent the formation of the strong π-π interaction between the phenyl rings to result in only slight red-shifted fluorescence [70]. Therefore, the

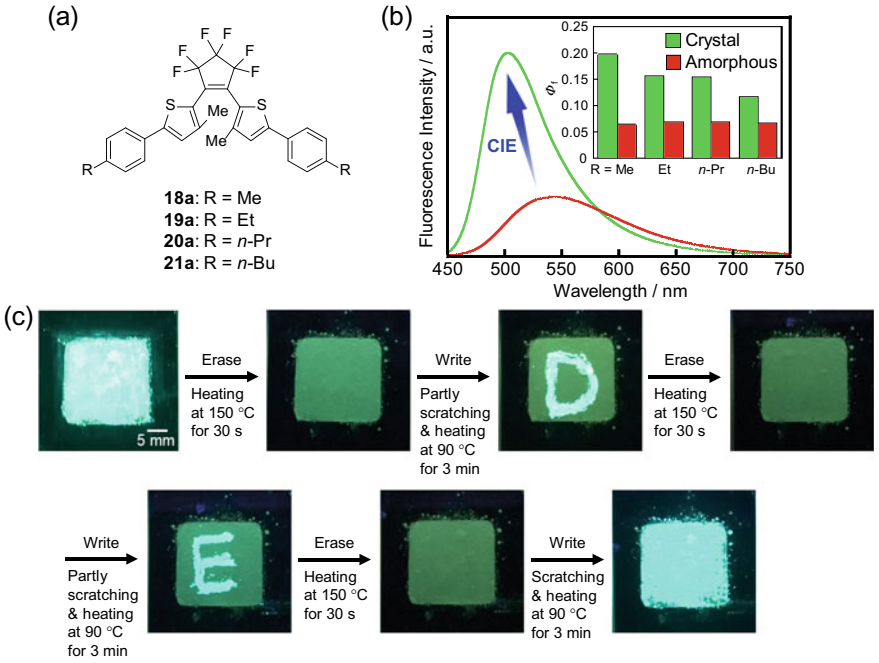

Fig. 15.17 **a** Molecular structures of inverse-type diarylethenes **18a-21a**, **b** fluorescence spectra of **18a** in the crystalline phase (green line) and in the amorphous phase (red line); inset shows the fluorescence quantum yields of **18a-21a** in the crystalline phase and in the amorphous phase, and **c** reversible fluorescence recording of **18a** by partly scratching and heating observed at room temperature upon excitation at 365 nm. Reprinted from Ref. [70]. Copyright 2019, with permission from Elsevier

inverse-type diarylethene **1a** and the derivatives exhibit different fluorescence colors depending on the intermolecular interaction in different states. In addition, **18a-21a** have crystallization-induced emission (CIE) characteristics to exhibit strong fluorescence in the crystalline phase compared in *n*-hexane and in the amorphous phase (Fig. 15.17b). The amorphous solid of **18a** which has the most remarkable CIE characteristics among **18a-21a** was crystallized after mechanical scratching followed by heating at 90 °C because the small crystal nuclei were fabricated by scratching and the growth of the crystal nuclei was performed by heating. As shown in Fig. 15.17c, reversible fluorescence recording based on CIE characteristics and mechanical scratching and heating induced crystallization was successfully demonstrated. By partly scratching and heating at 90 °C for 3 min for the amorphous solid that was prepared by heating the crystals at 150 °C, green fluorescent letters of "D" or "E" were clearly written. The letter was completely erased by heating at 150 °C for 30 s. As introduced up to this point, inverse-type diarylethenes having phenyl groups show unique behavior in the solid states, such as multicolor fluorescence depending on intermolecular interactions and responsiveness for external stimuli such as heat and scratching, which may be useful for potential applications such as in sensors and security materials.

15.5 Summary

In this chapter, we have introduced the solid-state fluorescence switching using diarylethene. The fluorescence switching can be achieved by combining a diarylethene with a fluorophore or using a fluorescent diarylethene in solution. On the other hand, in the solid states, it is difficult to obtain similar properties as in solution due to problems such as concentration quenching and environmental effect of the matrix. However, various types of solid-state fluorescence-switchable systems using the diarylethenes based on rational molecular design and smart experimental approach have been proposed and successfully demonstrated for practical applications, such as optical memory, display devices, and sensor materials. A series of the researches will advance the realization of the applications based on the fluorescence switching of the diarylethene.

References

1. Irie, M., Fukaminato, T., Matsuda, K., Kobatake, S.: Photochromism of diarylethene molecules and crystals: memories, switches, and actuators. Chem. Rev. **114**, 12174–12277 (2014)
2. Fukaminato, T., Kobatake, S., Kawai, T., Irie, M.: Three-dimensional erasable optical memory using a photochromic diarylethene single crystal as the recording medium. Proc. Japan Acad., Ser B **77**, 30–35 (2001)
3. Fukaminato, T., Kawai, T., Kobatake, S., Irie, M.: Fluorescence of photochromic 1,2-bis(3-methyl-2-thienyl)ethene. J. Phys. Chem. B **107**, 8372–8377 (2003)

4. Meng, X.L., Zhu, W.H., Zhang, Q., Feng, Y.L., Tan, W.J., Tian, H.: Novel bisthienylethenes containing naphthalimide as the center ethene bridge: photochromism and solvatochromism for combined nor and inhibit logic gates. J. Phys. Chem. B **112**, 15636–15645 (2008)
5. Zhu, W.H., Meng, X.L., Yang, Y.H., Zhang, Q., Xie, Y.S., Tian, H.: Bisthienylethenes containing a benzothiadiazole unit as a bridge: photochromic performance dependence on substitution position. Chem. Eur. J. **16**, 899–906 (2010)
6. Poon, C.T., Lam, W.H., Wong, H.L., Yam, V.W.W.: A versatile photochromic dithienylethene-containing beta-diketonate ligand: near-infrared photochromic behavior and photoswitchable luminescence properties upon incorporation of a boron(III) center. J. Am. Chem. Soc. **132**, 13992–13993 (2010)
7. Suzuki, K., Ubukata, T., Yokoyama, Y.: Dual-mode fluorescence switching of photochromic bisthiazolylcoumarin. Chem. Commun. **48**, 765–767 (2012)
8. Yagi, K., Irie, M.: Fluorescence property of photochromic diarylethenes with indole groups. Bull. Chem. Soc. Jpn. **76**, 1625–1628 (2003a)
9. Pu, S.Z., Li, H., Liu, G., Liu, W.J., Cui, S.Q., Fan, C.B.: Synthesis and the effects of substitution upon photochromic diarylethenes bearing an isoxazole moiety. Tetrahedron **67**, 1438–1447 (2011)
10. Pu, S.Z., Liu, G., Shen, L., Xu, J.K.: Efficient synthesis and properties of isomeric photochromic diarylethenes having a pyrrole unit. Org. Lett. **9**, 2139–2142 (2007)
11. Giraud, M., Leaustic, A., Charlot, M.F., Yu, P., Cesario, M., Philouze, C., Pansu, R., Nakatani, K., Ishow, E.: Synthesis and photochromism of two new 1,2-bis(thiazolyl)perfluorocyclopentenes with chelating sites. New J. Chem. **29**, 439–446 (2005)
12. Piard, J., Métivier, R., Giraud, M., Léaustic, A., Yu, P., Nakatani, K.: Photoswitching in diarylethene nanoparticles, a trade-off between bulk solid and solution: towards balanced photochromic and fluorescent properties. New J. Chem. **33**, 1420–1426 (2009)
13. Shibata, K., Kuroki, L., Fukaminato, T., Irie, M.: Fluorescence switching of a diarylethene derivative having oxazole rings. Chem. Lett. **37**, 832–833 (2008)
14. Uchida, K., Matsuoka, T., Kobatake, S., Yamaguchi, T., Irie, M.: Substituent effect on the photochromic reactivity of bis(2-thienyl)perfluorocyclopentenes. Tetrahedron **57**, 4559–4565 (2001)
15. Uno, K., Niikura, H., Morimoto, M., Ishibashi, Y., Miyasaka, H., Irie, M.: In situ preparation of highly fluorescent dyes upon photoirradiation. J. Am. Chem. Soc. **133**, 13558–13564 (2011)
16. Irie, M., Morimoto, M.: Photoswitchable turn-on mode fluorescent diarylethenes: strategies for controlling the switching response. Bull. Chem. Soc. Jpn. **91**, 237–250 (2017)
17. Cipolloni, M., Ortica, F., Bougdid, L., Moustrou, C., Mazzucato, U., Favaro, G.: New thermally irreversible and fluorescent photochromic diarylethenes. J. Phys. Chem. A **112**, 4765–4771 (2008)
18. Li, Z.Y., Xia, J.L., Liang, J.H., Yuan, J.J., Jin, G.J., Yin, J., Yu, G.A., Liu, S.H.: Synthesis of diarylethene derivatives containing various heterocycles and tuning of light-emitting properties in a turn-on fluorescent diarylethene system. Dyes Pigm. **90**, 290–296 (2011)
19. Pang, S.C., Hyun, H., Lee, S., Jang, D., Lee, M.J., Kang, S.H., Ahn, K.H.: Photoswitchable fluorescent diarylethene in a turn-on mode for live cell imaging. Chem. Commun. **48**, 3745–3747 (2012)
20. Jeong, Y.C., Park, D.G., Lee, I.S., Yang, S.I., Ahn, K.H.: Highly fluorescent photochromic diarylethene with an excellent fatigue property. J. Mater. Chem. **19**, 97–103 (2009)
21. Nakagawa, T., Miyasaka, Y., Yokoyama, Y.: Photochromism of a spiro-functionalized diarylethene derivative: multi-colour fluorescence modulation with a photon-quantitative photocyclization reactivity. Chem. Commun. **54**, 3207–3210 (2018)
22. Bens, A.T., Ern, J., Kuldova, K., Trommsdorff, H.P., Kryschi, C.: Reaction and excited state relaxation dynamics of photochromic dithienylethene derivatives. J. Lumin. **94**, 51–54 (2001)
23. Jeong, Y.C., Yang, S.I., Kim, E., Ahn, K.H.: Development of highly fluorescent photochromic material with high fatigue resistance. Tetrahedron **62**, 5855–5861 (2006a)
24. Kim, M.S., Kawai, T., Irie, M.: Synthesis of fluorescent amorphous diarylethenes. Chem. Lett., 702–703 (2001)

25. Yagi, K., Irie, M.: Photochromic and fluorescent properties of a diarylethene dimer. Chem. Lett. **32**, 848–849 (2003b)
26. Liu, H.H., Chen, Y.: The photochromism and fluorescence of diarylethenes with a imidazole bridge unit: a strategy for the design of turn-on fluorescent diarylethene system. J. Phys. Chem. A **113**, 5550–5553 (2009)
27. Kasatani, K., Kambe, S., Irie, M.: Photochromic reaction and fluorescence of dithienylethenes in the solid state. J. Photochem. Photobiol. A **122**, 11–15 (1999)
28. Jeong, Y.C., Yang, S.I., Ahn, K.-H., Kim, E.: Highly fluorescent photochromic diarylethene in the closed-ring form. Chem. Commun., 2503–2505 (2005)
29. Jeong, Y.C., Yang, S.I., Kim, E., Ahn, K.H.: A high-content diarylethene photochromic polymer for an efficient fluorescence modulation. Macromol. Rapid Commun. **27**, 1769–1773 (2006b)
30. Irie, M.: Diarylethenes for memories and switches. Chem. Rev. **100**, 1685–1716 (2000)
31. Fukaminato, T.: Single-molecule fluorescence photoswitching: design and synthesis of photoswitchable fluorescent molecules. J. Photochem. Photobiol. C **12**, 177–208 (2011)
32. Fukaminato, T., Ishida, S., Métivier, R.: Photochromic fluorophores at the molecular and nanoparticle levels: fundamentals and applications of diarylethenes. NPG Asia Materials **10**, 859–881 (2018)
33. Kim, D., Park, S.Y.: Multicolor fluorescence photoswitching: color-correlated versus color-specific switching. Adv. Opt. Mater. **6**, 1800678 (2018)
34. Tian, H., Yang, S.J.: Recent progresses on diarylethene based photochromic switches. Chem. Soc. Rev. **33**, 85–97 (2004)
35. Irie, M., Fukaminato, T., Sasaki, T., Tamai, N., Kawai, T.: Organic chemistry: A digital fluorescent molecular photoswitch. Nature **420**, 759–760 (2002)
36. Fukaminato, T., Sasaki, T., Kawai, T., Tamai, N., Irie, M.: Digital photoswitching of fluorescence based on the photochromism of diarylethene derivatives at a single-molecule level. J. Am. Chem. Soc. **126**, 14843–14849 (2004)
37. Fukaminato, T., Umemoto, T., Iwata, Y., Irie, M.: Direct measurement of photochromic durability at the single-molecule level. Chem. Lett. **34**, 676–677 (2005)
38. Fukaminato, T., Umemoto, T., Iwata, Y., Yokojima, S., Yoneyama, M., Nakamura, S., Irie, M.: Photochromxcism of diarylethene single molecules in polymer matrices. J. Am. Chem. Soc. **129**, 5932–5938 (2007)
39. Lim, S.J., An, B.K., Jung, S.D., Chung, M.A., Park, S.Y.: Photoswitchable organic nanoparticles and a polymer film employing multifunctional molecules with enhanced fluorescence emission and bistable photochromism. Angew. Chem. Int. Ed. **43**, 6346–6350 (2004)
40. An, B.K., Kwon, S.K., Jung, S.D., Park, S.Y.: Enhanced emission and its switching in fluorescent organic nanoparticles. J. Am. Chem. Soc. **124**, 14410–14415 (2002)
41. An, B.K., Lee, D.S., Lee, J.S., Park, Y.S., Song, H.S., Park, S.Y.: Strongly fluorescent organogel system comprising fibrillar self-assembly of a trifluoromethyl-based cyanostilbene derivative. J. Am. Chem. Soc. **126**, 10232–10233 (2004)
42. Yoon, S.J., Chung, J.W., Gierschner, J., Kim, K.S., Choi, M.G., Kim, D., Park, S.Y.: Multistimuli two-color luminescence switching via different slip-stacking of highly fluorescent molecular sheets. J. Am. Chem. Soc. **132**, 13675–13683 (2010)
43. Métivier, R., Badre, S., Meallet-Renault, R., Yu, P., Pansu, R.B., Nakatani, K.: Fluorescence photoswitching in polymer matrix: mutual influence between photochromic and fluorescent molecules by energy transfer processes. J. Phys. Chem. C **113**, 11916–11926 (2009)
44. Su, J., Fukaminato, T., Placial, J.P., Onodera, T., Suzuki, R., Oikawa, H., Brosseau, A., Brisset, F., Pansu, R., Nakatani, K., Métivier, R.: Giant amplification of photoswitching by a few photons in fluorescent photochromic organic nanoparticles. Angew. Chem. Int. Ed. **55**, 3662–3666 (2016)
45. Nakahama, T., Kitagawa, D., Sotome, H., Ito, S., Miyasaka, H., Kobatake, S.: Fluorescence on/off switching in polymers bearing diarylethene and fluorene in their side chains. J. Phys. Chem. C **121**, 6272–6281 (2017)
46. Nakahama, T., Kitagawa, D., Sotome, H., Fukaminato, T., Ito, S., Miyasaka, H., Kobatake, S.: Fluorescence on/off switching in nanoparticles consisting of two types of diarylethenes. ACS Omega **3**, 2374–2382 (2018)

47. Lim, S.J., An, B.K., Park, S.Y.: Bistable photoswitching in the film of fluorescent photochromic polymer: enhanced fluorescence emission and its high contrast switching. Macromolecules **38**, 6236–6239 (2005)
48. Lim, S.J., Seo, J., Park, S.Y.: Photochromic switching of excited-state intramolecular proton-transfer (ESIPT) fluorescence: a unique route to high-contrast memory switching and nondestructive readout. J. Am. Chem. Soc. **128**, 14542–14547 (2006)
49. Corredor, C.C., Huang, Z.L., Belfield, K.D.: Two-photon 3D optical data storage via fluorescence modulation of an efficient fluorene dye by a photochromic diarylethene. Adv. Mater. **18**, 2910–2914 (2006)
50. Corredor, C.C., Huang, Z.L., Belfield, K.D., Morales, A.R., Bondar, M.V.: Photochromic polymer composites for two-photon 3D optical data storage. Chem. Mater. **19**, 5165–5173 (2007)
51. Berberich, M., Krause, A.M., Orlandi, M., Scandola, F., Wurthner, F.: Toward fluorescent memories with nondestructive readout: photoswitching of fluorescence by intramolecular electron transfer in a diaryl ethene-perylene bisimide photochromic system. Angew. Chem. Int. Ed. **47**, 6616–6619 (2008)
52. Odo, Y., Fukaminato, T., Irie, M.: Photoswitching of fluorescence based on intramolecular electron transfer. Chem. Lett. **36**, 240–241 (2007)
53. Berberich, M., Natali, M., Spenst, P., Chiorboli, C., Scandola, F., Wurthner, F.: Nondestructive photoluminescence read-out by intramolecular electron transfer in a perylene bisimide-diarylethene dyad. Chem. Eur. J. **18**, 13651–13664 (2012)
54. Berberich, M., Würthner, F.: Terrylene bisimide-diarylethene photochromic switch. Chem. Sci. **3**, 2771–2777 (2012)
55. Fukaminato, T., Tanaka, M., Doi, T., Tamaoki, N., Katayama, T., Mallick, A., Ishibashi, Y., Miyasaka, H., Irie, M.: Fluorescence photoswitching of a diarylethene-perylenebisimide dyad based on intramolecular electron transfer. Photochem. Photobiol. Sci. **9**, 181–187 (2010)
56. Fukaminato, T., Doi, T., Tamaoki, N., Okuno, K., Ishibashi, Y., Miyasaka, H., Irie, M.: Single-molecule fluorescence photoswitching of a diarylethene−perylenebisimide dyad: non-destructive fluorescence readout. J. Am. Chem. Soc. **133**, 4984–4990 (2011)
57. Kim, S., Yoon, S.J., Park, S.Y.: Highly fluorescent chameleon nanoparticles and polymer films: multicomponent organic systems that combine FRET and photochromic switching. J. Am. Chem. Soc. **134**, 12091–12097 (2012)
58. Kim, D., Kwon, J.E., Park, S.Y.: Is color-specific photoswitching in dual-color fluorescence systems possible? Manipulating intermolecular energy transfer among two different fluorophores and one photoswitch. Adv. Opt. Mater. **4**, 790–797 (2016)
59. Bu, J., Watanabe, K., Hayasaka, H., Akagi, K.: Photochemically colour-tuneable white fluorescence illuminants consisting of conjugated polymer nanospheres. Nat. Commun. **5**, 3799 (2014)
60. Taguchi, M., Nakagawa, T., Nakashima, T., Adachi, C., Kawai, T.: Photo-patternable electroluminescence based on one-way photoisomerization reaction of tetraoxidized triangle terarylenes. Chem. Commun. **49**, 6373–6375 (2013)
61. Ishida, S., Kitagawa, D., Kobatake, S., Kim, S., Kurihara, S., Fukaminato, T.: Efficient "turn-off" fluorescence photoswitching in a highly fluorescent diarylethene single crystal. Chem. Commun. **55**, 5681–5684 (2019)
62. Morimoto, M., Kashihara, R., Mutoh, K., Kobayashi, Y., Abe, J., Sotome, H., Ito, S., Miyasaka, H., Irie, M.: Turn-on mode fluorescence photoswitching of diarylethene single crystals. Cryst. Eng. Commun. **18**, 7241–7248 (2016)
63. Sotome, H., Kitagawa, D., Nakahama, T., Ito, S., Kobatake, S., Irie, M., Miyasaka, H.: Cyclization reaction dynamics of an inverse type diarylethene derivative as revealed by time-resolved absorption and fluorescence spectroscopies. Phys. Chem. Chem. Phys. **21**, 8623–8632 (2019)
64. Kobatake, S., Uchida, K., Tsuchida, E., Irie, M.: Single-crystalline photochromism of diarylethenes: reactivity-structure relationship. Chem. Commun., 2804–2805 (2002)

65. Kitagawa, D., Nakahama, T., Mutoh, K., Kobayashi, Y., Abe, J., Sotome, H., Ito, S., Miyasaka, H., Kobatake, S.: Polymorphs of a diarylethene that exhibits strong emission and direct visualization of polymorphic phase transition process by fluorescence color change. Dyes Pigm. **139**, 233–238 (2017)
66. Irie, M., Uchida, K., Eriguchi, T., Tsuzuki, H.: Photochromism of single crystalline diarylethenes. Chem. Lett. **24**, 899–900 (1995)
67. Morimoto, M., Kobatake, S., Irie, M.: Multicolor photochromism of two- and three-component diarylethene crystals. J. Am. Chem. Soc. **125**, 11080–11087 (2003)
68. Uchida, K., Sumino, H., Shimobayashi, Y., Ushiogi, Y., Takata, A., Kojima, Y., Yokojima, S., Kobatake, S., Nakamura, S.: Unusual photochromic behavior of C3-methoxy-substituted bis(2-thienyl)perfluorocyclopentene. Bull. Chem. Soc. Jpn. **82**, 1441–1446 (2009)
69. Nakahama, T., Kitagawa, D., Sotome, H., Ito, S., Miyasaka, H., Kobatake, S.: Solid-state fluorescence behavior induced by photochemical ring-opening reaction of 1,2-bis(3-methyl-5-phenyl-2-thienyl)perfluorocyclopentene. Bull. Chem. Soc. Jpn. **91**, 153–157 (2018)
70. Nakahama, T., Kitagawa, D., Sotome, H., Ito, S., Miyasaka, H., Kobatake, S.: Crystallization-induced emission of 1,2-bis(3-methyl-5-(4-alkylphenyl)-2-thienyl)perfluorocyclopentenes: a mechanical and thermal recording system. Dyes Pigm. **160**, 450–456 (2019)

Chapter 16
Circularly Polarized Luminescence from Solid-State Chiral Luminophores

Yoshitane Imai

Abstract Solid-state chiral organic luminophores bearing various functionalities have been successfully developed. These chiral luminophores can emit circularly polarized luminescence (CPL) when wrapped with organic polymer films or inorganic crystal pellet in the solid state. The chiroptical properties of these chiral luminophores in the solid state and solution state are different. In the solid state, a precise chiral arrangement of the fluorescent units in the luminescent molecule generates characteristic CPL that is not observed in the solution state.

Keywords Chiral · Circular dichroism (CD) · Circularly polarized luminescence (CPL) · Fluorescence · Luminophore

16.1 Introduction

Organic molecules with chiroptical properties have attracted attention for the development of new functional organic compounds. The chiroptical properties of chiral organic compounds in their solid state are particularly important in the development of new optoelectronic materials. Specifically, circularly polarized luminescence (CPL) from chiral organic luminophores in their solid state has recently attracted significant attention in the field of optoelectronics for applications such as polarized 3D systems and security systems. [1–10]

In this chapter, the characteristic properties of solid-state CPL of the chiral organic luminophores are introduced. This will help in designing new solid-state circularly polarized luminophores.

Y. Imai (✉)
Kindai University, Osaka, Japan
e-mail: y-imai@apch.kindai.ac.jp

M. Sakamoto and H. Uekusa (eds.), *Advances in Organic Crystal Chemistry*,
https://doi.org/10.1007/978-981-15-5085-0_16

16.2 Non-classical Control of CPL in Solid-State, Axially Chiral Binaphthyl Luminophore Wrapped with Organic PMMA Polymer [11]

Axially chiral binaphthyl is a fundamental chiral unit that is used to introduce chirality in molecules and materials. This binaphthyl unit emits CPL as it is both chiral and fluorescent. In practical applications, CPL from the solid-state luminophore is exploited.

In this section, non-classical control of CPL by two solid-state, axially chiral binaphthyl luminophores is reported. Two nearly identical binaphthyl derivatives with the same (*S*)-axial chirality, open-type binaphthyl (*S*)-2,2′-diethoxy-1,1′-binaphthyl [(*S*)-**1**] and closed-type binaphthyl (*S*)-2,2′-(1,4-butylenedioxy)-1,1′-binaphthyl [(*S*)-**2**], were used (Fig. 16.1). Chiral polymer-wrapped binaphthyl luminophores, (*S*)-**1**/PMMA and (*S*)-**2**/PMMA, were prepared by spin-coating (*S*)-**1** and (*S*)-**2** with an organic polymer, poly(methyl methacrylate) (PMMA) (Fig. 16.1).

The solid-state CPL spectra of the open-type (*S*)-**1**/PMMA and closed-type (*S*)-**2**/PMMA are shown in Fig. 16.2a. Although luminescence quenching is the most serious drawback associated with solid-state organic luminophores, polymer-wrapped (*S*)-**1**/PMMA and (*S*)-**2**/PMMA can emit CPL even in the solid state. The absolute solid-state PL quantum yields (Φ_F) and CPL maxima (λ_{CPL}) for (*S*)-**1**/PMMA and (*S*)-**2**/PMMA were 45% at ≈ 373 nm and 46% at ≈ 375 nm, respectively.

These CPL spectra are almost identical in the solution state. Thus, the CPL from (*S*)-**1**/PMMA and (*S*)-**2**/PMMA originates from the electronic interactions in an isolated molecule in the solid state. The rovibrational modes and non-radiative processes are limited by wrapping the luminophores with PMMA. This is in contrast to those in the solution state. Therefore, the Φ_F values of (*S*)-**1**/PMMA and (*S*)-**2**/PMMA in the solid state are greater than those in the solution state. It is interesting to note that although (*S*)-**1**/PMMA and (*S*)-**2**/PMMA are composed of the same axial chiral binaphthyl, their CPL spectra are opposite in signs—the CPL spectra of (*S*)-**1**/PMMA is positive (+) in sign, while that of (*S*)-**2**/PMMA is negative (−) in sign. To quantitatively compare the degrees of CPL, we used the dimensionless Kuhn's anisotropy factor in the photo-excited state, which is defined as $g_{CPL} = 2(I_L - I_R)/(I_L$

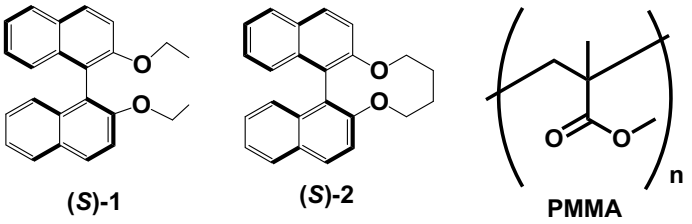

Fig. 16.1 Chiral binaphthyl luminophores (*S*)-**1** and (*S*)-**2** and organic polymer PMMA

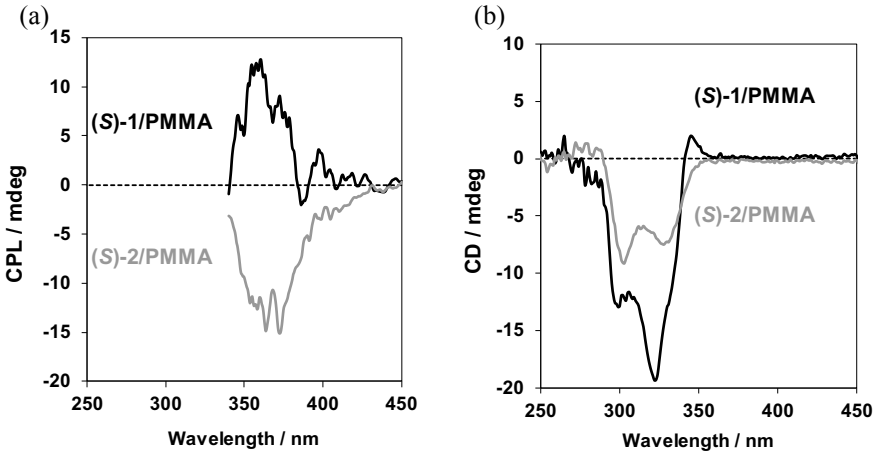

Fig. 16.2 Solid-state **a** CPL and **b** CD spectra for (*S*)-**1**/PMMA (black lines) and (*S*)-**2**/PMMA (gray lines)

$+ I_R$). Here, I_L and I_R are the intensities of the left- and right-handed CPL, respectively, upon excitation with unpolarized light. The g_{CPL} values were $\approx +7.9 \times 10^{-4}$ for (*S*)-**1**/PMMA and $\approx -1.6 \times 10^{-3}$ for (*S*)-**2**/PMMA.

To study the origin of the reversal in CPL sign, circular dichroism (CD) spectra of (*S*)-**1**/PMMA and (*S*)-**2**/PMMA were recorded (Fig. 16.2b). Several characteristic peaks from the ^1B_b moment in the binaphthyl unit were observed between 270 and 360 nm. To quantitatively evaluate the CD amplitude in the ground state, we evaluated the anisotropy factor. The magnitude of the circular polarization in the ground state (g_{CD}) is given by the relation $g_{CD} = (Abs_L – Abs_R)/[(Abs_L + Abs_R)/2]$, where Abs_L and Abs_R are the absorbances of the left and right circularly polarized light, respectively. Values of g_{CD} for (*S*)-**1**/PMMA and (*S*)-**2**/PMMA at their first Cotton CD bands were $\approx +3.5 \times 10^{-4}$ ($\lambda_{CD} = 345$ nm) and $\approx -2.7 \times 10^{-3}$ ($\lambda_{CD} = 328$ nm), respectively. Similar to CPL, the first Cotton CD bands of (*S*)-**1**/PMMA and (*S*)-**2**/PMMA were opposite in sign.

The CPL and CD spectra of solid-state (*S*)-**1**/PMMA and (*S*)-**2**/PMMA originate from isolated molecules rather than their aggregates in the PMMA film. It is known that the sign of CD signals originating from chiral binaphthyl units change according to the dihedral angles of binaphthyl. Thus, the opposite CPL and CD signs observed for (*S*)-**1**/PMMA and (*S*)-**2**/PMMA are attributable to the differences in the dihedral angles of the binaphthyl units in the ground and photo-excited states.

Generally, the inversion of the sign of CPL of a chiral luminophore requires an enantiomeric organic luminophore; however, the enantiomer is sometimes difficult to obtain. Therefore, controlling the sign of CPL of solid-state, axially chiral luminophore by adjusting the dihedral angle of the binaphthyl unit, without the need for an enantiomer, is instrumental in the development of novel, solid-state circularly polarized luminophores.

16.3 Non-classical Control of CPL in Solid-State, Axially Chiral Binaphthyl Luminophore Wrapped with Inorganic KBr Crystal [12]

In Sect. 16.2, it was seen that the sign of CPL of a polymer-wrapped axially chiral binaphthyl luminophore could be controlled by adjusting the dihedral angle of the binaphthyl unit.

In this section, the effect of an inorganic KBr crystal, instead of an organic polymer, on the CPL from a solid-state circularly polarized luminophore is discussed. Two almost identical chiral binaphthyl derivatives with the same (*R*)-axial chirality, open-type binaphthyl (*R*)-3,3′-bis(triphenylsilyl)-1,1′-bi-2-naphthol [(*R*)-**3**] and closed-type binaphthyl (*R*)-3,3′-bis(triphenylsilyl)-1,1′-binaphthyl-2,2′-diyl hydrogenphosphate [(*R*)-**4**], were used (Fig. 16.3). Chiral KBr-wrapped binaphthyl luminophores, (*R*)-**3**/KBr and (*R*)-**4**/KBr, were prepared by embedding (*R*)-**3** and (*R*)-**4** into KBr crystal, respectively.

(*R*)-**3**/KBr and (*R*)-**4**/KBr exhibited CPL at ≈ 372 and ≈ 365 nm (λ_{CPL}), with Φ_F = 0.08 and 0.29, respectively, without any significant quenching (Fig. 16.4a). The reason for the absence of CPL from KBr-wrapped (*R*)-(+)-1,1′-binaphthyl-2,2′-diol is not clearly understood. Besides, although (*R*)-**3** and (*R*)-**4** have the same axial chirality, the CPL sign of (*R*)-**3**/KBr was negative (−) while that of (*R*)-**4**/KBr was positive (+). The g_{CPL} values for (*R*)-**3**/KBr and (*R*)-**4**/KBr were ≈ -2.5×10^{-4} and ≈ $+2.2 \times 10^{-4}$, respectively.

The CD spectra of (*R*)-**3**/KBr and (*R*)-**4**/KBr show several peaks between 270 and 360 nm for vibronic π-π^* transitions, which are characteristic of naphthyl groups (Fig. 16.4b). The g_{CD} values of (*R*)-**3**/KBr and (*R*)-**4**/KBr at the first Cotton CD bands at 349 and 341 nm were ≈ -1.8×10^{-4} and ≈ $+4.4 \times 10^{-4}$, respectively. (*R*)-**3**/KBr and (*R*)-**4**/KBr also exhibited opposite CD signs for the first Cotton CD bands: The CD sign for (*R*)-**3**/KBr was negative (−), while that for (*R*)-**4**/KBr was positive (+).

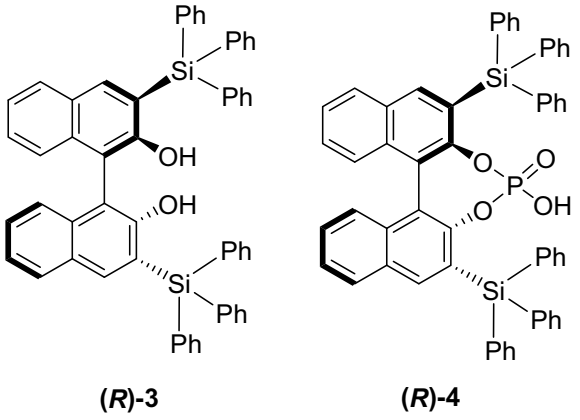

Fig. 16.3 Chiral binaphthyl luminophores (*R*)-**3** and (*R*)-**4**

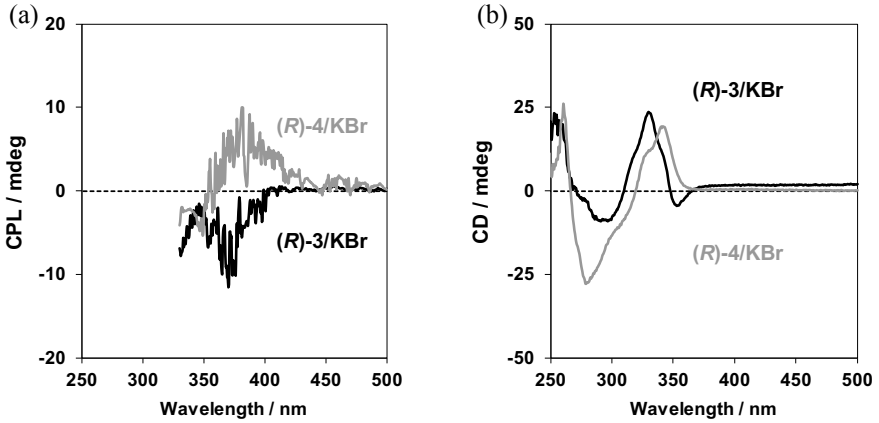

Fig. 16.4 Solid-state **a** CPL and **b** CD spectra of (*R*)-**3**/KBr (black lines) and (*R*)-**4**/KBr (gray lines)

These results suggested that the ground and photo-excited states of (*R*)-**3**/KBr and (*R*)-**4**/KBr have opposite chiralities.

Thus, inorganic KBr-wrapped binaphthyl circularly polarized luminophore can emit CPL in the solid state, and their sign can be controlled by the dihedral angle of the binaphthyl unit, while maintaining its atropchirality.

16.4 Characteristic Emission of CPL from Axially Chiral Binaphthyl Luminophore in the Solid State [13]

If the distance between a chiral source, such as binaphthyl, and achiral fluorescent units is large in an axially chiral binaphthyl luminescent system, CPL due to the two remote fluorescent moieties may not be emitted in the solution state, because the fluorescent units move freely. However, CPL may be emitted from the two remote fluorescent units in the solid state, owing to an effective chirality transfer from the axially chiral binaphthyl moiety to the remote fluorescent units.

Binaphthyl luminophore **5** consists of an axially chiral binaphthyl and two remote achiral fluorescent terthiophenes (Fig. 16.5). As expected, (*R*)- and (*S*)-**5** did not exhibited significant CPL in chloroform ($CHCl_3$) solution, presumably because of the highly flexible and long linkers between the binaphthyl and terthiophene units.

Next, binaphthyl luminophores (*R*)-**5**/KBr and (*S*)-**5**/KBr were prepared by embedding (*R*)-**5** and (*S*)-**5** into KBr crystal, respectively. As expected, (*R*)-**5**/KBr [or (*S*)-**5**/KBr] exhibited significant solid-state CPL at ≈ 413 nm (λ_{CPL}), with a g_{CPL} value of $\approx +5.0 \times 10^{-4}$ (Fig. 16.6a).

The solid-state CD and UV–Vis absorption spectra of (*R*)-**5**/KBr and (*S*)-**5**/KBr show several π–π^* transitions associated with the terthiophene groups of **5** in the

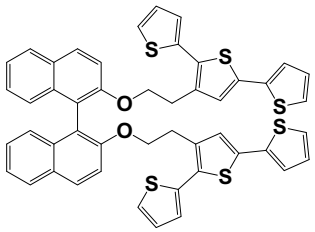

Fig. 16.5 Chiral binaphthyl-terthiophene luminophore **5**

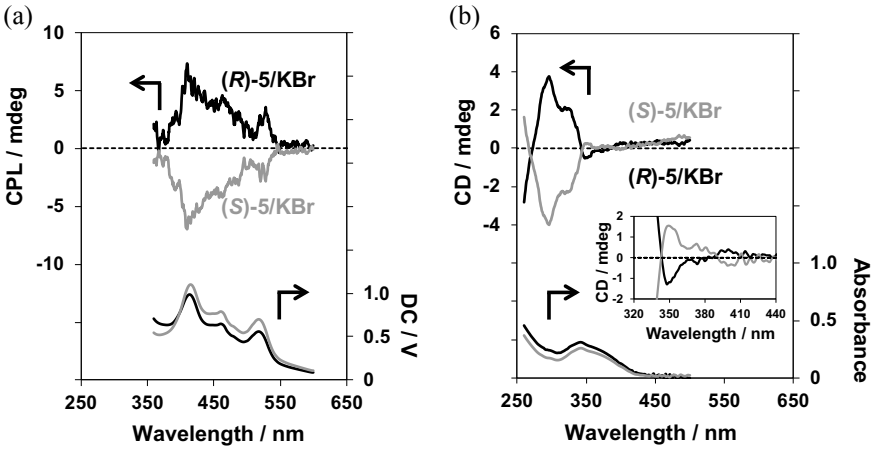

Fig. 16.6 Solid-state **a** CPL (upper panel) and PL (lower panel) spectra and **b** CD (upper panel) and UV–Vis absorption (lower panel) spectra of (*R*)-**5**/KBr (black lines) and (*S*)-**5**/KBr (gray lines)

range 260–360 nm (Fig. 16.6b). The g_{CD} value at the Cotton CD band (λ_{CD} = 342 nm) of (*R*)-**5** was $\approx -3.2 \times 10^{-5}$. The difference in the g_{CPL} and g_{CD} values can be possibly ascribed to the conformational changes in the solid-state ground and photo-excited states.

In the solid state, each molecule is surrounded by neighboring molecules and matrices, resulting in a densely packed state. The origin of CPL from the solid state may be due to the following two main factors: (i) efficient chirality transfer from the chiral binaphthyl unit to the fluorescent terthiophene units in the photo-excited state and (ii) the extremely limited molecular motion in the solid state.

Unlike the solution state, CPL from the solid state may be emitted from axially chiral binaphthyl luminophores bearing remote fluorescent units. This is because of the effective chirality transfer from the axially chiral binaphthyl unit to the tethered remote fluorescent units.

16.5 Non-classical Emission of CPL from Axially Chiral Binaphthyl Luminophore Wrapped with Organic PMMA Polymer [14]

Axially chiral 2,2′-bis(diphenylphosphino)-1,1′-binaphthyl (BINAP) is widely used as chiral ligands for asymmetric catalytic reactions (Fig. 16.7). However, the luminescence of (*R*)-BINAP in $CHCl_3$ solution is very weak.

In the above sections, we saw that CPL can be successfully induced and amplified in chiral binaphthyl luminophores by wrapping them with an organic polymer PMMA or inorganic crystal KBr.

Thus, for CPL emission from BINAP, chiral polymer-wrapped BINAP luminophores, (*R*)-BINAP/PMMA and (*S*)-BINAP/PMMA, were prepared by spin-coating (*R*)-BINAP and (*S*)-BINAP with PMMA films.

Surprisingly, (*R*)-BINAP/PMMA and (*S*)-BINAP/PMMA exhibited remarkable CPL at 355 nm (λ_{CPL}), with $\Phi_F = 0.03$ and $|g_{CPL}| = \approx 8.3 \times 10^{-4}$ (Fig. 16.8a). The solid-state CD and UV–Vis absorption spectra of (*R*)-BINAP/PMMA and (*S*)-BINAP/PMMA show that the $|g_{CD}|$ value of the first Cotton band is $\approx 2.3 \times 10^{-3}$ at $\lambda_{CD} = 335$ nm (Fig. 16.8b).

These CPL and CD signals arise from individual BINAP molecules in the PMMA film. The induction and amplification of CPL from doped PMMA films may be explained by the reduced thermally deactivated rovibrational modes of BINAP molecules and enhanced amount of oxygen (O_2) molecule introduced during doping into the PMMA film, which has a high glass transition temperature (~105 °C).

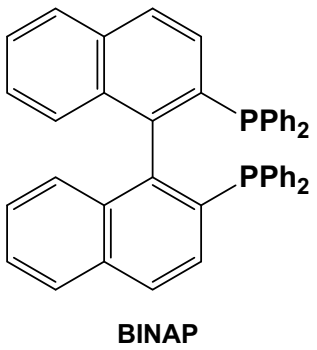

Fig. 16.7 Chiral binaphthyl luminophore BINAP

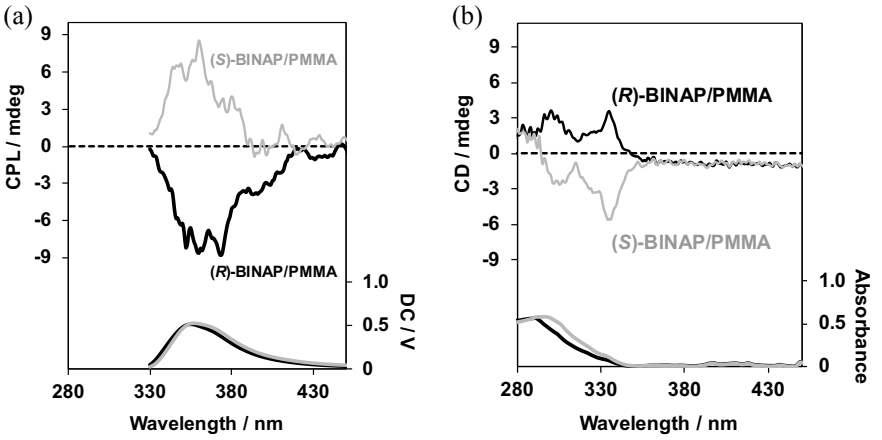

Fig. 16.8 Solid-state **a** CPL (upper panel) and PL (lower panel) spectra and **b** CD (upper panel) and UV–Vis absorption (lower panel) spectra of (*R*)-BINAP/PMMA (black lines) and (*S*)-BINAP/PMMA (gray lines)

16.6 Solid-State Aggregation-Induced Enhanced CPL from Chiral Perylene Diimide Luminophore [15]

Aggregation-induced enhanced CPL (AIEnh-CPL) has attracted much interest. AIEnh-CPL is almost always emitted from highly concentrated solutions.

Thus, solid-state AIEnh circularly polarized luminophores, N,N′-bis((1*R*)-phenylethyl)perylene-3,4,9,10-tetracarboxylic diimide/KBr [(*R,R*)-**BPP**/KBr] and its antipode [(*S,S*)-**BPP**/KBr], were prepared by doping chiral (*R,R*)-**BPP** and its antipode (*S,S*)-**BPP** into inorganic KBr crystal. The two **BPP**s have two chiral substituents and an extended π-electron planar perylene system (Fig. 16.9).

No significant CPL from chiral **BPP** (1.0×10^{-4} M) was observed in the solution state. However, remarkable AIEnh-CPL was observed from the solid-state, aggregated (*R,R*)-**BPP**, that is (*R,R*)-**BPP**/KBr, at 657 nm (λ_{CPL}), with a corresponding Φ_F of 0.09 (Fig. 16.10a). The CPL efficiency, $|g_{CPL}|$, of **BPP**/KBr is of the order of 10^{-3} ($|g_{CPL}| = \approx 2.0 \times 10^{-3}$).

Fig. 16.9 Chiral perylene diimide luminophore **BPP**

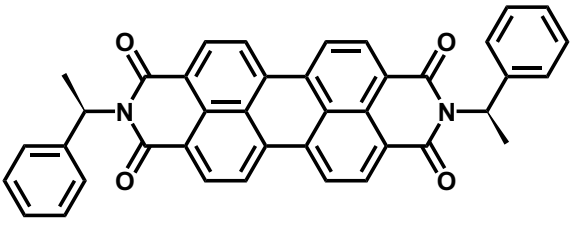

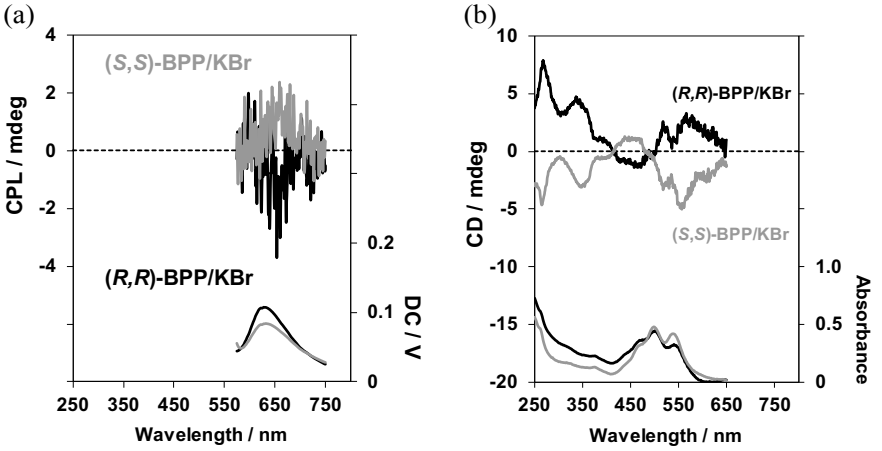

Fig. 16.10 Solid-state **a** CPL (upper panel) and PL (lower panel) spectra and **b** CD (upper panel) and UV–Vis absorption (lower panel) spectra of (*R,R*)-**BPP**/KBr (black lines) and (*S,S*)-**BPP**/KBr (gray lines)

The CD and UV–Vis absorption spectra of (*R,R*)-**BPP**/KBr and (*S,S*)-**BPP**/KBr were acquired (Fig. 16.10b). Several UV–Vis bands between 400 and 650 nm, which are characteristic of π-π* transitions between the intermolecular perylene units of multiple aggregated **BPP**, can be observed. The value of $|g_{CD}|$ at the first Cotton CD band of **BPP**/KBr was $\approx 5.4 \times 10^{-4}$ at 561 nm.

Consequently, in order to obtain stronger CPL, chiral polymer-wrapped luminophores, (*R,R*)-**BPP**/PMMA and (*S,S*)-**BPP**/PMMA, were prepared by doping (*R,R*)-**BPP** and (*S,S*)-**BPP**, respectively, into spin-coated films of PMMA. (*R,R*)-**BPP**/PMMA and (*S,S*)-**BPP**/PMMA emitted stronger AIEnh-CPL at 654 nm (λ_{CPL}), with a Φ_F of 0.40 (Fig. 16.11a). The luminescence originated from the lowest π–π* transitions between the perylene units. The $|g_{CPL}|$ value of **BPP**/PMMA was $\approx 2.4 \times 10^{-3}$, which is similar to that of **BPP**/KBr.

The corresponding CD spectra of (*R,R*)-**BPP**/PMMA and (*S,S*)-**BPP**/PMMA are also similar to that of **BPP**/KBr in the long wavelength region (Fig. 16.11b). The characteristic UV peaks originate from the π-π* transitions owing to the intermolecular interactions between multiple molecules. The $|g_{CD}|$ value at the first Cotton CD band is $\approx 3.1 \times 10^{-4}$, which is similar in magnitude to that of **BPP**/KBr.

A comparison of the anisotropy factors, $|g_{CPL}|$ and $|g_{CD}|$, reveals that $|g_{CPL}|$ is higher than the corresponding $|g_{CD}|$ value. This indicates that although the perylene units are stacked and twisted between the perylene units in the ground state, the twists increase in the photo-excited state in the solid state, as confirmed by the intense excimer CPL bands.

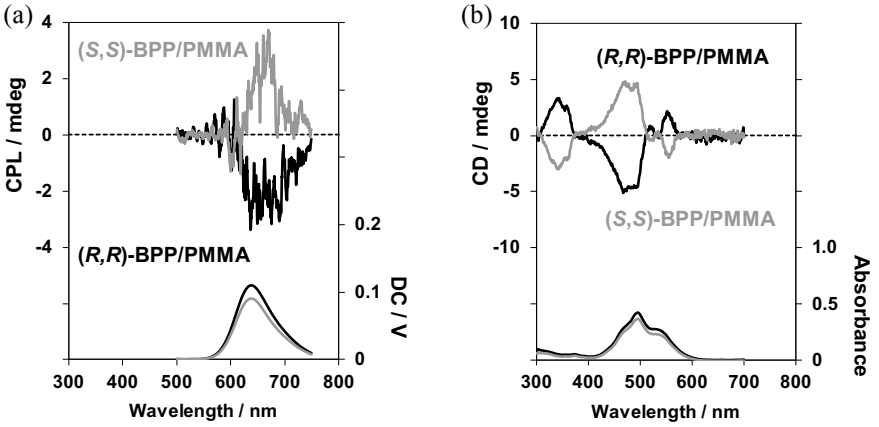

Fig. 16.11 Solid-state **a** CPL (upper panel) and PL (lower panel) spectra and **b** CD (upper panel) and UV–Vis absorption (lower panel) spectra of (*R,R*)-**BPP**/PMMA (black lines) and (*S,S*)-**BPP**/PMMA (gray lines)

16.7 Non-classical Control of AIEnh-CPL in Chiral Perylene Diimide Luminophores [16]

The CPL sign of an axially chiral binaphthyl luminophore can be controlled by adjusting the dihedral angle and chirality of the binaphthyl unit in the solid state. Thus, non-classical control of CPL sign in solid-state chiral AIEnh circularly polarized luminophores, using chiral units of the same absolute configuration, was attempted.

Solid-state AIEnh circularly polarized luminophores, N,N′-bis((1*R*)-naphthylethyl)perylene-3,4,9,10-tetracarboxylic diimide/PMMA [(*R*)-**1-BNP**/PMMA] and N,N′-bis((2*R*)-naphthylethyl)perylene-3,4,9,10-tetracarboxylic diimide/KBr [(*R*)-**2-BNP**/PMMA], were prepared by wrapping chiral (*R*)-**1-BNP** and (*R*)-**2-BNP**, respectively, with PMMA (Fig. 16.12). The naphthalene units in **1-BNP** and **2-BNP** bound differently.

No distinct CPL spectra from the two **BNP**s were obtained in $CHCl_3$ solution (1.0×10^{-4} M). This behavior was similar to that of **BPP**.

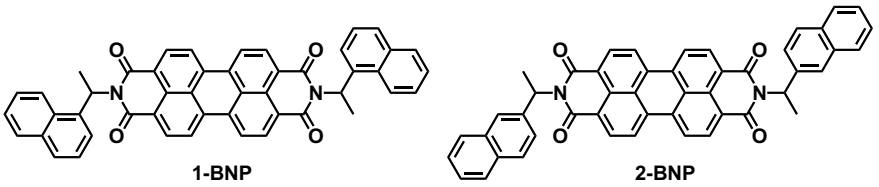

Fig. 16.12 Chiral perylene diimide luminophores **1-BNP** and **2-BNP**

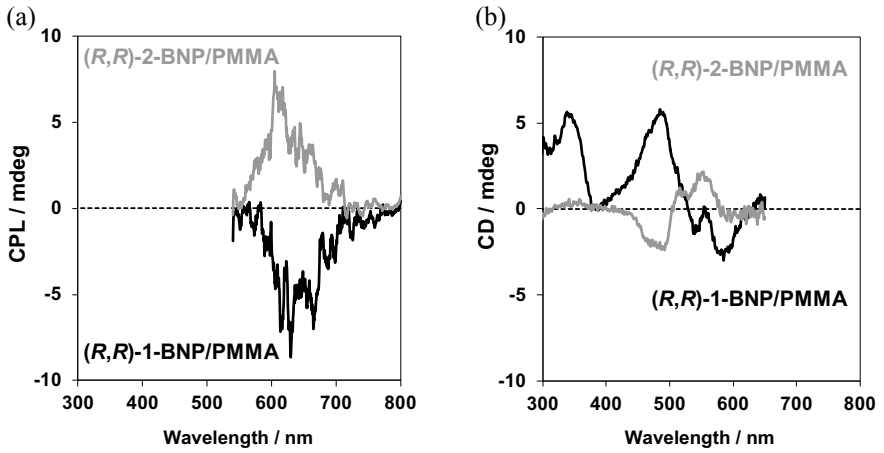

Fig. 16.13 Solid-state **a** CPL and **b** CD spectra of (*R,R*)-**1-BNP**/PMMA (black lines) and (*R,R*)-**2-BNP**/PMMA (gray lines)

Similar to **BPP**, solid-state (*R,R*)-**1-BNP**/PMMA and (*R,R*)-**2-BNP**/PMMA emitted AIEnh-CPL, which originated from the lowest π–π^* transitions of the perylene backbones (Fig. 16.13a).

The emission maxima of AIEnh-CPL (λ_{CPL}) of (*R,R*)-**1-BNP**/PMMA and (*R,R*)-**2-BNP**/PMMA were 630 and 605 nm, respectively, and their Φ_F values were 0.06 and 0.32, respectively. Surprisingly, the CPL signs of (*R,R*)-**1-BNP**/PMMA and (*R,R*)-**2-BNP**/PMMA were opposite, and the CPL spectra were almost mirror images of each other; CPL sign of (*R,R*)-**1-BNP**/PMMA was negative (−), while that of (*R,R*)-**2-BNP**/PMMA was positive (+). The g_{CPL} values of (*R,R*)-**1-BNP**/PMMA and (*R,R*)-**2-BNP**/PMMA were $\approx -3.9 \times 10^{-3}$ and $\approx +3.3 \times 10^{-3}$, respectively.

The characteristic CD bands originate from the π–π^* transitions owing to the intermolecular interactions between the perylene units (Fig. 16.13b). Similar to the CPL sign, the signs of the first Cotton CD bands of (*R,R*)-**1-BNP**/PMMA and (*R,R*)-**2-BNP**/PMMA were opposite; they were negative (−) ($\lambda_{CD} = 585$ nm) and positive (+) ($\lambda_{CD} = 553$ nm), respectively. The CD spectra are nearly mirror images of each other. The g_{CD} values of the first band in (*R,R*)-**1-BNP**/PMMA and (*R,R*)-**2-BNP**/PMMA are $\approx -1.5 \times 10^{-3}$ and $\approx +6.5 \times 10^{-4}$, respectively. In this case too, since $|g_{CPL}|$ is slightly higher than $|g_{CD}|$, the twists between the perylene backbones increase in the solid-state photo-excited state.

Thus, the sign of CPL emitted from solid-state chiral AIEnh circularly polarized luminophores can be tuned by changing the bonding position on the substituent, without having the need of a molecule with opposite chirality.

16.8 Non-classical Control of CPL in Solid-State Supramolecular Organic Luminophore Composed of 4-(2-Arylethynyl)-Benzoic Acid [17]

Most chiral organic luminophores exhibiting solid-state fluorescence are composed of a single component. Chiral supramolecular organic luminophores containing two organic molecules have different functionalities compared with luminophores containing a single molecule. A key property of chiral supramolecular luminophores is that their solid-state chiroptical properties can be easily altered by varying the component molecules. Effective functionalities due to the synergistic effects of packing and the properties of the component molecules can be obtained.

Thus, two chiral, two-component supramolecular organic luminophores, (*R*)-**6/7-Me** and (*R*)-**6/7-F** (composed of chiral (*R*)-(+)-1-phenylethylamine [(*R*)-**6**] and achiral 4-[2-(4-methylphenyl)ethynyl]-benzoic acid (**7-Me**) and (*R*)-**6** and achiral 4-[2-(4-fluorophenyl)ethynyl]-benzoic acid (**7-F**), respectively) were prepared via crystallization from an ethanol (EtOH) solution [Fig. 16.14].

Chiral KBr-wrapped supramolecular luminophores, (*R*)-**6/7-Me**/KBr and (*R*)-**6/7-F**/KBr, were prepared by embedding (*R*)-**6/7-Me** and (*R*)-**6/7-F,** respectively, into KBr crystals.

(*R*)-**6/7-Me**/KBr and (*R*)-**6/7-F**/KBr emit CPL at 379 nm (λ_{CPL}) and 420 nm (λ_{CPL}) in the solid state, respectively (Fig. 16.15a). Interestingly, although (*R*)-**6/7-Me**/KBr and (*R*)-**6/7-F**/KBr are composed of the same chiral molecule (*R*)-**6**, their CPL spectra are opposite in signs; the CPL signs of (*R*)-**6/7-Me**/KBr and (*R*)-**6/7-F**/KBr are negative (−) and positive (+), respectively, and the corresponding g_{CPL} values are $\approx -0.7 \times 10^{-3}$ and $\approx +4.8 \times 10^{-4}$.

The CD spectra of (*R*)-**6/7-Me**/KBr and (*R*)-**6/7-F**/KBr, originating due to the ethynylphenylene unit, are nearly mirror images (Fig. 16.15b). The g_{CD} values of the first band for (*R*)-**6/7-Me**/KBr and (*R*)-**6/7-F**/KBr are $\approx +1.0 \times 10^{-3}$ and $\approx -4.1 \times 10^{-3}$, respectively. Interestingly, the signs of the CD spectra are also opposite; they are positive (+) for (*R*)-**6/7-Me**/KBr and negative (−) for (*R*)-**6/7-F**/KBr. These results indicate that there is an effective chirality transfer from chiral (*R*)-**6** to the achiral fluorescent unit **7-Me** (or **7-F**) through complexation in the ground and photo-excited states.

To study the origin of the solid-state CD signal from these complexes, the X-ray crystal structures of (*R*)-**6/7-Me** and (*R*)-**6/7-F** were compared. The crystal structure of (*R*)-**6/7-Me** is shown in Fig. 16.16. The stoichiometry of (*R*)-**6/7-Me** is

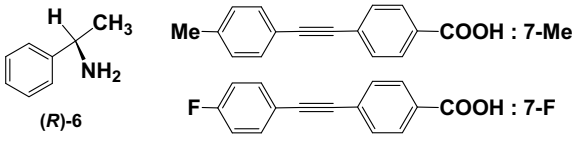

Fig. 16.14 Chiral component (*R*)-**6** and achiral luminescent components **7-Me** and **7-F**

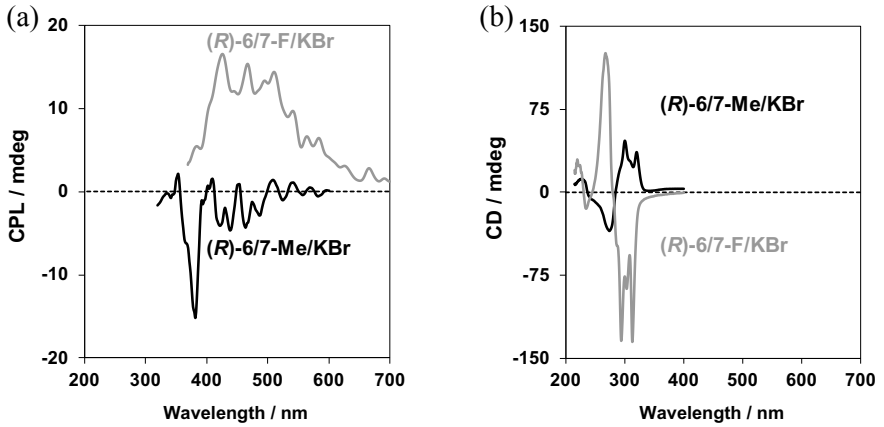

Fig. 16.15 Solid-state **a** CPL and **b** CD spectra of (*R*)-**6/7-Me**/KBr (black lines) and (*R*)-**6/7-F**/KBr (gray lines)

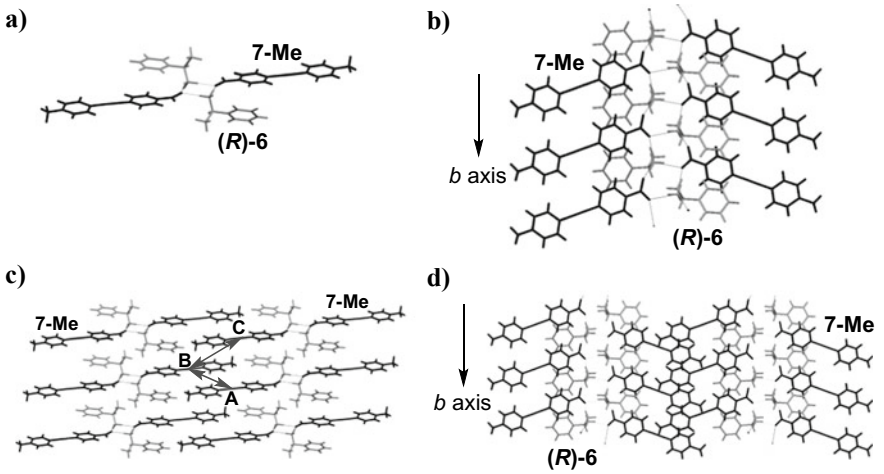

Fig. 16.16 Crystal structures of (*R*)-**6/7-Me**. **a** 2_1-helical columnar network structure along *b* axis. **b** View along *a* axis. **c** Packing structure along *b* axis. **d** View along *a* axis

(*R*)-**6**:**7-Me** = 1:1. This complex has a characteristic 2_1-helical columnar network structure along the *b* axis (Fig. 16.16a, b). This column is mainly composed of the carboxylate oxygen of the carboxylic acid anions and the ammonium hydrogen of the protonated amine. (*R*)-**6/7-Me** is formed by the self-assembly of these 2_1-helical columns, which is driven by the three intercolumnar benzene–benzene edge-to-face interactions (Fig. 16.16c, d).

In (*R*)-**6/7-F**, the stoichiometry is (*R*)-**6**:**7-F** = 1:1 [Fig. 16.17]. Similar to (*R*)-**6/7-Me**, this complex also has a 2_1-helical columnar network structure along the *a*

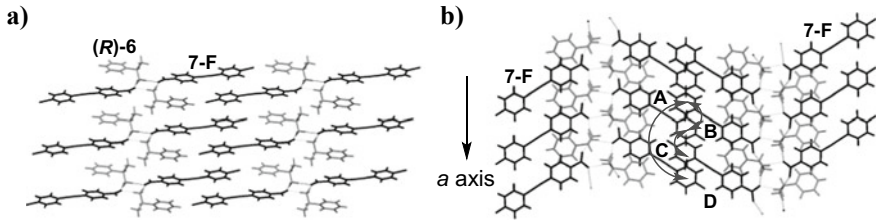

Fig. 16.17 Crystal structures of (*R*)-**6/7-F**. **a** Packing structure of 2_1-helical columnar network structure along *a* axis. **b** View along *b* axis

axis. (*R*)-**6/7-F** is formed by the self-assembly of these 2_1-helical columns, which is driven by the intercolumnar benzene–benzene edge-to-face and F···H interactions. Interestingly, despite the similar structures of the 2_1-helical columns in (*R*)-**6/7-Me** and (*R*)-**6/7-F**, as revealed by X-ray crystallography, the packing structures of the shared 2_1-helical columns are different (Figs. 16.16d and 16.17b).

CD intensities of this magnitude are likely to arise from the coupling of monomer electronic transitions between the neighboring **7-Me** or **7-F** components in crystals. When the CD spectra of the molecular pairs of **7-Me** and **7-F** in (*R*)-**6/7-Me** and (*R*)-**6/7-F** crystals were calculated by the ZINDO method, it was found that the sign of CD of (*R*)-**6/7-Me** (Fig. 16.16d) originated from molecular pair B-C rather than A-B, while the sign of CD of (*R*)-**6/7-F** (Fig. 16.17b) originated from molecular pairs A-B and A-D rather than B-C. In addition, the electronic transition in the monomer in each crystal has significant rotational strength because of the twisted molecular conformation around the C-COO bonds. Thus, the experimentally observed CD intensities are caused by this monomer distortion as well as by the coupling of monomer electronic transitions.

Thus, in two-component chiral supramolecular organic luminophores, the sign of solid-state CPL can be controlled not only by using a chiral molecule with opposite chirality but also by changing the bonding position of the substituent in the achiral fluorescent molecule (that is, by changing the packing structure of the fluorescent unit).

16.9 Conclusions

The development of optically active solid-state luminophores that can emit CPL with high functionalities, such as a high dissymmetry factor (g_{CPL}) and high quantum yield, (Φ_F) has attracted attention in chiroptical organic and inorganic material fields. Molecules are more rigidly constrained in the solid state than in solution because of the greater influence of neighboring molecules in the solid state. In this chapter, this afforded organic luminophores with novel functionalities, resulting from the synergy derived from the neighboring molecules in the solid state. For example, the chiral optical properties of organic luminophores can be controlled by changing the packing

structure of luminophores without using a chiral compound with opposite chirality. Solid-state organic luminophores are expected to aid the development of novel chiral aggregation-induced enhanced (AIEnh) CPL systems with various functionalities.

References

1. Kimoto, T., Amako, T., Tajima, N., Kuroda, R., Fujiki, M., Imai, Y.: Control of Solid-state Circularly Polarized Luminescence of Binaphthyl Organic Fluorophores through Environmental Changes. Asian J. Org. Chem. **2**, 404–410 (2013)
2. Amako, T., Harada, T., Suzuki, N., Mishima, K., Fujiki, M., Imai, Y.: Solid-state circularly polarized luminescence and circular dichroism of viscous binaphthyl compounds. RSC Adv. **3**, 23508–23513 (2013)
3. Nakabayashi, K., Amako, T., Tajima, N., Fujiki, M., Imai, Y.: Nonclassical dual control of circularly polarized luminescence modes of binaphthyl-pyrene organic fluorophores in fluidic and glassy media. Chem. Commun. **50**, 13228–13230 (2014)
4. Kitayama, Y., Nakabayashi, K., Wakabayashi, T., Tajima, N., Fujiki, M., Imai, Y.: Circularly polarized luminescence of biaryl atropisomers: subtle but significant structural dependency. RSC Adv. **5**, 410–415 (2015)
5. Amako, T., Nakabayashi, K., Sudo, A., Fujiki, M., Imai, Y.: Solid-state circularly polarised luminescence of atropisomeric fluorophores embedded in achiral myo-inositol-containing polyurethanes. Org. Biomol. Chem. **13**, 2913–2917 (2015)
6. Amako, T., Nakabayashi, K., Suzuki, N., Guo, S., Abdul Rahim, N.A., Harada, T., Fujiki, M., Imai, Y.: Pyrene magic: chiroptical enciphering and deciphering 1,3-dioxolane bearing two wirepullings to drive two remote pyrenes. Chem. Commun. **51**, 8237–8240 (2015)
7. Zheng, H., Li, W., Li, W., Wang, X., Tang, Z., Zhang, S.X., Xu, Y.: Uncovering the Circular Polarization Potential of Chiral Photonic Cellulose Films for Photonic Applications. Adv. Mater. **30**, 1705948 (2018)
8. Zhao, B., Pan, K., Deng, J.: Combining chiral helical polymer with achiral luminophores for generating full-color, on-off, and switchable circularly polarized luminescence. Macromolecules **52**, 376–384 (2019)
9. Jin, Q., Chen, S., Sang, Y., Guo, H., Dong, S., Han, J., Chen, W., Yang, X., Li, F., Duan, P.: Circularly polarized luminescence of achiral open-shell π-radicals. Chem. Commun. **55**, 6583–6586 (2019)
10. Chen, Y., Li, X., Li, N., Quan, Y., Cheng, Y., Tang, Y.: Strong circularly polarized electroluminescence based on chiral salen-Zn(II) complex monomer chromophores. Mater. Chem. Front. **3**, 867–873 (2019)
11. Kimoto, T., Tajima, N., Fujiki, M., Imai, Y.: Control of circularly polarized luminescence by open- and closed-type binaphthyl derivatives with the same axial chirality. Chem. Asian J **7**, 2836–2841 (2012)
12. Sato, T., Tajima, N., Ueno, H., Harada, T., Fujiki, M., Imai, Y.: Binaphthyl luminophores with triphenylsilyl groups: Sign inversion of circularly polarized luminescence and circular dichroism. Tetrahedron **72**, 7032–7038 (2016)
13. Taniguchi, N., Nakabayashi, K., Harada, T., Tajima, N., Shizuma, M., Fujiki, M., Imai, Y.: Circularly polarized luminescence of chiral binaphthyl with achiral terthiophene fluorophores. Chem. Lett. **44**, 598–600 (2015)
14. Kono, Y., Nakabayashi, K., Kitamura, S., Kuroda, R., Fujiki, M., Imai, Y.: A comparison of circularly polarised luminescent BINAP and BINAPO as chiral binaphthyl luminophores. Tetrahedron **71**, 3985–3989 (2015)
15. Taniguchi, A., Kaji, D., Hara, N., Murata, R., Akiyama, S., Harada, T., Sudo, A., Nishikawa, H., Imai, Y.: Solid-state aienh-circularly polarised luminescence of chiral perylene diimide fluorophores. RSC Adv. **9**, 1976–1981 (2019)

16. Watanabe, K., Taniguchi, A., Kaji, D., Hara, N., Hosoya, T., Kanesaka, A., Harada, T., Nishikawa, H., Imai, Y.: Non-classical control of solid-state aggregation-induced enhanced circularly polarized luminescence in chiral perylene diimides. Tetrahedron **75**, 2944–2948 (2019)
17. Nishiguchi, N., Kinuta, T., Nakano, Y., Harada, T., Tajima, N., Sato, T., Fujiki, M., Kuroda, R., Matsubara, Y., Imai, Y.: Control of solid-state chiral optical properties of a supramolecular organic fluorophore containing of 4-(2-arylethynyl)-benzoic acid. Chem. Asian J. **6**, 1092–1098 (2011)

Chapter 17
Azulene-Based Materials for Organic Field-Effect Transistors

Hiroshi Katagiri

Abstract Azulene is a non-alternant non-benzenoid hydrocarbon that has attracted much attention because of its large dipole moment and long-wavelength absorption properties that are derived from its unique molecular orbital geometry; its highest occupied and lowest unoccupied molecular orbitals are not mirror images. In this chapter, we describe the synthesis, structures, properties, and organic field-effect transistor (OFET) characteristics of 2-azulenyl end-capped oligomers and 2, 6-connected terazulene isomers, in which the azulene moieties deliver molecules that are flat and linear. These compounds show high-order orientations with herringbone packing in their crystalline states and typical OFET characteristics with high carrier mobilities. In particular, terazulene isomers are unique π-conjugated systems with asymmetrically distributed molecular orbitals, which leads to an unconventional concept: polarity control of OFET by molecular orbital distribution control. These findings provide a key approach for constructing various OFET materials and a basis for the accelerated development of the solid-state chemistry of azulene.

Keywords Azulene · π-Conjugation · Herringbone structure · Organic field-effect transistors · Dipole moment · Structure–property relationship

17.1 Introduction

Azulene consists of a five-membered ring and a seven-membered ring fused to form a stable bicyclic 10-π-electron system (Fig. 17.1). Since it has a dipole moment of 1.0 D, which is rare among hydrocarbons, and is blue in color, extending the π-electron system of azulene has been of interest. In particular, the polarized structure and small excitation energy of azulene are attractive in a π-conjugated system, and

H. Katagiri (✉)
Graduate School of Science and Engineering, Yamagata University,
Jonan Yonezawa 992-8510, Japan
e-mail: kgri7078@yz.yamagata-u.ac.jp

M. Sakamoto and H. Uekusa (eds.), *Advances in Organic Crystal Chemistry*,
https://doi.org/10.1007/978-981-15-5085-0_17

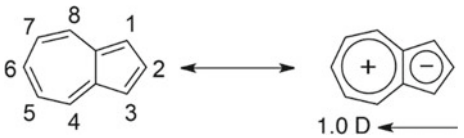

Fig. 17.1 Numbering and resonance structure of azulene

π-conjugated azulenes with narrow gaps between their highest occupied and lowest unoccupied orbitals (HOMO–LUMO gaps) have been synthesized and studied [1–3]. As recent topics of interest, the π-conjugated azulene molecule is expected to be useful as a dye-sensitized solar-cell material by taking advantage of its long-wavelength absorption characteristics [4, 5]. On the other hand, azulene compounds have mainly been researched in solution, with few solid-state reports having appeared in the literature before 2015 [6–8]. In this section, we describe the challenges involved in extending the structure of azulene at its 2- and 6-positions, the applications of such π-conjugated modifications to organic field-effect transistors (OFETs), and the invention of functional organic crystalline materials that use the features of azulene.

17.2 Study Design

17.2.1 Electronic Structure of Azulene

Azulene is classified as a non-alternant hydrocarbon, which is defined as a conjugated system of odd-numbered rings, such as a five-membered ring and a seven-membered ring, that has a low-symmetry molecular structure. Unlike naphthalene, which is an alternant hydrocarbon, the HOMO and LUMO of azulene are asymmetric, with atomic coefficients that differ greatly. Therefore, electron repulsion during excitation is small, and a lower than expected excitation energy is observed (Fig. 17.2) [9, 10]. The electrons in the HOMO of azulene have a high probability of being at the 1- and 3-positions, while the electrons in the LUMO have a high probability of being at the 2- and 6-positions; consequently, the effect of conjugation extension depends greatly on the position of the substituent [11–14]. In particular, the LUMO of azulene has large orbital coefficients on the carbon atoms at its 2- and 6-positions, while the HOMO has a nodal plane through these carbon atoms. Moreover, the energy difference between the HOMO and HOMO−1 is about 1 eV; therefore, linkages at the 2- and 6-positions can contribute greatly to lowering the LUMO energy of azulene. This observation provides an ideal design guideline for materials with π-electron conjugation, because this π-conjugated system can be expanded without destabilizing the compound by raising the HOMO energy.

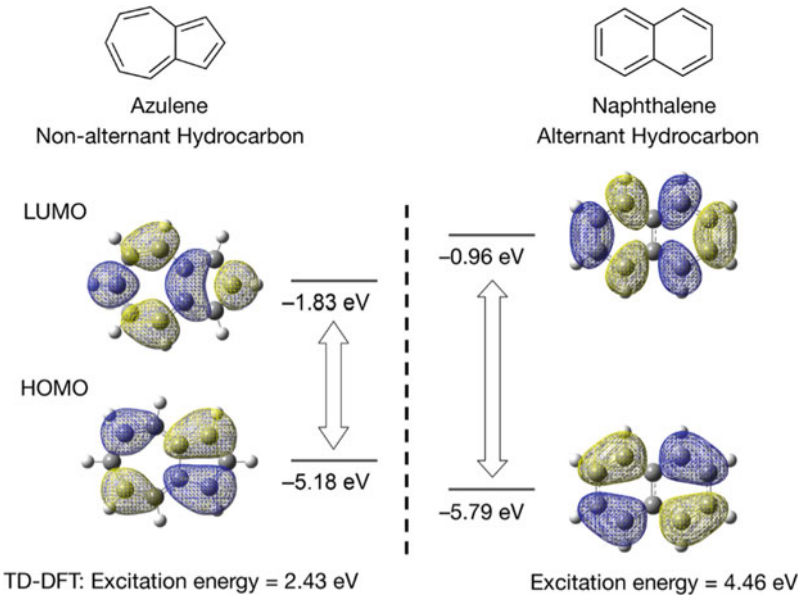

Fig. 17.2 Frontier orbitals of azulene and naphthalene calculated at the B3LYP/6-31G(d) level of theory

17.2.2 The Molecular Structure of an Ideal OFET Material

Organic crystalline materials based on π-conjugated compounds are typically used in OFETs, and a highly ordered molecular arrangement is required in the crystalline thin film of the active layer in order to realize high performance. As a result, planar and linear structural extensions have been widely used to increase dispersion forces by extending the π-electron system. In many cases, molecules with rigid planar structures show end-on orientations perpendicular to the substrate, which makes them suitable for use in typical lateral FET devices that conduct current in the planes of their organic thin films [15–17]. In particular, two-dimensional herringbone structures with edge-to-face configurations, such as pentacene, are representative high-performance organic transistor materials. The crystal structures of these polycyclic aromatic hydrocarbons have been systematically summarized, with these compounds widely recognized as having long and narrow molecular shapes and large aspect ratios (Fig. 17.3) [18, 19]. In order to obtain a molecular structure with a large aspect ratio, it is desirable to extend the structure of azulene at its 2- and 6-positions.

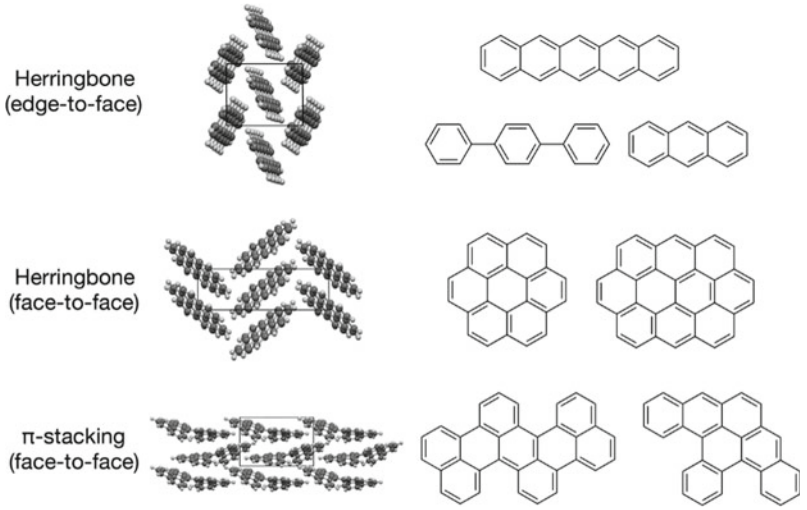

Fig. 17.3 Molecular packing motifs in the crystal structures of polycyclic aromatic hydrocarbons

17.2.3 Reactivity of Azulene

Azulene is preferentially electrophilically substituted at its 1- and 3-positions, where the HOMO coefficients are largest. Therefore, introducing substituents at the 2- and 6-positions of azulene is generally difficult. The conventional method (the Nozoe–Seto azulene synthesis), in which a cyanoacetate or a malonate ester is reacted with a tropone derivative in the presence of a base, as reported by Nozoe, Seto, and coworkers in 1956, is widely used to prepare azulenes (Scheme 17.1) [20, 21]. Not only are amino and hydroxyl groups selectively introduced at the 2-position, but the 1- and 3-positions, which are active sites for electrophilic substitution, are also protected by ester groups, which is advantageous. Therefore, a substituent can selectively be introduced at the 6-position by a subsequent electrophilic substitution reaction. The amino group can undergo a series of functional transformations via diazonium salts, and the ester group can easily be removed later by decarboxylation. Hence, this method is advantageous for constructing azulene skeletons with optional substituents at their 2- and 6-positions. In view of the electronic structure of azulene and the ideal molecular structure of an OFET material discussed in this section, we focused on structurally expanding azulene starting with its 2- and 6-positions. In addition, since

Scheme 17.1 The Nozoe–Seto azulene synthesis

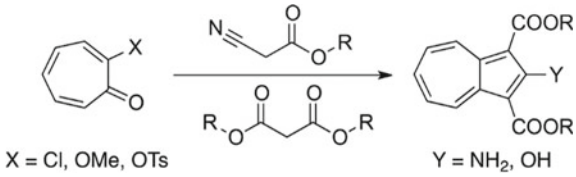

the dipole moment of azulene passes through its 2-and 6-positions, we concluded that structurally expanding azulene at these positions would lead to oligomers that reflected the magnitude and direction of the dipole moment of a single azulene molecule the most. In other words, structurally expanding azulene through its 2- and 6-positions uses the features of this molecule to their maximum benefit.

17.3 Azulenyl End-Capped Oligomers

17.3.1 Objective and Background

Sulfur-containing conjugated skeletons, such as bithiophene and thienothiophene, have been widely used as the basic skeletons of organic semiconductor materials because the large atomic radius of sulfur is advantageous for orbital overlap and intermolecular interactions. In particular, end-capping π-conjugated systems to produce aromatic oligomers that are end-capped with optional aromatic units on each end is an important basic strategy for the design of π-conjugated materials because a wide range of material groups can be prepared by combining the basic skeleton with end-cap groups [22, 23]. We synthesized two kinds of material (DAzBT, DAzTT; Fig. 17.4) with linearly extended π-conjugation, in which bithiophene or thieno [3,2-*b*] thiophene was end-capped with 2-azulenyl groups, and evaluated their structures, physical properties, and OFET characteristics.

17.3.2 Synthesizing DAzBT and DAzTT

The key substrate required for the introduction of the azulene moiety, namely 2-iodoazulene (**8**), was prepared according to the conventional Nozoe–Seto azulene synthesis methodology (Scheme 17.2). To that end, dimethyl 2-aminoazulene-1,3-dicarboxylate (**5**) was synthesized from methyl cyanoacetate and 2-chlorotropone (**4**), itself prepared from cyclopentadiene (**1**) as the starting material; **8** was obtained by a sequence that included chlorination, decarboxylation, and iodination via a diazonium salt [21]. The Suzuki–Miyaura cross-coupling reaction was then used to introduce the azulene framework. The bithiophene skeleton of DAzBT was constructed by the homocoupling reaction of the thiophene **10** following azulene introduction, while

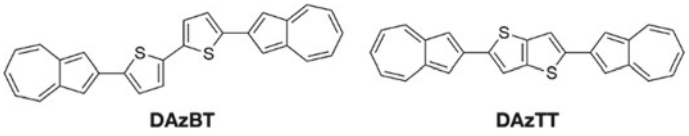

Fig. 17.4 Molecular structures of DAzBT and DAzTT

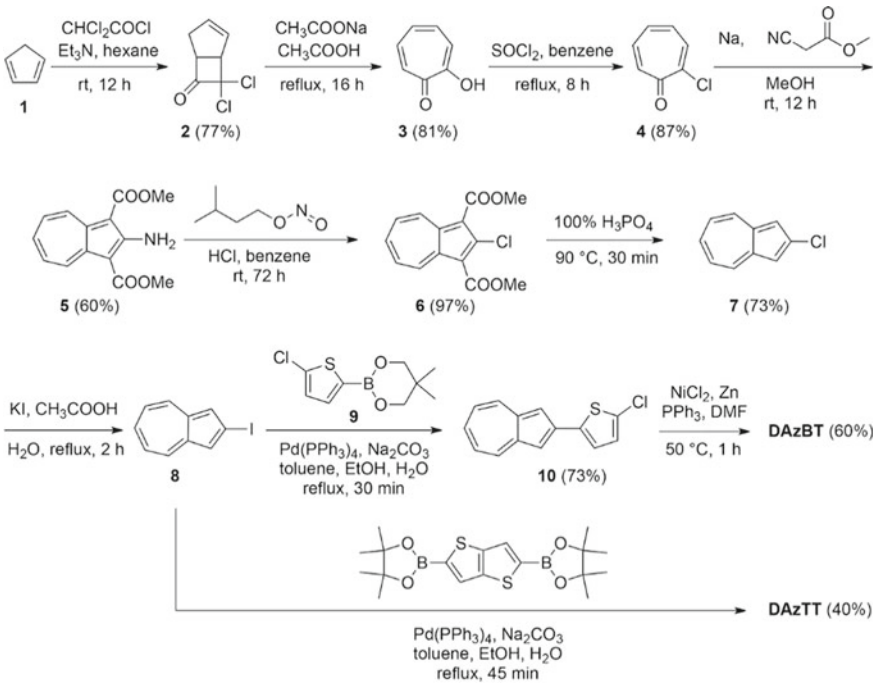

Scheme 17.2 Synthesis of DAzBT and DAzTT

azulene was introduced at two places in DAzTT through reaction with thienothiophene diboronic acid bis (pinacol) ester. DAzBT and DAzTT were purified by sublimation because they are poorly soluble in many organic solvents; both compounds are highly thermally stable.

17.3.3 Crystal Structures and Optical Properties of DAzBT and DAzTT

Single crystals of DAzBT and DAzTT obtained by sublimation were subjected to X-ray crystallography; both were found to be planar with herringbone-type packing structures (Fig. 17.5). Edge-to-edge-type layered structures were also observed along the molecular long axes. This overall structure is a typical packing pattern found for molecules with large aspect ratios, such as pentacene and oligothiophene, as discussed above. These molecules are closely packed, and no repulsion due to the dipole moment of azulene was observed. DAzTT has a denser structure with more interatomic contacts than DAzBT; packing coefficients of 73.8 and 73.1% were found for DAzTT and DAzBT, respectively. The ionization energy (IP) of each molecule was determined by atmospheric photoelectron spectroscopy; low values of −5.43 eV

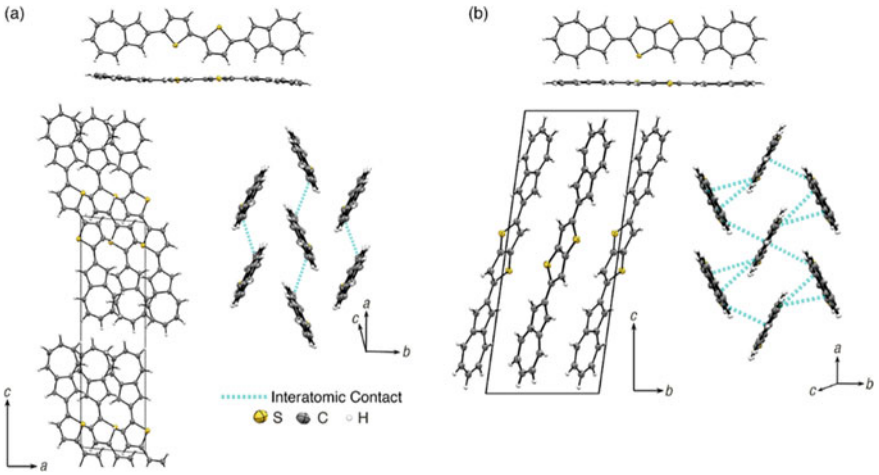

Fig. 17.5 Crystal packing structures of **a** DAzBT and **b** DAzTT. Reproduced from Ref. [24] with permission. Copyright 2012 American Chemical Society

(DAzBT) and −5.45 eV (DAzTT) were found, and high atmospheric stabilities were observed. Increases in the HOMO energy of azulene are suppressed by bonding at the 2-position, which lies on the nodal plane of the HOMO of azulene.

17.3.4 OFET Properties and Thin-Film Structures of DAzBT and DAzTT

Top-contact-type FET devices were fabricated using thin films of DAzBT and DAzTT prepared by the vacuum-evaporation method, and their OFET characteristics were evaluated. These devices exhibited FET properties typical of p-type semiconductors, with carrier mobilities of 2.4×10^{-2} cm^2/Vs (DAzBT) and 5.0×10^{-2} cm^2/Vs (DAzTT). DAzTT exhibited excellent carrier-transport behavior, and the superior properties of DAzTT are consistent with its crystal structure. These results are comparable to, or better than, similar end-capped compounds, such as naphthalene, phenanthrene, and naphthothiophene derivatives.

Thin-film X-ray diffraction analysis revealed the formation of two-dimensional conductive planes on the substrate surfaces through end-on molecular orientations on the substrate (Fig. 17.6).

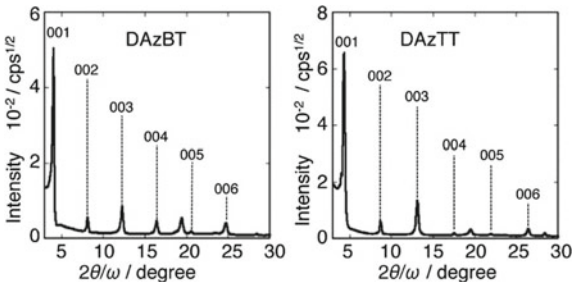

Fig. 17.6 Out-of-plane X-ray diffraction patterns of evaporated thin films of (left) DAzBT and (right) DAzTT on HMDS-treated Si/SiO_2 substrates. Reproduced from Ref. [24] with permission. Copyright 2012 American Chemical Society

17.4 Terazulene Isomers

17.4.1 Objective and Background

To the best of our knowledge, there is no example of a compound bearing multiple azulene moieties in which the dipole moment, a major feature of azulene, synergistically contributes to molecular function; in many cases, the physical properties are simply the result of the nature of the 10-π-electron system. To begin with, we designed terazulene (TAz1) with unidirectionally and linearly connected azulenes [25]. Since structural expansion at the 2- and 6-positions greatly contributes to the lowering of the LUMO energy, n-type semiconductor characteristics were expected to be expressed by conjugated systems with further expanded azulenes. Three other isomers of terazulene exist (TAz2, TAz3, TAz4; Fig. 17.7) resulting from different azulene orientations [26]. By investigating the structure–property relationships of these terazulene isomers, the effects on material properties of the intramolecular dipole moment and electronic state peculiar to azulene were clarified.

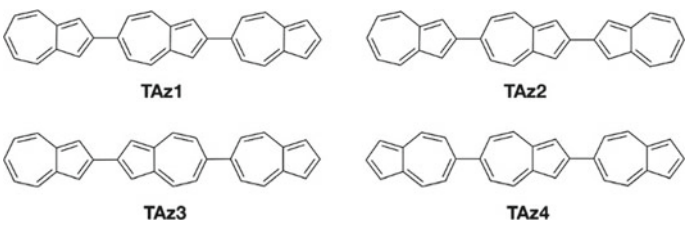

Fig. 17.7 Molecular structures of terazulene isomers

17.4.2 Synthesizing Terazulene Isomers

The Suzuki–Miyaura cross-coupling reaction was used to construct the azulene backbone (Scheme 17.3). The coupling substrates, namely 2-azulenylboronic acid ester [27], 6-bromoazulene [28], and 6-azulenylboronic acid ester [29], are known compounds and were synthesized from ethyl 2-aminoazulene-1,3-dicarboxylate, itself prepared by the Nozoe–Seto azulene synthesis. Here, the novel 2-chloroazulene-6-boronic acid ester **12**, synthesized by the diazotization of the 2-aminoazulene-6-boronic acid diester **11** [29], is a key compound used to synthesize all of the terazulenes and facilitates the sequential introduction of azulene backbone units based on the difference in reactivities of the 2- and 6-positions. We converted compound **12** into 2,6′-biazulene (**13**) and 6,6′-biazulene (**14**) by Suzuki–Miyaura cross-coupling reactions, followed by decarboxylation to chlorobiazulenes **15** and **16**. The four terazulene isomers were finally prepared by reactions with the corresponding boronic acid esters. All compounds were highly thermally stable and were purified by sublimation.

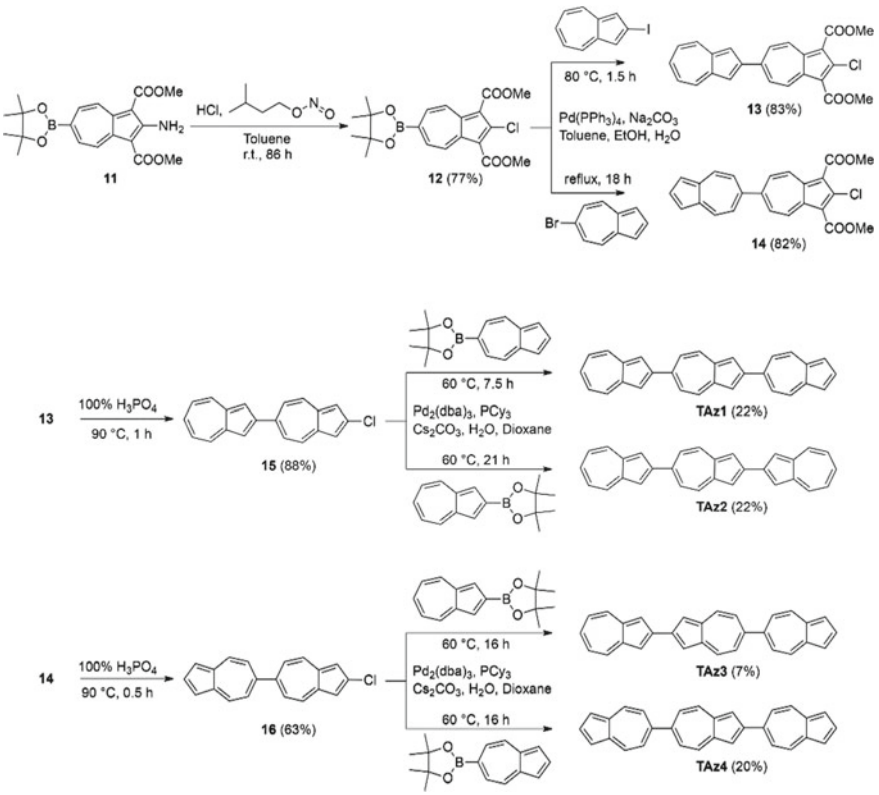

Scheme 17.3 Syntheses of terazulene isomers TAz1, TAz2, TAz3, and TAz4

17.4.3 Crystal Structures and Optical Properties of the Terazulene Isomers

Single crystals of the above-mentioned terazulenes obtained by sublimation were subjected to X-ray crystallography, which revealed that TAz1 and TAz2 are planar, while TAz3 and TAz4 have structures that are twisted about their 6,6′-bonds by about 50° (Fig. 17.8). The 6,6′-bond was also found to be twisted by about 50° in an isolated molecule structurally optimized by computational methods; this twist is believed to be caused by steric hindrance. On the other hand, the optimized structure of an isolated molecule connected through a 2,6′-bond was twisted by about 30°, which suggests that the planar structures observed in the crystals of TAz1 and TAz2 are due to intermolecular interactions in the single crystals. In addition, the optimized structure of the 2,2′-connected biazulene is planar, as observed in the crystal structures of TAz2 and TAz3. All terazulene isomers formed edge-to-face herringbone packing structures and were found to be packed in a layered manner along each molecular long axis. These structures also adopt the typical packing structure observed in molecules with large aspect ratios.

The optical properties of the terazulene isomers are summarized in Table 17.1. The IPs of films obtained by atmospheric photoelectron spectroscopy ranged from −5.45 to −5.56 eV; these values are not significantly different from the oxidation potential of azulene itself ($E_{1/2} = 0.54$ V vs. Fc/Fc^+) [30, 31] determined by cyclic voltammetry and the HOMO energy (−5.18 eV) determined by quantum chemical calculations. Therefore, the HOMO energy is largely unaffected by oligomerization. Furthermore, the energy gaps calculated from the absorption spectra were 1.56–1.63 eV, with LUMO energies calculated on the basis of these energies ranging from −3.83 to −3.93 eV. Consequently, lower LUMO energies were determined to be responsible for the smaller energy gaps; we conclude that this outcome is a major feature of azulenes structurally expanded at their 2- and 6-positions.

17.4.4 OFET Properties and Thin-Film Structures of the Terazulene Isomers

The FET characteristics of TAz1 are shown in Fig. 17.9. Interestingly, the TAz1 top-contact FET device showed only n-type semiconductor characteristics with a charge mobility of 0.29 cm^2/Vs, while the TAz2 and TAz3 devices exhibited ambipolar characteristics, with both n-type and p-type polarities, and TAz4 showed only n-type characteristics with a charge mobility of 0.15 cm^2/Vs. These results clearly reveal that the polarity of the semiconductor depends on the azulene orientation. In particular, TAz2 showed ambipolar character when an Al electrode was used, but only p-type character when an Au electrode was used, with a hole mobility of 1.32 cm^2/Vs. The unipolar p-type behavior of TAz2 is attributable to the higher LUMO energy of TAz2 compared to those of the other isomers.

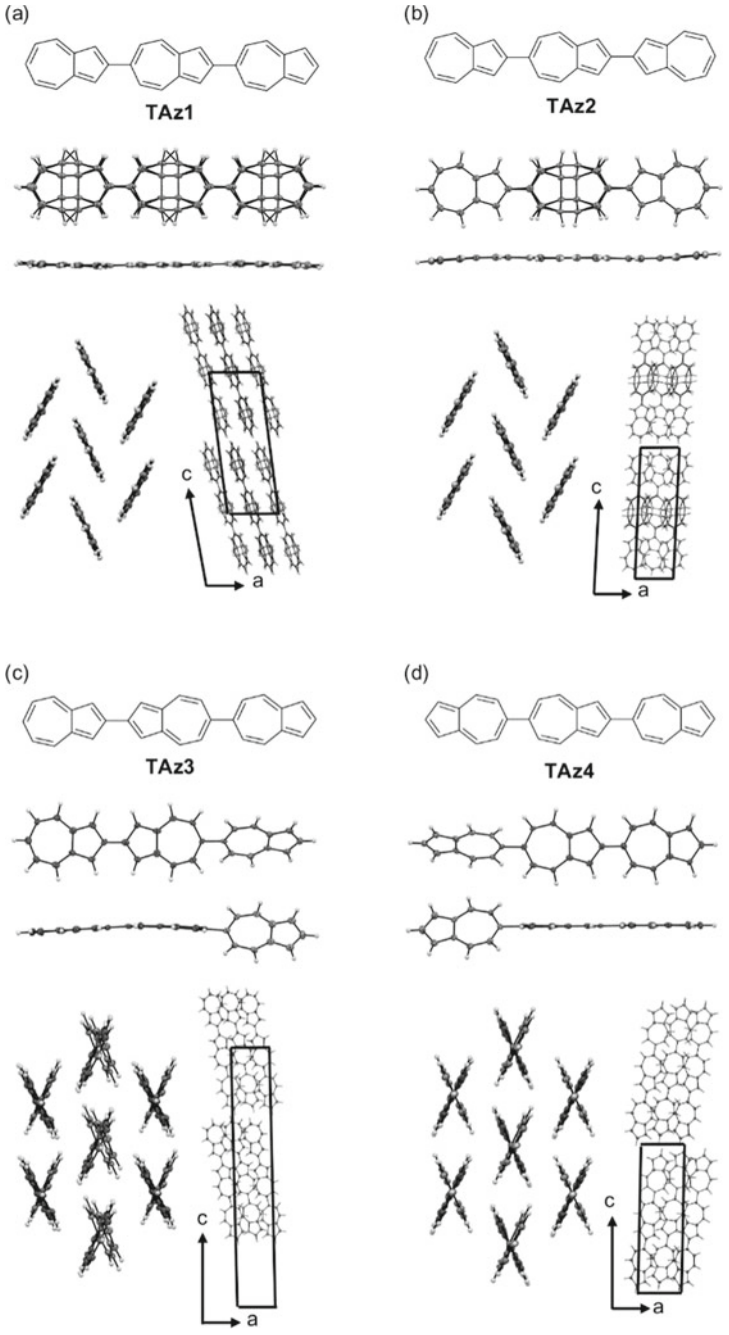

Fig. 17.8 Crystal packing structures of **a** TAz1, **b** TAz2, **c** TAz3, and **d** TAz4. Reproduced from Ref. [26] with permission. Copyright 2015 American Chemical Society

Table 17.1 Optical properties of terazulene isomers TAz1, TAz2, TAz3, and TAz4 in their film forms

Compound	λ_{onset} (nm)	$E^{a}_{g\text{-}abs}$ (eV)	HOMO[b] (eV)	LUMO[c] (eV)
TAz1	757	1.63	−5.56	−3.93
TAz2	764	1.62	−5.45	−3.83
TAz3	785	1.57	−5.47	−3.90
TAz4	795	1.56	−5.49	−3.93

[a]Determined from the absorption edge
[b]Determined by photoemission yield spectroscopy (PYS)
[c]LUMO energies calculated by adding the optical band gap (Eg-abs) to the HOMO energy

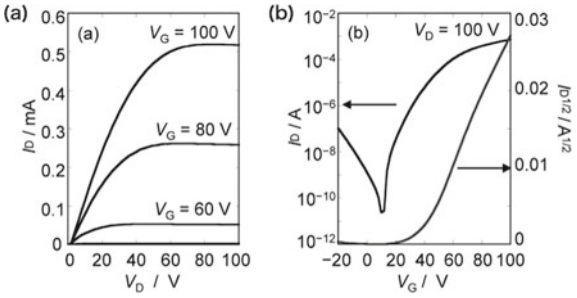

Fig. 17.9 OFET characteristics of top-contact devices fabricated with 2,6′:2′,6″-terazulene (TAz1) at $T_{sub} = 100$ °C, **a** output curves at various gate voltages, **b** transfer curves in the saturated region at a drain voltage of −100 V. Reproduced from Ref. [25] with permission. Copyright 2013 American Chemical Society

Grazing incidence wide-angle X-ray diffraction (GIWAXD) analysis of their thin films confirmed the end-on orientation of each molecule on the substrate and their in-plane herringbone structures (Fig. 17.10). The simulated GIWAXD profiles of TAz1–TAz4 based on their single-crystal structures are in good agreement with the experimental results, suggesting that the crystal structures of the thin films are almost identical to the structures of the single crystals. In-house XRD also revealed the well-defined crystalline characteristics of the TAz1–TAz4 thin films (Fig. 17.11); the out-of-plane XRD patterns show a series of peaks that are clearly assignable to (00*l*) reflections, while the in-plane XRD patterns of the terazulene isomers clearly show three typical peaks assignable to π-stacking orientations [(11*l*), (02*l*), (12*l*)] associated with the herringbone structures. The profiles and peak intensities were observed to gradually improve with increasing substrate temperature, T_{sub}.

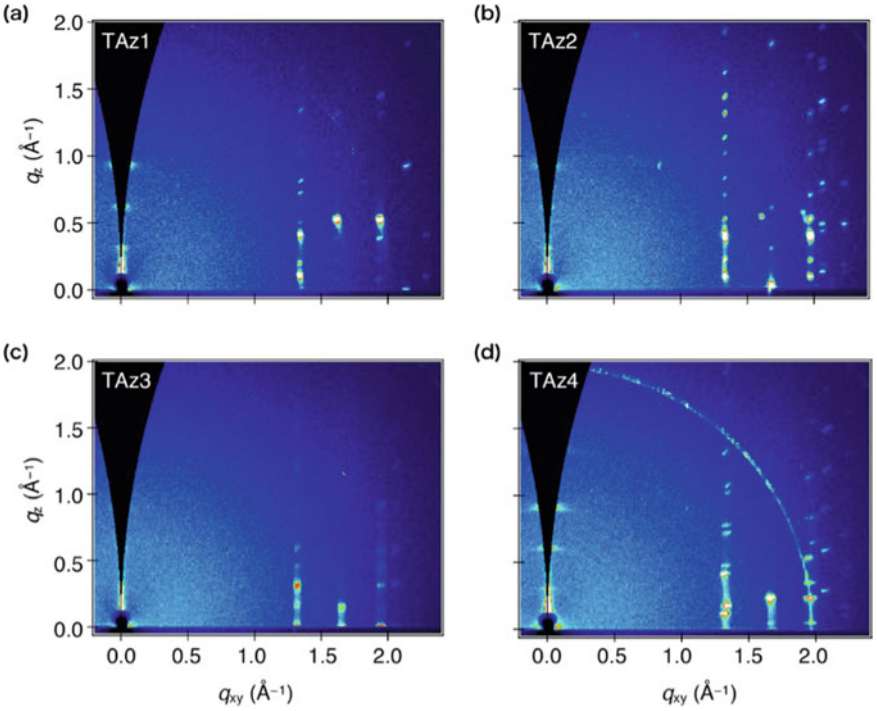

Fig. 17.10 2D GIXD images of evaporated thin films of **a** TAz1, **b** TAz2, **c** TAz3, and **d** TAz4 deposited onto ODTS-treated Si/SiO_2 at $T_{sub} = 100\,°C$. Reproduced from Ref. [26] with permission. Copyright 2015 American Chemical Society

17.4.5 Controlling OFET Polarity by Controlling the Molecular Orbital Distribution

The calculated molecular orbitals of the terazulene isomers are shown in Fig. 17.12. The LUMO of each isomer is favorably structured for electron transport because it is distributed over the entire molecule. On the other hand, the HOMOs are biased toward one of the ends of the TAz1 and TAz4 molecules, but are more distributed in TAz2 and TAz3. In other words, HOMO molecular overlap is disadvantageous for the hole transport in TAz1 and TAz4; hence, only n-type character was observed as a result. On the other hand, hole transport between molecules is possible in TAz2 and TAz3; hence, ambipolar behavior that combines both p-type and n-type character is observed. We refer to this concept as "polarity control of OFET by molecular orbital distribution control."

The molecular orbital features of the terazulene isomers are rationalized as follows. The LUMO of azulene itself shows high orbital densities at its 2- and 6-positions, which leads to strong coupling between the three azulene LUMOs in terazulene. Consequently, the LUMOs of the terazulene isomers are uniform and

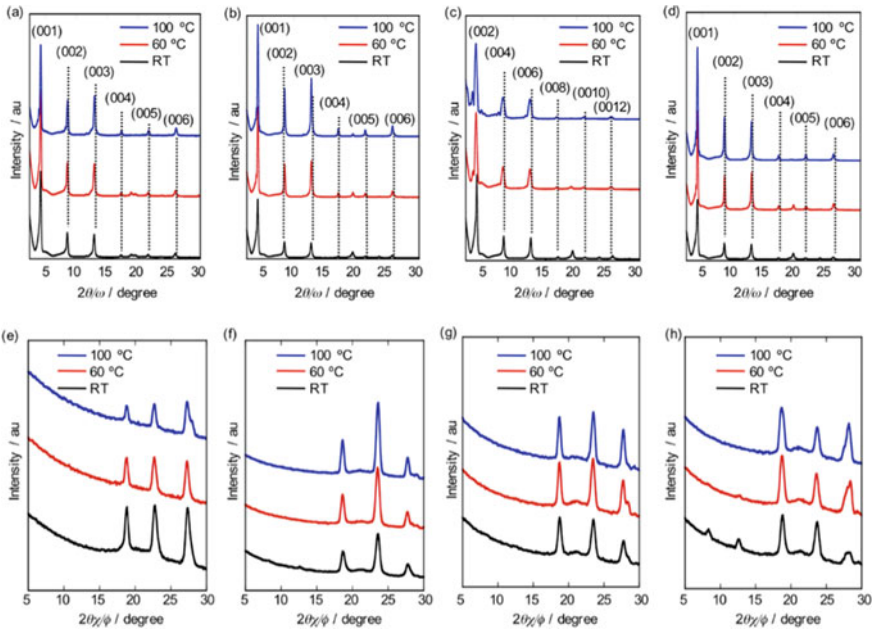

Fig. 17.11 XRD patterns of evaporated thin films of TAz1–TAz4 deposited onto ODTS-treated Si/SiO_2 substrates at different substrate temperatures. Out-of-plane X-ray diffraction patterns of **a** TAz1, **b** TAz2, **c** TAz3, and **d** TAz4. In-plane X-ray diffraction patterns of **e** TAz1, **f** TAz2, **g** TAz3, and **h** TAz4. Reproduced from Ref. [26] with permission. Copyright 2015 American Chemical Society

widely distributed over the three azulene units. In contrast, the HOMO of azulene itself has no orbital density at the 2- and 6-positions; consequently, coupling between the three HOMOs in each terazulene is weak. As a result, the three highest orbitals of terazulene, which are formed from the three HOMOs of the individual azulenes, are distributed in their respective azulene units. In the absence of conjugation, these three orbitals are degenerate and equally occupied. However, each terazulene has a dipole moment that creates an electrostatic potential gradient in the molecule and eliminates this degeneracy. Quantum chemical calculations reveal that the magnitude of the dipole moment of the terazulene isomer and the energy difference between the occupied orbitals and the orbital bias are correlated; TAz1, with the largest dipole moment shows the largest energy difference and orbital bias (Fig. 17.13). In other words, the dipole moment solves the occupied-orbital degeneracy issue, which leads to orbital deviations.

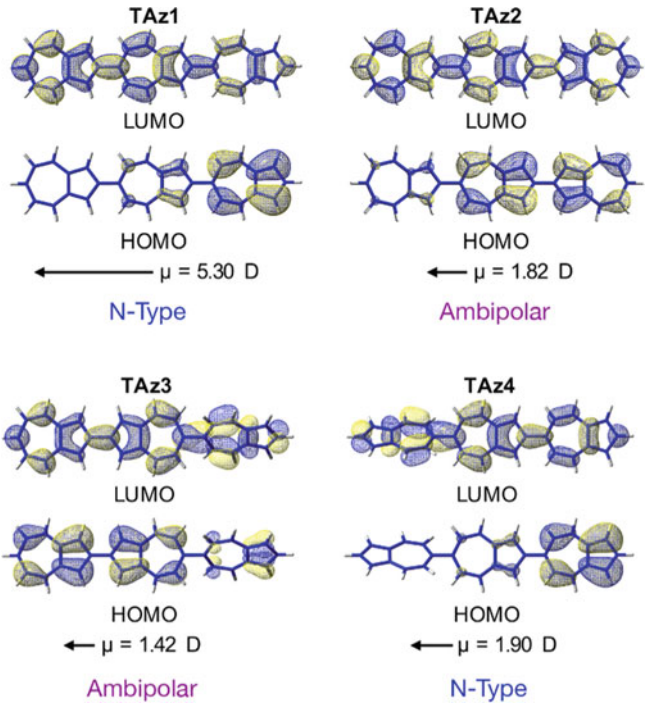

Fig. 17.12 Calculated frontier orbitals and dipole moments of TAz1, TAz2, TAz3, and TAz4 at the B3LYP/6-31G(d) level, and experimental semiconductor type

17.5 Conclusions and Scope

In this chapter, the usefulness of azulene as a unit for extending the π-conjugation of an organic semiconducting material was clarified. π-Conjugated systems linearly extended through the 2- and 6-positions of azulene are greatly advantageous for OFET applications from the perspectives of their electronic and crystal structures. It is significant that azulene, which has been developed through solution chemistry, has been applied to organic crystalline materials, especially the terazulene isomers, for which significant correlations have been recognized in their crystal structures, in the orbital interactions between units, their dipole moments, and semiconductor properties. A new synthetic method has recently been developed; consequently, it has recently become possible to efficiently introduce substituents at the 2- and 6-positions of azulene. In addition, the use of organic semiconducting materials as organic solid materials is also developing in recent years [32–38]. Together with developments in synthetic chemistry, π-conjugated systems based on azulene are expected to significantly progress in the future.

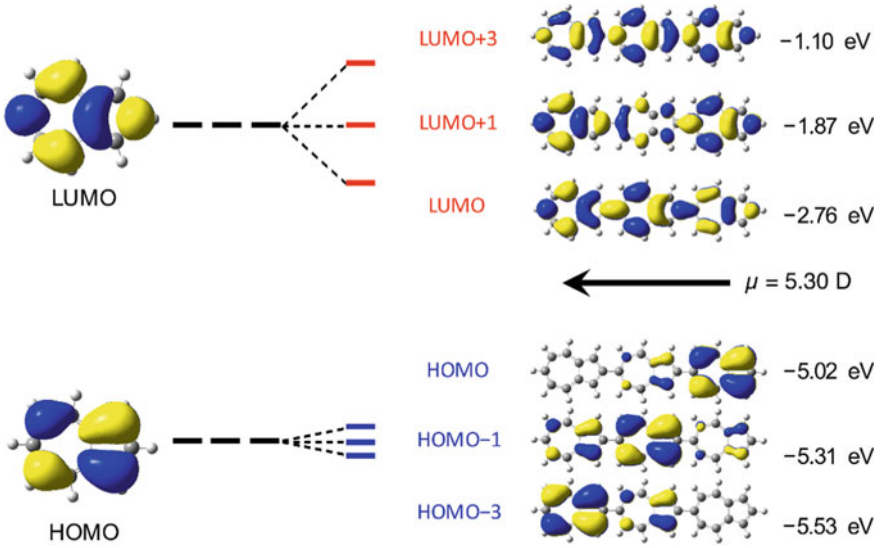

Fig. 17.13 Schematic representations of the molecular orbital distributions and energy levels in **TAz1**. The calculation was performed at B3LYP/6-31G(d) level. Reproduced from Ref. [25] with permission. Copyright 2013 American Chemical Society

Acknowledgements This study was supported by Grant-in-Aid for Young Scientist (B) (25870076 to H.K.) and for Scientific Research (C) (18K05071 to H.K.) from the Ministry of Education, Culture, Sports, Science and Technology (MEXT), and YU-COE (M) program from Yamagata University (M30-5 to H.K.).

References

1. Kurotobi, K., Kim, K.S., Noh, S.B., Kim, D., Osuka, A.: A quadruply azulene-fused porphyrin with intense near-IR absorption and a large two-photon absorption cross section. Angew. Chem. Int. Ed. **45**, 3944–3947 (2006)
2. Muranaka, A., Yonehara, M., Uchiyama, M.: Azulenocyanine: a new family of phthalocyanines with intense near-IR absorption. J. Am. Chem. Soc. **132**, 7844–7845 (2010)
3. Tang, T., Lin, T., Wang, F., He, C.: Azulene-based conjugated polymers with tuneable near-IR absorption up to 2.5 μm. Polym. Chem. **5**, 2980–2984 (2014)
4. Zhang, X.-H., Li, C., Wang, W.-B., Cheng, X.-X., Wang, X.-S., Zhang, B.-W.: Photophysical, electrochemical, and photoelectrochemical properties of new azulene-based dye molecules. J. Mater. Chem. **17**, 642–649 (2007)
5. Cowper, P., Pockett, A., Kociok-Köhn, G., Cameron, P.J., Lewis, S.E.: Azulene - thiophene - cyanoacrylic acid dyes with donor-π-acceptor structures. Synthesis, characterisation and evaluation in dye-sensitized solar cells, Tetrahedron **74**, 2775–2786 (2018)
6. Thanh, N.C., Ikai, M., Kajioka, T., Fujikawa, H., Taga, Y., Zhang, Y., Ogawa, S., Shimada, H., Miyahara, Y., Kuroda, S., Oda, M.: Synthesis of N, N, N′, N′-tetrasubstituted 1,3-bis(4-aminophenyl)azulenes and their application to a hole-injecting material in organic electroluminescent devices. Tetrahedron **62**, 11227–11239 (2006)

7. Smits, E.C.P., Setayesh, S., Anthopoulos, T.D., Buechel, M., Nijssen, W., Coehoorn, R., Blom, P.W.M., de Boer, B., de Leeuw, D.M.: Near-infrared light-emitting ambipolar organic field-effect transistors. Adv. Mater. **19**, 734–738 (2007)
8. Wöbkenberg, P.H., Labram, J.G., Swiecicki, J.-M., Parkhomenko, K., Sredojevic, D., Gisselbrecht, J.-P., de Leeuw, D.M., Bradley, D.D.C., Djukic, J.-P., Anthopoulos, T.D.: Ambipolar organic transistors and near-infrared phototransistors based on a solution-processable squarilium dye. J. Mater. Chem. **20**, 3673–3680 (2010)
9. Michl, J., Thulstrup, E.W.: Why is azulene blue and anthracene white? A simple mo picture. Tetrahedron **32**, 205–209 (1976)
10. Lemal, D.M., Goldman, G.D.: Synthesis of azulene, a blue hydrocarbon. J. Chem. Educ. **65**, 923–933 (1988)
11. Murai, M., Amir, E., Amir, R.J., Hawker, C.J.: Azulene-based conjugated polymers: unique seven-membered ring connectivity leading to stimuli-responsiveness. Chem. Sci. **3**, 2721–2725 (2012)
12. Amir, E., Murai, M., Amir, R.J., Chabinyc, M.L., Chabinyc, M.L., Hawker, C.J.: Conjugated oligomers incorporating azulene building blocks—seven—versus five-membered ring connectivity. Chem. Sci. **5**, 4483–4489 (2014)
13. Shevyakov, S.V., Li, H., Muthyala, R., Asato, A.E., Croney, J.C., Jameson, D.M., Liu, R.S.H.: Orbital control of the color and excited state properties of formylated and fluorinated derivatives of azulene†. J. Phys. Chem. A **107**, 3295–3299 (2003)
14. Shoji, T., Maruyama, A., Araki, T., Ito, S., Okujima, T.: Synthesis of 2- and 6-thienylazulenes by palladium-catalyzed direct arylation of 2- and 6-haloazulenes with thiophene derivatives. Org. Biomol. Chem. **13**, 10191–10197 (2015)
15. Anthony, J.E.: Functionalized acenes and heteroacenes for organic electronics. Chem. Rev. **106**, 5028–5048 (2006)
16. Mei, J., Diao, Y., Appleton, A.L., Fang, L., Bao, Z.: Integrated materials design of organic semiconductors for field-effect transistors. J. Am. Chem. Soc. **135**, 6724–6746 (2013)
17. Dong, H., Fu, X., Liu, J., Wang, Z., Hu, W.: 25th anniversary article: key points for high-mobility organic field-effect transistors. Adv. Mater. **25**, 6158–6183 (2013)
18. Gavezzotti, A., Desiraju, G.R.: A systematic analysis of packing energies and other packing parameters for fused-ring aromatic hydrocarbons. Acta Crystallogr., Sect. B: Struct. Sci. **44**, 427–434 (1988)
19. Desiraju, G.R., Gavezzotti, A.: Crystal structures of polynuclear aromatic hydrocarbons. Classification, rationalization and prediction from molecular structure. Acta Crystallogr., Sect. B: Struct. Sci. **45**, 473–482 (1989)
20. Nozoe, T., Seto, S., Matsumura, S., Asano, T.: Synthesis of azulene derivatives from troponoids and cyanoacetic ester. Proc. Japan Acad. **32**, 339–343 (1956)
21. Nozoe, T., Seto, S., Matsumura, S.: Synthesis of 2-substituted azulenes by nucleophilic substitution reactions of 2-haloazulene derivatives. Bull. Chem. Soc. Jpn **35**, 1990–1998 (1962)
22. Tian, H.K., Shi, J.W., He, B., Hu, N.H., Dong, S.Q., Yan, D.H., Zhang, J.P., Geng, Y.H., Wang, F.S.: Naphthyl and thionaphthyl end-capped oligothiophenes as organic semiconductors: effect of chain length and end-capping groups. Adv. Funct. Mater. **17**, 1940–1951 (2007)
23. Nicolas, Y., Blanchard, P., Roncali, J., Allain, M., Mercier, N., Deman, A.-L., Tardy, J.: Synthesis of a thermally stable hybrid acene-thiophene organic semiconductor via a soluble precursor. Org. Lett. **7**, 3513–3516 (2005)
24. Yamaguchi, Y., Maruya, Y., Katagiri, H., Nakayama, K.-I., Ohba, Y.: Synthesis, properties, and OFET characteristics of 5,5′-Di(2-azulenyl)-2,2′-bithiophene (DAzBT) and 2,5-Di(2-azulenyl)-thieno[3,2- b]thiophene (DAzTT). Org. Lett. **14**, 2316–2319 (2012)
25. Yamaguchi, Y., Ogawa, K., Nakayama, K.-I., Ohba, Y., Katagiri, H.: Terazulene: a high-performance n-type organic field-effect transistor based on molecular orbital distribution control. J. Am. Chem. Soc. **135**, 19095–19098 (2013)
26. Yamaguchi, Y., Takubo, M., Ogawa, K., Nakayama, K.-I., Koganezawa, T., Katagiri, H.: Terazulene isomers: polarity change of OFETs through molecular orbital distribution contrast. J. Am. Chem. Soc. **138**, 11335–11343 (2016)

27. Ito, S., Kubo, T., Morita, N., Matsui, Y., Watanabe, T., Ohta, A., Fujimori, K., Murafuji, T., Sugihara, Y., Tajiri, A.: Preparation of azulenyllithium and magnesium reagents utilizing halogen–metal exchange reaction of several iodoazulenes with organolithium or magnesium ate complex. Tetrahedron Lett. **45**, 2891–2894 (2004)
28. McDonald, R.N., Richmond, J.M., Curtis, J.R., Petty, H.E., Hoskins, T.L., Tajiri, A.: Nonbenzenoid aromatic systems. XII. Synthesis of 2-, 3-, and 6-substituted 2-(1-azulyl)ethanols and their tosylate esters. J. Org. Chem. **41**, 1811–1821 (1976)
29. Kurotobi, K., Tabata, H., Miyauchi, M., Murafuji, T., Sugihara, Y.: Coupling reaction of azulenyl-4,4,5,5-tetramethyl-1,3,2-dioxaborolanes with haloazulenes. Synthesis **2002**, 1013–1016 (2002)
30. Robinson, R.E., Holovics, T.C., Deplazes, S.F., Powell, D.R., Lushington, G.H., Thompson, W.H., Barybin, M.V.: Five possible isocyanoazulenes and electron-rich complexes thereof: a quantitative organometallic approach for probing electronic inhomogeneity of the azulenic framework. Organometallics **24**, 2386–2397 (2005)
31. Saitoh, M., Yano, J., NAKAZAWA, T., Sugihara, Y., Hashimoto, K.: Voltammetric behavior and electronic molecular structures of several azulenylketones. J. Electroanal. Chem. **418**, 139–145 (1996)
32. Yao, J., Cai, Z., Liu, Z., Yu, C., Luo, H., Yang, Y., Yang, S., Zhang, G., Zhang, D.: Tuning the semiconducting behaviors of new alternating dithienyldiketopyrrolopyrrole-azulene conjugated polymers by varying the linking positions of azulene. Macromolecules **48**, 2039–2047 (2015)
33. Xin, H., Ge, C., Yang, X., Gao, H., Yang, X., Gao, X.: Biazulene diimides: a new building block for organic electronic materials. Chem. Sci. **7**, 6701–6705 (2016)
34. Xin, H., Ge, C., Jiao, X., Yang, X., Rundel, K., McNeill, C.R., Gao, X.: Incorporation of 2,6-connected azulene units into the backbone of conjugated polymers: towards high-performance organic optoelectronic materials. Angew. Chem. Int. Ed. **57**, 1322–1326 (2017)
35. Xin, H., Li, J., Ge, C., Yang, X., Xue, T., Gao, X.: 6,6′-diaryl-substituted biazulene diimides for solution-processable high-performance n-type organic semiconductors. Mater. Chem. Front. **2**, 975–985 (2018)
36. Umeyama, T., Watanabe, Y., Miyata, T., Imahori, H.: Electron-rich five-membered ring of azulene as a donor unit in donor-acceptor alternating copolymers for polymer solar cell applications. Chem. Lett. **44**, 47–49 (2015)
37. Nishimura, H., Ishida, N., Shimazaki, A., Wakamiya, A., Saeki, A., Scott, L.T., Murata, Y.: Hole-transporting materials with a two-dimensionally expanded π-system around an azulene core for efficient perovskite solar cells. J. Am. Chem. Soc. **137**, 15656–15659 (2015)
38. Truong, M.A., Lee, J., Nakamura, T., Seo, J.Y., Jung, M., Ozaki, M., Shimazaki, A., Shioya, N., Hasegawa, T., Murata, Y., Zakeeruddin, S.M., Grätzel, M., Murdey, R., Wakamiya, A.: Influence of alkoxy chain length on the properties of two-dimensionally expanded azulene-core-based hole-transporting materials for efficient perovskite solar cells. Chem. Eur. J. **25**, 6741–6752 (2019)

Chapter 18
Electrochemical Functions of Nanostructured Liquid Crystals with Electronic and Ionic Conductivity

Masahiro Funahashi

Abstract Nanosegregated liquid crystals are effective to construct nanostructures in which an electronic function couples with an ionic transport. Polarization of ionic species can form local electric fields interacting with electronic charges. In electrochromism, an electrical double layer promotes charge injection from an anode or cathode to an active layer in which the injected charges are transported efficiently, due to the nanostructures of the liquid crystal phase. In chemical doping, dopant ions are accumulated in ion-conductive subdomains and separated from the electron transport channels. This type of the doping is interstitial doping which is different from substitutional doping observed in organic molecular crystals. Side-chain engineering is effective for construction of the nanosegregated liquid crystal phases. Imidazolium units connected to the terminal of alkyl chains of liquid crystalline oligothiophene derivatives promote formation of the nanosegregated structure in which ion-conductive and hole-transporting layers are integrated alternately. Oligosiloxane moieties have a liquid-like property although they induce nanosegregation in liquid crystal phases. Perylene bisimide derivatives bearing oligosiloxane moieties exhibit high solubilities in organic solvents and columnar phases at room temperature. Perylene bisimide derivative bearing two cyclotetrasiloxane rings and one triethylene oxide chain works as a mixed conductor. Polymerized thin films display electrochromism in organic electrolyte solutions and anisotropic electrical conductivity in the doped states.

Keywords Liquid crystalline semiconductor · Nanosegregation · Oligosiloxane · Electrochromism · Interstitial doping · Perylene bisimide · Oligothiophene

M. Funahashi (✉)
Department of Advanced Materials Science, Faculty of Engineering and Design, Kagawa University, 2217-20 Hayashi-cho, Takamatsu, Kagawa 761-0396, Japan
e-mail: m-funa@eng.kagawa-u.ac.jp

Health Research Institute, National Institute of Advanced Industrial Science and Technology, 2217-14 Hayashi-cho, Takamatsu, Kagawa 761-0395, Japan

M. Sakamoto and H. Uekusa (eds.), *Advances in Organic Crystal Chemistry*,
https://doi.org/10.1007/978-981-15-5085-0_18

18.1 Introduction

Molecular crystals consisting of molecules with extended π-conjugated units function as semiconductors, and they have been applied to organic electronic devices, such as field-effect transistors (FETs). Electronic charge carriers are transported between π-conjugated units via orbital overlaps and carrier mobilities strongly depend upon the supramolecular aggregation states of the crystals [1]. In addition, liquid crystals having extended π-conjugated units also work as semiconductors and applications to FETs, electroluminescence devices, and solar cells [2].

The theme of this chapter is to create new soft materials to couple of the electronic charge carrier transport with ionic polarization in nanosegregated liquid crystalline (LC) systems [3]. In contrast to molecular crystals, most characteristic feature of liquid crystals is a soft dynamic structure [4]. In liquid crystal materials, functional domains can be integrated in liquid crystal phases based on nanosegregation to produce multi-functional systems [5]. Aggregates of electro- and redox-active π-conjugated units and hydrophilic mantles are self-assembled in columnar or lamellar orders to form soft mixed conductors. In mixed conductors, ionic species polarize to form local electric fields interacting with electronic charge carriers by the application of the external DC bias, resulting in electro- and redox-active functions of the materials [6].

For this purpose, 'side chain engineering' is indispensable [7]. Electro- and redox-active materials have extended π-conjugated systems, which indicate strong π–π stacking interaction. In order to maintain the solubility and flexibility of thin films, rigid active units should be connected to flexible side chains. Moreover, the side chains also promote nanosegregation to form flexible nanostructures to induce electronic and electrochemical functions. The author found that oligosiloxane moieties do not only increase solubilities of LC materials but also promote formation of nanostructures to enhance electronic and electrochemical functions [8].

In the electrochromism, the electrical double layers formed at the cathode and anode promote hole or electron injection in the active layer, resulting in reduction or oxidation of the redox-active units [9]. Thin films of crystals have no nanopores through which ionic species penetrate and polarization based on the formation of electrical double layers therefore does not occur. In contrast, thin films of the nanostructured LC mixed conductors have nanochannels, in which ionic species are mobile. By the DC bias application in the presence of electrolytes, electrical double layers are immediately formed.

In the doping of nanostructured π-conjugated liquid crystals, ionic reductants diffuse through the ion channels of the LC thin films and reduce the electron deficient π-conjugated cores to increase the electron density. Dopant ions are separated from the electron-transporting π-stacks, and this polarized structure is categorized as an interstitial doping [10]. This is quite different from the substitution doping in the organic molecular crystals in which dopant molecules occupy the lattice points of the host crystals [11].

18.2 Electrochromism in Ionic π-Conjugated Liquid Crystals

In conventional electrochromism of organic materials, an organic thin film is dipped in an electrolyte solution, and a DC bias is applied to the thin film. Ionic species penetrate into the film, and an electrical double layer is produced at the interface between the organic layer and the electrode. Positive or negative charges are injected to the organic layer by the electric field formed at the interface, and consequently, colored cationic or anionic species are produced [9].

For a high-speed electrochromic process, fast ion diffusion in the thin films and efficient charge transfer from the electrode to the organic layer are indispensable. Moreover, effective charge carrier transport should make it possible to involve the active molecules separated from the electrode [12].

For this purpose, we designed nanosegregated LC mixed conductors; the molecules consist of an electro- and redox-active π-conjugated unit as well as an ionic moiety, as shown in Fig. 18.1. A phenylterthiophene moiety was adopted as a π-conjugated unit, and an imidazolium moiety was introduced at the terminal position of the alkyl side chain [13, 14].

These compounds exhibit a smectic A (SmA) phase at elevated temperatures. Figure 18.2a shows an X-ray diffraction pattern of the SmA phase of compound **3** and schematic illustration for the structure of the SmA phase. The X-ray diffraction pattern in the SmA phase suggested an anti-parallel arrangement of the LC molecules. Hole-transporting sublayers made from phenylterthiophene units as well as ion-conductive sublayers consisting of imidazolium cations and counter-anions are integrated alternately in the SmA phase, as shown in Fig. 18.2b.

Compound **3** was capillary filled into a LC cell consisting of two ITO-coated glass plates at the temperature of the isotropic liquid phase, and the sample was cooled to 100 °C. The sample changed to the SmA phase. When a DC bias was

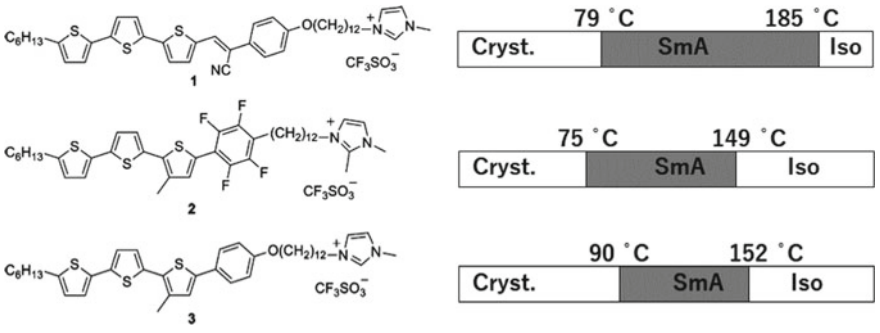

Fig. 18.1 Molecular structures of LC phenylterthiophene derivatives bearing imidazolium moieties. The abbreviations 'Cryst.', 'SmA', and 'Iso' are crystal, smectic A, and isotropic phases, respectively

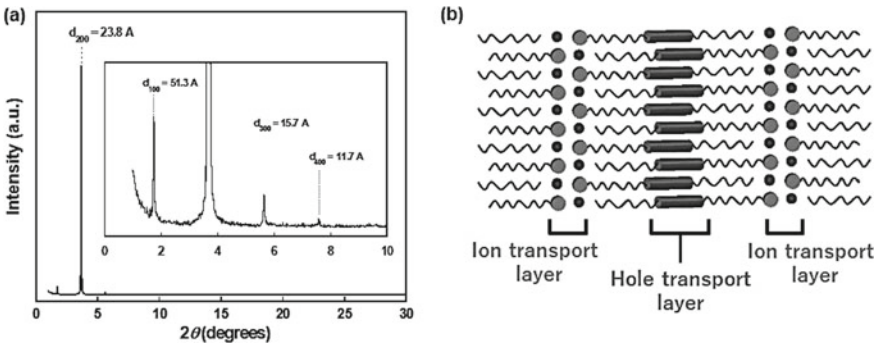

Fig. 18.2 **a** X-ray diffraction pattern in the SmA phase (100 °C) of compound **3**, **b** schematic illustration for the molecular aggregation structure of the SmA phase of compound **3**. Reprinted with the permission from Ref. [13]. Copyright 2008 American Chemical Society

applied to the sample, the color of the sample changed from yellow to dark blue (Fig. 18.3a). This color change was attributed to the formation of cation radical of the phenylterthiophene unit by the electrochemical oxidation at the anode.

Because of the presence of the ion-conductive layers, counter-anions immediately moved to the anode to form the electrical double layer. Subsequently, holes are injected to the hole-transporting sublayers, generating cation radicals of phenylterthiophene units. It should be noted that an electrolyte solution is not necessary unlike conventional organic electrochromic materials.

The response speed was enhanced when PEDOT-PSS thin layer was coated on the cathode because the oxidation of the π-conjugated unit of the LC molecules at the anode coupled with the reduction of doped PEDOT coated on the cathode. Figure 18.3b shows the electrochromic response in the SmA phase of compound **3** at 100 °C. Response speed was several ms, which should be attributed to rapid

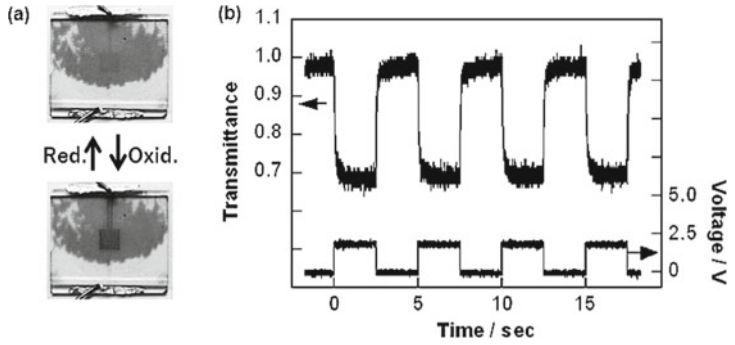

Fig. 18.3 **a** Color change of the sample in the SmA phase of compound **3** when DC bias (+1.5 V) was applied, **b** electrochromic response at 100 °C in the sample in which PEDOT/PSS layer was coated on the anode. Reprinted with the permission from Ref. [14]. Copyright 2010 American Chemical Society

formation of electrical double layers, due to the presence of the ion-conductive layers. Moreover, hole hopping between the π-conjugated units made it possible to oxidize distant LC molecules from the anode.

18.3 Nanosegregated π-Conjugated Liquid Crystals

18.3.1 Oligosiloxane Moieties as a Side Chain of Liquid Crystals

As shown in Sect. 18.2, nanosegregation is an effective method to functionalize LC materials by coupling the electronic transport with the ionic conductivity. An ionic moiety introduced to the terminal of the alkyl side chain played a significant role in the nanosegregation process. This fact indicates that not only a design of π-conjugated functional units but also an engineering of side chains is effective to create new functional LC materials.

Conventional liquid crystal molecules have rigid core units and flexible alkyl side chains. One of the driving forces to form smectic or columnar structures is nanosegregation between core units and alkyl side chains. Other than alkyl side chains, hydrophilic oligoethylene oxide chains, perfluoroalkyl groups with small polarizability are recognized to enhance nanosegregation and promote the formation of various superstructures in liquid crystal phases [15, 16]. Moreover, liquid crystals bearing ionic moieties such as imidazolium groups form ion-conductive liquid crystals which have one-dimensional columnar, two-dimensional lamellar, and three-dimensional bicontinuous cubic structures [17–19].

The authors have paid an attention to oligosiloxane chains as a flexible side chain of functional liquid crystals. Side-chain-type LC polymers consisting of a polysiloxane backbone and mesogenic side chains have been investigated for the application to LC elastomers [20]. Polysiloxanes bearing terthiophene side chains exhibit photoconductivity [21].

On the other hand, ferroelectric liquid crystals bearing pentamethyl-1,3-disiloxane or heptamethyl-1,3,5-trisiloxane chains at the terminals of alkyl side chains have also been synthesized. Because of nanosegregation, layer structures are stabilized and they sometimes indicate de Vries-type phase transition [22]. For rod-like liquid crystal molecules exhibiting smectic phases, not a few liquid crystals have been designed and synthesized. However, the advantage of oligosiloxane side chains has not been took for columnar liquid crystals except for only one example of hexaalokoxytriphenylene derivative [23].

The perylene bisimide derivatives have been known as red pigments and n-type semiconductors. Various *N*-alkylated derivatives have been synthesized; however, their solubilities in organic solvents are low and it is difficult to produce thin films for device applications by solution processes. We synthesized perylene bisimide derivatives bearing oligosiloxane chains at the terminals of alkyl side chains, as

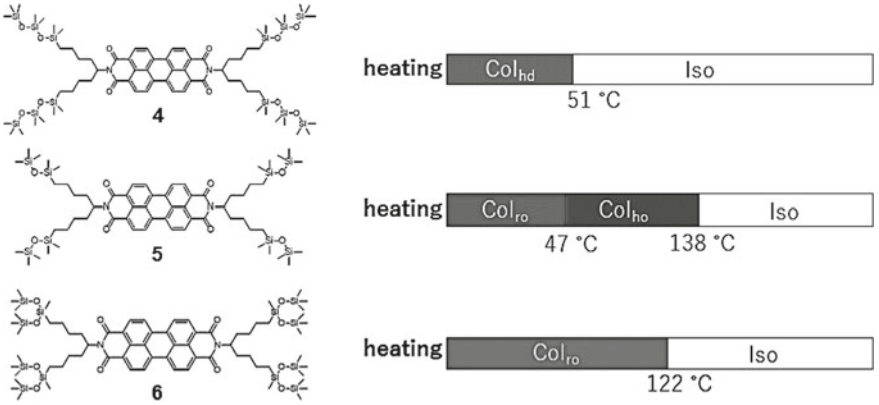

Fig. 18.4 Molecular structures of LC perylene bisimide derivatives bearing oligosiloxane chains and their phase transition temperatures. Col_{hd}, Col_{ho}, and Col_{ro} denote a columnar hexagonal disordered, columnar hexagonal ordered, and columnar rectangular ordered phase, respectively

shown in Fig. 18.4. Compounds **4**–**6** exhibit columnar phases over wide temperature ranges including room temperature and do not crystallize even when they are cooled to −100 °C [24–26].

Figure 18.5a shows X-ray diffraction patterns of compounds **4** and **5**. In columnar phases, the lattice constants were shorter than the molecular lengths, suggesting interdigitation of the oligosiloxane moieties. Interestingly, oligosiloxane chains stabilize the columnar structures because of nanosegregation in spite of the bulkiness of the oligosiloxane chains, compared to that of alkyl chains. These compounds exhibit ordered columnar phases in which the perylene bisimide cores stack periodically. The intermolecular distance within the columnar aggregates is 3.4 Å, which is a typical value for π–π stacking. Figure 18.5b displays a schematic illustration for the columnar phase of these compounds. Crystal-like one-dimensional π-stacks are surrounded by liquid-like mantle consisting of oligosiloxane moieties.

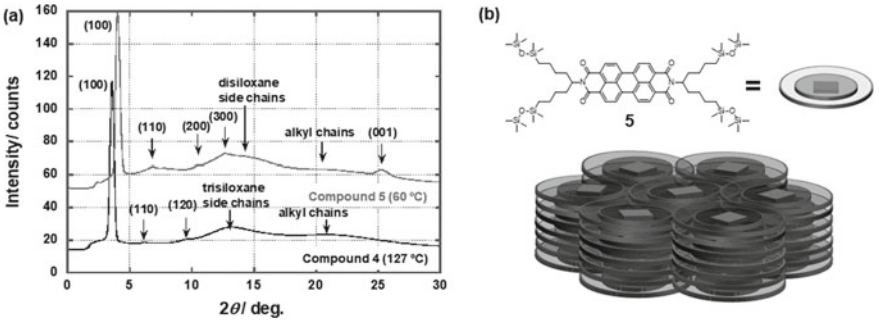

Fig. 18.5 **a** X-ray diffraction pattern of compounds **4** and **5** at room temperature, **b** schematic illustration of the columnar phase

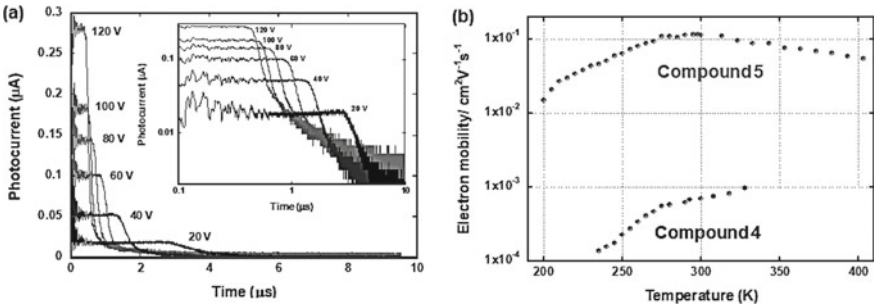

Fig. 18.6 **a** Transient photocurrent curves for electrons in the columnar ordered phase of compound **5** at room temperature. The sample thickness was 25 μm, and the wavelength of excitation light was 356 nm, **b** electron mobilities of compounds **4** and **5** as a function of the temperature. Reproduced from Ref. [27] with permission from the PCCP Owner Societies

Figure 18.6a shows transient photocurrent curves for electrons in the columnar phase of compound **5** at room temperature. Time-of-flight measurement revealed the high electron mobility exceeding 0.1 $cm^2\ V^{-1}\ s^{-1}$ at room temperature in the ordered columnar phases of these compounds [27]. This value is comparable to those of molecular crystals. This high electron mobility in the columnar phases should be attributed to the crystal-like π-stacks. As shown in Fig. 18.6b, the electron mobility of compound **5** was two orders of magnitude higher than that of compound **4** which exhibited a columnar phase without a periodical π–π stacking structure. In spite of these crystal-like structures, solubilities of these compounds in organic solvents are very high. For compound **5**, the solubility even in *n*-hexane exceeds 30 wt%. Therefore, thin films can be produced by solution processes, such as a spin-coating method.

18.3.2 Cyclotetrasiloxane Moiety as a Polymerizable Side Chain

Insolubilization of organic thin films is very significant for construction of multilayer structures. Particularly, in electrochemical applications, insolubilization of thin films is indispensable because they are dipped in organic electrolyte solutions.

In situ polymerization of LC films is an effective method to retain the macroscopic molecular alignments of the LC thin films as well as nanosegregated structures. The conventional in situ insolubilization of thin film states has been photopolymerization using LC materials bearing acrylate, methacrylate, 1,4-diene moieties [28, 29]. Nanostructured ion-conductive LC films were insolubilized by the UV light illumination [28]. Uniaxially aligned nematic LC films consisting of extended π-conjugated chromophores were polymerized by the UV light illumination and applied to electroluminescence devices [29]. Not only macroscopic molecular alignment but also

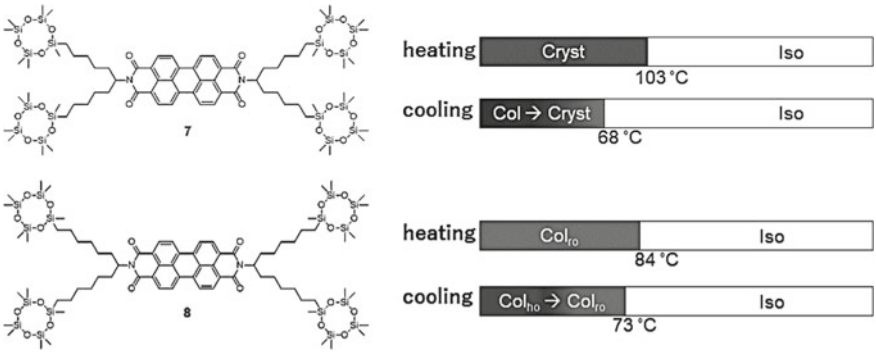

Fig. 18.7 Molecular structures of perylene bisimide derivatives bearing cyclotetrasiloxane rings and their phase transition property

nanosegregated structures were retained during the photopolymerization process. However, terminal polymerizable groups sometimes inhibit the formation of LC phases and do not increase solubility sufficiently.

Cyclotetrasiloxane moieties polymerize in the presence of an acid or base catalyst in solution states. However, they are inactive to UV light illumination and the photopolymerization method could not be adopted.

We synthesized perylene bisimide derivatives **7** and **8** which have four cyclotetrasiloxane rings at the terminals of alkyl chains (Fig. 18.7). The cyclotetrasiloxane ring is very bulky compared to conventional alkyl side chains; nevertheless, these compounds exhibit columnar phases at room temperature [30].

TOF measurements revealed a high electron mobility exceeding 0.1 cm^2/Vs in the columnar phase of compound **8** at room temperature. In spite of the presence of the bulky cycloterasiloxane rings, π-conjugated units are closely organized and form crystal-like order in the columnar phase.

The solubilities of these compounds are very high (>30 wt% for *n*-hexane), and thin films could be produced by the spin-coating method. On non-treated glass substrates, thin films with polydomain structures were produced. The domain size was around several ten μm and columnar aggregates aligned parallel to the surface of the substrates because of the surface tension at the air-solution interface.

Compound **8** polymerized in solution states in the presence of acid catalysts to form gelatinous precipitates. However, the precipitates were not soluble in organic solvents and thin films could not be produced. Figure 18.8a displays a schematic illustration of the in situ polymerization of the spin-coated film of compound **8**. The spin-coated thin films can be insolubilized by an exposure on acid vapors at 70 °C. The polymerization in the thin film proceeds via a ring-opening mechanism initiated by acid vapors. In an IR absorption spectrum of the thin film, only absorption band for Si–O stretching changed during the polymerization process, which support the ring-opening of the cyclotetrasiloxane rings purged into the mantle area of the columnar

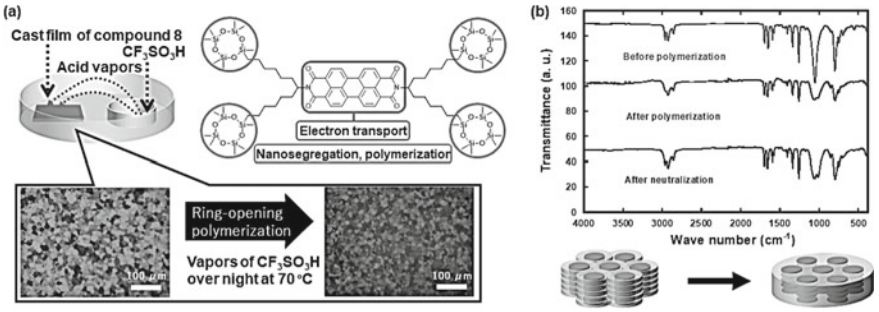

Fig. 18.8 **a** Illustration for acid-induced ring-opening polymerization in the thin film states of compound **8**, **b** IR spectra of the thin film before and after the polymerization

aggregates, as shown in Fig. 18.8b. The polymerized thin films are insoluble in CH_2Cl_2, tetrahydrofuran, toluene, acetonitrile, and acetone [31].

From the X-ray diffraction, polarizing optical micrographic study, and surface observation by atomic force microscopy (AFM), columnar structures in the thin films are retained during the polymerization process although structural disorder is increased. In the X-ray diffraction patterns of as-deposited and polymerized thin films, (100), diffraction peak indicating a columnar structure was retained during the insolubilization process, as shown in Fig. 18.9a. The AFM observation of the surface morphology of as-deposited thin films revealed plateaus and steps corresponding to the diameter of columnar aggregates, as shown in Fig. 18.9b. In the polymerized thin films, the nanostructures disappeared, indicating induction of structural disorder during the polymerization process, as shown in Fig. 18.9c.

By a friction transfer method, uniaxially aligned film was produced. A polarized absorption spectrum of the uniaxially aligned thin films in the as-deposited state

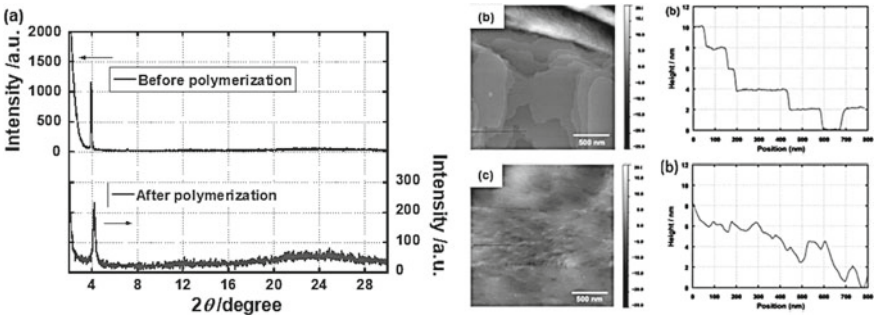

Fig. 18.9 **a** X-ray diffraction patterns of the spin-coated film of compound **8** before and after the in situ polymerization. Surface morphologies of the thin films of compound **8** measured by an AFM, **b** before and, **c** after the in situ polymerization. Reproduced from Ref. [31] by permission of The Royal Society of Chemistry

revealed a dichroic ratio of 5. This uniaxiality was retained during the acid-vapor-initialized polymerization, decreasing the dichroic ratio in the polarized absorption spectra to 3.

18.4 Nanosegregated Liquid Crystals with Electrochemical Functions

18.4.1 Liquid Crystalline Perylene Bisimide Hybridized with Lithium Salt

For electrochemical applications of nanosegregated liquid crystals, ion-conductive channels should be constructed in the liquid crystalline on the nanometer scale. In general, electrochemically active π-conjugated units and ionic moieties decrease the solubilities in organic solvents and raise up the phase transition temperatures, due to strong π–π and electrostatic interactions. Oligosiloxane moieties are effective to increase solubilities in organic solvents and suppress crystallization.

Oligoethylene oxide derivatives have been used for solid electrolytes because of lone pairs of oxygen atoms coordinating to metal cations. Perylene bisimide derivative **9** bearing two disiloxane chains and one triethylene oxide moiety was synthesized, as shown in Fig. 18.10. This compound exhibited a lamellar phase at room temperature. In the lamellar phase, the lattice constant determined by the X-ray diffraction was shorter than the double of the molecular length but longer than it, indicating a dimeric structure and the presence of hydrophilic sublayer consisting of triethylene oxide chains. The TOF measurement revealed that the electron mobility was on the order of 10^{-4} cm^2/Vs at room temperature [32].

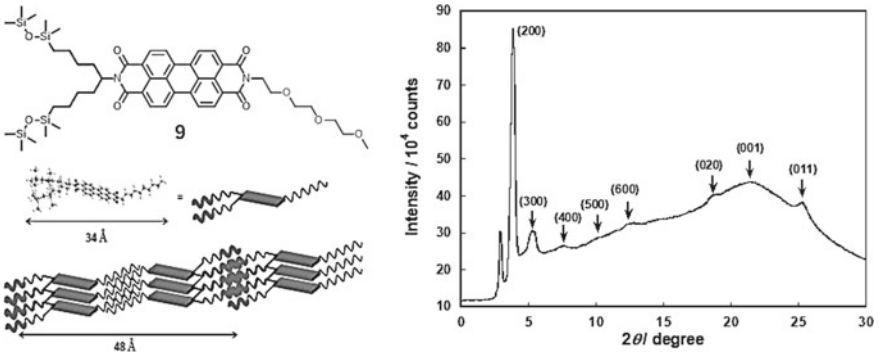

Fig. 18.10 Molecular structure of compound **9**, X-ray diffraction pattern of compound **9** at room temperature, and schematic for supramolecular aggregation structure. Reproduced from Ref. [32] by permission of The Royal Society of Chemistry

This compound retained the LC phase when 3 mol% of lithium triflate was doped. Lithium triflate should be absorbed in the hydrophilic sublayers consisting of triethylene oxide chains. The electron mobility did not change in the doped samples. This result indicated that the doped lithium and triflate ions should be adsorbed in the hydrophilic sublayers and separated from the electron transport layers consisting of electroactive perylene bisimide units.

18.4.2 Polymerizable Liquid Crystalline Mixed Conductor

In the usage of electrochemical application such as supercapacitors, butteries, and electrochromic devices, electrochemically active materials are operated in electrolyte solutions. Therefore, it is indispensable to insolubilize the thin films, retaining the nanosegregated structures formed in the as-deposited thin films. The cyclotetrasiloxane moiety is not only polymerizable but also promotes nanosegregation.

Perylene bisimide derivatives have been known as n-type semiconductors and redox-active materials. However, electrochromism of the monomeric and polymeric derivatives have unexpectedly been limited, perhaps because of difficulties in fabrication of homogeneous thin films which are durable in organic solvents. Polymers containing perylene bisimide units in their backbones indicated electrochromism in electrolyte solution [33].

Figure 18.11 shows molecular structures, phase transition properties, and supramolecular aggregation structures of compounds **10** and **11** [34]. Perylene bisimide derivative **10** has two polymerizable cyclotetrasiloxane rings and one triethylene oxide chain coordinating to ionic species. An alkylated analog **11** was also

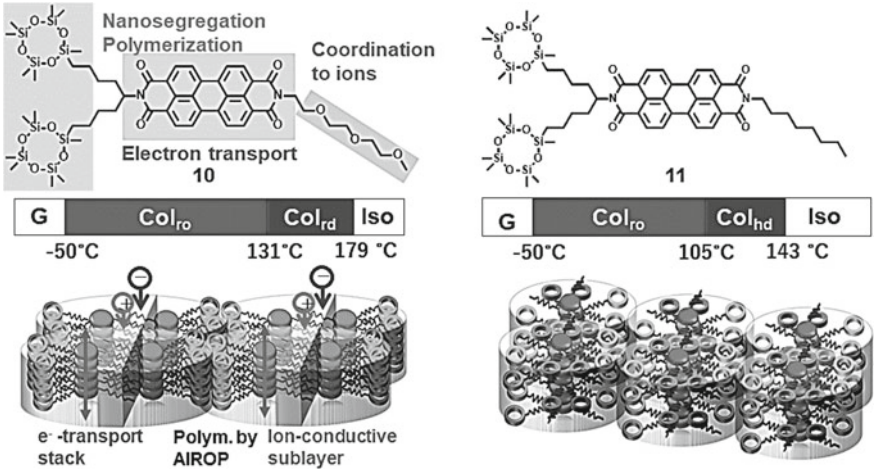

Fig. 18.11 Molecular structures and phase transition temperatures of compounds **10** and **11**. Reproduced from Ref. [34] by permission of The Royal Society of Chemistry

prepared. These compounds exhibit columnar phases at room temperature. However, the structures of the supramolecular aggregation were quite different; compound **10** formed columnar rectangular phase with a dimeric structure. In the columnar aggregates, ion-conductive sublayers consisting of triethylene oxide chains and electron-transporting π-stacks were formed separately. In contrast, conventional monomeric columnar aggregates were formed for compound **11**.

The triethylene oxide chains of compound **10** form hydrophilic sublayers within the columnar aggregates. This sublayer works as an ion-conductive layer. For electrochromism, ionic species penetrate into active film for the formation of an electrical double layer at the anode.

In electrochromism of organic thin films, the films are dipped in organic electrolyte solutions and the insolubilized thin films in the organic solvents are requisite. Compound **10** is soluble in various organic solutions and thin films can be produced by the spin-coating method. The as-deposited thin films are soluble in various organic solvents, and therefore, they could not retain in the electrolyte solution. The solubility of thin films of compound **10** in acetonitrile is relatively low and can retain the thin film state in acetonitrile solution of tetrabutylammonium perchlorate. However, the thin film was dissolved when a negative DC bias was applied to the thin film because anion radicals which have higher solubility in acetonitrile.

After insolubilization of the thin film by the acid vapor-induced ring-opening polymerization method, the thin film of compound **10** can retain not only in the neutral state but also even when they are reduced to anion radical and dianion states.

Insolubilized films of compound **10** by the ring-opening polymerization indicated electrochromism in an organic electrolyte solution, i.e., acetonitrile solution of tetrabutylammonium perchlorate. Figure 18.12a displays the color change of the polymerized thin film of compound **10** in the electrochromic process. As shown in Fig. 18.12b, two-step reversible reduction waves were observed for solution and film states. As shown in Fig. 18.12c, the reduction wave at -0.8 V and -1.2 V versus an Ag^+/Ag electrode were assigned to the generation of anion radicals and dianions of the perylene bisimide core, respectively. In this efficient electrochromism, the presence of the ion-conductive sublayers is significant. The absorption spectrum of the polymerized film of compound **10** during the electrochromism indicated that efficient generation of dianions of the perylene bisimide units by a two-electron reduction [34].

In contrast, for compound **11** which has no ion-conductive sublayers, electrochromism was not observed under the application of -1.5 V versus Ag^+/Ag electrode. Formation of electrical double layers by polarization of ionic species is requisite for electrochemical function. This nanosegregated structure in which redox-active π-stacks and ion-conductive sublayers are separated on a nanometer scale is effective for efficient electrochromic response.

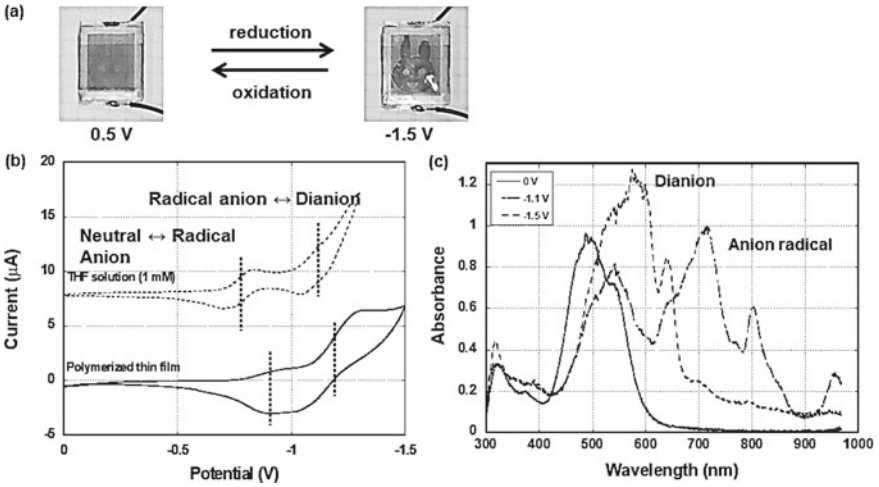

Fig. 18.12 **a** Color change of a polymerized film of compound **10** in the electrochromic process, **b** cyclic voltammogram of compound **10** in solution and film states (Ag^+/Ag standard), **c** absorption spectra of a thin film of compound **10** in the electrochromic process. Reproduced from Ref. [34] by permission of The Royal Society of Chemistry

18.4.3 Interstitial Doping in the Nanostructured Liquid Crystal

There are two categories of doping in semiconductors. The first is substitution doping, which is usually seen in inorganic semiconductors such as silicon and organic molecular crystals. In this case, semiconductor atoms or molecules located at crystal lattice points are substituted by chemical dopants. This type of doping in inorganic semiconductors has achieved a great success in industrial applications to produce various electronic devices. For the substitution doping in organic molecular systems, dopant molecules often perturb the molecular aggregation to increase energetic and structural disorders.

The second is interstitial doping, in which dopant atoms or molecules penetrate in the voids in crystal lattice, such as strontium titanate [35]. Organic crystals generally have insufficient voids for dopant molecules, and interstitial doping is difficult. In nanostructured liquid crystal phases, voids for dopant molecules can be designed properly to separate the dopant molecules from the carrier transport paths.

Gregg et al. synthesized LC perylene bisimide derivatives bearing an ammonium moiety as well as oligoethylene oxide chains, and the electrical conductivity of the LC perylene bisimide derivatives doped with sodium was measured under an inert atmosphere [36–39]. However, the all processes were carried out under an inert atmosphere and the measurement was done in the crystal phases of the compounds.

In contrast, compound **10** exhibits the columnar phase at room temperature and the electrical conductivity in the LC phase can be studied. Moreover, ionic reductant

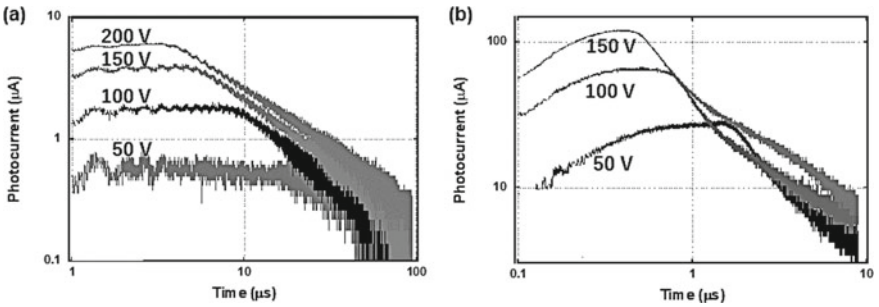

Fig. 18.13 Transient photocurrent curves for electrons in the columnar phases of (**a**) compound **10** and (**b**) compound **11**. The sample thickness was 15 μm and the wavelength of excitation light was 356 nm. Reproduced from Ref. [34] by permission of The Royal Society of Chemistry

can be used instead of sodium metal because of the presence of the ion-conductive sublayers.

Figure 18.13 shows transient photocurrent curves obtained by the TOF method for electrons in the columnar phases of compounds **10** and **11**. The TOF measurement revealed electron mobilities on the order of 10^{-3} cm^2 V^{-1} s^{-1} for the columnar phase of compound **10** and 10^{-2} cm^2 V^{-1} s^{-1} for the columnar phase of compound **11** at room temperature. These compounds exhibit efficient electron transport in the columnar phases, due to π–π stacking structures in the columnar phases [34].

The ion-conductive sublayers promoted ion diffusion into the films of compound **10**. Sodium dithionite is an inorganic reductant which can reduce the perylene bisimide core to the anion radical and dianion states. Thin films of compounds **10** and **11** with the thickness of 100 nm were produced by the spin-coating method. The spin-coated films were exposed on vapors of trifluoromethanesulfonic acid at 70 °C for 30 min to insolubilize the thin films. The as-deposited and polymerized thin films were dipped in alkaline solution of sodium dithionate.

In several ten minutes, color of as-deposited and polymerized thin films of compound **10** changed from red to blue in the doping process. Figure 18.14 displays time-dependent absorption spectra of the thin films of compound **10**. Both for as-deposited and polymerized thin films, absorption bands in the IR area grew first and next a band around 560 nm appeared. The color of the film changed from red to blue via brownish red. The absorption bands in the IR are and 560 nm are attributed to anion radical and dianion of perylene bisimide units, respectively. This result indicated that this doping process could produce anion radicals in the thin films of compound **10**.

In contrast, the color of the thin films of compound **11** was not changed by this doping process, indicating no generation of the anion radicals and dianions of the perylene bisimide core. Ionic dithionate anions should not penetrate in the thin films of compound **11** because hydrophobicity of the thin film and absence of ion-conductive sublayer in the columnar phase of compound **11**.

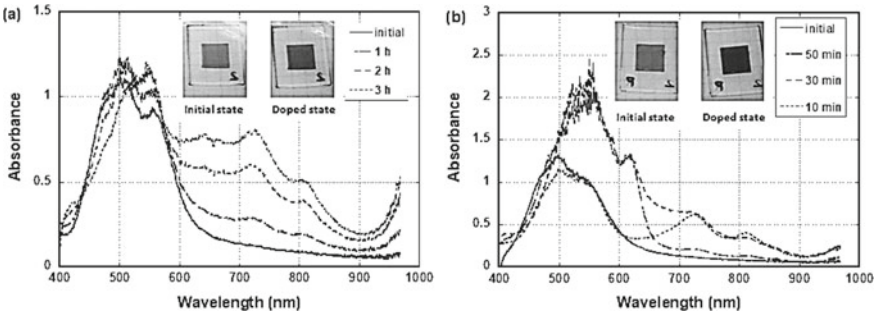

Fig. 18.14 Absorption spectra of **a** as-deposited and **b** polymerized thin films of compound **10** dipped in alkaline solution of sodium dithionate. Reproduced from Ref. [34] by permission of The Royal Society of Chemistry

For as-deposited and polymerized thin films of compound **10**, electrical conductivity was increased to 1×10^{-4} Scm^{-1} by 5 orders of magnitude compared to those of non-doped states by this doping process, as shown in Fig. 18.15a, b. The conductivities of as-deposited and polymerized films were on the same order. For as-deposited and polymerized thin films of compound **10**, the electrical conductivity increased to 3×10^{-10} and 1×10^{-9} by the factors of 40 and 5 in the doping process (Fig. 18.15c,

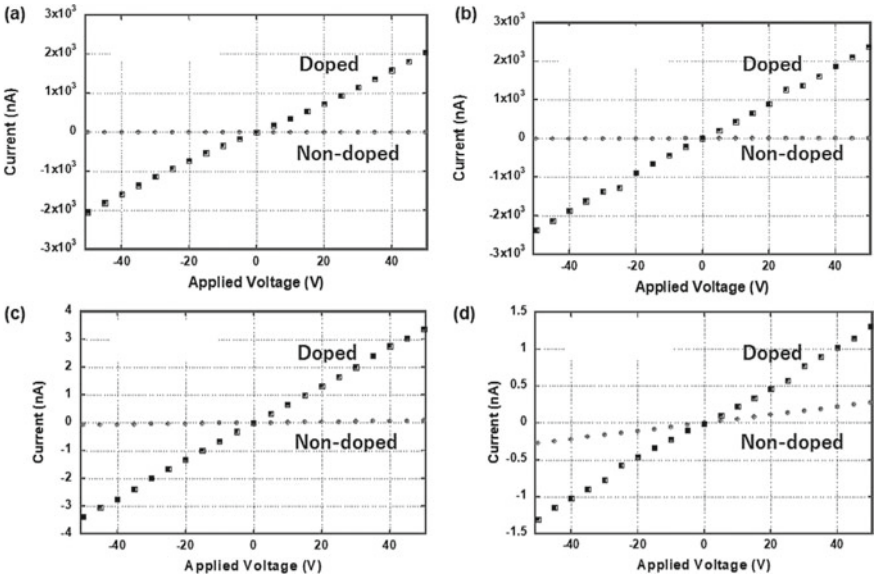

Fig. 18.15 Current–voltage characteristics of non-doped and doped thin films. **a** As-deposited and **b** polymerized films of compound **10**, **c** As-deposited and **d** polymerized films of compound **11**. Reproduced from Ref. [34] by permission of The Royal Society of Chemistry

d). The presence of ion-conductive sublayers is indispensable for efficient doping in the columnar phases [34].

Compared to thin films of molecular crystals, macroscopic molecular alignment is relatively easy in liquid crystalline thin films. While rubbed polyimide layer is effective for uniaxial alignment of nematic phase, this method is not successful in the uniaxial alignment of ordered smectic and columnar phases. For the columnar phases of compound **10**, a friction transfer method achieved production of uniaxial alignment of the columnar aggregates of the spin-coated thin films on four segmented electrodes, as shown in Fig. 18.16a.

Polarized absorption spectra of the uniaxially aligned thin films of compound **10** indicated the dichroic ratio of 12 and 4 in the as-deposited and polymerized states, respectively (Fig. 18.16b). Absorbance perpendicular to the friction direction was larger than that parallel to it because the columnar axis was parallel to the friction direction and the transition moment of perylene bisimide core was perpendicular to the direction.

Figure 18.16c shows current–voltage characteristics of uniaxially aligned thin films. The ratio of the electrical conductivities along and vertical to the columnar axis was 100 and 10 for the as-deposited and polymerized thin films of compound **10**. Because of the presence of π-stacks of perylene bisimide units, higher conductivity

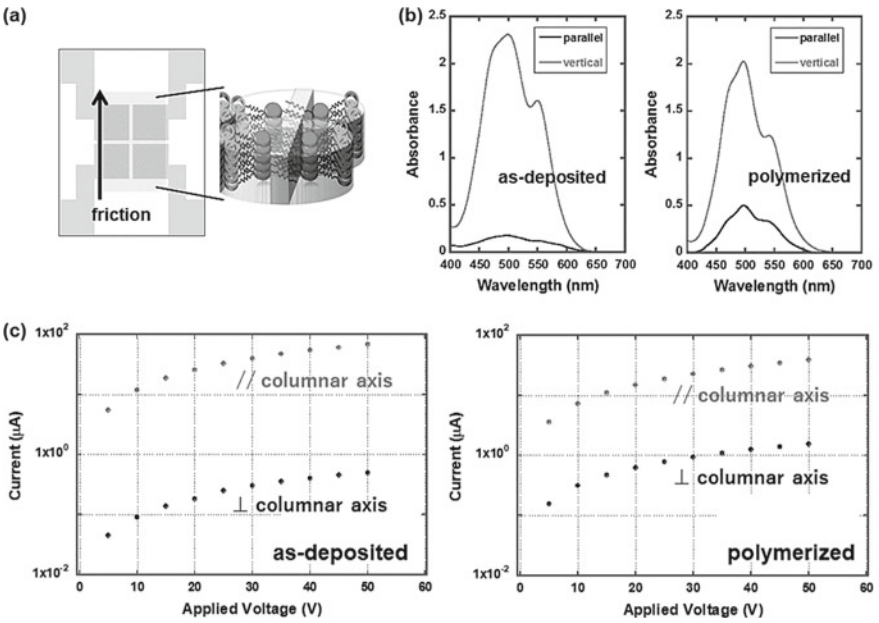

Fig. 18.16 **a** Schematic illustration of a sample for anisotropy measurement of electrical conductivity, **b** polarized absorption spectra of uniaxially aligned thin films of compound **10**, **c** current–voltage characteristics of uniaxially aligned thin films of compound **10**. Reproduced from Ref. [34] by permission of The Royal Society of Chemistry

along the columnar axis should be observed, while conductivity perpendicular to the columnar axis was low since the conducive π-stacks were surrounded by insulative mantles consisting of oligosiloxane moieties. During the polymerization process, structural disorder should be induced to decrease the anisotropy in the absorption and conductivity. However, the one-dimensionality of the electronic conduction was retained in the polymerization process [34].

18.5 Conclusion

Nanosegregated LC structures are effective to form electrical polarization from which electrochemical functions are derived. For the construction of nanosegregated structures, the side chain engineering is indispensable rather than design π-conjugated units. In particular, oligosiloxane side chains promote segregation between functional units and side chains to form soft nanostructures in the LC phases.

LC oligithiophene derivatives bearing an imidazolium unit at the terminal of the alkyl side chain exhibit nanosegregated smectic phases in which ion-conductive and hole-conductive sublayers are integrated separately. In the SmA phase, these compounds display electrochromism in the bulk state.

Perylene bisimide derivatives bearing oligosiloxane chains exhibit columnar phases at room temperature. In the columnar phases, one-dimensional electron-transporting π-stacks are surrounded by electrically insulative mantle consisting of oligosiloxane chains. The mantle is liquid-like and the bulk states of the columnar phases are waxy solid. However, they exhibit high electron mobilities, due to the crystal-like π-stacks of perylene bisimide units.

The cyclotetrasiloxane moiety is not only polymerizable but also promotes nanosegregation. Perylene bisimide derivatives bearing the cyclotetrasiloxane moieties can be insolubilized in the thin film state via ring-opening polymerization induced by the exposure on vapors of trifluoromethanesulfonic acid.

Perylene bisimide derivative bearing a triethylene oxide chain and two disiloxane chains exhibits a lamellar LC phase which can be hybridized with lithium salts. Perylene bisimide derivative bearing two cyclotetrasiloxane rings and one triethylene oxide chain exhibits a nanostructured columnar phase in which ion-conductive sublayers and electro- and redox-active π-stacks are integrated on a nanometer scale. This nanostructure is retained during the acid-induced polymerization process. The polymerized thin films display electrochromism between red and blue, due to the penetration of the ionic species and the rapid formation of electrical double layer.

In the doping of nanostructured π-conjugated liquid crystals, ionic reductants diffuse through the ion-conductive sublayers within the columnar aggregates and reduce the electron deficient π-conjugated cores to increase the electron density. Dopant ions are separated from the electron-transporting π-stacks and this polarized structure is categorized as an interstitial doping. Doped thin films which exhibit anisotropic conductivity could be produced.

References

1. Köhler, A., Bässler, H.: Electronic Processes in Organic Semiconductors: An Introduction. Wiley-VCH Verlag GmbH & Co. KGaA, Weinheim (2015)
2. Funahashi, M.: Development of liquid crystalline semiconductors with high Carrier mobility and their application to thin-film transistors. Polym. J. **41**, 459–469 (2009)
3. Kato, T., Yoshio, M., Ichikawa, T., Soberats, B., Ohno, H., Funahashi, M.: Transport of ions and electrons in nanostructured liquid crystals. Nat. Rev. Mater. **2**, 17001 (2017)
4. Kato, T., Mizoshita, N., Kishimoto, K.: Functional liquid-crystalline assemblies: self-organized soft materials. Angew. Chem. Int. Ed. **45**, 38 (2005)
5. Funahashi, M.: Nanostructured liquid-crystalline semiconductors—a new approach to soft matter electronics. J. Mater. Chem. C **2**, 7451 (2014)
6. Choi, N.-S., Chen, Z., Freunberger, S.A., Ji, X., Sun, Y.-K., Amine, K., Yushin, G., Nazar, L.F., Cho, J., Bruce, P.G.: Challenges facing lithium batteries and electrical double-layer capacitors. Angew. Chem. Int. Ed. **51**, 9994 (2012)
7. Seki, A., Funahashi, M.: Nanostructure formation based on the functionalized side chains in liquid-crystalline heteroaromatic compounds. Heterocycles **92**, 3 (2016)
8. Funahashi, M.: Integration of electro-active π-conjugated units in nanosegregated liquid-crystalline phases. Polym. J. **49**, 75 (2017)
9. Heuer, H.W., Wehrmann, R., Kirchmeyer, S.: Electrochromic window based on conducting Poly(3,4-ethylenedioxythiophene)–Poly(styrene sulfonate). Adv. Funct. Mater. **12**, 89–94 (2002)
10. Tosoni, S., Di Valentin, C., Pacchioni, G.: Effect of alkali metals interstitial doping on structural and electronic properties of WO_3. J. Phys. Chem. C **118**, 3000 (2014)
11. Lüssem, B., Riede, M., Leo, K.: Doping of organic semiconductors. Phys. Stat. Solid. C **210**, 9 (2013)
12. Sato, K., Ichinoi, R., Mizukami, R., Serikawa, T., Sasaki, Y., Lutkenhaus, J., Nishide, H., Oyaizu, K.: Diffusion-cooperative model for charge transport by redox-active nonconjugated polymers. J. Am. Chem. Soc. **140**, 1049 (2018)
13. Yazaki, S., Funahashi, M., Kato, T.: Electrochromic liquid crystals consisting of π-conjugated and ionic moieties. J. Am. Chem. Soc. **130**, 13206 (2008)
14. Yazaki, S., Funahashi, M., Kagimoto, J., Ohno, H., Kato, T.: Nanostructured liquid crystals combining ionic and electronic functions. J. Am. Chem. Soc. **132**, 7702 (2010)
15. Schenning, A.P.H.J., Kilbinger, A.F.M., Biscarini, F., Cavallini, M., Cooper, H.J., Derrick, P.J., Feast, W.J., Lazzaroni, R., Leclère, P., McDonell, L.A., Meijer, E.W., Meskers, S.C.J.: Supramolecular organization of α,α'-disubstituted sexithiophenes supramolecular organization of α,α'-disubstituted sexithiophenes. J. Am. Chem. Soc. **124**, 1269 (2002)
16. Sakurai, T., Tashiro, K., Honsho, Y., Saeki, A., Seki, S., Osuka, A., Muranaka, A., Uchiyama, M., Kim, J., Ha, S., Kato, K., Takata, M., Aida, T.: Electron- or hole-transporting nature selected by side-chain-directed π-stacking geometry: liquid crystalline fused metalloporphyrin dimers. J. Am. Chem. Soc. **133**, 6537 (2011)
17. Yoshio, M., Mukai, T., Ohno, H., Kato, T.: One-dimensional ion transport in self-organized columnar ionic liquids. J. Am. Chem. Soc. **126**, 4994 (2004)
18. Yasuda, T., Ooi, H., Morita, J., Akama, Y., Minoura, K., Funahashi, M., Shimomura, T., Kato, T.: π-conjugated oligothiophene-based polycatenar liquid crystals: self-organization and photoconductive, luminescent, and redox properties. Adv. Funct. Mater. **19**, 411 (2009)
19. Ichikawa, T., Yoshio, M., Hamasaki, A., Mukai, T., Ohno, H., Kato, T.: J. Am. Chem. Soc. **129**, 10662 (2007)
20. Küpfer, J., Finkelmann, H.: Nematic liquid single crystal elastomers. Macromol. Chem. Rap. Commun. **12**, 717 (1992)
21. Matsui, A., Funahashi, M., Tsuji, T., Kato, T.: Hole transport in liquid-crystalline polymers with a polysiloxane backbone and a phenylterthiophene moiety in the side chain. Chem. Eur. J. **16**, 13465–13472 (2010)

22. Lagerwall, J.P.F., Giesselmann, F.: Current topics in smectic liquid crystal research. Chem. Phys. Chem. **7**, 20 (2006)
23. Zelcer, A., Donnio, B., Bourgogne, C., Cukiernik, F.D., Guillon, D.: Mesomorphism of hybrid siloxane-triphenylene star-shaped oligomers. Chem. Mater. **19**, 1992 (2007)
24. Funahashi, M., Sonoda, A.: Liquid-crystalline perylene tetracarboxylic acid bisimide bearing oligosiloxane chains with high electron mobility and solubility. Org. Electron. **13**, 1633 (2012)
25. Funahashi, M., Sonoda, A.: High electron mobility in a columnar phase of liquid-crystalline perylene tetracarboxylic bisimide bearing oligosiloxane chains. J. Mater. Chem. **22**, 25190 (2012)
26. Funahashi, M., Takeuchi, N., Sonoda, A.: Liquid-crystalline perylene tetracarboxylic bisimide derivative bearing trisiloxan-2-yl moieties: Influence on mesomorphic property and electron transport. RSC Advances **6**, 18703 (2016)
27. Funahashi, M., Sonoda, A.: Electron transport characteristics in nanosegregated columnar phases of perylene tetracarboxylic bisimide derivatives bearing oligosiloxane chains. Phys. Chem. Chem. Phys. **16**, 7754 (2014)
28. Yoshio, M., Kagata, T., Hoshino, K., Mukai, T., Ohno, H., Kato, T.: One-dimensional ion-conductive polymer films: alignment and fixation of ionic channels formed by self-organization of polymerizable columnar liquid crystals. J. Am. Chem. Soc. **128**, 5570 (2006)
29. Aldred, M.P., Contoret, A.E.A., Farrar, S.R., Kelly, S.M., Mathieson, D., O'Neill, M., Tsoi, W.C., Vlachos, P.: A full color electroluminescent device and patterned photo alignment using light emitting liquid crystals. Adv. Mater. **17**, 1368 (2005)
30. Funahashi, M., Yamaoka, M., Takenami, K., Sonoda, A.: Liquid-crystalline perylene tetracarboxylic bisimide derivatives bearing cyclotetrasiloxane moieties. J. Mater. Chem. C **1**, 7872 (2013)
31. Takenami, K., Uemura, S., Funahashi, M.: In situ polymerization of liquid-crystalline thin films of electron-transporting perylene tetracarboxylic bisimide bearing cyclotetrasiloxane rings. RSC Adv. **6**, 5474 (2016)
32. Funahashi, M., Sonoda, A.: Liquid-crystalline perylene tetracarboxylic bisimide derivative bearing a triethylene oxide chain and complexation of the derivative with Li cations. Dalton Trans. **42**, 15987 (2013)
33. Lu, W., Gao, J.P., Wang, Z.Y., Qi, Y., Sacripante, G.G., Duff, J.D., Sundararajan, P.R.: electrochemical characterization, electrochroism, and voltage-dependent fluorescence of novel perylene-containing polyimides. Macromolecules **32**, 8880 (1999)
34. Funahashi, M.: Anisotropic electrical conductivity of n-doped thin films of polymerizable liquid-crystalline perylene bisimide bearing a triethylene oxide chain and cyclotetrasiloxane rings. Mater. Chem. Front. **1**, 1137 (2017)
35. Nakayama, R., Maesato, M., Yamamoto, T., Kageyama, H., Terashima, T., Kitagawa, H.: Heavy interstitial hydrogen doping into $SrTiO_3$. Chem. Commun. **54**, 12439 (2018)
36. Liu, S.-G., Sui, G., Cormier, R.A., Leblanc, R.M., Gregg, B.A.: Self-organizing liquid crystal perylene diimide thin films: spectroscopy, crystallinity, and molecular orientation. J. Phys. Chem. B **106**, 1307 (2002)
37. Chen, S.-G., Stradins, P., Gregg, B.A.: Doping highly ordered organic semiconductors: experimental results and fits to a self-consistent model of excitonic processes, doping, and transport. J. Phys. Chem. B **109**, 13451 (2005)
38. Gregg, B.A., Cormier, R.A.: Doping molecular semiconductors: n-type doping of a liquid crystal perylene diimide. J. Am. Chem. Soc. **123**, 7959 (2001)
39. Gregg, B.A., Kose, M.E.: Reversible switching between molecular and charge transfer phases in a liquid crystalline organic semiconductor. Chem. Mater. **20**, 5235 (2008)

Part IV
Chirality

Chapter 19
Kryptoracemates

Edward R. T. Tiekink

Abstract Racemic crystals normally crystallise in centrosymmetric space-groups containing equal numbers of enantiomers. More rarely, racemates may crystallise in non-centrosymmetric space-groups having glide symmetry or, even more rarely, in space-groups devoid of a centre of inversion, having no rotary-inversion axes nor glide plane. The latter class of crystals forms the subject of the present bibliographic review—a survey of kryptoracemic behaviour. The term kryptoracemic alludes to the presence of a hidden or non-crystallographic centre of inversion between two molecules that might otherwise be expected to crystallise in an achiral space-group, often about a centre of inversion. Herein, examples of molecules with stereogenic centres crystallising in one of the 65 Sohncke space-groups are described. Genuine kryptoracemates, i.e. crystals comprising only enantiomorphous pairs, are described followed by an overview of non-genuine kryptoracemates, whereby the crystal also contains other species such as solvent and/or counter-ions. A full-range, i.e. one to six, stereogenic centres are noted in genuine kryptoracemates. Examples will also be described, whereby there are more than one enantiomeric pair of molecules in the crystallographic asymmetric unit. A more diverse range of examples are available for non-genuine kryptoracemates. There are unbalanced species where in addition to the enantiomeric pair of molecules, there is another enantiomeric molecule present. There are examples of co-crystals, solvated species and salts. Finally, special examples will be highlighted where the counter-ions are chiral and where they are disparate, both circumstances promoting kryptoracemic behaviour.

Keywords Kryptoracemate · Molecular packing · Crystal structure · Crystallisation · Chirality

E. R. T. Tiekink (✉)
School of Science and Technology, Research Centre for Crystalline Materials, Sunway University, 5 Jalan Universiti, Bandar Sunway, Selangor Darul Ehsan 47500, Malaysia
e-mail: edwardt@sunway.edu.my

M. Sakamoto and H. Uekusa (eds.), *Advances in Organic Crystal Chemistry*,
https://doi.org/10.1007/978-981-15-5085-0_19

19.1 Introduction

The intriguing term *kryptoracemate* has been ascribed [1] to Ivan Bernal, a renowned chemical crystallographer with a particular interest in chirality in crystals, especially in metalorganic systems. It is understood that Ivan Bernal employed the term during a meeting of the American Crystallographic Association in the mid-1990s [2]. Clearly, the term refers to the crystallisation of racemic compounds. Less obvious is the origin of the prefix "*krypto*", which comes from the Greek and loosely translates as hidden. Thus, kryptoracemic behaviour refers to crystallisation of racemic molecules about a hidden, i.e. a non-crystallographic, centre of inversion. For organic molecules, the most recent comprehensive review of the topic by Fábián and Brock [3] highlights how rare this phenomenon is, accounting for only 0.1% of all-organic structures included in the Cambridge Structural Database (CSD) [4]; a complimentary survey of kryptoracemic behaviour in metalorganic systems has been published by Bernal and Watkins [5]. The aim of the present chapter is to alert the reader to this crystallographic peculiarity by surveying the structural characteristics of representative examples of all-organic molecules known with a certain degree of confidence to exhibit kryptoracemic behaviour.

There are at least three possible outcomes from the crystallisation from a solution of a racemic compound. In descending order of importance, these crystallisation outcomes are: (i) an ordered racemic crystal, (ii) a physical mixture comprising equal numbers of enantiopure crystals and (iii) a kryptoracemate; herein, solid solutions and enantiomorphous twins are ignored. Racemic compounds have equal numbers of the enantiomers in the crystal, i.e. an equal distribution of mirror images of the molecules. This is normally accomplished by having the molecules disposed about a crystallographic centre of inversion. There are exceptions to this general principle, whereby a racemate can crystallise in a non-centrosymmetric space-group, but a space-group having glide symmetry so that the criterion of having equal numbers of mirror images pertains. An early survey of this later phenomenon by Dalhus and Görbitz [6] revealed that 90% of crystals in this category crystallised in five non-centrosymmetric space-groups, namely *Pc*, *Cc*, $Pca2_1$, $Pna2_1$ and $Fdd2$. The second phenomenon leading to a physical mixture of crystals, or a conglomerate of homochiral crystals, is usually termed spontaneous resolution and was famously recognised by Pasteur in his work on ammonium sodium tartrate crystals [7]. The third crystallisation outcome for racemic compounds results in kryptoracemic crystals which are characterised as crystallising in space-groups lacking a centre of inversion, mirror planes and rotary-inversion centres, i.e. not having symmetry operators of the second kind, as discussed further below.

The reality is that most organic materials containing a pair of resolvable isomers (also those with meso-symmetry and achiral compounds) crystallise in one of the centrosymmetric space-groups leading to hetero-chiral crystals; this has been termed an enantiophilic trait [8]. It is estimated that 99% of molecules (neutral and charged) that can crystallise in a centrosymmetric space-group will do so [9]. This is probably

related to close-packing considerations: it is well established that 83% of all structures included in the CSD [4] crystallise in one of six space-groups out of a possible 230 space-groups (or 219 when the 11 pairs of enantiomorphic space-groups are counted once only), i.e. $P2_1/c$ (34.6%), $P\bar{1}$ (24.5%), $C2/c$ (8.4%), $P2_12_12_1$ (7.2%), $P2_1$ (5.2%) and $Pbca$ (3.3%), or alternative settings of these [9, 10]. The common feature of the indicated space-groups is that they are all are conducive to close-packing arrangements, which is optimised for spherical molecules. Thus, an odd-shaped molecule crystallising about a centre of inversion inherently becomes more spherical in shape. When enantiophilic behaviour [8] no longer prevails, enantiophobic behaviour comes to the fore resulting in the formation of conglomerates or, more rarely, kryptoracemates.

In terms of space-group symmetry, kryptoracemates are restricted in the adoption of these. As mentioned above, kryptoracemates can only crystallise in space-groups not having symmetry operators of the second kind. Thus, a kryptoracemate must crystallise in one of the 65 Sohncke space-groups (non-enantiogenic groups) which are characterised as not having a centre of inversion, rotary-inversion axes or glide planes, i.e. only have symmetry operations of the first kind; crystals adopting Sohncke space-groups are chiral. Further, the number of molecules in the crystallographic asymmetric unit, i.e. Z' (equals the number of formula units in a unit cell divided by the number of general positions for that unit cell), is greater than unity unless the molecule itself lies on a rotation axis [11].

The purpose of this overview is not to give a comprehensive list of all known kryptoracemates but rather to highlight the different classes of kryptoracemates that have been described in the crystallographic literature. As a starting point, a clarification of the term kryptoracemic compound is made, analogous to that now adopted for supramolecular isomers [12, 13]. A supramolecular isomer (SI) is a molecule/framework that can adopt a different structure, including with a different atomic connectivity, as opposed to a polymorph [14]. Often, this phenomenon was accompanied by a change in the counter-ion and/or solvent occluded in the crystal [12]. Subsequently, the term was modified to refer to a genuine SI [13], whereby the molecular formula was exactly the same, rather than the generic, all-encompassing SI [12]. Following this precedent, herein, kryptoracemates are divided into "genuine kryptoracemates", with only one type of species (molecule or zwitterion) in the crystal, and "more loosely defined kryptoracemates", which may include counter-ions, solvent, etc., in their crystals.

With the above division in mind, the following survey is arranged in terms of the number of chiral centres in the molecule and highlights different issues associated with the examples, for example, polymorphism, the availability of crystals of diastereoisomers, etc. The images herein are original, being generated from the Crystallographic Information Files (CIFs) [15] available through the CSD [4] employing DIAMOND [16] and QMol [17]. The chemical diagrams were drawn with ChemDraw™, and data analysis was aided by Mercury [18] and PLATON [19].

The respective CSD [4] REFCODES are included in the captions of the figures. Finally, while common names are employed in the text as much as possible, IUPAC names are included in the captions of the figures, as determined by MarvinSketch [20].

19.2 Genuine Kryptoracemates

A distinction is made herein between genuine and non-genuine kryptoracemates. While the basic definition is the same for both classes of compound, the influence of solvent or a counter-ion on the crystallisation outcome is virtually impossible to determine with absolute confidence. Hence, kryptoracemic crystals comprising enantiomorphic molecules are discussed first; in 19.3, kryptoracemic crystals having additional species present in the crystal will be described.

One of the very first molecules to exhibit kryptoracemic behaviour was DL-2-hydroxyphenylalanine (**1**), which in fact crystallises as a zwitterion [21]; images for **1** are shown in Fig. 19.1. There is one stereogenic centre in **1**, which crystallises in the monoclinic space-group $P2_1$ with $Z' = 2$, the asymmetric unit comprising a pair of ostensibly enantiomorphic molecules; the *S*-form is shown in Fig. 19.1. The overlap diagram, comprising the *S*-form and inverted *R*-form, displays an almost perfect overlap, as is often seen in kryptoracemates. However, in this case, the diagram is misleading. The enantiomeric molecules are related by a non-crystallographic centre of inversion located at 0.661, 0.390, 0.802. As the fractional atomic coordinates for the *R*-form were not available, this molecule was generated arbitrarily. While **1** is zwitterionic, the overwhelming majority of genuine kryptoracemates comprise neutral enantiomers.

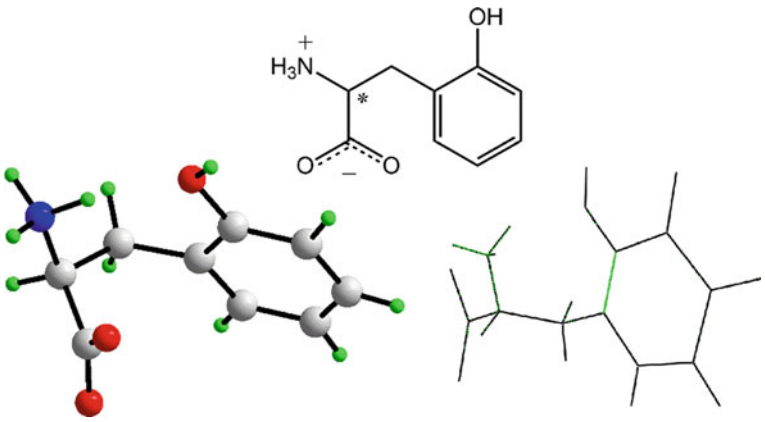

Fig. 19.1 Images for 2-azaniumyl-3-(2-hydroxyphenyl)propanoate (DTYROS), **1**: chemical diagram (upper view), molecular structure and overlay diagram

Figure 19.2 shows images for 4-azido-5-(biphenyl-4-yl)-5-hydroxy-3-methyl-2-oxo-2,5-dihydrofuran (**2**), a neutral molecule crystallising with $Z' = 2$ (space-group $P2_1$); the *R*-form is illustrated in the molecular diagram [22]. The overlap diagram highlights a close correspondence of the molecular structures in the independent tetrahydrofuranyl rings (*R*-form and inverted *S*-form) but differences in the orientations of the biphenyl residues.

In **3**, 2,4-dinitro-2,3-dichloro-3-thiolene-1,1-dioxide, rich in heteroatoms, a close overlap is again noted between the five-membered rings when the molecule in Fig. 19.3, i.e. the *S*-form, is overlapped with the inverted form [23]. The molecule crystallises in the orthorhombic space-group $P2_12_12_1$ with $Z' = 2$.

Kryptoracemic behaviour is not restricted to examples with $Z' = 2$, i.e. two independent molecules in the crystallographic asymmetric unit. This is illustrated for 1,6-dihydro-1,6-dimethyl-4-phenyl-1,2,3-triazine 2-oxide (**4**), where $Z' = 4$ (monoclinic, $P2_1$); **4** is another example of a formally charged species [24]. The asymmetric

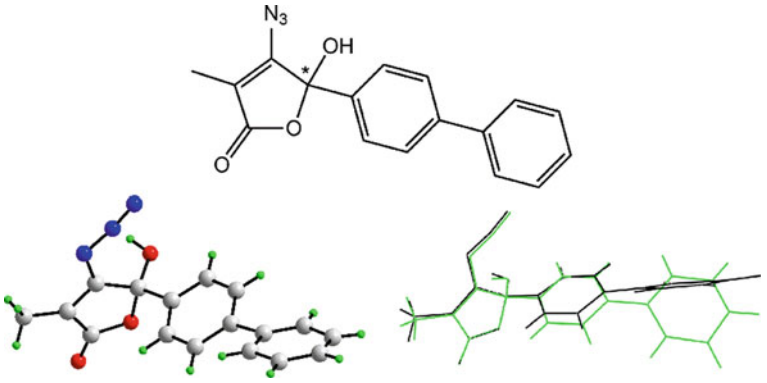

Fig. 19.2 Images for 4-azido-5-hydroxy-3-methyl-5-(4-phenylphenyl)-2,5-dihydrofuran-2-one (DIXPUW), **2**: chemical diagram, molecular structure and overlay diagram

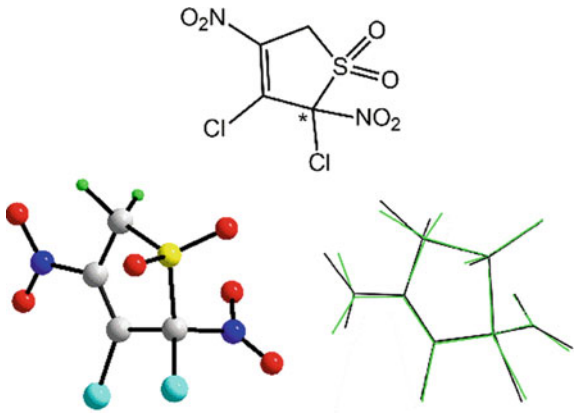

Fig. 19.3 Images for 2,3-dichloro-2,4-dinitro-2,5-dihydro-1λ^6-thiophene-1,1-dione (LACFEB), **3**: chemical diagram, molecular structure and overlay diagram

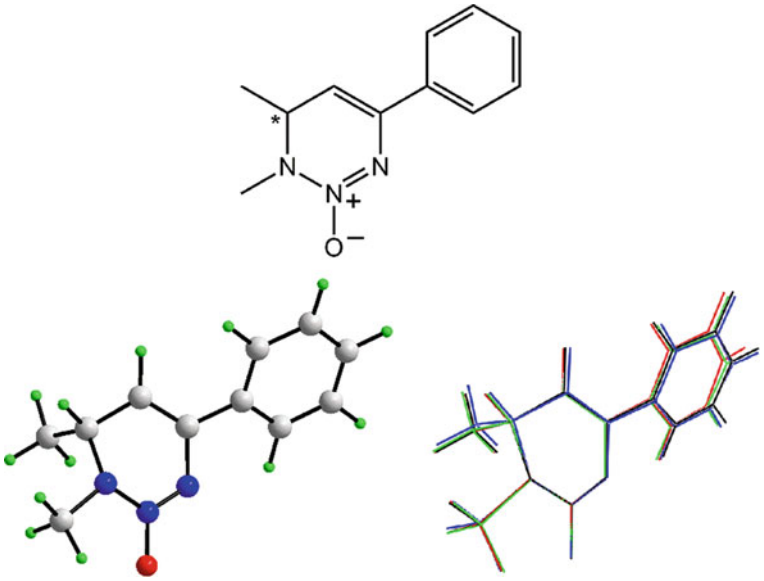

Fig. 19.4 Images for 1,6-dimethyl-4-phenyl-1,6-dihydro-1,2,3-triazin-2-ium-2-olate (FATFUB), **4**: chemical diagram, molecular structure and overlay diagram

unit of **4** comprises two independent pairs of enantiomeric molecules, neither of which is related by crystallographic symmetry. The illustrated molecule in Fig. 19.4 has the chiral centre being *R*. Thus, there are one further *R*-form and two *S*-forms in the asymmetric unit. The overlap diagram of the two *R*-forms with the inverted *S*-forms reveals high degree of concordance among the four independent molecular conformations.

Molecules of 8-methoxy-1-oxacyclotetradeca-2,13-dione (**5**) have a single stereogenic centre, with the *S*-form shown in Fig. 19.5. The kryptoracemate crystallises in the monoclinic space-group $P2_1, Z' = 2$ [25]. A centrosymmetric polymorph is also known for **5**, which exhibits similar unit cell parameters for the space-group $P2_1/c$, $Z' = 1$ [26]. The overlay diagram highlights the close agreement in the molecular conformations. The above observations raise two crucial issues when assessing the aetiology and even the validity of kryptoracemic behaviour.

The first important issue to be addressed relates to the correctness of the assigned space-group. In a series of publications spanning several decades [27–29], Marsh and colleagues periodically corrected space-group assignments. Particularly relevant to the present survey was the conclusion that the most often missed symmetry in space-group assignments, often leading to incorrect or even over-interpretation of chemistry/correlations with spectroscopy, was the presence of a centre of inversion [29]. With modern software, such as PLATON [19], it is likely that the number of errant structures will be/should be reduced.

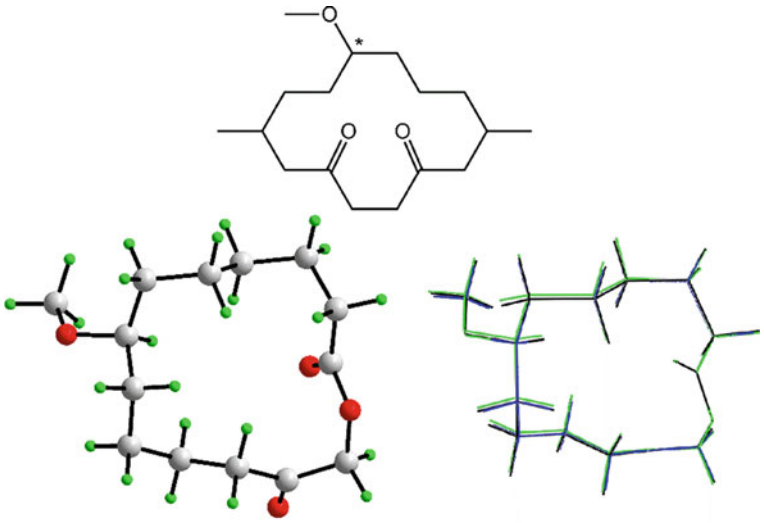

Fig. 19.5 Images for 8-methoxy-1-oxacyclotetradecane-2,13-dione (NIWHUX), **5**: chemical diagram, molecular structure and overlay diagram. In the latter, the blue trace represents the molecule found in the centrosymmetric crystal [26]

The question of mis-assigned space-groups notwithstanding, the second issue arising from the appearance of non-centrosymmetric and centrosymmetric polymorphs for **5**, remains largely unanswered. The crux of this question is: Why do kryptoracemates appear in the first place? The centrosymmetric structure of **5** indicates that enantiomers of **5** can and do crystallise in a centrosymmetric space-group, as might be expected. So, why the appearance of a non-centrosymmetric version, the kryptoracemate? As noted above, kryptoracemates crystallise with $Z' > 1$; thus far, the author has not come across a kryptoracemate with the molecule lying on a rotation axis. Thus, kryptoracemates may be considered a special case of the relatively large number of structures with $Z' > 1$. In a recent comprehensive review of this topic, Steed and Steed [30] indicate that 9% of all-organic crystals have $Z' > 1$ and include reasons for this phenomenon such as having awkward-shaped molecules, the vagaries of crystallisation techniques, thermodynamics, etc., or some combination of these. In the case of **5**, it might be that the observation of the kryptoracemic form may be the result of a rapid crystallisation, the kinetic form, the centrosymmetric form, the thermodynamic outcome.

Thus far, all of the discussed kryptoracemates discussed feature a single stereogenic centre only. However, two and more stereogenic centres may be found in kryptoracemates. An example of a kryptoracemate with two stereogenic centres is illustrated for 2,2′-dimethyl-2,2′,3,3′-tetrahydro-1,1′-bicyclopenta(a)naphthalenylidene (**6**) [31] in Fig. 19.6. In the illustrated molecule, both chiral centres are *R*. As seen above, the superimposition of the illustrated molecule with the inverted form shows

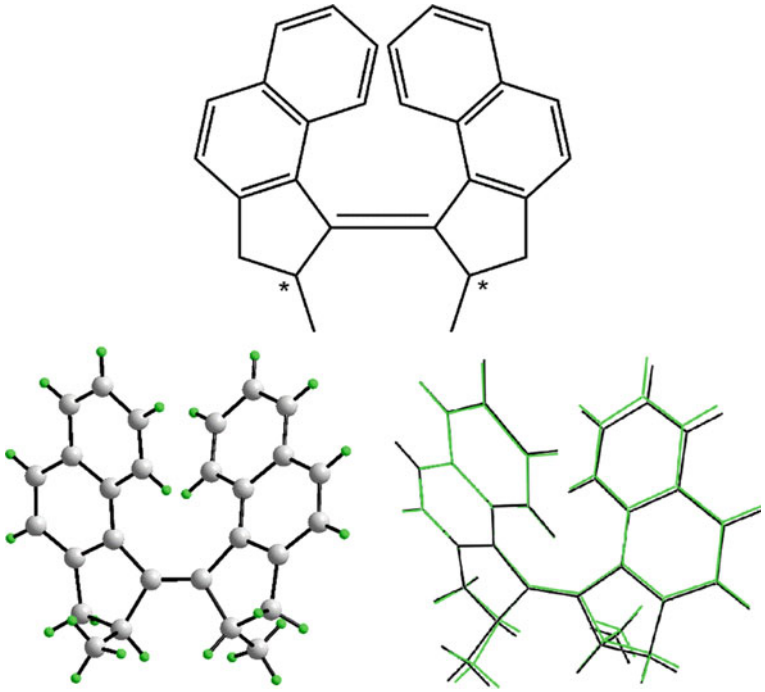

Fig. 19.6 Images for 2-methyl-1-{2-methyl-1H,2H,3H-cyclopenta[a]naphthalen-1-ylidene}-1H,2H,3H-cyclopenta[a]naphthalene (AQABID); **6**: chemical diagram, molecular structure and overlay diagram

a close correlation with the exception of the relative orientations of the methyl substituents.

In 2-[(3,5-dinitrobenzene)amido]cyclobutane-1-carboxylic acid (**7**) [32], the configurations at the sp^3-carbon atoms bearing the carboxylic acid and amino functionalities are *R* and *S*, respectively, as shown in Fig. 19.7. The overlap diagram again confirms the close similarity in the molecular conformations, especially in the four-membered rings. The presence of carboxylic acid functionality might be expected to promote the formation of a racemic crystal, whereby the carboxylic acid groups of each enantiomer associate about a centre of inversion via the familiar eight-membered $\{\cdots HOCO\}_2$ homo-synthon. However, while the $\{\cdots HOCO\}_2$ homo-synthon is formed between the two molecules in the crystal (orthorhombic, $P2_12_12_1$), the homo-synthon is non-symmetric. It is worth noting here that it is well established in the crystallographic literature that carboxylic acids form the eight-membered $\{\cdots HOCO\}_2$ homo-synthon in only about a third of the crystal structures where this is possible, being heavily susceptible to competing supramolecular synthons [33, 34].

In another variation of the theme, thus far, all of the chiral centres have been carbon-based. An attractive exception is found in the triazatriphosphinine derivative

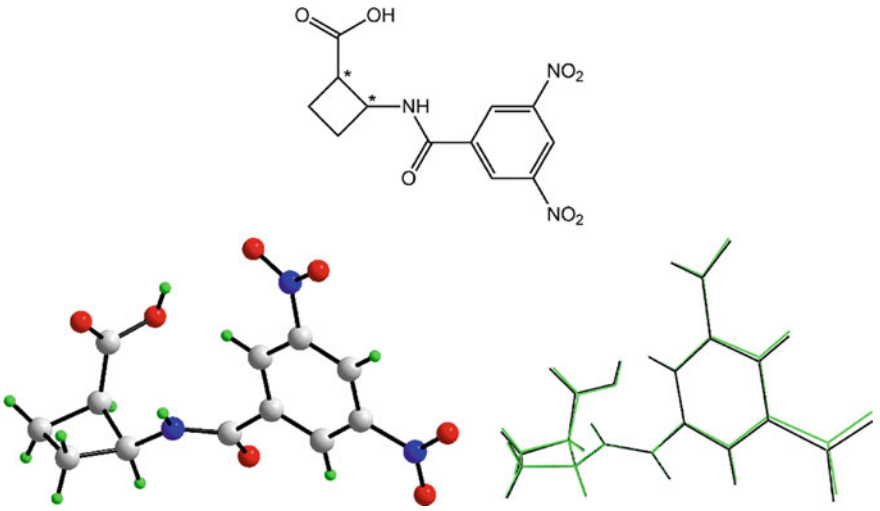

Fig. 19.7 Images for 2-[(3,5-dinitrobenzene)amido]cyclobutane-1-carboxylic acid (EGURIH); **7**: chemical diagram, molecular structure and overlay diagram

(**8**) [35]; the crystal is monoclinic, $P2_1$. As seen from Fig. 19.8, the two chiral centres are phosphorus-based with the configuration being *S* at the phosphorus centre bearing the chloride substituents and *R* at the second chiral phosphorus atom. Unlike several other structures, differences between the enantiomers are noted in the conformations of the nine-membered rings and in the relative orientations of two phenyl rings.

Three chiral centres are noted in the crystal of 1-acetoxy-7-cyano-5-methylbicyclo(3.2.0)heptan-2-one (**9**) [36]. For the illustrated molecule in Fig. 19.9, which crystallises in the monoclinic space-group $P2_1$, the configurations at the acetyl-, cyano- and methyl-substituted carbon atoms are *R*, *R* and *S*, respectively.

The structure of 6a-ethyl-1-(phenylsulphonyl)decahydro-4H-pyrrolo(3,2,1-ij)quinoline (**10**) [36] is notable for two reasons. First and foremost, there are four chiral centres in the molecule; see Fig. 19.10. The configurations about the centres bearing sulphur and nitrogen atoms are each *S*, while those about the carbon atoms bound to three carbon atoms are each *R*. Secondly, the crystal structure of a stereoisomer is known. The stereoisomer crystallises in the centrosymmetric space-group $P2_1/c$ with $Z' = 1$ with equal numbers of all *S*, *S*, *S*, *R* (and *R*, *R*, *R*, *S*) configurations [37].

Kryptoracemic crystals of the di-hydroxyl species, 1,2,3,4,5,6-hexahydro-2a,4a-(ethano)cyclopenta(fg)acenaphthylene-3,9-diol (**11**), feature four chiral centres in a monoclinic crystal with space-group $P2_1$ with $Z' = 4$ [38], i.e. with two pairs of crystallographic independent enantiomeric molecules. In the molecule illustrated in Fig. 19.11, the two hydroxyl-bearing carbon atoms each have an *S*-configuration while the other two chiral centres each have a *R*-configuration. Further interest in **11** rests with the observation that a polymorph is also known [38]. In this monoclinic crystal, there are one and one-half independent molecules in the asymmetric unit (Z'

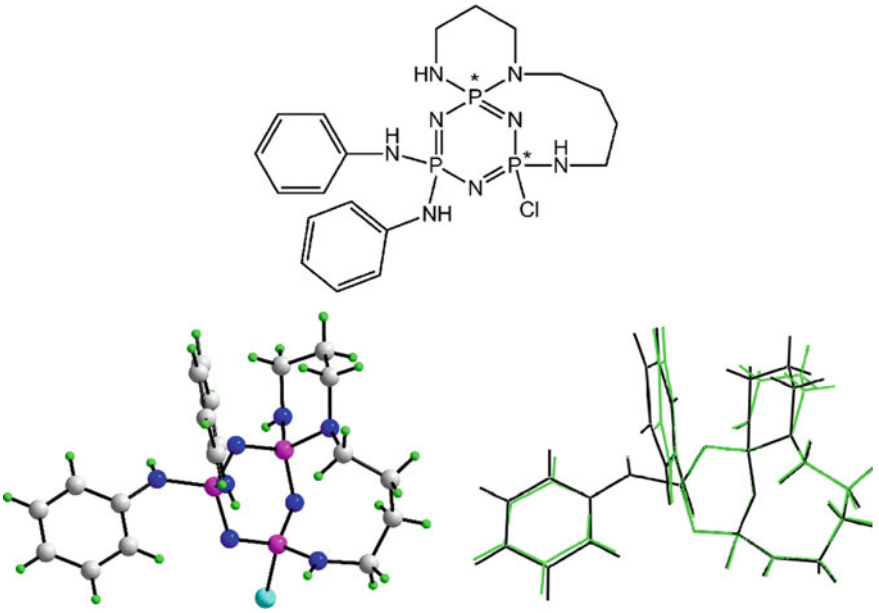

Fig. 19.8 Images for 12-chloro-14-*N*′,14-*N*-diphenyl-2,6,11,13,15,16-hexaaza-1λ^5,12 λ^5,14λ^5-triphosphatricyclo[10.3.1.0^{1,6}]hexadeca-1(16),12,14-triene-14,14-diamine (GAFJIH); **8**: chemical diagram, molecular structure and overlay diagram

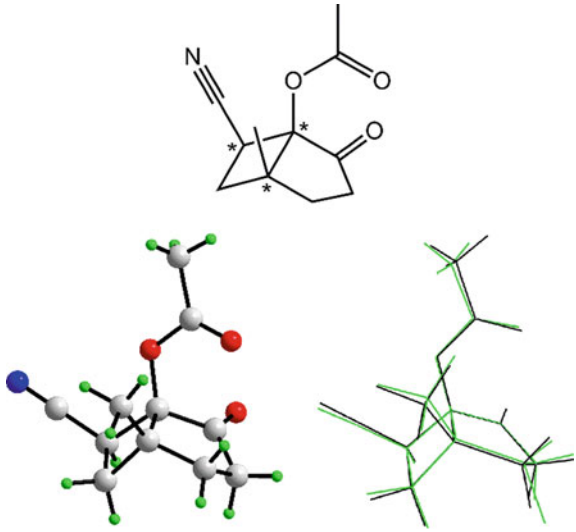

Fig. 19.9 Images for 7-cyano-5-methyl-2-oxobicyclo[3.2.0]heptan-1-yl acetate (BINGOU); **9**: chemical diagram, molecular structure and overlay diagram

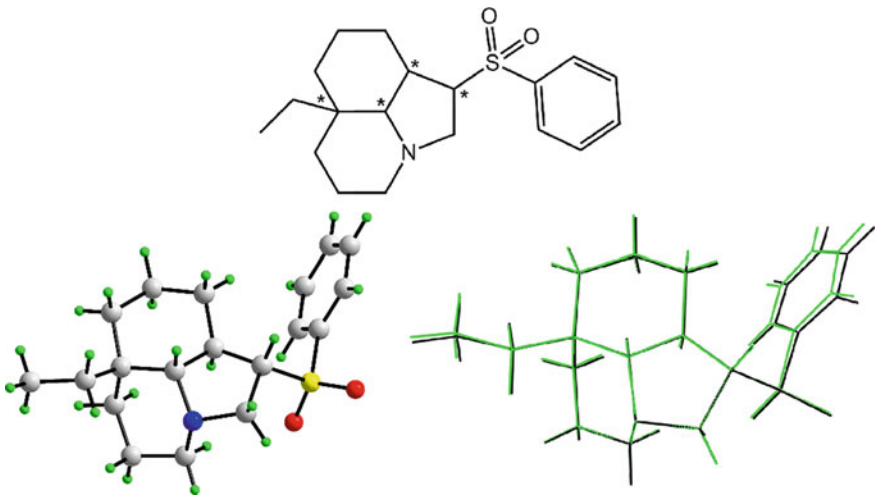

Fig. 19.10 Images for 3-(benzenesulphonyl)-8-ethyl-1-azatricyclo[6.3.1.$0^{4,12}$]dodecane (HILXUW); **10**: chemical diagram, molecular structure and overlay diagram

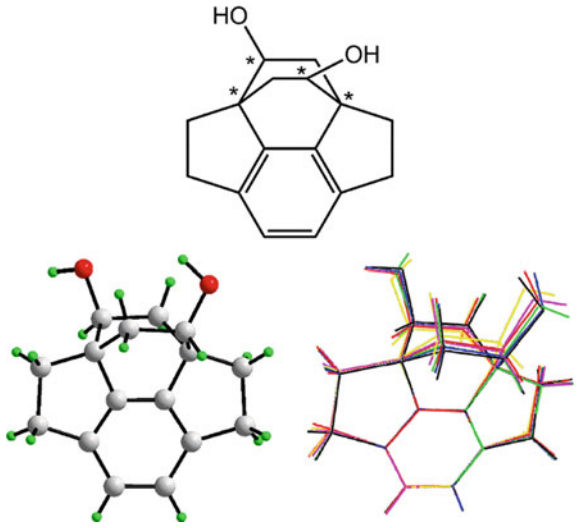

Fig. 19.11 Images for pentacyclo[5.5.2.$2^{1,4}$.$0^{4,14}$.$0^{10,13}$]hexadeca-7(14),8,10(13)-triene-2,15-diol (NOLFUP); **11**: chemical diagram, molecular structure and overlay diagram

= 1.5) with the space-group being *P*2/*c*. While one molecule lies in a general position (yellow image in the overlay diagram), the other is located about a twofold axis of symmetry (pink image). The overlay diagram of the six independent molecules in Fig. 11 highlights only small conformational differences in the molecules.

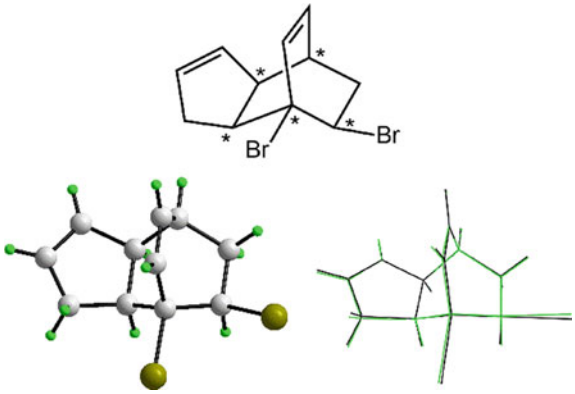

Fig. 19.12 Images for 7,11-dibromotricyclo[5.2.2.$0^{2,6}$]undeca-3,8-diene (QEWTES); **12**: chemical diagram, molecular structure and overlay diagram

The are five stereogenic centres in the dibromo derivative, 1,10-dibromotricyclo(5.2.2.02,6)undeca-4,8-diene (**12**) [39]; crystals belong to the orthorhombic space-group $P2_12_12_1$. In the illustrated molecule of Fig. 19.12, the chiral centres connecting the five- and six-membered rings each have an *S*-configuration and the remaining chiral centres are each *R*.

The final structure to be described among the genuine kryptoracemates is that of 4,7;13,16-diepoxy-9,18-dimethyl-1,10-dioxacyclo-octadecane-2,11-dione (**13**) [40]. The molecule crystallises in the monoclinic space-group $P2_1$ and with $Z' = 4$; i.e. there are two pairs of enantiomeric pairs related across a non-crystallographic centre of symmetry. The illustrated molecule of **13** in Fig. 19.13 has six stereogenic centres, each having a *R*-configuration. The overlap diagram of the two all-*R*-species with the inverted all-*S*-species shows a high degree of concordance in molecular conformation.

19.3 Non-genuine Kryptoracemates

In this section, representative examples of kryptoracemates with additional species incorporated in the crystal are described. These are solvates, salts and crystals with a combination of these. Enantiomeric pairs of chiral molecules are present in all examples as for the genuine kryptoracemates reviewed in 19.2 but so are other species. In most cases, it is likely that the presence of additional species does not have a significant influence on the observed kryptoracemic behaviour but, as will be demonstrated, certain counter-ions can be employed to force the formation of kryptoracemates.

The first structure to be described in this section may consider the result of an unbalanced crystallisation. In the crystal of *trans*-2-*N*,*N*′-dimethylaminomethyl-1,3-dithiolane-1,3-dioxide (**14**) [41], the chiral centres are the sulphoxide–sulphur atoms,

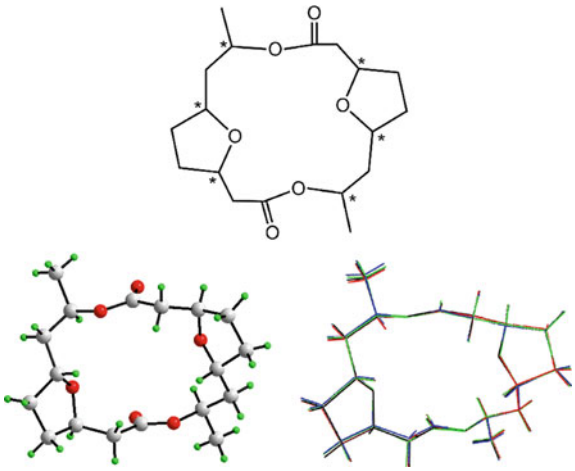

Fig. 19.13 Images for 5,14-dimethyl-4,13,19,20-tetraoxatricyclo[14.2.1.1^{7,10}]icosane-3,12-dione (NUYTAC); **13**: chemical diagram, molecular structure and overlay diagram

having *R*- and *S*-configurations in the molecule illustrated in Fig. 19.14. The molecule crystallises in the monoclinic space-group $P2_1$ with $Z' = 3$. Two of the molecules have the conformation shown in the molecular structure diagram of Fig. 19.14, and the third molecule has the opposite, i.e. *S*- and *R*-configurations. Hence, there is a deviation from the usual 1:1 enantiomeric ratio, hence the use of the term "unbalanced". In one sense, **14** can be considered a multi-component crystal of an enantiomeric pair of **14** co-crystallised with a *RS*-diastereoisomer.

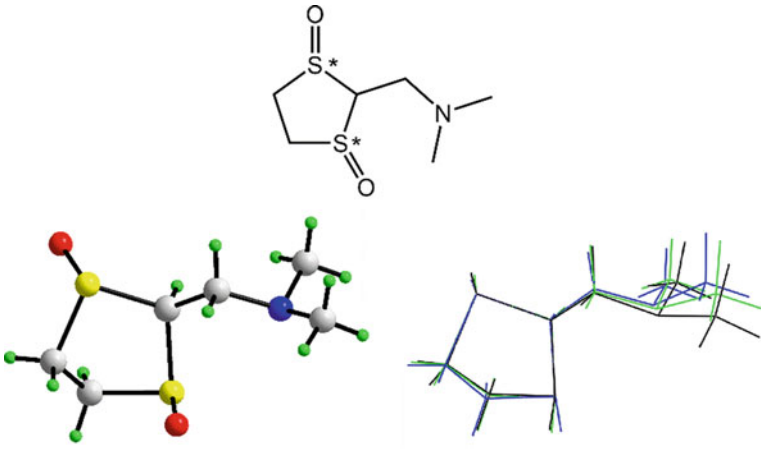

Fig. 19.14 Images for 2-[(dimethylamino)methyl]-1λ^4,3λ^4-dithiolane-1,3-dione (VEFMEZ); **14**: chemical diagram, molecular structure and overlay diagram

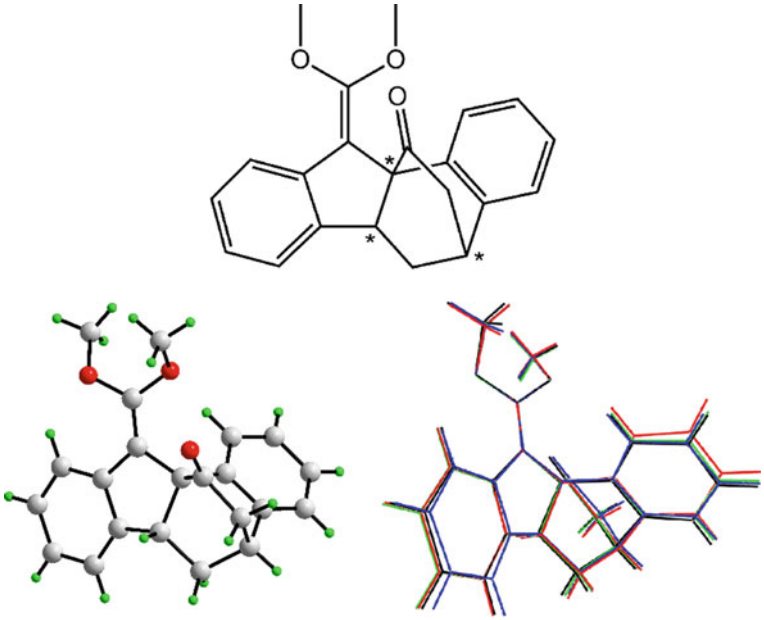

Fig. 19.15 Images for 2-(dimethoxymethylidene)pentacyclo[9.6.2.$0^{1,9}$.$0^{3,8}$.$0^{12,17}$]nonadeca-3(8),4,6,12,14,16-hexaen-18-one (SOQQOE); **15**: chemical diagram, molecular structure and overlay diagram

An analogous situation to **14** pertains in the crystal of 6-(dimethoxymethylene)-dibenzo(d,k)tricyclo(5.2.2.$0^{3,7}$)undeca-4,10-dien-8-one (**15**) [42], which crystallises in the triclinic space-group $P\bar{1}$ with $Z' = 4$. In this unbalanced crystal, three of molecules have the configuration shown in the molecular structure of Fig. 19.15, i.e. with *R*-configurations at the three chiral centres, and the fourth molecule has the all-*S*-configuration. Minor conformational differences in the orientations of some of the aromatic rings are noted in the overlay diagram (the inverted all-*S*-configuration is represented by the red image).

A more conventional co-crystal is evident for **16**, having a 2:1 composition of 3,3-dimethyl-4-(phenylsulphonyl)azetidin-2-one and *trans*-3-methyl-4-(phenylsulphonyl)azetidin-2-one; **16** crystallises in the monoclinic space-group $P2_1$ [43]. The illustrated molecule in Fig. 19.16 has an *R*-configuration around the chiral centre, and the overlay diagram between it and its inverted enantiomer suggests a conformational difference associated with the relative orientations of the phenyl sulphoxide residues. In the molecular packing, each of the amine-N–H atoms forms a similar weak hydrogen bond with a sulphoxide oxygen atom.

The carboxylic acid, syn-1-benzyl-4,5-diphenyl-2-methyl-4,5-dihydroimidazole-4-carboxylic acid, has been crystallised as its hemi-dichloromethane solvate (**17**) in the orthorhombic space-group $P2_12_12_1$ [44]. In the molecule illustrated in Fig. 19.17, the configuration of the carbon atom bearing the carboxylic acid is *S* and the other

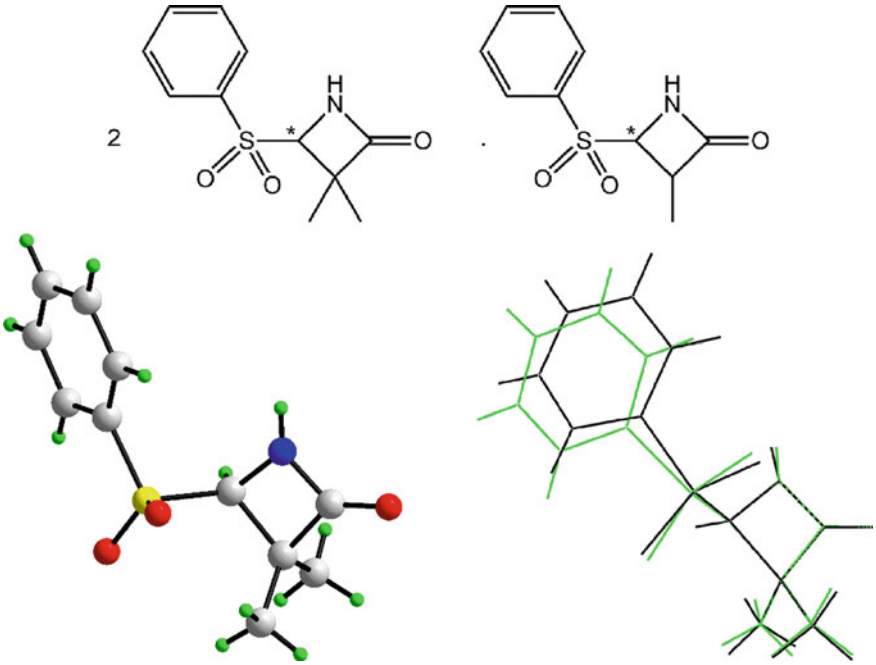

Fig. 19.16 Images for the 2:1 4-(benzenesulphonyl)-3-methylazetidin-2-one 4-(benzenesulphonyl)-3,3-dimethylazetidin-2-one co-crystal (ABADUD); **16**: chemical diagram, molecular structure of 4-(benzenesulphonyl)-3,3-dimethylazetidin-2-one and overlay diagram for an enantiomeric pair of 4-(benzenesulphonyl)-3,3-dimethylazetidin-2-one molecules

chiral centre is *R*. The overlay diagram is exceptional in that there are significant conformational differences in all but the methyl substituents about the central five-membered imidazole ring. In the crystal, each of the hydroxyl groups forms an intermolecular hydrogen-bonding interaction with an imidazole nitrogen atom rather than self-associating via hydroxyl-O–H···O(hydroxyl) hydrogen-bonding, as has been noted previously in cases of steric congestion [45] and in the presence of competing synthons [46].

Another solvate, this time a 3:2 hydrate is found in the orthorhombic ($P2_12_12_1$) crystals of 2,8-diisopropyl-5-trifluoromethyl-7,8-dihydro-1,12-iminobenzo(c)pyrido(4,3,2-ef)(1)-benzazepine (**18**) [47]. Just as for **15** and **16** described above, the composition of **18** can be considered as being unbalanced, with the crystallographic asymmetric unit comprising the illustrated molecule in Fig. 19.18, with an *S*-configuration at the chiral centre, two inverted organic molecules along with two water molecules of crystallisation. Different orientations of the isopropyl groups are evident in the overlay diagram. The independent molecules form different intermolecular interactions. The molecule with the *S*-configuration forms amine-N–H···N(amine) and N–H···N(pyridyl) hydrogen bonds. By contrast,

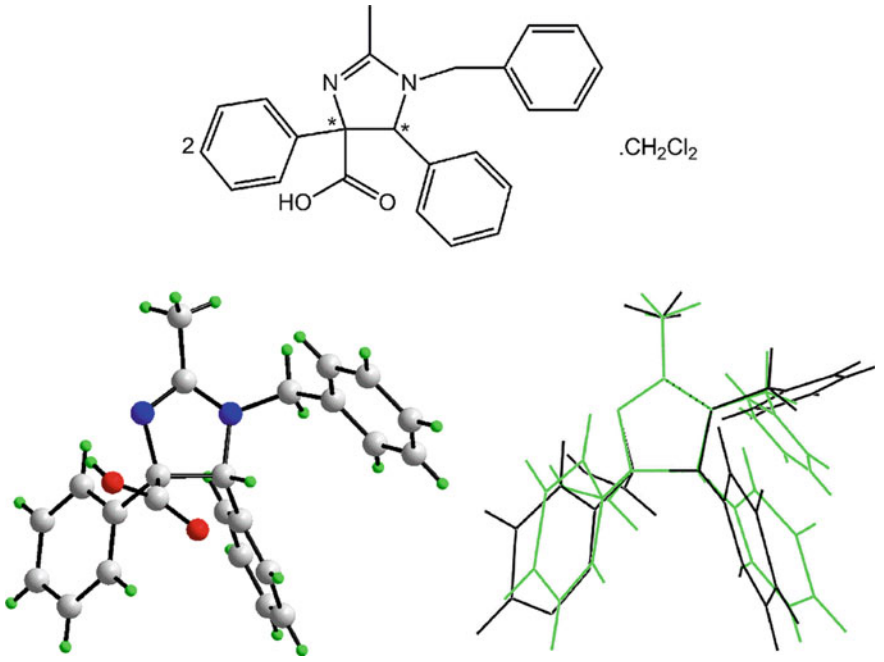

Fig. 19.17 Images for 1-benzyl-2-methyl-4,5-diphenyl-4,5-dihydro-1H-imidazole-4-carboxylic acid dichloromethane solvate (2:1) (KODQOK); **17**: chemical diagram, molecular structure of the carboxylic acid and overlay diagram for the enantiomeric carboxylic acids

each of the two molecules with a *R*-configuration forms amine-N–H···O(water) and N–H···N(amine) hydrogen bonds.

Attention is now directed towards the description of four salts. The first of these, namely the 1:1 salt 2-amino-N-(1-methyl-1,2-diphenylethyl)acetamide hydrochloride (**19**) [48], crystallises in the monoclinic space-group $P2_1$ with an enantiomeric pair of cations and two chloride counter-ions in the asymmetric unit. The chiral centre in the cation shown in Fig. 19.19 has an *R*-configuration. As noted above for **17**, non-trivial conformational differences are evident for the pendant groups in the overlay diagram. There is charge-assisted ammonium-N–H···Cl and ammonium-N–H···O(carbonyl) along with amino-N–H···Cl and amino-N–H···O(carbonyl) hydrogen-bonding operating in the molecular packing. The independent cations have distinctive hydrogen-bonding patterns, with the molecule shown in Fig. 19.19 forming ammonium-N–H···Cl and amino-N–H···O(carbonyl) hydrogen bonds as opposed to the enantiomer which forms two ammonium-N–H···Cl, one ammonium-N–H···O(carbonyl) and one amino-N–H···Cl hydrogen-bonding interactions.

A 1:1 ratio between cations and anions is also found in the crystal of 2-((2,8-bis(trifluoromethyl)quinolin-4-yl)(hydroxy)methyl)piperidinium 3,3,3-trifluoro-2-methoxy-2-phenylpropanoate (triclinic, $P\bar{1}$ with $Z' = 2$) [49]. The special

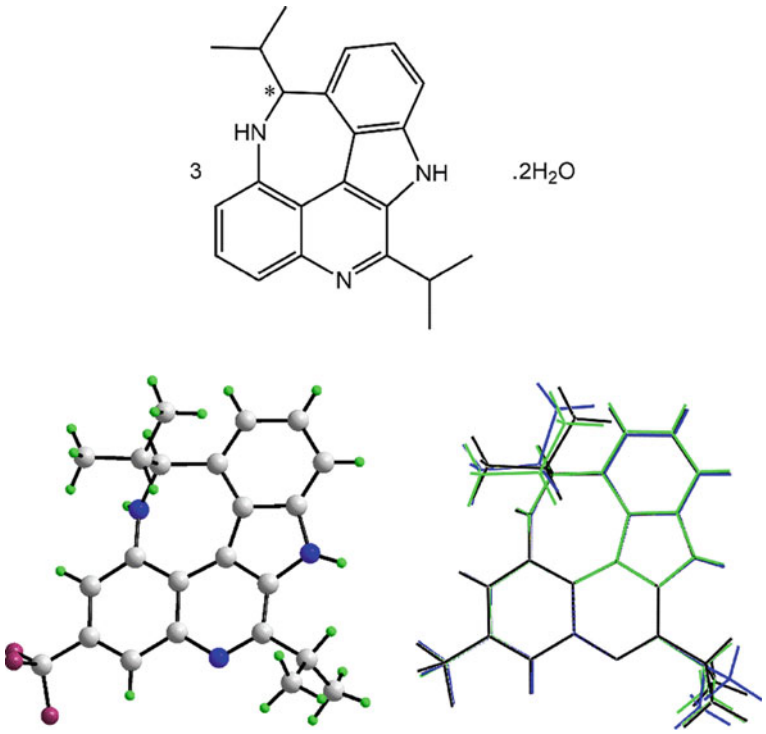

Fig. 19.18 Images for the 3:2 8,16-bis(propan-2-yl)-12-(trifluoromethyl)-9,15,19-triazapentacyclo[8.7.1.1^{3,17}.0^{2,7}.0^{14,18}]nonadeca-1(18),2(7),3,5,10,12,14,16-octaene hydrate (AWUVUJ); **18**: chemical diagram, molecular structure of 2,8-diisopropyl-5-trifluoromethyl-7,8-dihydro-1,12-iminobenzo(c)pyrido(4,3,2-ef)(1)benzazepine and overlay diagram of the organic molecules

feature of this structure is that the anions are chiral, and each has an *R*-configuration, precluding the adoption of a centrosymmetric space-group. The molecule illustrated in Fig. 19.20 has two chiral centres, with the carbon bearing the hydroxyl group being *S* and the other being *R*. The overlay diagram between this molecule and its pseudo-enantiomer mate indicates differences in the relative orientations of the piperidinium cations. The hydrogen-bonding interactions formed by the cations are quite similar, at least to a first approximation, with each of the hydroxyl groups participating in a charge-assisted O–H···O hydrogen bond with a carboxylate oxygen atom. Three of the four ammonium-N–H atoms are bifurcated. One hydrogen atom from each ammonium each group forms an intramolecular, charge-assisted N–H···O(hydroxyl) hydrogen bond, and the remaining charge-assisted hydrogen bonds are of the type N–H···O(carboxylate).

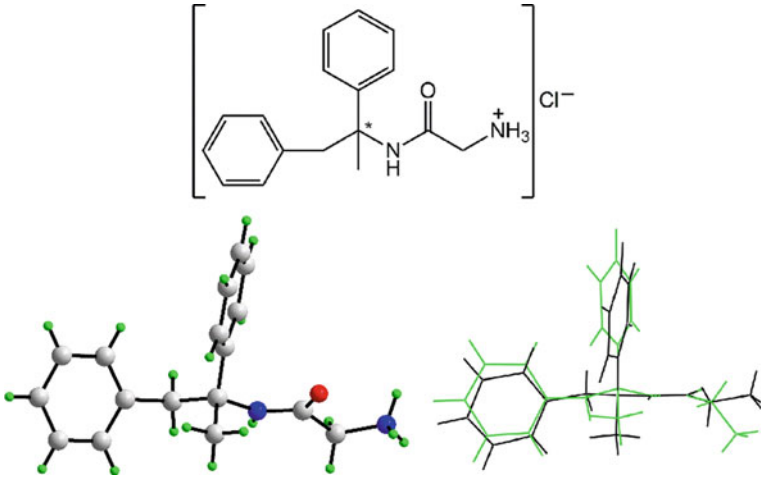

Fig. 19.19 Images for [(1,2-diphenylpropan-2-yl)carbamoyl]methanaminium chloride [MAPXUX]; **19**: chemical diagram, molecular structure of the cation and overlay diagram of the independent cations

The next structure to be described is also a 1:1 salt, i.e. bis(2-((2,8-bis(trifluoromethyl)quinolin-4-yl)(hydroxy)methyl)piperidinium) chloride 4-fluorobenzenesulphonate (orthorhombic, $P2_12_12_1$ with $Z' = 2$) [50]. The key difference in this case is that the two anions are distinct. For the molecule illustrated in Fig. 19.21, the chirality of the carbon connected to the hydroxyl group is *R* and the other chiral centre in the ring is *S*. As for **20**, there is a minor conformational difference in the piperidinium cations. Despite the presence of distinct anions, the hydrogen-bonding interactions at play in the crystal are comparable. Thus, each hydroxyl group forms a hydrogen bond to a sulphoxide oxygen atom, indeed to the same sulphoxide oxygen atom. The two ammonium-N-H atoms of each cation form charge-assisted hydrogen bonds to a chloride and to a sulphoxide oxygen atom.

The crystal of **21** is the second 2-{[2,7-bis(trifluoromethyl)quinolin-4-yl](hydroxy)methyl}piperidin-1-ium salt to be described. These species are of interest as the *R*,*S*-cation, as its chloride salt, commonly known as mefloquinium chloride, was found to be effective against malaria [51]. The salts **20** and **21** were prepared in attempts to resolve the enantiomers as the *S*,*R*-enantiomer causes toxic side effects and, in fact, were the structures that piqued the interest of the author in this field. Of the about 30 known [4] crystal structures of methloquine/mefloquinium, two are kryptoracemic. In another study [52], where crystallographic details were reported only extremely briefly, it was mentioned that in their attempts at chiral resolution, about the same ratio of kryptoracemates was isolated. These numbers exceed greatly the estimated 0.1% frequency for this behaviour and may suggest a propensity of these molecules towards kryptoracemic behaviour. However, it is more likely that the "McCrone axiom" is apt here [53]: paraphrasing, the more effort one puts into discovering different forms of crystals, the more likely it is that new forms will

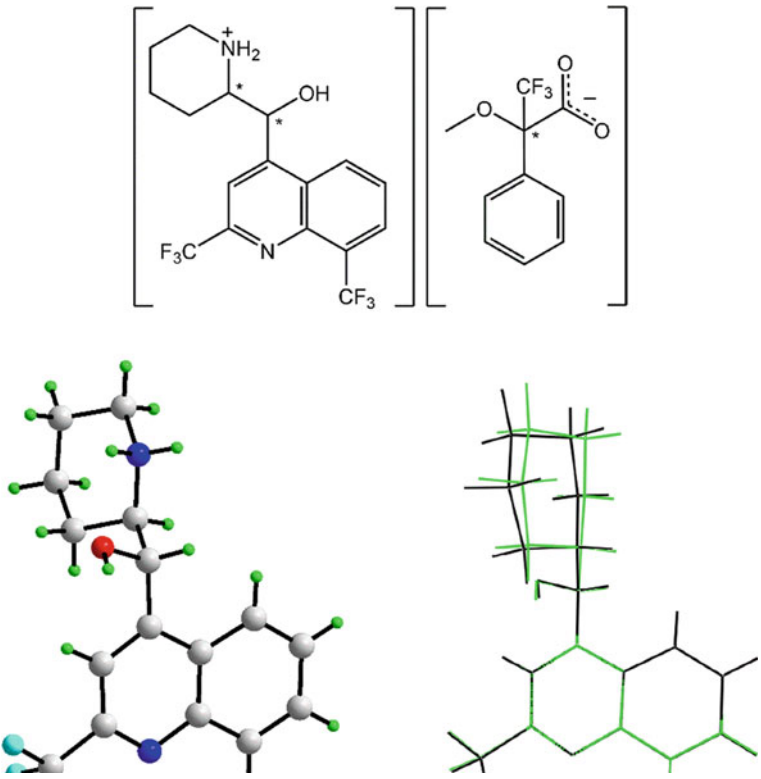

Fig. 19.20 Images for 2-{[2,7-bis(trifluoromethyl)quinolin-4-yl](hydroxy)methyl}piperidin-1-ium 3,3,3-trifluoro-2-methoxy-2-phenylpropanoate [ENIPUO]; **20**: chemical diagram, molecular structure of one cation and overlay diagram of the cations

be discovered. This axiom is clearly vindicated by computational chemistry investigations which indicate that many calculated polymorphic forms of a molecule may differ in Gibbs free energies by only a few kcal/mol [54, 55].

One last kryptoracemate example is included for the sake of completeness, namely a salt solvate, *cis*-2-phenyl-3-methoxycarbonyl-pyrrolidinium oxalate hemihydrate (22) [56]. The crystallographic asymmetric unit in the monoclinic space-group $P2_1$ comprises two cations, two anions and a water molecule of crystallisation. The cation represented in Fig. 19.22 has *S*- and *R*-configurations at the carbon atoms carrying the phenyl and ester groups, respectively. As is normally the case, the agreement in conformation between the illustrated and inverted mates is close as seen in the overlay diagram. The hydrogen-bonding profiles exhibited by the cations are quite similar with one ammonium-N–H atom of each forming a donor interaction to the water molecule of crystallisation. In the same way, the second ammonium-N–H atom of each cation is bifurcated. For the illustrated molecule in Fig. 19.22, this atom bridges the carbonyl oxygen atom of the carboxylic acid group and a carboxylate oxygen

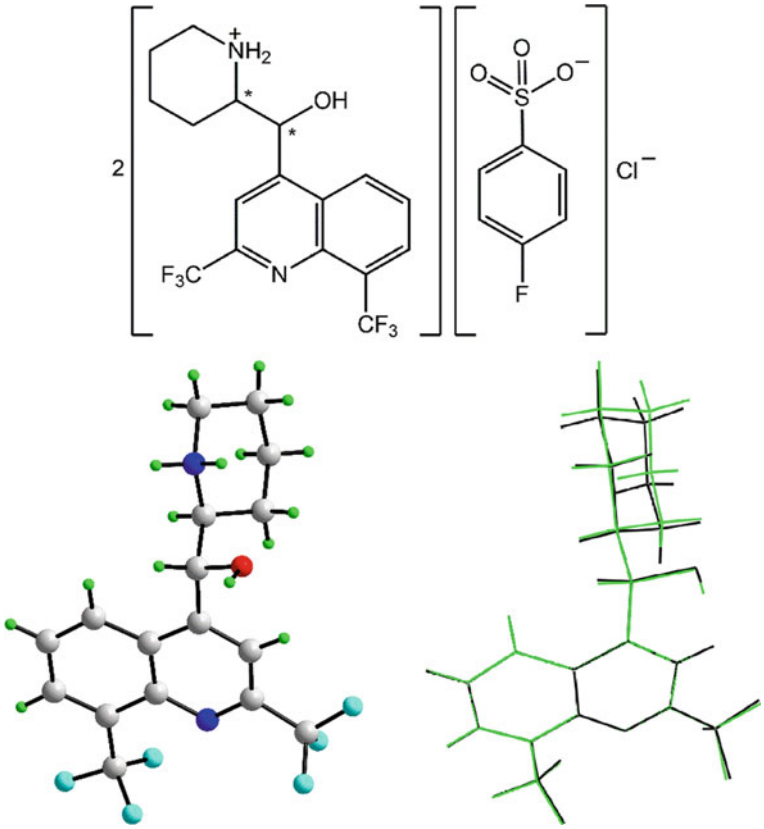

Fig. 19.21 Images for 2-{[2,7-bis(trifluoromethyl)quinolin-4-yl](hydroxy)methyl}piperidin-1-ium chloride 4-fluorobenzene-1-sulphonate [ELAMAH]; **21**: chemical diagram, molecular structure of one cation and overlay diagram

atom of the same oxalate anion, thereby forming a five-membered {H···OCCO} synthon. A slight difference occurs in the case of the second cation. Although a five-membered {H···OCCO} synthon is still formed, one, weaker, hydrogen bond involves the hydroxy group of the oxalate anion (rather than a carbonyl) resulting in a significantly longer N–H···O hydrogen bond.

19.4 Overview

The intention of the present survey of reported kryptoracemic crystals highlights the structural diversity of this rare class of crystal, making up only 0.1% of all-organic crystals [3]. The genuine or pure kryptoracemates—containing pseudo-racemic pairs only—have molecules related to a non-crystallographic centre of symmetry with

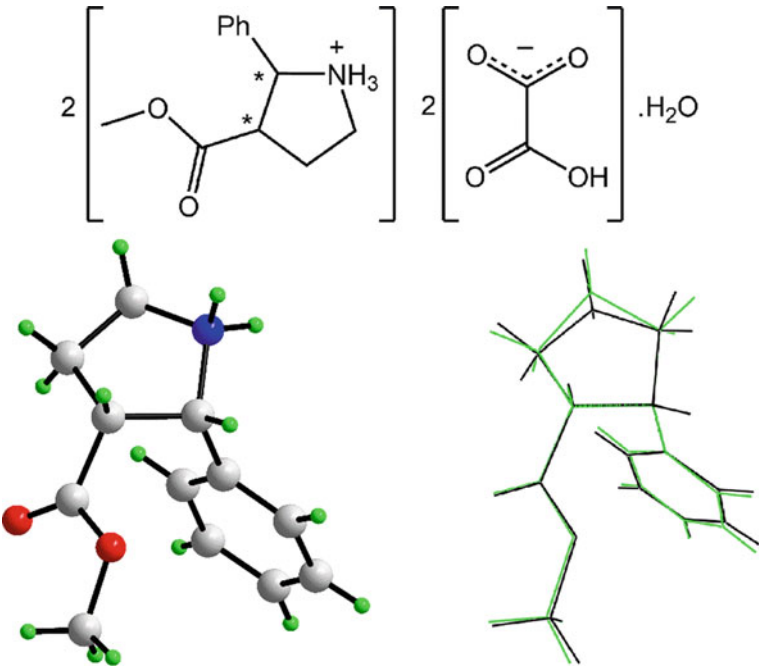

Fig. 19.22 Images for 3-(methoxycarbonyl)-2-phenylpyrrolidin-1-ium hydrogen oxalate hemihydrate [FAHQUB]; **22**: chemical diagram, molecular structure of one of the cations and overlay diagram of the cations

only minor conformational differences. Similar observations pertain to non-genuine kryptoracemates which contain additional species (solvent and counter-ions) in their crystals in addition to pseudo-racemic pairs. Kryptoracemates can only crystallise in Sohncke space-groups and the overwhelming majority of genuine examples crystallised in three space-groups: $P1$ (15%), $P2_1$ (52%) and $P2_12_12_1$ (33%). For the non-genuine kryptoracemates, a possible reason for this behaviour may relate to the presence of additional species and the influence these have on the supramolecular association operating in the crystals, something unlikely to "pertain" in the genuine kryptoracemates.

At present, it is probably fair to opine that most of the reported kryptoracemates are the product of serendipity and that systematic studies are likely to uphold the McCrone axiom [53] but prove to be most rewarding at the same time [57]. Certainly, a rationale of this behaviour will prove useful in the understanding of the crystallisation phenomenon in general.

References

1. Morales, G.A., Fronczek, F.R.: A kryptoracemic hydroperoxide. Acta Crystallogr. **C52**, 1266–1268 (1996)
2. Bernal, I.: ACA Annual Meeting, Montreal, Quebec, Canada. Abstract 4a.1.e (1995)
3. Fábián, L., Brock, C.P.: A list of organic kryptoracemates. Acta Crystallogr. B **66**, 94–103 (2010)
4. Taylor, R., Wood, P.A.: A million crystal structures: the whole is greater than the sum of its parts. Chem. Rev. **119**, 9427–9477 (2019)
5. Bernal, I., Watkins, S.: A list of organometallic kryptoracemates. Acta Crystallogr. **C71**, 216–221 (2015)
6. Dalhus, B., Görbitz, C.H.: Non-centrosymmetric racemates: space-group frequencies and conformational similarities between crystallographically independent molecules. Acta Crystallogr. **B56**, 715–719 (2000)
7. Flack, H.D.: Louis Pasteur's discovery of molecular chirality and spontaneous resolution in 1848, together with a complete review of his crystallographic and chemical work. Acta Crystallogr. **A65**, 371–389 (2009)
8. Pérez-García, L., Amabilino, D.B.: Spontaneous resolution, whence and whither: from enantiomorphic solids to chiral liquid crystals, monolayers and macro- and supra-molecular polymers and assemblies. Chem. Soc. Rev. **36**, 941–967 (2007)
9. Pidcock, E., Motherwell, W.D.S., Cole, J.C.: A database survey of molecular and crystallographic symmetry. Acta Crystallogr. **B59**, 634–640 (2003)
10. Brock, C.P., Dunitz, J.D.: Towards a grammar of crystal packing. Chem. Mater **6**, 1118–1127 (1994)
11. Flack, H.D.: Chiral and achiral crystal structures. Helv. Chim. Acta **86**, 905–921 (2003)
12. Moulton, B., Zaworotko, M.J.: From molecules to crystal engineering: supramolecular isomerism and polymorphism in network solids. Chem. Rev. **101**, 1629–1658 (2001)
13. Zhang, J.-P., Huang, X.-C., Chen, X.-M.: Supramolecular isomerism in coordination polymers. Chem. Soc. Rev. **38**, 2385–2396 (2009)
14. Cruz-Cabeza, A.J., Reutzel-Edens, S.M., Bernstein, J.: Facts and fictions about polymorphism. J. Chem. Soc. Rev. **44**, 8619–8635 (2015)
15. Hall, S.R., Allen, F.H., Brown, I.D.: The Crystallographic Information File (CIF): a new standard archive file for crystallography. Acta Crystallogr. **A47**, 655–685 (1991)
16. Brandenburg, K., Putz, H.: DIAMOND—crystal and molecular structure visualization. Crystal Impact GbR, Bonn, Germany (2006)
17. Gans, J.D., Shalloway, D.: Qmol: a program for molecular visualization on Windows-based PCs. J. Molec. Graphics Model **19**, 557–559 (2001)
18. Macrae, C.F., Edgington, P.R., McCabe, P., Pidcock, E., Shields, G.P., Taylor, R., Towler, M., van de Streek, J.: Mercury: visualization and analysis of crystal structures. J. Appl. Cryst **39**, 453–457 (2006)
19. Spek, A.L.: Structure validation in chemical crystallography. Acta Crystallogr. **D65**, 148–155 (2009)
20. ChemAxon: Marvinsketch. http://www.chemaxon.com. Accessed 1 Nov 2019) (2010)
21. Mostad, A., Romming, C., Tressum, L.: The crystal and molecular structure of (2-hydroxyphenyl)alanine (o-tyrosine). Acta Chem. Scand **29**, 171–176 (1975)
22. Patonay, T., Jekó, J., Juhász-Tóth, E.: Synthesis of highly substituted 2H-azirine-2-carboxylates via 3-Azido-4-oxobut-2-enoates. Eur. J. Org. Chem **125**, 1441–1448 (2008)
23. Berestovitskaya, V.M., Litvinov, I.A., Efremova, I.E., Lapshina, L.V., Krivolapov, D.B., Gubaidullin, A.T.: Halo derivatives of 2,4-dinitrothiolene 1,1-dioxides: synthesis and structure. Russ. J. Gen. Chem **72**, 1111–1118 (2002)
24. Ohsawa, A., Arai, H., Ohnishi, H., Kaihoh, T., Itoh, T., Yamaguchi, K., Igeta, H., Iitaka, Y.: Sodium borohydride reduction of 1,2,3-triazine derivatives. J. Pharm. Soc. Jpn. **105**, 1122–1130 (1985)

25. Erhardt, S., Macgregor, S.A., McCullough, K.J., Savill, K., Taylor B.J.: Model studies of β-scission ring-opening reactions of cyclohexyloxy radicals: application to thermal rearrangements of dispiro-1,2,4-trioxanes. Org. Lett. 5569–5572 (2007)
26. McCullough, K.J., Hursthouse, M.B., Coles, S.J.: Private Communication to the Cambridge Structural Database. Refcode NIWHUX01 (1993)
27. Santarsieroa, B.D., Marsh, R.E. (1922–2017): Acta Crystallogr. **C73**, 1038–1039 (2017)
28. Marsh, R.E.: The importance of weak reflections in resolving the centrosymmetric-noncentrosymmetric ambiguity: a cautionary tale. Acta Crystallogr. **B37**, 1985–1988 (1981)
29. Marsh, R.E., Spek, A.L.: Use of software to search for higher symmetry: space group C2. Acta Crystallogr. **B57**, 800–805 (2001)
30. Steed, K.S., Steed, J.W.: Packing problems: High Z' crystal structures and their relationship to cocrystals, inclusion compounds, and polymorphism. Chem. Rev. **115**, 2895–2933 (2015)
31. ter Wiel, M.K.J., van Delden, R.A., Meetsma, A., Feringa, B.L.: Increased speed of rotation for the smallest light-driven molecular motor. J. Am. Chem. Soc **125**, 15076–15086 (2003)
32. Aitken, D.J., Gauzy, C., Pereira, E.: A short synthesis of the cis-cyclobutane β-aminoacid skeleton using a [2+2] cycloaddition strategy. Tetrahedron Lett **43**, 6177–6179 (2002)
33. Allen, F.H., Motherwell, W.D.S., Raithby, P.R., Shields, G.P., Taylor, R.: Systematic analysis of the probabilities of formation of bimolecular hydrogen-bonded ring motifs in organic crystal structures. New J. Chem **23**, 25–34 (1999)
34. Tiekink, E.R.T.: Supramolecular assembly based on "emerging" intermolecular interactions of particular interest to coordination chemists. Coord. Chem. Rev. **345**, 209–248 (2017)
35. Beşli, S., Coles, S.J., Davies, D.B., Hursthouse, M.B., Ibişoğlu, H., Kiliç, A., Shaw, R.A.: Retention of configuration in the nucleophilic substitution reactions of some nine-membered ansa derivatives of cyclotriphosphazatriene. Chem. Eur. J **10**, 4915–4920 (2004)
36. Furusaki, A., Abe, K., Matsumoto, T.: X-ray structure of (1RS, 5RS, 7SR)-1-acetoxy-7-cyano-5-methylbicyclo[3.2.0]heptan-2-one, a photocycloadduct of 2-acetoxy-3-methyl-2-cyclopenten-1-one and acrylonitrile. Bull. Chem. Soc. Jpn. **55**, 611–612 (1982)
37. Coldham, I., Burrell, A.J.M., White, L.E., Adams, H., Oram, N.: Highly efficient synthesis of tricyclic amines by a cyclization/cycloaddition cascade: total syntheses of aspidospermine, aspidospermidine, and quebrachamine. Angew. Chem. Int. Ed. **46**, 6159–6162 (2007)
38. Savinsky,R., Hopf, H., Dix, I., Jones, P.G.: Partially hydrogenated [2.2]paracyclophanes as precursors in polycyclic hydrocarbon chemistry. Eur. J. Org. Chem. 4595–4606 (2001)
39. Su, K.-J., Mieusset, J.-L., Arion, V.B., Brecker, L., Brinker, U.H.: Cope rearrangement versus a novel tandem retro-Diels—Alder—Diels—Alder reaction with role reversal. Org. Lett **9**, 113–115 (2007)
40. Kalesse, M., Wartchow, R.: Structural features for the promotion of optimal stacking in the solid state. Tetrahedron **54**, 8015–8024 (1998)
41. Gültekin, Z., Hökelek, T.: Crystal structure of *trans*-(1*RS*,3*RS*)-2-*N*,*N*′-Dimethylaminomethyl-1,3-dithiolane-1,3-dioxide. Anal. Sci. X-Ray Struct. Anal. Online **22**, x9–x10 (2006)
42. Heileman, M.J., Moore, H.W.: Generation and intramolecular cyclization of (2-ethenylphenyl)bisketenes. Synthesis of benzofuranones. Tetrahedron Lett. **39**, 3643–3646 (1998)
43. Basak, A., Bag, S.S., Mazumdar, P.A., Bertolasi, V., Das A.K.: Molecular recognition in β-lactams: The crystal packing in 4-sulfonyl β-lactams. J. Chem. Res. 318–321 (2004)
44. Sharma, V., Tepe, J.J.: Diastereochemical diversity of imidazoline scaffolds via substrate controlled TMSCl mediated cycloaddition of azlactones. Org. Lett **7**, 5091–5094 (2005)
45. Brock, C.P., Duncan, L.L.: Anomalous space-group frequencies for monoalcohols. CnHmO. Chem. Mater. **6**, 1307–1312 (1994)
46. Bis, J.A., Vishweshwar, P., Weyna, D., Zaworotko, M.J.: Hierarchy of supramolecular synthons: persistent hydroxyl···pyridine hydrogen bonds in cocrystals that contain a cyano acceptor. Molec. Pharma. **4**, 401–416 (2007)
47. Al-Khashashneh, A.M., El-Abadelah, M.M., Boese, R.: Novel synthesis of model dihydroazepine-fused indolo[2,3-c]quinolines. Heterocycles **60**, 73–87 (2003)

48. Lewis, G.R., Steele, G., McBride L., Florence, A.J., Kennedy, A.R., Shankland, N., David, W.I.F., Shankland, K., Teat, S.J.: Hydrophobic versus hydrophilic: ionic competition in remacemide salt structures. Cryst. Growth Des. **5**, 427–438 (2005)
49. Wardell, J.L., Wardell, S.M.S.V., Tiekink, E.R.T.: A kryptoracemic salt: 2-{[2,8-bis(trifluoromethyl)quinolin-4-yl](hydroxy)methyl}piperidin-1-ium (+)-3,3,3-trifluoro-2-methoxy-2-phenylpropanoate. Acta Crystallogr. **E57**, 872–877 (2016)
50. Jotani, M.M., Wardell, J.L., Tiekink, E.R.T.: Crystal structure and Hirshfeld analysis of the kryptoracemate: bis(mefloquinium) chloride p-fluorobenzenesulphonate. Z. Kristallogr. Cryst. Mater. **231**, 247–255 (2016)
51. Nevin, R.L.: A serious nightmare: psychiatric and neurologic adverse reactions to mefloquine are serious adverse reactions. Pharmacol. Res. Perspect **5**, e00328 (2017)
52. Engwerda, A.H.J., Maassen, R., Tinnemans, P., Meekes, H., Rutjes, F.P.J.T., Vlieg, E.: Attrition-enhanced deracemization of the antimalaria drug mefloquine. Angew. Chem. Int. Ed **58**, 1670–1673 (2019)
53. Haleblian, J., McCrone, W.: Pharmaceutical applications of polymorphism. J. Pharm. Sci **58**, 911–929 (1969)
54. Gavezzotti, A., Filippini, G.: Polymorphic forms of organic crystals at room conditions: thermodynamic and structural implications. J. Am. Chem. Soc **117**, 12299–12305 (1995)
55. Price, S.L.: Is zeroth order crystal structure prediction (CSP_0) coming to maturity? What should we aim for in an ideal crystal structure prediction code? Faraday Discuss **211**, 9–30 (2018)
56. Suresh, S., Periasamy, M.: Synthesis of *cis*-2-aryl-3-pyrrolidine carboxylic esters via diastereoselective cyclization of γ-imino esters using a $TiCl_4/Et_3N$ reagent system. Tetrahedron Lett **45**, 6291–6293 (2004)
57. Laubenstein, R., Şerb, M.-D., Englert, U., Raabe, G., Braun, T., Braun, B.: Is it all in the hinge? A kryptoracemate and three of its alternative racemic polymorphs of an aminonitrile. Chem. Commun **52**, 1214–1217 (2016)

Chapter 20
Twenty-Five Years' History, Mechanism, and Generality of Preferential Enrichment as a Complexity Phenomenon

Rui Tamura, Hiroki Takahashi, and Gérard Coquerel

Abstract Described here are the history, mechanism, and generality of 'preferential enrichment (PE)' which is a spontaneous chiral resolution phenomenon observed upon recrystallization of certain kinds of chiral racemic organic compounds from organic or aqueous solvents. The use of dimorphic cocrystals of chiral racemic compounds and achiral coformers could greatly expand the scope of PE. A thorough mechanistic investigation through (i) the direct observation of crystallization processes by using in situ techniques such as attenuated total reflectance infrared spectroscopy, temperature-controlled video-microscopy, and time-resolved X-ray powder diffraction measurement, (ii) the graph set analysis of crystal structures of deposited crystals, (iii) the kinetic/thermodynamic studies on the unique solubility properties of two enantiomers, and (iv) the observation of equilibrium behavior of an added labeled compound in solution and in the solid phases under PE conditions, together with (v) the construction of the corresponding ternary phase diagram, has indicated that PE is ascribed to an event of nonequilibrium 'complexity system.'

Keywords Preferential enrichment · Spontaneous chiral resolution · Phase transition · Chiral symmetry breaking · Complexity system

R. Tamura (✉) · H. Takahashi
Graduate School of Human and Environmental Studies, Kyoto University, Kyoto 606-8501, Japan
e-mail: tamura.rui.45x@st.kyoto-u.ac.jp

H. Takahashi
e-mail: takahashi.hiroki.2x@kyoto-u.ac.jp

G. Coquerel
Normandie Universuté, SMS, EA 3233, Université Rouen, Crystal Genesis Unit, 76821 Mont Saint-Aignan Cedex, France
e-mail: gerard.coquerel@univ-rouen.fr

M. Sakamoto and H. Uekusa (eds.), *Advances in Organic Crystal Chemistry*,
https://doi.org/10.1007/978-981-15-5085-0_20

20.1 Introduction

The ‘complexity theory’ developed rapidly since the 1970s is regarded as one of the paradigm shifts or epoch-making revolutions of natural science in the twentieth century [1, 2], together with the birth and establishment of ‘quantum mechanics’ and ‘Einsteinian general theory of relativity’ at the beginning of the same century [3]. Nowadays, a concept of the nonlinear complexity theory is recognized to govern a variety of dynamic behaviors observed in both natural and social sciences [4–8]. In the ‘nonequilibrium (or out of equilibrium) complexity system,’ symmetry breaking occurs easily in concert with a phase transition of a chaotic or dissipative state to another one. In other words, fluctuation in a nonequilibrium state induces a phase transition to trigger the symmetry breaking, and eventually, the nonlinear amplification of fluctuation leads to dissymmetric circumstances [4–8]. A typical example is the birth of the universe by the cosmic inflation followed by big bang starting from a quantum fluctuation according to the ‘uncertainty principle of energy and time’ as a hypothetical explanation [3]. Other familiar and important examples include many body interactions of multiple elements responsible for the nonlinearity [9]; intermolecular interactions can give nonequilibrium objects such as cells [10], bubbles [11], and metastable crystals [12], which may have strong links to the origin of the selected chirality of life.

In this context, twenty-five years ago, we discovered an unprecedented, spontaneous chiral resolution phenomenon, referred to as ‘preferential enrichment (PE),’ which was applicable to a certain kind of racemic organic salt crystals [13, 14]. Since that time, it has been proved that generally, PE originates from regular chiral fluctuation and symmetry breaking which occurs immediately after polymorphic transition during crystallization. In more detail, by repeating simple recrystallization of certain kinds of racemic mixed crystals (solid solutions) under nonequilibrium conditions using high supersaturation, a regularly alternating enrichment of two enantiomers occurs largely in the mother liquor and slightly in the deposited crystals with full reproducibility in the absence of an external chiral source (Fig. 20.1a) [15–19]. This is, in essence, a completely opposite phenomenon to the well-known ‘preferential crystallization (PC)’ of racemic conglomerates composed of a mixture of homochiral R and S crystals [20–22]. PC discovered by Gernez in the nineteenth century has been recognized to be a common chiral resolution method by seeding a nearly racemic solution with a very small amount of enantiomerically pure crystals (Fig. 20.1b) [23, 24]. In PC, it is in the deposited crystals that substantial enrichment occurs by recrystallization, and at the same time, slight enrichment of the opposite enantiomer always takes place in the mother liquor. Please refer to the cited literatures [15–22] for the comparison of PE with PC and the significance of these complementary two phenomena in the field of chiral separation by crystallization.

Here, at first, we focus on the history and features, and the recently clarified mechanism, requirements and generality concerning PE. Then, our strategy and the outcome with respect to the recent application of PE to racemic dimorphic (two components) cocrystals are introduced. Eventually, we have recognized that PE is ascribed to an

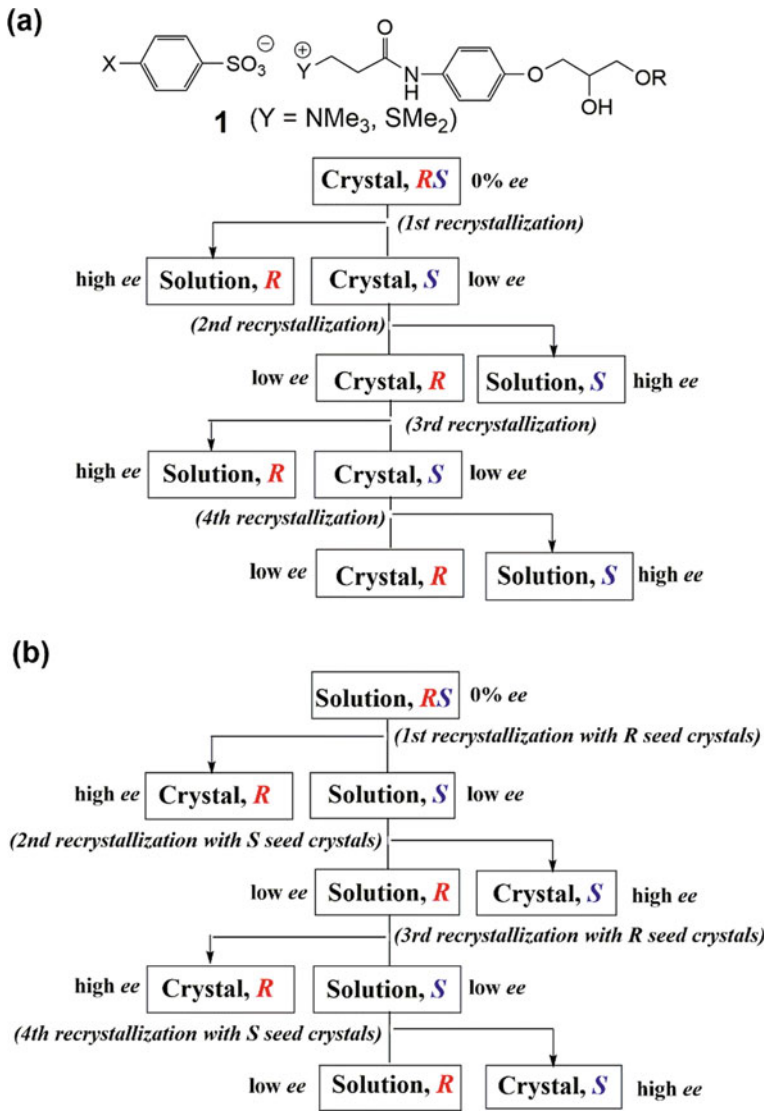

Fig. 20.1 Chiral resolution by **a** preferential enrichment (PE) of a racemic mixed crystal in the case of substantial enrichment of *R* enantiomer in solution after the first recrystallization of the first-generation of chiral organic salts **1** and **b** preferential crystallization (PC) of racemic conglomerates

event of complexity system; the processes in PE such as (a) molecular aggregation in solution, (b) formation of metastable crystalline phases, (c) polymorphic transition (or phase transition), and (d) substantial enrichment of one enantiomer in the mother liquor correspond to the following terminologies of complexity theory; (a′)

dissipative self-organization, (b′) emergence of new order and chaos, (c′) phase transition between chaos and/or order, and (d′) chiral symmetry breaking and increasing returns, respectively [1, 2, 4–8].

20.2 History and Features of PE

In 1993, accidentally Ushio and Tamura found an unprecedented spontaneous chiral resolution phenomenon during recrystallization of a chiral racemic antiallergenic drug named 'Suplatast Tosylate (**1a**)' which is an organic salt (Fig. 20.2) [13]. In 1998, this new phenomenon was referred to as 'preferential enrichment (PE)' [14]. In 2002, we proposed the general mechanism of PE with respect to a series of the first

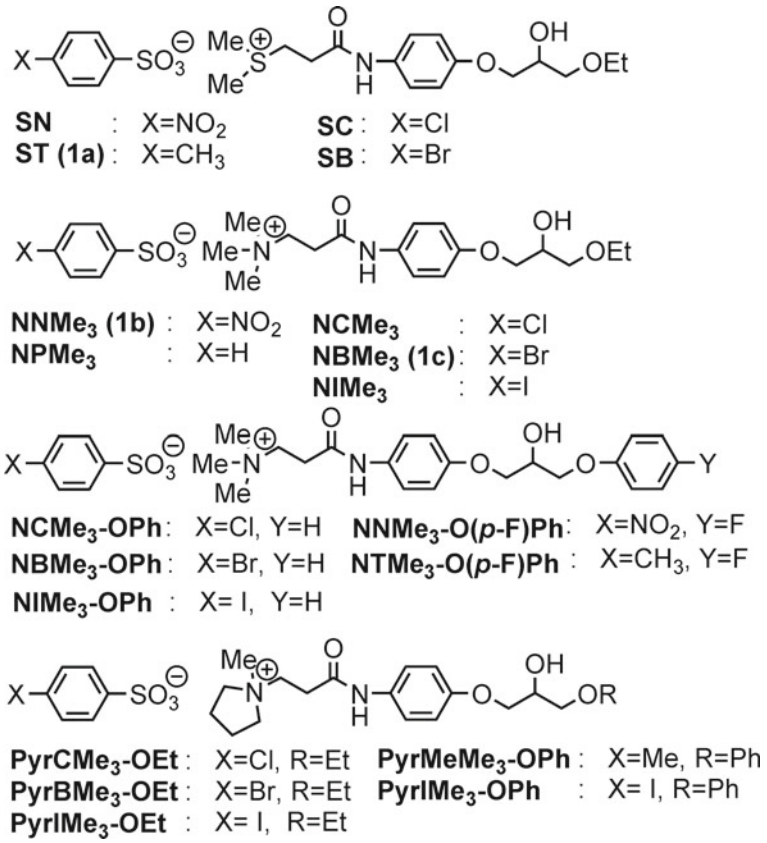

Fig. 20.2 Molecular structures of the first-generation of racemic organic salts **1** showing PE. Abbreviated names representing each molecular structure, like **ST** for compound **1a**, are also indicated

generation of chiral racemic organic salts **1** (Fig. 20.2), which were the derivatives of racemic **1a**, in terms of a unique polymorphic transition occurring during crystallization (Fig. 20.3) [25, 26]. The propriety of this proposed mechanism was verified by the

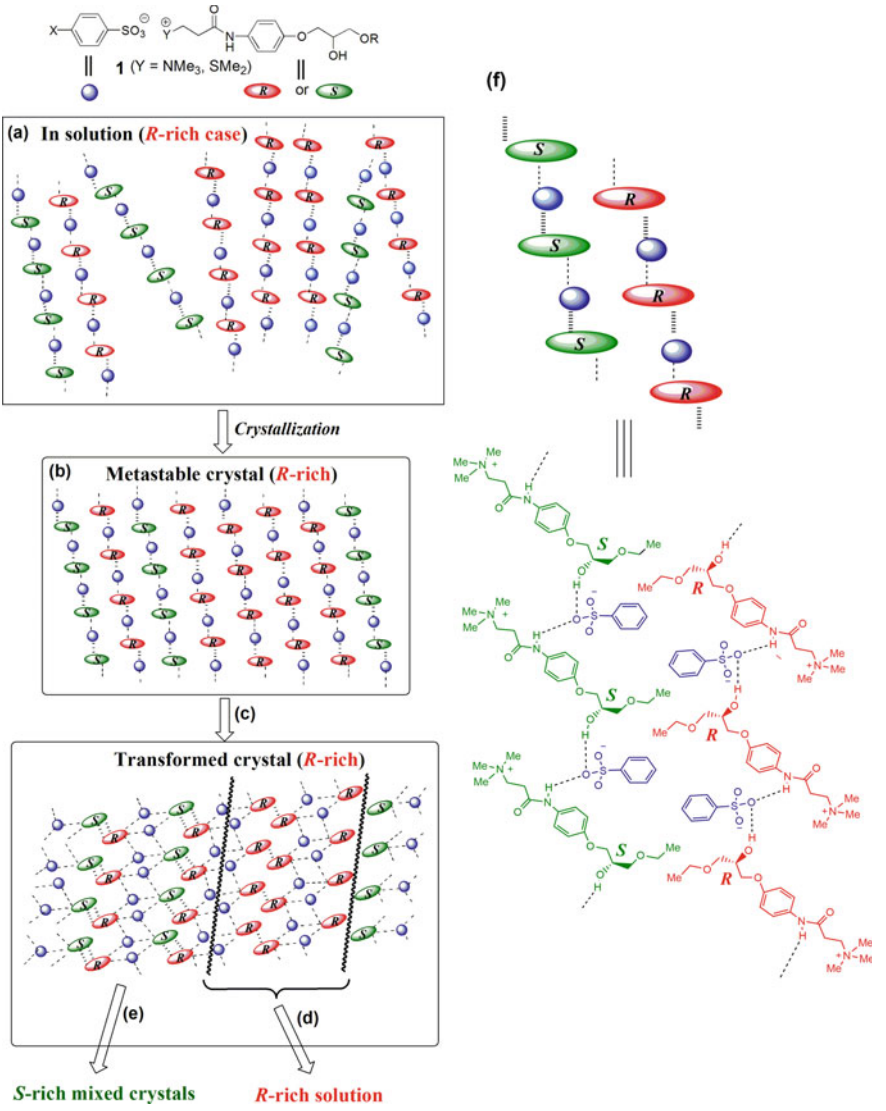

Fig. 20.3 Mechanism of PE in the case of crystallization of the supersaturated solution of slightly R-enriched compounds **1**. Homochiral 1D molecular association (**a**, **f**) in the supersaturated solution and **b**, **f** in the metastable crystals, **c** polymorphic transition followed by **d** selective redissolution of the excess R enantiomer into the mother liquor, and **e** deposition of nonracemic mixed crystals slightly enriched with the opposite S enantiomer

following four experimental and theoretical studies; (1) the polymorphic transition process could be directly followed by using in situ techniques such as attenuated total reflectance FT infrared (ATR-FTIR) spectroscopy [25–30], temperature-controlled (TC) video-microscopy [31], and time-resolved X-ray powder diffraction (XRPD) measurement [31], (2) the regular enrichment of one enantiomer in the mother liquor was successfully rationalized by the kinetic/thermodynamic studies on the solubility properties of two enantiomers [32], (3) the crystal structures of the deposited fine polycrystalline powder samples were solved from the XRPD data by the direct-space approach employing the Monte Carlo method with the subsequent Rietveld refinement [26, 27, 29], and the resulting brittle crystal structures were characterized in terms of the occurrence of partial crystal disintegration of the once deposited crystals on the basis of the graph set analysis of hydrogen bond motifs [33], and (4) a ternary phase diagram that is fully in accord with all experimental data and the elucidated mechanism of PE was proposed [32].

Consequently, PE with regard to the first generation of racemic organic salts **1** was found to be initiated by the solvent-assisted solid-to-solid transformation of a metastable polymorphic form into another thermodynamically more stable one during crystallization from the supersaturated solution of the racemic organic salts composed of two enantiomers without the aid of any external chiral element (Fig. 20.3c) [15–19]. Most notably, this polymorphic transition process was accompanied by selective redissolution of the excess one enantiomer from the incomplete hydrogen bonding sites inside the transformed disordered crystal lattice into the mother liquor until the deposited crystals were slightly enriched with the opposite enantiomer (<10% ee) with full reproducibility (Fig. 20.3d, e). Thus, the interplay of (i) such a solvent-assisted solid-to-solid polymorphic transition (Fig. 20.3c), (ii) the subsequent selective redissolution process of the excess one enantiomer from the deposited brittle mixed crystals (Fig. 20.3d), (iii) the regular enrichment of one enantiomer in the mother liquor, and (iv) the deposition of eventually disintegrated, powdered mixed crystals which can retain the resulting fairly-random alignment of two enantiomers inside the crystal lattice so as to memorize the regular chiral fluctuation and symmetry breaking (Fig. 20.3e) turned out to be responsible for this unique chiral resolution phenomenon.

Furthermore, on the basis of the requirements of PE clarified for a series of the first generation of racemic organic salts **1**, we have successfully expanded the scope of PE to common racemic crystals, such as (1) an acidic chiral nonsteroidal anti-inflammatory drug (ketoprofen) [34] and (2) the second generation of dimorphic cocrystals composed of (a) a racemic neutral or basic α-amino acid (Phe, Leu, or Arg) and an achiral dicarboxylic acid (fumaric acid or oxalic acid) as the coformer (cocrystal former) [35–38] and (b) a racemic acidic anti-hyperlipoproteinemia drug (CPPPA) and an achiral isonicotinamide as the coformer (Fig. 20.4) [39]. Although a little bit modified mechanism was necessary for each of these cocrystals, these results strongly support the generality of our initially proposed requirements and mechanism of PE clarified for a series of the first generation of racemic organic salts **1**. Thus, PE is expected to become a general chiral resolution method by crystallization, with high flexibility and versatility, and full reproducibility.

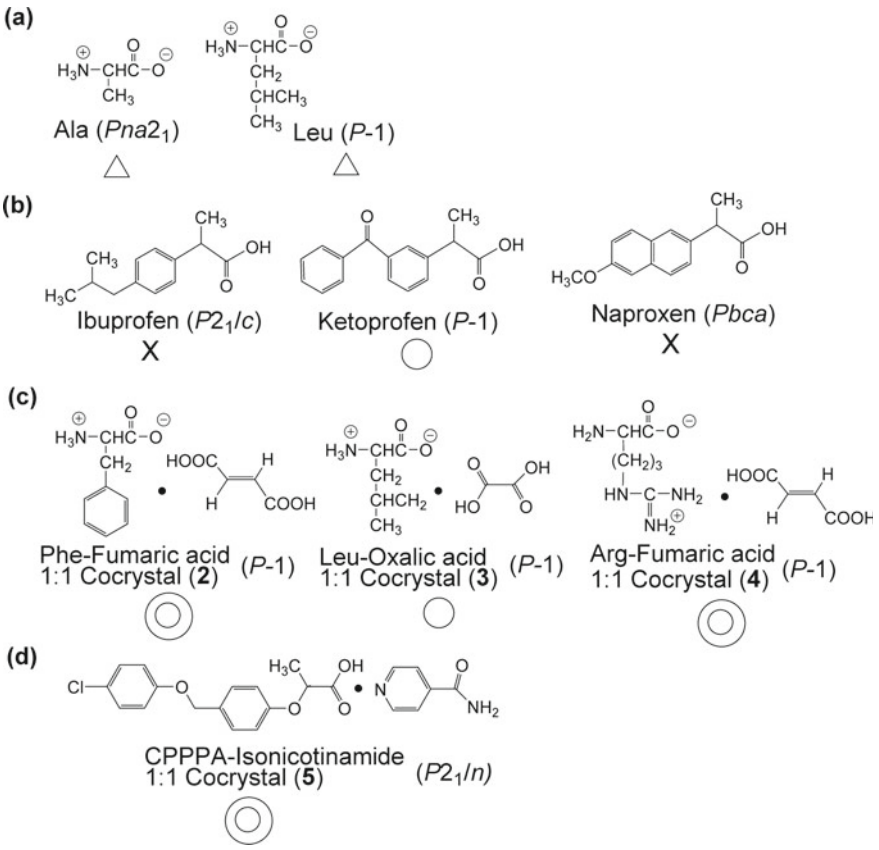

Fig. 20.4 Molecular structures and space groups of the racemic crystals of **a** neutral α-amino acids, **b** acidic nonsteroidal anti-inflammatory drugs, **c** cocrystals (**2**-**4**) of α-amino acids with achiral dicarboxylic acids, and **d** cocrystal (**5**) of acidic CPPPA and achiral isonicotinamide, treated in this article. The double circle, single circle, triangle and cross signs indicate the occurrence of an excellent, good, fair, or no PE, respectively

20.3 First Generation of Organic Salts

The five requirements indispensable for the occurrence of PE with respect to the first generation of racemic organic salts **1** are summarized below in connection with the elucidated mechanism (Fig. 20.3) [15–19, 25–33, 40]:

(i) Sufficient Solubility Difference: The choice of crystallization solvents is one of the most crucial factors. In more detail, the solubility of the enantiomerically enriched sample must be much higher (twice or preferably more) than that of the corresponding racemic one; this implies the high possibility of preferential formation of homochiral one-dimensional (1D) R and S chains even in a racemic solution (Fig. 20.3a). Such a solubility difference considerably

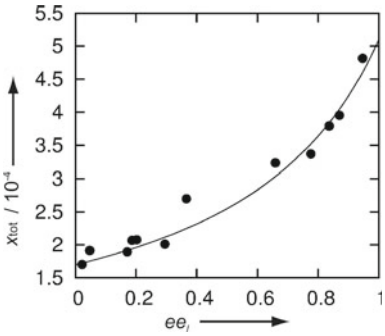

Fig. 20.5 Nonlinear solubility properties of **1c** observed during the PE experiment carried out in EtOH at 25 °C. The plot of the total mole fraction (X_{tot}) of **1c** versus the ee value (ee_l) in the mother liquor. Data cited from Ref. [32]

affects the ee value reached in the mother liquor at the end of crystallization; the larger the difference is, the higher the reached ee value in the mother liquor is. Furthermore, the combined use of supersolubility (a solubility obtained by dissolving the sample in a solvent on heating followed by being cooled) measurement under various conditions, measurement of the total solubility of the two enantiomers of **1** at each reached ee value in the mother liquor during the PE experiment [32], and number-averaged molecular weight measurement by vapor pressure osmometry [25], together with the molecular dynamic simulation of the oligomer models [25], supported a homochiral 1D assembly in preference to a heterochiral one in the racemic solutions of **1** showing PE and proved the nonlinearly increasing total solubility of the two enantiomers with increasing ee value in the mother liquor (Fig. 20.5).

(ii) Unique Crystal Structure: The stable non-racemic crystals obtained at the end of each PE experiment must have a disordered molecular arrangement mainly containing heterochiral RS cyclic dimer chains as well as homochiral 1D R and S chains (Figs. 20.3e and 20.6) [33].

(iii) Polymorphic Transition: A solid-to-solid polymorphic transition of the initially formed metastable mixed crystals composed of a random alignment of the homochiral 1D R and S chains into the stable mixed crystals mainly comprising heterochiral RS cyclic dimer chains mentioned in the above requirement (ii) should occur during crystallization (Figs. 20.3b, c and 20.6). This polymorphic transition could be monitored by means of in situ ATR-FTIR spectroscopy [25–30], real-time TC video-microscopy (Fig. 20.7) [31], and time-resolved in situ XRPD measurement (Fig. 20.8) [31]. The occurrence of polymorphic transition during crystallization was further supported by two different types of unique melting point diagrams obtained experimentally for two typical first generation of chiral organic salts (**1b** and **1c**) showing an excellent PE phenomenon (Fig. 20.9); for **1b**, two end-of-fusion curves intersect at 35% ee [25], while for **1c**, the two curves are located closely to each other without intersection [40]. The following three conclusions were drawn from these two diagrams; (1) their crystalline nature falls into a racemic mixed crystal (i.e., solid solution), (2) the existence of two polymorphic phases is necessary for PE, and 3) the

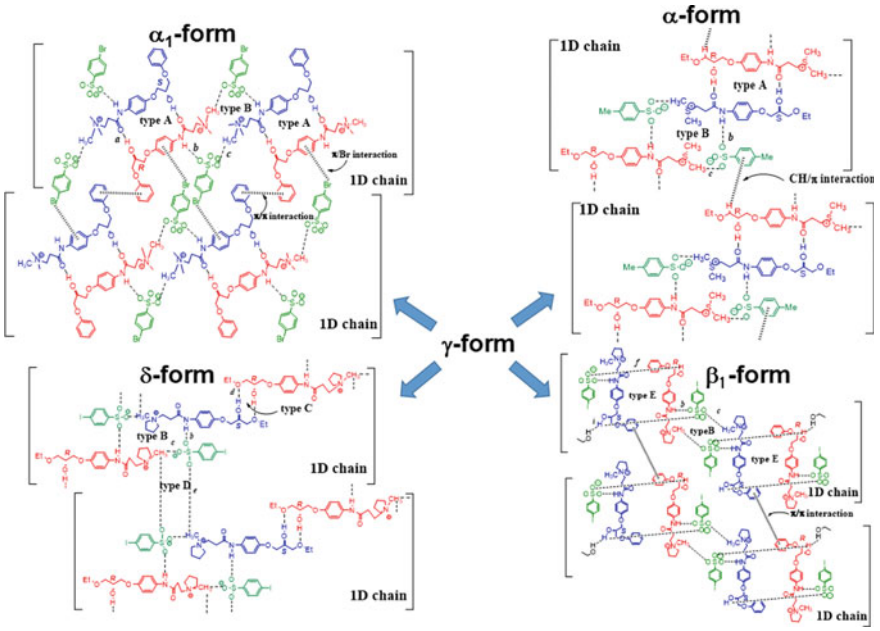

Fig. 20.6 Schematic representation of typical crystal structures of the deposited crystals obtained after the polymorphic transition of the metastable γ-form crystals inducing PE. Actually obtained nonracemic crystals have a disordered crystal structure. Graph set assignments for centrosymmetric cyclic dimers are as follows: Type A, $R_2^2(24)$; Type B, $R_4^4(22)$; Type C, $R_2^2(10)$; Type D, $R_4^4(12)$, Type E, $R_4^4(28)$. Data cited from Ref. [33]

free energy difference between the two polymorphs is small enough to allow a polymorphic transition to proceed at a moderate rate during crystallization.

(iv) Selective Redissolution of Excess One Enantiomer: At the end of the above polymorphic transition, the transformed disordered crystals become brittle due to the formation of incomplete hydrogen bonding sites which result from the irregular alignment of R and S chains in the metastable crystal lattice (Fig. 20.3b). This was rationalized by characterizing the crystal structures of the deposited crystals on the basis of the graph set analysis of hydrogen bond motifs (Fig. 20.6) [33]. Consequently, selective redissolution of the excess one enantiomer from the fragile transformed crystals into the mother liquor occurs until the deposited crystals were slightly enriched with the opposite enantiomer (Fig. 20.3d).

(v) Deposition of Non-racemic Mixed Crystals: The transformed deposited non-racemic mixed crystals must not undergo an additional solvent-mediated polymorphic transition into racemic compound crystals of 0%; thereby, the occurrence of the regular chiral fluctuation and symmetry breaking can be memorized.

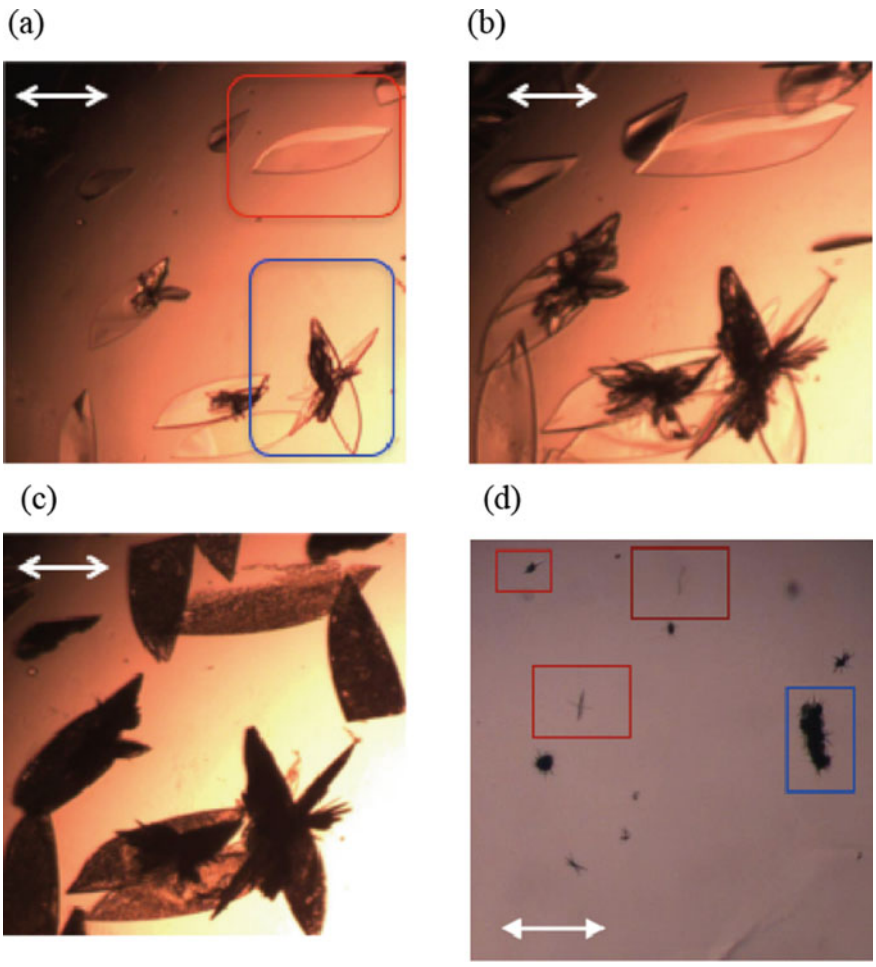

Fig. 20.7 Time sequence showing microscope images of racemic **1c** during crystallization from the 10-fold supersaturated EtOH/2-PrOH (1/1 v/v) solution at 20 °C. **a** The metastable leaf-shaped and the stable dendrite crystals nucleated onto the leaf-shaped crystals are highlighted as red and blue squares, respectively. The left-side inset indicates the magnification of the right-side crystals. **b** The stable crystals grow on the surface of the metastable crystals. **c** The metastable crystals started to dissolve when the solution was heated to 70 °C. **d** Dissolution of leaf-shaped and stable dendrite crystals. The white arrow corresponds to 50 μm. Reprinted with permission from Ref. [31]: Copyright 2020 American Chemical Society

Based on these requirements and mechanism of PE, we proposed a ternary phase diagram that is fully consistent with all experimental data obtained for the first generation of organic salts **1** showing PE (Fig. 20.10). The explanation concerning this diagram cited from Ref. [32]. is as follows. 'In this diagram, the first-formed metastable phase I has a composition of S_1 and L_1 in the solid and liquid phases, respectively. The unchangeable Ω_{10} (overall composition), the changeable S_1 and L_1,

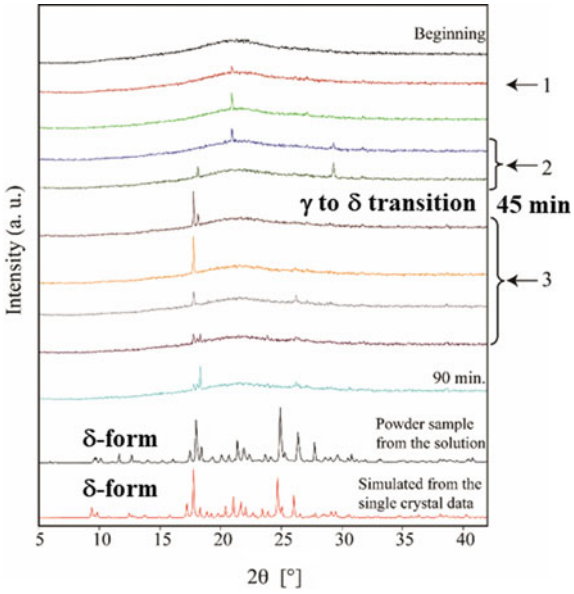

Fig. 20.8 In situ XRPD patterns of **1c**. Conditions: In EtOH/2-PrOH (1/1 v/v, 11-fold supersaturation), at 10 °C, and time interval 9 min. These in situ diffraction patterns were compared with that of the dry final powder sample and that simulated from the single crystal data (δ-form) of racemic **1c**. Major transition points are denoted by arrows 1–3. Reprinted with permission from Ref. [31]: Copyright 2020 American Chemical Society

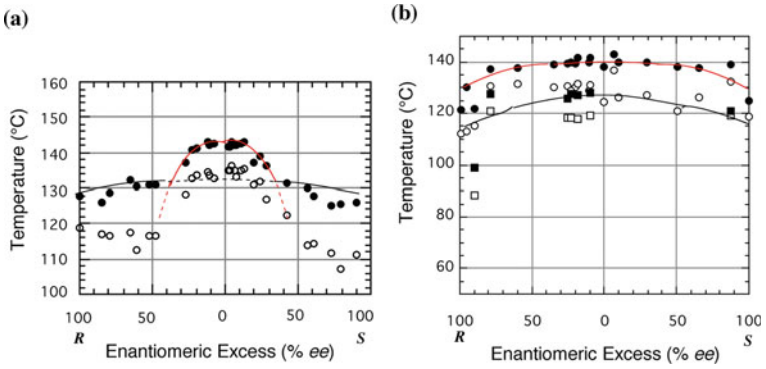

Fig. 20.9 Melting point diagrams of **a 1b** and **b 1c**. White and black circles represent the temperatures of the beginning and the end of fusion of the stable polymorph, respectively, while white and black squares in panel (**a**) are those of the metastable polymorph. Data cited from Refs. [25] and [40]

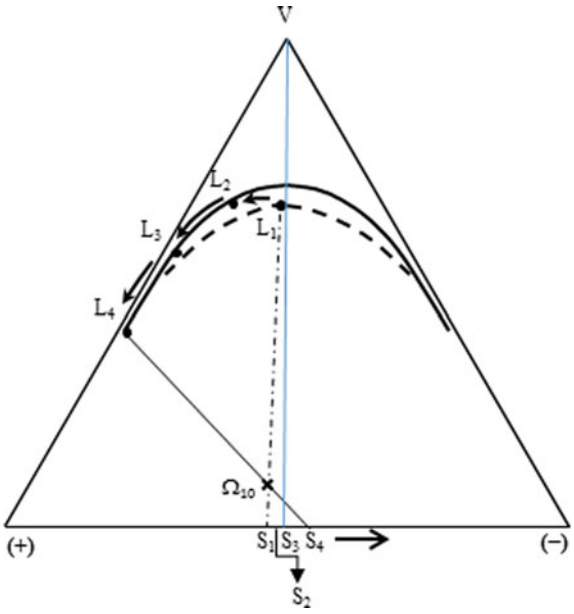

Fig. 20.10 Ternary phase diagram for PE. V is the point of 100% solvent. Ω_{10} represents the amount ratio of ternary components in the tenfold supersaturated solution. S_1 and L_1 indicate the initial compositions in the solid and liquid phases, respectively, immediately after the first crystallization. The next process is an irreversible transition from the phase I to another more stable phase II, resulting in the liquid phase change from L_1 to L_2 and the solid phase change from S_1 to S_2. The last change from L_3 to L_4 is accompanied by that from S_3 to S_4 and thereby irreversible transition from (+)-rich to (−)-rich (around 5% ee) crystals which is a macroscopic chiral symmetry breaking phenomenon unique to PE. Data cited from Ref. [32]

and point V (100% solvent) are aligned as shown by the dashed-dotted line, meaning that an ideal behavior is expected for the first-formed metastable mixed crystals. Then, phase I undergoes an irreversible solid-to-solid polymorphic transition to give another more stable phase II, which comprises S_2 and L_2 and the tie line is no more aligned with the point V. The liquid phase L_2 is more enriched with the (+)-enantiomer than the solid phase S_2, because this evolution is represented by an anticlockwise rotation of the tie line around Ω_{10}. If the solid phase is composed of a normal racemic compound, the rotation of the tie line should stop at L_3 (S_3 is 0% ee). However, the PE process is a "reversed entrainment effect" that has gained some momentum, and it keeps going beyond the 50:50 ratio of (+)- and (−)-enantiomers in the solid phase, showing that it is a nonequilibrium process. In practice, the solid phase S_4 is slightly enriched with the opposite (−)-enantiomer, resulting in a macroscopic chiral symmetry breaking phenomenon.'

Accordingly, the technical and phenomenal features of PE are summarized as follows:

(a) Usual stagnant crystallization conditions without either vigorous stirring or abrasive grinding can be applied to the PE experiment, except that approximately four to 25-fold supersaturated solutions are employed because the supersolubility of the racemates showing PE is considerably higher than the solubility at 25 °C. The attainment of such a high supersolubility is closely associated with the preferential formation of homochiral 1D R and S chains even in the racemic solution. Usually, at the supersaturated concentrations below fourfold, PE does not efficiently occur.
(b) Racemic or non-racemic samples less than 10% ee are more suitable for the PE experiment than those of higher ee values to achieve a very efficient resolution, resulting in the regular deposition of non-racemic mixed crystals slightly enriched (around 5% ee) with the opposite enantiomer.
(c) When the original supersaturated solution used for crystallization is strictly racemic (0.0% ee), the probability for either the R or the S enantiomer to be enriched in the mother liquor after the first crystallization is 0.5. This is because initial capricious formation of the first-formed non-racemic metastable crystal nucleus should determine which enantiomer is enriched in the mother liquor thereafter. Since generally the racemic synthesis of 1.0 mol of a chiral compound produces a racemic sample with a standard deviation of ca. 1.3×10^{-10}% ee, it is noteworthy that chiral amplification of nearly 10^{12}-fold occurs easily during the PE process [32].
(d) Only racemic or non-racemic samples have to be crystalline to implement the PE experiment efficiently. It does not matter whether the enantiomerically enriched samples with high ee values exist as solids or oils; this is in sharp contrast to PC of racemic conglomerate crystals.
(e) Seed crystals are not necessary at all and should not be added to induce crystallization, because PE is sometimes inhibited by them.

20.4 Ketoprofen [34]

To extend the scope of PE to pharmaceutically relevant compounds, we carried out an extensive search using the Cambridge Structural Database (CSD) regarding chiral nonsteroidal anti-inflammatory drugs (NSAID) with an appropriate crystal structure exhibiting PE, according to the requirement (ii) in the Sect. 20.3. We found that ibuprofen (space group: $P2_1/c$), ketoprofen (P–1), and naproxen (*Pbca*) (Fig. 20.4) have the desired stable racemic crystal structure containing RS dimer chains as well as homochiral 1D R and S chains (Fig. 20.11). Among them, only ketoprofen with a relatively high eutectic point at 82% ee satisfied all the five requirements (i)–(v) for the occurrence of PE listed in the Sect. 20.3. Indeed, ketoprofen showed a good PE phenomenon as long as crystallization began from tenfold supersaturated H_2O–EtOH (v/v 1:1) solution of non-racemic ketoprofen of more than 1% ee at –16 °C (Fig. 20.12), despite being a single-component organic crystal. However, ibuprofen

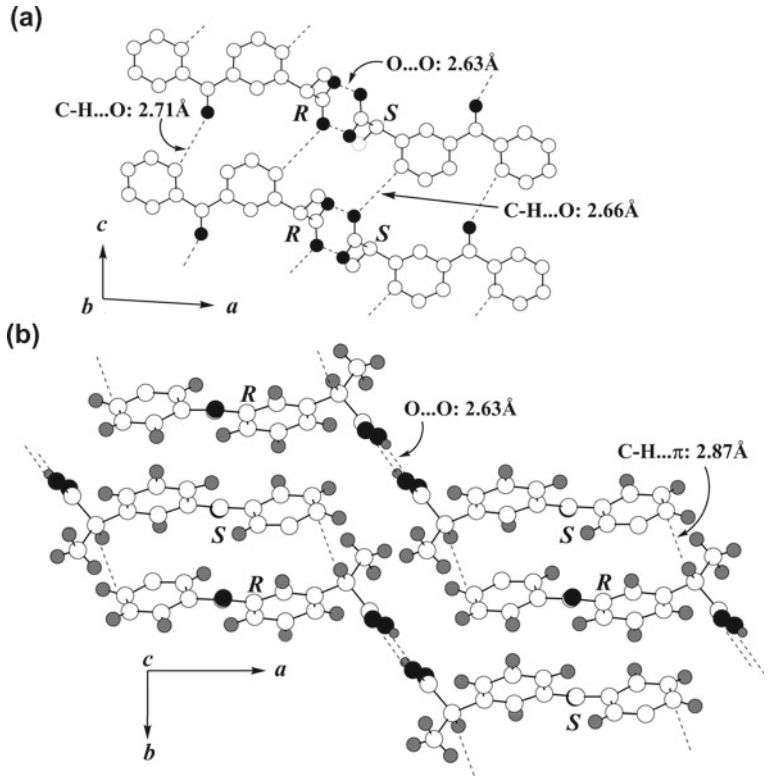

Fig. 20.11 Crystal structure of (*RS*)-ketoprofen. **a** A view down the *b*-axis. **b** A view down the*c*-axis. See Fig. S2 for a view down the *a*-axis. Reproduced from Ref. [34] with permission from The Royal Society of Chemistry

and naproxen failed to show PE due to no occurrence of polymorphic transition during crystallization.

20.5 Second Generation of Organic Cocrystals

From the successful case of PE for the single-component ketoprofen (Sect. 20.4), we learned that a common racemic compound with a relatively high eutectic ee value can behave like a quasi-mixed crystal and show a good PE phenomenon by carefully choosing nonequilibrium crystallization conditions so as to induce a desired polymorphic transition. Therefore, we focused on dimorphic cocrystals which have a high potential of showing a polymorphism and inducing polymorphic transition during crystallization [41]. It is anticipated that the cocrystal formation would contribute to producing the requisite molecular arrangement in the crystal by converting a racemic

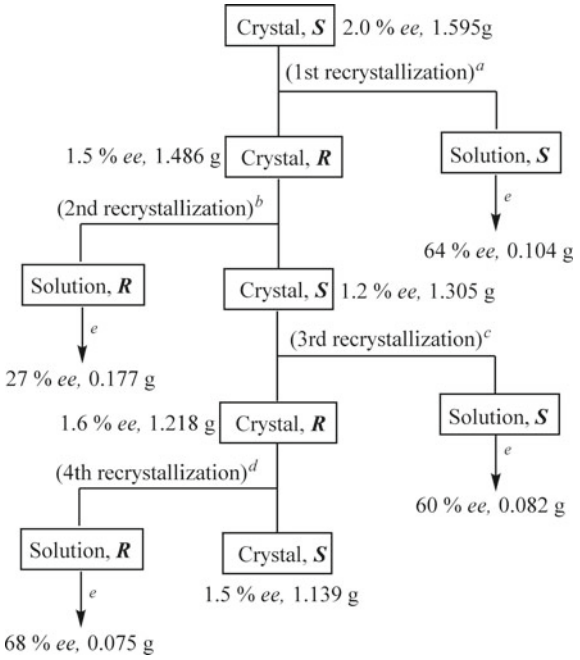

Fig. 20.12 Preferential enrichment of ketoprofen. Conditions: [a] H_2O-EtOH (v/v 1:1, 3.7 mL) at −16 °C for 4 days; [b] H_2O-EtOH (v/v 1:1, 2.8 mL) at −16 °C for 4 days; [c] H_2O-EtOH, (v/v 1:1, 2.4 mL) at −16 °C for 4 days; [d] H_2O-EtOH (v/v 1:1, 2.2 mL) at −16 °C for 4 days; [e] removal of the solvent by evaporation. Data cited from Ref. [34]

compound crystal with a low eutectic ee value into a quasi-mixed crystal with a very high eutectic ee value (Fig. 20.13a, b), which can permit the formation of brittle deposited crystals after polymorphic transition under supersaturated crystallization conditions (Fig. 20.13c–e).

Accordingly, we carried out an extensive CSD search to find out an appropriate cocrystal composed of a racemic neutral α-amino acid and an achiral dicarboxylic acid as the model compound. Consequently, we found that the 1:1 cocrystal (**2**) of DL-Phe (phenylalanine) and fumaric acid (Fig. 20.4), which has a space group of *P*–1 and a high eutectic ee value, satisfied all the five requirements and indeed showed an efficient PE phenomenon, whereas free DL-Phe failed to show a polymorphic transition and thereby PE [35]. Furthermore, we found that the 1:1 cocrystal (**3**) (*P*–1) of DL-Leu (leucine) and oxalic acid [36] or the 1:1 cocrystal (**4**) (*P*–1) of DL-Arg (arginine) and fumaric acid [37] exhibited an improved or an excellent PE phenomenon, respectively, although free DL-Leu or DL-Arg showed a poor or no PE phenomenon, respectively (Fig. 20.4) [37, 38]. However, the cocrystals of other α-amino acids such as Val, Leu, Ile, Met, Ser, Tyr, and Ala with fumaric acid or oxalic acid failed to show PE [37]. Based on these findings of cocrystals **2**–**4** exhibiting PE, next, we focused on finding the cocrystals with a space group of *P*–1 which are composed of chiral acidic drugs and achiral basic coformers by the CSD search.

First, to improve the efficiency of PE with respect to ketoprofen, we tried co-crystallization using various basic coformers. However, no cocrystal was formed due to a large solubility difference between the two components in various solvents;

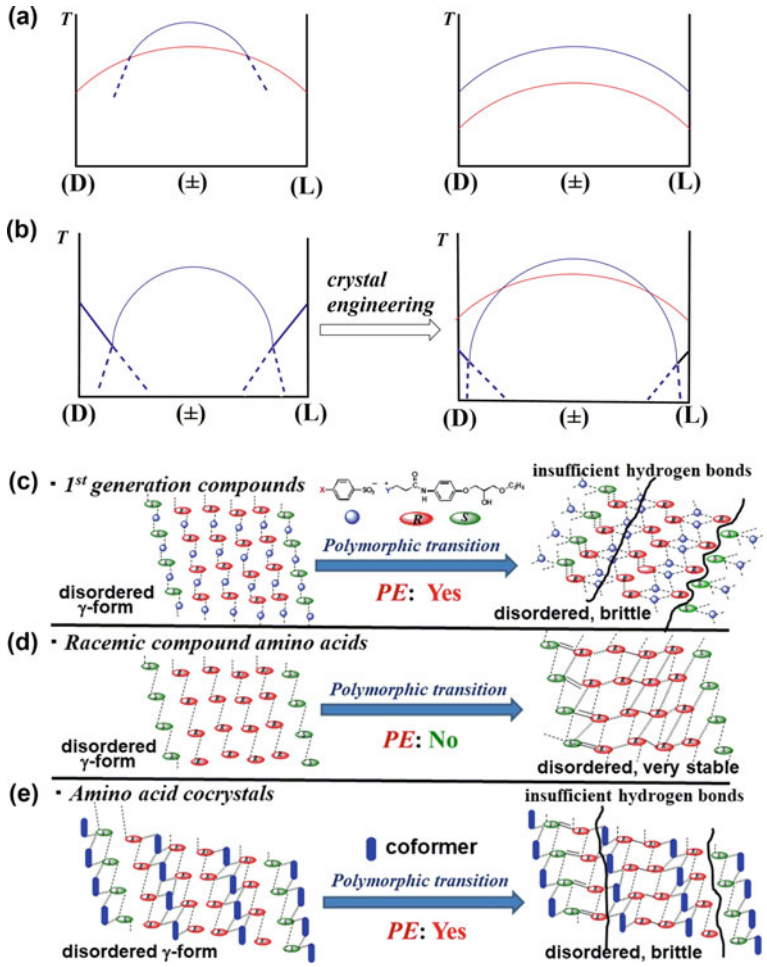

Fig. 20.13 Schematic melting point diagrams (**a**, **b**) with a polymorphism essential to induce PE and advantage of co-crystallization of racemic compound crystals (**c**–**e**). **a** Two typical diagrams of a mixed crystal capable of showing PE with respect to organic salts **1** corresponding to Fig. 20.9 and **b** a concept on transformation of a common racemic compound with a low eutectic ee value into a quasi-mixed crystal with a high eutectic ee value with an appropriate polymorphism by crystal engineering. For clarity, only the end of fusion curves are indicated. A polymorphic transition of a metastable disordered γ-form crystal into **c** a brittle disordered crystal capable of inducing PE for the first-generation of organic salts, **d** a very stable disordered crystal unable to induce PE due to hydrogen bonding networks, and **e** a brittle disordered crystal capable of inducing PE with the aid of coformers. Two handwritten lines in panels **c** and **e** indicate the brittle sites in the crystal lattices due to the weak electrostatic interactions and no hydrogen bond

racemic ketoprofen always showed much higher solubility than coformers [39]. Next, although the cocrystal of racemic naproxen with bipyridine or piperazine was successfully prepared, both cocrystals failed to show PE because of the violation of the solubility requirement (i) in the Sect. 20.3; the solubility of the pure enantiomer was lower than that of the racemate in various solvents [42]. Furthermore, the crystal structure of the cocrystal of racemic ibuprofen with 4,4′-ethane-1,2-diyldipyridine (P–1) or nicotinamide ($Pca2_1$) was known. However, these cocrystals failed to exhibit PE, because they did not have an appropriate crystal structure described in the requirement (ii) [39]. Instead we have found that the 1:1 cocrystal (**5**) ($P2_1/n$) of racemic CPPPA [anti-hyperlipoproteinemia drug (EMD 31 647)] and isonicotinamide (Fig. 20.4), shows an excellent PE phenomenon [39].

20.5.1 Phenylalanine-Fumaric Acid Cocrystal (2) [35]

The 1:1 cocrystal (**2**) of DL-Phe and fumaric acid, which has a eutectic ee value as high as 99% in water, satisfied all the requirements (i)–(v) and thereby showed an efficient PE phenomenon (Fig. 20.14). The XRPD pattern of the deposited non-

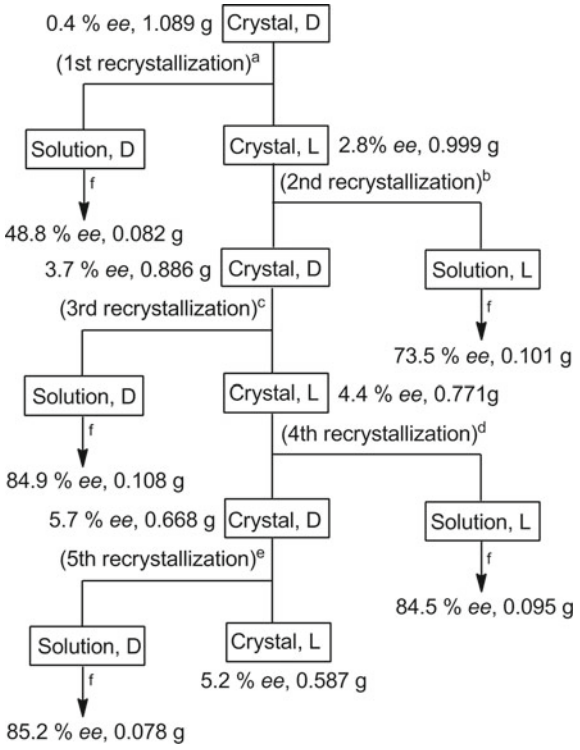

Fig. 20.14 Successive recrystallization of cocrystal **2**. Conditions: [a]H_2O (10.0 mL, six-fold supersaturation) at 5 °C for 60 h. [b]H_2O (9.2 mL) at 5 °C for 48 h. [c]H_2O (8.7 mL) at 5 °C for 42 h. [d]H_2O (7.8 mL) at 5 °C for 24 h. [e]H_2O (6.9 mL) at 5 °C for 24 h. [f]Removal of the solvent by evaporation. Data cited from Ref. [35]

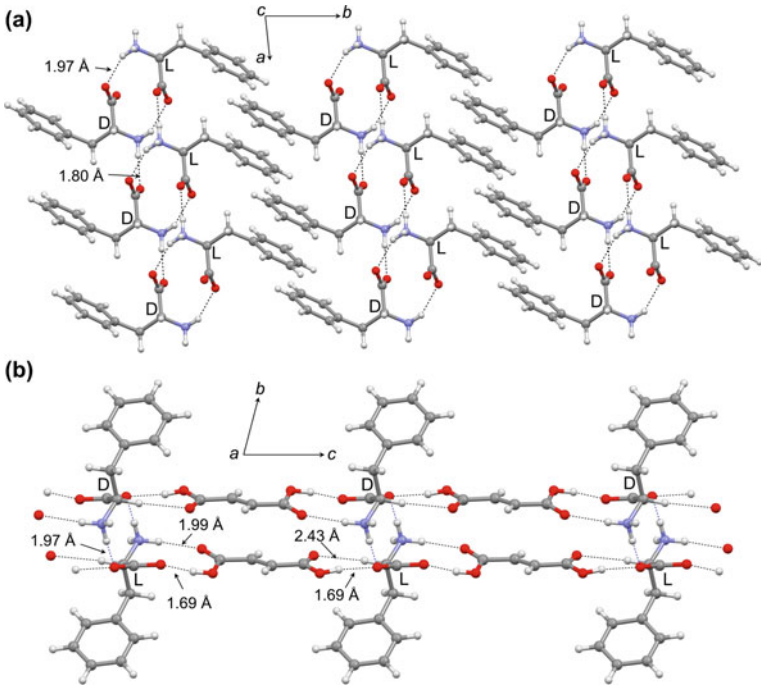

Fig. 20.15 Crystal structure of DL-cocrystal **2**. **a** A view down the *c*-axis. Fumaric acid molecules were omitted for clarity. **b** A view down the *a*-axis. The carbon, oxygen, nitrogen, and hydrogen atoms are represented by grey, red, blue, and white circles, respectively. Reprinted with permission from Ref. [35]: Copyright 2020 American Chemical Society

racemic crystals obtained at the end of PE experiment of the DL-cocrystal was identical to that simulated from the X-ray crystallographic data of the single crystal of DL-**2**. Based on this crystal structure (Fig. 20.15), the mechanism of PE most likely involves the following successive processes (in the case of starting from a slightly L-rich solution, Fig. 20.16): (1) preferential formation of homochiral 1D D and L chains of type A in the supersaturated solution, (2) a solid-to-solid polymorphic transition of the metastable mixed crystals composed of the same homochiral D and L chains of type A into the stable heterochiral cyclic dimer chains of type B, and (3) partial crystal disintegration in the irregular molecular alignment area allowing the redissolution of the excess L enantiomer into the mother liquor until the deposited crystals are slightly enriched with the opposite D enantiomer. This mechanism is quite similar to the case of the first generation of organic salts (Fig. 20.3).

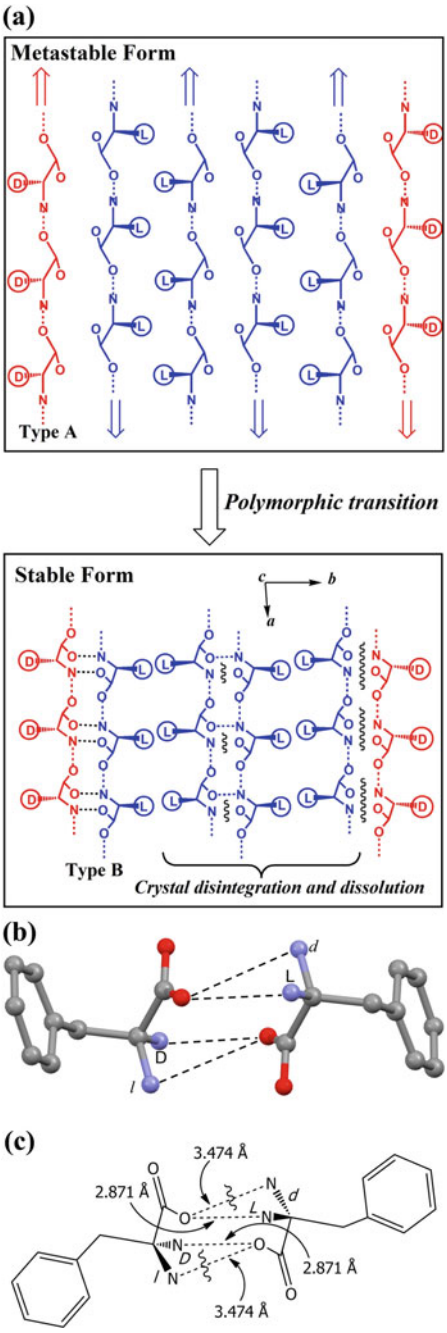

Fig. 20.16 The proposed mode of polymorphic transition of racemic or nonracemic cocrystal **2**. **a** Transformation of a metastable form into a stable one. This is the case in which an even number (four in this case) of homochiral L chains are surrounded by two D chains in the metastable form, resulting in partial crystal disintegration after polymorphic transition. **b** Hypothetical type B cyclic dimer chain structure in the cocrystal with orientational disorder at the position of the amino group on an asymmetric carbon atom. **c** Schematic illustration of panel b. Reprinted with permission from Ref. [35]: Copyright 2020 American Chemical Society

20.5.2 Leucine-Oxalic Acid Cocrystal (3) [36]

Although the 1:1 cocrystal (**3**) of DL-Leu and oxalic acid has a eutectic ee value as high as >98% in H_2O–EtOH (v/v 2:1) at 25 °C, only modest PE phenomenon was observed even when successive crystallization was performed from a slightly enantiomerically enriched (5.0% ee) fivefold supersaturated solution at 5 °C [36] (Fig. 20.17).

Interestingly, the crystal structure of the stable DL-**3** was quite different from those of the first generation of organic salts and DL-**2**, although the space group was *P*–1. Namely, the crystal structure was composed of a pair of 2D D and L sheets (Fig. 20.18a, b). Accordingly, the mechanism of PE was different from the previous ones. A new mechanism consistent with all the experimental data was proposed to involve the following processes in the case of using a slightly L-rich sample: (1) preferential formation of homochiral 1D D and L chains of Leu through the intermediary of oxalic acid in the supersaturated solution, (2) direct nucleation (phase transition) from the slightly L-rich molecular cluster to give the stable, slightly L-rich mixed crystalline phase composed of 2D D and L sheets (Fig. 20.18c), and (3) preferential redissolution of the L sheets from the area of irregular and brittle sheets packing in the crystals, in which an even number of L sheets (four sheets in this case) are surrounded by two D sheets, into the mother liquor until the deposited crystals are slightly enriched with the opposite D enantiomer (Fig. 20.18c). Thus, the ee value in the mother liquor cannot increase largely, because the ee value of the resulting D-rich deposited crystals is as low as less than 1.0%.

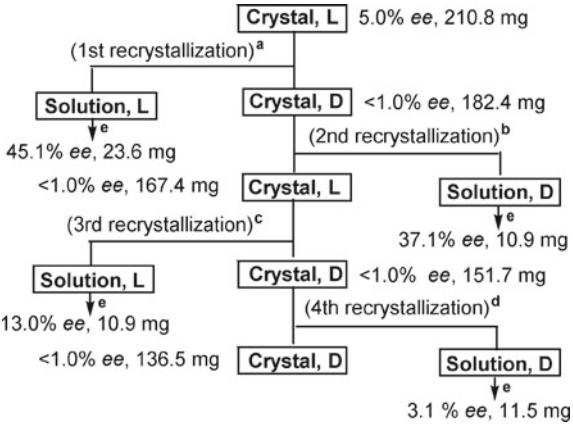

Fig. 20.17 Preferential enrichment experiment of cocrystal **3** by using a fivefold supersaturated solution in H_2O/EtOH (2/1 v/v), compared with the solubility at 25 °C (Table 1). Conditions: **a** H_2O/EtOH (2/1 v/v) (2.0 mL) at 5 °C for 7days. **b** H_2O/EtOH (2/1 v/v) (1.6 mL) at 5 °C for 4 days. **c** H_2O/EtOH (2/1 v/v) (1.5 mL) at 5 °C for 5 days. **d** H_2O/EtOH (2/1 v/v) (1.3 mL) at 5 °C for 4 days. **e** Removal of the solvent by evaporation. Data cited from Ref. [36]

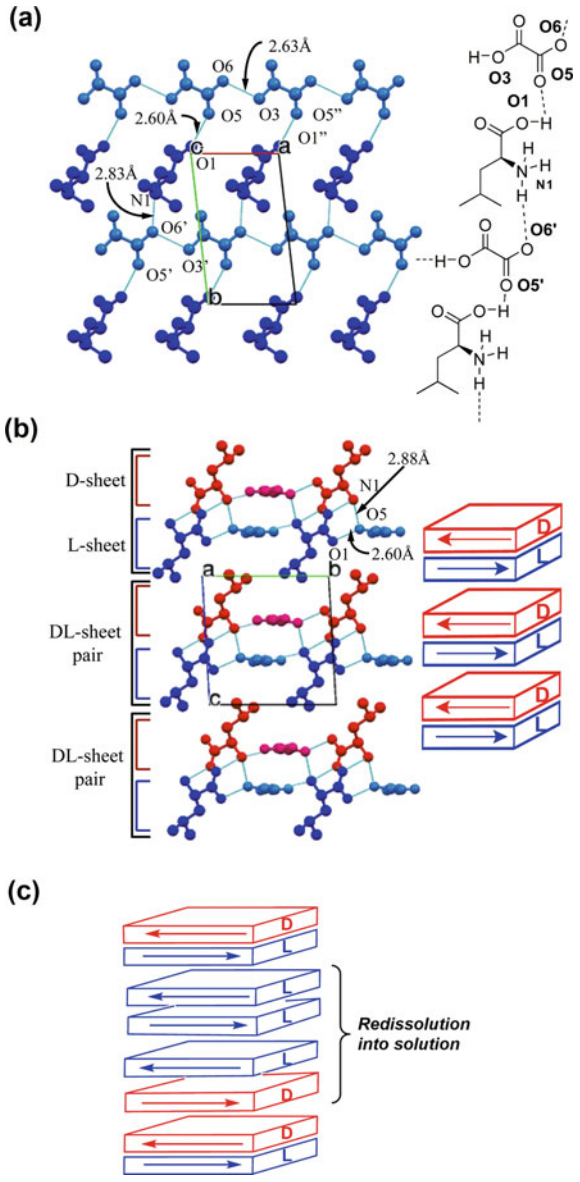

Fig. 20.18 Crystal structure of DL-cocrystal **3** and the mechanism of PE. **a** 2D Homochiral sheet structure on the *ab* plane (left) and schematic representation of the 1D homochiral chain in the sheet structure (right). **b** Heterochiral 1D chain structure along the *b*-axis and stacking modes of 2D D and L sheets and DL sheet pairs along the *c*-axis. D-Leu (red), L-Leu (blue) and oxalic acid (sky blue and magenta). Hydrogen atoms are omitted for clarity. The arrows show the direction of alternating homochiral 1D chains alignment in the 2D D and L sheets. **c** Proposed mode of the selective redissolution of the excess L sheets from the deposited crystal. The arrows show the direction of alternating homochiral 1D chains alignment in the 2D D and L sheets. Data cited from Ref. [36]

20.5.3 Arginine-Fumaric Acid Cocrystal (4) [37]

DL-Arg formed a 1:1 cocrystal (space group: $P\bar{1}$, $C2/c$, or $P2_1/c$) with fumaric acid, malonic acid, or oxalic acid, respectively. Among these three cocrystals with very high eutectic ee values (>95%), only the cocrystal (**4**) of DL-Arg and fumaric acid showed an excellent PE phenomenon (Fig. 20.19), although in this instance a

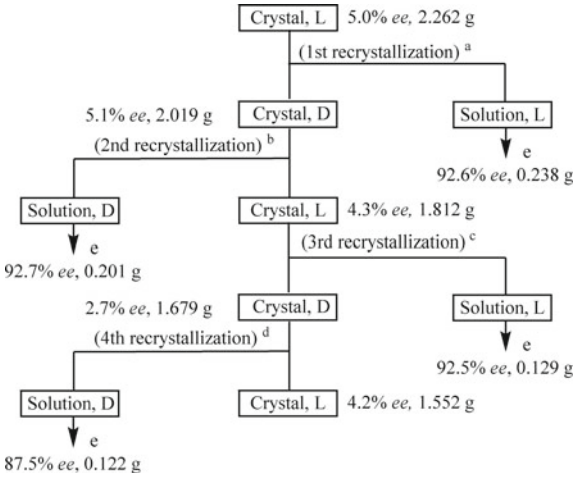

Fig. 20.19 Preferential enrichment experiment of cocrystal **4** using an 8-fold supersaturated H_2O-EtOH (1:1 v/v) solution. Conditions: **a** H_2O-EtOH (8.8 mL) at 5 °C for 6 days, **b** H_2O-EtOH, (7.9 mL) at 5 °C for 4 days, **c** H_2O-EtOH (7.1 mL) at 5 °C for 5 days, **d** H_2O-EtOH (6.6 mL) at 5 °C for 4 days, **e** removal of the solvent by evaporation. Data cited from Ref. [37]

polymorphic transition was not observed during crystallization by in situ ATR-FTIR spectroscopy, TC video-microscopy, and in situ time-resolved XRPD measurement. Therefore, in this case, a direct nucleation (phase transition) from the molecular clusters present in the supersaturated solution giving mixed crystals is most likely to induce the chiral symmetry breaking and thereby PE. The crystal structure of the stable racemic cocrystal **4** is shown in Fig. 20.20.

Furthermore, in this PE experiment, a total amount of two enantiomers dissolved in the mother liquor was kept constant despite the increasing ee value of one enantiomer in the mother liquor during crystallization, in contrast to the case of the first generation of organic salts [32]. More interestingly, by adding a minute amount (0.1 wt % of the

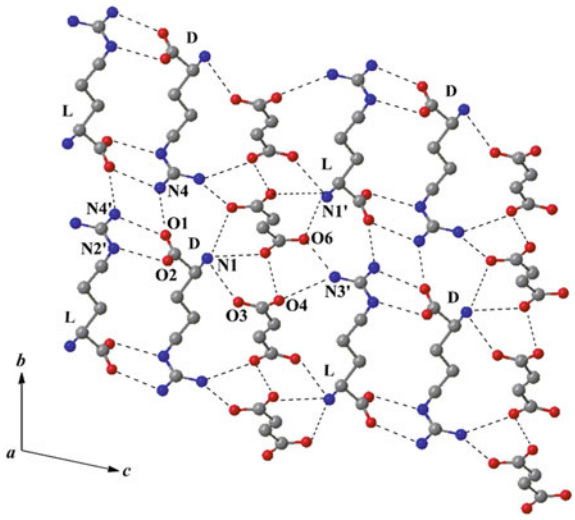

Fig. 20.20 Crystal structure of DL-cocrystal **4**. Data cited from Ref. [37]

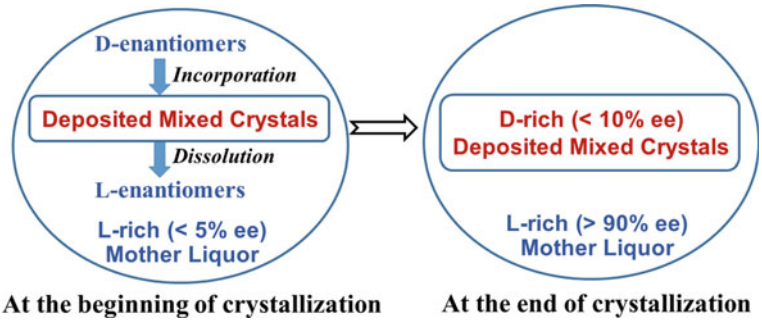

Fig. 20.21 Schematic representation of the exchange processes of two enantiomers between the solid and the solution phases in the case of the PE experiment starting from a slightly L-rich supersaturated solution. Selective dissolution of the excess L enantiomers from the deposited mixed crystals into the mother liquor and selective incorporation of D enantiomer from the mother liquor into the deposited crystals occur to give slightly D-rich deposited mixed crystals and highly L-rich mother liquor eventually

total Arg mass) of $^{13}C_6$-L-Arg to the slightly D or L-rich suspension of cocrystal **4** at a different time (2.5, 6, or 144 h) after the beginning of precipitation, we found that 95, 93, or 75% of the labeled L-Arg, respectively, was incorporated deeply inside the L-rich deposited crystals in the case of starting from the slightly D-rich suspension, whereas in the case of starting from the slightly L-rich suspension, 50 or only 12% of the labeled L-Arg was mainly incorporated into the surface area of D-rich deposited crystals by the addition at 2.5 or 144 h, respectively. Apparently, an exchange of opposite enantiomers between the solid and the liquid phases was noted [43].

Based on these experimental results obtained during the duration from 5 min to 144 h after crystallization began, the mechanism of this PE phenomenon in the case of using a slightly L-rich supersaturated solution is most likely to involve a crucial exchange process between the D enantiomer in the mother liquor and the L enantiomer in the solid phase during crystallization so that the ee value in the mother liquor gradually increases by the following double effects; (i) impoverishing the minor D enantiomer in the mother liquor and (ii) enriching the mother liquor by the L enantiomer which was already in excess in the original supersaturated solution (Fig. 20.21).

20.5.4 CPPPA-Isonicotinamide Cocrystal (5) [39]

Free CPPPA of 0.0% ee did not show a PE phenomenon at all under any crystallization conditions. However, when non-racemic free CPPPA of 1.0% ee were repeatedly recrystallized from the fivefold supersaturated 2-PrOH solution at 20 °C only under stagnant conditions without stirring, a modest PE phenomenon was observed.

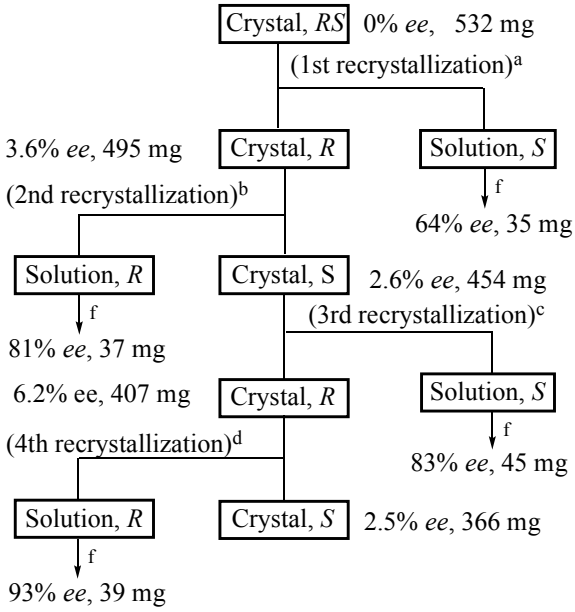

Fig. 20.22 Preferential enrichment experiment of cocrystal **5** using the fivefold supersaturated 2-PrOH solution at 20 °C. Conditions: **a** 2-PrOH (3.8 mL) for 5 days. **b** 2-PrOH (3.5 mL) for 5 days. **c** 2-PrOH (3.2 mL) for 3 days. **d** 2-PrOH (2.9 mL) for 3 days. **f** Removal of the solvent by evaporation

When recrystallization of the 1:1 cocrystal (**5**) of racemic CPPPA and isonicotinamide (INA) was repeatedly carried out from the fivefold supersaturated 2-PrOH solution at 20 °C with initial stirring until crystallization began and subsequently under stagnant conditions, the ee value in the mother liquor reached 93% after the fourth recrystallization (Fig. 20.22). In this case, the occurrence of polymorphic transition during crystallization was not observed by the in situ ATR-FTIR spectroscopy, similarly to the case of the cocrystal (**4**) of Arg and fumaric acid.

The unique crystal structure of this stable racemic cocrystal **5** is shown in Fig. 20.23a, b. Interestingly, the space group was not $P\bar{1}$ but $P2_1/n$. From this crystal structure, it is assumed that a corrugated homochiral 2D R or S sheet with a large dipole moment (6.36 D per CPPPA-INA unit), which is formed by homochiral 2D aggregation of R or S molecules, is fairly stable in 2-PrOH (Fig. 20.23a, b). On the other hand, a pair of homochiral 2D sheets (RR or SS sheet pair) are formed by stacking in an antiparallel manner so as to cancel the dipole moment in the solid phase, so that RR and SS sheet pairs stack alternately to form the unique racemic crystal structure (Fig. 20.23b).

Furthermore, a total amount of two enantiomers dissolved in the mother liquor was kept constant despite the increasing ee value of one enantiomer in the mother liquor during crystallization, similarly to the case of the cocrystal **4**, but different from the cases of the first generation of organic salts **1** (Fig. 20.5) [32]. Therefore, the mechanism of PE regarding the cocrystal **5** should be quite different from those of other compounds showing PE.

Based on the unique crystal structure of the racemic cocrystal **5** and the additional fact that the deposited crystals with very low ee values obtained at the end of PE

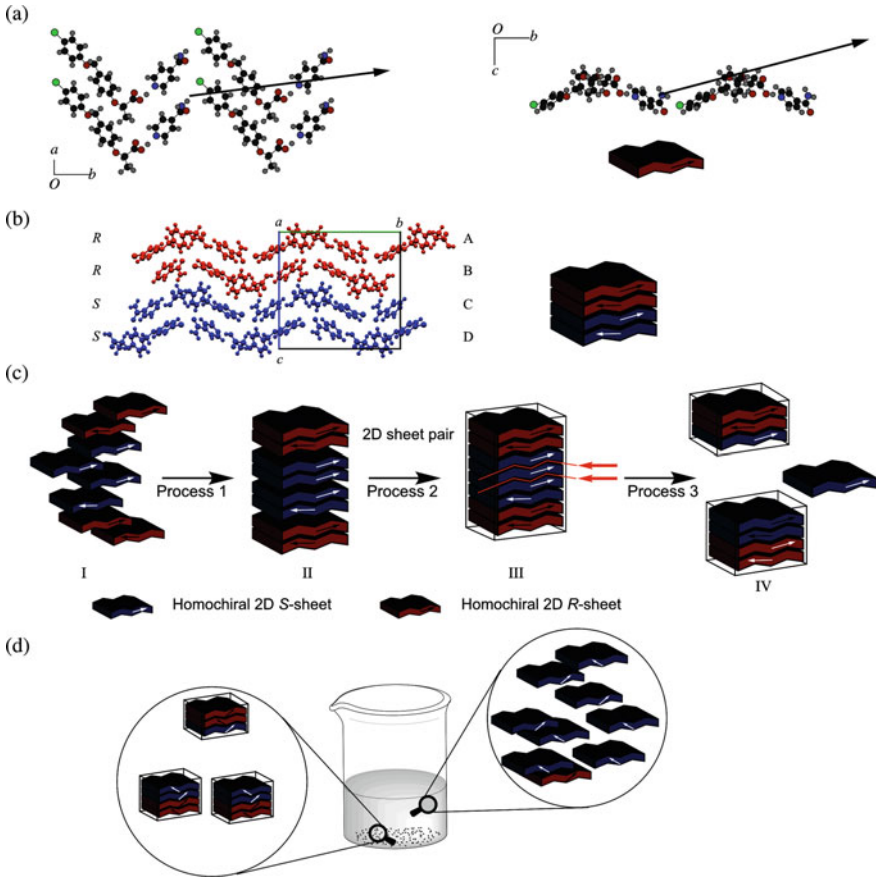

Fig. 20.23 Crystal structure (**a**, **b**) of DL-cocrystal **5** and the mechanism (**c**, **d**) of PE. **a** Left: The stacking manner of, e.g., four CPPPA-INA units in the homochiral 2D sheet on the *ab* plane. Right: The same homochiral 2D sheet viewed down the *a* axis and its schematic representation. The black arrows indicate the direction of total dipole moment of the same four CPPPA-INA uints. **b** The stacked layer structure of antiparallel homochiral 2D sheet pairs along the *c* axis and its schematic representation. **c** Mechanism of a large enantiomeric enrichment in the mother liquor and a slight enrichment of the opposite enantiomer in the deposited crystals. From the less stable stacking sites indicated by the orange arrows (structure III), the excess S-sheet dissolved into the mother liquor. **d** Schematic drawing of 2D sheets dissolved in the mother liquor and stacked in the solid phase at the end of the PE experiment. Reproduced from Ref. [39] by permission of Wiley Ltd.

experiment were always second harmonic generation (SHG)-positive indicating the formation of homochiral domains inside the crystals, it is assumed that an irregular arrangement of homochiral 2D R and S sheets occurs during crystallization under nonequilibrium conditions using high supersaturation (process 1 and structure II in Fig. 20.23c); (i) the respective homochiral 2D R and S sheets stack predominantly in an antiparallel manner, but to some extent in a parallel manner to form somewhat

irregular homochiral sheet pairs, and (ii) the homochiral 2D sheets pairs stack to give partially irregular arrangement in the crystals. As a result, the resulting brittle deposited mixed crystals contain the less stable parallel stacking sites indicated by the outside orange arrows (structure III), where the excess homochiral 2D sheet (an S sheet in the present case) dissolves into the mother liquor to result in the slightly R-rich crystal (process 3 and structure IV). Thus, it is reasonable to consider that a large molecular dipole moment of the CPPPA-INA unit and the weak interactions (only CH/O and CH/π interactions) between homochiral 2D sheets are responsible for the observed PE phenomenon.

20.6 Conclusions and Prospects

Through the 25 years' studies on the mechanism and generality of PE, we have confirmed that PE is attributed to an event of complexity system and applicable to not only certain kinds of mixed crystals which we discovered for the first time, but also various quasi-mixed crystals prepared by co-crystallization of common racemic compounds with achiral coformers. The mechanism of PE has turned out to be quite flexible depending on the molecular and crystal structures. Since various compounds which satisfied all the five requirements listed in this article could show a PE phenomenon with very high probability, we believe that it is easy to find out new compounds showing PE according to this simple protocol, i.e., the five requirements. Furthermore, it is noteworthy that SHG measurement of deposited crystals can serve as a facile method at the first-stage screening to explore new candidate compounds showing PE or confirm the occurrence of PE for newly found compounds.

Thus, we anticipate that PE can be used as a general chiral resolution method by simple crystallization, with high flexibility and versatility, and full reproducibility, similarly to PC of racemic conglomerates.

References

1. Prigogine, I.: The End of Certainty. The Free Press, New York (1977)
2. Prigogine, I., Stengers, I.: Order Out of Chaos: Man's New Dialogue with Nature. Bantam Books, New York (1984)
3. Lightman, A.: The Discoveries. Vintage Books, New York (2005)
4. Waldrop, M.M.: Complexity. Simon & Schuster Paperbacks, New York (1992)
5. Kauffman, S.A.: At Home in the Universe. Oxford University Press, New York (1995)
6. Kauffman, S.A.: Investigations. Oxford University Press, New York (2000)
7. Mainzer, K.: Symmetry and Complexity. World Scientific (2005)
8. Mainzer, K.: Thinking in Complexity. Springer, Berlin (2007)
9. Di Bella, S., Ratner, M.A., Marks, T.J.: Design of chromophoric molecular assemblies with large second-order optical nonlinearities. A theoretical analysis of the role of intermolecular interactions. J. Am. Chem. Soc. **114**, 5842–5849 (1992)
10. Bustamante, C., Liphardt, J., Ritort, F.: The nonequilibrium thermodynamics of small systems. Phys. Today **58**, 43–48 (2005)

11. Kwak, H.Y., Panton, R.L.: Gas bubble formation in nonequilibrium water–gas solutions. J. Chem. Phys. **78**, 5795–5799 (1983)
12. Mann, S., Heywood, B.R., Rajam, S., Birchall, J.D.: Controlled crystallization of $CaCO_3$ under stearic acid monolayers. Nature **334**, 692–695 (1988)
13. Ushio, T., Tamura, R., Takahashi, H., Yamamoto, K.: Unusual enantiomeric resolution phenomenon observed upon recrystallization of a racemic compound. Angew. Chem. Int. Ed. **35**, 2372–2374 (1996)
14. Tamura, R., Takahashi, H., Hitotsu, K., Nakjima, Y., Ushio, T., Toda, F.: Unusual disordered crystal structure of a racemate exhibiting a novel enantiomeric resolution: preferential enrichment. Angew. Chem. Int. Ed. **37**, 2876–2878 (1998)
15. Tamura, R.: Engineering crystallography: from molecule to crystal to functional form. In: Roberts, K., Docherty, R., Tamura, R. (eds.), pp. 353–364. Springer, Dordrecht (2017)
16. Tamura, R., Iwama, S., Gonnade, R.G.: Control of polymorphic transition inducing preferential enrichment. CrystEngComm **13**, 5269–5280 (2011)
17. Tamura, R., Iwama, S., Takahashi, H.: Chiral symmetry breaking phenomenon caused by a phase transition. Symmetry **2**, 112–135 (2010)
18. Tamura, R., Takahashi, H., Fujimoto, D., Ushio, T.: Mechanism and scope of preferential enrichment, a symmetry-breaking enantiomeric resolution phenomenon. Top. Curr. Chem. **269**, 53–82 (2007)
19. Tamura, R., Ushio, T.: Enantiomer separation. In: Toda, F. (ed.), pp. 135–163. Kluwer Academic Publishers, Dordrecht (2004)
20. Coquerel, G.: Advances in organic crystal chemistry: comprehensive reviews 2015. In: Tamura, R., Miyata, M. (eds.), pp. 393–420. Springer, Tokyo (2015)
21. Kellogg, R.M.: Advances in organic crystal chemistry: comprehensive reviews 2015. In: Tamura, R., Miyata, M. (eds.), pp. 421–443. Springer, Tokyo (2015)
22. Coquerel, G.: Preferential crystallization. Top. Curr. Chem. **269**, 1–51 (2007)
23. Pasteur, L.: Recherches sur les relations qui peuvent exister entre la forme crystalline, la composition chimique et le sens de la polarisation rotatoire. Ann. Chim. Phys. **24**, 442–459 (1848)
24. Jacques, J., Collet, A., Wilen, S.H.: Enantiomers, Racemates and Resolutions. Krieger, Malabar (1994)
25. Tamura, R., Fujimoto, D., Lepp, Z., Misaki, K., Miura, H., Takahashi, H., Ushio, T., Nakai, T., Hirotsu, K.: Mechanism of preferential enrichment, an unusual enantiomeric resolution phenomenon caused by polymorphic transition during crystallization of mixed crystals composed of two enantiomers. J. Am. Chem. Soc. **124**, 13139–13153 (2002)
26. Fujimoto, D., Tamura, R., Lepp, Z., Takahashi, H., Ushio, T.: Mechanism of a new type of solvent-assisted solid-to-solid polymorphic transition causing preferential enrichment: prominent influence of C(sp2)H–O interaction on the control of a crystal structure. Cryst. Growth Des. **3**, 973–979 (2003)
27. Miura, H., Ushio, T., Nagai, K., Fujimoto, D., Lepp, Z., Takahashi, H., Tamura, R.: Crystallization of a desired metastable polymorph by pseudoseeding, crystal structure solution from its powder X-ray diffraction data, and confirmation of polymorphic transition. Cryst. Growth Des. **3**, 959–965 (2003)
28. Horiguchi, M., Okuhara, S., Shimona, E., Fujimoto, D., Takahashi, H., Tsue, H., Tamura, R.: Mechanistic flexibility of solvent-assisted solid-to-solid polymorphic transition causing preferential enrichment: significant contribution of π/π and CH/π interactions as well as hydrogen bonds. Cryst. Growth Des. **7**, 1643–1652 (2007)
29. Horiguchi, M., Okuhara, S., Shimona, E., Fujimoto, D., Takahashi, H., Tsue, H., Tamura, R.: Control of the mode of polymorphic transition inducing preferential enrichment by modifying the molecular structure or adding seed crystals: significant influence of CH/F hydrogen bonds. Cryst. Growth Des. **8**, 540–548 (2008)
30. Horiguchi, M., Yabunaka, S., Iwama, S., Shimona, E., Lepp, Z., Takahashi, H., Tsue, H., Tamura, R.: Case study on the effects of molecular structure on the mode of polymorphic transition inducing preferential enrichment. Eur. J. Org. Chem. 3496–3505 (2008)

31. Takahashi, H., Iwama, S., Clevers, S., Veesler, S., Coquerel, G., Tsue, H., Tamura, R.: In situ observation of polymorphic transition during crystallization of organic compounds showing preferential enrichment by means of temperature-controlled video-microscopy and time-resolved X-ray powder diffraction. Cryst. Growth Des. **17**, 671–676 (2017)
32. Uchida, Y., Iwama, S., Coquerel, G., Tamura, R.: A kinetic/thermodynamic origin of regular chiral fluctuation or symmetry breaking unique to preferential enrichment. Chem. Eur. J. **22**, 11660–11666 (2016)
33. Iwama, S., Takahashi, H., Tsue, H., Tamura, R.: Case study on the interpretation of crystal structures inducing preferential enrichment based on the graph set analysis of hydrogen bond motifs. Cryst. Growth Des. **15**, 3052–3062 (2015)
34. Gonnade, R.G., Iwama, S., Sugiwake, R., Manoj, K., Takahashi, H., Tsue, H., Tamura, R.: Occurrence of spontaneous resolution of ketoprofen with a racemic crystal structure by simple crystallization under nonequilibrium preferential enrichment conditions. Chem. Commun. **48**, 2791–2793 (2012)
35. Gonnade, R.G., Iwama, S., Mori, Y., Takahashi, H., Tsue, H., Tamura, R.: Observation of efficient preferential enrichment phenomenon for a cocrystal of (DL)-phenylalanine and fumaric acid under nonequilibrium crystallization conditions. Cryst. Growth Des. **11**, 607–615 (2011)
36. Manoj, K., Takahashi, H., Morita, Y., Gonnade, R.G., Iwama, S., Tsue, H., Tamura, R.: Preferential enrichment of DL-leucine using cocrystal formation with oxalic acid under nonequilibrium crystallization conditions. Chiralty **27**, 405–410 (2015)
37. Iwama, S., Kuyama, K., Mori, Y., Manoj, K., Gonnade, R.G., Suzuki, K., Hughes, C.E., Williams, P.A., Harris, K.D.M., Veesler, S., Takahashi, H., Tsue, H., Tamura, R.: Highly efficient chiral resolution of DL-arginine by cocrystal formation followed by recrystallization under preferential enrichment conditions. Chem. Eur. J. **20**, 10343–10350 (2014)
38. Iwama, S., Horiguchi, M., Sato, H., Uchida, Y., Takahashi, H., Tsue, H., Tamura, R.: Observation of the preferential enrichment phenomenon for essential α-amino acids with a racemic crystal structure. Cryst. Growth Des. **10**, 2668–2675 (2010)
39. Takhashi, H., Numao, Y., Motokawa, J., Clevers, S., Coquerel, G., Tsue, H., Tamura, R.: A novel mechanism of preferential enrichment phenomenon observed for the cocrystal of (RS)-2-{4-[(4-chlorophenoxy)methyl]phenoxy}propionic acid and isonicotinamide. Chem. Eur. J. **25**, 16405–16413 (2019)
40. Takahashi, H., Tamura, R., Fujimoto, D., Lepp, Z., Kobayashi, K., Ushio, T.: Preferential enrichment: full crystallographic analysis of the unusual phenomenon in the mixed crystals' version. Chirality **14**, 541–547 (2002)
41. Aakeroy, C.B., Sinha, A.S. (eds.): Co-Crystals: Preparation, Characterization and Applications. Royal Society of Chemistry, London (2018)
42. Manoj, K., Tamura, R., Takahashi, H., Tsue, H.: Crystal engineering of homochiral molecular organization of naproxen in cocrystals and their thermal phase transformation studies. CrystEngComm **16**, 5811–5819 (2014)
43. De Saint Jores, C.: Towards a deeper understanding of preferential enrichment. A case study: DL arginine fumarate in ethanol-water 5-5 mixture, Ph.D. thesis, University of Rouen, 2018

Chapter 21
Asymmetric Synthesis Involving Dynamic Enantioselective Crystallization

Masami Sakamoto

Abstract An approach to obtain products with high enantiomeric purity by utilizing the chirality generated by crystallizing organic materials is introduced. If a racemic mixture forms a conglomerate in which each single crystal is assembled from a single-handed enantiomer, it is possible to resolve each enantiomer from the racemic mixture by the preferential crystallization method. Furthermore, when preferential crystallization is applied under conditions in which fast racemization proceeds in the mother liquor, it becomes possible to converge the entire system to the desired single-handed enantiomer. This method is called crystallization-induced enantiomer transformation (CIET), a type of crystallization-induced stereoisomer transformation (CIST), and is a total resolution method realized by amino acids, pharmaceutical intermediates, axially chiral materials, etc. In recent years, even dynamic systems with relatively low racemization rates have been applied to chiral amplification by attrition-enhanced deracemization. In this chapter, recent advances in asymmetric synthesis by a methodology combining a chemical reaction that forms a chiral center from prochiral starting materials with deracemization by dynamic enantioselective crystallization are introduced. This method is applied to various asymmetric syntheses and is a phenomenon in which crystals of a product with high enantiomeric purity can be obtained only by crystallizing the product from the reaction system in solution. Various types of reactions have been developed by adjusting the conditions for the reversible reaction or the racemization of asymmetric centers with enantioselective crystallization. This method will be widely developed in the future and is also applicable on an industrial scale.

Keywords Crystal chirality · Conglomerate · Asymmetric synthesis · Absolute asymmetric synthesis · Total resolution · Deracemization · Dynamic crystallization

M. Sakamoto (✉)
Department of Applied Chemistry and Biotechnology, Graduate School of Engineering, Chiba University, Yayoi-cho, Inage-ku, Chiba 263-8522, Japan
e-mail: sakamotom@faculty.chiba-u.jp

M. Sakamoto and H. Uekusa (eds.), *Advances in Organic Crystal Chemistry*,
https://doi.org/10.1007/978-981-15-5085-0_21

21.1 Introduction

Optically active compounds are in high demand in the fields of pharmaceuticals, foods, functional materials, etc., hence the development of efficient and highly selective synthetic methods is strongly required. The optical resolution process by preferential crystallization has evolved into a practical method for optically resolving racemates economically and easily, and has been carried out on an industrial scale [1–3]. Furthermore, the dynamic crystallization method via racemization in the process of crystallization can completely separate the required enantiomers from the mixture of racemates by deracemization [4–8]. In addition, Viedma ripening, for which many successful examples have been reported in recent years, is a deracemization process by grinding and stirring crystals using glass beads under conditions where racemization proceeds in a racemic mixture of conglomerate crystals [9].

The crystal of a racemate can be roughly classified into three categories that focus on individual crystals: (i) the racemic compound is composed of an equivalent amount of both enantiomers, (ii) a racemic conglomerate consists of a single enantiomer, and (iii) the racemic solid solution in which both enantiomers are arranged at random in a single crystal. All racemic materials studied crystallize as one of these three kinds of crystals [10–13]. Preferential crystallization is not available for all the crystals of a racemate, and only a racemic conglomerate of the crystal (ii) was utilized for resolution.

The space groups of crystals are classified into 280 kinds, of which 65 are chiral space groups. Table 21.1 shows the space groups of crystals registered in the Cambridge Crystallographic Data Center (CCDC) as of August 2019, including the first 11 that occur most frequently, which accounts for 90% of the total. Among

Table 21.1 11 preferred space groups and frequency of crystalline compounds in CSD-2019 (total number: 957,506)

Space group number	Space group	Frequency (%) Top 11 > 90%	Frequency (%) among chiral space groups
14	$P2_1/c$	34.4	
2	*P*-1	24.8	
15	*C*2/c	8.3	
19[a]	$P2_12_12_1$	7.1	32.8
4[a]	$P2_1$	5.1	23.7
61	*P*bca	3.3	
33	$Pna2_1$	1.4	
62	*P*nma	1.0	
9	*C*c	1.0	
1[a]	*P*1	1.0	4.4
5[a]	*C*2	0.9	3.9

[a]Chiral space group

them, the chiral space groups are $P2_12_12_1$, $P2_1$, P1, C2, which is 14.1% of the total [14]. Since this data includes crystal structure analysis data of optically active compounds, the ratio of chiral crystallization of achiral compounds and formation of conglomerates is considered to be somewhat lower, around 5-10%. However, there are some substance groups where only half crystallize in a chiral space group, and there are cases where the synthesis of 50 types of derivatives does not afford any chiral space groups. Although the intermolecular interactions of both enantiomers can be predicted to some extent, they are still not fully elucidated but are dependent on chance.

Therefore, when performing a reaction using a chiral crystal or utilizing optical resolution by crystallization, it is preferable to target a substance group whose substituents can be easily changed. Unlike studies applying to a variety of derivatives with different substituents, such as asymmetric synthesis using chiral catalysts, chiral crystallization is a bottleneck for asymmetric synthesis using crystal chirality. In order to avoid this bottleneck, a diastereomeric reaction can be used by introducing optically active substituents into the molecule, or by forming chiral ion pairs (salts), co-crystals, or chiral inclusion compounds (host–guest complexes). Many valuable methods have been adopted that lead to chiral environments in crystal lattices [15–20].

21.2 Total Resolution from Racemates by Dynamic Crystallization

Pasteur was able to manually separate sodium ammonium tartrate crystals to obtain an enantiopure compound, based on the geometric chirality of the contours of the conglomerate crystal. However, it is difficult to visually divide most crystals, because they do not show geometric chirality by such an outline [21]. So far, conglomerate crystals have been used for optical resolution of racemates by general preferential crystallization methods, which are important methods indispensable for resolution processes on an industrial scale, especially in the fields of medicine, agrochemicals, and foods [22].

In the industrial preferential crystallization process, various improvements have been made to obtain crystals with as high an enantiomeric purity as possible, but it is necessary to reduce the amount of crystals obtained by one crystallization, because the opposite enantiomer that is excessive in the mother liquor crystallizes. (Fig. 21.1a). Furthermore, the maximum resolution is only 50:50, and there is a problem that one enantiomer must be discarded. Therefore, total resolution to selectively obtain only the required enantiomer by crystallization under conditions where racemization occurs rapidly has been performed with some substrates (Fig. 21.1b).

When a racemic mixture of a conglomerate is crystallized from a supersaturated solution, the molecule repeatedly aggregates and dissolves, until the first chiral crystal nucleus is eventually formed. As molecules of the same enantiomer gather further

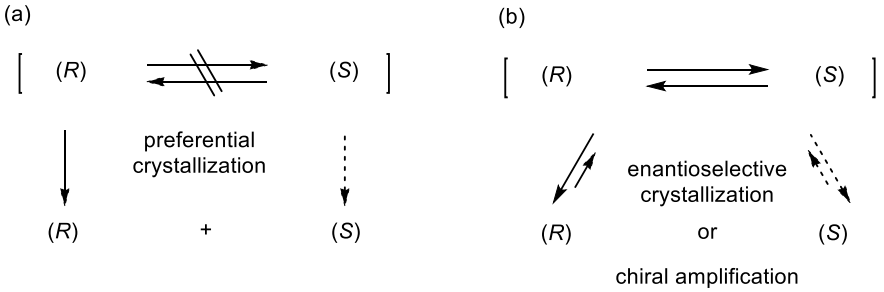

Fig. 21.1 **a** Preferential crystallization of racemic conglomerate and **b** dynamic enantioselective crystallization (total resolution by chiral amplification)

in the crystal nucleus and crystals grow, the crystallized enantiomer decreases in the mother liquor, but it is supplied through racemization in solution and the equilibrium state is maintained. In this way, enantiomerically pure crystals are obtained without special optical resolution methods such as exposure to a chiral stationary phase.

The first example of dynamic enantioselective crystallization is the crystallization of quaternary ammonium iodides from solvents reported by Havinga et al. [23]. They proposed that the second crystal nuclei grow from microcrystals derived from the first mother crystals, and also demonstrated the effect of stirring, by which crystals of high purity can be obtained reproducibly. The effect of stirring has been studied in detail with sodium chlorate by Kondepudi et al. [24].

The phenomenon of nonlinear increase of one enantiomer is explained by "Ostwald ripening." When there is a difference in the size of fine particles (microcrystals) deposited from a supersaturated solution, this is a phenomenon in which small particles disappear and large particles gradually become larger with the passage of time [25]. Since the solubility of small particles is higher than that of large particles, they gradually disappear and aggregate toward the larger particles by the Gibbs–Thomson effect.

In order to obtain crystals with high optical purity, fast racemization in the mother liquor compared to the rate of crystal growth is required. Therefore, in dynamic crystallization under conditions of low racemization rates, asymmetric amplification to high enantiomeric purity is difficult. However, a method that allows chiral amplification even in a system with a low racemization rate has been developed. Viedma sealed a saturated solution containing crystals of racemic sodium chlorate and glass beads and continued the grinding with stirring for a few days. All of the crystals were completely converted into crystals of a single-handed enantiomer [9, 26]. This asymmetric transformation is called attrition-enhanced deracemization (Viedma ripening) and is a solid-to-solid deracemization reaction, which is distinguished from the dynamic preferential crystallization method via deracemization from solution-to-solid [27, 28]. His experiment used sodium chlorate, which is an achiral inorganic molecule, but other groups have recently succeeded using many organic molecules.

As mentioned above, chiral amplification using dynamic enantioselective crystallization is a very effective resolution method because the desired enantiomer can be completely resolved in one crystallization [7, 8]. Several successful examples of chiral amplification have been reported so far, and their application to amino acid derivatives and in the pharmaceutical field is particularly remarkable (Fig. 21.2). The amino acid derivatives **1**–**11** [5, 26, 29–38] and the naproxen derivative **12** [39, 40] all use a racemization reaction via deprotonation at the α-position of the carbonyl group. The required optically active enantiomers are selectively obtained with high enantiomeric purity by filtration, and some compounds have been developed industrially.

Deracemization of racemic diarylsuccinamides **13** affording a conglomerate was also developed under basic conditions by the solvent evaporation method or attrition-enhanced deracemization with specific ee values [41, 42].

The racemization reaction is most frequently reported by abstraction of the acidic protons at the α-position of carbonyl groups, but asymmetric amplification accompanied by racemization of quaternary chiral centers has also been reported. The chiral center of isoindolinone **14** is an aminal structure and is stable in nonpolar solvents; however, racemization proceeds under basic conditions or in an alcoholic solvent. Asymmetric amplification from a racemate to over 90% ee has been achieved by crystallization while promoting racemization in the presence of 1,8-diazabicyclo[5.4.0]undec-7-ene (DBU) [43]. Similarly, for the racemization by ring-opening and ring-closing of the aminal carbon, 100% ee optical purity has been reported even for asymmetric amplification of pyrrolinone **15** [44].

Spiropyrans **16** and spirooxazines **17** also have quaternary chiral centers. These compounds are photochromic materials that undergo reversible color change owing to ring-opening and ring-closing reactions by photolysis or thermal reaction. Asymmetric amplification has been achieved by dynamic crystallization of racemic spiropyrans and spirooxazines, which afforded racemic conglomerate crystals by the solvent evaporation method or attrition-enhanced deracemization [45].

Deracemization of allylsulfoxide **18** was developed by Meekes under grinding conditions in ether refluxing conditions, where the racemization process involved 2,3-sigmatropic rearrangement [46].

An example of preferential crystallization accompanied by racemization (atropisomerization) by axial rotation has been reported [47]. Pincock et al. reported that binaphthyl **19** was melted and crystallized at 150 °C to obtain an optically active solid. Binaphthyl is a racemic crystal upon crystallization from solution, but deracemization is achieved by satisfying two conditions: forming a conglomerate at high temperature and rapid racemization by axial rotation during crystallization. Furthermore, when the melted materials were stirred during crystallization, the reproducibility of obtaining high purity crystals improved with high optical purity of 90% ee or more [48].

We found that an analog of pyrimidine bases **20** having aryl groups on the nitrogen atom formed conglomerates [49]. These compounds have stable C–N axial chirality and do not racemize at room temperature; however, axial rotation occurs at high temperature. A small amount of solvent was added to crystals of **20**. After dissolution

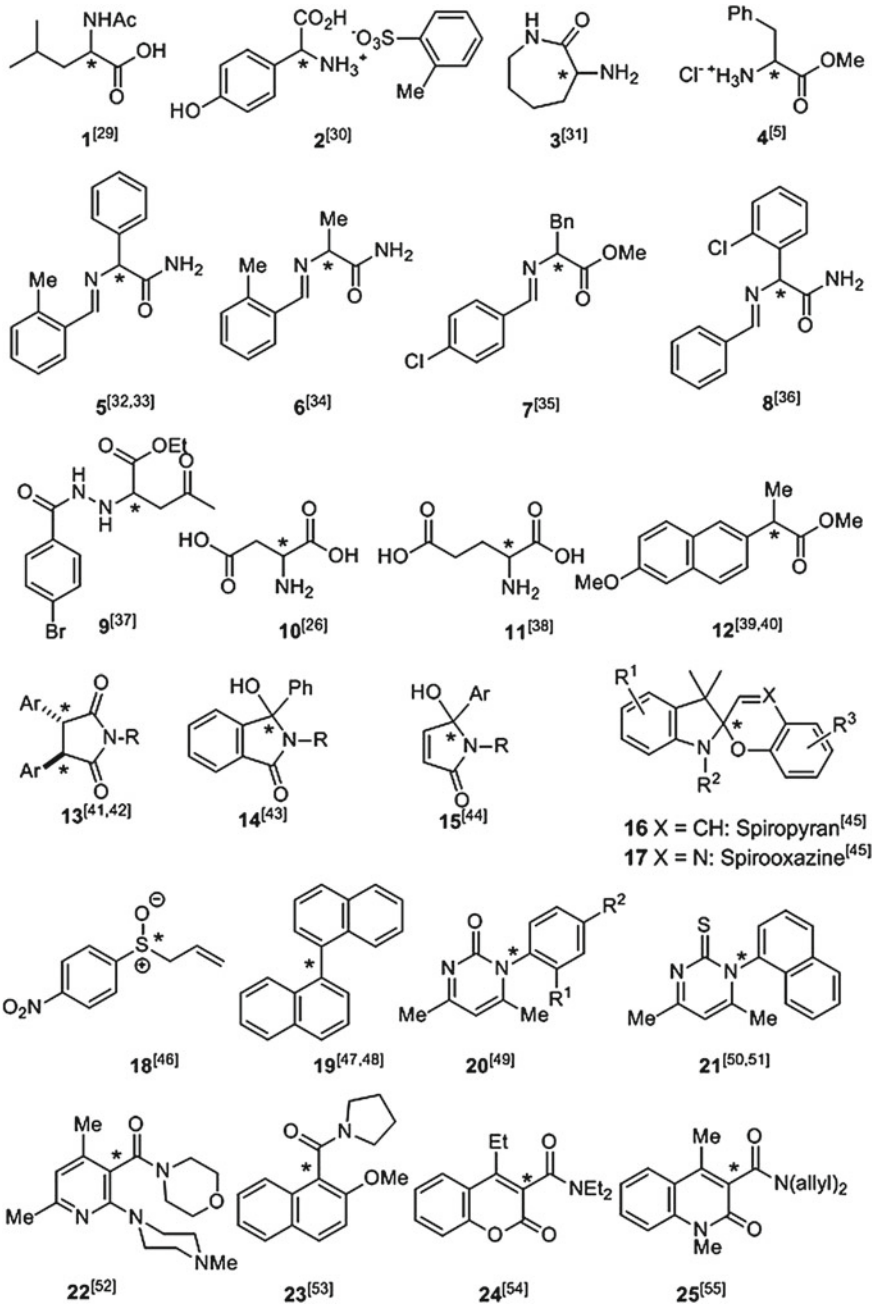

Fig. 21.2 Successful examples of dynamic enantioselective crystallization using conglomerates

at 200 °C, a small amount of seed crystals was added and crystallization was carried out while gradually cooling to obtain crystals with high optical purity of 90% ee or more.

In addition, there is a substrate suitable for deracemization by crystallization. Pyrimidinethione **21** having a naphthyl group on the nitrogen atom forms a conglomerate. The solvent is gradually evaporated from the toluene solution at 100 °C to give 91% ee of crystals [50, 51].

Nicotinamide **22** also gave a conglomerate ($P2_1$ space group) and has a half-life of racemization of about 3 h in chloroform at 20 °C. It was melted at 160 °C (mp 148 °C), gradually cooled to 125 °C with stirring, and solidified by adding a small amount of seed crystals, giving 83–92% ee of crystals [52]. To obtain a high ee of crystals with good reproducibility by deracemization from the melt, seeding is necessary, because only 6-42% ee was obtained without seeding. On the other hand, attrition with stirring in hexane at 70 °C always gave 99% ee crystals after 3 days.

Similar aromatic amide derivatives **23**–**25** exhibited axial chirality, and afforded conglomerate crystals [53–55]. Their activation free energies are around 20–22 k cal mol^{-1}, which means that their axial chirality can be easily controlled thermodynamically. Optically active compounds were easily obtained by enantioselective crystallization from the melt with specific ees; however, the chirality was gradually lost by dissolving into solvent even at room temperature. The chirality was efficiently utilized for many asymmetric reactions at low temperature and by using adequate solvent properties.

21.3 Absolute Asymmetric Synthesis by the Combined Methodology of Chiral Center Generation and Dynamic Enantioselective Crystallization

Focusing on developing a more effective and convenient absolute asymmetric synthesis using crystal chirality, an asymmetric synthetic method combining a reaction that generates a chiral center from a prochiral molecule with dynamic crystallization was developed (Fig. 21.3). Optically active materials can be obtained by simultaneously carrying out the chemical reaction and dynamic crystallization without an external chiral source. This approach starts with prochiral materials that can provide chiral products via reversible condensation reactions. Application to the Mannich reaction has been reported by Tsogoeva et al. [37] and to an aldol condensation by Bolm et al. [56]. We also developed some new reaction systems and summarize them together with some valuable results developed by other groups.

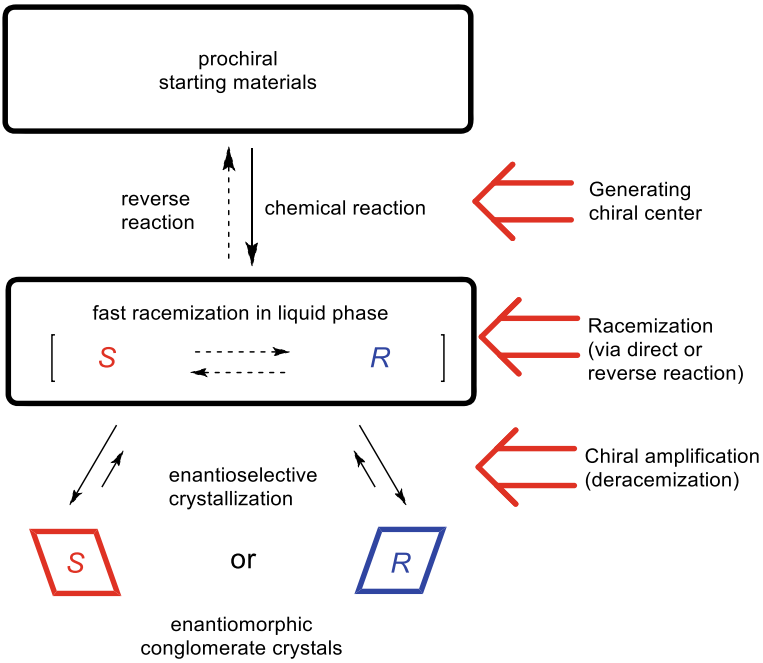

Fig. 21.3 Chirogenic scheme from prochiral starting materials followed by dynamic enantioselective crystallization

21.3.1 Asymmetric Stereoisomerization Involving Dynamic Crystallization

An asymmetric stereoisomerization from a prochiral form to a chiral form involving the isomerization of 2,3-disubstituted succinimides was developed (Fig. 21.4) [41]. Symmetrical diphenylmaleimides were reduced with hydrogen in the presence of platinum oxide to give the corresponding *cis*-diphenylsuccinimides. These materials were in prochiral *meso* form, but in the presence of a base, rapid isomerization took place to the thermodynamically stable chiral *trans* form with both enantiomers. Among the *trans* isomers with various substituents, it was found that **26a** (R = Pr), **26b** (R = *i*-Pr), and **26c** (R = o-tolyl) gave racemic conglomerates.

A catalytic amount of base (DBU) was added to a mixed solution of chloroform and hexane of **26a** or **26b**, and the crystals of the *trans* form were quantitatively deracemized to an enantiomeric purity of 80–90% ee simply by allowing the solvent to evaporate naturally with stirring. Although the formation ratio of the (+)-form or (−)-form by spontaneous crystallization was almost the same, seeding with a small amount of seed crystals could promote crystals with the same stereochemistry as the seed crystals to be selectively amplified. In the case of **26c**, isomerization occurred to the *trans* form during purification of the *cis* form. Dynamic preferential

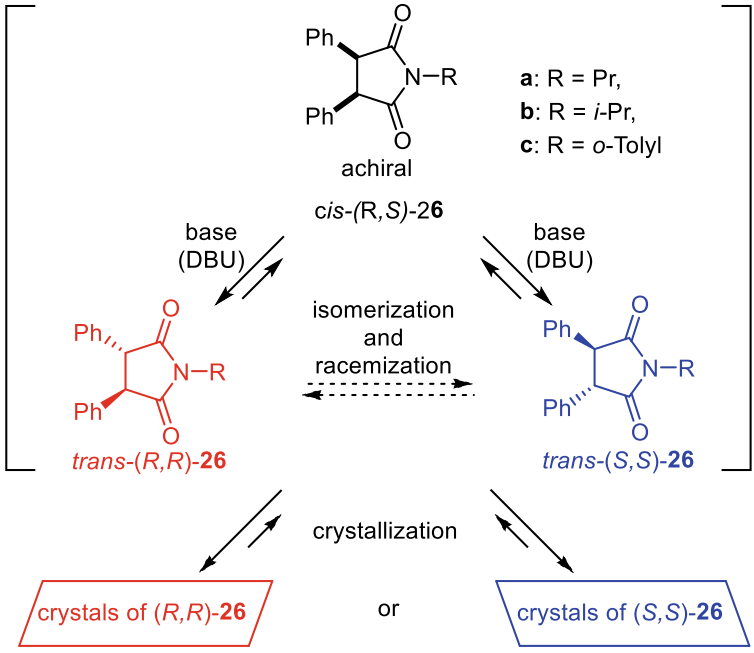

Fig. 21.4 Asymmetric isomerization followed by dynamic crystallization under achiral conditions

crystallization could then be carried out using the racemic mixture of the *trans* isomer as a starting material, and deracemization to the *trans*-**26c** of high enantiomeric purity was observed.

21.3.2 Asymmetric Synthesis Using Reversible aza-Michael Addition Reaction Followed by Attrition-Enhanced Deracemization

Vlieg et al. succeeded in obtaining β-aminoketone **27** in 100% ee by applying the Viedma ripening method to the reversible aza-Michael addition reaction of anisidine to an enone (Fig. 21.5) [57]. When anisidine was reacted with an enone in ethanol, conglomerate adduct **27** crystallized. The reaction mixture was kept in suspension with stirring in the presence of DBU, and deracemization was promoted through the reverse reaction leading to one-handed enantiomorphic crystals.

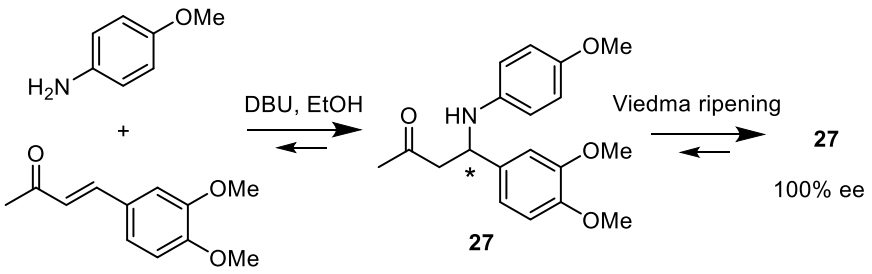

Fig. 21.5 Asymmetric synthesis followed by dynamic crystallization under achiral conditions

21.3.3 Asymmetric Synthesis of Amino Acid Derivatives and Their Precursors

We also developed asymmetric amplification reactions combining the reversible Michael addition reaction and the dynamic crystallization of conglomerate crystals (Fig. 21.6) [58]. Michael reaction of phenethylamine and aroylacrylamide **28** in the presence of a catalytic amount of DBU in a mixed solvent of EtOH and heptane

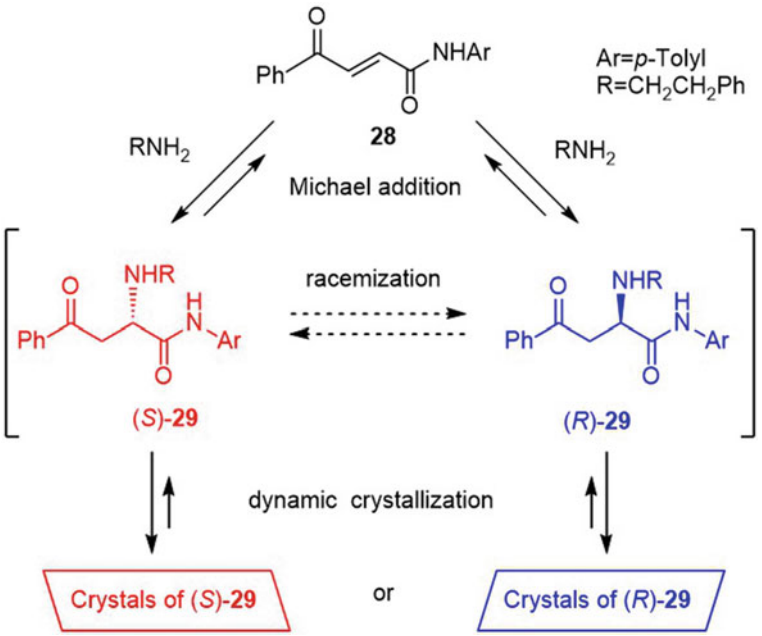

Fig. 21.6 Asymmetric synthesis using reversible Michael addition followed by dynamic crystallization in achiral conditions

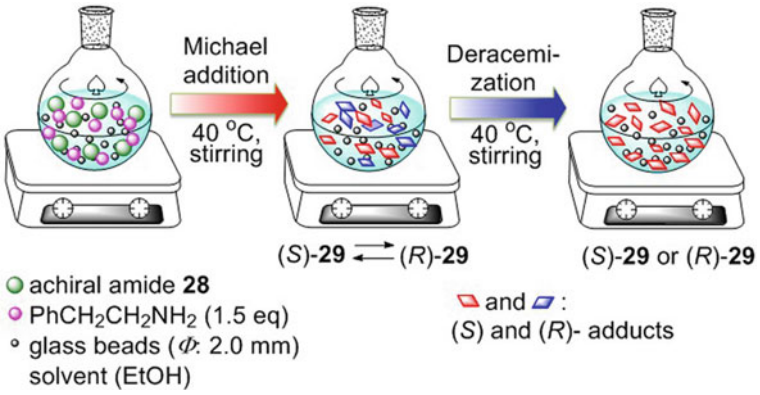

Fig. 21.7 Asymmetric synthesis of α-amino amide by conjugate addition and attrition-enhanced deracemization

efficiently occurred to give a white precipitate of an amino acid derivative **29**. Continuous suspension with stirring until complete evaporation of the solvent quantitatively gave **29** with 46% ee. The rate of racemization by the reverse reaction was insufficient even in the presence of DBU, and it was difficult to obtain a product with higher optical purity by the solvent evaporation method.

Next, we examined conjugate addition followed by attrition-enhanced deracemization (Viedma ripening). Arolyacrylamide **28** was reacted with 1.5 eq of phenethylamine in EtOH with or without glass beads (Fig. 21.7). The cycloaddition reaction proceeded smoothly and the solid of adduct amino amide **29** appeared immediately. The reaction mixture was continuously stirred over several days while monitoring the ee value. In solution, the racemization proceeded by reverse conjugate addition reaction and deracemization by Viedma ripening.

When we used glass beads with a stir bar, the ee value started to increase after 14 days, reaching 95% ee after 22 days. The ee was measured for both the mother liquor and the solid. The ee value of the solid after 22 days was 99%, while that of the mother liquor was nearly racemic. Without glass beads and with only a stir bar, the starting time was delayed to 25 days; furthermore, the rate of deracemization became slow and took as many as 45 days to reach a stationary state with the same ee value as that obtained with glass beads. Thus, the use of glass beads was effective in accelerating the rate of deracemization. This reversible reaction was also efficiently accelerated by DBU in aprotic solvent; however, DBU in protic solvent was not as effective. When DBU (0.5 eq) was added to the reaction system, some effect appeared on the starting point of deracemization; however, the inclination of the line of deracemization was almost the same. This reaction afforded the asymmetric synthesis of an amino acid derivative by reversible Michael addition.

In these procedures, both enantiomers appeared randomly in each batch at almost the same probability. Once the achiral substrates, **28** and phenethylamine, were suspended in solution, the reaction occurred to give both enantiomers of the product

in equal amounts. As the reaction progressed, the solution became saturated with the poorly soluble product, and both enantiomers of the product precipitated in equal amounts as racemic conglomerate crystals. The solid of **28** was gradually replaced with the solid of product **29**. The initial symmetry of this solid state was broken due to either local statistical fluctuations in ee or a local difference in crystal size distribution between the enantiomers. Subsequently, grinding of the crystals in combination with solution-phase racemization caused complete deracemization of the solids. The reaction proceeded quantitatively, and the yield of the filtered solid product was 90 with 99% ee.

As described above, moderate chiral induction of 45% ee was achieved in a couple of days by conjugate addition followed by the dynamic preferential crystallization method. On the other hand, a considerably higher ee value was obtained with the second method by using Viedma ripening, although several days were required for effective deracemization even in the presence of DBU. Therefore, we examined combining the methodology of both procedures to obtain optically pure crystals in a short period of time. First, benzoylacrylamide **28** and phenethylamine (1.3 eq) were reacted in a mixed solvent of MeOH and hexane, and the reaction mixture was vigorously stirred while evaporating solvent at 40 °C. It took about a half-day to remove all the solvent. The ee value of the solid of adduct **29** was around 15%. To the solid, ethanol as a solvent, DBU (0.5 eq), and glass beads were added, and the suspended mixture was stirred vigorously. The changes in ee values for the reaction mixture (including both mother liquor and crystals) were plotted. Deracemization began in a short time and the ee increased to 95% in only 8 or 9 days. In all cases, the final ee value of the separated solid was 99%. Thus, we shortened the reaction time significantly by dynamic preferential crystallization followed by attrition-enhanced deracemization.

The next example is the asymmetric synthesis of an aspartic acid derivative, succinopyridine **30** (Fig. 21.8) [59]. This material crystallizes in the chiral space group of $P2_12_12_1$ and is used as an optical element due to its second-harmonic generation (SHG) properties. As described above, the aza-Michael addition is reversible and is successful in chiral amplification by dynamic crystallization. The pyridinium cation of **30** adjacent to the carboxylate anion also suggests that direct deprotonation would lead to racemization of this material.

The racemization rate of optically active **30** was measured in 90 °C water, and the half-life was found to be 115 min. The use of 10% aqueous AcOH reduced the half-life to 20 min. In this case, when D_2O was used instead of H_2O, deuterated **30** was formed at the chiral center accompanied by small amounts of maleic acid and fumaric acid. These facts suggested that the racemization of the chiral center did not occur by a reversible reaction but by deprotonation involving the enol form as a major pathway.

When an equal amount of maleic acid and pyridine was reacted in water at 90 °C, succinopyridine precipitated readily. Acetic acid was added to form a 60% aqueous acetic acid solution, and the reaction mixture maintained suspension with stirring at the same temperature using glass beads. The ee value rose after 8 days and reached 99% ee after 16 days. A higher concentration of acetic acid, about 75% in water,

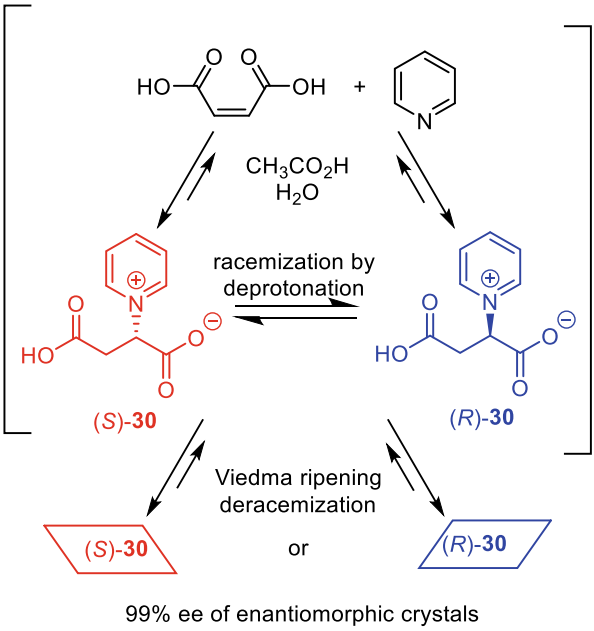

Fig. 21.8 Asymmetric synthesis using Michael addition followed by dynamic crystallization involving deracemization by deprotonation

reduced the induction period, and deracemization started after 4 days and gave 80% ee of the solid after 7 days.

Kawasaki et al. reported a valuable synthetic example of an amino acid precursor by the Strecker reaction followed by crystallization with racemization in the presence of a base leading to α-aminonitrile **31** in up to 96% ee (Fig. 21.9) [60, 61].

Noorduin et al. also reported the Strecker reaction to Viedma ripening for the absolute asymmetric synthesis of highly sterically hindered α-amino acids, and the enantiomerically pure α-amino acids **32**, *tert*-leucine, and α-(1-adamantyl)glycine were obtained (Fig. 21.10) [62].

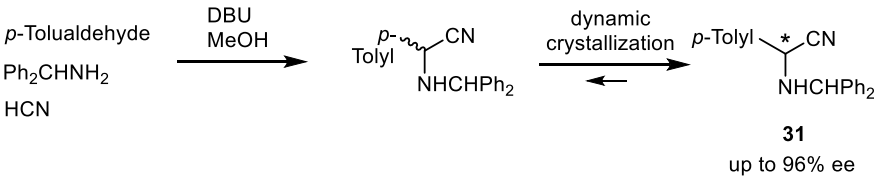

Fig. 21.9 Asymmetric Strecker synthesis followed by dynamic crystallization

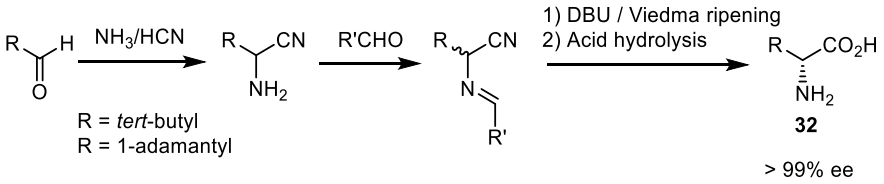

Fig. 21.10 Asymmetric Strecker synthesis followed by Viedma ripening

21.3.4 Asymmetric Synthesis Involving Photochemical Reaction Followed by Dynamic Enantioselective Crystallization

The above reactions involved both thermal chemical reactions and thermal racemization processes (TT-type, Fig. 21.11). We also developed an asymmetric synthesis

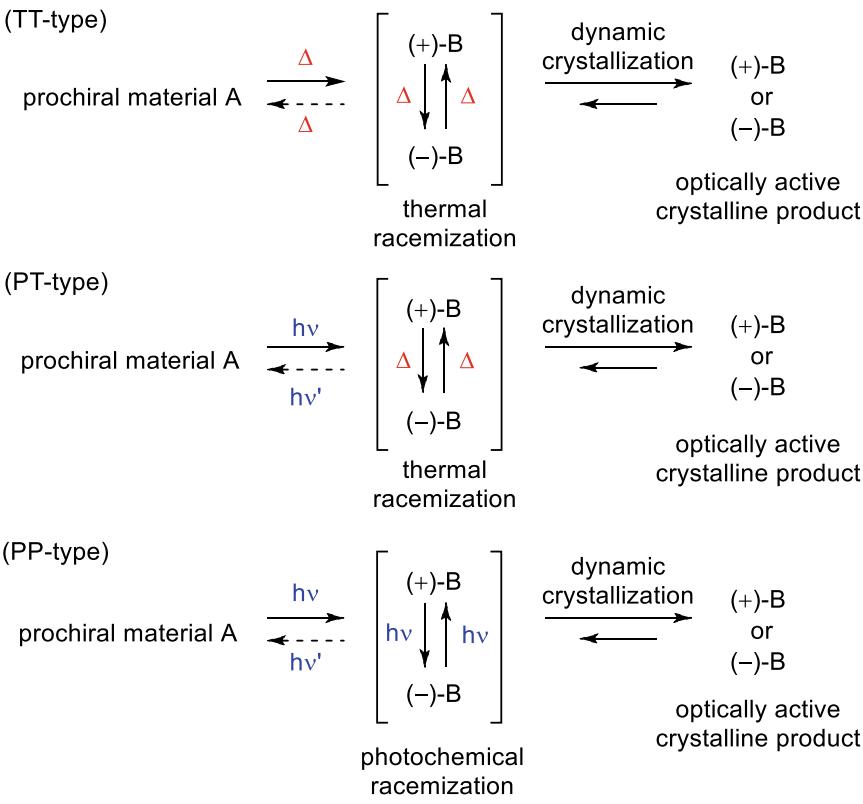

Fig. 21.11 Three types of asymmetric reactions involving dynamic crystallization

by a reversible photochemical reaction as a new asymmetric reaction system. It is an absolute asymmetric synthesis of the PP-type by photochemical reaction and photochemical racemization.

When prochiral ethyl 6-bromochromone-2-carboxylate **33** was used as a starting material, the photodimer **34** was obtained as a conglomerate of the C2 crystal space group. A reversible reaction process by light irradiation using the same wavelength of light was also observed (Fig. 21.12) [63]. When a 0.01 M acetonitrile solution of **33** was irradiated at 20 °C while gradually evaporating the solvent, crystalline optically active dimer **34** was obtained; however, the enantiomeric purity was only 29% ee. It was possible to increase the ee to 50% by adding a small amount of seed crystals during crystallization.

Next, the acetonitrile solution was irradiated at low temperature to promote crystallization without evaporation of solvent. When a 0.01 M acetonitrile solution of **33** was irradiated at −40 °C, dimer **34** was obtained with 38% ee without adding seed crystals. The enantiomeric purity could be increased up to 80% ee by adding a small amount of seed crystals.

We also examined the photoreaction using sunlight, because both monomer **33** and dimer **34** showed absorption in the long wavelength region over 400 nm. When a

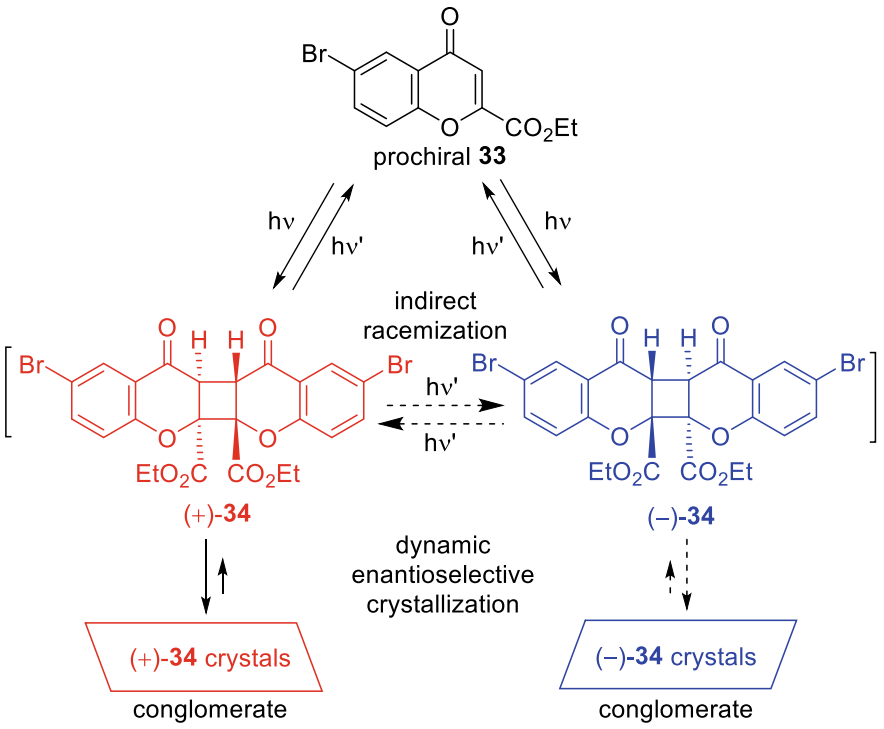

Fig. 21.12 Asymmetric synthesis by reversible photodimerization of chromone carboxylates followed by enantioselective crystallization

0.01 M acetonitrile solution of **33** was irradiated by sunlight outdoors on a clear day at a temperature of 10–20 °C, the dimer precipitated as a white solid by stirring for about 6 h until the solvent was evaporated. When seed crystals were not used, **34** was obtained with low ee or as a racemate. On the other hand, when seed crystals were added, the dimer having the same chirality as the seed crystals was obtained in 15–30% ee. Thus, an optically active substance could be obtained simply by irradiating a solution of a prochiral compound with sunlight.

For the above PP-type asymmetric reaction system, efficient racemization did not proceed and optical purity was only up to 80% ee due to competition of light absorption between the product and the starting material. Therefore, an asymmetric synthesis of PT-type (photochemical reaction and thermal racemization) was designed, in which the photoreaction was used as a trigger to generate an asymmetric center, followed by thermal racemization for the fast racemization process (Fig. 21.13).

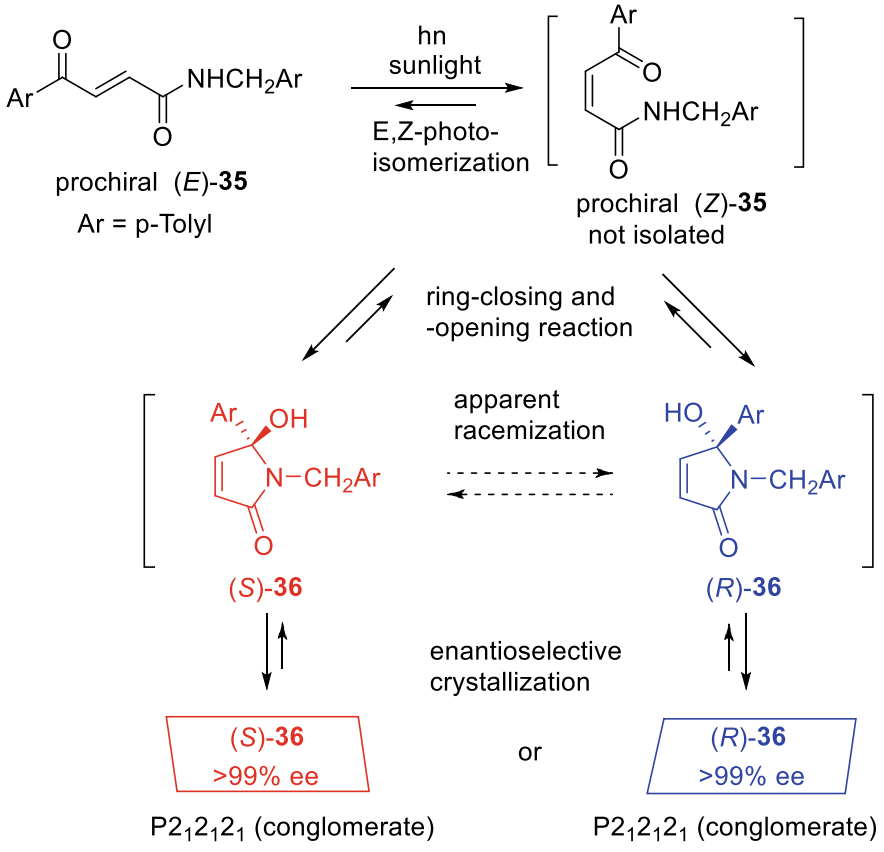

Fig. 21.13 Asymmetric synthesis by photochemical reaction using natural sunlight followed by thermal racemization process

Prochiral aroylacrylamide **35** has an enone structure, and the photoisomerization reaction was expected to convert the *E*-form to the *Z*-form (Fig. 21.13) [44]. Thermodynamically stable (*E*)-**35** was isomerized to the *Z*-form by irradiation of light. The *Z*-form is much more stable than normal *Z*-enones due to the intramolecular hydrogen bond between the carbonyl oxygen of the ketone and the NH group. Furthermore, the NH of the amide and the nearby carbonyl carbon resulted in an intramolecular cyclization reaction to give the pyrrolinone **36**. It was revealed that **36** formed a conglomerate with a crystal space group of $P2_12_12_1$. Since pyrrolinone **36** has an aminal skeleton, a racemization reaction is expected due to the (*Z*)-**35** mediated ring-opening process and deracemization by application of the stereoselective dynamic crystallization method (asymmetric amplification).

The asymmetric center of **36** was stable in low polar solvents such as benzene, hexane and chloroform and in aprotic solvents, and racemization did not proceed at room temperature. An increase in racemization rate was observed in methanol, with a half-life at 20 °C of 161 min. The half-life was shortened to 11.5 min at 35 °C. When DBU was added as a base catalyst, racemization was further promoted; however, isomerization from (*Z*)-**35** to (*E*)-**35** was also induced at the same time. In order to obtain **36** of high optical purity, it was necessary to continue irradiation with light in order to promote isomerization of the alkenyl group while promoting racemization by DBU.

The experimental procedure for the actual asymmetric synthesis is very simple. The prochiral (*E*)-**35** and 0.1 equivalents of DBU were dissolved in a mixed solvent of methanol and chloroform, and irradiated with light at 365 nm using an LED while stirring at room temperature until the solvent was completely evaporated. The optical purity of precipitated **36** after solvent evaporation was analyzed using HPLC with a chiral column. In all the experiments, **36** was reproducibly obtained at 98–99.9% ee.

The chirality was random in each batch, but by adding a small amount of seed crystals, it was possible to obtain **36** having the same chirality as the added seed crystals. We also succeeded in an asymmetric reaction using sunlight. Enamide (*E*)-**35** has an absorption edge up to 420 nm and can be isomerized by sunlight. The prochiral (*E*)-**35** was dissolved in a mixed solvent of methanol and chloroform, 0.1 equivalents of DBU was added, and the mixture was irradiated with sunlight with stirring until the solvent was completely evaporated. When the experiment was conducted 10 times, **36** was obtained with an optical purity of 99% ee or more in all, with 7 in the *R*-form and 3 in the *S*-form.

In this reaction system, the pyrrolinone derivative could be obtained with high enantiomeric purity simply by irradiating the solution of prochiral compound with LED light or sunlight outdoors (Fig. 21.14). Pyrrolinone is an important skeleton found in many pharmaceutical intermediates, and the control of the stereochemistry is an important research topic.

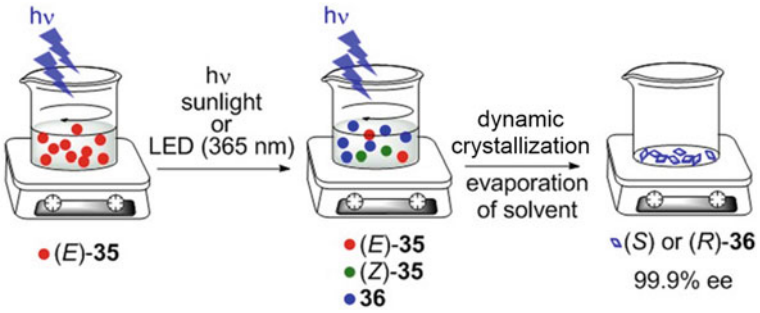

Fig. 21.14 Photochemical reaction of **35** followed by crystallization, leading to the optically active pyrrolinone **36**

21.3.5 Generation and Amplification of Chirality via Diels–Alder Reaction and Dynamic Crystallization

The Diels–Alder (DA) reaction is one of the most fundamental and illustrious reactions in organic chemistry, providing access to a variety of polycyclic heterocycles. The DA reaction is well-known to be a concerted electro-cycloaddition reaction and to involve a reversible process. We applied this reaction system to the asymmetric synthesis involving dynamic stereoselective crystallization as shown in Fig. 21.15 [64]. The primary DA reaction of 2-methylfuran with *N*-phenylmaleimide provides chiral materials from prochiral starting substrates and the racemization of (±)–**37** might be promoted by a reversible process. One of the most important requirements in this reaction system is that the DA adduct **37** should afford a racemic conglomerate in the $P2_12_12_1$ space group (Fig. 21.16).

When 2-methylfuran and *N*-phenylmaleimide were reacted in $CDCl_3$ under homogeneous conditions, at the early stage of the reaction, both *exo*- and *endo*-adducts formed equally, but the *endo*-adduct gradually decreased, and the ratio of *exo* to *endo* reached 8:1. When the reaction was performed on a preparative scale and concentration, the crystalline *exo*-adduct precipitated and was removed from the reaction system. Finally, the products converged to the *exo*-adduct, which was isolated in 90% yield accompanied by a trace amount of the *endo*-adduct.

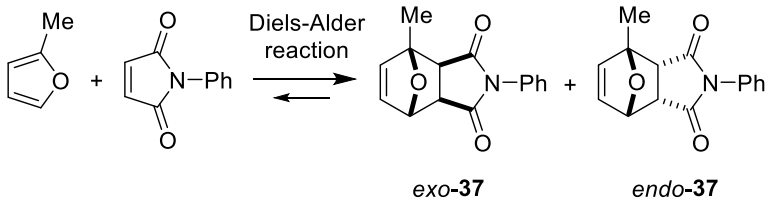

Fig. 21.15 Diels–Alder reaction of *N*-phenylmaleimide and 2-methylfuran

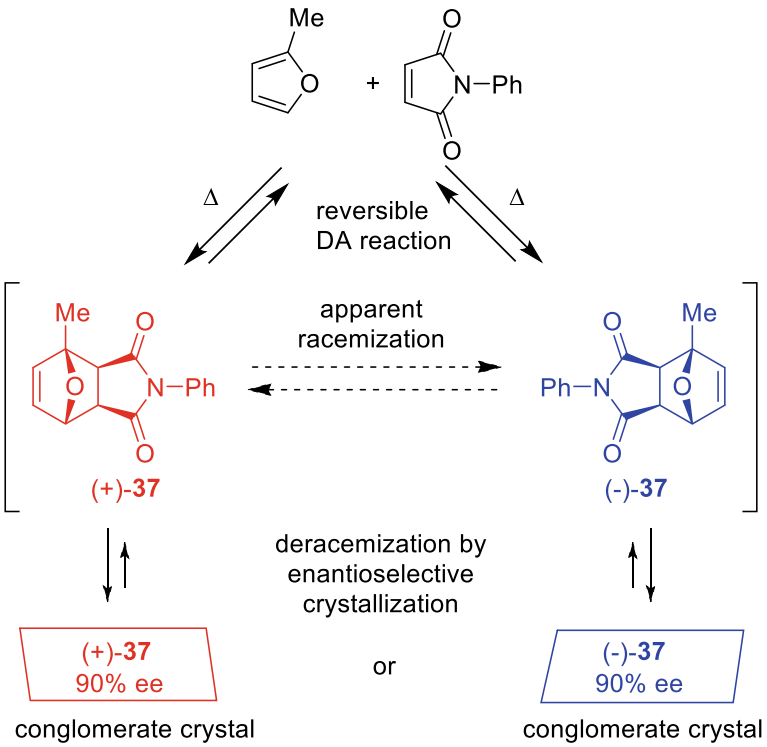

Fig. 21.16 Absolute asymmetric synthesis by Diels–Alder reaction involving dynamic enantioselective crystallization

Another important requirement to apply this asymmetric DA reaction using dynamic stereoselective crystallization is the rate of the reverse reaction under the same conditions. The reverse reaction without catalyst was quite slow, however, it was found that trifluoroacetic acid (TFA) accelerated not only the reversible DA reaction and but also the DA reaction without side reactions.

Next, we examined the asymmetric DA reaction involving dynamic enantioselective crystallization. When a heptane solution of *N*-phenylmaleimide, 2-methylfuran (15.0 eq), and TFA (0–1.0 eq) was stirred in the presence of glass beads at 80 °C in a sealed tube, the crystalline *exo*-adduct appeared quickly. The solution was kept in suspension by stirring for several days at the same temperature, and the change in ee value of *exo*-**37** by attrition-enhanced deracemization was monitored by HPLC using a chiral column.

When we stirred achiral *N*-phenylmaleimide and 2-methylfuran without TFA in a heptane solution, the induction period until deracemization started was several days. Deracemization began gradually after 15 days, but once initiated, the ee value sharply increased up to 90% ee as shown in Fig. 21.17, line 1. The attrition of crystals using glass beads was quite effective for deracemization, since deracemization was not

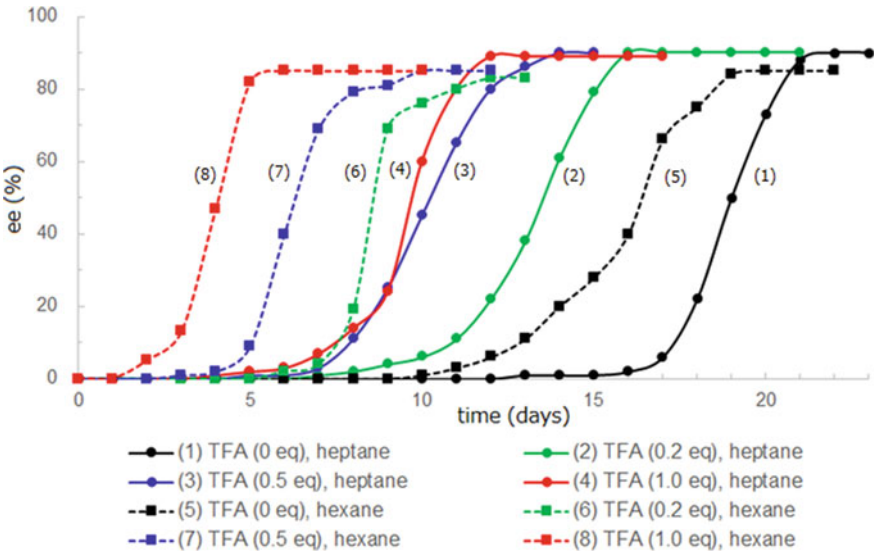

Fig. 21.17 Asymmetric Diels–Alder reaction followed by attrition-enhanced deracemization using glass beads applied to achiral *N*-phenylmaleimide (100 mg, 0.578 mmol) and 2-methylfuran (710 mg, 8.67 mmol) in hexane or heptane (1.00 mL) at 80 °C with or without TFA (0–1.0 eq)

observed under suspension without glass beads even after 30 days. Furthermore, the induction period could be reduced by the use of TFA as an acid catalyst (lines 2–4). TFA accelerated not only the DA cycloaddition reaction but also the *retro*-DA reaction without promoting other side reactions. As the amount of TFA increased, there was a tendency toward both a reduction in the induction period and an acceleration in deracemization, with deracemization starting at the fourth day leading to 90% ee after 11 days (line 4).

When using hexane instead of heptane, deracemization proceeded much faster (lines 5–8). Deracemization started after ten days and reached 86% ee after 19 days without TFA (line 5). TFA influenced both the reduction of induction and deracemization periods, affording a 86% ee of *exo*-**37** after only five days by the use of 1.0 eq of TFA (line 8).

However, the maximum ee value of the solid obtained from the reaction in hexane was slightly lower than that in heptane (86% vs. 90%). The solubility of the DA adduct may play an important role in deracemization with its repeated dissolution and crystallization processes. Hexane had a slightly higher solubility for the DA adduct than heptane at 80 °C in a sealed tube, resulting in the shorter deracemization time and lower ee value of the solid.

The first example of asymmetric DA reaction was developed involving stereoselective dynamic crystallization via a reversible process.

The first example of asymmetric DA reaction was developed involving stereoselective dynamic crystallization via a reversible process.

21.4 Conclusion and Future Prospects—The Fascination of Organic Crystals and the Prospect for New Asymmetric Reactions

Asymmetric chemistry using chirality that is naturally expressed by crystallization of organic compounds was introduced from the viewpoint of asymmetric synthesis. More than 160 years have passed since Pasteur separated sodium ammonium tartrate crystals by hand to obtain optically pure compounds, but the attractiveness of such crystals has yet to be exhausted, with new chemistry being developed every day.

Optical resolution of racemates utilizing the properties of conglomerates is important as a simple and inexpensive resolution method. Furthermore, in the case of rapid racemization in the process of crystallization, total resolution by deracemization from a racemate to one enantiomer becomes possible. We introduced examples of incorporating synthetic processes for amino acids, medicines and agrochemicals, and applications to axially asymmetric compounds. Deracemization by dynamic crystallization includes liquid–solid dynamic preferential crystallization, which promotes crystallization from a supersaturated solution, and Viedma ripening by asymmetric amplification in solid–solid form, which is being developed in new reaction systems.

In addition, the asymmetric synthetic process combining a reaction that generates a chiral center from a prochiral substrate with dynamic crystallization is a phenomenon in which chirality is manifested and amplification occurs only by reaction in solution and crystallization. This method is expected to be developed for a variety of reaction systems. However, the above-mentioned methods are only applicable to chiral crystals and conglomerates, and chiral crystallization is the largest bottleneck. Future developments such as technology that can arbitrarily control the crystal structure and chirality, and prediction of crystal structure due to advances in computational chemistry are eagerly anticipated.

References

1. Sheldon, R.A.: Chirotechnology: Industrial Synthesis of Optically Active Compounds. CRC Press, New York (1993)
2. Collins, A.N., Sheldrake, G.N., Crosby, J.: Chirality in Industry: The Commercial Manufacture and Applications of Optically Active Compounds. Wiley, New York (1992)
3. Polenske, D., Lorenz, H., Seidel-Morgenstern, A.: Potential of different techniques of preferential crystallization for enantioseparation of racemic compound forming systems. Chirality **21**, 728–737 (2009)
4. Collet, A.: Separation and purification of enantiomers by crystallisation methods. Enantiomer **4**, 157–172 (1999)
5. Yoshioka, R.: Optical resolution and crystallization-induced asymmetric transformation of amino acids and pharmaceutical intermediates. Top. Curr. Chem. **269**, 83–132 (2007)
6. Sakamoto, M, Mino, T.: Asymmetric reaction using molecular chirality controlled by spontaneous crystallization. In: Y. Mastai (ed) Advances in Crystallization Processes, InTech, pp. 59–80, (2012)

7. Kellogg, R.M., How to Pasteur's tweezers. In: Tamura R, Miyata, M. (eds) Advances in Organic Crystal Chemistry, comprehensive reviews 2015, pp. 421–443. Springer (2015)
8. Sakamoto, M., Mino, T.: Total resolution of racemates by dynamic preferential crystallization. In: Tamura, R. Miyata, M. (eds) Advances in Organic Crystal Chemistry, Comprehensive Reviews 2015, pp. 445–462. Springer (2015)
9. Viedma, C.: Chiral symmetry breaking during crystallization: complete chiral purity induced by nonlinear autocatalysis and recycling. Phys. Rev. Lett. **94**, 065504 (2005)
10. Jacques, J., Collet, A., Wilen, S.H.: Enantiomers Racemates and Resolutions. Krieger Publishing, Malabar, FL (1994)
11. Schmidt, G.M.J.: Photodimerization in the solid state. Pure Appl. Chem. **27**, 647–678 (1971)
12. Green, B.S., Lahav, M., Rabinovich, D.: Asymmetric synthesis via reactions in chiral crystals. Acc. Chem. Res. **12**, 191–197 (1979)
13. Sakamoto, M.: Absolute asymmetric synthesis from achiral molecules in the chiral crystalline environment. Chem. Eur. J. **3**, 684–689 (1997)
14. https://www.ccdc.cam.ac.uk/
15. Ramamurthy, V., Venkatesan, K.: Photochemical reactions of organic crystals. Chem. Rev. **87**, 433–481 (1987)
16. Scheffer, J.R., Garcia-Garibay, M., Nalamasu, O.: The influence of the molecular crystalline environment on organic photorearrangemens, In: A. Padwa (ed) Organic Photochemistry, pp. 249–347. **8**, Marcel Dekker, New York (1987)
17. Vaida, M., Popovitz-Biro, R., Leiserowitz, L., Lahav, M.: Probing reaction pathways via asymmetric transformations in chiral and centrosymmetric crystals. In: Ramamurthy, V. (ed) Photochemistry in Organized and Constrained Media, pp. 247–302. Wiley, New York (1991)
18. M. Sakamoto, Absolute Asymmetric Photochemistry Using Spontaneous Chiral Crystallization. Chiral Photochemistry, V. Ramamurthy (Ed) Marcel Dekker New York: 415–446 (2004)
19. Sakamoto, M.: Spontaneous chiral crystallization of achiral materials and absolute asymmetric photochemical transformation using the chiral crystalline environment. J. Photochem. Photobiol. C: Photochem. Rev. **7**, 183–196 (2006)
20. Sakamoto, M., Mino, T., Fujita, T.: Generation and control of chirality by crystallization: asymmetric synthesis using the crystal chirality in fluid media. Yuki Gosei Kagaku Kyokaishi **68**, 1047–1056 (2010)
21. Pasteur, L.: Recherches sur les relations qui peuvent exister entre la forme crystalline et la composition chimique, et le sens de la polarisation rotatoire. Ann. Chim. Phys. **24**, 442–459 (1848)
22. Saigo, K.: Optical resolution and amplification of artificial chiral compounds. Yuki Gosei Kagaku Kyokaishi **43**, 1144–1154 (1985)
23. Havinga, E.: Spontaneous formation of optically active substances. Biochem. Biophys. Acta. **13**, 171–174 (1954)
24. Kondepudi, D.K., Kaufman, R.J., Singh, N.: Chiral symmetry breaking in sodium chlorate crystallization. Science **250**, 975–976 (1990)
25. Ostwald, W.: Studies on the formation and inversion of solids. First paper: supersaturation and supercooling. Z. Phys. Chem. Stoechiom. Verwandtschaftsl **22**, 289–330 (1897)
26. Viedma, C., Ortiz, J.E., de Torres, T., Izumi, T., Blackmond, D.G.: Evolution of solid phase homochirality for a proteinogenic amino acid. J. Am. Chem. Soc. **130**, 15274–15275 (2008)
27. Coquerel, G.: Crystallization of molecular systems from solution: phase diagrams, supersaturation and other basic concepts. Chem. Soc. Rev. **43**, 2286–2300 (2014)
28. Coquerel, G.: Chiral discrimination in the solid state: application to resolution and deracemization. In: Tamura, R., Miyata, M. (eds) Advances in Organic Crystal Chemistry, Comprehensive Reviews 2015, pp. 393–420, Springer (2015)
29. Hongo, C., Yamada, S., Chibata, I.: Asymmetric transformation of N-acetyl-DL-leucine. Bull. Chem. Soc. Jpn **54**, 3291–3295 (1981)
30. Yamada, S., Hongo, C., Yoshioka, R., Chibata, I.: Method for the racemization of optically active amino acids. J. Org. Chem. **48**, 843–846 (1983)

31. Boyle Jr., W.J., Sifniades, S., Van Peppen, J.F.: Asymmetric transformation of α-amino-ε-caprolactam, a lysine precursor. J. Org. Chem. **44**, 4841–4847 (1979)
32. Noorduin, W.L., Bode, A.A.C., van der Meijden, M., Meekes, H., van Etteger, A.F., van Enckevort, W.J.P., Christianen, P.C.M., Kaptein, B., Kellogg, R.M., Rasing, T., Vlieg, E.: Complete chiral symmetry breaking of an amino acid derivative directed by circularly polarized light. Nat. Chem. **1**, 729–732 (2009)
33. Noorduin, W.L., Izumi, T., Millemaggi, A., Leeman, M., Meekes, H., van Enckevort, W.J.P., Kellogg, R.M., Kaptein, B., Vlieg, E., Blackmond, D.G.: Emergence of a single solid chiral state from a nearly racemic amino acid derivative. J. Am. Chem. Soc. **130**, 1158–1159 (2008)
34. Leeman, M., Noorduin, W.L., Millemaggi, A., Vlieg, E., Meekes, H., van Enckevort, W.J.P., Kaptein, B., Kellogg, R.M.: Efficient Havinga-Kondepudi resolution of conglomerate amino acid derivatives by slow cooling and abrasive grinding. Cryst. Eng. Comm. **12**, 2051–2053 (2010)
35. Obara, Y., Matsumoto, H., Arai, K., Tsuchiya, S.: Optical resolution of N-(substituted phenylmethylidene)phenylalanine methyl esters. Jpn. Kokai Tokkyo Koho, 1986, JP6100165 (1986)
36. Hein, J.E., Huynh, C.B., Viedma, C., Kellogg, R.M., Blackmond, D.G.: Pasteur's tweezers revisited: on the mechanism of attrition-enhanced deracemization and resolution of chiral conglomerate solids. J. Am. Chem. Soc. **134**, 12629–12636 (2012)
37. Tsogoeva, S.B., Wei, S., Freund, M., Mauksch, M.: Generation of highly enantioenriched crystalline products in reversible asymmetric reactions with racemic or achiral catalysts. Angew. Chem. Int. Ed. **48**, 590–594 (2009)
38. Spix, L., Meekes, H., Blaauw, R.H., van Enckevort, W.J.P., Vlieg, E.E.: Complete deracemization of proteinogenic glutamic acid using Viedma ripening on a metastable conglomerate. Cryst. Growth Des. **12**, 5796–5799 (2012)
39. Lopez, F.J., Ferrino, S.A., Reyes, M.S., Roman, R.: Asymmetric transformation of the second kind of racemic naproxen. Tetrahedron. Asymm. **8**, 2497–2500 (1977)
40. Noorduin, W.L., Kaptein, B., Meekes, H., van Enckevort, W.J.P., Kellogg, R.M., Vlieg, E.: Fast attrition-enhanced deracemization of naproxen by a gradual in situ feed. Angew. Chem. Int. Ed. **48**, 4581–4583 (2009)
41. Hachiya, S., Kasashima, Y., Yagishita, F., Mino, T., Masu, H., Sakamoto, M.: Asymmetric transformation by dynamic crystallization of achiral succinimides. Chem. Commun. **49**, 4776–4778 (2013)
42. Engwerda, A.H.J., Mertens, J.C.J., Tinnemans, P., Meekes, H., Rutjes, F.P.J.T., Vlieg, E.: Solid-phase conversion of four stereoisomers into a single enantiomer. Angew. Chem. Int. Ed. **57**, 15441–15444 (2018)
43. Yagishita, F., Ishikawa, H., Onuki, T., Hachiya, S., Mino, T., Sakamoto, M.: Total spontaneous resolution by deracemization of isoindolinones. Angew. Chem. Int. Ed. **51**, 13023–13025 (2012)
44. Sakamoto, M., Shiratsuki, K., Uemura, N., Ishikawa, H., Yoshida, Y., Kasashima, Y., Mino, T.: Asymmetric synthesis by using natural sunlight under absolute achiral conditions. Chem. Eur. J. **23**, 1717–1721 (2017)
45. Ishikawa, H., Uemura, N., Saito, R., Yoshida, Y., Mino, T., Kasashima, Y., Sakamoto, M.: Chiral symmetry breaking of spiropyrans and spirooxazines by dynamic enantioselective crystallization. Chem. Eur. J. **25**, 9758–9763 (2019)
46. Engwerda, A.H.J., Koning, N., Tinnemans, P., Meekes, H., Bickelhaupt, F.M., Rutjes, F.P.J.T., Vlieg, E.: Deracemization of a racemic allylic sulfoxide using Viedma ripening. Cryst. Growth Des. **17**, 4454–4457 (2017)
47. Pincock, R.E., Perkins, R.R., Ma, A.S., Wilson, K.R.: Probability distribution of enantiomorphous forms in spontaneous generation of optically active substances. Science **174**, 1018–1020 (1971)
48. Kondepudi, D.K., Laudadio, J., Asakura, K.: Chiral symmetry breaking in stirred crystallization of 1,1′-binaphthyl melt. J. Am. Chem. Soc. **121**, 1448–1451 (1999)

49. Sakamoto, M., Utsumi, N., Ando, M., Saeki, M., Mino, T., Fujita, T., Katoh, A., Nishio, T., Kashima, C.: Breaking the symmetry of axially chiral N-Aryl-2(1H)-pyrimidinones by spontaneous crystallization. Angew. Chem. Int. Ed. **42**, 4360–4363 (2003)
50. Sakamoto, M., Unosawa, A., Kobaru, S., Fujita, K., Mino, T., Fujita, T.: An asymmetric SNAr reaction using the molecular chirality in a crystal. Chem. Commun. **34**, 3586–3588 (2007)
51. Engwerda, A.H.J., van Schayik, P., Jagtenberg, H., Meekes, H., Rutjes, F.P.J.T., Vlieg, E.: Solid phase deracemization of an atropisomer. Cryst. Growth Des. **17**, 5583–5585 (2017)
52. Yagishita, F., Okamoto, K., Kamataki, N., Kanno, S., Mino, T., Kasashima, Y., Sakamoto, M.: Chiral symmetry breaking of axially chiral nicotinamide by crystallization from the melt. Chem. Lett. **42**, 1508–1511 (2013)
53. Sakamoto, M., Unosawa, A., Kobaru, S., Saito, A., Kasashima, Y., Mino, T., Fujita, T.: Asymmetric photocycloaddition in solution of a chiral crystallized naphthamide. Angew. Chem. Int. Ed. **44**, 5523–5526 (2005)
54. Sakamoto, M., Kato, M., Aida, Y., Fujita, K., Mino, T., Fujita, T.: Photosensitized 2 + 2 cycloaddition reaction using homochirality generated by spontaneous crystallization. J. Am. Chem. Soc. **130**, 1132 (2008)
55. Yagishita, F., Mino, T., Fujita, T., Sakamoto, M.: Two-step asymmetric reaction using the frozen chirality generated by spontaneous crystallization. Org. Lett. **14**, 2638–2641 (2012)
56. Flock, A.M., Reucher, C.M.M., Bolm, C.: Enantioenrichment by iterative retro-aldol/aldol reaction catalyzed by an achiral or racemic base. Chem. Eur. J. **16**, 3918–3921 (2010)
57. Steendam, R.R.E., Verkade, J.M.M., van Benthem, T.J.B., Meekes, H., van Enckevort, W.J.P., Raap, J., Rutjes, F.P.J.T., Vlieg, E.: Emergence of single-molecular chirality from achiral reactants. Nature Commun. **5**, 5543–5550 (2014)
58. Kaji, Y., Uemura, N., Kasashima, Y., Ishikawa, H., Yoshida, Y., Mino, T., Sakamoto, M.: asymmetric synthesis of an amino acid derivative from achiral aroyl acrylamide by reversible michael addition and preferential crystallization. Chem. Eur. J. **22**, 16429–16432 (2016)
59. Uemura, N., Sano, K., Matsumoto, A., Yoshida, Y., Mino, T., Sakamoto, M.: Asymmetric synthesis of aspartic acid derivative from prochiral maleic acid and pyridine under achiral conditions. Chem. Asian J. **14**, 4150–4153 (2019)
60. Miyagawa, S., Yoshimura, K., Yamazaki, Y., Takamatsu, N., Kuraishi, T., Tetsuya, A., Tokunaga, S., Yuji, K., Kawasaki, T.: Asymmetric strecker reaction arising from the molecular orientation of an achiral imine at the single-crystal face: enantioenriched l- and d-amino acids. Angew. Chem. Int. Ed. **56**, 1055–1058 (2017)
61. Kawasaki, T., Takamatsu, N., Aiba, S., Tokunaga, Y.: Spontaneous formation and amplification of an enantioenriched α-amino nitrile: a chiral precursor for Strecker amino acid synthesis. Chem. Commun. **51**, 14377–14380 (2015)
62. Baglai, I., Leeman, M., Wurst, K., Kaptein, B., Kellogg, R.M., Noorduin, W.L.: The strecker reaction coupled to Viedma ripening: a simple route to highly hindered enantiomerically pure amino acids. Chem. Commun. **54**, 10832–10834 (2018)
63. Ishikawa, H., Uemura, N., Yagishita, F., Baba, N., Yoshida, Y., Mino, T., Kasashima, Y., Sakamoto, M.: Asymmetric synthesis involving reversible photodimerization of a prochiral flavonoid followed by crystallization. Eur. J. Org. Chem. **2017**, 6878–6881 (2017)
64. Uemura, N., Toyoda, S., Ishikawa, H., Yoshida, Y., Mino, T., Kasashima, Y., Sakamoto, M.: Asymmetric Diels–Alder reaction involving dynamic enantioselective crystallization. J. Org. Chem. **83**, 9300–9304 (2018)

Chapter 22
Molecular Recognition by Inclusion Crystals of Chiral Host Molecules Having Trityl and Related Bulky Groups

Motohiro Akazome and Shoji Matsumoto

Abstract Molecular recognition by inclusion phenomena is a useful application of organic crystals. So, in this research, first, we discuss how several recent examples of inclusion crystal methods have been overviewed in the optical resolution field. Then, we focus on the installation of trityl and related bulky groups, which enable compounds possible to settle guest molecules to form inclusion crystals. Some hosts of amines and amino-acid derivatives having trityl or 9-phenyl-9-xanthenyl groups include several neutral guests to construct inclusion crystals and achieve structural isomer separation and optical resolution. Finally, we report how salts between *N*-trityltyrosine and *tert*-butylamine include 1-(1-naphtyl)ethanol with high enantioselectivity of 96% ee (*R*). Through this review, we recognize trityl and related bulky groups as crystal engineering tools that conduct inclusion ability to host candidates. Single-crystal X-ray analyses of these inclusion crystals show us that inclusion with low enantioselectivity is often due to the statistically disordered structure of guests. The method of suppressing this statistic disorder to reach high enantioselective inclusion remains unknown.

Keywords Molecular recognition · Inclusion crystals · Amino acid · Trityl group

22.1 Introduction

In the comprehensive reviews of our previous book (2015), we dealt with chiral recognition with inclusion crystals of amino-acid derivatives having trityl groups [1]. We will expand on the former review by summarizing the five-year progress of molecular recognition with inclusion crystals of chiral substance-based host molecules with bulky groups.

M. Akazome (✉) · S. Matsumoto
Department of Applied Chemistry and Biotechnology, Graduate School of Engineering, Chiba University, 1-33 Yayoi-cho, Inage-ku, Chiba 263-8522, Japan
e-mail: akazome@faculty.chiba-u.jp

M. Sakamoto and H. Uekusa (eds.), *Advances in Organic Crystal Chemistry*,
https://doi.org/10.1007/978-981-15-5085-0_22

Many approaches to performing optical resolution of racemic compounds have been developed [2]. Three major optical resolution methods are listed with brief accounts of their procedures in Fig. 22.1.

Generally, acidic or basic compounds are easily separated because basic or acidic optical resolution reagents are applicable to the diastereomeric salt method (Fig. 22.1a) [3, 4]. However, racemic neutral compounds do not form salts, so diastereomeric salt methods are not applicable. The covalent diastereomer method is considered a reliable optical resolution method for neutral compounds such as alcohols and ketones (Fig. 22.1b). Racemic neutral compounds are transformed to the diastereomers by covalent bonding formation with chiral auxiliaries. After the diastereomers are separated by column chromatography or fractional crystallization, they are decomposed to recover an enantiomer of original compounds.

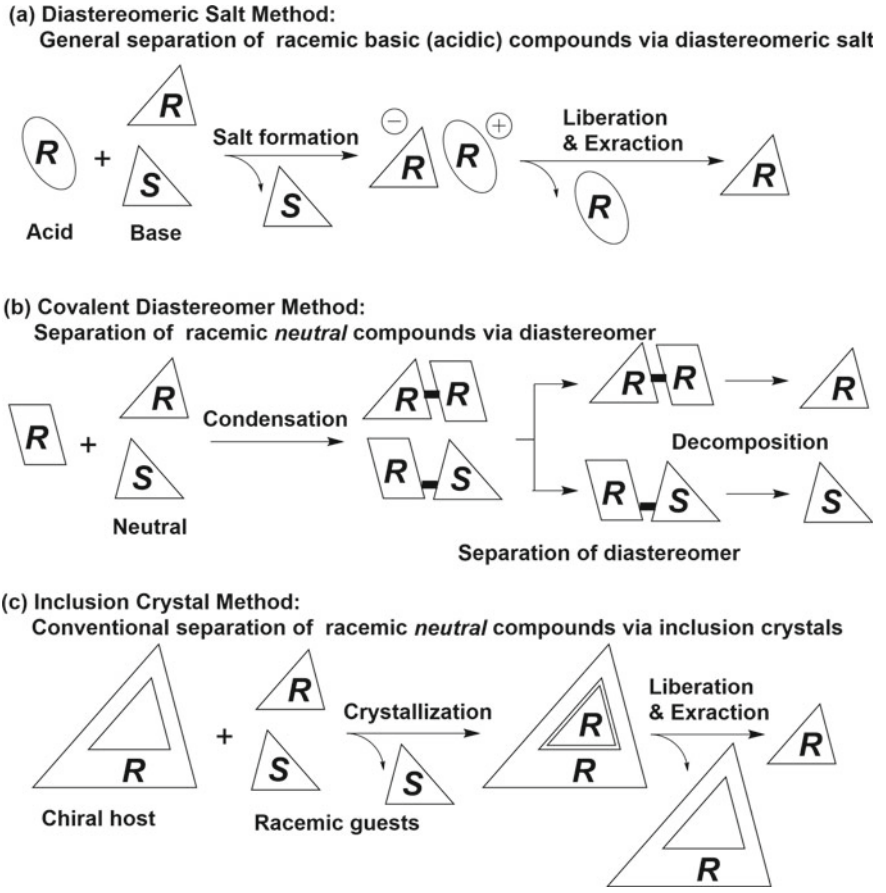

Fig. 22.1 Some optical resolution methods. **a** Diastereomeric salt method. **b** Covalent diastereomer method. **c** Inclusion crystal method

Choosing reversible and convenient covalent bonding formation in the functional groups of amides, sulfoxides, nitrile, and so on is more difficult than with alcohols and ketones. The inclusion crystal method must conveniently separate one enantiomer from racemic compounds for all of these neutral compounds, including alcohols and ketones (Fig. 22.1c) [5–7]. Because inclusion crystals are obtained by co-crystallization without a covalent bonding formation between hosts and guests, the recovery of optically separated guests—in which guests are released by dissolution or heating of inclusion crystals—is quite easy.

However, inclusion crystals consist of weaker intermolecular interactions such as hydrogen bonds and van der Waals interactions instead of ion pairs and covalent bonds. Therefore, the molecular design of the host is an important consideration in the construction of inclusion crystals with guest molecules.

22.2 Recent Examples of Molecular Recognition by Inclusion Crystals

22.2.1 Chiral Recognition by Inclusion Crystals

In 1983, Toda reported on optical resolution by the inclusion crystal method using a chiral 1,6-bis(2-chlorophenyl)-1,6-diphenylhexa-2,4-diyne-1,6-diol, which is classified as a wheel-and-axle type (Fig. 22.2a) [8]. This chiral diol host included 3-methylcyclohexanone and 3-methylcyclopentanone enantioselectively.

More recently, Nassibeni and Weber reported on a borneol dumb-bell host with methylcyclohexanones and 2-butanols (Fig. 22.2b) [9]. Achiral 4-methylcyclohexanones formed 1:2 (host/guest) inclusion crystals. With other methylcyclohexanones, 1:1 inclusion crystals were obtained and 2- and 3-methylcyclohexanones were included in 72% ee (*S*) and 57% ee (*S*) with statistic disorder of these guest molecules.

Barton and Caira's group reported on the inclusion of TETROL with cyclohexanone and 2-, 3-, and 4-methylcyclohexanone (abbreviation: **Cy**, **2-MeCy**, **3-MeCy**, and **4-MeCy**) that form 1:1 complexes (Fig. 22.2c) [10]. Notably, the **2-** and **3-MeCy**s were included in the axial conformation of their methyl groups. But the methyl group of the included **4-MeCy** took the more favorable equatorial conformation. Enantiomeric excesses of **2- and 3-MeCy**s in the inclusion crystals are 13% and 20% ee for (*R*)-enantiomer, respectively. The reason for this low selectivity is confirmed by the single-crystal X-ray analysis that showed both (*R*)- and (*S*)-enantiomers were observed as a statistically disordered structure in the same void space. In addition, Barton found interesting inclusion phenomena of these cyclohexanones concerning TETROL in the competition experiments [11]. Crystallization of TETROL in the presence of an equimolar mixture of **2-**, **3-**, and **4-MeCy** gave inclusion crystals with a mixture of three guests, where the ratios were 79: 14: 7, respectively. The host's selectivity might be described as **2-MeCy** > > **3- MeCy** > **4-MeCy**. Conversely,

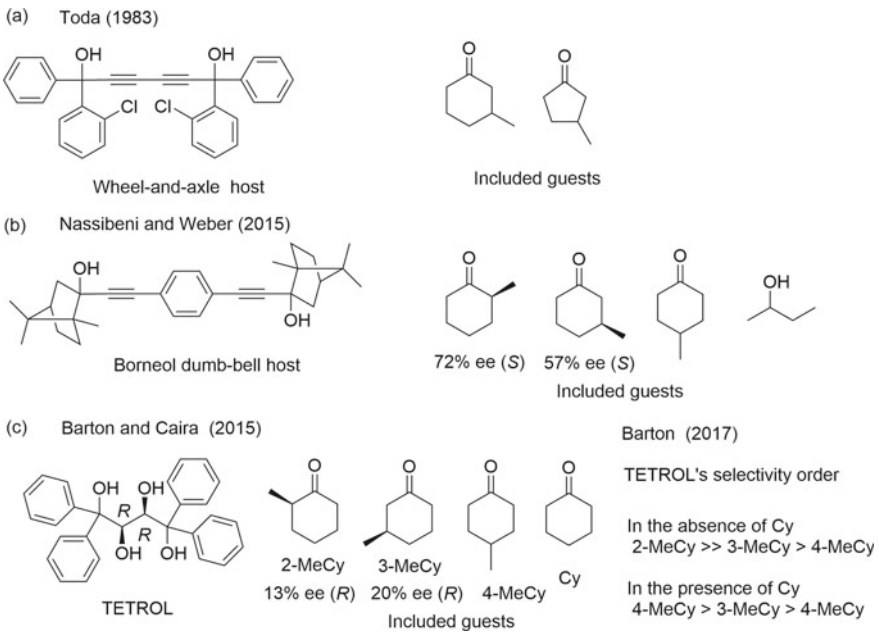

Fig. 22.2 Structure of hosts and guest molecules in inclusion crystals

TETROL in the presence of the equimolar mixture of **Cy** and **2-**, **3-**, and **4-MeCy** crystallized with a mixture of four guests, at the ratios of 52: 5: 13: 30, respectively. The host's selectivity might be described as **Cy** > **4-MeCy** > **3-MeCy** > **2-MeCy**. The selectivity order of TETROL for the three isomeric **MeCy**s was reversed whether **Cy** was present or not. Here, **Cy** was overwhelmingly favored over any of **MeCy**s from the results of equimolar binary or ternary competition including **Cy**. Interestingly, the coexistence of **Cy** altered the host behavior of the inclusion crystals.

This TETROL host is related to TADDOL, which Toda [12] and Seebach [13] studied in the early stages of inclusion crystal development. TADDOL is also a famous diol host that can include ketones enantioselectively.

Generally, optical resolution can reliably obtain one enantiomer from a racemic compound. However, half of the undesirable opposite enantiomers remained after optical resolution. When the guests are racemizable in the crystallization process, the thermodynamic controlled crystallization yields a more stable compound with enantioselectivity, which is called "crystallization-induced dynamic resolution" (CIDR).

As shown in the useful application of inclusion crystals in Fig. 22.3, Kaku and Tsunoda's group have been developing this CIDR of racemic ketones using a TADDOL-type host since 1997. Recently, deracemization of α-monosubstituted cyclopentanones as new substrates was achieved [14]. This CIDR transformed racemic α-alkylcyclopentanone into the *R*-form (97% ee) in an 89% yield.

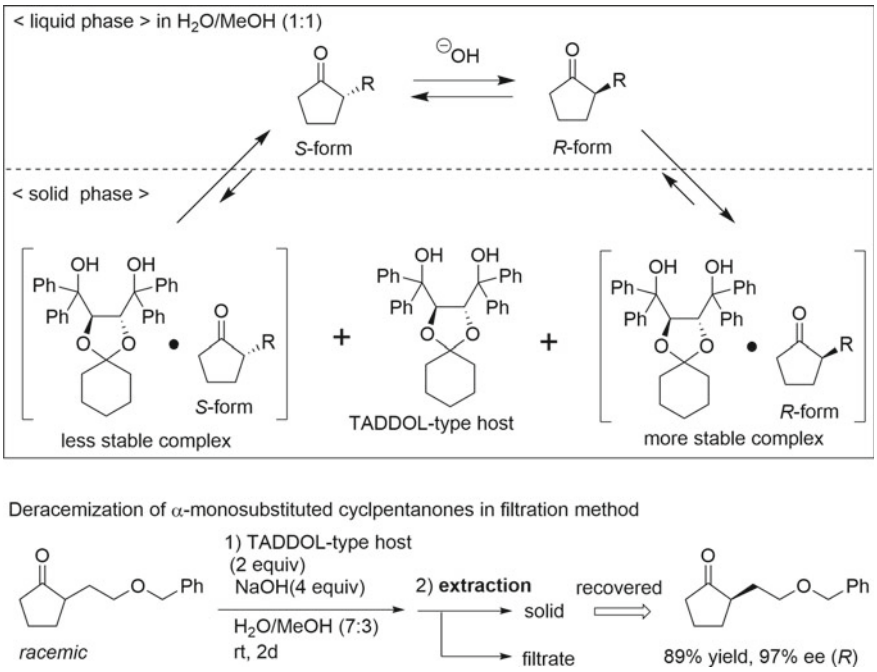

Fig. 22.3 Crystallization-induced dynamic resolution of racemic ketones using TADDOL-type host

22.2.2 Chiral Recognition by Inclusion Crystals of Amino-Acid Derivatives

Here, we discuss three works [15–17] on molecular recognition by chiral amino-acid derivatives to review the progress of inclusion crystals over the past five years. Kodama's two papers addressed intriguing crystalline hosts that have binary structures to combine the organic salt of amino-acid derivatives with urea [15] and hydrazide [16] functional moieties. Hu's paper reported that a chiral cyclic peptide derived from (*S*)-proline included both enantiomers of BINOL to form a 1:1 complex of (3*S*,6*S*)-dipeptide and *rac*-BINOL [17]. When this phenomenon was applied to non-racemic BINOL as the guest, inclusion crystals were deposited to include perfectly racemic BINOL; however, enantiomeric enrichment of BINOL in the solution occurred to obtain optically pure BINOL from the filtrate.

In 2016, Kodama reported that salt of urea-modified phenylalanine and an achiral amine included alkyl aryl sulfoxides with high enantioselectivity (Fig. 22.4) [15]. The binary structure built up with the salt of ammonium carboxylate and urea functional moiety makes the host design unique. In this case, combining urea-modified phenylalanine and diphenylmethylamine formed 1:1 (host/guest) inclusion crystals with methyl phenyl sulfoxide in 89% ee (*R*). Single-crystal X-ray analyses were performed

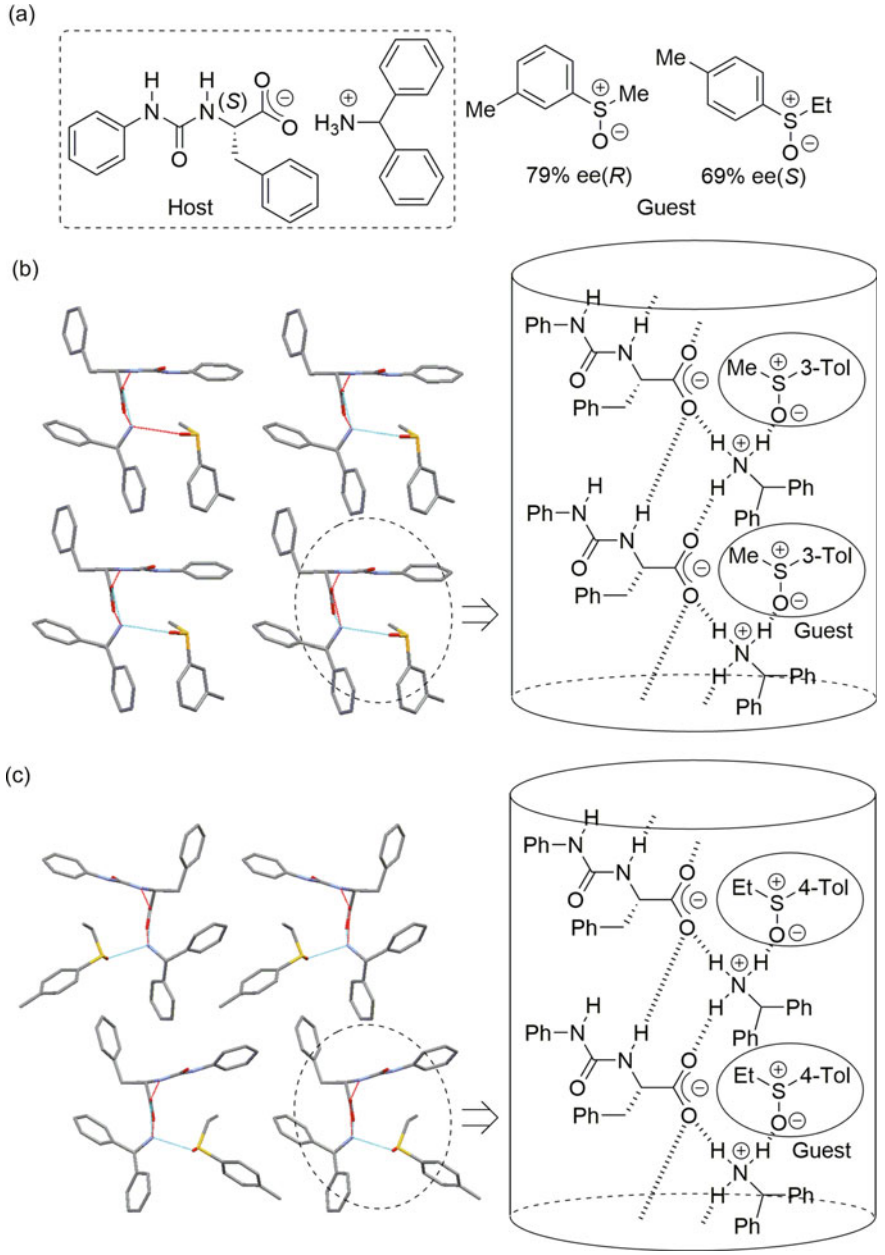

Fig. 22.4 Kodama's urea-modified phenylalanine salt host. **a** Host and guest structures. **b** Methyl 3-tolyl sulfoxide-included crystals (CCDC-1478529: space group $P1$). **c** Ethyl 4-tolyl sulfoxide-included crystals (CCDC-1478530: $P2_1$)

on two other inclusion crystals with methyl 3-tolyl sulfoxide (space group $P1$) and ethyl 4-tolyl sulfoxide ($P2_1$) (Fig. 22.4b and c). Both crystal structures had a similar one-dimensional hydrogen bonding network, and the network made a column structure from the host–guest complex. The two crystal structures differed in the direction these columns were assembled, space group $P1$ arranges them in a parallel direction, $P2_1$ arranges them in an antiparallel direction.

The hydrogen bond of phenyl-urea moiety with an oxygen atom of the carboxylate made a rigid L-shaped conformation of the host, which is essential to creating the asymmetric cavity for one preferable enantiomer of sulfoxides.

When triphenylmethylamine used an amine part instead of diphenylmethylamine, the urea-modified phenylalanine salt crystallized without guest molecules. The amine part was also necessary to form inclusion crystals.

More recently, Kodama reported on enantioseparation of sulfoxides and nitriles by inclusion crystallization with chiral organic salts based on phenylalanine [16]. The host also has a binary structure composed of a hydrazide functional moiety and a salt between a 4-hydroxybenzoic acid and chiral amine part of a phenylalanine derivative (Fig. 22.5a).

The salt forms a one-dimensional columnar structure with a 2_1-helical hydrogen bonding network (Fig. 22.5b). In inclusion crystals, (*S*)-form (98% ee) of ethyl phenyl sulfoxide was captured by hydrogen bonding with the phenolic hydroxy group of the host and settling in the inclusion cavity formed between these host columns. The phenyl hydrazide moiety needs to bind with an oxygen atom of carboxylate and become an inclusion cavity wall to recognize guest shapes.

Similarly, several nitriles with high enantioselectivity up to 92% ee (*S*) were also included in this host.

Many recent asymmetric syntheses in organic chemistry achieved high enantioselectivity. However, insufficient results give non-racemic compounds and might require additional optical resolution. Such non-racemic mixtures of enantiomers are base materials for optical resolution. Fogassy considers the enrichment of non-racemic mixtures of enantiomers an important part of the resolution processes [18].

Hu reported that (3*S*,6*S*)-dipeptide derived from (*S*)-proline includes both enantiomers of BINOL to form a 1:1 complex of (3*S*,6*S*)-dipeptide and *rac*-BINOL (Fig. 22.6) [17]. As the result, the enantiomer excess of the BINOL guest in inclusion crystals is zero, making it impossible to separate racemic BINOL. However, this inclusion phenomenon of racemic compounds can still use the method of enantiomeric enrichment in solutions. This is a unique example of optical resolution for non-racemic compounds. The *rac*-BINOL was deposited as a 1:1 complex, and enantiopure (*R*)- or (*S*)-BINOL was obtained from the filtrate. When 10% ee and 80% ee of (*R*)-BINOL were applied for enantiomeric enrichment, yields of 90% and 96% were obtained, respectively, based on the amount of enantiomeric pure BINOL (> 99% ee).

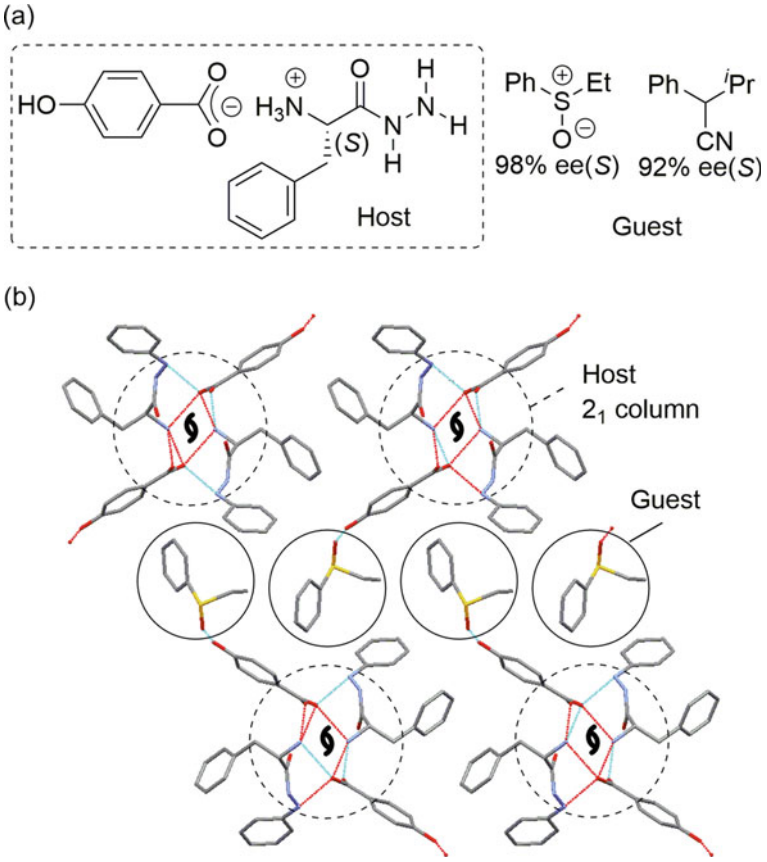

Fig. 22.5 Kodama's host design of amino-acid-based salt having a hydrazide functional moiety. **a** Host and guest structures. **b** Crystal structure of (*S*)-ethyl phenyl sulfoxide-included crystals (CCDC-1577954)

22.3 Installation of Trityl and Related Groups to Construct Inclusion Crystals

22.3.1 Trityl and Related Groups as Crystal Engineering Tools to Construct Inclusion Crystals

Trityl groups and related bulky aryl groups are recognized as functional tools for supramolecular chemistry including crystal engineering. In 2016, Sauvage [19] Stoddart [20], and Feringa [21] were awarded the Nobel Prize in Chemistry. They developed molecules with controllable movements like a tiny lift, artificial muscles, and minuscule motors.

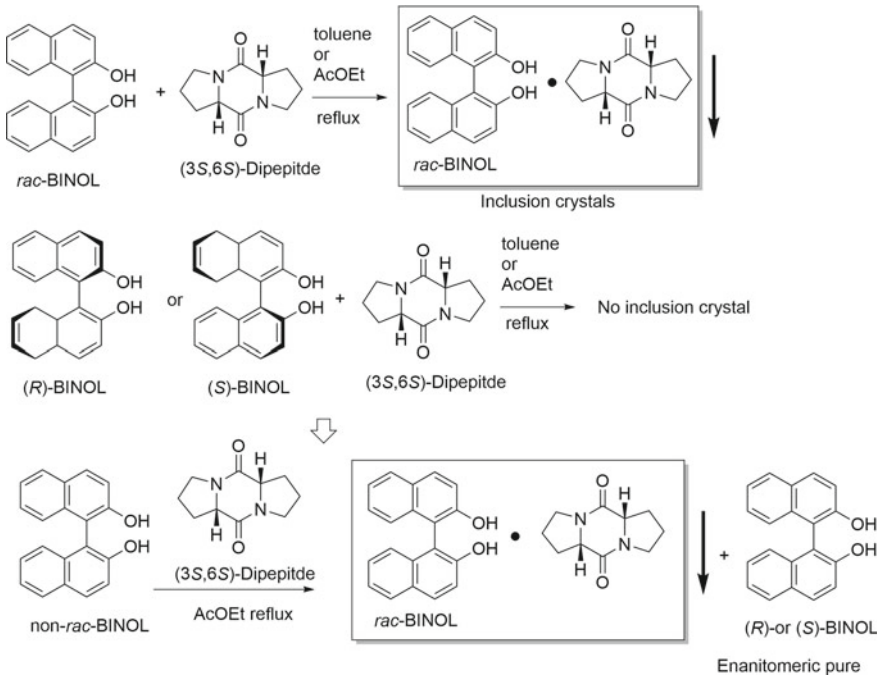

Fig. 22.6 Enantiomeric enrichment of non-racemic BINOL by heterocomplexation of (3*S*,6*S*)-dipeptide in a solution

They used bulky groups (such as a trityl group) as a molecular gear for the design and production of molecular machines regardless of solid or solution states, the stopper of rotaxane, etc. In this area, symmetrically beautiful triphenylmethyl or triptycene groups can fascinate us as molecular gears in intelligent molecular machines. In the early stage of molecular machines, Mislow studied these groups as propeller and dynamic molecular gear (Fig. 22.7) [22, 23].

In organic synthesis, the simple trityl group is a well-known protective group of amino groups [24]. Although the trityl group is readily introduced in the nitrogen atom of the amino group via trityl cation intermediate under acidic conditions, the trityl groups are to be kept stable under basic conditions but are easily removed under acidic conditions. We also have to remember that the amino group loses a hydrogen atom—which can potentially capture a guest using hydrogen bonds—instead of obtaining a trityl group. However, this is not always negative because the installed bulky trityl group often improves the inclusion ability of hosts by suppressing their inherent hydrogen bonding properties.

In the rest of this section, we summarize recent examples of molecular design for constructing inclusion crystals with neutral guests using trityl and related bulky groups as useful crystal engineering tools. Akazome used the suppression effect of a trityl group on the amide hydrogen bond in the related inclusion crystals of *N*,

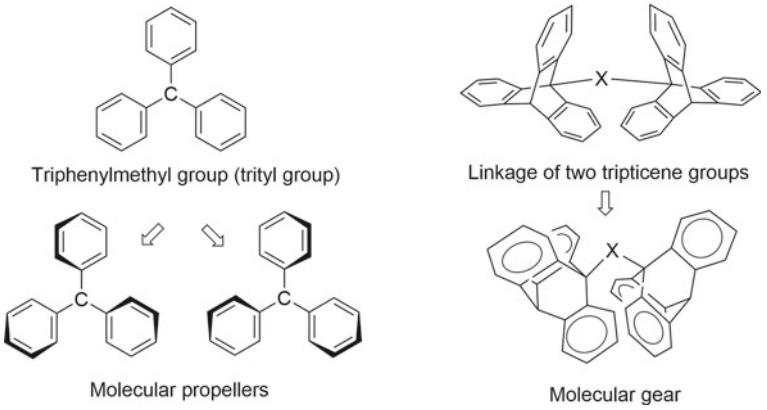

Fig. 22.7 Molecular propeller and gear consisting of trityl group and linkage of two triptycene groups

N'-ditritylamino-amide [1, 25]. Figure 22.8 illustrates our host design based on the compensation of hydrogen bonds broken by trityl groups. *N*-Methylacetamide has hydrogen bond donor (H–N) and acceptor (CO) groups that form a one-dimensional hydrogen bonding network, and the hydrogen bonds between them will be broken by installed bulky trityl groups. At the same time, the trityl groups make cavities in which guest molecules are captured. When a guest suitably compensates the loss of the inherent hydrogen bonds, the hydrogen bonds from host–guest interactions will form inclusion crystals.

Rychlewska found that bis(triphenylacetamides) of chiral 1,2-diamines construct inclusion crystals for suppression of amide NH$\cdots$O=C hydrogen bonds (Fig. 22.9) [26]. This host included CH_2Cl_2, H_2O, $CHCl_3$, and Me_2CO to form 1:1 (host/guest) inclusion crystals. In the 1:2 (host/guest) inclusion crystals of dimethyl sulfoxide, hydrogen bonding only occurs between the host and the guest molecules (Fig. 22.9b).

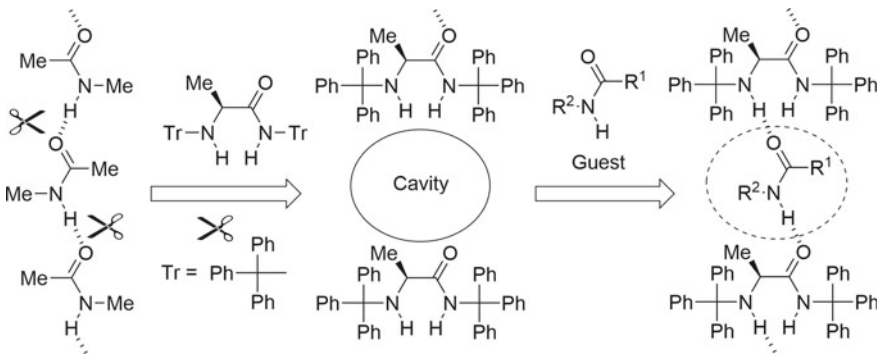

Fig. 22.8 Akazome's host designed to capture amide guests to compensate for loss of hydrogen bonds broken by trityl groups

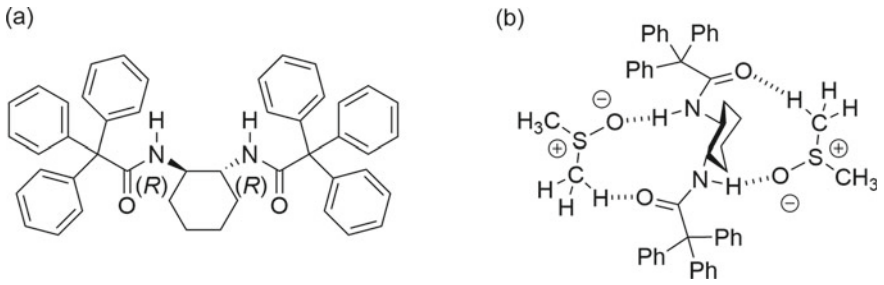

Fig. 22.9 **a** Rychlewska's bis(triphenylacetamides) host of chiral 1,2-diamines. **b** Schematic drawing of host–guest interactions in inclusion crystals with dimethyl sulfoxide guest

This host also included methanol, ethanol, and 2-propanol accompanied with one water molecule. But longer-chain alcohol molecules such as *n*-butanol and *sec*-butanol were not included. Furthermore, inclusion of chiral molecules was unsuccessful. However, further modification of this host molecule might bring enantioselective inclusion.

As another example, inclusion ability was obtained by introducing a trityl group to the structure. A silatrane has a unique structure with an intramolecular Si-N coordination bond. Introduction of the trityl group to the amino group of [1-[(*N*-methyl-*N*-tritylamino)methyl]silatrane brings inclusion ability for this tritylated product (Fig. 22.10) [27]. Inclusion crystals of 1:1 (host/guest) with a benzene molecule were obtained after the recrystallization from a mixture of benzene and heptane. The X-ray diffraction study shows that the geometry of the coordination center of silicon and the existence of an intramolecular Si-N coordination bond are typical for silatranes. The trityl group made a void to include a benzene molecule.

In the organic chemistry, we often need to separate racemic compounds and a mixture of structural isomers. For example, there are mixtures of *o*-, *m*-, and *p*-disubstituted benzenes, of linear and branched alkanes, etc. Even if the host molecules are achiral, they can recognize one structural isomer from a mixture of isomers based on whether the molecular shapes match the void that occurred in the crystal lattice or not.

In 2019, Barton and her coworkers developed a new wheel-and-axle host design of achiral diamines that have two 9-phenyl-9-xanthenyl or (9-phenyl-9-thioxanthenyl) groups with structures similar to a trityl group. The xanthenyl and thioxanthenyl

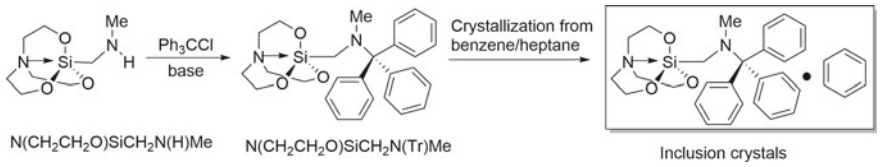

Fig. 22.10 Formation of inclusion crystals by tritylated 1-[(*N*-methyl)methyl]silatrane

groups are conformationally restricted by oxygen and sulfur atoms bridged over two phenyl groups, respectively (Fig. 22. 11).

These hosts formed inclusion crystals to recognize molecular shapes of many guests that have five- or six-membered rings [28–32]. As a few typical and practical examples, we introduce Barton's separation of structural isomers (C8 aromatic fraction of crude oil) briefly using these hosts. From an equimolar quaternary guest mixture (EB, o-Xy, m-Xy, p-Xy), the 1:1 complex of **H1** ($X = S$) included EB, *o*-Xy, *m*-Xy, and *p*-Xy in guest ratios (25.1:2.5:4.1:68.3) and that of **H2** ($X = O$) included them in guest ratios (5.2:1.5:1.3:92.0). This result means that ethylenediamine having two (9-phenyl-9-xanthenyl) groups (**H2**) recognized the shape of the *p*-Xy guest molecules and included it predominately in the cavity formed in their crystal lattice.

A similar trend was also observed in selective inclusion from a mixture of anisoles. From an equimolar quaternary guest mixture (ANI, 2MANI, 3MANI, 4MANI), the 1:1 complex of **H1** ($X = S$) included ANI, 2MANI, 3MANI, and 4MANI in guest ratios (29.0:3.0:21.9:46.1) and that of **H2** ($X = O$) included them in guest ratios (11.3:1.5:4.6:82.6). **H2** included 4MANI predominately, where 4-methylamisole (4MANI) had a structure similar to ethylbenzene (EB). Barton also reports inclusion crystals of cyclohexane-1,4-diamines having two 9-phenyl-9-xanthenyl or (9-phenyl-9-thioxanthenyl) groups [32].

Although these hosts are achiral structures at this stage, 9-phenyl-9-xanthenyl and 9-phenyl-9-thioxanthenyl groups would be good candidates for crystal engineering tools to construct inclusion crystals. The synthetic methods of these xanthenyl groups are as easy as the trityl group's. When these xanthenyl groups are introduced to chiral amines, enantioselective inclusion may occur by the host.

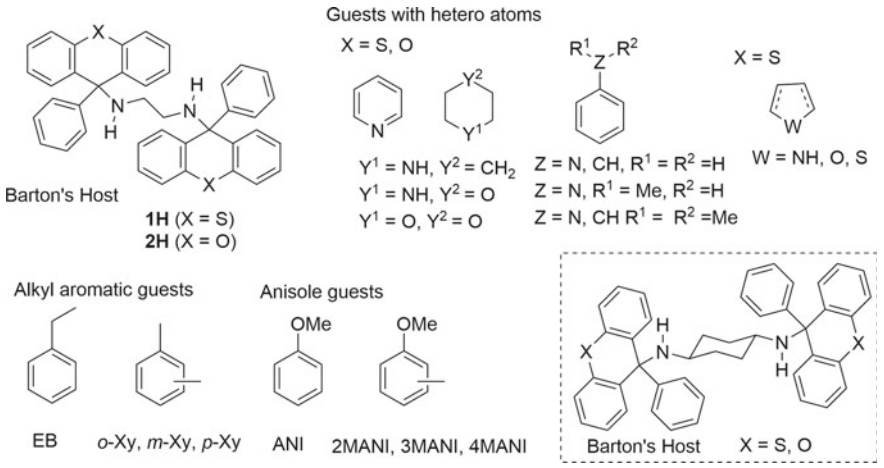

Fig. 22.11 Barton's alkanediamine hosts having 9-phenyl-9-xanthenyl and (9-phenyl-9-thioxanthenyl) groups and examined guests

22.3.2 *Enantioselective Inclusion of Alcohols Into Salts Between* N-*Trityl* (S)-*Tyrosine and Tert-Butylamine [33]*

In 2012, we reported that *N*-tritylamino acid *tert*-butylamine salts enantioselectively included aliphatic alcohol (Fig. 22.12) [34]. Salts between carboxylic acids and primary amines have an inherent one-dimensional hydrogen bonding network. In this work, we utilized trityl groups to break the hydrogen bonds and form inclusion cavities, and alcohols were included to compensate for the loss of hydrogen bonds. In *tert*-butylammonium salts of *N*-tritylphenylalanine, enantioselective inclusion of 1-chloro-2-propanol was observed in 69% ee(*S*). This salt host included only alkanols and benzyl alcohol, but 1-arylethanols such as 1-phenylethanol were not included at all.

Here, we report additional developments of *N*-tritylamino acid *tert*-butylamine salts. In our previous work, the enantioselective inclusion ability of phenylalanine was superior to five other amino acids we examined (Ala, Val, Leu, Ile, Phe, and Phg (an abbreviation for phenylglycine)). Among about twenty naturally occurring amino acids, the structure of tyrosine is close to phenylalanine, whereas the hydroxy group is in the *para*-position of the phenyl group. We theorize whether the hydroxyl group incorporates the hydrogen bonding network and affects their inclusion ability and enantioselectivity (Fig. 22.13).

To evaluate the ability of the host to include secondary alcohols with enantioselectivity, we chose several 1-arylethanols as *racemic* alcohols. The crystalline host (*tert*-butylammonium salts of *N*-trityltyrosine: Tr-Tyr·tBuNH$_2$) and *racemic* 1-arylethanols (4 equiv.) were dissolved in toluene and recrystallized by diffusion of hexane vapor. The Tr-Tyr·tBuNH$_2$ included the corresponding alcohols to yield 1:1 inclusion crystals, which were collected by filtration and confirmed by a ^{1}H NMR spectra. After inclusion crystals were dissolved in chloroform, a 1 M aqueous NaOH

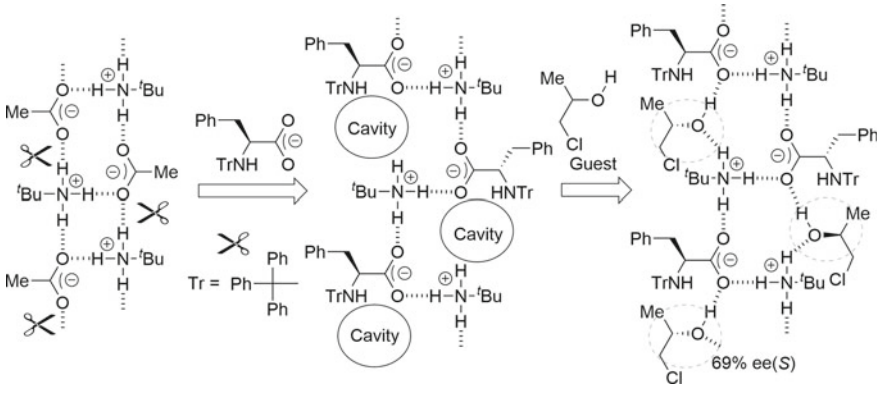

Fig. 22.12 Crystallization of Tr-Phe·tBuNH$_2$ with alcohols to prepare inclusion crystals

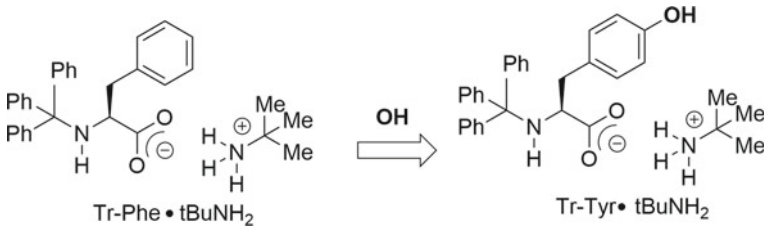

Fig. 22.13 Host structure of Tr-Phe·tBuNH$_2$ and Tr-Tyr·tBuNH$_2$

solution was used to move Tr-Tyr into the aqueous phase. The included alcohol was recovered from the organic phase, and the enantiomeric excesses of the alcohol were estimated by chiral HPLC (CHIRALCELs OB-H and OD-H and CHIRALPAK IB) analysis. The results are summarized in Table 22.1.

The predominant configurations of 1-phenyl, 1-(2-tolyl), and 1-(3-tolyl)ethanols that included in the host were (*R*)-enantiomer with enantiomeric excesses of 46%, 56%, and 53%, respectively.

We carried out single-crystal X-ray analysis of inclusion crystals with 1-phenylethanol to clarify the mechanism of enantioselective inclusion and the effect of hydroxy group (Fig. 22.14). The results show that the HO group and carboxylate of tyrosine captured 1-phenylethanol molecules (host/guest = 1:1) and constructed a cyclic hydrogen bonding network to form a 2:2 cluster (Tr-Tyr·tBuNH$_2$). We observed that one N-H group of *tert*-butylammonium formed an N-H$\cdots\pi$ interaction with the phenolic side chain of Tyr, and all other protic hydrogen atoms participated in normal hydrogen bonds in the crystal structure. Two hosts of Tr-Tyr·tBuNH$_2$ and two guests of 1-phenylethanol were included in an asymmetric unit. An enantiopure (*R*)-1-phenylethanol was observed in one recognition site, but both enantiomers of the alcohols (*R*:*S* = 45:55) were included in another recognition site. As a result of the statistically disordered structure, the enantiomeric excess of (*R*)-1-phenylethanol in this crystal was calculated to be 45%, which is very close to 46% in bulk solids. The tolerance of the disordered structure decreased its enantioselectivity.

Inclusion crystals of Tr-Tyr·tBuNH$_2$ with 1-(4-tolyl)ethanol and 1-(1-naphthyl)ethanol were also subjected to single-crystal X-ray analyses. As shown in Fig. 22.15, these crystal structures are similar to that of 1-phenylethanol mentioned

Table 22.1 Alcohols included in salts of *tert*-butylammonium *N*-trityltyrosine

Entry	Alcohol guest	ee (%)	Predominant configuration
1	1-phenylethanol	46	*R*
2	1-(2-tolyl)ethanol	56	*R*
3	1-(3-tolyl)ethanol	53	*R*
4	1-(4-tolyl)ethanol	3	*R*
5	1-(1-naphtyl)ethanol	96	*R*

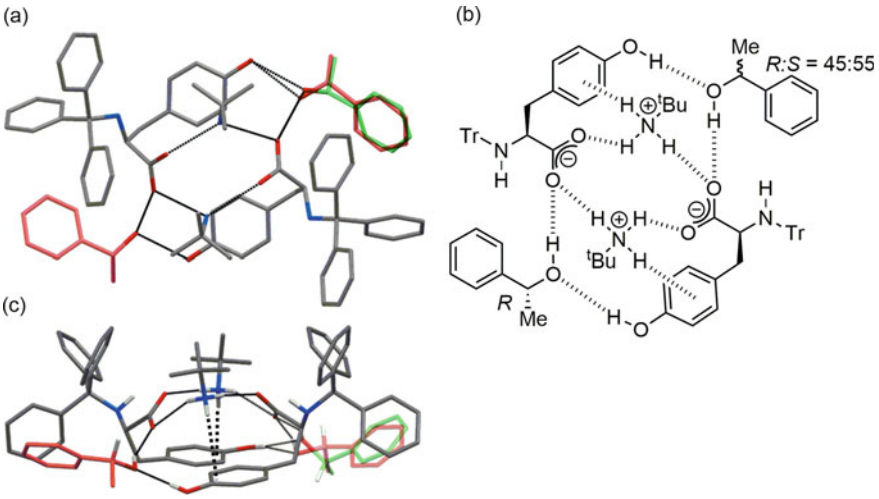

Fig. 22.14 Crystal structures of Tr-Tyr·tBuNH$_2$ with 1-phenylethanol (CCDC-1949797). **a** Top view of 2:2 cluster. (b) Schematic drawing of hydrogen bonds (c) Side view to clarify NH-π interaction

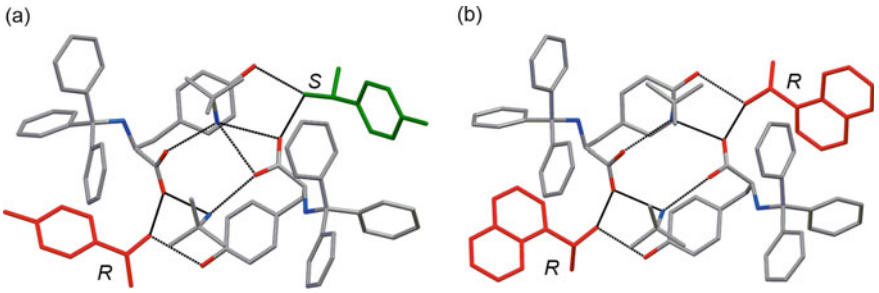

Fig. 22.15 Crystal structures of Tr-Tyr·tBuNH$_2$ with **a** 1-(4-tolyl)ethanol (CCDC-1949798) and **b** 1-(1-naphtyl)ethanol guest (CCDC-1949799)

above. The 2:2 clusters (Tr-Tyr·tBuNH$_2$) have the same cyclic hydrogen bonding network in which HO groups of alcohols are captured by the HO group and carboxylate of tyrosine.

Notably, both enantiomers of 1-(4-tolyl)ethanol were included in each cavity without statistic disorders even though the space group ($P2_1$) was identical to 1-phenylethanol. This result showed that the bulk solids of the enantiomeric excess resulted in 3% ee (*R*).

Conversely, inclusion crystals of 1-(1-naphthyl)ethanol suppressed the disordered structure in which the same (*R*)-enantiomer settled in each cavity. Similarly, the enantiomeric excess of bulk solids reached up to 96% (*R*) in Table 22.1. Notably, the

asymmetric unit consisted of two hosts and two guests, while the space group was $P1$.

The three crystal structures mentioned above have the same cyclic hydrogen bonding network to form 2:2 clusters (Tr-Tyr·tBuNH$_2$).

Figure 22.16 shows the difference between phenylalanine and tyrosine. In the case of Tyr, a one-dimensional hydrogen bonding network of ammonium carboxylate was broken and terminated by a phenolic hydroxy group of Tyr. As a result, larger secondary alcohol guests settled between hosts with the distance expanded from 9.27 to 11.15 Å. Although the phenyl group of Phe interacted with one phenyl group of a trityl group by a C-H$\cdots\pi$ interaction, the phenyl group of Tyr interacted with one hydrogen atom of the ammonium group by a N-H$\cdots\pi$ interaction, and the phenolic HO group also made a hydrogen bond with an oxygen atom of the guest alcohol. The conformational change of the side chain induced a new 2:2 cluster structure (Tr-Tyr·tBuNH$_2$).

As mentioned above, we found that Tr-Tyr·tBuNH$_2$ salt included 1-arylethanols to form the similar 2:2 clusters (Tr-Tyr·tBuNH$_2$). The structure of these inclusion crystals had the generality to become a great potential inclusion host. However, the statistic disorder must be suppressed and high enantiomeric excesses must be gained.

22.4 Conclusion

We reviewed the recent progress of the molecular recognition by inclusion phenomena regarded as a useful application of organic crystals.

In the first half of this review, we covered recent examples of molecular recognition by inclusion crystalline hosts: a dumb-bell type host [9], TETROL [10, 11] and TADDOL [14], and amino-acid-based hosts [15–17]. Some chiral hosts have achieved high enantioselective inclusion for cyclic ketones (up to 97% ee), sulfoxides (up to 98% ee), and nitriles (up to 92% ee).

In the latter half, we focused on the installation of trityl and related bulky groups, which enable compounds to settle guest molecules to form inclusion crystals. In fact, some hosts of amines [26–32] having trityl or 9-phenyl-9-xanthenyl groups included several neutral guests to construct inclusion crystals. In particular, we demonstrated that salts between *N*-trityl-tyrosine and *tert*-butylamine include 1-(1-naphthyl)ethanol in 96% ee (*R*) [33].

Inclusion crystal methods are still being refined to achieve structural isomer separation and optical resolution for neutral compounds. The trityl and related bulky groups might be recognized as crystal engineering tools that have the inclusion ability to host candidates. However, single-crystal X-ray analyses of these inclusion crystals showed us that inclusion with low enantioselectivity was often owing to statistically disordered structures, meaning both enantiomers settled in one recognition site. Therefore, the method of suppressing this statistic disorder with low enantioselectivity remains unknown.

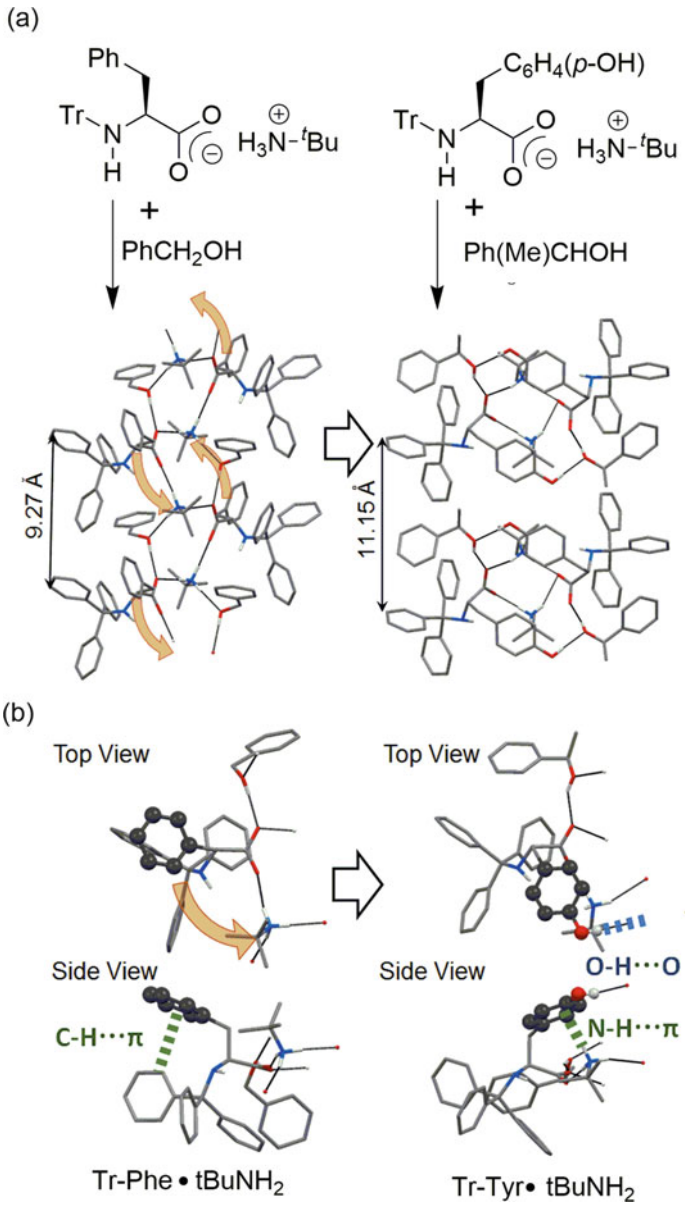

Fig. 22.16 Comparison of crystal structures of Tr-Phe·tBuNH$_2$ with benzyl alcohol (CCDC-1949796) and Tr-Tyr•tBuNH$_2$ with 1-phenylethanol (CCDC-1949797). **a** Hydrogen bonding network. **b** Conformational difference between Tr-Phe and Tr-Tyr·tBuNH$_2$ in inclusion crystals

References

1. Akazome, M.: Chiral recognition by inclusion crystals of amino-acid derivatives having trityl groups, in Tamura R., Miyata M. (eds.) Advances in Organic Crystal Chemistry, pp. 463 − 482, Springer, Japan, (2015)
2. Fogassy, E., Nógrádi, M., Kozma, D., Egri, G., Pálovics, E., Kiss, V.: Optical resolution methods. Org. Biomol. Chem. **4**, 3011–3030 (2006)
3. Siedlecka, R.: Recent developments in optical resolution. Tetrahedron **69**, 6331–6363 (2013)
4. Faigel, F., Fogassy, E., Nógrádi, M., Pálovics, E., Schindler, J.: Strategies in optical resolution: a practical guide. Tetrahedron: Asymmetry **19**, 519 − 536 (2008)
5. Toda, F., Bishop, R.: Separations and reactions in organic supramolecular chemistry; perspectives in supramolecular chemistry **8** Wiley, Chichester, (2004)
6. Toda, F. (ed.): Enantiomer separation: Fundamentals and practical methods. Kluwer Academic Publishers, Dordrecht (2004)
7. Kurilov, D.V., Vinogradov, M.G.: Preparative separation structurally related and racemic hydroxyl-containing compound through the formation of crystalline molecular complexes. Russ. Chem. Rev. **77**, 621–631 (2008)
8. Toda, F.: comprehensive supramolecular chemistry. in: Lehn J.-M. (ed.) Solid-state supramolecular chemistry: Crystal engineering, pp. 465–516, Pergamon, Oxford, (1996)
9. Batisai, E., Nassimbeni, L.R., Weber, E.: Inclusion compounds of a borneol dumb-bell host with methylcyclohexanones and 2-butanols: structures and resolutions. CrystEngComm **17**, 4205–4209 (2015)
10. Barton, B., Caira, M.R., Hosten, E.C., McCleland, C.W., Weitz, S.: Clathrates of TETROL: further aspects of the selective inclusion of methylcyclohexanones in their energetically unfavorable axial methyl conformations. J. Org. Chem. **80**, 7184–7192 (2015)
11. Barton, B., Dorfling, S.-L., Hosten, E.C.: Cyclohexanone-driven discriminatory behavior change of host compound (+)-(2R,3R)-TETROL for isomeric methylcyclohexanone guests. Cryst. Growth Des. **17**, 6725–6732 (2017)
12. Toda, F.: Molecular recognition. Bioorg. Chem. **19**, 157–168 (1991)
13. Seebach, D., Beck, A.K., Heckel, A.: TADDOLs, their derivatives, and TADDOL analogues: versatile chiral auxiliaries. Angew. Chem. Int. Ed. **40**, 92–138 (2001)
14. Kaku, H., Ito, M., Horikawa, M., Tsunoda, T.: Deracemization of α-monosubstituted cyclopentanones in the presence of a TADDOL-type host molecule. Tetrahedron **74**, 124–129 (2018)
15. Kodama, K., Morita, R., Hirose, T.: Formation of ternary inclusion crystal and enantioseparation of alkyl aryl sulfoxides by the salt of urea-modified L-phenylalanine and an achiral amine. Cryst. Growth Des. **16**, 5206–5213 (2016)
16. Kodama, K., Kanai, H., Shimomura, Y., Hirose, T.: Enantioseparation of sulfoxides and nitriles by inclusion crystallization with chiral organic salts based on L-phenylalanine. Eur. J. Org. Chem. 1726–1729 (2018)
17. Hu, X., Yang, Y., Shi, S., Shan, Z.: Effects of solvent on inclusion complexation of a chiral dipeptide toward racemic BINOL. Chirality **28**, 784–788 (2016)
18. Faigl, F., Fogassy, E., Nógrádi, M., Pálovics, E., Schindler, J.: Separation of non-racemic mixtures of enantiomers: an essential part of optical resolution. Org. Biomol. Chem. **8**, 947–959 (2010)
19. Niess, F., Duplan, V., Sauvage, J.-P.: Molecular muscles: from species in solution to materials and devices. Chem. Lett. **43**, 964–974 (2014)
20. Balzani, V., Credi, A., Raymo, F.M., Stoddart, J.F.: Artificial molecular machines. Angew. Chem. Int. Ed. **39**, 3348–3391 (2000)
21. Kassem, S., van Leeuwen, T., Lubbe, A.S., Wilson, M.R., Feringa, B.L., Leigh, D.A.: Artificial molecular motors. Chem. Soc. Rev. **46**, 2592–2621 (2017)
22. Mislow, K.: Stereochemical consequences of correlated rotation in molecular propellers. Acc. Chem. Res. **9**, 26–33 (1976)

23. Iwamura, H., Mislow, K.: Stereochemical consequences of dynamic gearing Acc. Chem. Res. **21**, 175–182 (1988)
24. Wuts, P.G.M.: Greene's Protective Groups in Organic Synthesis, 5th edn, pp. 1056–1057. John Wiley & Sons Inc, New Jersey (2014)
25. Megumi, K., Yokota, S., Matsumoto, S., Akazome, M.: Enantioselective inclusion of amide guests into a chiral N, N'-ditrityl aminoamide host to compensate the loss of hydrogen bonds broken by installation of trityl groups. Tetrahedron Lett. **54**, 707–710 (2013)
26. Bendzińska-Berus, W., Warżajtis, B., Gajewy, J., Kwit, M., Rychlewska, U.: Trityl group as an crystal engineering tool for construction of inclusion compounds and for suppression of amide NH···O = C hydrogen bonds. Cryst. Growth Des. **17**, 2560–2568 (2017)
27. Lazareva, N.F., Sterkhova, I.V., Lazarev, I.M., Smirnov, V.I.: 1-[(*N*-Methyl-*N*-tritylamino)methyl]silatrane: synthesis and structure. Polyhedron **117**, 377–380 (2016)
28. Barton, B., McCleland, C.W., Caira, M.R., de Jager, L., Hosten, E.C.: Crystal X-ray diffraction and molecular modeling considerations elucidate the factors responsible for the opposing host behavior of two isostructural xanthenyl- and thioxanthenyl-derived host compounds. Cryst. Growth Des. **19**, 2396–2418 (2019)
29. Barton, B., de Jager, L., Hosten, E.C.: Comparing the host behaviour of N, N'-bis(9-phenyl-9-thioxanthenyl)ethylenediamine and N, N'-bis(9-phenyl-9-xanthenyl)ethylenediamine in the presence of various alkylated aromatic and aniline guests: crystal engineering considerations. CrystEngComm **21**, 4387–4400 (2019)
30. Barton, B., de Jager, L., Hosten, E.C.: Host behavior of N, N'-bis(9-phenyl-9-thioxanthenyl)ethylenediamine in the presence of aromatic and aliphatic five-membered heterocyclic guests: selectivity correlations with Hirshfeld surface analyses. Cryst. Growth Des. **19**, 1268–1281 (2019)
31. Barton, B., de Jager, L., Hosten, E.C.: Minor modifications afford improved host selectivities in xanthenyl-type host systems. Cryst. Eng. Comm. **21**, 3000–3013 (2019)
32. Barton, B., Jooste, D.V., Hosten, E.C.: Synthesis and assessment of compounds trans-*N*,*N*'-bis(9-phenyl-9-xanthenyl)cyclohexane-1,4-diamine and trans-*N*,*N*'-bis(9-phenyl-9-thioxanthenyl)cyclohexane-1,4-diamine as hosts for potential xylene and ethylbenzene guests. J. Inclusion Phenom. Macrocyclic Chem. **93**, 333–346 (2019)
33. Akazome, M., Ikegaya, M., Megumi, K., Matsumoto, S.: Enantioselective inclusion of alcohols into salts between *N*-trityl (*S*)-amino acids and amines. Joint Congress of Asian Crystallization Technology Symposium-2014 (ACTS-2014) and 11th International Workshop on Crystal Growth of Organic Materials (CGOM11), PC-42, Nara (2014)
34. Megumi, K., Nadiah Binti Mohd Arif, F., Matsumoto, S., Akazome, M.: Design and evaluation of salts between *N*-trityl amino acid and tert-butylamine as inclusion crystals of alcohols. Cryst. Growth Des. **12**, 5680 − 5685 (2012)

Chapter 23
Asymmetric Catalysis and Chromatographic Enantiomer Separation by Homochiral Metal–Organic Framework: Recent Advances

Koichi Tanaka

Abstract In this review, we report the recent progress in homochiral metal–organic frameworks (MOFs), a new class of porous materials, consisting of metal–oxo clusters and multifunctional ligands for heterogeneous asymmetric catalysis and enantiomer separation. The asymmetric catalysis section is subdivided based on the types of reactions that have recently been successfully performed using chiral MOFs as a heterogeneous catalyst. In the second part, we give some examples from recent studies highlighting enantiomer separation using chiral MOFs as a novel chiral stationary phase for high-performance liquid chromatography.

Keyword Chiral metal–organic frameworks · Chiral asymmetric catalysis · Chromatographic enantioselective separation · Crystal structure

23.1 Introduction

In the last decade, metal–organic frameworks (MOFs) have attracted much attention for various applications, such as gas storage, separation, sensing, and catalysis [1]. Chiral MOFs show great potential as asymmetric catalysts [2] and chiral stationary phases (CSPs) for enantiomer separation by high-performance liquid chromatography (HPLC) [3]. Several structural features of chiral MOFs play crucial roles in the above-mentioned applications, such as their large internal surface area, high adsorption capacity, permanent porosity, and thermal stability. In this review, we describe the recent progress in asymmetric catalysis and chiral HPLC separation using chiral MOFs. Asymmetric catalysis is an essential area of chiral chemistry, and it efficiently assists in the synthesis of valuable chiral organic compounds. The use of homochiral MOFs as asymmetric catalysts is eco-friendly owing to their many advantages, including mild reaction conditions, high enantioselectivity, easy

K. Tanaka (✉)
Department of Chemistry and Materials Engineering, Faculty of Chemistry, Materials and Bioengineering, Kansai University, Suita, Osaka 564-8680, Japan
e-mail: ktanaka@kansai-u.ac.jp

M. Sakamoto and H. Uekusa (eds.), *Advances in Organic Crystal Chemistry*,
https://doi.org/10.1007/978-981-15-5085-0_23

product purification, and catalyst reusability. Because of the numerous benefits of homochiral MOF catalysts, a variety of chiral MOFs have been designed and investigated as asymmetric catalysts. A large number of chiral stationary phases based on crown ethers, polysaccharides, and cyclodextrins have been reported for separation of enantiomers. In addition, chiral MOFs show great potential as the chiral stationary phase for enantiomer separation by HPLC. The advantages of chiral MOFs over other chiral stationary phases are their well-ordered frameworks with defined chiral pores that are accessible to potential substrates and their controllable functionalities by varying the chiral linkers and metal ions. This review highlights the recent successful applications of chiral MOFs in the fields of asymmetric catalysis and chromatographic enantiomer separation from 2012 until the present.

23.2 Asymmetric Catalysis

23.2.1 Ring-Opening Reaction of Meso-Epoxides with Aromatic Amines

In 2008, Tanaka and co-workers [4] reported synthesis of (*R*)-**MOF-1** by treating (*R*)-2,2'-dihydroxyl-1,1'-binaphthalene-5,5'-dicarboxylic acid **1** with $Cu(NO_3)_2$ under solvothermal conditions. The resulting two-dimensional infinite $[Cu_2(\mathbf{1})_2(H_2O)_2]\cdot MeOH\cdot H_2O$ framework contains copper paddle wheels as secondary building units (SBU**s**) stacked along the *b* axis with an interlayer Cu–Cu distance of 15.6 Å (Fig. 23.1). Using (*R*)-**MOF-1** as a catalyst for asymmetric ring-opening reactions of cyclohexene oxide with some aniline derivatives to furnish the corresponding optically active β-amino alcohols resulted in good yields with excellent enantioselectivities (Table 23.1) [5]. Hirao et al. [6] reported the mechanism of this catalytic reaction by QM/MM computational study. The QM/MM calculations showed that the reaction consists of two major steps. In the first step, ring-opening of the epoxide occurs to form an intermediate with an alkoxide ion, and the strong binding of the alkoxide ion to the Cu(II) center results in cleavage of one of the four coordination bonds of the copper with carboxylate ligands. In the second step, proton transfer occurs from the aniline to the alkoxide oxygen atom to form the β-amino alcohol. The transition state for the ring-opening step in formation of the (*R*,*R*)-isomer is stabilized by CH–π interactions, whereas such interactions are absent in the transition state for formation of the (*S*,*S*)-isomer. Tanaka et al. [5] synthesized (*R*)-**MOF-2** by solvothermal reaction of the chiral organic linker (*R*)-2,2'-diethoxy-1,1'-binaphthyl-4,4'-di(5-isophthalic acid) **2** and $Zn(NO_3)_2\cdot 6H_2O$ in a mixed solvent (*N*,*N*-dimethylacetamide–EtOH) at 110°C for 2 days. X-ray diffraction analysis revealed that a rigid MOF was constructed around two pentacoordinated Zn(II) cations with a nearest Zn···Zn distance of 3.384(2) Å (Fig. 23.2), which were bridged by three carboxyl groups from three different

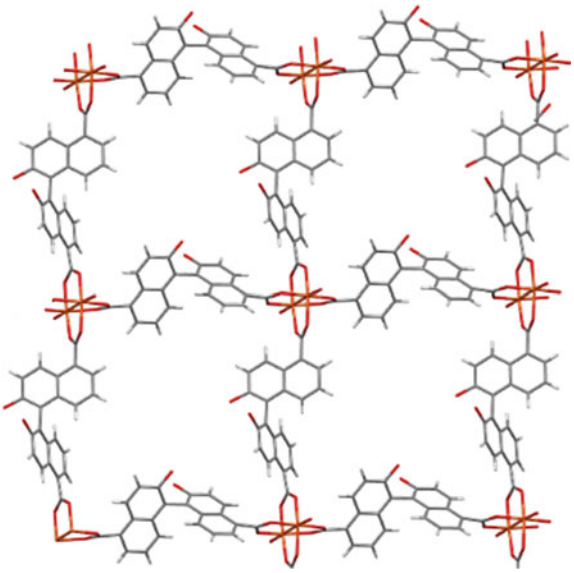

Fig. 23.1 X-ray structure of (*R*)-**MOF-1**

Table 23.1 Asymmetric epoxide ring-opening of cyclohexene oxide catalyzed by (*R*)-**MOF-1**

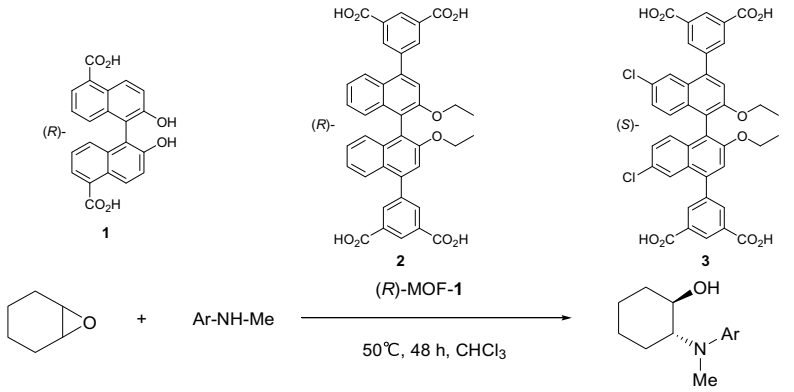

Entry	Ar	Yield (%)	Ee (%)
1	Ph	86	85
2	2-MeC_6H_4	19	43
3	3-MeC_6H_4	90	78
4	4-MeC_6H_4	94	92
5	4-MeOC_6H_4	87	95
6	4-ClC_6H_4	85	82

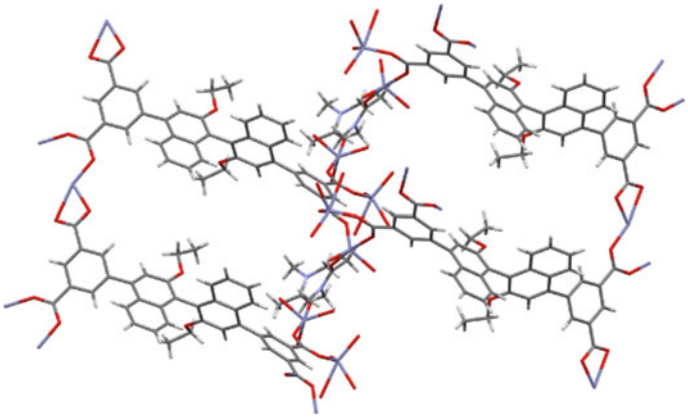

Fig. 23.2 X-ray structure of (*R*)-**MOF-2**

Table 23.2 Asymmetric epoxide ring-opening of cis-stilbene oxide catalyzed by (*S*)-**MOF-3**

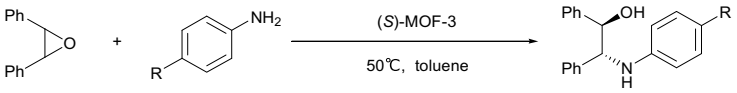

Entry	R	Time (h)	Yield (%)	Ee (%)
1	H	15	91	85
2	Me	70	78	75
3	MeO	63	70	62
4	F	63	95	89
5	Cl	63	70	58
6	Br	63	72	31

chiral ligands. (*R*)-**MOF-2** exhibited good enantioselectivities toward the ring-opening reaction of *cis*-stilbene oxide with aniline or *N*-methyl aniline. Zhao and co-workers [7] reported synthesis of (*S*)-**MOF-3** from (*S*)-6,6'-dichloro-2,2'-diethoxyl-1,1'-binaphthyl-4,4'-bis(5-isophthalic acid) **3** and its good catalytic activity for the asymmetric ring-opening reaction of *cis*-stilbene oxide with several anilines (Table 23.2).

23.2.2 Oxidation of Sulfides to Sulfoxides

Tanaka and co-workers [8] described a **MOF-1** catalyzed oxidation of unsymmetrical sulfides. Various sulfides were oxidized with hydrogen peroxide or its complex with

Table 23.3 Oxidation of sulfides to sulfoxides with hydrogen peroxide catalyzed by (*R*)-**MOF-1**

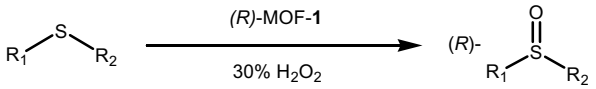

Entry	R_1	R_2	Yield (%)	Ee (%)
1	Me	Ph	44	56
2	Et	Ph	67	58
3	Me	4-MeC_6H_4	35	39
4	Me	4-$MeOC_6H_4$	69	40
5	Me	4-ClC_6H_4	53	41
6	Me	2-ClC_6H_4	6	13
7	H_2C=CH	Ph	15	64
8	Me	2-Naphthyl	27	65
9	Me	$PhCH_2$	79	80
10	Ph	$PhCH_2$	26	23

urea in the presence of 0.04 mol% of **MOF-1** under mild conditions to give sulfoxides with high enantioselectivity up to 80% *ee* in favor of the *R* isomer (Table 23.3). It is important that no sulfones were formed and that **MOF-1** can be separated by simple filtration from the reaction mixture and reused.

23.2.3 Michael Reaction

Lin and co-workers [9] extensively investigated the catalytic activities of Ru- and Rh-complex-based BINAP-derived chiral MOFs. **MOF-4·Ru** was synthesized by reaction of $ZrCl_4$ with 4,4'-bis-(4-carboxyphenylethynyl)BINAP **4**, followed by modification of **MOF-4** with [Ru(cod)(2-Me-allyl)$_2$]. The **MOF-4·Ru** catalyst showed impressive enantioselectivity in 1,4-addition of arylboronic acids to cyclohex-2-en-1-one to afford (*S*)-3-arylcyclohexan-1-ones with yields of 80%–99% and enantioselectivities of > 99% ee.

Enantioselective addition of phenylboronic acids to *N*-tosyl benzaldehyde imines readily occurred in the presence of 3 mol% **MOF-5·Rh(acac)** synthesized from ligand **5**. Optically active substituted (*S*)-*N*-tosyldiphenylamines were obtained with

~ 99% enantioselectivity in high yield (Table 23.4) [10]. A homogeneous catalyst used as a reference showed lower activity and asymmetric induction.

23.2.4 Cyanosilylation

Cui and co-workers [11] synthesized vanadium(V)-containing cage-type (*S*)-**MOF-6** with metal–salen fragments from dicarboxylic acid **6**. (*S*)-**MOF-6** showed high enantioselectivity in addition of trimethylsilyl cyanide to aromatic and heteroaromatic aldehydes to form the cyanohydrin silyl ether with a high ee value in the presence of 1 mol% (*S*)-**MOF-6** (Table 23.5). They suggested that the low ee value of the adduct obtained from anthracene-9-carbaldehyde could be related to steric hindrance. A homogeneous catalyst prepared from dimethyl VO (salen) dicarboxylate showed considerably lower asymmetric induction of 51% ee with 42.6% conversion.

23.2.5 Henry Reaction

Jiang et al. [12] reported synthesis of the three-dimensional (3D) chiral metallosalen-based chiral MOF $[Cd_2(Cu(salen))(DMF)_3]\cdot DMF\cdot 3H_2O$ (*R*)-**MOF-7** with a one-dimensional open channel. In the presence of 1 mol% (*R*)-**MOF-7** and $(i\text{-Pr})_2$EtN as a co-catalyst, nitromethane enantioselectively added to various aliphatic, aromatic, and heteroaromatic aldehydes to give the corresponding (*R*)-adducts (Table 23.6). For most of the reactions, the yields were high and the ee values exceeded 90%. The exceptions were sterically hindered aldehydes, such as naphthalene-1-carbaldehyde and anthracene-9-carbaldehyde, and 4-nitrobenzaldehyde. Pyrene-1-carbaldehyde failed to react under the reaction conditions, presumably because of its large size, which prevents it from accessing the catalytic sites inside the pores of (*R*)-**MOF-7**.

23.2.6 Morita–Baylis–Hillman Reaction

Hu et al. [13] reported synthesis of a chiral ionic liquid moiety of a L-pyrrolidin-2-ylimidazole-decorated homochiral UiO-68-type MOF, followed by impregnating UiO-68-type coordination polymer in a toluene solution of $Ti(Oi\text{-Pr})_4$ and subsequent hydrolysis of the latter inside **MOF-8** pores. The obtained porous TiO_2@**MOF-8** composite catalyst was an efficient asymmetric heterogeneous catalyst in the Morita–Baylis–Hillman reaction. Addition of methyl acrylate to substituted benzaldehydes in the presence of 2 mol% TiO_2@**MOF-8** afforded the corresponding (*R*)-products in high yield with excellent enantiomeric purity (Table 23.7).

Table 23.4 Michael addition of phenylboronic acids to *N*-tosyl benzaldehyde imines

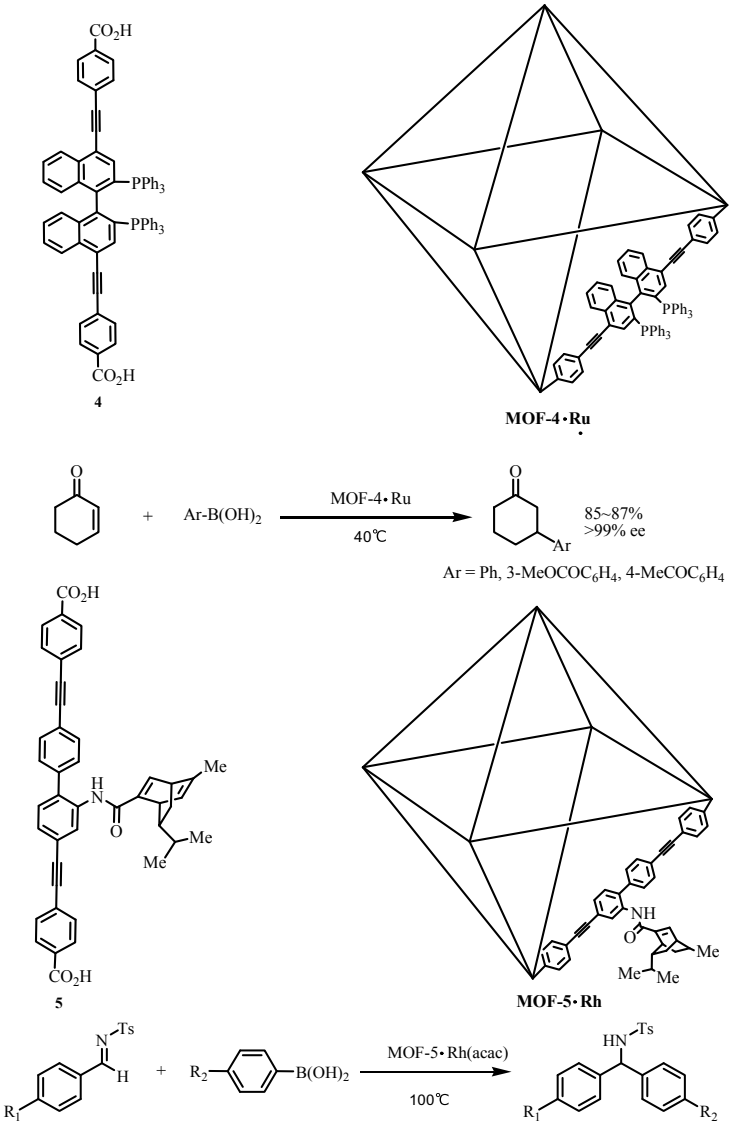

(continued)

Table 23.4 (continued)

Entry	R_1	R_2	Yield (%)	**Ee (%)**
1	Cl	H	99	**98**
2	Cl	F	95	**99**
3	Cl	OMe	80	**97**
4	H	F	97	**99**
5	H	OMe	96	**97**
6	OMe	H	98	**99**
7	OMe	F	99	**>99**

Table 23.5 Cyanosilylation of aldehydes in the presence of (*S*)-**MOF-6**

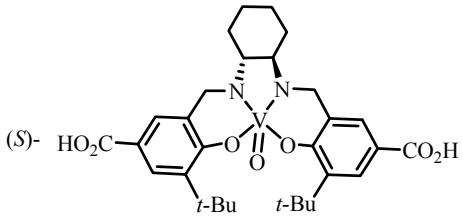

6

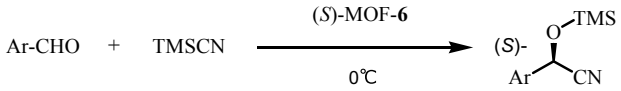

Entry	Ar	Yield (%)	Ee (%)
1	Ph	93	92 (*S*)
2	4-BrC_6H_4	94	92 (*S*)
3	4-MeC_6H_4	90	92 (*S*)
4	3-$MeOC_6H_4$	92	95 (*S*)
5	4-$MeOC_6H_4$	90	94 (*S*)
6	1-Naphthyl	91	92 (*R*)
7	2-Naphthyl	90	95 (*S*)
8	2-Thiophenyl	92	92 (*S*)
9	9-Anthryl	62	35 (*S*)
10	9-Anthryl	20	90 (*S*)

Table 23.6 H reaction of aldehydes with nitromethane catalyzed by (*R*)-**MOF-7**

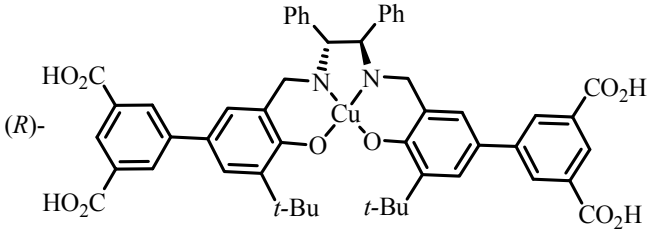

7

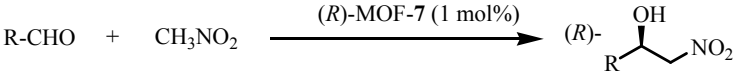

Entry	R	Yield (%)	Ee (%)
1	*n*-Bu	98	91
2	cyclohexyl	84	92
3	Ph	71	95
4	2-MeC_6H_4	83	93
5	2-MeOC_6H_4	88	98
6	2-BrC_6H_4	75	93
7	2-$NO_2C_6H_4$	73	91
8	2-furyl	86	93
9	2-pyridyl	98	93
10	1-naphthyl	31	81
11	9-anthracyl	11	45

23.2.7 Diels–Alder Reaction

In 2016, Tanaka et al. [14] prepared novel homochiral biphenol-based (*R*)-**MOF-9** by the solvothermal reaction of the chiral organic (*R*)-2,2'-dihydroxy-1,1'-binaphthyl-4,4'-dibenzoic acid **9** ligand and $Cu(NO_3)_2{\cdot}3H_2O$ in a mixed solvent (DMF–H_2O) at 55 °C for 4 days. The MOF crystallized in the trigonal *R*32 space group (Fig. 23.3). Synthesized chiral (*R*)-**MOF-9** was found to be an effective asymmetric catalyst in the Diels–Alder reaction between isoprene and *N*-ethyl maleimide, with up to 81% yield and 75% ee. The optimized conditions for the reaction were explored, and it was found that the best yield was obtained when the reaction was performed at 0°C for 48 h in EtOAc solvent. The scope of the reaction was investigated with various *N*-substituted maleimides with isoprene, and lower reactivity and enantioselectivity were obtained for bulky substrates because of their weak interactions with chiral (*R*)-**MOF-9** (Table 23.8).

Table 23.7 Morita–Baylis–Hillman reaction of benzaldehydes with methyl acrylate catalyzed by TiO_2@**MOF-8**

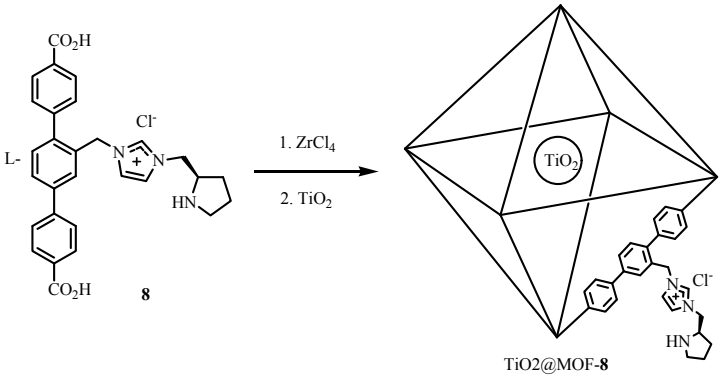

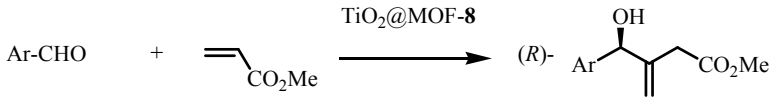

Entry	Ar	Yield (%)	Ee (%)
1	2-$MeOC_6H_4$	88	90
2	3-$MeOC_6H_4$	93	97
3	4-$MeOC_6H_4$	99	99
4	2-MeC_6H_4	68	85
5	3-MeC_6H_4	85	93
6	4-MeC_6H_4	97	96
7	2-$NO_2C_6H_4$	44	87
8	3-$NO_2C_6H_4$	56	95
9	4-$NO_2C_6H_4$	64	98

Cui and co-workers [15] prepared Cr(salen)-based (*R,R*)-**MOF-10** from (*R,R*)-(−)-*N,N'*-bis(3-carboxyl-5-*tert*-butylsalicylidene)-1,2-cyclohexanediamine **10** and demonstrated its ability as a catalyst for a variety of asymmetric organic transformations. The Diels–Alder reaction was explored with a range of methyl-substituted dienes, which successfully reacted with acrolein in the presence of 5 mol% (*R,R*)-**MOF-10**, affording the corresponding products with up to 91% ee (Table 23.9). The catalytic activity of (*R,R*)-**MOF-10** in hetero-Diels–Alder reactions was also evaluated. The reactions proceeded smoothly with substituted benzaldehydes and Danishefsky dienes, and the desired products were obtained with up to 79% ee (Table 23.10).

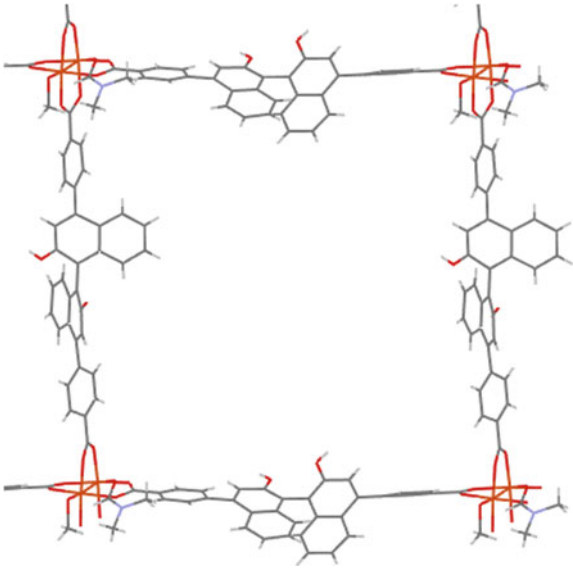

Fig. 23.3 X-ray structure of (*R*)-**MOF-9**

23.2.8 Friedel–Crafts Alkylation

In 2012, Lin and co-workers [16] constructed novel chiral (*R*)-**MOF-11** with Brønsted acid sites from (*R*)-1,1'-binaphthyl-2,2'-phosphoric acid derivative **11** and $Cu(NO_3)_2$. (*R*)-**MOF-11** was found to be an active catalyst for the Friedel–Crafts reaction between indoles and *N*-sulfonyl aldimines. The reaction preferentially formed the corresponding *R* isomer (Table 23.11). Interestingly, methyl ester ligand **11** predominantly formed the *S* isomer.

In 2018, Tanaka and co-workers [18] reported the first highly enantioselective Friedel–Crafts alkylation of *N,N*-dialkylanilines with *trans*-β-nitrostyrene catalyzed by homochiral (*R*)-**MOF-12** [17] constructed from (*R*)-2,2'-dihydroxy-1,1'-binaphthyl-6,6'-dicarboxylic acid **12** (Fig. 23.4). The Friedel–Crafts reaction was explored with a range of *N,N*-dialkylanilines, which successfully reacted with *trans*-*β*-nitrostyrene in the presence of 20 mol% of the evacuated MOF, affording the corresponding products in excellent yields (~96%) and enantioselectivities (~98% ee) (Table 23.12). Sterically more bulky *N,N*-dibenzylaniline showed poor catalytic efficiency in terms of both the product yield (5%) and enantioselectivity (26% ee). This may be because of the weaker encapsulation of the sterically bulky reactant in the chiral cavities of (*R*)-**MOF-12**. The catalyst was separated by filtration and successfully used for two further catalytic cycles without loss of catalytic activity. On the basis of the above results, the reaction was extended to pyrrole and *N*-methyl pyrrole, and it was found that (*R*)-**MOF-12** can also efficiently catalyzed the reaction

Table 23.8 Diels–Alder reaction of isoprene with *N*-substituted maleimides catalyzed by (*R*)-**MOF-9**

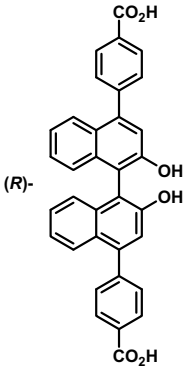

9

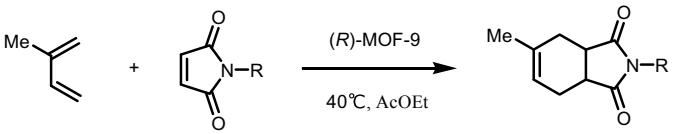

Entry	R	Yield (%)	Ee (%)
1	Me	37	37
2	Et	81	75
3	*n*-Pr	11	5
4	Ph	17	7
5	Cyclohexyl	18	0

with β-nitrostyrene, affording both 1:1 adduct and 1:2 adduct in excellent enantioselectivities and good diastereoselectivities; the results are summarized in Table 23.13. We propose a stereochemical model for the transition state of the reaction, based on the experimental results and the configurations of the products. The NO_2 group of *β*-nitrostyrene coordinates with the Lewis acidic Cu site through an oxygen atom. Preferential attack of the *para*-position of *N,N*-dimethylaniline on the *Si*-face of *β*-nitrostyrene in the confined spaces in (*R*)-**MOF-12** leads to the *R*-configured product (Fig. 23.5).

Table 23.9 Asymmetric Diels–Alder reactions catalyzed by Cr(salen)-based (*R,R*)-**MOF-10**

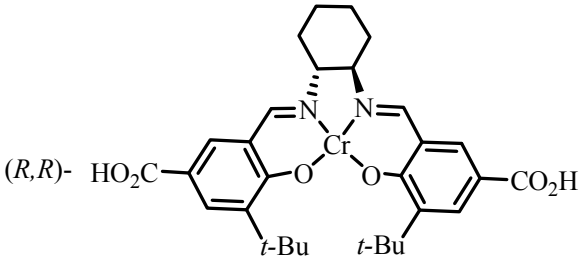

10

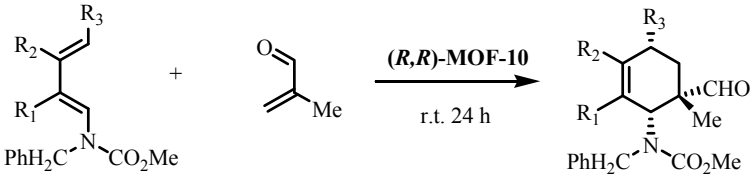

Entry	R_1	R_2	R_3	Yield (%)	Ee (%)
1	H	H	H	90	87
2	Me	H	H	32	86
3	H	Me	H	79	91
4	H	H	Me	30	87

Table 23.10 Asymmetric hetero-Diels–Alder reactions catalyzed by Cr(salen)-based (*R,R*)-**MOF-10**

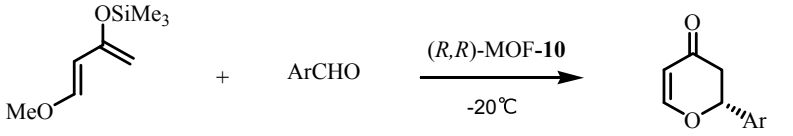

Entry	Ar	Yield (%)	Ee (%)
1	Ph	87	78
2	2-FC_6H_4	89	78
3	4-FC_6H_4	84	79
4	4-BrC_6H_4	86	72
5	3-$NO_2C_6H_4$	83	75
6	4-$NO_2C_6H_4$	77	75

Table 23.11 Enantioselective Friedel–Crafts reactions of indole with *N*-sulfonyl aldimines

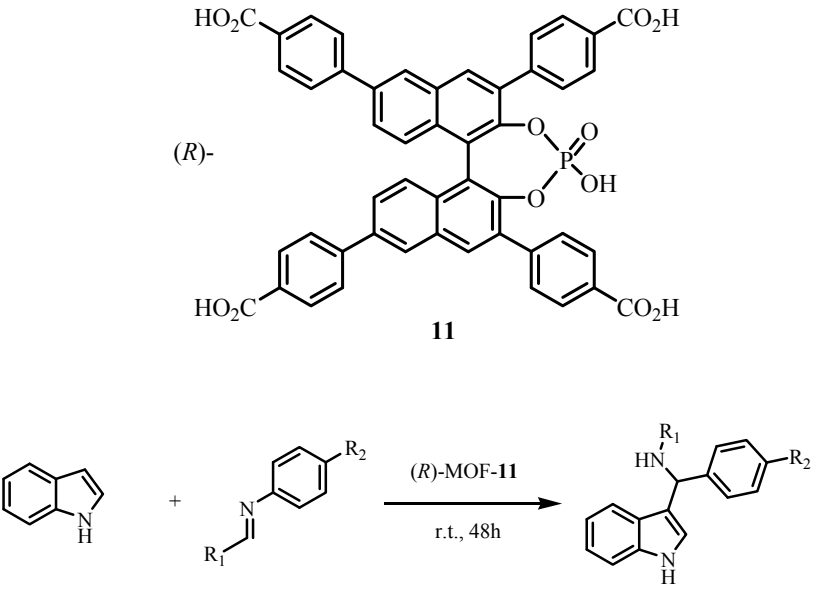

Entry	R_1	R_2	Yield (%)	Ee (%)
1	Bs	H	39	42
2	Bs	H	38	39
3	Ts	H	32	44
4	Ts	Br	42	40
5	Ts	Cl	45	29

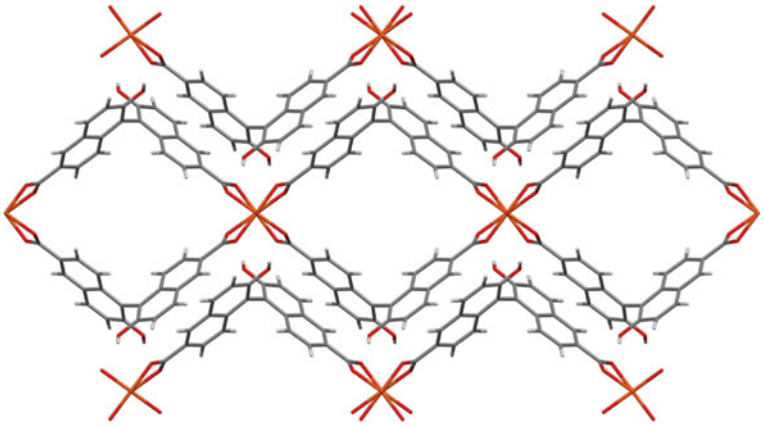

Fig. 23.4 X-ray structure of (*R*)-**MOF-12**

Table 23.12 Enantioselective Friedel–Crafts reactions of dialkylanilines with β-nitrostyrene catalyzed by (*R*)-**MOF-12**

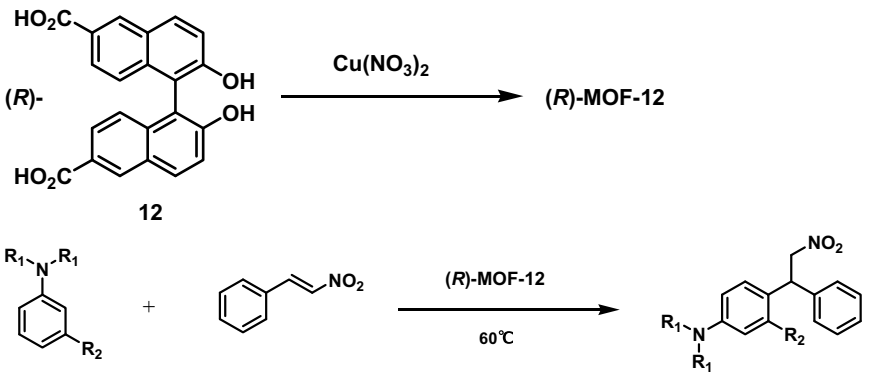

Entry	R_1	R_2	Solv.	Time (h)	Yield (%)	Ee (%)
1	Me	H	EtOH	48	95	98 (R)
2	Et	H	2-PrOH	72	91	95
3	n-Pr	H	2-PrOH	72	46	84
4	CH_2Ph	H	EtOH	72	5	26
5	Me	Me	EtOH	48	93	97
6	Me	Cl	EtOH	72	56	98
7	Me	OMe	2-PrOH	48	96	94
8		$-(CH_2)_5-$	EtOH	72	62	99

Table 23.13 Enantio- and diastereoselective Friedel–Crafts reactions of pyrroles with β-nitrostyrene catalyzed by (*R*)-**MOF-12**

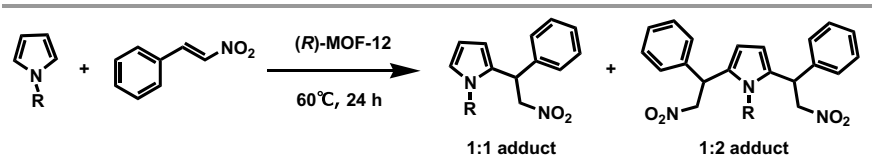

Entry	R	Solv.	1:1 adduct		1:2 adduct		
			Yield (%)	Ee (%)	Yield(%)	Ee(%)	Dr
1	H	2-PrOH	44	75	21	93	69:31
2	Me	EtOH	44	80	15	97	81:19

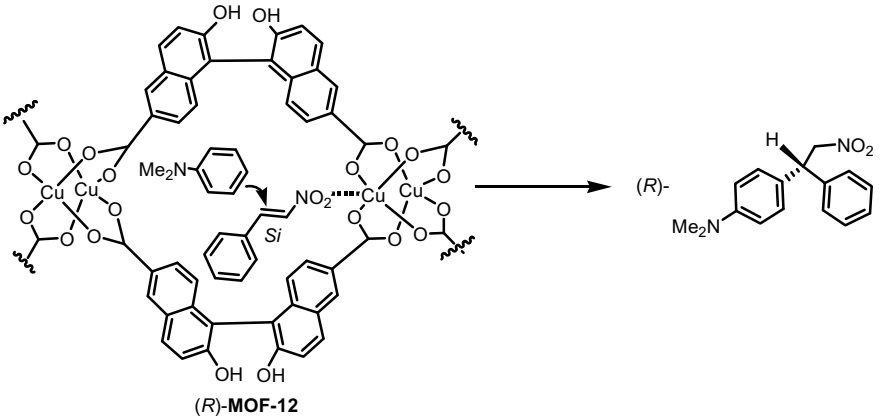

Fig. 23.5 A plausible mechanism of the asymmetric Friedel–Crafts reaction by (*R*)-**MOF-12**

23.3 Chromatographic Enantiomer Separation

In 2012, Tanaka et al. [19, 20] reported HPLC enantiomer separation of various types of sulfoxides, *sec*-alcohols, β-lactams, benzoins, flavanones, and epoxides using a (*R*)-**MOF-12**-silica composite as the chiral stationary phase. The (*R*)-**MOF-12**-silica composite was synthesized from a mixture of (*R*)-**12**, $Cu(NO_3)_2$, and monodisperse spherical silica gel (particle size 7 μm) in DMF under solvothermal conditions. A suspension of the (*R*)-**MOF-12**-silica composite in hexane/2-PrOH was slurry-packed into a stainless steel column (150 mm × 4.6 mm). The separation factors were larger for unsubstituted and *p*-substituted sulfoxides than their *o*- and *m*-substituted isomers. Thus, the shapes of the *p*-substituted sulfoxides matched the cavity of (*R*)-**MOF-12** (6.2 Å × 6.2 Å). Enantioseparation of *o*-substituted sulfoxides was incomplete, probably because of steric constraints. The (*S*)-isomer of the sulfoxides eluted first, followed by the (*R*)-isomer in most cases. This suggests inclusion of the (*R*)-enantiomer in the cavity of (*R*)-**MOF-12**, probably promoted by intermolecular hydrogen-bonding interactions between the phenolic OH group of (*R*)-**MOF-12** and the sulfinyl group. Indeed, polar substituents, such as Cl, at the *o*-position of the phenyl group disturbed this hydrogen-bond formation and led to poor enantioselectivity (Fig. 23.6).

In 2013, Yuan et al. [21] reported successful HPLC resolution of racemates, such as 1-(4-chlorophenyl)ethanol, furoin, benzoin, flavanone, Troger's base, BINOL, 1,2-diphenyl-1,2-ethanediol, warfarin sodium, 3-benzyloxy-1,2-propanediol, and 3,5-dinitro-*N*-(1-phenylethyl)benzamide using the chiral $[(CH_3)_2NH_2][CD(bpdc)_{1.5}]$ MOF as the chiral stationary phase. Tang and co-workers [22] designed a non-interpenetrated 3D homochiral MOF using enantiopure pyridyl-functionalized salen [(*N*-(4-pyridylmethyl)-L-leucine·HBr)] as a starting material. It was also used as the chiral stationary phase for HPLC to enantioseparate racemic drugs (ibuprofen,

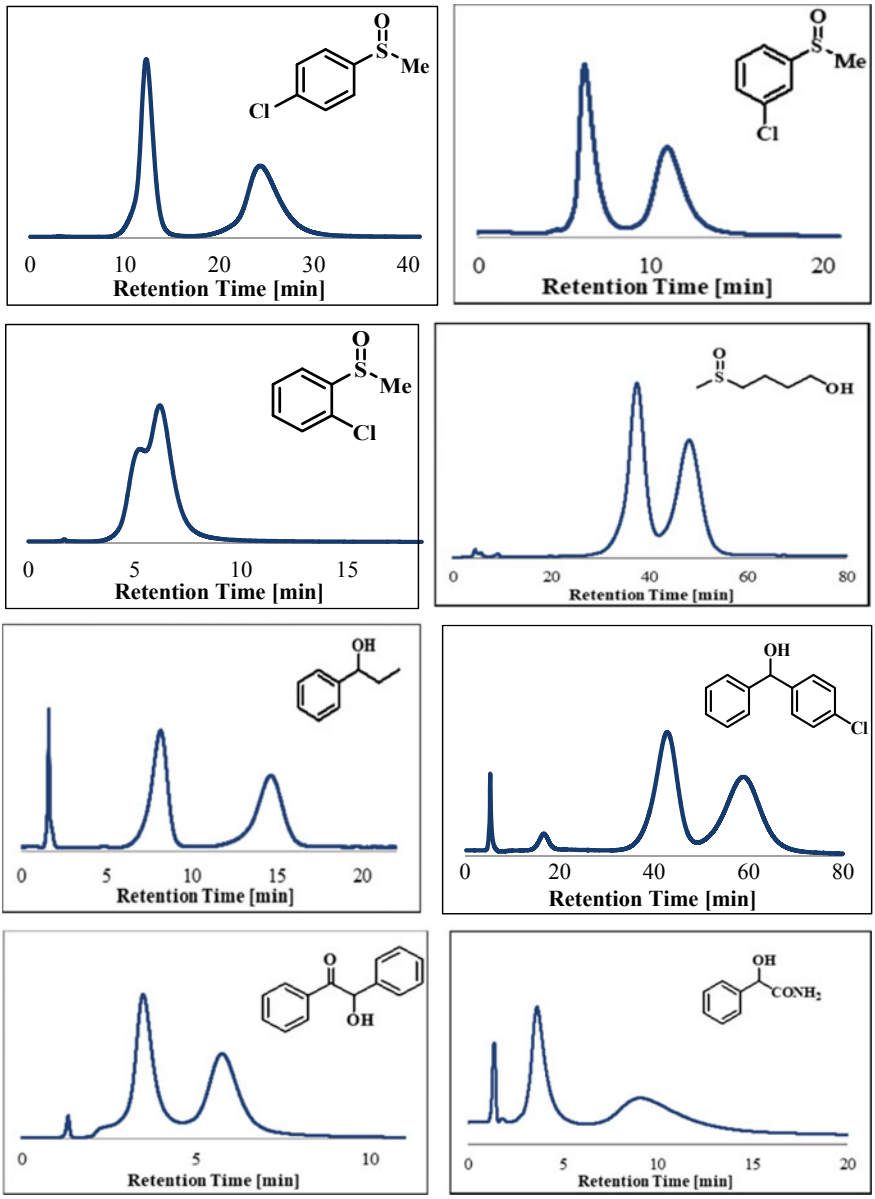

Fig. 23.6 HPLC chromatograms on (*R*)-**MOF-12** column for the separation of racemates

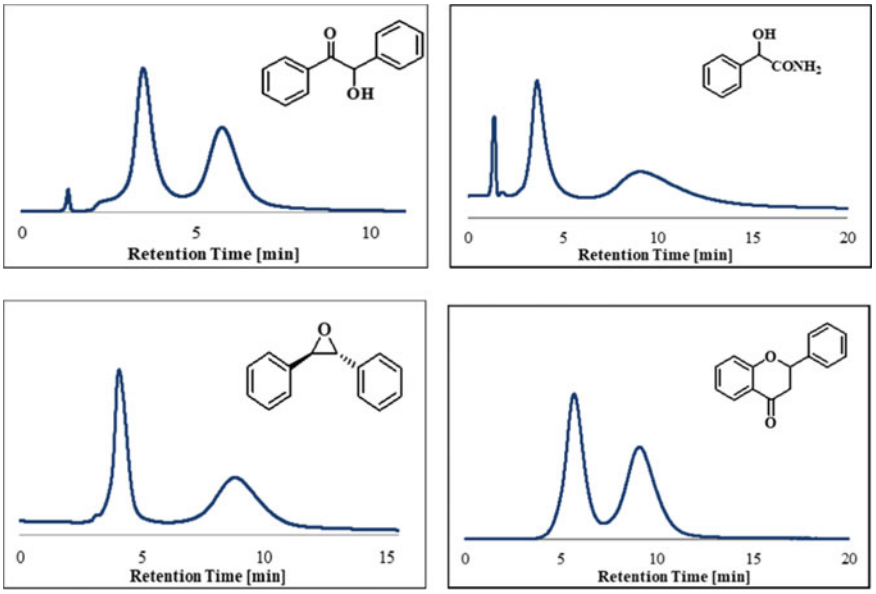

Fig. 23.6 (continued)

1-phenyl-1-propanol, benzoin, ketoprofen, and naproxen), and it showed excellent performance in enantioseparation. Cui et al. [23] reported two homochiral 1,10-biphenol-based MOFs with chiral dihydroxyl and dimethoxy groups, respectively. A MOF containing chiral dihydroxyl auxiliaries was used as the chiral stationary phase of HPLC for enantioseparation of 1-phenylethylamine, 1-(4-fluorophenyl)ethylamine, 1-phenylpropylamine, and 1-naphthalen-1-yl-ethylamine.

In 2019, Tanaka et al. [24] reported a new homochiral MOF (*R*)-**MOF-13** with an expanded open cage (10.7 Å × 10.7 Å) (Fig. 23.7) based on the (*R*)-3,3'-bis(6-carboxy-2-naphthyl)-2,2'-dihydroxy-1,1'-binaphthyl ligand and used it as a novel chiral stationary phase for HPLC. (*R*)-**MOF-13** showed excellent performance for enantiomeric separation of several racemates, including *sec*-alcohols, sulfoxides, epoxides, lactone, 1,3-dioxolan-2-one, and oxazolidinone, in HPLC (Fig. 23.8).

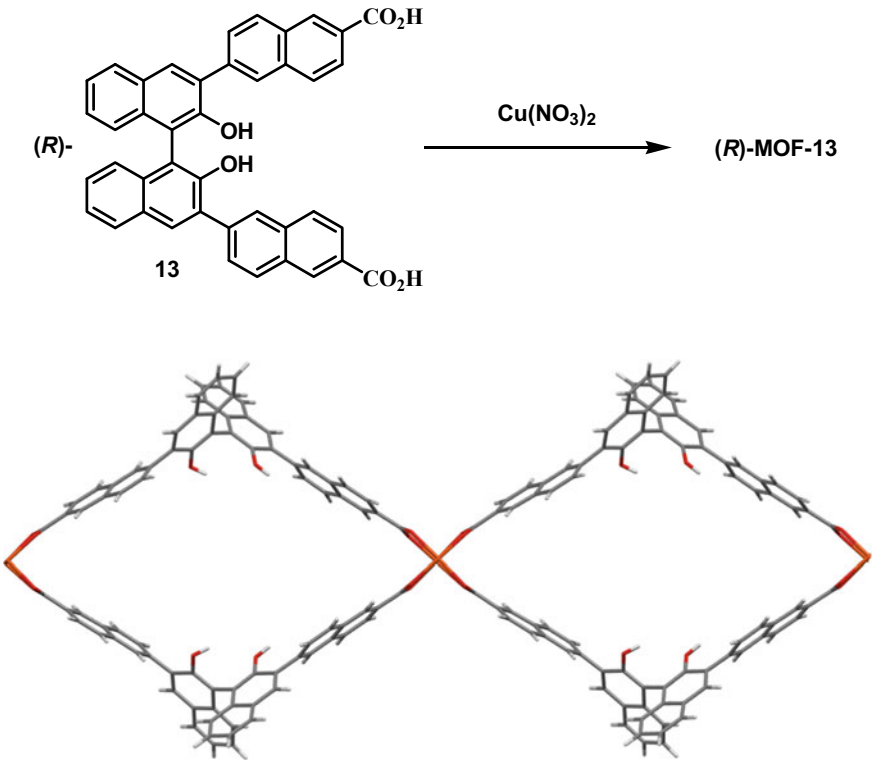

Fig. 23.7 X-ray structure of (*R*)-**MOF-13**

23.4 Conclusions

In this review, we summarize the recent progress in synthesis of novel chiral MOFs and their applications as heterogeneous catalysts in asymmetric reactions and as the chiral stationary phase of HPLC. Chiral MOFs have proven to be remarkable heterogeneous catalysts in asymmetric reactions affording high yields and excellent enantioselectivities of reactions comparable with those of homogeneous catalysts. Chromatographic separation with chiral MOFs has rapidly expanded in recent years, and more suitable chiral MOFs will be designed for separation of various organic racemates in the near future.

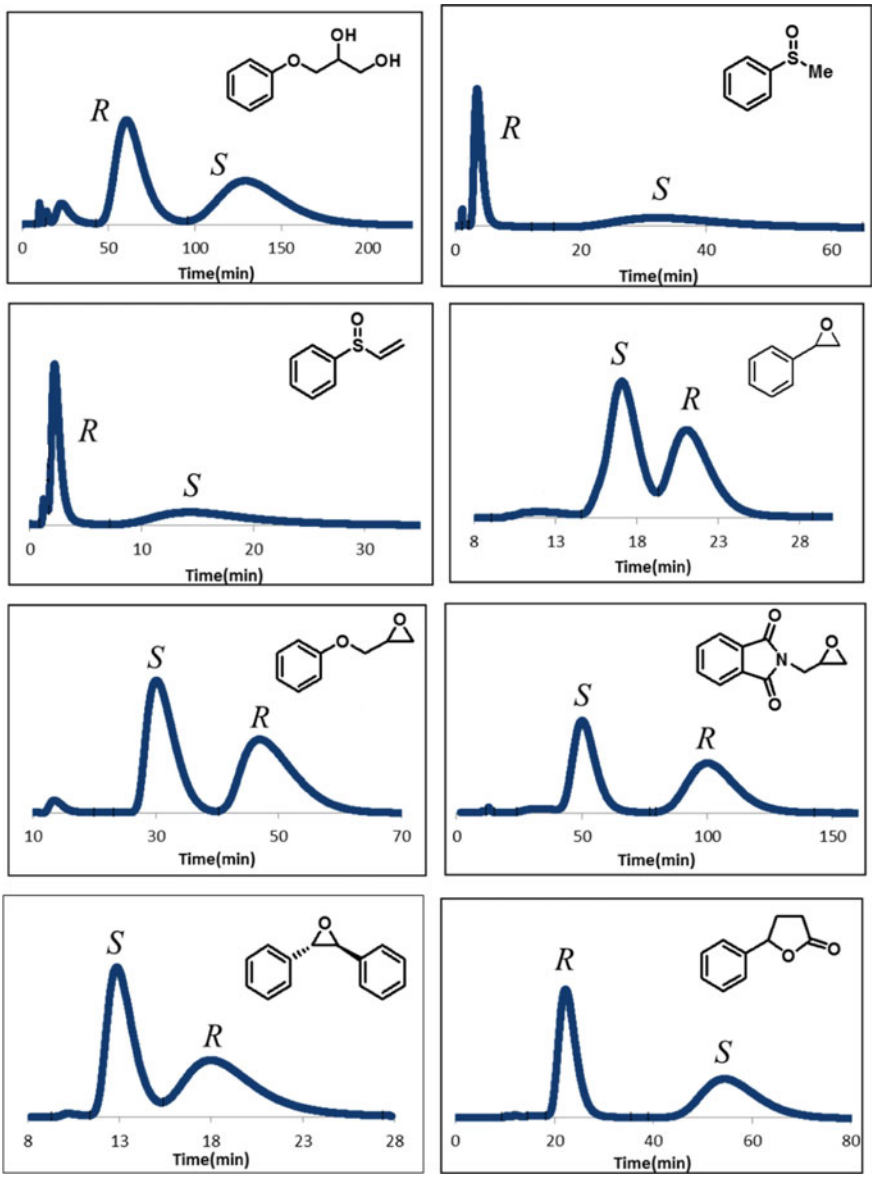

Fig. 23.8 HPLC chromatograms on (*R*)-**MOF-13** column for the separation of racemates

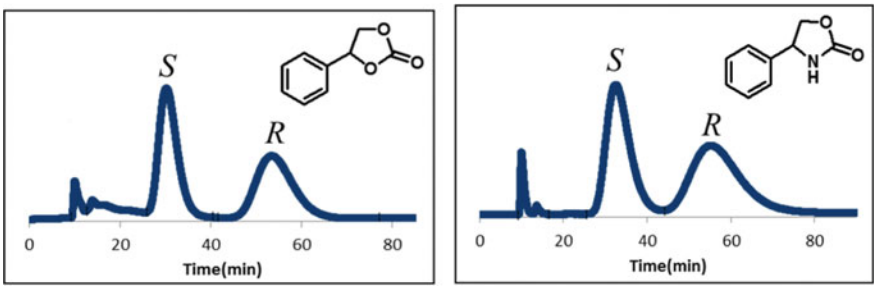

Fig. 23.8 (continued)

References

1. Cook, T.R., Zheng, Y., Stang, P.J.: Metal − organic frameworks and self-assembled supramolecular coordination complexes: comparing and contrasting the design, synthesis, and functionality of metal − organic materials. Chem. Rev. **113**, 734–777 (2009)
2. Ma, L., Abney, C., Lin, W.: Enatioselective catalysis with homochiral metal–organic frameworks. Chem. Soc. Rev. **38**, 1248–1256 (2009)
3. Peluso, P., Mamane, V., Cossu, S.: Homochiral metal-organic frameworks and their application in chromatography enantioseparation. J. Chromatogr. A **1363**, 11–26 (2014)
4. Tanaka, K., Oda, S., Shiro, M.: A novel chiral porous metal–organic framework: Asymmetric ring opening reaction of epoxide with amine in the chiral open space. Chem. Commun., 820–822 (2008)
5. Tanaka, K., Kinoshita, M., Kayahara, J., Uebayashi, Y., Nakaji, K., Morrawiak, M., Urbanczyk-Lipkowska, Z.: Asymmetric ring-opening reaction of *meso*-epoxides with aromatic amines using homochiral metal–organic frameworks as recyclable heterogeneous catalysts. RSC Adv. **8**, 28146–28159 (2018)
6. Doitomi, K., Xu, K., Hirao, H.: The mechanism of an asymmetric ring-opening reaction of epoxide with amine catalyzed by a metal–organic framework: insights from combined quantum mechanics and molecular mechanics calculations. Dalton Trans. **46**, 3470–3481 (2017)
7. Regati, S., He, Y., Thimmaiah, M., Li, P., Xiang, S., Chen, B., Cong-Gui Zhao, J.: Enantioselective ring-opening of *meso*-epoxides by aromatic amines catalyzed by a homochiral metal–organic framework. Chem. Commun., **49**, 9836–9838 (2013)
8. Tanaka, K., Kubo, K., Iida, K., Otani, K., Murase, T., Yanamoto, D., Shiro, M.: Asymmetric catalytic sulfoxidation with H_2O_2 using chiral copper metal–organic framework crystals. Asian J. Org. Chem. **2**, 1055–1060 (2013)
9. Falkowski, J.M., Sawano, T., Zhang, T., Tsun, G., Chen, Y., Lockard, J.V., Lin, W.: Privileged phosphine-based metal–organic frameworks for broad-scope asymmetric catalysis. J. Am. Chem. Soc. **136**, 5213–5216 (2014)
10. Sawano, T., Ji, P., McIsaac, A.R., Lin, Z., Abney, C.W., Lin, W.: The first chiral diene-based metal–organic frameworks for highly enantioselective carbon–carbon bond formation reactions. Chem. Sci. **6**, 7163–7168 (2015)
11. Xi, W., Liu, Y., Xia, Q., Li, Z., Cui, Y.: Direct and post-synthesis incorporation of chiral metallosalen catalysts into metal–organic frameworks for asymmetric organic transformations. Chem. Eur. J. **21**, 12581–12585 (2015)
12. Fan, Y., Ren, Y., Li, J., Yue, C., Jiang, H.: Enhanced activity and enantioselectivity of Henry reaction by the postsynthetic reduction modification for a chiral Cu(salen)-based metal–organic framework. Inorg. Chem. **57**, 11986–11994 (2018)

13. Hu, Y., Liu, C., Wang, J., Ren, X., Kan, X., Dong, Y.: TiO_2@UiO-68-CIL: A metal–organic-framework-based bifunctional composite catalyst for a one-pot sequential asymmetric Morita–Baylis–Hillman reaction. Inorg. Chem. **58**, 4722–4730 (2019)
14. Tanaka, K., Nagase, S., Anami, T., Wierzbick, M., Urbanczyk-Lipkowska, Z.: Enantioselective Diels-Alder reaction in the confined space of homochiral metal–organic frameworks. RSC Adv. **6**, 111436–111439 (2016)
15. Xia, Q., Liu, Y., Li, Z., Gong, W., Cui, Y.: A Cr(salen)-based metal–organic framework as a versatile catalyst for efficient asymmetric transformations. Chem. Commun. **52**, 13167–13170 (2016)
16. Zheng, M., Liu, Y., Wang, C., Liu, S., Lin, W.: Cavity-induced enantioselectivity reversal in a chiral metal–organic framework Brønsted acid catalyst. Chem. Sci. **3**, 2623–2627 (2012)
17. Cui, Y., Ngo, H.L., White, P.S., Lin, W.: Homochiral 3D open frameworks assembled from 1- and 2-D coordination polymers. Chem. Comm., 994–995 (2003)
18. Tanaka, K., Sakuragi, K., Ozaki, H., Takada, Y.: Highly enantioselective Friedel-Crafts alkylation of N, N-dialkylanilines with trans-β-nitrostyrene catalyzed by a homochiral metal–organic framework. Chem. Commun. **54**, 6328–6331 (2018)
19. Tanaka, K., Muraoka, T., Hirayama, D., Ohnishi, A.: Highly efficient chromatographic resolution of sulfoxides using a new homochiral MOF–silica composite. Chem. Commun. **48**, 8577–8579 (2012)
20. Tanaka, K., Muraoka, T., Otubo, Y., Takahashi, H., Ohnishi, A.: HPLC enantioseparation on a homochiral MOF–silica composite as a novel chiral stationary phase. RSC Adv. **6**, 21293–21301 (2016)
21. Zhang, M., Pu, Z., Chen, X., Gong, X., Zhu, A., Yuan, L.: Chiral recognition of a 3D chiral nanoporous metal–organic framework. Chem. Commun. **49**, 5201–5203 (2013)
22. Kuang, X., Ma, Y., Su, H., Zhang, J., Dong, Y., Tang, B.: High-performance liquid chromatographic enantioseparation of racemic drugs based on homochiral metal–organic framework. Anal. Chem. **86**, 1277–1281 (2014)
23. Peng, Y., Gong, T., Zhang, K., Lin, X., Liu, Y., Jiang, J., Cui, Y.: Engineering chiral porous metal–organic frameworks for enantioselective adsorption and separation. Nat. Commun. **5**, 4406 (2014)
24. Tanaka, K., Kawakita, T., Morawiak, M., Urbanczyk-Lipkowska, Z.: A novel homochiral metal–organic framework with an expanded open cage based on (*R*)-3,3'-bis(6-carboxy-2-naphthyl)-2,2'-dihydroxy-1,1'-binaphthyl: synthesis, X-ray structure and efficient HPLC enantiomer separation. CrystEngComm **21**, 487–493 (2019)

Part V
Solid-State Reaction

Chapter 24
Solid-State Polymerization of Conjugated Acetylene Compounds to Form π-Conjugated Polymers

Shuji Okada, Yoko Tatewaki, and Ryohei Yamakado

Abstract Since polydiacetylene derivatives are synthesized by the solid-state polymerization of butadiyne monomers, the structures of the monomers determining their alignment in the crystals are very important. By applying the molecular design strategies to obtain polymerizable monomers, several monomers with interesting structures and properties, i.e., monomers with electron-donating aromatic rings directly attached to the butadiyne moiety, gel-formable butadiyne monomers with 3,4,5-alkyloxyphenyl groups, monomers with a phenylene group sandwiched by two butadiyne moieties, and a ring monomer with two butadiyne moieties to form a tubular polymer, were synthesized and characterized.

Keywords Acetylenic compound · Solid-state polymerization · Polydiacetylene · Donor substituent · Gel · Tubular polymer

24.1 Introduction

π- Conjugated polymers are quite important materials for electronics and photonics, and their applications are based on electrical conducting and semiconducting properties, linear and nonlinear optical properties, photovoltaic property, etc. Similar to conventional polymers, most of π-conjugated polymers are synthesized in the solution state. Meanwhile, polydiacetylene is a unique π-conjugated polymer obtained by the solid-state polymerization of butadiyne monomers. Although some butadiyne monomers have been known to give colored materials in their crystalline states [1],

S. Okada (✉) · R. Yamakado
Graduate School of Organic Materials Science, Yamagata University, 4-3-16 Jonan, Yonezawa 992-8510, Japan
e-mail: okadas@yz.yamagata-u.ac.jp

R. Yamakado
e-mail: yamakado@yz.yamagata-u.ac.jp

Y. Tatewaki
Division of Applied Chemistry, Tokyo University of Agriculture and Technology, 2-24-16 Naka-Cho, Koganei 184-8588, Japan
e-mail: ytatewa@cc.tuat.ac.jp

M. Sakamoto and H. Uekusa (eds.), *Advances in Organic Crystal Chemistry*,
https://doi.org/10.1007/978-981-15-5085-0_24

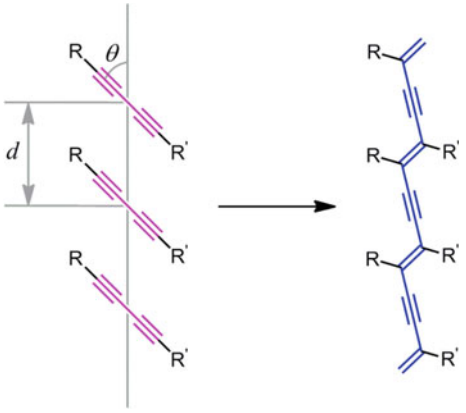

Fig. 24.1 Solid-state polymerization scheme of butadiyne monomers (left) to the corresponding polydiacetylene (right). Distance d and angle θ are the packing parameters of the monomers. The appropriate conditions for the polymerization are $d \approx 5$ Å and $\theta \approx 45°$

the reaction and the products were first clarified by G. Wegner [2]. The monomer used was hexa-2,4-diyne-1,6-diyl bis(*p*-toluenesulfonate) (PTS), and the crystal reacted thermally was subjected by X-ray crystallographic analysis. The reaction scheme was explained to be 1,4-addition polymerization of butadiyne monomers to give polymers with a π-conjugated backbone composed of the alternating sequence of the carbon-carbon double and triple bonds. Since the mobile range of molecules in the crystals is limited, monomer arrangement in the crystals is definitely important for smooth progress of the polymerization in the crystals. The conditions for the solid-state polymerization of the butadiyne monomers to give polydiacetylenes have been found as follows: Distance d between the adjacent monomer molecules along the translation direction, which coincides to the polymerization direction, is approximately 5 Å, and angle θ between the translation direction and the direction of the linear butadiyne rod structure in the monomer is approximately 45° as shown in Fig. 24.1 [3, 4]. Hereafter, in this chapter, butadiyne moieties and their conjugated substituents are shown in magenta color, and polydiacetylene backbones are shown in blue color in the chemical structures. The polymerization can be stimulated by thermal treatment, photoirradiation, and irradiation of high-energy electromagnetic waves such as X-ray and γ-ray, depending on the monomers. Since the polymerization progresses under the crystal lattice control, i.e., generally topochemical, and topotactic in some cases, the stereoregular polymer structures are obtained. From the point of view of polymer synthesis, stereoregular synthesis is one of the important subjects, and the solid-state polymerization satisfies this point. Another important issue in polymer synthesis is the molecular-weight control. Since the polymerization direction in the crystals is fixed along a certain crystallographic axis, we can control the molecular weight by the length of the crystal along the polymerization direction. In the two-dimensional crystals, synthesis of a polydiacetylene molecule by polymerization from a stimulated monomer to the monomer beside a defect has been demonstrated [5]. Nanocrystals of butadiyne monomers with controlled sizes are also useful to prepare molecular-weight-controlled polydiacetylenes when the

polymerization occurs from one crystal surface to the other surface on the opposite side [6, 7].

Due to the formation of the π-conjugated backbones after the polymerization, the resulting polydiacetylenes usually have the excitonic absorption bands with the maxima in the wavelength region approximately between 500 and 700 nm, showing characteristic blue to red colors. As mentioned later, when the materials after the solid-state reaction of butadiyne derivatives do not show such characteristic bands, the reaction may not proceed in the 1,4-addtion manner to form the polydiacetylene structure. Although the backbone structure of polydiacetylene is fixed to the ene-yne alternating sequence, its color varies depending on the structural conditions. Generally, it is believed that blue color corresponds to planer extended π-conjugated backbone and red color corresponds to slightly disordered or undulated π-conjugated backbone, respectively. Thus, the polymer color can be altered through conformational changes of the substituents triggered by external stimuli, which result in conformational changes of the π-conjugated backbone. Based on this mechanism, a variety of bio- and chemo-sensors have been developed [8, 9].

Meanwhile, applications of polydiacetylenes for electronics and photonics have been started first as third-order nonlinear optical materials. In 1969, the third-order nonlinear optical susceptibilities ($\chi^{(3)}$s) of polydiacetylenes evaluated by third-harmonic generation (THG) were reported to be comparable to or more than those of semiconductors, which have been known as the materials with large $\chi^{(3)}$s [10]. On the other hand, although many of π-conjugated polymers have been investigated as conducting polymers, electrical conductivities of polydiacetylenes are generally poor. This is because high crystallinity of the polymer prevents dopant immersion and effective chemical doping of the π-conjugated backbones cannot be achieved. Semiconducting electrical conductivities in the crystalline states were reported, for example, for the polydiacetylene obtained by polymerization of the doped monomer crystals or doping during polymerization [11].

In this article, we review some polydiacetylenes prepared to improve their physical properties. The first topic contains polydiacetylenes substituted by electron-donating aromatic rings directly bound to the backbone. They may be used as hole-transport materials. Also, if they form charge-transfer complexes by combining with appropriate electron-accepting species, electrically conducting monomers and polymers may be obtained. The second topic is related to polydiacetylenes with fibrous morphology. When the π-conjugated backbones are formed along the fiber direction, the resulting fibrous crystals may be used as conducting wires for molecular electronics. The third topic is related to polymerization of the monomers with two butadiyne moieties, which may give ladder-type polydiacetylenes with unique properties.

24.2 Aryl-Substituted Butadiyne Monomers

In order to develop materials for all-optical switching devices, studies on further improvement of the third-order nonlinear optical properties of polydiacetylenes were performed. Although it was clearly demonstrated that the large $\chi^{(3)}$s were originated from polarization along the π-conjugated backbones, their enhancement has not been easy because the substituents of the conventional polydiacetylenes are composed of methylene chains and the π-conjugated backbone structures are quite similar among them. Thus, attachment of π-conjugated substituents to the backbone to modify the π-conjugated structures was proposed to increase $\chi^{(3)}$s. However, in the early stage of the research on polydiacetylenes, only few diphenylbutadiyne derivatives were known to be polymerizable in the solid state [12, 13]. Many of diphenylbutadiyne monomers do not align in the polymerizable stack in the crystals resulting in stable compounds. In order to obtain polymerizable butadiyne monomers with one aromatic ring at least, key structures for the polymerizable stacks were extracted from the crystal structures of the polymerizable monomers. They were methylene group with the bent structure for easy stacking, the alkyl chain for intermolecular packing, urethane or amide groups to form intermolecular hydrogen bonding, and fluorinated aromatics with the characteristic electronic effect [14]. By using these structural features, various polydiacetylenes with π-conjugation between the backbone and the substituents have been prepared and characterized [15]. For example, symmetrical diphenylbutadiyne derivatives with fluorinated substituents such as fluorine atoms or trifluoromethyl groups were often found to be polymerizable [16] although polymerization probabilities of asymmetrical derivatives with one fluorinated phenyl group became low [17]. Introduction of urethane group in the alkyl substituent has been known to be effective to obtain polydiacetylenes from symmetrically substituted monomers [18], and polymerization probabilities of arylbutadiyne derivatives were found to be improved by attaching the alkyl-urethane group [19, 20]. By using this urethane substituent effect, the solid-state polymerization of butadiyne derivatives with electron-donating aromatic rings were studied.

24.2.1 Aniline and Carbazole Derivatives

Aniline and carbazole rings work as electron-donating substituents. Thus, 4-(dimethylamino)phenyl [21, 22], 4-(*N*-carbazolyl)phenyl [23], and 3-(*N*-phenyl)carbazolyl [24] groups were introduced as one of the butadiyne substituents, and the other substituent contained butylene and urethane groups (Fig. 24.2). Although all compounds prepared showed absorption in the visible region after UV irradiation, their diffuse reflectance spectra were able to be roughly classified into two types. One is the spectra with absorption maxima in the wavelength range between 580 and 672 nm (Fig. 24.3a). This type of absorption is typical for polydiacetylenes as mentioned in the introduction. The other spectra showed absorbance

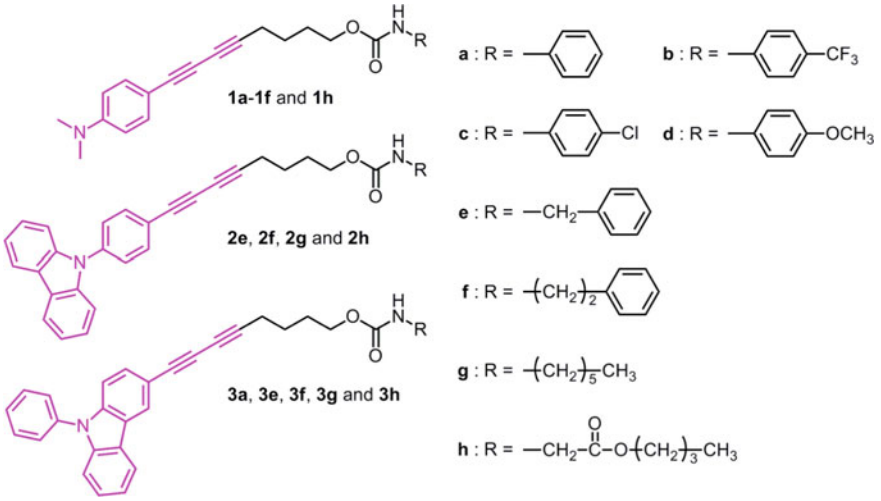

Fig. 24.2 Structures of butadiyne monomers with 4-(dimethylamino)phenyl, 4-(*N*-carbazolyl)phenyl or 3-(*N*-phenyl)carbazolyl group

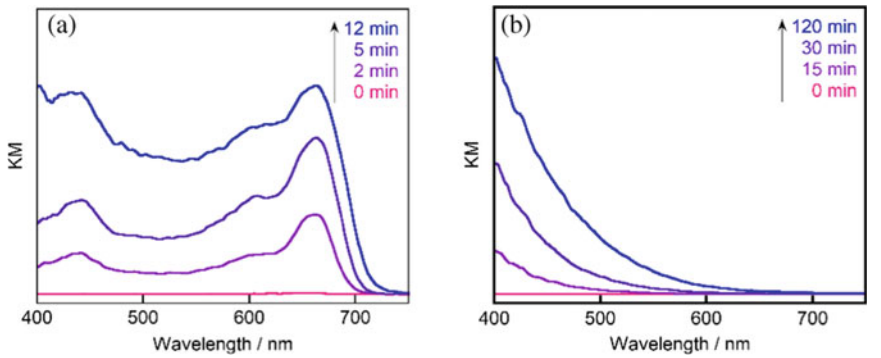

Fig. 24.3 Typical examples of two types of diffuse reflectance spectra of the butadiyne derivatives obtained during irradiation of UV light at 254 nm: **a** Spectra of **1b** with absorption maxima in the visible region and **b** spectra of **1d** without no absorption maxima in the visible region

increase from the absorption edge to the shorter-wavelength side without absorption maxima in the visible region (Fig. 24.3b). Absorption of this type is often observed for mono-substituted butadiyne derivatives [25, 26]. Although these spectral differences have been recognized [27], the structural differences have not been clearly explained. Fortunately, since eight crystal structures of compounds **1** and **2** were able to be solved, the relation between the absorption spectra and the reaction scheme was found. Table 24.1 summarizes some important data obtained by the X-ray crystallographic analysis to explain the polymerization scheme and the absorption maximum of the polymers. Geometrical relations of the distances between

Table 24.1 Monomer conformation, packing parameters d and θ, carbon-carbon distance between adjacent molecules, and absorption maximum wavelength (λ_{max}) of the polymer

Compound	Butylene conformation[a]	d^b/Å	θ^b/°	C1···C2[c] C3···C4[c]/Å	C1···C4[c]/Å	λ_{max}/nm
1a	*gtg*	5.19	47.4	4.47	3.83	637
1b	*ttt*	4.99	51.6	4.34–4.35	3.97	660
1c	*gtg*	5.16	48.1	4.45	3.86	672
1d	*ttt*	4.97–5.07	70.5–71.3	4.73–4.85	5.10–5.27	–
1e	*gtg,ttt*	5.94	41.1, 53.3–55.7	5.09–5.12, 5.29–5.45	3.97, 4.77	–
1f	*ttt*	5.11	45.7	4.35–4.37	3.66	610
2e	*ttt*	5.09	61.4	4.63	4.67	–
2f	*ggg*	5.07–5.17	48.5–49.8	4.29–4.50	3.85–3.94	580

[a]Symbols *g* and *t* indicate *gauche* and *trans* forms of ethylenes in the butylene group between butadiyne and urethane moieties
[b]See Fig. 24.1
[c]See Fig. 24.4

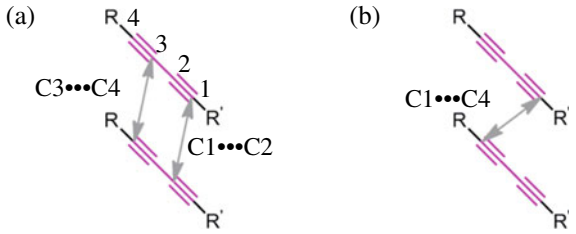

Fig. 24.4 Reacting carbons of adjacent butadiyne monomers for **a** 1,2-addition and **b** 1,4-addition, respectively. Substituent R corresponds to aryl groups of compounds **1** and **2**, and butadiyne carbons are numbered from the R' side. Symbol C$m\cdots$Cn indicates the distance between carbon m and carbon n between the adjacent monomers

acetylenic carbons of the adjacent monomers are shown in Fig. 24.4. Distances C1$\cdots$C2 and C3$\cdots$C4 (d_{12}) in Fig. 24.4a are related to reactivity via the 1,2-addition scheme while distance C1$\cdots$C4 (d_{14}) in Fig. 24.4b is for the 1,4-addition scheme. Focusing on the compounds showing absorption maxima, ds are 4.99–5.19 Å near 5 Å and θs are 45.7–51.6° near 45°, which satisfy the condition for 1,4-addition polymerization. In these compounds, the d_{14}s are shorter than the corresponding d_{12}s, suggesting 1,4-addition is much easier. Among the compounds without absorption maximum, **1e** has a large d value of 5.94 Å, which is an obstacle for the polymerization. From the point of view of the monomer alignment, all analyzed monomers except **1e** have intermolecular hydrogen bonding between the urethane groups along the monomer stacking direction. However, for **1e**, the hydrogen-bonding direction and the stacking direction are different, which causes the large d value. For **1d** and **2e**, the d_{14}s are longer than the corresponding d_{12}s, which induces 1,2-addition rather than 1,4-addition. From these results, it is concluded that the absorption bands in the visible region like in Fig. 24.3a are essential for the polydiacetylene structure obtained by 1,4-addition. For the monomer showing the spectra like in Fig. 24.3b, the regular polydiacetylene structure should not be obtained. It is interesting that all-*trans* conformation of butylene in the monomers is not essential in the regularly polymerizable stack.

Except for the monomers in Table 24.1, **2g**, **2h**, **3e**, **3f**, **3g,** and **3h** showed excitonic absorption bands of polydiacetylene, while **1h** and **3a** did not. Regarding to the hole-transport property, higher HOMO levels are important. For the monomers, the DFT calculation results suggested that the HOMO energy order from lower to higher levels was **2** < **3** < **1**. However, measured ionization potentials of the polymerized **1c**, **2 h,** and **3e** were 5.9, 5.4, and 5.2 eV, respectively. Thus, the HOMO energy order of the polymers was estimated to be **1** < **2** < **3**. One of the possible reasons for the experimental low HOMO level of the polymer of **1** may be its oxidation due to the higher HOMO level than the others. Since the ionization potential of polydiacetylene from 1,6-di(*N*-carbazolyl)butadiyne (DCHD) [28], which is a well-known monomer substituted by carbazolyl groups without conjugation to the butadiyne moiety, was obtained to be 6.2 eV in the same measuring conditions, the conjugation effect of

carbazolyl group to the polymer backbone in **2** and **3** seemed to be effective to elevate the HOMO levels.

As was demonstrated by the calculation results on the HOMO levels, **1** has the highest energy among them, and formation of the charge-transfer complexes with electron acceptors was expected. However, strong acceptors such as tetracyanoethylene (TCNE) and 7,7,8,8-tetracyanoquinodimethane (TCNQ) were reported to react with ethynylaniline derivatives [29, 30]. Thus, weaker acceptors of 2,4,7-trinitrofluorenone (TNF), 2,3-dichloro-5,6-dicyano-*p*-benzoquinone (DDQ), *p*-benzoquinone, and chloranil were mixed with **1h** [21]. When solution of **1h** was combined with acceptor solutions, the color changes were clearly observed for TNF and DDQ. From their NMR studies, it was found that TNF formed the charge-transfer complex with **1h** but DDQ reacted with **1h** to give a product with a cyclobutene ring due to the [2 + 2] cycloaddition of –C≡C– in **1h** and –CCN=CCN– in DDQ. Even in the case of weaker acceptors of *p*-benzoquinone and chloranil, their co-grinding with **1h** resulted in color-changed products due to charge-transfer complex formation. All products from **1h**, i.e., the adduct with DDQ and the charge-transfer complexes with TNF, *p*-benzoquinone, and chloranil, showed a broad absorption band in the visible region in their diffuse reflectance spectra, and the absorption edge wavelengths were between approximately 750 and 1000 nm, depending on the compounds.

24.2.2 Pyrene Derivatives

Pyrene is an aromatic hydrocarbon with electron-donating ability and fluorescent property, and 1-pyrenyl group was introduced as a substituent of butadiyne as shown in Fig. 24.5. When UV light at 254 nm was irradiated to yellowish compound **4**, the color turned green [31]. From the absorption spectra, it was found that the new band with the maximum at approximately 620 nm appeared by UV irradiation, and this band was assigned to the polydiacetylene structure. Greenish color of the polymer is explained by the color mixing of yellow from the pyrenyl group and blue from the polymer backbone. Since the absorption edge wavelength of monomer

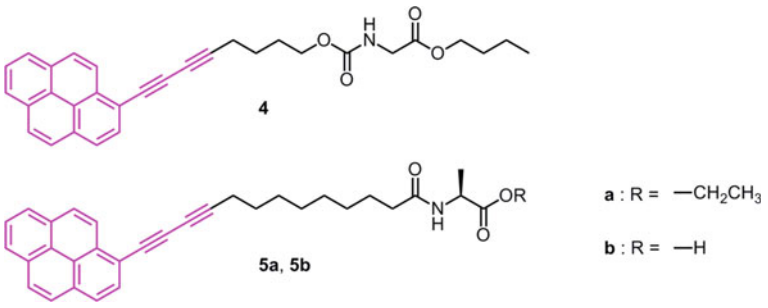

Fig. 24.5 Structures of butadiyne monomers with 1-pyrenyl group

4 is longer than 400 nm, photopolymerization can be stimulated even by UV light at 302 and 365 nm, which is contrast to the polymerization of the conventional butadiyne monomers. This clearly indicates the conjugation effect of the pyrenyl group to the butadiyne moiety. Since the absorption spectra of the polymers obtained by irradiation of the UV light at different wavelengths almost coincided, the polymer structures were found to be the same irrespective of the irradiated wavelength.

Synthesis of compounds **5a** and **5b** with the alanine residue at the end was inspired by the butadiyne derivatives with an alkyl group instead of the pyrenyl group of **5a** and **5b**, which formed nanoassembled structures [32]. Upon irradiation of UV light at 254 or 365 nm, **5a** polymerized to be the polydiacetylene with absorption maximum at 624 nm while **5b** polymerized in irregular manner [33]. For these compounds, the reprecipitation method [34], in which acetone solution of the compound was injected into pure water with vigorous stirring, was applied to form nanoaggregates. The sizes of nanoaggregates prepared at ambient temperature were approximately 105 nm for **5a** and 50 nm for **5b**, which increased by elevating temperature. When the preparation temperature was set at 60 °C, a part of **5a** coagulated to form helical nanoribbon structures with the typical width and length of approximately 100 nm and more than 1 μm, respectively. The origin of the helicity is considered to be chirality of the alanine residue. For **5b**, circle domain structures with the size of hundreds of nanometers were observed. Upon UV irradiation, both aggregates did not show characteristic bands of polydiacetylene suggesting that the main reaction was not 1,4-addition. Namely, monomer stacking structures of **5a** are different between the crystals and the nanoaggregates.

24.2.3 Tetrathiafulvalene Derivative

Tetrathiafulvalene (TTF) is a strong electron donor, which is often used to prepare charge-transfer complexes by combining with electron acceptors like TCNQ. Thus, monomer **6** with the TTF moiety in Fig. 24.6 was synthesized, and its polymerization behaviors were investigated in the crystals and the nanoaggregates [35]. Size of the nanoaggregates obtained by the reprecipitation method was 80 ± 10 nm. Although **6** in the crystalline state showed the absorption band at approximately 580 nm upon

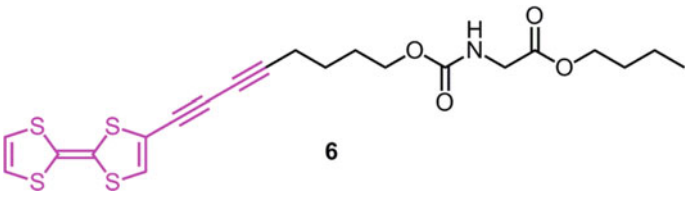

6

Fig. 24.6 Structure of a monomer with a butadiyne moiety connected to a tetrathiafulvalene ring

irradiation of UV light at 254 nm, no absorption peaks were observed for the nanoaggregates in the same condition, indicating different stacking structures between the crystals and the nanoaggregates. The charge-transfer complex of **6** with 2,5-difluoro-7,7,8,8-tetracyanoquinodimethane (F_2TCNQ) in the nanoaggregate states was also prepared by the reprecipitation method using acetone solution of **6** and F_2TCNQ in the mixing ratio of 1:1 for injection to pure water. The nanoaggregate size was approximately 140 ± 70 nm. Since the absorption bands in the visible-NIR spectra, assigned to TTF radical cation and F_2TCNQ radical anion, were confirmed, the charge-transfer complex seemed to be formed. However, upon UV irradiation, the complexed monomer showed absorption decrease suggesting that the charge-transfer state was decomposed and the regular solid-state polymerization did not progress at least.

24.3 Monomers Showing Fibrous Morphology

When we can prepare fibrous crystals of butadiyne monomers and stimulate the solid-state polymerization along the fibrous direction, fibers with large mechanical strength may be realized. In addition, they may be also used as conducting wires for molecular electronics, if fiber diameters are down to a nanoscale and appropriate doping is carried out. When nanowires are prepared in solvent in high concentration, the gel state generally appears. Although some gel-formable polydiacetylenes have been reported [36–38], the monomer structures were slightly complicated. Thus, simplified structures were designed. Since 3,4,5-alkyloxyphenyl group, which can be derived from gallic acid, is a useful substituent for nanoassembling of functional species, it was introduced at both ends of the butadiyne monomers [39, 40]. Urethane or amide groups were placed between the end groups and the central butadiyne moiety to ensure the formation of the polymerizable stacks by intermolecular hydrogen bonding. Structures of the related monomers are shown in Fig. 24.7.

In monomers **7** and **8**, the methylene numbers between butadiyne and urethane moieties are different, i.e., four for **7** and three for **8**, respectively. The C=O vibration of **7** and **8** with dodecyloxy groups is approximately 1700 cm^{-1}, while that of the corresponding methoxy derivatives is approximately 1725 cm^{-1}, indicating that intermolecular hydrogen bonding becomes stronger by attaching long alkyl chains. However, there is large difference in the melting points of **7** and **8**, i.e., 74 and 109 °C, respectively, and stacking difference depending on the methylene chain number was found to be also an important factor for determining the physical properties besides the hydrogen bonding. Upon UV irradiation, the absorption bands at the longest wavelength of both monomers appear approximately at 580 nm. Conversion from a monomer to the corresponding polymer by γ-ray irradiation of **7** was higher than that of **8**. For monomers **9**–**11**, the hydrogen-bonding group was changed to amide group, and its direction and position were changed. The melting points reflecting crystallization states were investigated using DSC in detail, and, at least, two polymorphs were found for each of **9**–**11**. Upon UV irradiation, the absorption bands

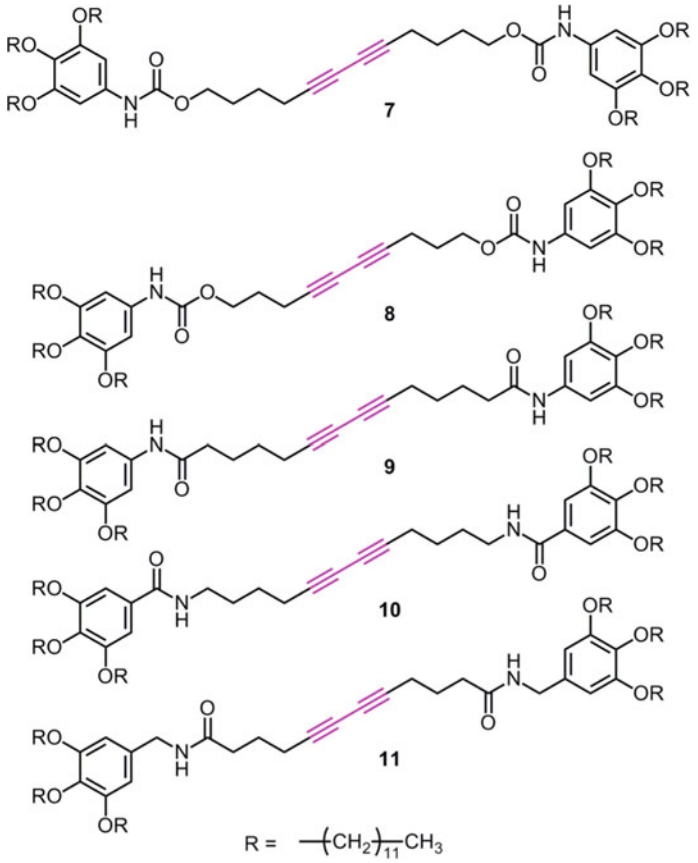

Fig. 24.7 Structures of butadiyne monomers with 3,4,5-tri(dodecyloxy)phenyl groups

at the longest wavelength of **9**, **9, 10**, and **11** were approximately at 640, 570, and 530 nm, respectively, and these wavelengths varied depending on the crystallization conditions except for **11**.

Gel formation was confirmed as follows. The solution with a determined concentration was prepared in a test tube and was cooled in an ice bath. When the test tubes were turned upside down and the materials inside did not flow and was fixed, the mixture was decided to be in the gel state. For chloroform and tetrahydrofuran, all compounds did not form gels even in the solution with the 5wt% concentration. The results for other solvents are summarized in Table 24.2. In these experimental conditions, the urethane derivatives form gels in carbon tetrachloride and toluene but not in diethyl ether. Meanwhile, opposite results were obtained for the amide derivatives. In general, transparent or translucent gels were formed in nonpolar solvents, and opaque gels were formed in polar solvents. These appearance differences were

Table 24.2 Gel formability of **7**–**11** in various solvents

Solvent	Gel formability[a]				
	7	**8**	**9**	**10**	**11**
Hexane	T(1)	T(1)	T(2)	T(3)	T(1)
Cyclohexane	T(1)	T(1)	T(3)	T(3)	T(3)
Carbon tetrachloride	T(2)	T(1)	–	–	–
Toluene	T(2)	T(2)	–	–	–
Diethyl ether	–	–	T(2)	O(3)	O(2)
Ethyl acetate	O(1)	O(1)	O(2)	O(1)	O(2)
Acetone	O(2)	O(1)	O(1)	O(1)	O(2)
Ethanol	–	O(1)	O(1)	O(5)	O(1)

[a]Symbols for the gel formability: T, formation of transparent or translucent gels; O, formation of opaque gels; –, no gel formation even in the 5wt% concentration solution. Numbers in parentheses are minimum concentration for gel formation in wt%

originated from their nanostructures, which were confirmed by the SEM observation of the corresponding xerogels. For the transparent or translucent gels, the fibers thinner than 100 nm were observed (Fig. 24.8a). However, for the opaque gels, the fibers thicker than 400 nm, which is comparable to the visible-light wavelengths, were found (Fig. 24.8b), and they causes light scattering. All these gels were found to be photopolymerizable. Although gels from **7** and **8** were reported to be nonpolymerizable [39], their polymerizable gels were able to be obtained in the conditions different from the reported ones.

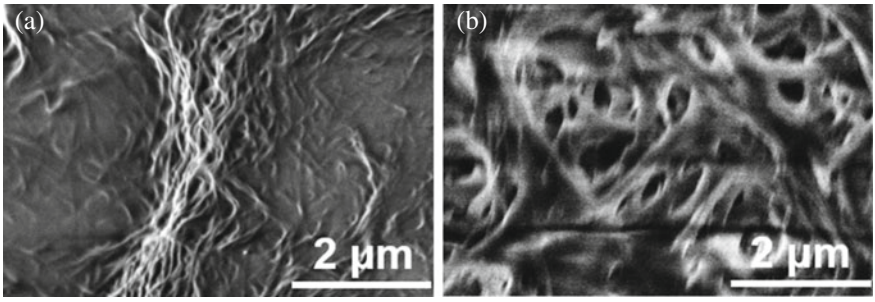

Fig. 24.8 SEM images of xerogels of **10** obtained from **a** cyclohexane and **b** ethyl acetate. They correspond to transparent and opaque gels, respectively. Reprinted with permission from ref. [40]. Copyright 2017 by the Chemical Society of Japan

24.4 Monomers with Two Butadiyne Moieties

When the monomers have two polymerizable moieties and are fully polymerized, one-dimensional ladder polymers or two-dimensional network polymers can be obtained depending on the monomer structures and the polymerization sites, which will be discussed later. Stepwise polymerization scheme of the monomers with two butadiyne moieties to form the ladder polymers are displayed in Fig. 24.9. In previous studies, the monomers with two butadiyne moieties have already been synthesized. For monomers with two butadiyne moieties connected by a methylene chain, both moieties reacted to give the ladder polymer when the methylene numbers are eight and four. When the methylene number is two, only one butadiyne moiety reacted to form the single-chain polydiacetylene. This result suggested that polymerization of a butadiyne moiety affects the conformation of another butadiyne near the polymerized butadiyne moiety [41]. Similar interference between two butadiyne moieties was also observed for the monomers with two diphenylbutadiyne moieties and amide groups [42]. Meanwhile, polymerization of the monomers with two butadiyne moieties connected by acetylene sequence of $-(C{\equiv}C)_n-$ was also investigated. For the monomer with $n = 0$, i.e., octatetrayne, asymmetric polymerization was progressed, and butadiynyl-substituted polydiacetylene with deep blue color was first formed [43]. The further polymerization stimulated by the thermal treatment gave less-crystalline brownish polymers [44]. For the monomers with $n = 1$ and 2, i.e., decapentayne and dodecahexayne [45, 46], the first step of polymerization is the same as the tetrayne derivatives, and the second step of polymerization also progressed to form ladder polymers, in which two conjugated backbones were

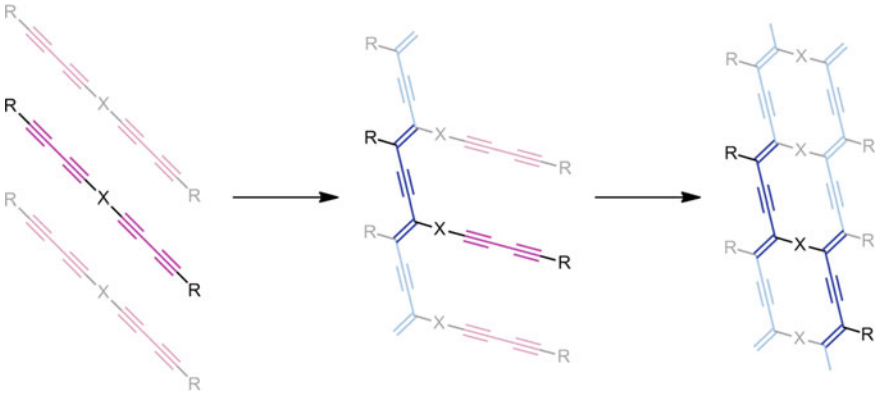

Fig. 24.9 Stepwise polymerization scheme of the monomers with two butadiyne moieties to form the ladder-type polydiacetylene. A monomer and the corresponding monomer unit are highlighted. One of the butadiyne moieties of the monomer (left) polymerizes via 1,4-addition to form single-chain polydiacetylene (middle), in which butadiyne moieties remains in the substituents. The following 1,4-addition polymerization of the butadiyne moieties in the substituents gives ladder-type polydiacetylene (right)

connected by conjugated acetylenes in each repeating unit. The resulting polymers showed unique absorption bands at the longer wavelength than the excitonic bands of the polydiacetylene, which were considered to be originated from π-conjugation between two π-conjugated backbones. On the other hand, in the case of the monomer with two butadiyne moieties connected by $-(CH{=}CH)_3-$ in the all-*trans* form, regular polymerization did not occur [47].

24.4.1 Monomers with Phenylene Linkage

As mentioned above, when the π-conjugated linkage is introduced between two butadiyne moieties, π-conjugation between two polydiacetylene backbones is expected. Since phenylene group can be another π-conjugated linkage, the related compounds of **12** and **13** in Fig. 24.10 with phenylene and 2,3,5,6-tetrafluorophenylene groups, respectively, were synthesized, and their polymerization behaviors were studied [48]. It was found that **12** was photostable and **13** polymerized to give the single-chain polydiacetylene, whose further polymerization was impossible. Thus, two approaches were performed to change their polymerization conditions.

The first one was cocrystallization of these two monomers [49]. Solid-state polymerization of the cocrystals affords copolymers of polydiacetylene, whose properties may be modified depending on the mixing ratio of the comonomers. Although the monomer structures of **12** and **13** are the same except the central phenylene groups, their crystal structures are apparently different because of different polymerization behaviors. Thus, cocrystallization conditions were first investigated. Single melting point and single crystal-structure of the crystals were confirmed by the DSC and powder X-ray diffraction measurements, respectively, as evidences of cocrystal formation. The cocrystals of **12** and **13** were prepared by the slow-evaporation method using dichloromethane. The melting points of **12** and **13** are 120 and 140 °C, respectively. When the molar mixing ratio of **13** was low, two endothermic peaks were observed in the temperature range up to 150 °C in the DSC thermograms. However, when the molar mixing ratio of **13** was approximately 60% or more,

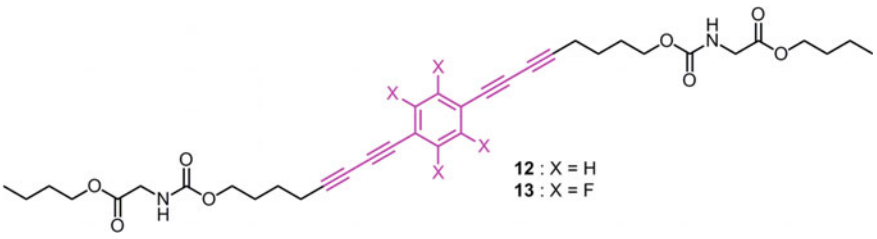

Fig. 24.10 Structures of bis(butadiynyl)benzene derivatives

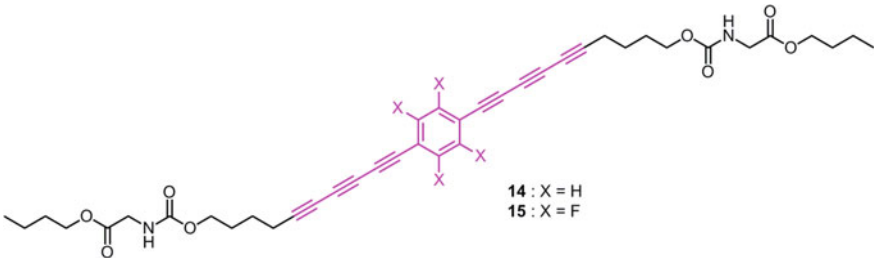

Fig. 24.11 Structures of bis(hexatriynyl)benzene derivatives

single melting point around 140 °C was observed. Because of the specific interaction between arenes and the corresponding perfluoroarenes [50], formation of the 1:1 cocrystals was considered. However, this cocrystal combination was found to be not the case. In the powder X-ray diffraction experiments, both diffraction peaks of **12** and **13** were observed when the molar ratio of **13** was low. However, as the molar ratio of **13** increased, the diffraction peaks corresponding to **12** disappeared and only the diffraction peaks similar to **13** remained. This indicates that **12** is incorporated in the crystal lattice of **13**. Actually, the cocrystals with the 3:7 mixing ratio of **12**:**13** were found to be photopolymerizable to show the absorption band around 700 nm.

The second approach was to extend conjugated acetylenic moieties from butadiyne to hexatriyne [51]. Generally, reactivity of butadiyne derivatives is less than that of the corresponding more acetylene-conjugated compounds. Accordingly, hexatriyne derivatives **14** and **15** in Fig. 24.11 were expected to be more reactive than the corresponding butadiyne derivatives **12** and **13**, respectively. Actually, in addition to **15**, polymerization of **14** was also confirmed irrespective of no polymerization of the corresponding butadiyne derivative **12**. Photopolymerization of these monomers was able to be stimulated by irradiation of UV light at 254 and 365 nm. Upon irradiation of UV light at 254 nm, **14** first showed the absorption peaks at 637 and 586 nm with a shoulder band at the longer wavelength of approximately 690 nm. The similar absorption bands were also observed when irradiated with UV light at 365 nm. In contrast, **15** showed different absorption spectra depending on the irradiated wavelengths. When **15** was irradiated with UV light at 254 nm, the absorption peak at 622 nm with a shoulder band at approximately 580 nm, whose structures were similar to the absorption peaks at 637 and 586 nm of **14** and characteristic of polydiacetylene, were observed. Meanwhile, upon irradiation of UV light at 365 nm to **15**, the absorption peak appeared at the wavelength approximately 100 nm longer, i.e., a small band at 743 nm with the broad band at 654 nm. Although the reason for the different behavior of **15** depending on the irradiated wavelengths is unclear, the produced polymer with absorption at the longer wavelengths may be unstable to UV light at 254 nm. From the FT-IR spectra to monitor intensity changes of the C≡C stretching vibration peak depending on UV irradiation time, conversion of **14** by UV light at 254 nm was found to be low but that of **15** by UV light at 365 nm was estimated to be approximately 60%. This meant approximately half of the hexatriyne moieties

reacted. From the detailed analysis of **15** using ^{13}C-NMR spectra, it was clarified that one of two hexatriyne moieties reacted to form the single-chain polydiacetylene. The 1,4-polymerization sites were found to be at the first acetylenic carbon next to the methylene chain and the fourth acetylenic carbon from the methylene chain, i.e., polydiacetylene substituted by 2-[4-(hexatriynyl)phenyl]ethynyl groups was formed. Although further polymerization was attempted on cocrystals of **13** with **12** and crystals of **14** and **15**, it was hard to obtain the polymers with two polydiacetylene backbones linked by arylene groups from these monomers.

24.4.2 Ring Monomer with Nonconjugated Linkage

As ladder polymers are obtained from linear monomers with two butadiyne moieties, tubular polymers are expected to be formed from ring monomers with butadiyne moieties. There were several examples of the ring monomers with one or two butadiyne moieties [13, 52, 53]. If some parts of the ring structure are composed of methylene chains, the resulting tubular polymers seem to be soft in contrast to rigid tubular polymers like carbon nanotubes. Molecular inclusion ability in the polymer tubes may show interesting phenomena such as specific molecular transport and specific interaction between the tube wall and included molecules.

As described in Sect. 24.3, butadiyne derivatives with 3,4,5-alkyloxyphenyl groups at ends give polydiacetylenes with nanofibrous morphology. Based on this molecular design, synthesis of a tubular polydiacetylene was planned [54]. Compound **10** was selected as a basic structure, and one of dodecyl groups on the phenyl rings was converted to the nonylene linkage by design to connect two butadiyne derivatives, resulting in a ring monomer **16** (Fig. 24.12). It was actually synthesized by the copper-catalyzed oxidative coupling reaction of the precursor **17** (Fig. 24.12). The structure of **16**, purified finally by the gel permeation chromatography, was confirmed by the following features. In the ^{1}H-NMR spectrum, the terminal acetylene protons were not detected. Although aromatic protons of **17** were observed at the same chemical shift due to free rotation of the aromatic ring, those of **16** were observed as a pair of doublet peaks suggesting the fixed ring structure. The MALDI-TOF mass spectrum clearly indicated existence of the species with the molecular weight corresponding to **16**. Interestingly, in spite of similar molecular weights, melting point of **16** is much higher than that of **17**, i.e., 153.5 and 107.3 °C, respectively.

Cyclic compound **16** was found to crystallize in two modifications I and II. It is not surprising because **10** as the basic structure also showed more than one crystalline forms. Modification I solidified from chloroform-methanol mixture showed the absorption bands around 500 nm characteristic of polydiacetylene upon UV irradiation. In contrast, absorption changes of modification II solidified from chloroform-hexane mixture were similar to those displayed in Fig. 24.3b indicating irregular polymerization. When the solution of **16** in chloroform-methanol mixture was drop-casted and dried, the nanofibrous structures with the diameter of 80 ± 30 nm like in

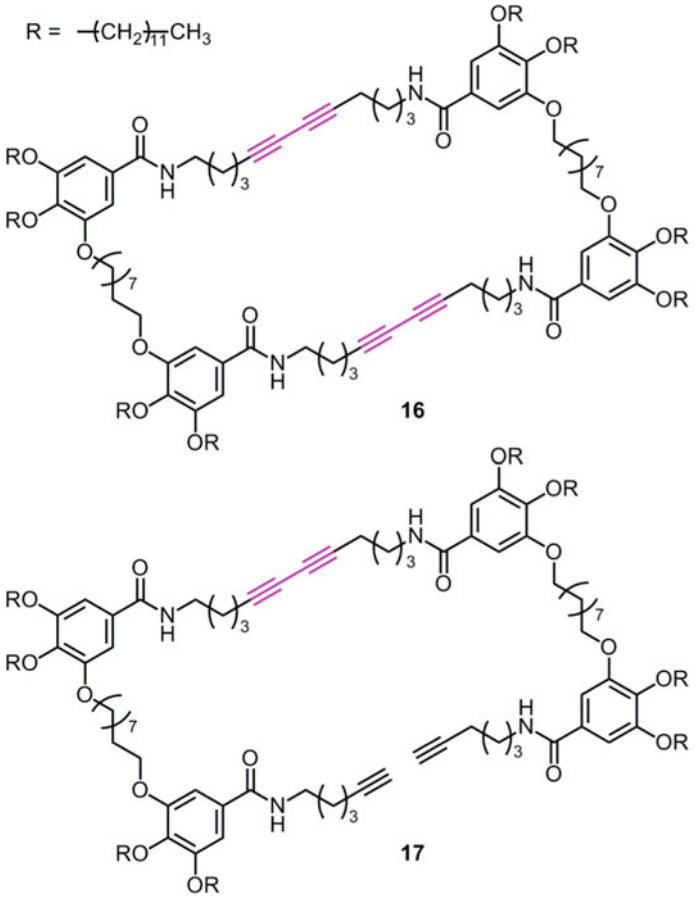

Fig. 24.12 Structures of macrocyclic monomer **16** with two butadiyne moieties and its precursor **17**

Fig. 24.7a were confirmed by the SEM observation. Modification II did not show clear fine fibrous structures. From the Raman spectra, the conversion due to photopolymerization was estimated. In modification I, the monomer showed the C≡C stretching vibration peak at 2250 cm^{-1}, and it almost disappeared upon prolonged UV irradiation. Instead, a new peak at 2106 cm^{-1}corresponding to the stretching vibration of C≡C within the polydiacetylene backbones gradually appeared depending on UV irradiation time, indicating almost full conversion. Even in modification II, almost full conversion was also confirmed.

As mentioned above, the linear monomers with two butadiyne moieties may give one-dimensional ladder polymers or two-dimensional network polymers depending on the monomer structures and the polymerization sites. Similarly, the ring monomers

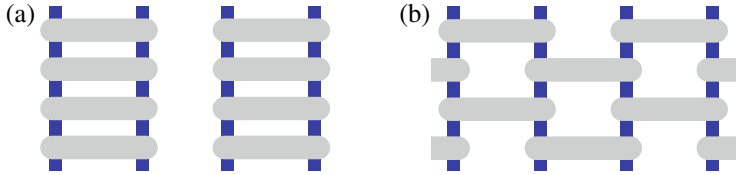

Fig. 24.13 Possible regular polymerization schemes of **16**: **a** one-dimensional tubular polymers obtained from parallel stacking of the macrocyclic monomers and **b** two-dimensional porous crosslinked polymers obtained from alternating stacking of the macrocyclic monomers. Horizontal gray bars and vertical blue lines indicate the side views of the ring structures and π-conjugated backbones, respectively

with two butadiyne moieties may afford one-dimensional tubular polymers or two-dimensional porous crosslinked polymers as shown in Fig. 24.13. In general, one-dimensional polymers are relatively soluble, but two-dimensional crosslinked polymers are not. Since the polymerized samples of **16** were soluble in organic solvents, they should not be the fully crosslinked polymers but the tubular polymers.

24.5 Conclusion

In order to obtain polydiacetylenes with specific functions, several types of conjugated acetylene monomers, which have the substituents to modify the properties of the resulting polymer and hydrogen-bonding groups to align the monomers in the polymerizable stacks in the crystals, were prepared.

For the monomers with electron-donating aromatic rings, *N*,*N*-dimethylaniline, *N*-phenylcarbazol, pyrene, and TTF rings were directly attached to the butadiyne moiety as one of the butadiyne substituents in **1**–**6**. They are generally polymerizable. From the X-ray crystallographic analysis of some monomers, the intermolecular C–C distances related to polymerization were obtained, and the relation between these distances and the absorption spectra in the course of photopolymerization was clarified. When the spectra have the absorption maxima in the wavelength region approximately between 500 and 700 nm, d_{14}s are shorter than d_{12}s, and 1,4-addition to form polydiacetylene is actually advantageous. This corresponds to the fact that the absorption bands have been recognized to excitons characteristic of polydiacetylene. When the spectra show no maximum in the visible region and monotonical absorbance increase from the absorption edge to the shorter-wavelength side, d_{12}s are shorter than d_{14}s or ds are too long, suggesting that the regular 1,4-addition polymerization is no longer possible in these cases. Due to substitution of the electron-donating rings, the HOMO levels of some polydiacetylenes increased to be higher than those of the conventional polydiacetylenes. Although optical and electronic properties of the pyrenyl derivatives have not been elucidated in detail, the helical nanostructure was formed by introducing the chiral substituent. The charge-transfer

complexes of the monomers with aniline or TTF ring were able to be prepared. However, their solid-state polymerization was not successful.

Monomers with phenylene or tetrafluorophenylene group sandwiched by two butadiyne or hexatriyne moieties were prepared and polymerized. By cocrystallization of nonpolymerizable monomer **12** and polymerizable monomer **13**, polydiacetylene copolymers, whose molar ratio of **13** was not less than approximately 60%, were obtained. Both monomers **14** and **15** with hexatriyne moieties were polymerizable. However, only one of the conjugated acetylenes reacted to form the single-chain polydiacetylene and the polymers with two polydiacetylene backbones connected by phenylene linkages seemed to be difficult to be synthesized.

Gel-formable butadiyne monomers **7**–**11** were able to be obtained by a simple molecular design, in which 3,4,5-alkyloxyphenyl groups and hydrogen-bonding groups were introduced. The nanofibrous structures as a microscopic view of the gels were confirmed, and the macroscopic appearance of the gels depending on the solvent used was explained by the fiber thicknesses. By extending the linear molecular design of **10** into a ring shape, a macrocyclic monomer **16** with two butadiyne moieties was synthesized, and the corresponding tubular polymer seemed to be obtained.

By applying appropriate combination of functional groups and hydrogen-bonding groups to conjugated acetylene monomers, π-conjugated polymers with desired optical and electronic functions can be synthesized via the solid-state polymerization. Further challenges to prepare polydiacetylenes with the single crystalline feature advantageous to improve a variety of physical properties will be continued.

Acknowledgements Many of the results introduced in this chapter have been obtained in collaboration with professors in Yamagata University and the graduate and undergraduate students of our laboratory, whose names are shown in the references. The authors thank them for their contribution and effort.

References

1. Dunitz, J.D., Robertson, J.M.: The crystal and molecular structure of certain dicarboxylic acids. Part III. Diacetylenedicarboxylic acid dehydrate. J. Chem. Soc., 1145–1156 (1947)
2. Wegner, G.: Topochemische Reaktionen von Monomeren mit konjugierten Dreifachbindungen I. Mitt.: Polymerisation von Derivaten des 2.4-Hexadiin-1.6-diols im kristallinen Zustand. Z. Naturforsch. **24b**, 824–832 (1969)
3. Baughman, R.H., Yee, K.C.: Solid-state polymerization oflinear and cyclic acetylenes. Macromol. Rev. **13**, 219–239 (1978)
4. Enkelmann, V.: Structural aspects of the topochemical polymerization of diacetylenes. in: Cantow H.J. (ed.) Polydiacetylenes, Advances in Polymer Science, vol. 63, pp. 91–136, Springer, Berlin (1984)
5. Okawa, Y., Aono, M.: Linear chain polymerization initiated by a scanning tunneling microscope tip at designated positions. J. Chem. Phys. **115**, 2317–2322 (2001)
6. Okada, S., Nakanishi, H.: Recent progress in polydiacetylene material research for nonlinear optics. Int. J. Nonlinear Opt. Phys. **3**, 501–509 (1994)

7. Okada, S., Oikawa, H.: Reactions and orientational control of organic nanocrystals. In: Tamura, R., Miyata, M. (eds.) Advances in Organic Crystal Chemistry, Comprehensive Reviews 2015, pp. 485–501, Springer, Tokyo (2015)
8. Ahn, D.J., Kim, J.-M.: Fluorogenic polydiacetylene supramolecules: Immobilization, micropatterning, and application to label-free chemosensors. Acc. Chem. Res. **41**, 805–816 (2008)
9. Chen, X., Zhou, G., Peng, X., Yoon, J.: Biosensors and chemosensors based on the optical responses of polydiacetylenes. Chem. Soc. Rev. **41**, 4610–4630 (2012)
10. Sauteret, C., Hermann, J.-P., Frey, R., Pradère, F., Ducuing, J., Baughman, R.H., Chance, R.R.: Optical nonlinearities in one-dimensional-conjugated polymer crystals. Phys. Rev. Lett. **36**, 956–959 (1976)
11. Nakanishi, H., Mizutani, F., Kato, M., Hasumi, K.: Semiconducting single crystals of polydiacetylenes. J. Polym. Sci., Polym. Lett. Ed. **21**, 983–987 (1983)
12. Wegner, G.: Topochemical reactions of monomers with conjugated triple bonds. III. Solid-state reactivity of derivatives of diphenyldiacetylene. J. Polym. Sci., Polym. Lett. Ed. **9**, 133–144 (1971)
13. Baughman, R.H., Yee, K.C.: Solid-state polymerization of a cyclic diacetylene. J. Polym. Sci., Polym. Chem. Ed. **12**, 2467–2475 (1974)
14. Nakanishi, H., Matsuda, H., Okada, S., Kato, M.: Preparation and nonlinear optical properties of novel polydiacetylenes. in: Saegusa T., Higashimura H., Abe A. (eds.) Frontiers of Macromolecular Science, pp. 469–474, Blackwell, Oxford (1989)
15. Sarkar, A., Okada, S., Matsuzawa, H., Matsuda, H., Nakanishi, H.: Novel polydiacetylenes for optical materials: Beyond the conventional polydiacetylenes. J. Mater. Chem. **10**, 819–828 (2000)
16. Nakanishi, H., Matsuda, H., Okada, S., Kato, M.: Nonlinear optical properties of polydiacetylenes with conjugation between the main chain and the substituents, in Kobayashi T. (ed.) Nonlinear Optics of Organics and Semiconductors, Springer Proceedings in Physics, vol. 36, pp. 155–162, Springer, Berlin (1989)
17. Okada, S., Ohsugi, M., Masaki, A., Matsuda, H., Takaragi, S., Nakanishi, H.: Preparation and nonlinear optical property of polydiacetylenes from unsymmetrical diphenylbutadiynes with trifluoromethyl substituents. Mol. Cryst. Liq. Cryst. **183**, 81–90 (1990)
18. Patel, G.N., Khanna, Y.P., Ivory, D.M., Sowa, J.M., Chance, R.R.: Polymer conversions in the γ-ray polymerization of urethane-substituted diacetylenes. J. Polym. Sci., Polym. Phys. Ed. **17**, 899–903 (1979)
19. Kim, W.H., Kodali, N.B., Kumar, J., Tripathy, S.K., Novel, A.: Soluble Poly(diacetylene) Containing an Aromatic Substituent. Macromolecules **27**, 1819–1824 (1994)
20. Sarkar, A., Okada, S., Nakanishi, H., Matsuda, H.: Polydiacetylenes from asymmetrically substituted diacetylenes containing heteroaryl side groups for third-order nonlinear optical properties. Macromolecules **31**, 9174–9180 (1998)
21. Ishii, S., Kaneko, S., Tatewaki, Y., Okada, S.: Synthesis and solid-state polymerization of 4-(dimethylamino)phenylbutadiyne derivatives and their charge-transfer complexes. Mol. Cryst. Liq. Cryst. **580**, 64–68 (2013)
22. Ikeshima, M., Katagiri, H., Fujiwara, W., Tokito, S., Okada, S.: Synthesis, crystal structures, and solid-state polymerization of 8-[4-(dimethylamino)phenyl]octa-5,7-diynyl carbamates. Cryst. Growth Des. **18**, 5991–6000 (2018)
23. Ikeshima, M., Mamada, M., Katagiri, H., Minami, T., Okada, S., Tokito, S.: Synthesis and solid-state polymerization of diacetylene derivatives with an *N*-carbazolylphenyl group. Bull. Chem. Soc. Jpn. **88**, 843–849 (2015)
24. Ikeshima, M., Mamada, M., Minami, T., Tokito, S., Okada, S.: Synthesis and solid-state polymerization of diacetylene derivatives directly substituted by a phenylcarbazole moiety. Polym. J. **48**, 1013–1018 (2016)
25. Okada, S., Matsuda, H., Otsuka, M., Kikuchi, N., Hayamizu, K., Nakanishi, H., Kato, M.: Synthesis and solid-state polymerization of ω-(1,3-butadiynyl) substituted 1-alkanol and alkanoic acid. Bull. Chem. Soc. Jpn. **67**, 455–461 (1994)

26. Watanabe, J., Yokoyama, H., Okada, S., Takaragi, S., Matsuda, H., Nakanishi, H.: Solid-state polymerization of monophenylbutadiyne derivatives. Mol. Cryst. Liq. Cryst. **505**, 203–209 (2009)
27. Okada, S., Matsuda, H., Otsuka, M., Nakanishi, H., Kato, M.: Synthesis and solid-state polymerization of ω-(4-aryl-1,3-butadiynyl) substituted 1-alkanol and alkanoic acid. Bull. Chem. Soc. Jpn. **67**, 483–489 (1994)
28. Enkelmann, V., Schleier, G., Wegner, G., Eichele, H., Schwoerer, M.: Structure, luminescence and polymerization of a diacetylene crystal: 1,6-di-(n-carbazolyl)-2,4 hexadiin (DCH). Chem. Phys. Lett. **52**, 314–319 (1977)
29. Michinobu, T., May, J.C., Lim, J.H., Boudon, C., Gisselbrecht, J.-P., Seiler, P., Gross, M., Biaggio, I., Diederich, F.: A new class of organic donor–acceptor molecules with large third-order optical nonlinearities. Chem. Commun., 737–739 (2005)
30. Kivala, M., Boudon, C., Gisselbrecht, J.-P., Seiler, P., Gross, M., Diederich, F.: A novel reaction of 7,7,8,8-tetracyanoquinodimethane (TCNQ): Charge-transfer chromophores by [2 + 2] cycloaddition with alkynes. Chem. Commun., 4731–4733 (2007)
31. Tatewaki, Y., Shibata, H., Shibuya, T., Watanabe, K., Ishii, S., Okada, S.: Solid-state polymerization of a pyrenylbutadiyne derivative. in: Kawabe Y., Kawase M. (eds.) Polymer Photonics and Novel Optical Technologies, pp. 152–155, Photonics World Consortium, Chitose (2011)
32. Cheng, Q., Yamamoto, M., Stevens, R.C.: Amino acid terminated polydiacetylene lipidmicrostructures: morphology and chromatic transition. Langmuir **16**, 5333–5342 (2000)
33. Tatewaki, Y., Sato, A., Ito, S., Inayama, S., Okada, S.: Synthesis and solid-state polymerization of L-alanine derivatives with a (1-pyrenyl)butadiynyl group. Mol. Cryst. Liq. Cryst. **580**, 58–63 (2013)
34. Kasai, H., Nalwa, H.S., Oikawa, H., Okada, S., Matsuda, H., Minami, N., Kakuta, A., Ono, K., Mukoh, A., Nakanishi, H.: A novel preparation method of organic microcrystals. Jpn. J. Appl. Phys. **31**, L1132–L1134 (1992)
35. Imai, M., Tatewaki, Y., Okada, S.: Preparation and physical properties of nanoaggregates composed of charge-transfer complexes containing butadiyne derivatives with tetrathiafulvalene moieties. Jpn. J. Appl. Phys. **53**, 05FA02-1–7 (2014)
36. Frankel, D.A., O'Brien, D.F.: Supramolecular assemblies of diacetylenic aldonamides. J. Am. Chem. Soc. **113**, 7436–7437 (1991)
37. Fuhrhop, J.-H., Blumtritt, P., Lehmann, C., Luger, P.: Supramolecular assemblies, a crystal structure, and a polymer of *N*-diacetylenic gluconamides. J. Am. Chem. Soc. **113**, 7437–7439 (1991)
38. Fujita, N., Sakamoto, Y., Shirakawa, M., Ojima, M., Fujii, A., Ozaki, M., Shinkai, S.: Polydiacetylene Nanofibers Created in Low-Molecular-Weight Gels by Post Modification: Control of Blue and Red Phases by the Odd − Even Effect in Alkyl Chains. J. Am. Chem. Soc. **129**, 4134–4135 (2007)
39. Takahashi, R., Nunokawa, T., Shibuya, T., Tomita, R., Tatewaki, Y., Okada, S., Kimura, T., Shimada, S., Matsuda, H.: Synthesis and solid-state polymerization of butadiyne derivatives with trialkoxyphenylurethane groups. Bull. Chem. Soc. Jpn. **85**, 236–244 (2012)
40. Kikuchi, K., Tatewaki, Y., Okada, S.: Self-assembly and solid-state polymerization of butadiyne derivatives with amide and trialkoxyphenyl groups. Bull. Chem. Soc. Jpn. **90**, 298–305 (2017)
41. Matsuzawa, H., Okada, S., Sarkar, A., Matsuda, H., Nakanishi, H.: Synthesis of ladder polymers containing polydiacetylene backbones connected with methylene chains and their properties. J. Polym. Sci. Pt. A: Polym. Chem. **37**, 3537–3548 (1999)
42. Matsuo, H., Okada, S., Nakanishi, H., Matsuda, H., Takaragi, S.: Solid-state polymerization of monomers possessing two diphenylbutadiyne moieties with amido groups to form ladder polymers. Polym. J. **34**, 825–834 (2002)
43. Okada, S., Hayamizu, K., Matsuda, H., Masaki, A., Nakanishi, H.: Structures of the polymers obtained by the solid-state polymerization of diyne, triyne, and tetrayne with long alkyl substituents. Bull. Chem. Soc. Jpn. **64**, 857–863 (1991)
44. Okada, S., Matsuda, H., Masaki, A., Nakanishi, H., Hayamizu, K.: Novel linear and ladder polymers from tetraynes for nonlinear optics. in: Singer K.D. (ed.) Nonlinear Optical Properties of Organic Materials IV, Proceedings of SPIE, vol. 1560, pp. 25–34, SPIE, Bellingham (1991)

45. Okada, S., Nakanishi, H., Matsuzawa, H., Katagi, H., Oshikiri, T., Kasai, H., Sarkar, A., Oikawa, H., Rangel-Rojo, R., Fukuda, T., Matsuda, H.: Improved third-order nonlinear optical properties of polydiacetylene derivatives. in: Eich M., Kuzyk M.G. (eds.) Organic Nonlinear Optical Materials, Proceedings of SPIE, vol. 3796, pp. 76–87, SPIE, Bellingham (1999)
46. Okada, S., Hayamizu, K., Matsuda, H., Masaki, A., Minami, N., Nakanishi, H.: Solid-state polymerization of 15,17,19,21,23,25-tetracontahexayne. Macromolecules **27**, 6259–6266 (1994)
47. Higuchi, K., Sasamura, K., Mizuguchi, K., Tatewaki, Y., Okada, S.: Synthesis and solid-state polymerization of monomers with conjugated diyne–triene–diyne structure. Polymer **54**, 2901–2906 (2013)
48. Matsuzawa, H., Okada, S., Sarkar, A., Matsuda, H., Nakanishi, H.: Synthesis of polydiacetylenes from novel monomers having two diacetylene units linked by an arylene group. Polym. J. **33**, 182–189 (2001)
49. Sasamura, K., Okada, S.: Preparation of mixed crystals composed of 1,4-bis(butadiynyl)phenylene derivatives and the solid-state copolymerization. Polym. Bull. **76**, 1675–1683 (2019)
50. Coates, G.W., Dunn, A.R., Henling, L.M., Dougherty, D.A., Grubbs, R.H.: Phenyl-perfluorophenylstacking interactions: A new strategy for supermolecule construction. Angew. Chem. Int. Ed. Engl. **36**, 248–251 (1997)
51. Sasamura, K., Mizuguchi, K., Tatewaki, Y., Okada, S.: Solid-state polymerization of 1,4-bis(hexatriynyl)benzene derivatives. Polym. J. **50**, 1159–1167 (2018)
52. Xu, Y., Smith, M.D., Geer, M.F., Pellechia, P.J., Brown, J.C., Wibowo, A.C., Shimizu, L.S.: Thermal reaction of a columnar assembled diacetylene macrocycle. J. Am. Chem. Soc. **132**, 5334–5335 (2010)
53. Nagasawa, J., Yoshida, M., Tamaoki, N.: Synthesis, gelation properties and photopolymerization of macrocyclic diacetylenedicarboxamides derived from L-glutamic acid and *trans*-1,4-cyclohexanediol. Eur. J. Org. Chem., 2247–2255 (2011)
54. Kikuchi, K., Tatewaki, Y., Okada, S.: Synthesis and solid-state polymerization of a macrocyclic compound with two butadiyne units. Bull. Chem. Soc. Jpn. **90**, 387–394 (2017)

Chapter 25
Click Chemistry to Metal-Organic Frameworks as a Synthetic Tool for MOF and Applications for Functional Materials

Kazuki Sada and Kenta Kokado

Abstract Metal-organic Frameworks (MOF) are a new class of functional crystalline materials with the large nanopores and open frame structures. The controlled nanoporous structures attract for various applications such as gas sorption, catalysis, biomedical applications, and transport materials for electronic and photophysical devices. For the large demands on preparing the advanced functional materials based on the MOF, the functionalization of the MOF has been attracted significant attention for controlling the environments of the nanopores in the past decade. Among them, the most fruitful approach is post-synthetic modification (PSM) of the MOF.The PSM is defined as the modification of the organic ligands in the frameworks of the MOF by chemical reactions, especially organic reactions, after the formation of the MOF as crystalline materials. In this review, we focus the PSM of the MOF by copper(I)-catalyzed azide–alkyne cycloaddition (CuAAC) and the related reactions that have many advantages such as diverse substrates, mild conditions, high yields, high 1,4-regio-selectivity, and high orthogonality for other organic reactions, and wide availability of the media. Furthermore, we discuss the control of the functions of the MOF and the preparation of the functional composites based on the MOF by the CuAAC of the MOF. Therefore, this review includes the following four topics: the exploration of CuAAC reaction for PSM in MOF, the development of other click reactions for PSM, the function-oriented PSM by CuAAC reaction, and networking and biocongujation of MOF.

Keywords Metal-Organic frameworks (MOF) · Post-synthetic modifications (PSM) · Click reaction · Copper(I)-catalyzed azide–alkyne cycloaddition (CuAAC) · Composites

K. Sada (✉) · K. Kokado
Department of Chemistry, Graduate School of Science, and Graduate School of Chemical Sciences and Engineering, Hokkaido University, Kita 10, Nishi 8, Kita-Ku, Sapporo 060-0810, Japan
e-mail: sadatcm@sci.hokudai.ac.jp

M. Sakamoto and H. Uekusa (eds.), *Advances in Organic Crystal Chemistry*,
https://doi.org/10.1007/978-981-15-5085-0_25

25.1 Introduction

Metal-organic Frameworks (MOF) are a new class of crystalline materials composed of polytropic ridged organic ligands and metal ions as shown schematically in Fig. 25.1a. They are self-organized to form an infinite periodic framework structure as the crystalline lattice due to the rigidity and large space of the organic ligands and multivalence of the metal ions. The most important feature of the MOF is the robust framework structures with large nanopores. The infinite combinations of the metal ions and the organic ligands provide large numbers of nanoporous materials with different porosities [1–3]. Moreover, as compared to other inorganic porous materials, such as zeolite and mesoporous silica, they can be easily synthesized under relatively mild conditions. From the library of the MOF, we can now design the frameworks of the MOF as well as the size and shape of the nanopores. The controlled nanoporous structures are useful for various applications such as storage and separation of gases [4, 5], heterogeneous catalysis [6] or supports for the immobilization of homogeneous catalysts [7, 8], drug delivery and bioimaging [9, 10], and transport materials for electronic and photophysical devices [11, 12].

For these many demands on preparing advanced functional materials based on the nanoporous structures of the MOF [13, 14], the methodology for the modification of the MOF has attracted significant attention for controlling the environments of the nanopores. The most successful approach is post-synthetic modification (PSM) [15–17], as shown in Fig. 25.1b. PSM is defined as the modification of the organic ligands in the frameworks of the MOF by chemical reactions, especially organic reactions, after the formation of the MOF as crystalline materials. This approach has the advantage for the preparation of the MOF with the functional groups that are sensitive or degradable under the solvothermal conditions used in the preparation of the MOF. PSM has become a powerful tool for the rational functionalization starting from the readily available MOF with the reactive functional groups on the organic ligands. The nanopores large enough for the organic reactions and the high stability against some organic reagents enable us to use many organic reactions for the PSM. This should be the most prominent difference between the MOF and the other nanoporous materials, especially the inclusion crystals of organic host molecules. The strong electrostatic interaction and coordination bonds between the metal ions and the organic ligands as the connectivity should contribute to the high stability, compared to the weak non-covalent bonds such as hydrogen bonds and π-π stacking among the host molecules in the inclusion crystals.

Although there are some early examples for the PSM of the MOF, in 2007, Cohen and coworker pointed out the significance of the PSM of the MOF [18]. They demonstrated the chemical modification of the amino-tagged MOF derived from IRMOF-3 prepared from 2-aminoterephthalic acid and Zn(II) ion. Isocyanates and acid anhydrides directly reacted with the amino group in the organic ligand of the MOF to convert the amide and urethane groups without loss of the crystallinity and the nanoporous structures of the MOF. This report suggested that the MOF has a relatively high stability against the organic reagents, and the organic reagents

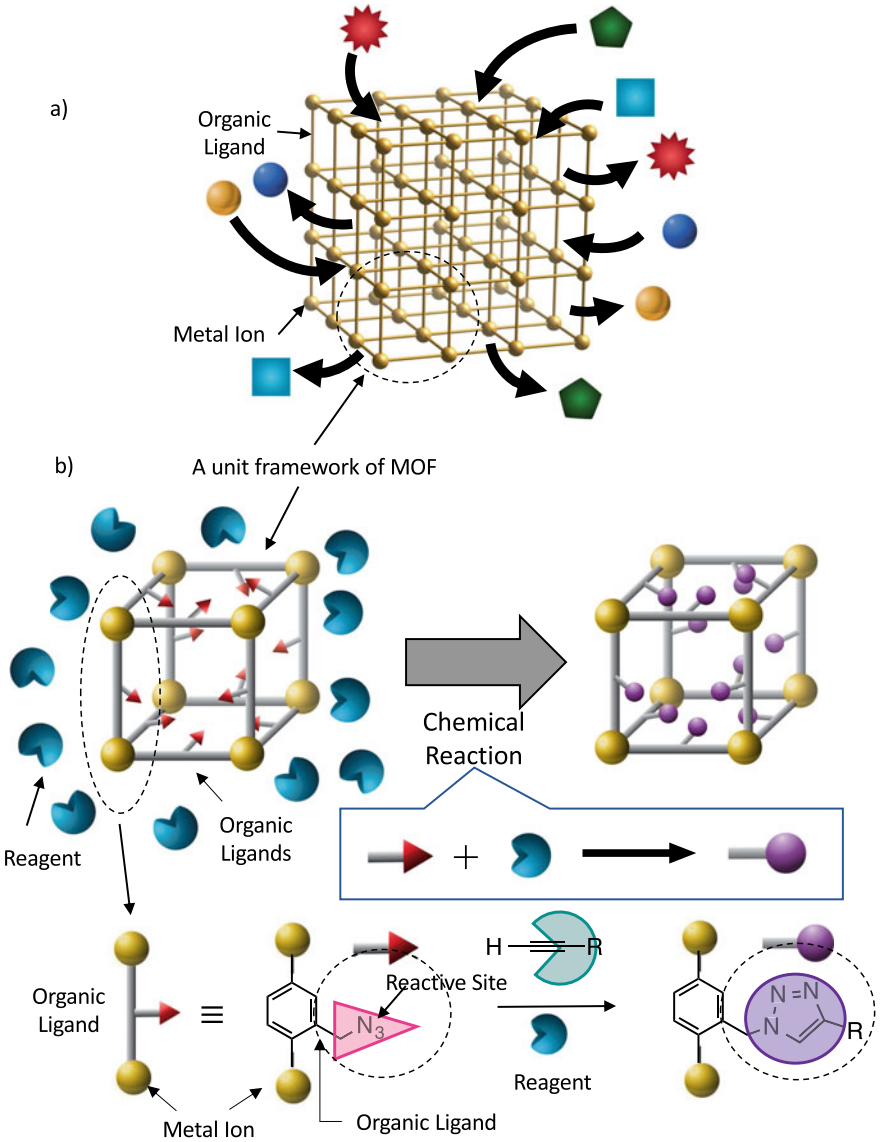

Fig. 25.1 Schematic drawings of **a** metal-organic frameworks (MOF) and **b** post-synthetic modifications (PSM) of MOF

smaller than the size of the nanopores could access and react inside the MOF. More interestingly, the easy functionalization of the MOF by the covalent bonds of the functional groups should be readily available, which are accessible to unique physical and chemical properties that are rarely presented in the pristine MOF. A high

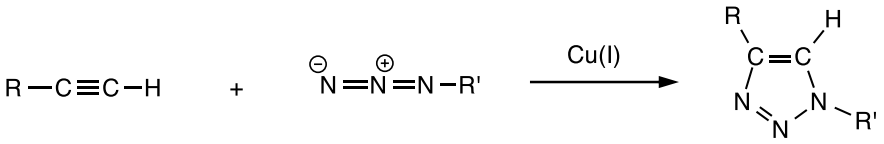

Scheme 25.1 Copper(I)-catalyzed azide–alkyne cycloaddition (CuAAC)

number of organic reactions for the modifications of the organic ligands in various MOF has been attempted to establish the PSM of the MOF [15–17].

Among the organic synthetic reactions, the copper(I)-catalyzed azide–alkyne cycloaddition (CuAAC) or the Huisgen 1,3-dipolar cycloaddition (Scheme 25.1) is one of the most useful organic reactions, due to its diverse substrates, mild conditions, high yields, high 1,4-regio-selectivity, high orthogonality for other organic reactions, and wide availability of the media [19, 20] Generally, the CuAAC reaction takes place just by mixing two substrates. As the results, they are called click chemistry or the click reaction [21, 22]. The discovery of CuAAC dates back to the 1960s, and the important improvement reported in 2002 is the utility of the copper(I) ion as a catalyst [19]. Due to the high specific reaction between the azide and the alkyne, CuAAC has been broadly exploited in the fabrication and modification of various functional materials including organic polymers [23, 24]. In recent years, CuAAC was also employed in the research field of porous organic polymers (POPs) and covalent-organic frameworks (COFs) [25]. In this review, we summarize the PSM of the MOF by the CuAAC reaction, and applications for the preparations of the functional materials based on the MOF. The progress of the recent research on the following three items, the exploration of the CuAAC reaction for the PSM in the MOF, the development of other click reactions for the PSM, and the function-oriented PSM by the CuAAC reaction, include the control of gas sorption, the development of new MOF catalysts by introducing homogeneous catalysts, the scaffold of the polymer and network materials, and the conjugations of the MOF with biomacromolecules.

25.2 CuAAC (Huisgen Cyclization) Reaction for Post-synthetic Modification (PSM) Ofthe MOF

According to a literature survey, the post-synthetic modifications by CuAAC are classified into the four main types of reactions: (1) azide-tagged MOF modified by alkynes, (2) alkyne-tagged MOF modified by azides, (3) one-pot, two-step modification of amino-tagged MOF by alkynes through in situ formation of azide-tagged MOF, and (4) azide-tagged MOF modified by the ring strain-promoting click reaction (SPAAC)without a copper catalyst as summarized in Scheme 25.2. Thus, we now review them chronologically.

In 2008, Sada et al. reported the first example for the PSM of the MOF using CuAAC [26].Terphenyldicarboxylic acid having two azide groups (AzTPDC) was

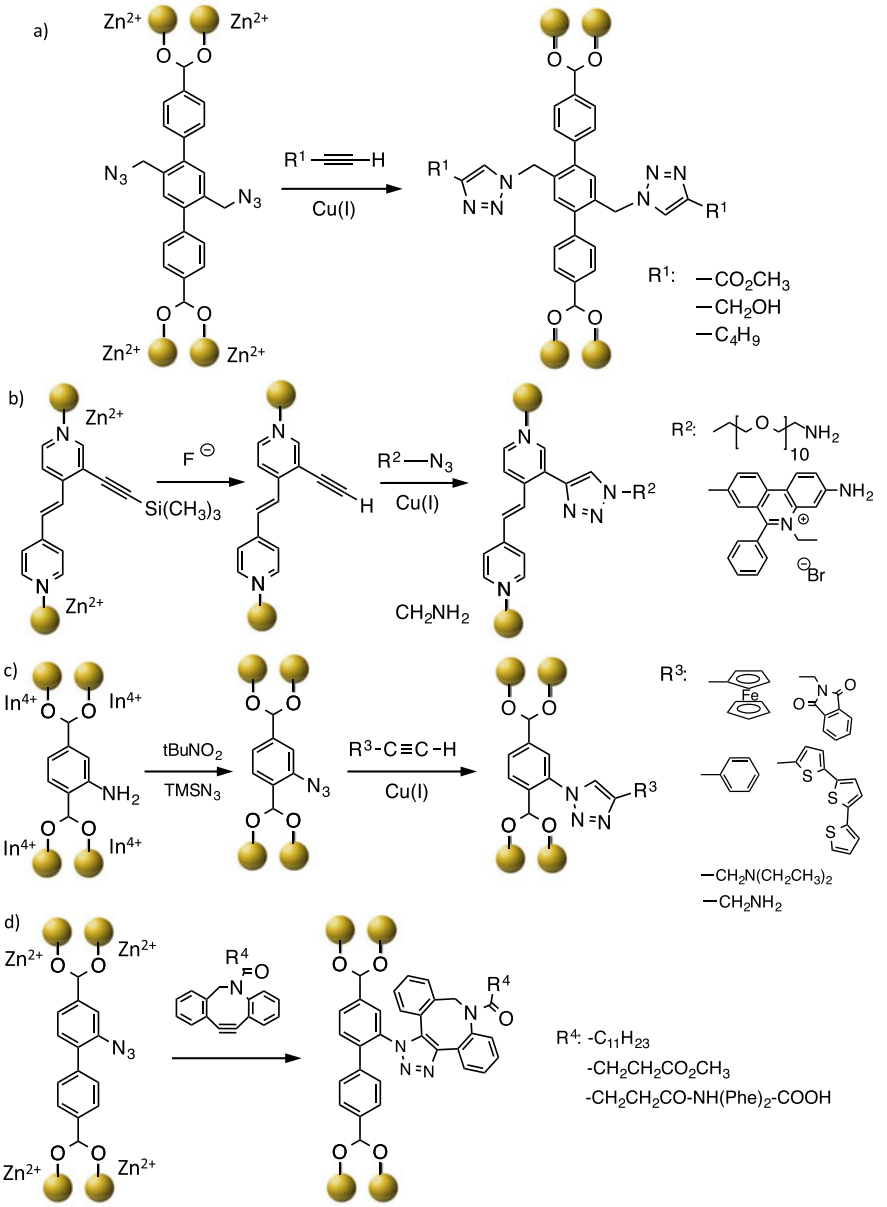

Scheme 25.2 Post-synthetic modifications (PSM) of the MOF by the CuAAC; **a** azide-tagged MOF modified by alkynes, **b** alkyne-tagged MOF modified by azides, **c** one-pot, two-step modification of amino-tagged MOF by alkynes through *in situ* formation of azide-tagged MOF, and **d** azide-tagged MOFs modified by the ring strain-promoting click reaction (SPAAC) without a copper catalyst

dissolved in *N,N*-diethylformamide (DEF) with zinc nitrate hexahydrate, followed by heating at 80°C to yield a pale yellow cubic-shaped crystal of N3-MOF-16 (Scheme 25.2a). Since it showed a similar powder X-ray diffraction pattern as IRMOF-16 consisting of zinc (II) ion and terphenyl dicarboxylic acid, it has the same infinite periodic lattice structure with the formation of the cluster of Zn_4-O-$(OOCR)_6$ from the six organic ligands as the connectivity of IRMOF-16. To this MOF, various terminal alkynes, such as methyl propiolate, propargyl alcohol, 1-hexyne, and propargylamine, caused the CuAAC reaction in the presence of copper bromide in DEF. The characteristic FT-IR band around 2100 cm^{-1} for the azide group completely disappeared in 30 min and ^1H NMR measurement after the acid hydrolysis represented the new peaks from the triazole ring. Also notably, since the X-ray diffraction pattern before and after the reaction did not change, the crystallinity of the MOF was found to be preserved during the click reaction. Therefore, this system should be one of the examples of the PSM for the MOF.

In the same year, Nguyen and coworkers reported surface modifications of a trimethylsilyl (TMS)-protected alkyne-tagged MOF by the same reaction after the deprotection of the TMS group by tetrabutylammonium fluoride (TBAF) [27, 28] (Scheme 25.2b). In this reaction, the alkyne-tagged MOF was reacted with azides introduced from the external solution. A strong fluorescence was observed only on the surface of the MOF after the treatment of the azide with ethidium bromide as a fluorophore. As another example, the surface hydrophilicity and wettability of the MOF could be changed by employing CuAAC with the azide-terminated polyethylene glycol (PEG). Subsequently, the same authors synthesized the core-shell MOF modified with two different azides by controlling the deprotecting reagents of the TMS-protected alkyne-tagged MOF [28]. In the multiple deprotection and CuAAC, the crystallinity and the nanoporous structure of the MOF were well maintained.

Since the organic ligand having an azide group is not commercially available for the PSM of the MOF, it is necessary to synthesize them through the several steps of organic reactions. This should be a drawback for the CuAAC for the PSM. In 2010, Farrusseng and colleagues reported a one-pot, two-step PSM from aminoterephthalic acid as the common starting material by the direct conversion of the amino group to the azide group [29] (Scheme 25.2c). They first prepared a series of MOF, called DMOF-$NH_2$and MIL-68(In)-NH_2. The PSM of the amino group to the azide group in the MOF was then done by the treatment of nitrite tert-butyl and trimethylsilylazide in a THF solution at room temperature, followed by the CuAAC with the terminal alkynes in the presence of copper (I) hexafluorophosphate. The resulting MOF was achieved by quantitative modification of the organic ligand. The surface area of the pores by this modification was reduced to 9–18% of the original MOF, and the pore volume by 6–14%. This method is applicable to other MOF such as IRMOF-3, MIL-101-NH_2, CAU-1, and MIL-53 providing many functional modified MOF. They also demonstrated that a large number of alkynes, such as phenylacetylene, propargylamine, 1-hexyne, propargyl alcohol, and propiolic acid, can be used to react with the MOF. Since the first step has a low efficiency due to the low diffusion rate in the nanopores, a high excess amount of trimethylsilylazide should be required for the quantitative conversion. Some limitation to the type of functional groups of the

alkynes, for example, DMOF-NH_2crystals, was easily dissolved by the treatment with propiolic acid. According to the nitrogen adsorption measurement, the adsorption surface area and pore volume are reduced in accordance with the conversion yields. Therefore, the size of the nanopores can be finely controlled by the PSM. Inspired by this method, Giambastiani and coworkers reported the unconventional double derivatizations of the amine-tagged MOF (UMCM-1 and MIXMOF-5) by treatment of single organic/organometallic acetylene derivatives for the first modification of the click reaction [30]. The binary and ternary mixtures of the alkynes in variable molar ratios were carried out for multi-modification by the single-step click reaction for the MOF catalysts.

Finally, in recent years, the ring strain-promoting click reaction (SPAAC)has been spotlighted [31, 32] because the cyclization takes place without the assistance of the metal ion, then this reaction was used for the PSM of the MOF. Rosi and coworkers prepared BioMOF (N_3-bio-MOF-100) equipped with the azide group (Scheme 25.2d). The click reaction of the azide groups in the MOF proceeded almost quantitatively by the treatment of a 11,12-didehydrodibenzoazosine (DIBAC) derivative having a ring strain triple bond to the azide group [33]. It should be noted that one equivalent was used for the azide groups in the MOF without any metal ions under very mild conditions. The active ester with DIBAC was also quantitatively modified, and further modification using the phenylalanine dimer could be achieved. In addition, Wöll and coworkers compared CuAAC and SPAAC for the PSM of MOF thin films **(SURMOF)** on gold substrates and reported the usefulness of SPAAC [34]. This process should be of importance to overcome the intrinsic toxicity from conventional Cu catalyst for CuAAC and significantly broaden its utilization in biomedical applications.

25.3 Post-synthetic Modification of MOF by Click Reaction Other Than CuAAC

As mentioned in the previous section, with the progress of click chemistry, not only the original CuAAC but also various reactions have come to be recognized as the click reactions. We focus on them in this section. Cohen et al. reported a tandem post-modification method of the MOF using a reverse electron-requested Diels–Alder reaction of vinyl compounds for 1,2,4,5-tetrazine (Scheme 25.3a) [35]. They first synthesized UMCM-1-NH_2 from aminoterephthalic acid and zinc(II) ion followed by the condensation reaction with 1-pentenic anhydride. For these MOF, it was allowed to quantitatively react with dimethyl 1,2,4,5-tetrazine-3,6-dicarboxylate to generate a dihydropyridazine skeleton ring. By the tandem modification, a large pore surface area derived from UMCM (4000 m^2/g) decreased after the first amidation (3600 m^2/g) and the subsequent Diels–Alder reaction (2800 m^2/g) according to the nitrogen adsorption measurement. When a similar tandem modification of IRMOF-3 with the smaller nanopores was attempted, the first step reaction quantitatively

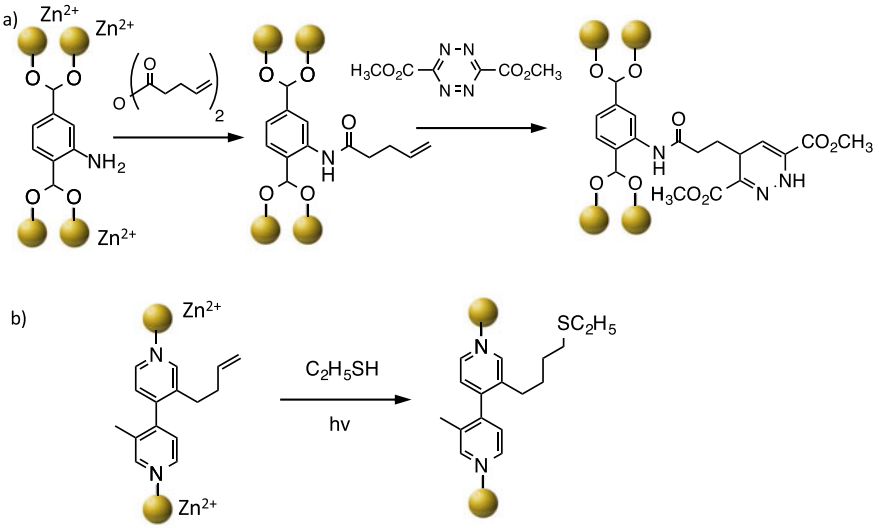

Scheme 25.3 Post-synthetic modifications (PSM) of the MOF by the click reactions other than the CuAAC; a a reverse electron-requested Diels–Alder reaction, and b the light-induced thiol-ene click reaction

occurred, but the Diels–Alder reaction proceeded with 20% or less chemical yield. The bulkiness of the substrate restricted the transport in the relative small pores of the MOF.

Another important click reaction is PSM of the MOF by the light-induced thiol-ene click reaction. Rieger and coworkers reported the light-induced click reaction to MOF from 9,10-triptycenedicarboxylic acid and 2-(1-butenyl)-2'-methyl-4,4'-bipyridyl as the organic ligands. They formed a paddle-wheel-type zinc (II) cluster, and the thiol-ene click reaction between the carbon-carbon double bond and thiols was carried out by UV irradiation with ethanethiol (Scheme 25.3b) [36]. The organic ligand is thioetherified in high yield. Since the thioether should be sensitive to metal coordination, quantitatively introduction of the thioether by PSM should have an advantage. In addition to the thiol-ene click reaction, they reported various PSM other than the click reaction, such as the introduction of the diol by osmium oxidation, the borylation by hydroboration reaction, and the epoxidation with dimethyldioxirane. They should expand the utility of the PSM for the functionalization of the MOF.

25.4 Function-Oriented MOF by CuAAC-PSM

As described in the previous section, CuAAC and the related reactions have been applied for the PSM to control the functions of the MOF. The variations in the organic ligands and the substrates for the CuAAC, either alkynes or azides, should provide

a high number of functionalized MOF by the PSM. The easy and mild reaction conditions might be advantage of the CuAAC for the modification of the MOF or the construction of the MOF conjugates with other functional materials. In addition, the high yield should be important for the functionalization with mixed ligands and mixed substrates for the fabrication of multi-variate functionalized MOF. In this section, we summarized some trials for controlling the functions of the MOF modified by the CuAAC.

For gas storage, the PSM should be effective tool for controlling the capability of gas sorption. Zhou et al. have reported the control of the functional group amount of the pore surface by mixing several types of ligands during the MOF synthesis(Scheme 25.4a) [37]. In this report, they prepared PCN-58 and PCN-59 consisting of zirconium (IV) ions and terphenyldicaboxylic acid ligands. A series of organic ligands equipped with zero to four azide groups in the benzene ring of the ligands were prepared and the mixed organic ligands were subjected to solvothermal synthesis to form various MOF with the various organic ligand ratios. The multi-variate MOF has a good reactivity for various alkynes in the pores as well as on the

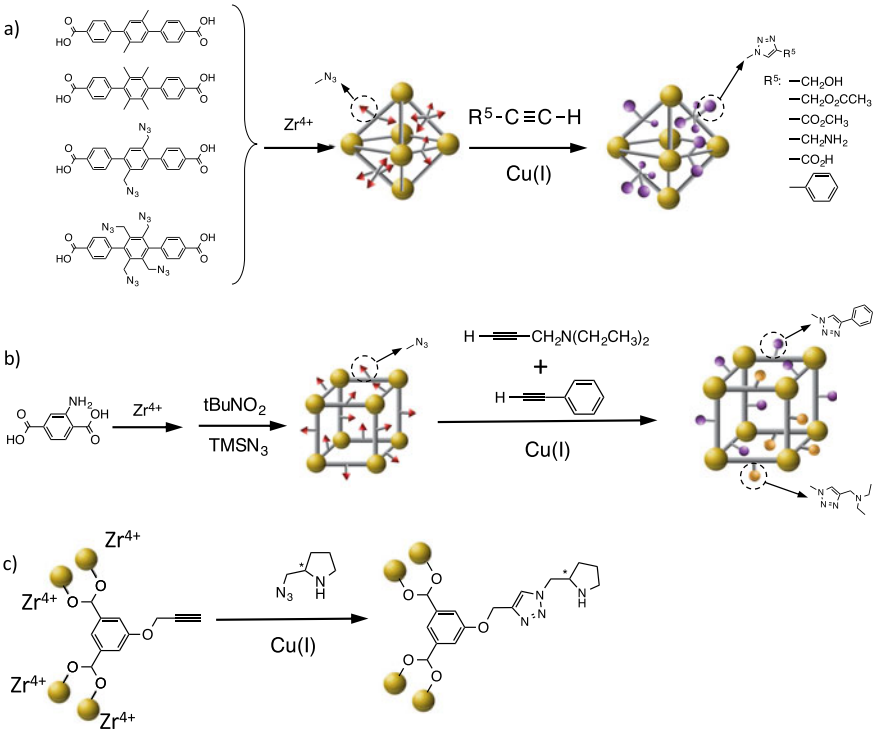

Scheme 25.4 Preparation of function-oriented MOF by the CuAAC; **a** the multi-variate MOF for gas sorption, **b** the multi-variate MOFfor catalysis, and **c** the MOF having the asymmetric organocatalyst

surface under the CuAAC conditions. In particular, the PCN-58 and PCN-59 modified with propargylamine having the four azide groups provided the greatest uptake of carbon dioxide compared to that of nitrogen. The affinity for carbon dioxide could be controlled by the modification of the amine functionality. After this approach, Zhao and coworkers reported the amine-triazole-tagged MIL-101 byCuAAC with a series of acetylene-containing amines from the azide-tagged MOF [38], and the obtained modified MOF was used for CO_2 adsorption. The improved CO_2 uptake ability increased up to 128.3 cm^3/g at 1 atm and 273 K, and a significantly enhanced selectivity to CO_2 over N_2 was observed. More recently, the preparation of the azide-tagged NU-1000 and the subsequent click reaction with alkynes have been reported [39], and the alkyne-tagged UiO-68 was also prepared and used for CuAAC with a series of azides by Wang and coworkers [40]. They controlled the gas sorption by the steric dimensions of the external substrate which affected the preference of guest adsorption.

MOFare promising as a catalyst, but there have also been attempts to improve the catalytic ability of the MOF by the PSM using the CuAAC. Farrusseng and coworkers introduced both the organic base derived from *N,N*-diethylpropargylamine as a catalytic site and the phenyl ring from phenylacetylene as a lipophilic site into the framework of DMOF-$NH_2$by a one-pot, two-step CuAAC (Scheme 25.4b) [41] and used for the transesterification of aliphatic esters. The transesterification reaction proceeded in a higher yield, when both alkynes were used for the PSM compared to those modified by only one of the two. The improved affinity with the substrate by introducing the lipophilic group (phenyl group) enhanced the catalytic activity. In the cases of the bulky alcohols, the transesterification reaction did not proceed, indicating the size selectivity of the substrate due to the pore size. More recently, Duan and coworkers reported the preparation of the MOF with chiral 2-azidomethylpyrrolidine by CuAAC as the asymmetric catalytic site(Scheme 25.4c) [42]. This MOF was used for asymmetric aldol reaction between 4-nitrobenzaldehyde and cyclohexanone with a 75% yield and 71%ee. The size selectivity of the substrates was also observed. Furthermore, the switching of the chirality of 2-azidomethylpyrrolidine in the PSM provided the product with the opposite chirality and the similar yield and enantioselectivity. This PSM should be used to construct the desired chiral nanopores for asymmetric catalysis. Gao and coworkers reported the catalytic MOF derived from UiO-67-N_3 by the CuAAC for the Knoevenagel condensation between benzaldehyde and ethyl cyanoacetate. The triazole group formed by CuAAC acted as the crucial active site for Knoevenagel condensation [43].

25.5 Networking and Biocongujation of MOF by CuAAC-PSM

The open framework structures of the MOF should be useful as the template for polymerization and networking. Sada et al. reported the polymerization of organic ligands

on the open framework of the MOF as the monomers by CuAAC with external guest monomers added to the solution (Scheme 25.5a) [44]. The azide-tagged MOF (N_3-IRMOF-16) consisting of AzTPDC and Zn(II) ions was treated with pentaerythritoltetrapropargyl ether (CL4) as a cross-linker under the standard CuAAC conditions, followed by the demetallation reaction of the MOF by an acid or base solution. The decomposition of the coordination bonds proceeded from the outside to the inside of the MOF within a few minutes to generate the polymer gels with a well-defined polyhedron shape similar to those of the starting MOF. The other MOF such as KUMOF and UiOMOF could be converted to the polymer gels with the well-defined polyhedral structures. They extended this method to the preparation of polymer gels with an anisotropic swelling behavior [45] and box-like polymer gels by core-shell MOF prepared by the epitaxial growth of unreactive and reactive organic ligands [46]. This method was applied to the polymer syntheses with the specific degree of polymerization controlled by the lattice structure of the MOF [47]. More recently, Tsotsalas reported porphyrin polymer thin films by PSM using CuAAC on the surface-anchored MOF (SURMOF) as the template [48]. The SURMOF with the azide groups prepared by a layer-by-layer technique was crosslinked with trimeric acetylene to give the

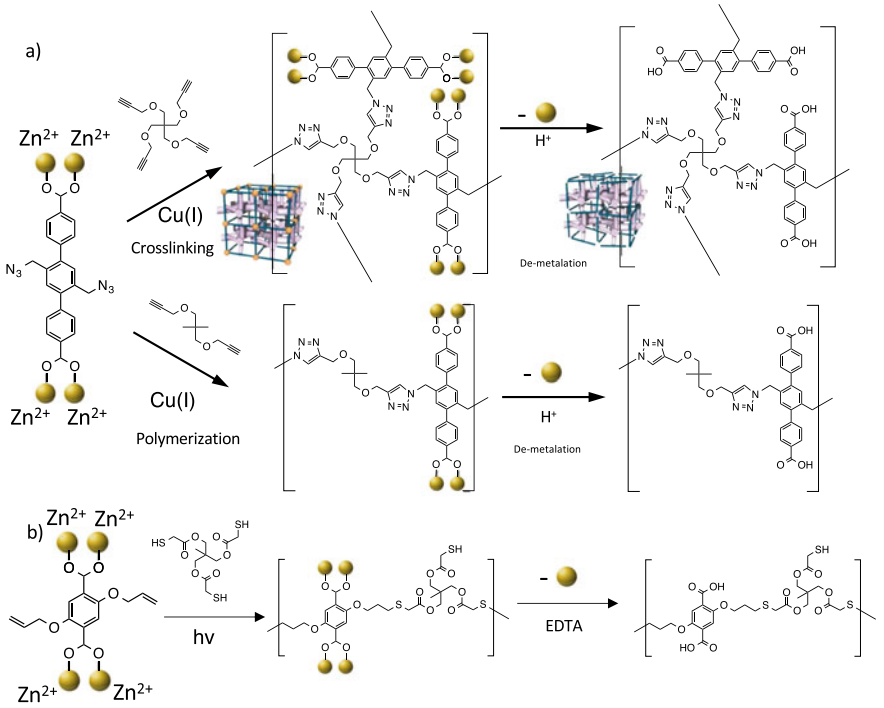

Scheme 25.5 Networking and polymerization of the organic ligands in the MOF by the PSM; **a** the CuAAC between the azide-tagged MOF and the multiple alkynes, and **b** the light-induced thiol-ene reaction between the alkene-tagged MOF and the multiple thiol

porphyrin-based organic thin films after removal of metal ions by immersing in an EDTA solution. The morphology and thickness of the porphyrin polymer thin films were not significantly changed during the decomposition of the coordination bonds. The open framework of the MOF acts as a template for the two-dimensional polymer thin film. The generation of singlet oxygen by visible light irradiation was monitored for its antimicrobial activity. The other reactions such as light-induced thiol-ene click reaction (Scheme 25.5b) and the coupling reaction of the terminal alkynes were used for the crosslinking of the organic ligands in SURMOF by the same group [49, 50].

The bioconjugation of the MOF and biomacromolecules has attracted considerable interest as functional composites. As described in the previous section, SPAAC should expand the possibility of the utility for the PSM of the MOF by the CuACC. One of the earlier examples of the bioconjugates of the MOF was reported by Mirkin and coworkers in 2014 [51]. DNA oligonucleotides were covalently functionalized to the surface of the nanoparticles of UiO-66-N_3 by the CuACC (Fig. 25.2a). Due to the limitation in the pore size of UiO-66, the click reaction only occurred on the surface, and UiO-66 was mostly covered by DNA. Gas sorption revealed that the open framework was preserved throughout the chemical transformation. Moreover, after the modification, DNA-conjugated UiO-66-nanoparticles exhibit increased stability

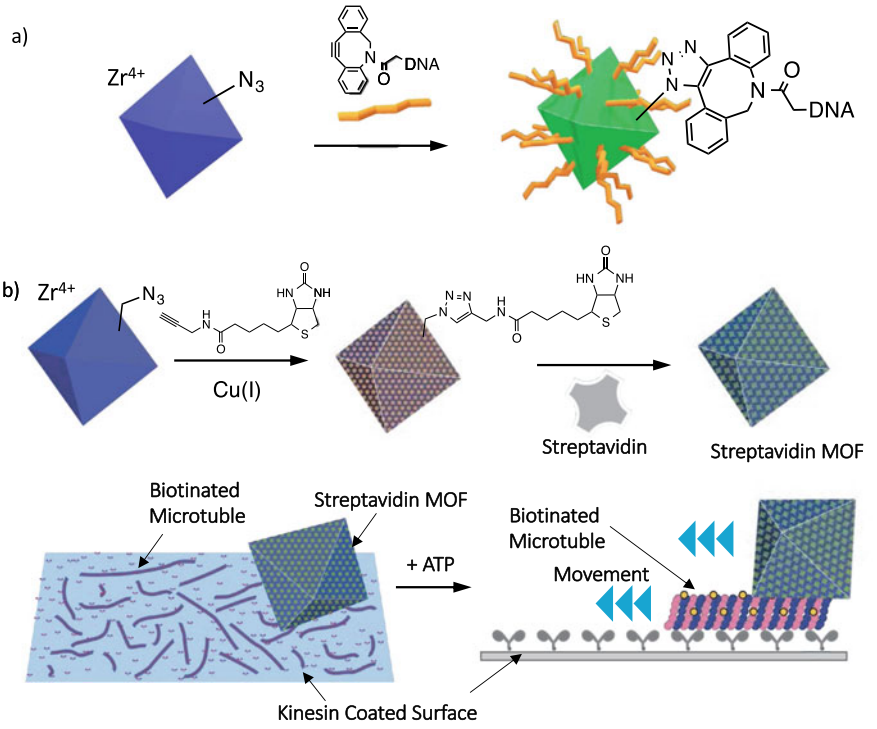

Fig. 25.2 Bioconjugated MOF; **a** DNA-conjugated MOF and **b** self-propelling of MOF-microtube conjugateon the kinesin-coated surface in the presence of ATP

and enhanced cellular uptake as compared to the pristine MOF nanoparticles. More recently, Willner et al. reported similar DNA-conjugated UiO-68 nanoparticles for a dye/drug loading device and their controlled release by stimuli-responsiveness of the DNA duplex [52, 53]. As another important application, nontoxic UiO-66 nanoparticles were synthesized by Forgan and coworkers. The surface of UiO-66 was wrapped with amphiphilic PEG by the CuAAC [54]. More recently, the bioconjugation of the MOF and microtubule was prepared by the CuACC between MOF and biotin, followed by the conjugation among the streptavidin, biotinated-microtubes, and streptavidin-MOF. Thus, the MOF were self-propelled on a kinesin-coated surface in the presence of ATP as the fuel for the biomotor (Fig. 25.2b) [55]. Thus, the covalent linkage between the MOF and biomacromolecules can be easily achieved by the CuAAC as the PSM, and should become an important tool for the construction of new biomedical devices.

25.6 Concluding Remarks

During the post-synthetic modification of the MOF, many functional groups were successfully tagged into/onto the pristine MOFs by the CuAAC toward targeted applications. The mild conditions and the wide tolerance for the functional groups of the reagents and the solvents in the CuAAC seem to play a key role for the PSM of the MOF. In other words, the PSM of the MOF by the CuAAC should become one of the most important strategies for the fabrication of functional composite materials of the MOF. Furthermore, although not detailed in this review, the CuAAC has been used for synthesizing organic ridged ligands for the formation of the MOF. The click chemistry has significantly contributed to the progress of the MOF research. We look forward to further development of functional materials through the combination of click chemistry and MOF.

References

1. Kitagawa, S., Kitaura, R., Noro, S.: Functional Porous Coordination Polymers. Angew. Chem. Int. Ed. **43**, 2334–2375 (2004)
2. Stock, N., Biswas, S.: synthesis of metal-organic frameworks (MOFs): routes to various MOF topologies, morphologies, and composites. Chem. Rev. **112**, 933–969 (2012)
3. Furukawa, H., Cordova, K.E., O'Keeffe, M., Yaghi, O.M.: The chemistry and applications of metal-organic frameworks. Science **341**, 1230444 (2013)
4. Suh, M.P., Park, H.J., Prasad, T.K., Lim, D.-W.: Hydrogen storage in metal-organic frameworks. Chem. Rev. **112**, 782–835 (2012)
5. Murray, L.J., Dincă, M., Long, J.R.: Hydrogen storage in metal–organic frameworks. Chem. Soc. Rev. **38**, 1294–1314 (2009)
6. Corma, A., García, H., Llabrés i Xamena, F.X.: Engineering metal organic frameworks for heterogeneous catalysis. Chem. Rev. **110**, 4606–4655 (2010)

7. Yoon, M., Srirambalaji, R., Kim, K.: Homochiral metal-organic frameworks for asymmetric heterogeneous catalysis. Chem. Rev. **112**, 1196–1231 (2012)
8. Farrusseng, D., Aguado, S., Pinel, C.: Metal-Organic frameworks: opportunities for catalysis. Angew. Chem. Int. Ed. **48**, 7502–7513 (2009)
9. Della Rocca, J., Liu, D., Lin, W.: Nanoscale metal–organic frameworks for biomedical imaging and drug delivery. Acc. Chem. Res. **44**, 957–968 (2011)
10. Horcajada, P., Gref, R., Baati, T., Allan, P.K., Maurin, G., Couvreur, P., Férey, G., Morris, R.E., Serre, C.: Metal-organic frameworks in biomedicine. Chem. Rev. **112**, 1232–1268 (2012)
11. Stavila, V., Talin, A.A., Allendorf, M.D.: MOF-based electronic and optoelectronic devices. Chem. Soc. Rev. **43**, 5994–6010 (2014)
12. Hu, Z., Deibert, B.J., Li, J.: Luminescent metal-organic frameworks for chemical sensing and explosive detection. Chem. Soc. Rev. **43**, 5815–5840 (2014)
13. Férey, G.: Hybrid porous solids: Past, present, future. Chem. Soc. Rev. **37**, 191–214 (2008)
14. Kuppler, R.J., Timmons, D.J., Fang, Q.-R., Li, J.-R., Makal, T.A., Young, M.D., Yuan, D., Zhao, D., Zhuang, W., Zhou, H.-C.: Potential applications of metal-organic frameworks. Coord. Chem. Rev. **253**, 3042–3066 (2009)
15. Cohen, S.M.: Postsynthetic methods for the functionalization of metal-organic frameworks. Chem. Rev. **112**, 970–1000 (2012)
16. Cohen, S.M.: The postsynthetic renaissance in porous solids. J. Am. Chem. Soc. **139**, 2855–2863 (2017)
17. Tanabe, K.K., Cohen, S.M.: Postsynthetic modification of metal-organic frameworks—A progress report. Chem. Soc. Rev. **40**, 498–519 (2011)
18. Wang, Z., Cohen, S.M.: Postsynthetic covalent modification of a neutral metal-organic framework. J. Am. Chem Soc. **129**, 12368–12369 (2007)
19. Rostovtsev, V.V., Green, L.G., Fokin, V.V., Sharpless, K.B.: A stepwise huisgen cycloaddition process: Copper(I)-catalyzed regioselective "ligation" of azides and terminal alkynes. Angew. Chem. Int. Ed. **41**, 2596–2599 (2002)
20. Kolb, H.C., Finn, M.G., Sharpless, K.B.: Click chemistry: Diverse chemical function from a few good reactions. Angew. Chemie Int. Ed. **40**, 2004–2021 (2001)
21. Wang, C., Ikhlef, D., Kahlal, S., Saillard, J.-Y., Astruc, D.: Metal-catalyzed azide-alkyne "click" reactions: Mechanistic overview and recent trends. Coord. Chem. Rev. **316**, 1–20 (2016)
22. Liang, L., Astruc, D.: The copper(I)-catalyzed alkyne-azide cycloaddition (CuAAC) "click" reaction and its applications. An overview. Coord. Chem. Rev. **255**, 2933–2945 (2011)
23. Binder, W.H., Sachsenhofer, R.: "Click" chemistry in polymer and materials science. Macromol. Rapid Commun. **28**, 15–54 (2007)
24. Doehler, D., Michael, P., Binder, W.H.: CuAAC-based click chemistry in self-healing polymers. Acc. Chem. Res. **50**, 2610–2620 (2017)
25. Li, P.-Z., Wang, X.-J., Zhao, Y.: Click chemistry as a versatile reaction for construction and modification of metal-organic frameworks. Coord. Chem. Rev. **380**, 484–518 (2019)
26. Goto, Y., Sato, H., Shinkai, S., Sada, K.: "Clickable" metal-organic framework. J. Am. Chem. Soc. **130**, 14354–14355 (2008)
27. Gadzikwa, T., Lu, G., Stern, C.L., Wilson, S.R., Hupp, J.T., Nguyen, S.T.: Covalent surface modification of a metal-organic framework: Selective surface engineering via Cu^{I}-catalyzed Huisgen cycloaddition, Chem. Commun., 5493–5495 (2008)
28. Gadzikwa, T., Farha, O.K., Malliakas, C.D., Kanatzidis, M.G., Hupp, J.T., Nguyen, S.T.: Selective bifunctional modification of a non-catenated metal-organic framework material via "click" chemistry. J. Am. Chem. Soc. **131**, 13613–13615 (2009)
29. Savonnet, M., Bazer-Bachi, D., Bats, N., Perez-Pellitero, J., Jeanneau, E., Lecocq, V., Pinel, C., Farrusseng, D.: Generic postfunctionalization route from amino-derived metal-organic frameworks. J. Am. Chem. Soc. **132**, 4518–4519 (2010)
30. Tuci, G., Rossin, A., Xu, X., Ranocchiari, M., van Bokhoven, J.A., Luconi, L., Manet, I., Melucci, M., Giambastiani, G.: "Click" on MOFs: A versatile tool for the multimodal derivatization of N-3-Decorated metal organic frameworks. Chem. Mater. **25**, 2297–2308 (2013)

31. Agard, N.J., Prescher, J.A., Bertozzi, C.R.: A strain-promoted [3 + 2] azide − alkyne cycloaddition for covalent modification of biomolecules in living systems. J. Am. Chem. Soc. **126**, 15046–15047 (2004)
32. Sletten, E.M., Bertozzi, C.R.: Bioorthogonal chemistry: Fishing for selectivity in a sea of functionality. Angew. Chem. Int. Ed. **48**, 6974–6998 (2009)
33. Liu, C., Li, T., Rosi, N.L.: Strain-promoted "click" modification of a mesoporous metal-organic framework. J. Am. Chem. Soc. **134**, 18886–18888 (2012)
34. Wang, Z., Liu, J., Arslan, H.K., Grosjean, S., Hagendorn, T., Gliemann, H., Braese, S., Woell, C.: post-synthetic modification of metal-organic framework thin films using click chemistry: the importance of strained C-C triple bonds. Langmuir **29**, 15958–15964 (2013)
35. Chen, C., Allen, C.A., Cohen, S.M.: tandem postsynthetic modification of metal-organic frameworks using an inverse-electron-demand diels-alder reaction. Inorg. Chem. **50**, 10534–10536 (2011)
36. Hindelang, K., Kronast, A., Vagin, S.I., Rieger, B.: Functionalization of metal-organic frameworks through the postsynthetic transformation of olefin side groups. Chem. Eur. J. **19**, 8244–8252 (2013)
37. Jiang, H.-L., Feng, D., Liu, T.-F., Li, J.-R., Zhou, H.-C.: Pore surface engineering with controlled loadings of functional groups via click chemistry in highly stable metal-organic frameworks. J. Am. Chem. Soc. **134**, 14690–14693 (2012)
38. Li, P.Z., Wang, X.J., Tan, R.H.D., Zhang, Q., Zou, R., Zhao, Y.: Rationally "clicked" post-modification of a highly stable metal-organic framework and its high improvement on CO_2-selective capture. RSC Adv. **3**, 15566–15570 (2013)
39. Deria, P., Bury, W., Hupp, J.T., Farha, O.K.: Versatile functionalization of the NU-1000 platform by solvent-assisted ligand incorporation. Chem. Commun. **50**, 1965–1968 (2014)
40. Li, B., Gui, B., Hu, G., Yuan, D., Wang, C.: postsynthetic modification of an alkyne-tagged zirconium metal-organic framework via a "click" reaction. Inorg. Chem. **54**, 5139–5141 (2015)
41. Savonnet, M., Camarata, A., Canivet, J., Bazer-Bachi, D., Bats, N., Lecocq, V., Pinel, C., Farrusseng, D.: Tailoring metal-organic framework catalysts by click chemistry. Dalt. Trans. **41**, 3945–3948 (2012)
42. Zhu, W., He, C., Wu, P., Wu, X., Duan, C.: "Click" post-synthetic modification of metal-organic frameworks with chiral functional adduct for heterogeneous asymmetric catalysis. Dalt. Trans. **41**, 3072–3077 (2012)
43. Yi, X.C., Xi, F.G., Qi, Y., Gao, E.Q.: Synthesis and click modification of an azido-functionalized Zr(IV) metal-organic framework and a catalytic study. RSC Adv. **5**, 893–900 (2015)
44. Ishiwata, T., Furukawa, Y., Sugikawa, K., Kokado, K., Sada, K.: Transformation of metal-organic framework to polymer gel by cross-linking the organic ligands preorganized in metal-organic framework. J. Am. Chem. Soc. **135**, 5427–5432 (2013)
45. Ishiwata, T., Kokado, K., Sada, K.: Anisotropically swelling gels attained through axis-dependent crosslinking of mof crystals. Angew. Chem. Int. Ed. **56**, 2608–2612 (2017)
46. Ishiwata, T., Michibata, A., Kokado, K., Ferlay, S., Hosseini, M.W., Sada, K.: Box-like gel capsules from heterostructures based on a core–shell MOF as a template of crystal crosslinking. Chem. Commun. **54**, 1437–1440 (2018)
47. Anan, S., Mochizuki, Y., Kokado, K., Sada, K.: step-growth copolymerization between an immobilized monomer and a mobile monomer in metal-organic frameworks. Angew. Chem. Int. Ed. **58**, 8018–8023 (2019)
48. Zhou, W., Begum, S., Wang, Z., Krolla, P., Wagner, D., Braese, S., Woell, C., Tsotsalas, M.: High antimicrobial activity of metal-organic framework-templated porphyrin polymer thin films. ACS Appl. Mater. Interfaces. **10**, 1528–1533 (2018)
49. Lindemann, P., Tsotsalas, M., Shishatskiy, S., Abetz, V., Krolla-Sidenstein, P., Azucena, C., Monnereau, L., Beyer, A., Goelzhaeuser, A., Mugnaini, V., Gliemann, H., Braese, S., Woell, C.: Preparation of freestanding conjugated microporous polymer nanomembranes for gas separation. Chem. Mater. **26**, 7189–7193 (2014)
50. Wang, Z., Blaszczyk, A., Fuhr, O., Heissler, S., Woell, C., Mayor, M.: Molecular weaving via surface-templated epitaxy of crystalline coordination networks. Nat. Commun. **8**, 14442 (2017)

51. Morris, W., Briley, W.E., Auyeung, E., Cabezas, M.D., Mirkin, C.A.: Nucleic acid-metal organic framework (MOF) nanoparticle conjugates. J. Am. Chem. Soc. **136**, 7261–7264 (2014)
52. Kahn, J.S., Freage, L., Enkin, N., Garcia, M.A.A., Willner, I.: stimuli-responsive DNA-functionalized metal-organic frameworks (MOFs). Adv. Mater. **29**, 1602782 (2017)
53. Chen, W.-H., Yu, X., Liao, W.-C., Sohn, Y.S., Cecconello, A., Kozell, A., Nechushtai, R., Willner, I.: ATP-Responsive aptamer-based metal-organic framework nanoparticles (NMOFs) for the controlled release of loads and drugs. Adv. Funct. Mater. **27**, 1702102 (2017)
54. Lazaro, I.A., Haddad, S., Sacca, S., Orellana-Tavra, C., Fairen-Jimenez, D., Forgan, R.S.: Selective surface PEGylation of UiO-66 nanoparticles for enhanced stability, cell uptake, and pH-responsive drug delivery. CHEM **2**, 561–578 (2017)
55. Ito, M., Ishiwata, T., Anan, S., Kokado, K., Inoue, D., Kabir, A.M.R., Kakugo, A., Sada, K.: Construction and gliding of metal-organic frameworks and microtubule conjugates. ChemistrySelect **1**, 5358–5362 (2016)